BEILSTEIN JOURNAL OF NANOTECHNOLOGY

Organic–inorganic nanosystems

Edited by Paul Ziemann

Imprint

Beilstein Journal of Nanotechnology
www.bjnano.org
ISSN 2190-4286
Email: journals-support@beilstein-institut.de

The *Beilstein Journal of Nanotechnology* is published by the Beilstein-Institut zur Förderung der Chemischen Wissenschaften.

Beilstein-Institut zur Förderung der Chemischen Wissenschaften
Trakehner Straße 7–9
60487 Frankfurt am Main
Germany
www.beilstein-institut.de

Beilstein Journal of Nanotechnology

Organic–inorganic nanosystems

Paul Ziemann

Editorial

Open Access

Address:
Institute of Solid State Physics, Ulm University, 89081 Ulm, Germany

Email:
Paul Ziemann - paul.ziemann@uni-ulm.de

Beilstein J. Nanotechnol. **2011,** *2,* 363–364.
doi:10.3762/bjnano.2.41

Received: 30 June 2011
Accepted: 02 July 2011
Published: 12 July 2011

This article is part of the Thematic Series "Organic–inorganic nanosystems".

Editor-in-Chief: T. Schimmel

A natural goal of most nanoscience projects, independent of the specific subfield they belong to, is to create a system providing novel functions which originate from the properties of its constituent nanoscale parts. Although the preparation of individual nanoobjects such as dots or wires of various materials is in principle possible, the analysis of their chemical and physical properties still poses a serious experimental challenge. Thus, to arrive at a certain minimum level of signal strength for a given analysis technique, in most cases ensembles of nanoobjects are needed. However, this immediately results in the requirement for a narrow size distribution of the nanoobjects, else their desired new size dependent properties will be completely smeared out. Additional conditions such as control of the chemical composition of the structures or of their spatial arrangement add further difficulties to the preparation. Finally, excluding time consuming, and thus costly, sequential top-down methods, one is almost naturally led to self-organizing bottom-up processes.

At this point organic–inorganic nanosystems enter the stage. Imagine an organic moiety such as a diblock-copolymer, in an appropriate solvent, forming an even more complex building block such as a nanoscaled micelle, which, in turn, can be deposited onto an inorganic substrate such as a Si-wafer by dip coating. Due to the presence of a complex hierarchy of interactions, such as those between copolymers, or copolymer–solvent, solvent–substrate or copolymer–substrate interactions, a rich spectrum of resulting micellar arrangements on top of a given inorganic substrate will emerge. This variety can be even further extended by the application to pre-patterned substrates acting as templates.

In the above example, diblock-copolymers will form spherical micelles within a certain window of block lengths in a properly chosen solvent, and such micelles can be used as carriers for a metal precursor during their self-organization on top of a substrate. This specific case is immediately generalized to the idea of depositing molecular, macromolecular or supramolecular organic species on top of inorganic platforms. By exploiting molecular self-organization, one finally arrives at a functional system with novel properties.

Much progress has been made during the last decade based on this idea of exploiting the self-organization of organic building blocks on top of inorganic supports, and a huge number of self-assembled structures have been prepared. A direct application

of this approach is to use such assemblies as templates or masks for subsequent further deposition or etching steps. Applied in this way, the method is a direct extension of the seminal work by Fischer and Zingsheim on hexagonal ordered arrays of polystyrene colloids serving as masks for subsequent metal evaporations [1].

In other cases, based on precursor loaded micelles or, more generally, colloids, the organic carriers are completely removed after their self-organization by various plasma treatments while the precursor compounds are transformed into metal oxides or, finally, into metals. In this way, hexagonal ordered arrays of metal nanoparticles can be obtained with controllable particle size and inter-particle distance. In that case, the organic–inorganic nanosystem simply serves as an intermediate step towards the sought after particle arrangement. An application of this technique for the preparation of magnetic nanoparticles is described in another recent Thematic Series about the preparation, properties and applications of magnetic nanoparticles in the *Beilstein Journal of Nanotechnology* [2].

In the present context, the wide field of ligand-stabilized nanoparticles should also be mentioned. Here, each particle represents an organic–inorganic system, opening up almost unlimited possibilities for the chemical functionalization of the particles and, hence, making them into selective docking stations for other molecules. Exploiting this selectivity, various chemical sensors have been developed with specific applications in biology and medicine. Closely related to this topic are drug delivery "absorption-active" nanoparticles, which are again surface functionalized organic–inorganic systems that can be specifically targeted towards tumor cells.

Up to this point, the organic part of the considered hybrids provided self-organization and specificity for subsequent chemical reactions or, in the simplest case, served as a spacer to avoid aggregation in a system of corresponding nanoobjects. However, there is yet another highly active field where the organic component delivers the sought after functionality of a device: Organic electronics. Here, doped π-conjugated oligomers and polymers play an important role due to their semiconducting behavior. As in standard electronics, the combination of p- and n-doped organic components leads to device applications such as organic light emitting diodes (OLED), organic field effect transistors (OFET) and organic solar cells, to name but a few. In all cases, the organic component must be brought into contact with a conducting electrode, usually a metal or a highly doped semiconductor. Each of these contacts represents an organic–inorganic interface with gradients on the nanoscale. Due to the importance of these interfaces on the transport properties of the devices, the electronic properties of various arrangements of organic molecules on top of metals must be studied. For the analysis of single molecules, the most promising technique is Scanning Tunneling Microscopy (STM) and its spectroscopic variant (STS), while for larger coverages standard photoelectron spectroscopies such UPS or XPS – often synchrotron based – also play an important role.

This broad spectrum of preparational approaches, analytical tools and sought after functionalities, all related to organic–inorganic nanosystems, are addressed in the present thematic series. The topic naturally demands an interdisciplinary cooperation between chemists and physicists, experimentalists and theoreticians, and this is reflected in the statistics of the authors contributing to this series. Practically all contributions have been at least in part funded by the German Science Foundation (DFG), many of them within the Collaborative Research Center (SFB) 569 dealing with the *"Hierarchical Structure Formation and Function of Organic–Inorganic Nanosystems"*. Thus, in addition to acknowledging the contributions of all authors and their teams, I would especially like to thank DFG for generous long term support. Special thanks also go to Barbara Jörg, Ursula von Gliscynski, and Frank-Dieter Kuchta for providing us with their advice over many years.

Paul Ziemann

Ulm, July 2011

References

1. Fischer, U. C.; Zingsheim, H. P. *J. Vac. Sci. Technol.* **1981,** *19,* 881–885. doi:10.1116/1.571227
2. Wiedwald, U.; Ziemann, P. *Beilstein J. Nanotechnol.* **2010,** *1,* 21–23. doi:10.3762/bjnano.1.4

Beilstein Journal of Nanotechnology

Intermolecular vs molecule–substrate interactions: A combined STM and theoretical study of supramolecular phases on graphene/Ru(0001)

Michael Roos[1], Benedikt Uhl[1], Daniela Künzel[2], Harry E. Hoster[1,§], Axel Groß[2] and R. Jürgen Behm[*1]

Full Research Paper

Open Access

Address:
[1]Institute of Surface Chemistry and Catalysis, Ulm University, D-89069 Ulm, Germany and [2]Institute of Theoretical Chemistry, Ulm University, D-89069 Ulm, Germany

Email:
R. Jürgen Behm[*] - juergen.behm@uni-ulm.de

* Corresponding author
§ Present address: TUM CREATE Centre for Electromobility, 62 Nanyang Drive, Singapore

Keywords:
graphene film; intermolecular interaction; large organic molecules; substrate–adsorbate interaction; supramolecular structure

Beilstein J. Nanotechnol. **2011,** *2,* 365–373.
doi:10.3762/bjnano.2.42

Received: 30 March 2011
Accepted: 20 May 2011
Published: 12 July 2011

This article is part of the Thematic Series "Organic–inorganic nanosystems".

Guest Editor: P. Ziemann

Abstract

The competition between intermolecular interactions and long-range lateral variations in the substrate–adsorbate interaction was studied by scanning tunnelling microscopy (STM) and force field based calculations, by comparing the phase formation of (sub-) monolayers of the organic molecules (i) 2-phenyl-4,6-bis(6-(pyridin-3-yl)-4-(pyridin-3-yl)pyridin-2-yl)pyrimidine (3,3'-BTP) and (ii) 3,4,9,10-perylene tetracarboxylic-dianhydride (PTCDA) on graphene/Ru(0001). For PTCDA adsorption, a 2D adlayer phase was formed, which extended over large areas, while for 3,3'-BTP adsorption linear or ring like structures were formed, which exclusively populated the areas between the maxima of the moiré structure of the buckled graphene layer. The consequences for the competing intermolecular interactions and corrugation in the adsorption potential are discussed and compared with the theoretical results.

Introduction

It is well known that the formation of highly ordered 2D supramolecular networks on smooth surfaces, such as metal substrates or highly oriented pyrolytic graphite (HOPG), is mainly governed by the intermolecular interactions between adjacent molecules due to hydrogen bonding [1-4], covalent bonding [5,6], or, in the case of metal organic networks, by metal–ligand interactions [1,7-9]. In these cases, the interactions between the adlayer and the substrate, or more specifically, the local variations in that interaction, play a minor role. These interactions mainly determine the orientation of the resulting supramolecular structure with respect to the underlying substrate lattice [3,6,10-14]. This is mainly due to the fact

that lateral variations in the interaction between the surface and a single bonding center in the admolecule, arising from the atomic structure of the surface, largely average out because of the imperfect match of the different bonding centers in the adsorbed molecule and the surface lattice. The situation is distinctly different if the adsorption potential is corrugated on a much larger length scale, exceeding that of the size of these admolecules, which is typically in the order of a few nanometers. Such long-range corrugations, however, are rather rare.

One example of this effect is in metal supported graphene films. In the case of Ru as a support, it is known from LEED structure analysis and theory that the lattice mismatch between the graphene layer and the underlying metal substrate results in a buckling of the graphene layer and therefore in a distinct height corrugation of 1.5 Å [15,16]. The graphene/Ru(0001) surface is also known to exhibit a lateral corrugation of 30 Å, which is comparable with the outer dimensions of the molecules used in this study. Representative images of the graphene/Ru(0001) surface presented in Figure 1 underline the highly ordered long-range periodicity of the graphene adlayer with its characteristic moiré pattern (Figure 1a) and resolve the atomic structure in the high resolution image (Figure 1b). In the latter image, two different areas are marked, denoting the positions on top of the maxima of the moiré lattice of the graphene film ("hill positions" - H) and the lower parts between the maxima ("valley positions" - V). These are taken as representative for the different adsorption sites on the graphene/Ru(0001) surface. Recently, we demonstrated, for the adsorption of 2-phenyl-4,6-bis(6-(pyridin-2-yl)-4-(pyridin-4-yl)pyridin-2-yl)pyrimidine (2,4'-BTP) molecules on a Ru(0001) supported graphene film, that such surfaces indeed exhibit not only a height corrugation but also a distinct corrugation in the adsorption potential [17]. This was explained by a mechanism in which the variation in the adsorption potential exceeds the intermolecular interactions, which favors population of the energetically favorable valley as compared to the formation of a 2D adlayer phase covering the entire surface, or islands of that phase covering part of the surface. Comparable structures were reported for graphene/Rh(111) [18]. Pronounced lateral variations in the adsorption potential on metal supported graphene monolayer films were previously reported also for metal deposition on such surfaces, e.g., for Ir on graphene/Ir(111) [19,20] or for Pt on graphene/Ru(0001) [21-23].

In this paper we extend this study, by comparing the adsorption behavior of two different types of molecular systems with distinctly different intermolecular interactions, namely (i) 2-phenyl-4,6-bis(6-(pyridin-3-yl)-4-(pyridin-3-yl)pyridin-2-yl)pyrimidine (3,3'-BTP) [24,25] and (ii) 3,4,9,10-perylene tetracarboxylic dianhydride (PTCDA) on graphene/Ru(0001). Schematic representations and space filling models of these molecules are presented in Figure 2. For both molecules, the intermolecular interactions are dominated by hydrogen bonds. In the case of the 3,3'-BTP the numbers 3,3' indicate the position of the outer nitrogen atoms which are responsible for

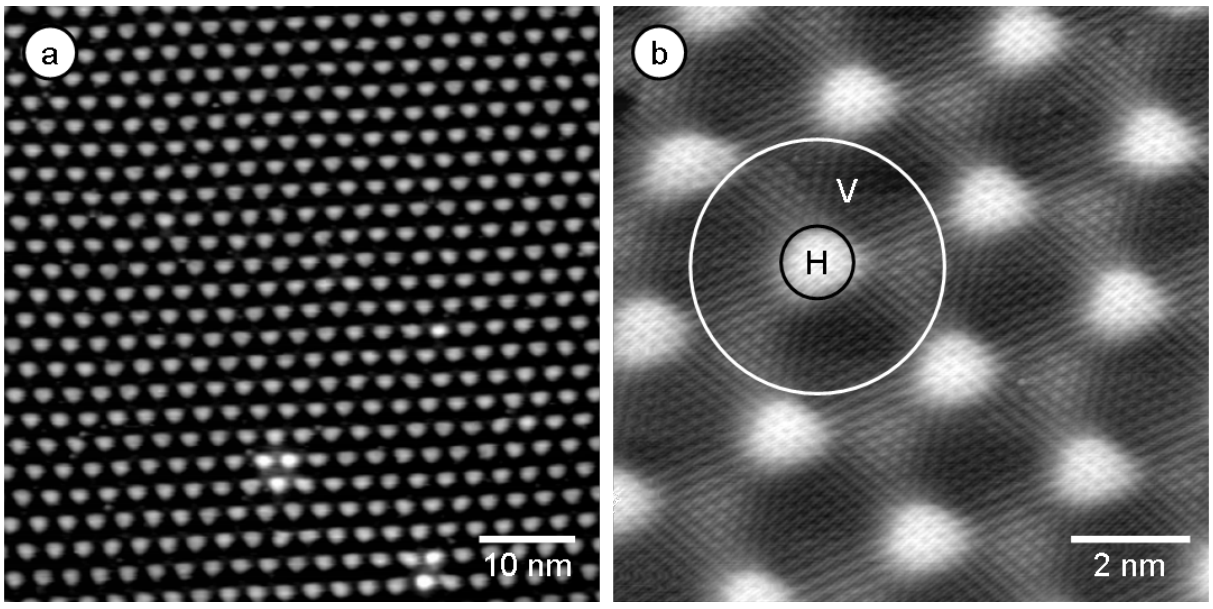

Figure 1: (a) Defect free graphene/Ru(0001) surface with typical moiré superstructure (U_T = −1.30 V, I_T = 60 pA, T = 130 K, 62 nm × 62 nm). (b) Atomically resolved STM image of the graphene/Ru(0001) surface (U_T = 0 V, I_T = 178 pA, T = 300 K, 10 nm × 10 nm) with different superimposed adsorption areas (H) = hill, (V) = valley.

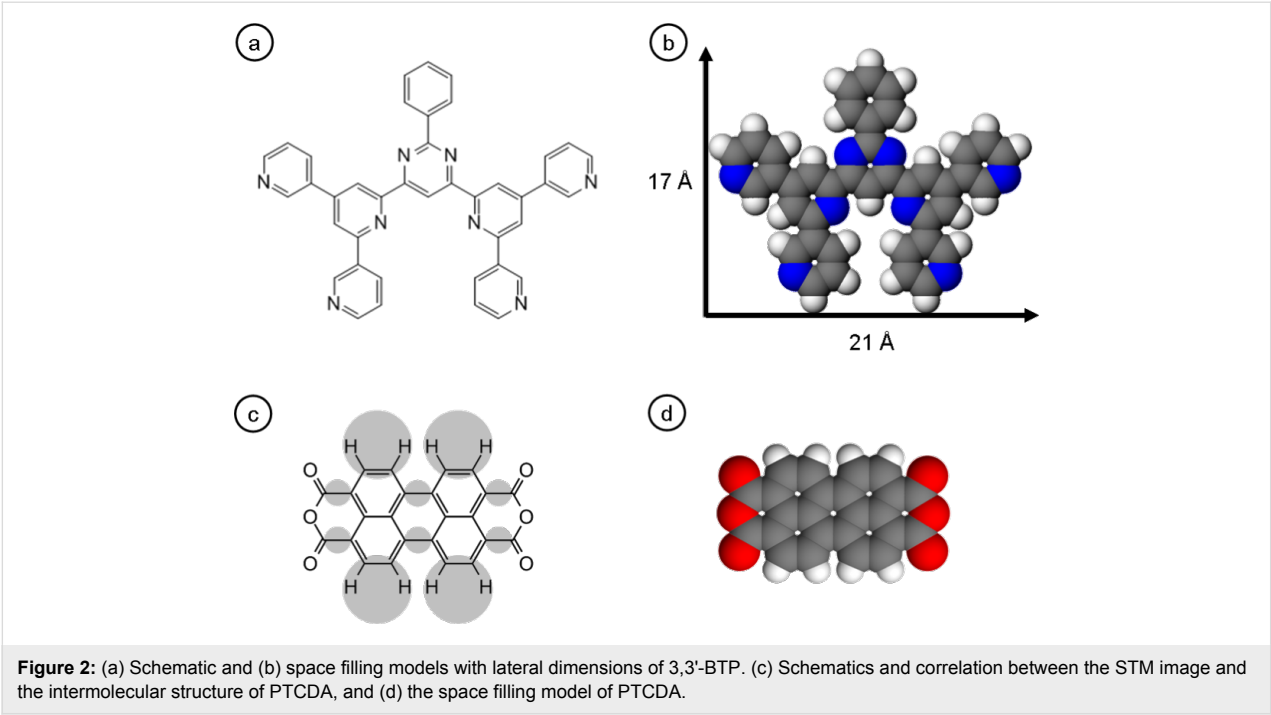

Figure 2: (a) Schematic and (b) space filling models with lateral dimensions of 3,3'-BTP. (c) Schematics and correlation between the STM image and the intermolecular structure of PTCDA, and (d) the space filling model of PTCDA.

hydrogen bonding between adjacent molecules. The strengths of these hydrogen bonds, however, are rather different for the two molecules. In the case of the 3,3'-BTP molecules, weak C–H···N-type hydrogen bonds are formed which are typically in the range of 100 meV [25]. The C–H···O-type hydrogen bonds formed between PTCDA molecules are somewhat stronger and result in intermolecular interactions in the range of 130 meV [26].

In the following, we first present STM observations of the adlayer phases formed by these molecules on graphene/Ru(0001) and compare these with adlayers of the corresponding phases on HOPG as a model for a low corrugation substrate. Subsequently, we present results of theoretical considerations, including force field based calculations of the interaction between the graphene/Ru(0001) substrate and adsorbed molecules, and discuss the consequences for the adlayer phase formation.

Results and Discussion

STM imaging

Figure 3a shows an exemplary STM image of a low coverage 3,3'-BTP adlayer on graphene/Ru(0001), with sub-molecular resolution. We can clearly identify the molecules and the hexagonally arranged hills of the graphene adlayer (see marked triangle). The molecules are exclusively adsorbed in the valleys of the graphene film, while the hills remain unoccupied. This limitation to specific adsorption sites in combination with the distinct positions of the hydrogen bond donors and acceptors within the molecule results in the formation of 1D chain structures (Figure 3b), similar to findings recently reported for the adsorption of PTCDI molecules on graphene/Rh(111) [18].

Due to the position of the N atoms and of the resulting hydrogen bonds between the 3,3'-BTP molecules, the attachment of an additional molecule at the end of a molecular chain is not restricted to an anti-parallel arrangement, but can occur also at an angle of 60° with respect to the last molecule in the chain. The former is responsible for linear chain structures, the latter will lead to curved chain-like structures or hexagonal and triangular ring structures. Such structures consist mostly of six molecules and are formed around a hill (Figure 3a and Figure 3b). The inner diameter of these units leaves enough space for an additional molecule on top of the enclosed hill, which in some cases are trapped on these sites. These additional molecules seem to be freely rotating, as evidenced by their diffuse shape. Figure 3b shows the different possible adsorption geometries. The long range order, however, is rather poor, with only relatively small units and chain-like arrangements. The hills of the graphene act as spacers between individual molecular units. Due to the resulting separation of approximately 10 Å between adjacent units, intermolecular interactions between them can be neglected. The fact that the hills remain unoccupied for 3,3'-BTP on graphene/Ru(0001) indicates that these sites are significantly less favorable than the valley sites, i.e., the corrugation of the adsorption potential exceeds possible additional intermolecular interactions between the different units.

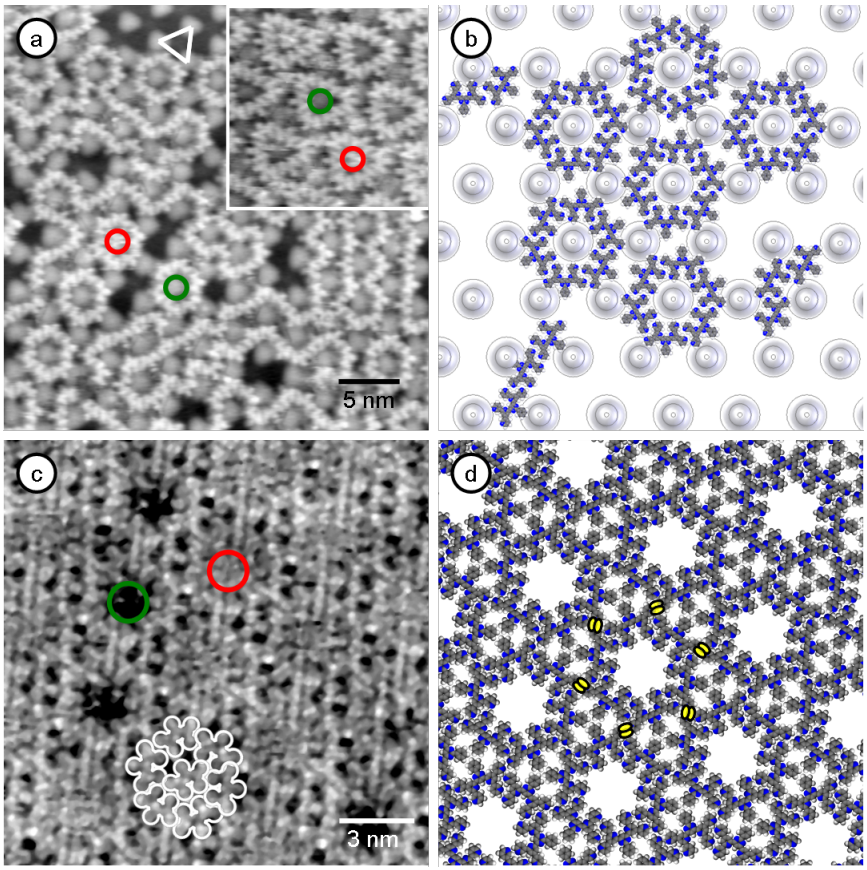

Figure 3: (a) STM image of 3,3'-BTP molecules on graphene (U_T = −2.36 V, I_T = 30 pA, T = 115 K, 35 nm × 35 nm). The inset shows the triangular structure with randomly filled (red) and unfilled (green) cavities (U_T = −2.36 V, I_T = 30 pA, T = 115 K, 9 nm × 9 nm). (b) True to scale model of 3,3'-BTP molecules on graphene illustrates the steric hindrance. (c) 3,3'-BTP on HOPG (U_T = −1.20 V, I_T = 44.7 pA, T = 300 K, 17 nm × 17 nm); The same hydrogen bonding configuration and hexagonal network, but without spacing between the hexagons. (d) Model of 3,3'-BTP on HOPG. Each molecule shares two hydrogen bonds with its adjacent hexagon (yellow ellipses).

Adsorption of 3,3'-BTP-molecules on HOPG led to networks with similar types of building blocks as formed on graphene/Ru(0001). At both the solid–liquid and the solid–gas interface we predominantly found a chiral 2D hexagonal network consisting of ring-like units of six molecules (Figure 3d) [24]. At the solid–gas interface, the resulting hexagonal network seems to be the most stable phase, as indicated by its coexistence with a 2D gas at lower coverage. Again, these rings provide enough space for adsorption of an additional central molecule. In this network, the hexagonal units are interconnected, i.e., there are not only interactions between the molecules within the hexagons, but also between molecules of adjacent hexagons (marked yellow in Figure 3d). This is in contrast to the clear separation between the rings on graphene/Ru(0001). In addition to the 2D hexagonal network, several 2D phases consisting of linear arrangements of 3,3'-BTP molecules were observed on HOPG [24]. These linear networks are characterized by their anti-parallel arrangement of the molecules. Similar to the adsorption of 2,4'-BTP molecules [4,12] on Ag thin films, these linear networks also exhibit intermolecular bonds between the linear elements. Finally, it is interesting to note that comparable 2D phases based on bent structures with 60° angles between different linear parts were not observed on HOPG. Molecular models show that in such phases hydrogen bonds are not possible between adjacent strings, leaving them energetically less favorable compared to phases based on linear structures.

The influence of thermal activation on the structure formation is illustrated in a series of snapshots recorded at 2 frames per second (fps, every 10th image shown) at room temperature with a home built video-STM (Figure 4). Upon imaging at higher tunnel current (smaller tip–sample distance), tip induced removal of 3,3'-BTP molecules from a fully covered graphene/Ru(0001) surface led to a local molecule-free surface area. Switching back to normal tunnelling conditions, 3,3'-BTP molecules diffused in from the surrounding area and re-populated this area. This re-occupation proceeds via growth of chain-like aggregates of the molecules, which follow the valley structure

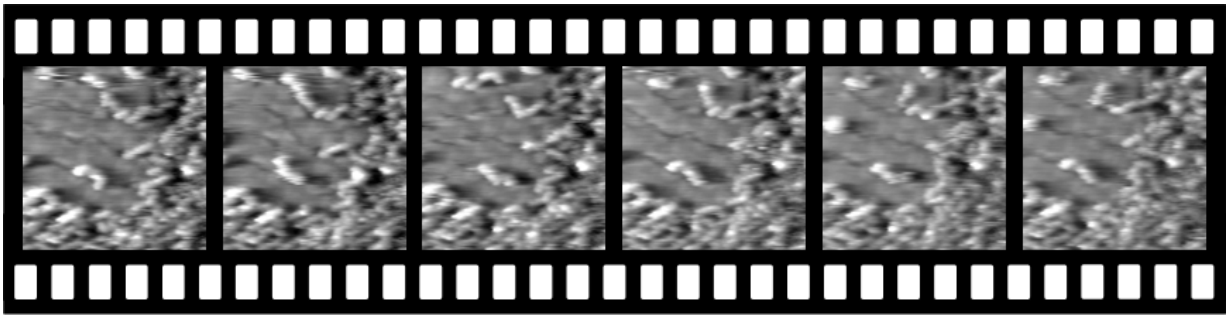

Figure 4: Sequence of time resolved images recorded at 2 fps showing every 10th image (time between single frames 5 s). Graphene/Ru(0001) partly covered with 3,3'-BTP molecules.

of the graphene while the hills remain unoccupied. Hence, even at room temperature thermal activation is not sufficient for growing over the graphene hills, reflecting the pronounced lateral corrugation of the 3,3'-BTP adsorption potential on the graphene/Ru(0001) surface.

Figure 5 shows the network formation of PTCDA molecules on graphene/Ru(0001). Even in the sub-monolayer regime, the molecules arrange in a periodic herringbone-like arrangement (Figure 5), similar to the phases described for other substrates such as HOPG [27-29] and various metal substrates such as

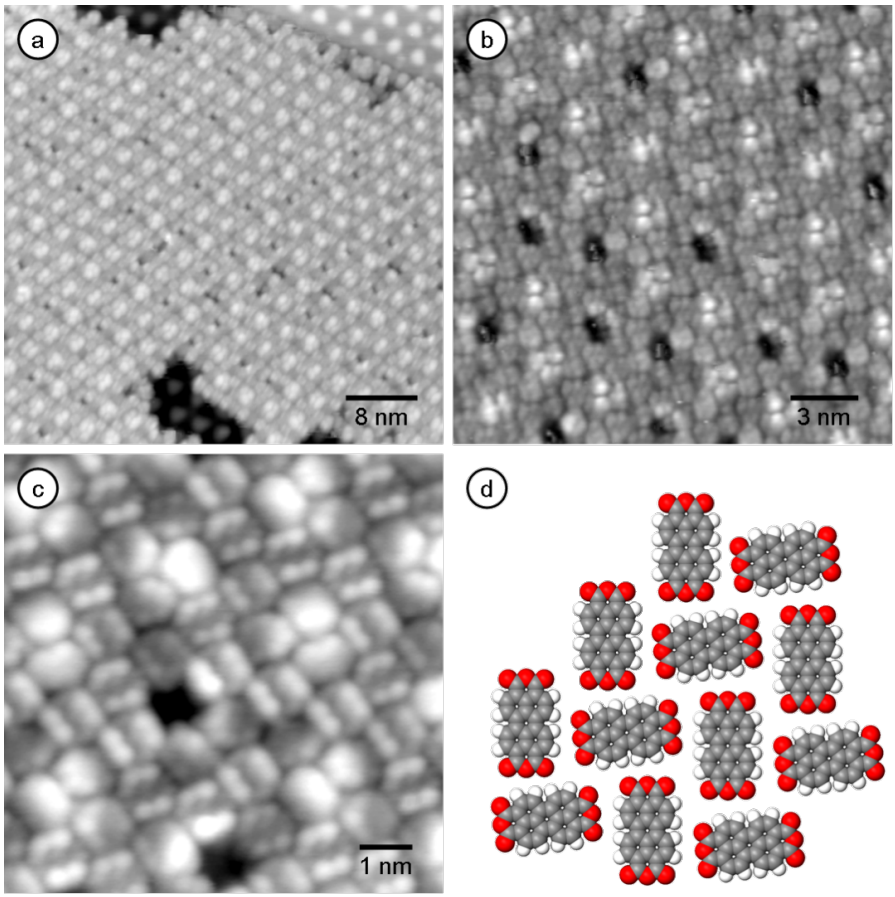

Figure 5: (a) Sub-monolayer of PTCDA on graphene/Ru(0001) (U_T = −0.61 V, I_T = 180 pA, T = 125 K, 49 nm × 49 nm) with simultaneous imaging of the underlying moiré of the graphene layer. (b) Not all hills are covered with PTCDA molecules. Fuzzy impression of molecules on hills indicative of (frustrated) rotation (U_T = −0.88 V, I_T = 50 pA, T = 125 K, 19 nm × 19 nm). (c) Sub-molecular resolution image revealing the adsorption geometry of the PTCDA molecules. (8 nm × 8 nm, U_T = 0.97 V, I_T = 110 pA, T = 125 K) (d) Model of the adsorption geometry of PTCDA molecules.

Au(111) [30-34], Ag(110) [35] or Cu(110) [36]. In contrast to the weakly interacting BTP molecules, the PTCDA adlayer covers the entire surface, i.e., the PTCDA molecules follow the up and down of the moiré superstructure of the graphene/Ru(0001) layer (Figure 5a). Since the unit cell of the herringbone structure does not fit perfectly to the periodicity of the underlying graphene/Ru(0001) substrate, an additional long-range structural modulation is obtained. The image in Figure 5a resolves both the PTCDA molecular adlayer and, in a hole of the adlayer, the underlying moiré structure with its hills and valleys. While the majority of the hills are covered by the PTCDA adlayer, some also result in local defects within the network and produce distinct voids of about the size of one molecule (Figure 5a–c). These voids indicate that the graphene/Ru(0001) substrate also exhibits a significant corrugation in the adsorption potential for PTCDA, although this is less pronounced, relative to intermolecular interactions, than for 3,3'-BTP. Figure 5c shows a sub-molecular resolution image of PTCDA on graphene/Ru(0001). Comparison with the model of a single PTCDA molecule in Figure 2c reveals the same sub-molecular structural details within the molecule. Similar structural results have recently been reported for the adsorption of PTCDA on SiC(0001) where the PTCDA film is grown over the corrugated surface without any disturbance due to the different adsorption sites [37].

Calculations

To determine the corrugation of the adsorption potential, we summed up the different contributions to the adsorption energy (molecule–graphene and molecule–Ru interaction) and subtracted the adsorption energy of a "hill" site from that of a "valley" position. Table 1 and Table 2 show the differences between these sites for different force fields. Clearly, the calculated binding energies strongly depend on the force field used, as found before in force field calculations addressing 3,3'-BTP adsorption on graphite [38]. Nevertheless, although the absolute values may vary with the applied force field, the differences between binding energies at the two sites, reflecting the lateral corrugation of the potential energy of the substrate, are reasonably close, both for 3,3'-BTP and PTCDA.

The corrugation of the adsorption energy can be compared with the intermolecular interactions. For the adsorption of 3,3'-BTP molecules, the STM images shown above reveal that very similar hexagonal local units are formed upon adsorption on HOPG and on graphene/Ru(0001). On both surfaces, these units consist of six molecules in a hexagonal arrangement. The main difference lies in the spacing between the different units. In the case of graphene/Ru(0001), they are separated by the hills of the graphene. On HOPG, in contrast, they are interconnected and therefore additionally stabilized by hydrogen bonds between adjacent molecules of neighboring units. The additional double hydrogen bonds are in the range of 0.14 eV per double bond [25]. Therefore the additional stabilization of a single molecule within a unit is only 0.07 eV per molecule (half of the double bond). Comparing this value with the potential energy corrugation, which depending on the applied force field varies between 0.625 and 0.985 eV per molecule (Table 1), we see that these additional intermolecular interactions which apply for higher adsorbate densities would be much lower than the corrugation of the adsorption potential. Hence, at sub-monolayer coverage it is energetically preferable to adsorb only in valley sites and their connections, rather than to form islands of 2D interconnected networks which would also occupy hill sites. Therefore, the tendency to avoid the hills can be easily rationalized by comparing the intermolecular interactions and the corrugation in the 3,3'-BTP-substrate interactions.

Table 1: Adsorption energies for 3,3'-BTP on graphene for different adsorption sites and corrugation Δ*E* in eV.

	hill	valley	Δ*E*
Compass	−3.346	−3.971	−0.625
CVFF	−6.120	−7.105	−0.985
Dreiding, Gasteiger	−3.400	−4.093	−0.693
Dreiding, QEq	−3.388	−4.013	−0.625
UFF, Gasteiger	−3.889	−4.669	−0.780
UFF, QEq	−3.853	−4.538	−0.685

Table 2: Adsorption energies of PTCDA for different adsorption sites and corrugation Δ*E* in eV.

	hill	valley	Δ*E*
Compass	−1.889	−2.324	−0.435
CVFF	−3.405	−4.095	−0.690
Dreiding, Gasteiger	−2.417	−2.875	−0.458
Dreiding, QEq	−3.037	−3.587	−0.550
UFF, Gasteiger	−2.248	−2.739	−0.491
UFF, QEq	−2.600	−3.171	−0.571

The same procedure was applied for PTCDA molecules adsorbed on graphene/Ru(0001). Figure 6 shows the adsorption geometry for a single PTCDA molecule (a) on a valley and (b) on a hill position, with top and side view of the adsorption geometry. Table 2 shows the calculated adsorption energy for both the hill and the valley position and the resulting corrugation of the adsorption potential ΔE for PTCDA molecules on graphene/Ru(0001) for different force fields. Dependent on the applied force field, the resulting Δ*E* ranges from −0.435 to −0.690 eV. To rationalize the different behavior of the PTCDA

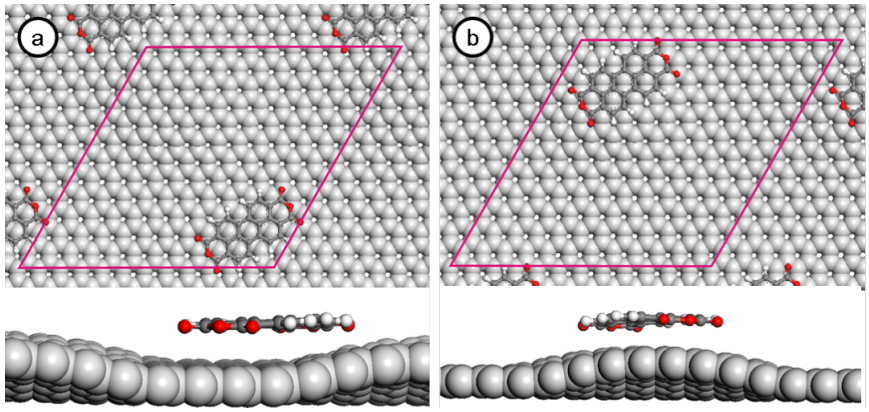

Figure 6: Optimized structure of PTCDA in (a) the valley position and (b) the hill position.

molecules, we again compare the corrugation of the adsorption energy with the intermolecular interaction between adjacent molecules in the herringbone configuration of PTCDA. Recent DFT calculations by Mura et al. [26] have shown that the stabilization energy per molecule is between −0.585 and −0.67 eV per molecule, depending on the exact herringbone structure [26]. Comparing these values with the values for the corrugation of the adsorption potential between the different adsorption states (see above) reveals that the additional intermolecular stabilization energies for the PTCDA molecules (over)compensate for the corrugation within the adsorption potential. Hence in this case, formation of islands of a 2D network is energetically favorable compared to a phase with 1D strings between the hills or ring units around the hills of the graphene/Ru(0001) substrate, in perfect agreement with the experimental findings.

These results illustrate the detail of microscopic understanding that can be extracted from combined STM experiments and state-of-the-art calculations. They also support the validity of structural concepts for the self assembly of supramolecular networks for cases where the adsorption potential on the substrate is highly corrugated, instead of the normal 'smooth' substrates.

Conclusion

We have shown by STM imaging that (i) there are distinct differences in the adlayer structures of 3,3'-BTP on HOPG compared to 3,3'-BTP on graphene/Ru(0001), while (ii) for PTCDA, similar structures are formed on both substrates. In the first case, the adlayer forms 1D chains around the hills of the graphene/Ru(0001), but a 2D interconnected network on HOPG, while in the second case 2D networks are formed on both substrates. Qualitatively, these differences can be explained by the competition between intermolecular interactions and the lateral variation of the adsorption potential, i.e., of the molecule–substrate interactions. In the case of the 3,3'-BTP molecules, the intermolecular interactions are significantly weaker than the potential energy corrugation of the surface, rendering the occupation of hill sites, and hence the formation of 2D networks, energetically unfavorable. In the case of PTCDA molecules, the lateral corrugation of the adsorption potential must be overcompensated by stronger intermolecular interactions. These ideas are fully supported on a quantitative scale by a combination of force field and density functional theory based calculations, which reveal much stronger intermolecular interactions for PTCDA than for 3,3'-BTP, while the difference in binding energy on valley sites (favorable) and on hill sites (unfavorable), and hence the lateral corrugation of the adsorption potential on the graphene/Ru(0001) substrate, is of similar magnitude for both molecules.

Experimental

Experiments

The experiments were performed in a standard ultrahigh vacuum (UHV) system (base pressure 2×10^{-10} mbar), equipped with a commercial variable temperature scanning tunneling microscope (STM) (Specs, STM 150 "Aarhus") and facilities for sample preparation, such as an Ar^+ ion sputter gun and evaporation sources for the deposition of organic molecules.

A Ru(0001) crystal (Mateck) was cleaned by standard procedures, including 3–4 cycles of Ar^+ ion sputtering (0.5 kV Ar^+ ions, 5 μA cm^{-2}, 15 min), followed by flash annealing to 1650 K. Remaining carbon impurities were removed by oxidation, involving oxygen adsorption (10 L O_2: 1 L = 1.33×10^{-6} mbar s^{-1}) and subsequent repeated flash annealing to 1650 K. The freshly prepared surface exhibited 50–200 nm wide, atomically flat terraces, separated by monolayer steps. The graphene layer was prepared by exposing the Ru(0001)

surface to ethylene for prolonged time at elevated temperatures (5×10^{-9} mbar ethylene, 2 h at 1000 K). The structural quality of the graphene layer was checked by STM in constant current mode at temperatures of around 100 K.

3,3'-BTP molecules (provided by U. Ziener, Ulm University) were deposited from a home-built, resistively heated, Knudsen cell at 583 K. The PTCDA molecules (Merck, 98% purity) were evaporated from a commercial evaporation source (Ventiotec, OVD-3) at 628 K. Prior to evaporation, the PTCDA was cleaned in UHV by a temperature gradient sublimation technique using a resistively heated quartz tube. After deposition the sample was annealed to 583 K to improve the structural quality of the molecular film.

Theoretical Methods

To complement and rationalize the experimental findings above, force field calculations were performed to determine the site specific adsorption energies for 3,3'-BTP and PTCDA on graphene/Ru(0001). Due to the large size of the system, quantum chemical calculations were too computationally expensive. The surface was modelled with three layers of Ru and one layer of graphene on top, using a commensurate lattice with a (12 × 12) graphene unit cell on a (11 × 11) Ru(0001) cell with a lattice constant of 29.96 Å, in agreement with experiment, using the coordinates obtained in recent density functional theory calculations from a combined experimental and theoretical study [39]. These surfaces coordinates were then kept fixed in the subsequent relaxation of adsorbed PTCDA and BTP molecules. The interactions between molecule–graphene and molecule–Ru were treated as being additive. For the modelling of the molecule–graphene interactions, a single molecule was placed on top of the two different adsorption sites ("hill" and "valley") and four different force fields were used to optimize the adsorption geometry of the adsorbate (Compass [40], CVFF [41], Dreiding [42], and UFF [43] as implemented in the Accelrys Materials Studio program package). Note that the "hill" position does not correspond to a true local minimum, so the structure optimization was performed for the internal molecular degrees of freedom with the center of mass of the molecule being on top of the hill. For Dreiding and UFF, we applied both the Gasteiger [44] and the QEq charging method [45]. For a reliable description of the interactions between the molecules and the ruthenium surface, force fields are normally not well suited since they do not accurately reproduce metallic properties. Instead, we used a semi-empirical dispersion correction scheme [46,47], which was originally used for the inclusion of van der Waals interactions in standard DFT calculations. These two contributions (adsorbate–graphene and adsorbate–metal) were then added in order to obtain total adsorption energies of the molecules on the graphene/Ru(0001) substrate.

Acknowledgements

Financial support for this work was obtained from the Deutsche Forschungsgemeinschaft (DFG) via the Collaborative Research Project (SFB) 569 (projects A8 and B11). We wish to thank U. Ziener for providing the 3,3'-BTP molecules and M.-L. Bocquet for the coordinates of the graphene/Ru(0001) system.

References

1. Barth, J. V.; Constantini, G.; Kern, K. *Nature* **2005,** *437,* 671–679. doi:10.1038/nature04166
2. Forrest, S. R. *Chem. Rev.* **1997,** *97,* 1793–1896. doi:10.1021/cr941014o
3. Barth, J. V. *Annu. Rev. Phys. Chem.* **2007,** *58,* 375–407. doi:10.1146/annurev.physchem.56.092503.141259
4. Roos, M.; Hoster, H. E.; Breitruck, A.; Behm, R. J. *Phys. Chem. Chem. Phys.* **2007,** *9,* 5672–5679. doi:10.1039/b708578h
5. Grill, L.; Dyer, M.; Lafferentz, L.; Persson, M.; Peters, M. V.; Hecht, S. *Nat. Nanotechnol.* **2007,** *2,* 687–691. doi:10.1038/nnano.2007.346
6. Bartels, L. *Nat. Chem.* **2010,** *2,* 87–95. doi:10.1038/nchem.517
7. Lin, N.; Stepanow, S.; Vidal, F.; Kern, K.; Alam, M. S.; Strömsdörfer, S.; Dremov, V.; Müller, P.; Landa, A.; Ruben, M. *Dalton Trans.* **2006,** *2006,* 2794–2800. doi:10.1039/B515728E
8. Breitruck, A.; Hoster, H. E.; Meier, C.; Ziener, U.; Behm, R. J. *Surf. Sci.* **2007,** *601,* 4200–4205. doi:10.1016/j.susc.2007.04.173
9. Schlikum, U.; Decker, R.; Klappenberger, F.; Zoppellaro, G.; Klyatskaya, S.; Ruben, M.; Silanes, I.; Arnau, A.; Kern, K.; Brune, H.; Barth, J. V. *Nano Lett.* **2007,** *7,* 3813–3817. doi:10.1021/nl072466m
10. Klappenberger, F.; Canas-Ventura, M. E.; Clair, S.; Pons, S.; Schlikum, U.; Qu, Z.-R.; Strunskus, T.; Comisso, A.; Wöll, C.; Brune, H.; De Vita, A.; Ruben, M.; Barth, J. V. *ChemPhysChem* **2008,** *9,* 2522–2530. doi:10.1002/cphc.200800590
11. Hermann, B. A.; Rohr, C.; Balbás Gambra, M.; Maleki, A.; Malarek, M. S.; Frey, E.; Franosch, T. *Phys. Rev. B* **2010,** *82,* 165451. doi:10.1103/PhysRevB.82.165451
12. Hoster, H. E.; Roos, M.; Breitruck, A.; Meier, C.; Tonigold, K.; Waldmann, T.; Ziener, U.; Behm, R. J. *Langmuir* **2007,** *23,* 11570–11579. doi:10.1021/la701382n
13. Waldmann, T.; Reichert, R.; Hoster, H. *ChemPhysChem* **2010,** *11,* 1513–1517. doi:10.1002/cphc.200901028
14. Zhang, Y.; Forrest, S. R. *Phys. Rev. Lett.* **1993,** *71,* 2765–2768. doi:10.1103/PhysRevLett.71.2765
15. Marchini, S.; Günther, S.; Wintterlin, J. *Phys. Rev. B* **2007,** *76,* 075429. doi:10.1103/PhysRevB.76.075429
16. Moritz, W.; Wang, B.; Bocquet, M.-L.; Brugger, T.; Greber, T.; Wintterlin, J.; Günther, S. *Phys. Rev. Lett.* **2010,** *104,* 136102. doi:10.1103/PhysRevLett.104.136102
17. Roos, M.; Künzel, D.; Uhl, B.; Huang, H.-H.; Alves, O. B.; Hoster, H. E.; Groß, A.; Behm, R. J. *J. Am. Chem. Soc.* **2011,** *133,* 9208–9211. doi:10.1021/ja2025855
18. Pollard, A. J.; Perkins, E. L.; Smith, N. A.; Saywell, A.; Goretzki, G.; Phillips, A. G.; Argent, S. P.; Sachdev, H.; Müller, F.; Hüfner, S.; Gsell, S.; Fischer, M.; Schreck, M.; Osterwalder, J.; Greber, T.; Berner, S.; Champness, N. R.; Beton, P. H. *Angew. Chem., Int. Ed.* **2010,** *122,* 1838–1843. doi:10.1002/anie.200905503
19. N'Diaye, A. T.; Bleikamp, S.; Feibelman, P. J.; Michely, T. *Phys. Rev. Lett.* **2006,** *97,* 215501. doi:10.1103/PhysRevLett.97.215501

20. N'Diaye, A. T.; Gerber, T.; Busse, C.; Myslivecek, J.; Coraux, J.; Michely, T. *New J. Phys.* **2009,** *11,* 103045. doi:10.1088/1367-2630/11/10/103045
21. Donner, K.; Jakob, P. *J. Chem. Phys.* **2009,** *131,* 164701. doi:10.1063/1.3246166
22. Zhou, Z.; Gao, F.; Goodman, D. W. *Surf. Sci.* **2010,** *604,* L31–L38. doi:10.1016/j.susc.2010.03.008
23. Lorenz, C. U.; Engstfeld, A.; Alves, O. B.; Hoster, H. E.; Behm, R. J. unpublished work, 2011.
24. Meier, C.; Roos, M.; Künzel, D.; Breitruck, A.; Hoster, H. E.; Landfester, K.; Groß, A.; Behm, R. J.; Ziener, U. *J. Phys. Chem. C* **2010,** *114,* 1268–1277. doi:10.1021/jp910029z
25. Meier, C.; Ziener, U.; Landfester, K.; Weihrich, P. *J. Phys. Chem. B* **2005,** *109,* 21015–21027. doi:10.1021/jp054271d
26. Mura, M.; Sun, X.; Silly, F.; Jonkman, H. T.; Briggs, G. A. D.; Castell, M. R.; Kantorovich, L. N. *Phys. Rev. B* **2010,** *81,* 195412. doi:10.1103/PhysRevB.81.195412
27. Ludwig, C.; Gompf, B.; Glatz, W.; Petersen, J.; Eisenmenger, W.; Möbus, M.; Zimmermann, U.; Karl, N. *Z. Phys. B* **1992,** *86,* 397–404. doi:10.1007/BF01323733
28. Ludwig, C.; Gompf, B.; Petersen, J.; Strohmaier, R.; Eisenmenger, W. *Z. Phys. B* **1994,** *93,* 365–373. doi:10.1007/BF01312708
29. Hoshino, A.; Isoda, S.; Kurata, H.; Kobayashi, T. *J. Appl. Phys.* **1994,** *76,* 4113–4120. doi:10.1063/1.357361
30. Fenter, P.; Burrows, P. E.; Eisenberger, P.; Forrest, S. R. *J. Cryst. Growth* **1995,** *152,* 65–72. doi:10.1016/0022-0248(95)00064-X
31. Nicoara, N.; Román, E.; Gómez-Rodíguez, J. M.; Martín-Gago, J. A.; Méndez, J. *Org. Electron.* **2006,** *7,* 287–294. doi:10.1016/j.orgel.2006.03.010
32. Tautz, F. S. *Prog. Surf. Sci.* **2007,** *82,* 479–520. doi:10.1016/j.progsurf.2007.09.001
33. Weiss, C.; Wagner, C.; Temirov, R.; Tautz, F. S. *J. Am. Chem. Soc.* **2010,** *132,* 11864–11865. doi:10.1021/ja104332t
34. Kilian, L.; Hauschild, A.; Temirov, R.; Soubatch, S.; Schöll, A.; Bendounan, A.; Reinert, F.; Lee, T.-L.; Tautz, F. S.; Sokolowski, M.; Umbach, E. *Phys. Rev. Lett.* **2008,** *100,* 136103. doi:10.1103/PhysRevLett.100.136103
35. Seidel, C.; Awater, C.; Liu, X. D.; Ellerbrake, R.; Fuchs, H. *Surf. Sci.* **1997,** *371,* 123–130. doi:10.1016/S0039-6028(96)00981-8
36. Stöhr, M.; Gabriel, M.; Möller, R. *Surf. Sci.* **2002,** *507–510,* 330–334. doi:10.1016/S0039-6028(02)01266-9
37. Wang, Q. H.; Hersam, M. C. *Nat. Chem.* **2009,** *1,* 206–211. doi:10.1038/nchem.212
38. Künzel, D.; Markert, T.; Groß, A.; Benoit, D. M. *Phys. Chem. Chem. Phys.* **2009,** *11,* 8867–8878. doi:10.1039/b907443k
39. Wang, B.; Bocquet, M.-L.; Marchini, S.; Günther, S.; Wintterlin, J. *Phys. Chem. Chem. Phys.* **2008,** *10,* 3530–3534. doi:10.1039/B801785A
40. Sun, H. *J. Phys. Chem. B* **1998,** *102,* 7338–7364. doi:10.1021/jp980939v
41. Hagler, A. T.; Huler, E.; Lifson, S. *J. Am. Chem. Soc.* **1974,** *96,* 5319–5327. doi:10.1021/ja00824a004
42. Mayo, S.; Olafson, B.; Goddard, W. A., III. *J. Phys. Chem.* **1990,** *94,* 8897–8909. doi:10.1021/j100389a010
43. Rappé, A. K.; Casewit, C. J.; Colwell, K. S.; Goddard, W. A., III; Skiff, W. M. *J. Am. Chem. Soc.* **1992,** *114,* 10024–10035. doi:10.1021/ja00051a040
44. Gasteiger, J.; Marsili, M. *Tetrahedron* **1980,** *36,* 3219–3288. doi:10.1016/0040-4020(80)80168-2
45. Rappé, A. K.; Goddard, W. A., III. *J. Phys. Chem.* **1991,** *95,* 3358–3363. doi:10.1021/j100161a070
46. Grimme, S. *J. Comput. Chem.* **2006,** *27,* 1787–1799. doi:10.1002/jcc.20495
47. Grimme, S.; Antony, J.; Ehrlich, S.; Krieg, H. *J. Chem. Phys.* **2010,** *132,* 154104. doi:10.1063/1.3382344

License and Terms

Beilstein Journal of Nanotechnology

Characterization of protein adsorption onto FePt nanoparticles using dual-focus fluorescence correlation spectroscopy

Pauline Maffre[1], Karin Nienhaus[1], Faheem Amin[2], Wolfgang J. Parak[2] and G. Ulrich Nienhaus[*1,3]

Full Research Paper

Open Access

Address:
[1]Institute of Applied Physics and Center for Functional Nanostructures, Karlsruhe Institute of Technology (KIT), Wolfgang-Gaede-Straße 1, 76131 Karlsruhe, Germany, [2]Department of Physics, Philipps University Marburg, Renthof 7, 35037 Marburg, Germany, and [3]Department of Physics, University of Illinois at Urbana-Champaign, 1110 West Green Street, Urbana, IL 61801, USA

Email:
Karin Nienhaus - Karin.nienhaus@kit.edu; G. Ulrich Nienhaus[*] - uli@illinois.edu

* Corresponding author

Keywords:
apolipoprotein; dual-focus fluorescence correlation spectroscopy; human serum albumin; nanoparticle; protein adsorption

Beilstein J. Nanotechnol. **2011,** *2,* 374–383.
doi:10.3762/bjnano.2.43

Received: 18 April 2011
Accepted: 06 June 2011
Published: 12 July 2011

This article is part of the Thematic Series "Organic–inorganic nanosystems".

Guest Editor: P. Ziemann

Abstract

Using dual-focus fluorescence correlation spectroscopy, we have analyzed the adsorption of three human blood serum proteins, namely serum albumin, apolipoprotein A-I and apolipoprotein E4, onto polymer-coated, fluorescently labeled FePt nanoparticles (~12 nm diameter) carrying negatively charged carboxyl groups on their surface. For all three proteins, a step-wise increase in hydrodynamic radius with protein concentration was observed, strongly suggesting the formation of protein monolayers that enclose the nanoparticles. Consistent with this interpretation, the absolute increase in hydrodynamic radius can be correlated with the molecular shapes of the proteins known from X-ray crystallography and solution experiments, indicating that the proteins bind on the nanoparticles in specific orientations. The equilibrium dissociation coefficients, measuring the affinity of the proteins to the nanoparticles, were observed to differ by almost four orders of magnitude. These variations can be understood in terms of the electrostatic properties of the proteins. From structure-based calculations of the surface potentials, positively charged patches of different extents can be revealed, through which the proteins interact electrostatically with the negatively charged nanoparticle surfaces.

Introduction

Recent years have seen enormous advances in the field of nanotechnology. A huge variety of nanoparticles (NPs), defined as objects with all three spatial dimensions in the range of 1–100 nm, has been developed, with well-controlled physicochemical properties including size, shape, charge, chemical composition and solubility. Many

of these NPs have already found their way into consumer products.

Owing to their small size, NPs may potentially invade all parts of the human body including tissues, cells and even subcellular compartments. Consequently, they hold great promise as tools for biomedical applications such as targeted drug delivery [1] or gene therapy [2]. However, NPs often exhibit properties distinctly different from those of the bulk material. For example, an enhanced surface reactivity may be observed due to their large surface-to-volume ratio [3] and, therefore, NPs may also pose a biological hazard [4,5].

Upon incorporation into the body, NPs become exposed to biological fluids such as lung epithelial lining fluid or blood plasma, which contain a variety of dissolved molecules, especially proteins. Depending on the properties of its surface, a NP may adsorb proteins and other biomolecules from the fluid to a lesser or greater extent. A protein coating layer, the so-called 'protein corona', forms and can completely enshroud the NP [6-11]. Consequently, at least the initial encounter of a NP with a cell is governed by the properties of the protein corona rather than those of the NP surface [12]. NP–protein interactions are typically weaker than chemical bonds and still comparable to the thermal energy at physiological temperatures. Therefore, the protein corona is not static but fluctuates in time due to incessant protein association and dissociation events. Upon biofluid exposure, the NP surface will quickly become coated with those proteins that are prevalent in the fluid and that have high binding rate coefficients. However, these proteins may subsequently be replaced by less prevalent proteins with higher binding affinity. Eventually, equilibrium will be established, so that the relative abundance of proteins in the corona is determined by their binding strength to the NP and their concentrations in the biofluid. We note that this simple equilibrium binding model is likely an oversimplification that needs further elaboration because proteins are complex physical systems that can assume a large number of different conformations [13,14]. The net free energies involved in NP–protein interactions can match or even exceed the entire internal stabilization energy of proteins. Their structures may change upon contact with a NP surface, up to the point that they entirely unfold. Such effects are known from the development of nanostructured surface coatings designed to prevent unspecific biomolecular adsorption ('biofilms') [15-17], which is an important issue for various fields including biotechnology (e.g., biosensors, bioanalytics) and biomedical devices (e.g., implants and catheters).

To be able to control the biological effects of NPs, such as prevention of uptake or targeted delivery to specific cells or tissues, it is of utmost importance to understand the structural and dynamic properties of the protein corona at the molecular level. Recently, we have used quantitative fluorescence microscopy, especially fluorescence correlation spectroscopy (FCS), to study protein adsorption of human serum albumin (HSA) on polymer-coated FePt NPs with an overall diameter of 11 nm [11]. HSA is the major soluble constituent of human blood plasma. It serves primarily as a carrier protein for steroids, fatty acids, and thyroid hormones [18]. We found that, at concentrations typically found in blood serum, ~20 HSA molecules adsorb as a monolayer of ~3.3 nm thickness on these NPs, and time-resolved fluorescence quenching experiments revealed a typical protein residence time of ~100 s [11]. For transferrin [8], an important blood plasma protein involved in iron transport and delivery, we observed formation of a 7 nm thick protein corona.

The FCS method is based on the analysis of the duration of brief bursts of photons from individual fluorescence emitters, diffusing through an observation volume of about 1 fL in a confocal microscope [19-23]. Autocorrelation analysis of the fluorescence intensity time traces yields the characteristic time scale of diffusion, τ_D. Based on the well-known spatial extension of the observation volume, the diffusion coefficient, D, and, by using the Stokes–Einstein equation (see Experimental), the hydrodynamic radius of the fluorescent particle, R_H, can be calculated. Consequently, a NP size increase due to protein adsorption onto the NP surfaces can be measured via an increase of τ_D. Knowledge of the molecule detection function (MDF), i.e., the probability to detect a fluorescence photon from a molecule at a given position in the sample volume, is key to the precise quantitative analysis of an FCS experiment [24]. The MDF depends on the intensity distribution of the focused laser beam used for excitation, the distribution of detection efficiencies of photons emanating from the observation volume and the photophysical properties of the fluorophores. It is sensitive to various parameters of the optical setup, including the refractive index mismatch between the sample solution and the immersion medium, variations in cover-slide thickness and astigmatism of the laser beam. Only by extremely careful calibration procedures and measurements can the subnanometer precision required for studying protein adsorption on NPs be achieved.

Dual-focus FCS (2fFCS) is a variant of the FCS method that includes an absolute calibration standard and promises to make high-precision particle size measurements much easier [25]. In 2fFCS, two laterally shifted, partially overlapping laser foci are positioned in the sample at a known, fixed separation. (Further details are given in Experimental.) Accurate diffusion coefficients can be obtained by a combined ('global') analysis, for each of the two detection volumes, of the autocorrelation func-

tion of the photon arrival times, i.e., the probability to detect a photon at time, $t + \tau$, given that a photon was detected at time t, and the cross-correlation between the two volumes, i.e., the probability to detect a photon from one volume at $t + \tau$, given that a photon was detected in the other volume at time t.

Here we have employed the 2fFCS method to quantify the equilibrium binding of three abundant blood plasma proteins to FePt NPs, HSA (which was included to ensure that our previously reported data [11] can be reproduced with our new technique) and the apolipoproteins apoA-I and apoE4. These two proteins function as transporters for lipid molecules in the blood by binding a large number of lipid and cholesterol molecules to form water-soluble lipoproteins, and they direct the lipids to their correct destinations in the body [26-28].

Results and Discussion

Protein equilibrium binding to FePt NPs

For studying the interaction of serum proteins with NPs by 2fFCS, we employed the same type of NP as in our previous work [11], namely, FePt cores that were rendered fluorescent by incorporating a small number of red fluorescent dye molecules (DY-636) in the polymer-coating surrounding the core [29]. The polymer shell contained a large number of carboxyl groups endowing the NPs with an overall negative charge and excellent colloidal stability [30].

To determine the affinity of the proteins to the NPs as well as the increase in R_H, we took 2fFCS data on NPs freely diffusing in solutions, which contained the proteins at concentrations varying over several orders of magnitude. NP concentrations in the nanomolar range ensured that roughly only one NP resided in the detection volume on average, so that the intensity fluctuations, on which the FCS method is based, were large. The protein concentration was varied on a logarithmic scale in a selected range appropriate for observing the transition from uncoated to coated NPs. Examples of measured correlation curves are depicted in Figure 1 for HSA, apoA-I and apoE4 (top to bottom). In the left column, representative correlation curves are shown at one selected protein concentration, i.e., autocorrelation curves for the two foci and the cross-correlation curve. Note that FCS data and, therefore, also the derived R_H values, are averages determined from a few thousand single-particle bursts. The autocorrelation curves in Figure 1 display two decay processes. The step on the millisecond time scale is due to NP diffusion and, therefore, reveals the particle size, whereas the step on the microsecond time scale arises from dye photophysics and is not of interest here. It originates from interconversion to the triplet state; fluorophores cease to emit fluorescence until they return to the ground state and can be excited again. Note that this process is strongly suppressed in the cross-correlation function because of its short time scale and the small overlap of the two detection volumes.

In the right column of Figure 1, cross-correlation curves are plotted for different protein concentrations in the solution, normalized to 1 at $\tau = 0.1$ ms (for ease of comparison). Evidently, the curves shift toward longer times with increasing protein concentration, indicating that the effective size of the NPs grows due to protein adsorption. The effect is small, however, so precise data are needed for a quantitative analysis of protein binding.

Figure 2 shows the dependence of R_H on the logarithm of the protein concentration, as obtained from the 2fFCS correlation data. For all three proteins, R_H increases in a stepwise fashion with protein concentration, as we previously reported for HSA and transferrin [8,11], which indicates a limited loading capacity of the NPs. This behavior can be understood if we assume that the protein molecules form a monolayer around the NPs, with a well-defined thickness, ΔR_H, and binding affinity, K'_D, as quantified by the protein concentration at the midpoint of the binding transition (vide infra). Once the monolayer is formed, the NP size remains constant, and the tendency to further accrete protein is essentially zero.

The data in Figure 2 can be analyzed quantitatively by using the following model. The hydrodynamic radius, R_H, of a spherical object is given by

$$R_H = \sqrt[3]{\frac{3}{4\pi}V}. \quad (1)$$

Consequently, we can express the dependence of R_H on the number of bound proteins by

$$R_H(N) = \sqrt[3]{\frac{3}{4\pi}(V_0 + NV_P)}. \quad (2)$$

Note that we make the assumption that the protein-coated NP can still be well approximated by a sphere. In Equation 2, V_0 is the volume of the NP, and N is the number and V_P the molecular volume of the adsorbed proteins. (Proteins have a typical density of 1.35 g/mL, so their volume is, to a good approximation, proportional to their mass). By introducing the radius of the bare NP, $R_H(0)$, and the coefficient $c = V_P/V_0$,

$$R_H(N) = R_H(0)\sqrt[3]{1 + cN}. \quad (3)$$

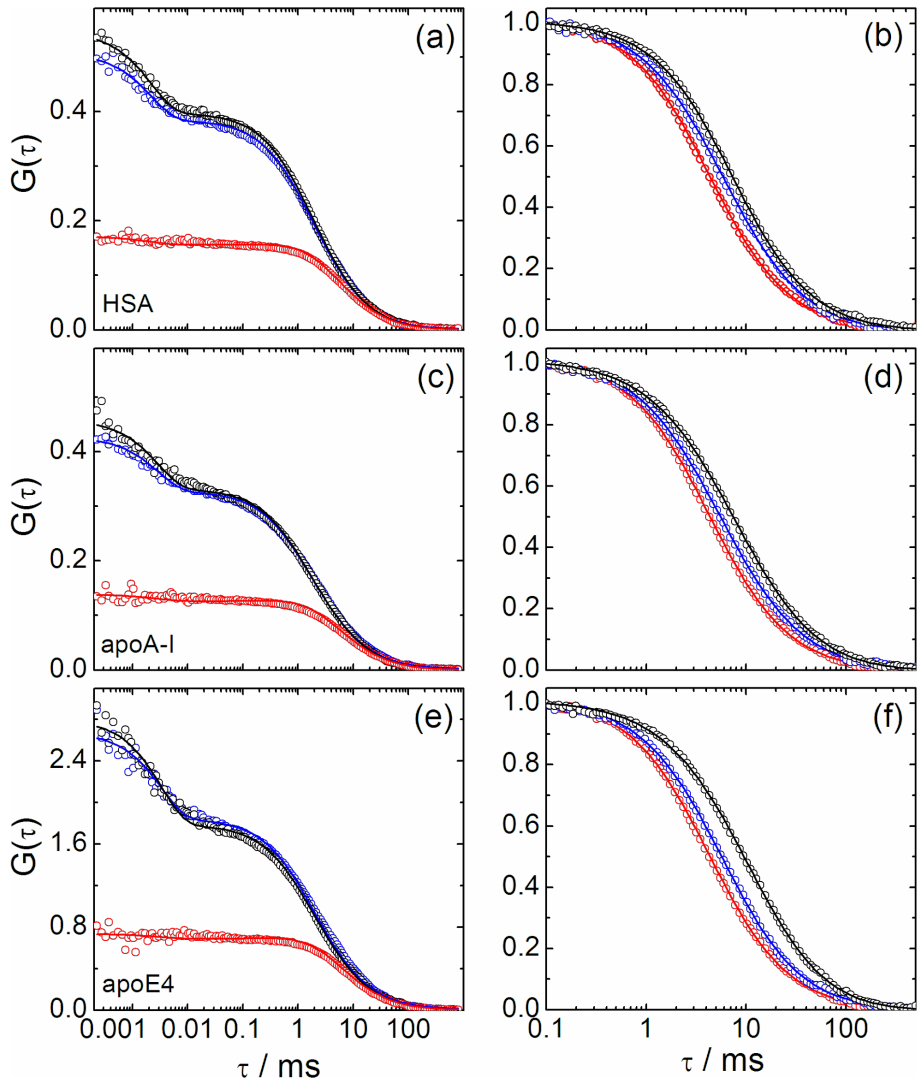

Figure 1: Fluorescence intensity correlation curves of NPs dissolved in buffer solutions of (a, b) HSA, (c, d) apoA-I, and (e, f) apoE4. (a, c, e) Measured (symbols) and fitted (lines) 2fFCS autocorrelation (black and blue) and cross-correlation (red) functions of polymer-coated FePt NPs in the presence of (a) 400 μM HSA, (c) 285 μM apoA-I and (e) 7.2 μM apoE4. (b, d, f) Measured (symbols) and fitted (lines) cross-correlation curves of NPs in buffer solution (red) and in the presence of serum proteins at two concentrations, normalized to 1 at τ = 0.1 ms. (b) 6.3 and 400 μM HSA (blue, black); (d) 36 and 285 μM apoA-I (blue, black); (f) 14 nM and 7.2 μM apoE4 (blue, black).

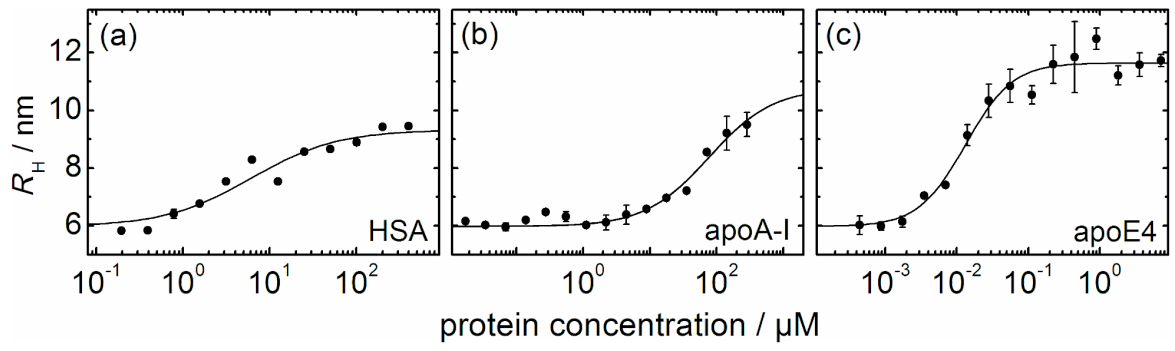

Figure 2: Hydrodynamic radius R_H, of the FePt NPs, plotted as a function of the concentration of (a) HSA, (b) apoA-I and (c) apoE4. The curves (solid lines) were fitted according to Equation 3 and Equation 5; best-fit parameters are compiled in Table 1.

Consequently, upon complete formation of the protein corona,

$$R_H(N_{max}) = R_H(0) + \Delta R_H = R_H(0)\sqrt[3]{1 + cN_{max}}, \quad (4)$$

where the maximum number of proteins binding to the NP is denoted by N_{max}. We model the dependence of N on the concentration of free protein, [P], by the Hill equation [11],

$$N = N_{max}\frac{1}{1 + (K'_D / [P])^n}. \quad (5)$$

Here, the equilibrium dissociation coefficient, K'_D, denotes the midpoint of the transition, i.e., the concentration of protein molecules free in the solution at half coverage. It quantifies the strength of the NP–protein interaction. The Hill coefficient, n, controls the steepness of the curve; it contains information about the cooperativity of binding. The lines in Figure 2 represent fits of Equations 3 and 5 to the data. Because all the FePt NPs were from the same batch, their hydrodynamic radius, $R_H(0)$ = (6.0 ± 0.1) nm, was taken as a global parameter in the fit for all three proteins. The best-fit parameters in Table 1 will be discussed in relation to the molecular structures of the proteins in the following subsections.

Structure of the protein corona

Comparison of the data in Figure 2 shows that the thickness of the protein corona, ΔR_H, is a characteristic of the particular protein species adsorbed. In our previous studies with HSA [11] and transferrin [8], we noticed that the thickness of the protein corona was correlated with the molecular dimensions of the proteins as obtained from the X-ray structures. These observations gave additional support to our claim that the corona consists of a monolayer of proteins adsorbed in specific orientations. Considering the strengths of Coulombic interactions, the molecular orientations are likely to be governed by patches of positive surface charge on the protein that preferentially interact with the negatively charged NP surface. In this subsection, we discuss the thickness of the corona in relation to the molecular shapes and electrostatic properties of the adsorbed proteins.

Figure 3a (left) shows a cartoon representation of the molecular structure of HSA, a protein with a molecular mass of 67 kDa [18]. It can be approximated by an equilateral triangular prism, with sides of ~8 nm and a height of ~3 nm (Figure 3a, middle). The ~3 nm radius increase upon adsorption of HSA, observed with 2fFCS (Figure 2a), completely agrees with our previous data [11], which led us to the suggestion that HSA molecules adsorb via their triangular surfaces onto the NPs. Also shown in Figure 3a (right) are space-filling models colored so as to visualize the electrostatic surface potentials. One of the triangular protein surfaces shows a pronounced positive patch, which is likely to promote the interaction with the negatively charged carboxyl groups on the NP surfaces (red arrow, Figure 3a). Overall, about 27 HSA molecules fit into the volume generated by the size increase of the NP (Table 1).

Lipid-free human apoA-I is the principal component of high-density lipoprotein (HDL) and plays an essential role in lipid transport and metabolism. This protein has a molecular mass of 28 kDa. X-ray crystallography revealed a two-domain structure, with a N-terminal domain forming a four-helix bundle and a structurally less well organized C-terminal domain (Figure 3b, left) [32-34]. In solution, apoA-I appears to be more flexible than in the crystalline state [35,36]. Based on analytical ultracentrifugation, viscometric, and fluorescence studies, its overall shape has been described by a prolate ellipsoid with an axial ratio of 5.5:1 [37,38]. Due to mutual interactions, the C-terminal domain is kept in close proximity to the N-terminal helix bundle, contributing significantly to the stability of the lipid-free conformation [39]. Förster resonance energy transfer (FRET) studies have indicated that the inter-domain distance in solution is even smaller than in the crystal structure [39]. Figure 3b (middle) gives a crude depiction of the structure of apoA-I in solution. On its surface, there are two rather extended negatively charged patches (marked by blue arrows in Figure 3b, right) that have been associated with the recognition of the ATP-binding cassette transporter A1 (ABCA1) [34]. In close vicinity to the larger patch, a small area of positive electrostatic potential is visible, which would be favorable for the interaction with our negatively charged NPs (red arrows in Figure 3b). By attaching with this patch to the NP surface, the

Table 1: Parameters of protein adsorption onto FePt NPs.

Protein	$R_H(N_{max})$ (nm)	ΔR_H (nm)	K'_D (μM)	n	N_{max}
HSA	9.3 ± 0.3	3.3 ± 0.3	9.9 ± 4.7	0.9 ± 0.2	27 ± 3
ApoA-I	10.8 ± 1.5	4.8 ± 1.4	140 ± 60	1.0 ± 0.3	52 ± 10
ApoE4	11.7 ± 0.3	5.7 ± 0.2	0.021 ± 0.003	1.4 ± 0.2	65 ± 3

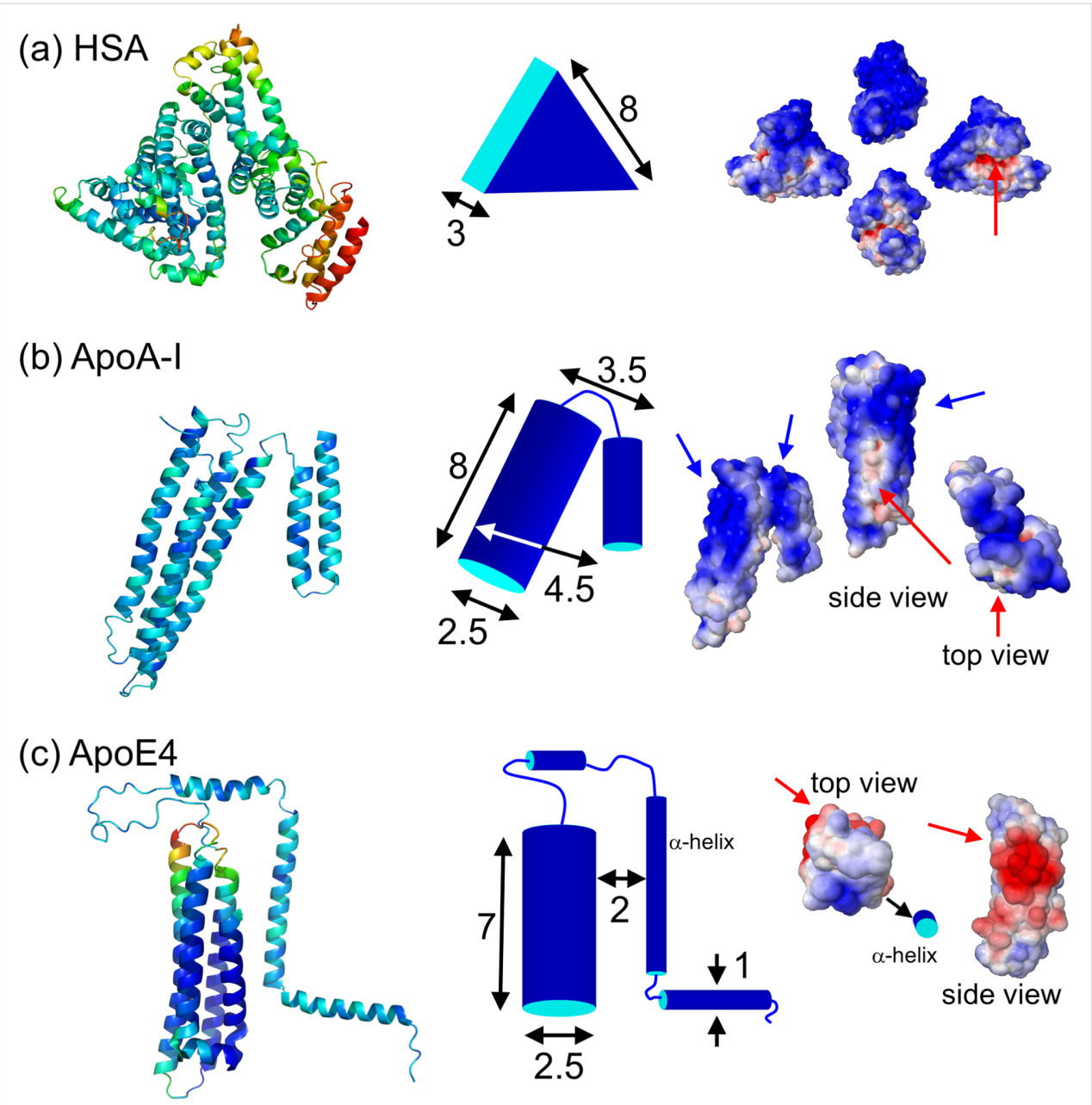

Figure 3: Structural depictions of (a) HSA, (b) apoA-I and (c) apoE4. Left column: Cartoon representations of HSA (protein data bank accession (pdb) code 1AO6), apoE4 (pdb code 1GS9) and apoA-I (pdb code 2A01). For apoE4, only the structure of the 22-K domain (4-helix bundle) has been solved. Center column: Simplified representations of the proteins including approximate dimensions (in nm). Right column: Space-filling models colored to indicate their surface electrostatics at pH 7.4 (blue: negative potential, red: positive potential; range from −5 k_BT/e to +5 k_BT/e; calculated online at http://kryptonite.nbcr.net/pdb2pqr/ [31]).

apoA-I molecules are expected to form a layer of ~4–5 nm thickness, which is in good agreement with our experimental findings (Figure 2b). The protein corona consists of on the order of 50 apoA-I molecules (Table 1).

Human apoE4 is another member of the family of soluble apolipoproteins [26]. The 34 kDa protein preferentially binds to very low-density lipoprotein (VLDL) and intermediate-density lipoprotein and has a high affinity for the low-density lipoprotein (LDL) receptor. Similarly to apoA-I, apoE4 also has two structural domains (Figure 3c, left), a N-terminal elongated four-helix bundle and a C-terminal, highly α-helical domain of yet unknown structure [40]. Recently, it was reported that apoE4 is not globular but, similar to apoA-I, ellipsoidal, with an axial ratio of ~7:1 [41]. A salt bridge between Arg61 in the N-terminal domain and Glu255 in the C-terminal domain

presumably stabilizes an extended helical structure at the C-terminus to support the interaction with large VLDLs [26,42].

Adsorption of apoE4 causes the largest increase in R_H for the three proteins studied here, by ~6 nm (Figure 2c, Table 1). Unlike the other two proteins, apoE4 has an extended, positively charged surface patch on its N-terminal domain that seems predestined to bind to the negatively charged NPs (Figure 3c). Related to the assumed position of the C-terminal α-helix, the patch is located almost on the opposite side of the four helix bundle, as indicated in Figure 3c (right). An electron paramagnetic resonance study of apoE4 has implied that the C-terminal domain forms a long α-helix that is arranged parallel to the helix bundle at a distance of ~2 nm [43]. If we assume that the four-helix bundle of apoE4 lies flat on the NP surface, binding with its positively charged patch, and if we add the typical diameter of a single α-helix separated by 2 nm, we obtain an overall thickness of 5–6 nm for the protein corona, which closely matches the observed ΔR_H (Figure 2c, Table 1). About 65 apoE4 molecules will attach to the NP upon complete formation of the protein corona (Table 1).

Protein binding affinity

The apolipoproteins differ in their binding affinities for the negatively charged FePt NPs by almost four orders of magnitude, with K'_D (apoE4) = 0.021 ± 0.003 μM and K'_D (apoA-I) = 140 ± 60 μM (Table 1). HSA has an intermediate K'_D of 9.9 ± 4.7 μM. The affinities can be correlated with the surface potentials. The high affinity of apoE4 to the negatively charged NPs most likely arises from Coulomb interactions involving the large patch of positive charge of apoE4 (Figure 3c). The positively charged patch on the HSA surface is less pronounced (Figure 3a) and, consequently, the binding affinity is greatly reduced. For apoA-I, there is only a weak area of positive surface potential (Figure 3b), consistent with the low affinity toward the NPs.

For HSA binding to FePt NPs, we have previously reported a Hill coefficient $n < 1$ [11], which is indicative of anti-cooperative binding, meaning that the binding affinity effectively decreases as more HSA molecules adsorb onto the NPs. This finding can be explained by mutual repulsion of the HSA molecules on the NP surface. Note that HSA exists in blood serum in high concentrations and, thus, should not have a tendency to aggregate. For apoA-I, we found $n = 1$, the non-cooperative case, whereas apoE4 was observed to bind to the NPs in a cooperative manner, with $n = 1.4$. This result may be related to the known tendency of apoE4 to form oligomers in solution [41]. Apparently, apoE4 molecules have interfaces by which they can mutually exert attractive interactions. Consequently, a cooperative effect of apoE4 binding to NPs can be explained by the additional stabilization of an apoE4 molecule on the NP in the presence of a neighboring apoE4 molecule.

Conclusion

By using 2fFCS, we have quantitatively analyzed the adsorption of three blood serum proteins onto FePt NPs. All three proteins gave rise to a well-defined increase in NP size upon binding. The thickness of the protein corona can be related to a particular orientation of the protein, based on the knowledge of its molecular structure. For apolipoproteins, this result is rather intriguing because they are very flexible and are known to undergo large structural changes upon lipid binding [44]. We have shown that the widely different binding affinities of the three proteins can be related to the presence of positively charged surface patches on the proteins. It is unlikely that the surface charge distribution will be similar if the protein structure changes markedly upon binding. Consequently, the observation of positively charged patches on the proteins, which appear to mediate the interaction with our negatively charged NPs, further supports our view that the apolipoproteins do not significantly change their structures upon NP binding. However, the evidence from 2fFCS presented here is rather indirect. In future studies, we shall employ more structure-specific spectroscopic methods such as single-particle FRET, which may yield more detailed insights into the structural properties of the protein corona surrounding NPs.

Experimental

Sample preparation

FePt NP cores were synthesized according to published protocols [45] and coated with an amphiphilic polymer synthesized from dodecylamine and poly(isobutylene-*alt*-maleic anhydride). They carry carboxylic acid groups on their surfaces, making them water-soluble. The polymer shell was labeled with the amino-modified fluorescent dye DY-636 (Dyomics, Jena, Germany).

2fFCS measurements were performed in PBS buffer, pH 7.4 (Dulbecco's PBS without Ca^{2+} and Mg^{2+}, PAA Labs, Cölbe, Germany). All proteins were purchased from Sigma (Sigma–Aldrich, St. Louis, MO). NP solutions at (1 ± 0.5) nM were mixed with equal volumes of solutions containing the proteins at varying concentrations. Because of the high affinity of apoE4 to the FePt NPs, the NP concentration was reduced to (0.1 ± 0.05) nM to ensure that only a small fraction of apoE4 proteins was bound to the NPs even at the lowest protein concentrations studied. All protein solutions were prepared by repeated dilution of a single stock solution. The apoE4 dilution series was prepared 2 h before mixing with the NPs to allow the sample to equilibrate between monomers and oligomers [41]. The experiments with apoA-I were limited to below 300 μM

because of aggregation problems at higher concentrations. The lack of data in the high-concentration range (Figure 2b) was compensated by enhanced data statistics at the lower concentrations. The NPs were incubated with the proteins for 10 min prior to the measurement.

2fFCS setup

The 2fFCS setup is based on a time-resolved confocal microscopy system (Microtime 200, PicoQuant, Berlin, Germany). Instead of using a single excitation laser, the light from two identical, orthogonally polarized pulsed 640 nm diode lasers (LDH-P-C-640B, Picoquant, Berlin, Germany) was combined by a polarizing beam splitter (Figure 4). The lasers were pulsed alternately, each with a repetition rate of 20 MHz, so that the time lag between successive pulses was 25 ns and, thus, much longer than the fluorescence lifetime of the DY-636 dyes (~0.5 ns [46]). Both lasers were coupled into a polarization retaining optical fiber. After exiting the fiber, the light was again collimated into a parallel light beam consisting of a train of laser pulses with alternating orthogonal polarizations. The beam was passed through a dichroic mirror (470/635 nm) and then a Nomarski DIC prism (U-DICTHC, Olympus, Hamburg, Germany), which deflects the laser pulses into two different directions, according to their polarization, into the objective (UPLSAPO 60XW, Olympus) of the inverted microscope (IX71, Olympus). Two overlapping excitation foci (Figure 4) were generated in the sample, with a lateral shift of 404 nm in our setup. The fluorescence light was collected by the same objective and passed through the prism and the dichroic mirror. After the pinhole (150 µm), the light was collimated, split and focused onto two avalanche photodiode (APD) detectors (SPCM-AQR-13, Perkin Elmer, Rodgau, Germany). A single-photon counting card (HydraHarp 400 picosecond event timer und TCSPC module, PicoQuant) recorded the detected photons with picosecond time resolution, so that the photons could be assigned unambiguously to the excitation in one or the other of the two foci. Autocorrelation functions for each detection volume as well as cross-correlation functions between the two detection volumes were calculated from the photon arrival time traces.

Data collection

For data collection, a few microliters of the sample solution were placed between two standard microscope cover slips separated by a 200 µm thick mylar foil with a 1 mm wide channel for the sample solution in the middle.

Samples were illuminated continuously for 8 min, with the power of each laser adjusted to 3 µW. For NP concentrations of 1 nM (0.1 nM), ~10,000 (1,000) single molecule bursts were analyzed. The temperature was measured during the experiments and accounted for in the determination of the diffusion coefficient, D, according to the Stokes–Einstein relation,

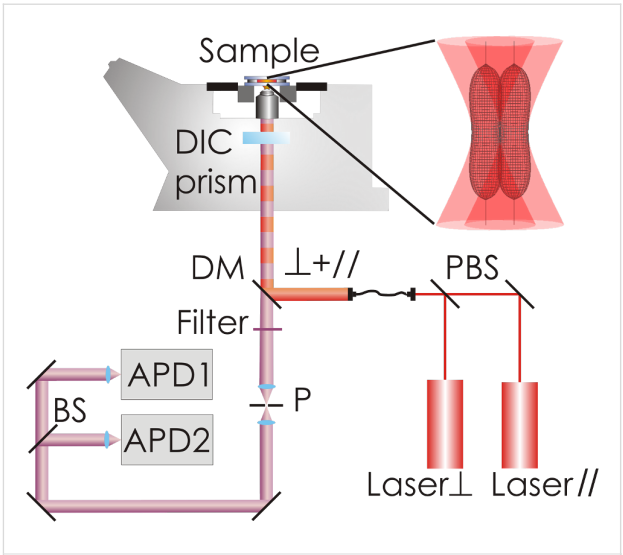

Figure 4: Schematic of the 2fFCS system. DM: dichroic mirror; BS: beam splitter; PBS: polarizing beam splitter; APD: avalanche photo diode; P: pinhole.

$$R_{\mathrm{H}} = \frac{k_{\mathrm{B}}T}{6\pi\eta D}, \tag{6}$$

with hydrodynamic radius R_{H}, Boltzmann constant k_{B}, temperature T, and viscosity η. Three independent series of measurements were taken and averaged.

Data analysis

In conventional FCS, the MDF is typically approximated by a three-dimensional Gaussian profile. However, this assumption is rather crude. In 2fFCS, data fitting is facilitated by a new, semi-empirical two-parameter model describing the MDF [25]. In each lateral (x,y-)plane along the optical axis, z, the MDF is, for both foci, modeled by a two-dimensional Gaussian function, $U(x,y)$, of width $w(z)$ and amplitude $\kappa(z)/w^2(z)$,

$$U(x,y) = \frac{\kappa(z)}{w^2(z)}\exp\left[-\frac{2}{w^2(z)}(x^2+y^2)\right], \tag{7}$$

with

$$w(z) = w_0\left[1+\left(\frac{\lambda_{\mathrm{exc}}z}{\pi w_0^2 n}\right)^2\right]^{1/2}, \tag{8}$$

$$\kappa(z) = 1 - \exp\left(-\frac{2a^2}{R^2(z)}\right), \quad (9)$$

$$R(z) = R_0\left[1 + \left(\frac{\lambda_{em} z}{\pi R_0^2 n}\right)^2\right]^{1/2}. \quad (10)$$

In these equations, λ_{exc} and λ_{em} are the excitation and the center emission wavelengths, respectively; n is the refractive index of the immersion medium and a is the radius of the confocal aperture divided by the magnification. R_0 and w_0 are a priori unknown model parameters that are determined by the fit.

As the emitted photons are registered as a function of time, they can be assigned to one of the two foci. Therefore, three correlation functions can be calculated from the data from each of the two foci, that is, the two auto-correlation functions and the cross-correlation function. Actually, a cross-correlation between two detectors is also performed to calculate the autocorrelation functions, so to avoid afterpulsing artifacts of the APDs. All three correlation functions are fitted globally, according to

$$g(t,\delta) = \frac{\varepsilon_1\varepsilon_2 c}{4}\sqrt{\frac{\pi}{Dt}}\int_{-\infty}^{\infty} dz_1 \int_{-\infty}^{\infty} dz_2 \frac{\kappa(z_1)\kappa(z_2)}{8Dt + w^2(z_1) + w^2(z_2)} \times \exp\left[-\frac{(z_2 - z_1)^2}{4Dt} - \frac{2\delta^2}{8Dt + w^2(z_1) + w^2(z_2)}\right]. \quad (11)$$

The coefficients ε_1 and ε_2 take the proper weighting of the two polarization channels, due to the different excitation powers and detection efficiencies, into account. For the auto-correlation curves, the spatial separation of the two foci, δ, is set to zero, and $\varepsilon_1\varepsilon_2$ is replaced by ${\varepsilon_1}^2$ or ${\varepsilon_2}^2$.

The correlation analysis was performed with the SymphoTime software (PicoQuant). FCS experiments are notoriously sensitive to the presence of large aggregates, therefore, those parts of the time traces that showed excessively high intensities were excluded from the correlation analysis. Changes in viscosity due to the increasing protein concentration were taken into account by using a linear approximation for the contribution of the solute to the solution viscosity, based on the intrinsic viscosity of HSA of 4.2 cm^3/g, as specified by the supplier (Sigma–Aldrich, St. Louis, MO), and of apoA-I (9.2 cm^3/g) [47]. The viscosity change due to apoE4 has, to the best of our knowledge, not yet been determined. However, the viscosity effect of apoE4 is minimal in our experiments because its high affinity to the NPs required the use of lower concentrations.

Acknowledgements

We thank Stefan Brandholt for technical assistance. This work was supported by the Deutsche Forschungsgemeinschaft (DFG) through the Center for Functional Nanostructures (CFN) and Schwerpunktprogramm (SPP) 1313, grants NI291/7, NI291/8 and PA794/4.

References

1. Maesaki, S. *Curr. Pharm. Des.* **2002,** *8,* 433–440.
2. Lewin, M.; Carlesso, N.; Tung, C.-H.; Tang, X.-W.; Cory, D.; Scadden, D. T.; Weissleder, R. *Nat. Biotechnol.* **2000,** *18,* 410–414. doi:10.1038/74464
3. Savolainen, K.; Alenius, H.; Norppa, H.; Pylkkänen, L.; Tuomi, T.; Kasper, G. *Toxicology* **2010,** *269,* 92–104. doi:10.1016/j.tox.2010.01.013
4. Lehmann, A. D.; Parak, W. J.; Zhang, F.; Ali, Z.; Röcker, C.; Nienhaus, G. U.; Gehr, P.; Rothen-Rutishauser, B. *Small* **2010,** *6,* 753–762. doi:10.1002/smll.200901770
5. Lunov, O.; Syrovets, T.; Büchele, B.; Jiang, X.; Röcker, C.; Tron, K.; Nienhaus, G. U.; Walther, P.; Mailänder, V.; Landfester, K.; Simmet, T. *Biomaterials* **2010,** *31,* 5063–5071. doi:10.1016/j.biomaterials.2010.03.023
6. Casals, E.; Pfaller, T.; Duschl, A.; Oostingh, G. J.; Puntes, V. *ACS Nano* **2010,** *4,* 3623–3632. doi:10.1021/nn901372t
7. Cedervall, T.; Lynch, I.; Lindman, S.; Berggård, T.; Thulin, E.; Nilsson, H.; Dawson, K. A.; Linse, S. *Proc. Natl. Acad. Sci. U. S. A.* **2007,** *104,* 2050–2055. doi:10.1073/pnas.0608582104
8. Jiang, X.; Weise, S.; Hafner, M.; Röcker, C.; Zhang, F.; Parak, W. J.; Nienhaus, G. U. *J. R. Soc., Interface* **2010,** *7* (Suppl. 1), S5–S13. doi:10.1098/rsif.2009.0272.focus
9. Lundqvist, M.; Stigler, J.; Elia, G.; Lynch, I.; Cedervall, T.; Dawson, K. A. *Proc. Natl. Acad. Sci. U. S. A.* **2008,** *105,* 14265–14270. doi:10.1073/pnas.0805135105
10. Monopoli, M. P.; Walczyk, D.; Campbell, A.; Elia, G.; Lynch, I.; Baldelli Bombelli, F.; Dawson, K. A. *J. Am. Chem. Soc.* **2011,** *133,* 2525–2534. doi:10.1021/ja107583h
11. Röcker, C.; Pötzl, M.; Zhang, F.; Parak, W. J.; Nienhaus, G. U. *Nat. Nanotechnol.* **2009,** *4,* 577–580. doi:10.1038/nnano.2009.195
12. Stark, W. J. *Angew. Chem., Int. Ed. Engl.* **2011,** *50,* 1242–1258. doi:10.1002/anie.200906684
13. Frauenfelder, H.; Nienhaus, G. U.; Johnson, J. B. *Ber. Bunsenges. Phys. Chem.* **1991,** *95,* 272–278.
14. Nienhaus, G. U.; Müller, J. D.; McMahon, B. H.; Frauenfelder, H. *Physica D* **1997,** *107,* 297–311. doi:10.1016/S0167-2789(97)00097-3
15. Heyes, C. D.; Groll, J.; Möller, M.; Nienhaus, G. U. *Mol. BioSyst.* **2007,** *3,* 419–430. doi:10.1039/b700055n
16. Heyes, C. D.; Kobitski, A. Y.; Amirgoulova, E. V.; Nienhaus, G. U. *J. Phys. Chem. B* **2004,** *108,* 13387–13394. doi:10.1021/jp049057o
17. Amirgoulova, E. V.; Groll, J.; Heyes, C. D.; Ameringer, T.; Röcker, C.; Möller, M.; Nienhaus, G. U. *ChemPhysChem* **2004,** *5,* 552–555. doi:10.1002/cphc.200400024
18. He, X. M.; Carter, D. C. *Nature* **1992,** *358,* 209–215. doi:10.1038/358209a0
19. Rigler, R.; Elson, E. S. *Fluorescence Correlation Spectroscopy: Theory and Applications;* Springer, 2011.
20. Maiti, S.; Haupts, U.; Webb, W. W. *Proc. Natl. Acad. Sci. U. S. A.* **1997,** *94,* 11753–11757. doi:10.1073/pnas.94.22.11753

21. Lamb, D. C.; Schenk, A.; Röcker, C.; Scalfi-Happ, C.; Nienhaus, G. U. *Biophys. J.* **2000,** *79,* 1129–1138. doi:10.1016/S0006-3495(00)76366-1
22. Schenk, A.; Ivanchenko, S.; Röcker, C.; Wiedenmann, J.; Nienhaus, G. U. *Biophys. J.* **2004,** *86,* 384–394. doi:10.1016/S0006-3495(04)74114-4
23. Zemanová, L.; Schenk, A.; Valler, M. J.; Nienhaus, G. U.; Heilker, R. *Drug Discovery Today* **2003,** *8,* 1085–1093. doi:10.1016/S1359-6446(03)02833-2
24. Enderlein, J.; Gregor, I.; Patra, D.; Dertinger, T.; Kaupp, U. B. *ChemPhysChem* **2005,** *6,* 2324–2336. doi:10.1002/cphc.200500414
25. Dertinger, T.; Pacheco, V.; von der Hocht, I.; Hartmann, R.; Gregor, I.; Enderlein, J. *ChemPhysChem* **2007,** *8,* 433–443. doi:10.1002/cphc.200600638
26. Hatters, D. M.; Peters-Libeu, C. A.; Weisgraber, K. H. *Trends Biochem. Sci.* **2006,** *31,* 445–454. doi:10.1016/j.tibs.2006.06.008
27. Marcel, Y. L.; Kiss, R. S. *Curr. Opin. Lipidol.* **2003,** *14,* 151–157. doi:10.1097/00041433-200304000-00006
28. Alaupovic, P. *Methods Enzymol.* **1996,** *263,* 32–60. doi:10.1016/S0076-6879(96)63004-3
29. Pellegrino, T.; Manna, L.; Kudera, S.; Liedl, T.; Koktysh, D.; Rogach, A. L.; Keller, S.; Rädler, J.; Natile, G.; Parak, W. J. *Nano Lett.* **2004,** *4,* 703–707. doi:10.1021/nl035172j
30. Lin, C.-A.; Sperling, R. A.; Li, J. K.; Yang, T.-Y.; Li, P.-Y.; Zanella, M.; Chang, W. H.; Parak, W. J. *Small* **2008,** *4,* 334–341. doi:10.1002/smll.200700654
31. Dolinsky, T. J.; Nielsen, J. E.; McCammon, J. A.; Baker, N. A. *Nucleic Acids Res.* **2004,** *32,* W665–667. doi:10.1093/nar/gkh381
32. Saito, H.; Dhanasekaran, P.; Nguyen, D.; Holvoet, P.; Lund-Katz, S.; Phillips, M. C. *J. Biol. Chem.* **2003,** *278,* 23227–23232. doi:10.1074/jbc.M303365200
33. Silva, R. A. G. D.; Hilliard, G. M.; Fang, J.; Macha, S.; Davidson, W. S. *Biochemistry* **2005,** *44,* 2759–2769. doi:10.1021/bi047717+
34. Ajees, A. A.; Anantharamaiah, G. M.; Mishra, V. K.; Hussain, M. M.; Murthy, H. M. K. *Proc. Natl. Acad. Sci. U. S. A.* **2006,** *103,* 2126–2131. doi:10.1073/pnas.0506877103
35. Davidson, W. S.; Thompson, T. B. *J. Biol. Chem.* **2007,** *282,* 22249–22253. doi:10.1074/jbc.R700014200
36. Thomas, M. J.; Bhat, S.; Sorci-Thomas, M. G. *J. Lipid Res.* **2008,** *49,* 1875–1883. doi:10.1194/jlr.R800010-JLR200
37. Barbeau, D. L.; Jonas, A.; Teng, T.-L.; Scanu, A. M. *Biochemistry* **1979,** *18,* 362–369. doi:10.1021/bi00569a021
38. Davidson, W. S.; Arnvig-McGuire, K.; Kennedy, A.; Kosman, J.; Hazlett, T. L.; Jonas, A. *Biochemistry* **1999,** *38,* 14387–14395. doi:10.1021/bi991428h
39. Koyama, M.; Tanaka, M.; Dhanasekaran, P.; Lund-Katz, S.; Phillips, M. C.; Saito, H. *Biochemistry* **2009,** *48,* 2529–2537. doi:10.1021/bi802317v
40. Wilson, C.; Wardell, M. R.; Weisgraber, K. H.; Mahley, R. W.; Agard, D. A. *Science* **1991,** *252,* 1817–1822. doi:10.1126/science.2063194
41. Garai, K.; Frieden, C. *Biochemistry* **2010,** *49,* 9533–9541. doi:10.1021/bi101407m
42. Chou, C.-Y.; Lin, Y.-L.; Huang, Y.-C.; Sheu, S.-Y.; Lin, T.-H.; Tsay, H.-J.; Chang, G.-G.; Shiao, M.-S. *Biophys. J.* **2005,** *88,* 455–466. doi:10.1529/biophysj.104.046813
43. Hatters, D. M.; Budamagunta, M. S.; Voss, J. C.; Weisgraber, K. H. *J. Biol. Chem.* **2005,** *280,* 34288–34295. doi:10.1074/jbc.M506044200
44. Shih, A. Y.; Sligar, S. G.; Schulten, K. J. R. *Soc., Interface* **2009,** *6,* 863–871. doi:10.1098/rsif.2009.0173
45. Sun, S.; Murray, C. B.; Weller, D.; Folks, L.; Moser, A. *Science* **2000,** *287,* 1989–1992. doi:10.1126/science.287.5460.1989
46. Buschmann, V.; Weston, K. D.; Sauer, M. *Bioconjugate Chem.* **2003,** *14,* 195–204. doi:10.1021/bc025600x
47. Edelstein, C.; Scanu, A. M. *J. Biol. Chem.* **1980,** *255,* 5747–5754.

License and Terms

The definitive version of this article is the electronic one which can be found at: doi:10.3762/bjnano.2.43

Beilstein Journal of Nanotechnology

Influence of water on the properties of an Au/Mpy/Pd metal/molecule/metal junction

Jan Kučera and Axel Groß*

Full Research Paper

Open Access

Address:
Institute of Theoretical Chemistry, Ulm University, D-89069 Ulm, Germany

Email:
Jan Kučera - jan.kucera@uni-ulm.de; Axel Groß* - axel.gross@uni-ulm.de

* Corresponding author

Keywords:
density functional calculations; self-assembled monolayers; water adsorption

Beilstein J. Nanotechnol. **2011,** *2,* 384–393.
doi:10.3762/bjnano.2.44

Received: 18 April 2011
Accepted: 09 June 2011
Published: 12 July 2011

This article is part of the Thematic Series "Organic–inorganic nanosystems".

Guest Editor: P. Ziemann

Abstract

The geometric and electronic structure of the metal–molecule interface in metal/molecule/metal junctions is of great interest since it affects the functionality of such units in possible nanoelectronic devices. We have investigated the interaction between water and a palladium monolayer of a Au(111)/4-mercaptopyridine/Pd junction by means of DFT calculations. A relatively strong bond between water and the palladium monolayer of the Au/Mpy/Pd complex is observed via a one-fold bond between the oxygen atom of the water molecule and a Pd atom. An isolated H_2O molecule adsorbs preferentially in a flat-lying geometry on top of a palladium atom that is at the same time also bound to the nitrogen atom of a Mpy molecule of the underlying self-assembled monolayer. The electronic structure of these Pd atoms is considerably modified which is reflected in a reduced local density of states at the Fermi energy. At higher coverages, water can be arranged in a hexagonal ice-like bilayer structure in analogy to water on bulk metal surfaces, but with a much stronger binding which is dominated by O–Pd bonds.

Introduction

Recently, an elegant electrochemical method for the metalization of molecular layers assembled on surfaces has been established [1]. Within the procedure, a solution containing metal cations is brought into contact with a self-assembled monolayer (SAM) consisting of organic molecules on a metal substrate, thus forming metal cation/molecule complexes. Then the cationic solution is exchanged with a cation-free electrolyte, and the cation/molecule complexes are reduced under potential control resulting in a metal layer on top of the SAM. The application of this technique led recently to the preparation of various metal/SAM/metal junctions on Au(111) electrodes, involving SAMs formed by 4-mercaptopyridine (Mpy) [1], 4-aminothiophenol (ATP) [2], thiazole [3], or 1,4-dicyanobenzene [4] molecules covered by monolayers of Pd [1], Pt [5], or

Rh [6], respectively. In addition, further progress extended the limits of the method towards the preparation of a prototypical Au/Mpy/Pd/Mpy/Pt double decker junction [7].

These achievements can eventually open the way towards the rational design of future bionanoelectronics in which the organic (molecule) and inorganic (metal) units will communicate with each other. Yet, there are many fundamental questions open with respect to the factors that play a crucial role in the preparation, characterization, and operation of metal/SAM/metal junctions. Among those, the elucidation of the microscopic structure of the metal–molecule interface is of particular importance since it influences the functionality of possible devices to a large extent. The knowledge about the metal–molecule contact on an atomic level is still limited because of the considerable complexity of this hybrid system which makes the experimental clarification of microscopic details rather difficult. Here the combination of experimental approaches together with modern methods of quantum chemistry might help to shed light on the microscopic structure of the constituents of the contacts [2,7-9].

The structure of the Pd layers prepared on Au/Mpy and Au/ATP SAMs was recently the subject of several experimental and theoretical studies [7-12]. Experimental ultraviolet photoelectron spectroscopy (UPS) revealed a relatively large reorganization of the valence band of the palladium monolayer with respect to bulk Pd [7,8]. For both the Mpy- and the ATP-SAM the density of states (DOS) of the Pd monolayer was found to be significantly reduced at the Fermi level with the maximum of the DOS shifted to about −1.8 eV below the Fermi energy.

Two possible scenarios have been considered as an explanation for the observed DOS of the palladium layers. Either the DOS might be modified due to the strong SAM–Pd interaction, or additional species from the liquid environment bound to the Pd layer could affect the Pd DOS [7,10,12]. In the case of SAMs formed by ATP molecules, periodic density functional theory (DFT) calculations of the bare Au/ATP/Pd junction, assuming a $(\sqrt{3}\times\sqrt{3})$ structure of the ATP molecules, were able to reproduce the experimentally observed downshift of the Pd DOS reasonably well [2,12] under the assumption that the amino groups of the ATP molecules become dehydrogenated upon the metalization. The isolated nitrogen atom of the dehydrogenated amino group interacts strongly with three Pd atoms thus causing the strong modification of the DOS.

In the case of the Au/Mpy/Pd junction, on the other hand, the DFT calculations for the bare system only yield a negligible downshift of the DOS [10], in contrast to the experimental results. The nitrogen atom of the Mpy molecule that is part of the aromatic ring interacts directly with only one atom of the Pd layer. The DOS of the Pd atoms not bound to the nitrogen atom remains rather bulk-like such that no significant reduction of the DOS at the Fermi level results. Only upon the consideration of additional adsorbents, such as sulfur, nitrogen, thiolates, amines, or H on the Pd layer, can a downshift of the DOS in agreement with the experiment be obtained in the calculations [12]. However, there is no clear experimental evidence yet with respect to the presence of these adsorbates on the Pd layer. Hence it is fair to say that the reason for the strong downshift of the Pd DOS in the Au/Mpy/Pd junction is still unclear.

The electrochemical metalization of the SAMs occurs in the presence of an aqueous electrolyte. In order to obtain a complete understanding of the factors influencing the geometric and electronic structure of the Au/Mpy/Pd junctions, it is important to clarify the role of the water–palladium interaction on the properties of the metal layer. Furthermore, under ambient conditions there is always a certain concentration of water molecules, and hence an understanding of the water–metal layer interaction is of interest from the point of view of future application of these junctions as electronic devices.

There have been numerous studies addressing the properties of water–metal interfaces, both from an experimental as well as from a theoretical point of view [13-21], but there are still questions remaining. For example, it is not clear whether water at close-packed metal surfaces is crystalline or liquid at room temperature [19]. Again, progress in the clarification of structure benefits from a close collaboration between experiment and theory [22-24].

According to DFT calculations, the interaction between water and flat metal surfaces is relatively weak [16,18]. For example, the energy gain upon the adsorption of a H_2O monomer on Pd(111) is about −0.33 eV [18]. Single H_2O molecules on metal surfaces preferentially occupy top site positions creating a one-fold oxygen–metal bond, with O–H bonds oriented parallel to the surface [25]. Layers of water on (111) metal surfaces are traditionally assumed to be arranged in an ice-like hexagonal bilayer structure with every second water molecule bound to the metal surface via the oxygen atom. The other water molecules have one hydrogen atom either pointing away from the surface (H_{up}) or towards the surface (H_{down}). In such an arrangement the adsorption energy related to one H_2O in the gas phase is higher compared to the adsorption energy of a single water molecule, e.g., for the H_{down} structure on Pd(111) it is −0.56 eV per molecule. However, the dominating contribution is coming from intermolecular hydrogen bonds rather then from water–molecule interactions [16,18]. Consequently, because of the rather weak metal–water interaction the electronic structure

of the metal substrate remains almost unaffected upon the water adsorption [26]. On the other hand, the adsorbed water bilayers become strongly polarized which leads to a significant work function change upon water adsorption on more strongly interacting transition metal surfaces such as, e.g., Pd/Au(111) [19].

In this paper, we use periodic DFT calculations to focus on the interaction of water molecules with the palladium monolayer prepared on a 4-mercaptopyridine SAM on Au(111), forming a Au/Mpy/Pd/H_2O complex. We determine the stability of an isolated water molecule, as well as of a water layer arranged in a hexagonal bilayer, at the preferential adsorption sites on the densely packed palladium monolayer of the Au/Mpy/Pd system. In addition, we concentrate on the structural and electronic modification of the Au/Mpy/Pd complex upon water adsorption. In particular we will discuss the character of the palladium local density of states (LDOS) in the presence of water and compare the findings with experimental UPS spectra of the corresponding system.

Results and Discussion

Before addressing the water adsorption on the Au/Mpy/Pd junction, we will first briefly discuss the structural details of the bare $(\sqrt{3}\times\sqrt{3})$R30° Au/Mpy/Pd complex. This structure was adopted as the initial configuration for all geometry optimizations of the complexes with water. In this structure, there is one Mpy molecule and three metal atoms per layer in the unit cell. Mpy molecules are bound to the gold substrate via a two-fold S–Au bond at the near-bridge fcc site, which was previously determined as the most stable site of the molecule in the $(\sqrt{3}\times\sqrt{3})$R30° structure on the Au(111) surface [27]. Note that the plane of the Mpy aromatic ring is tilted by 34° with respect to the Au(111) surface normal. The connection between the Mpy molecule and the densely packed palladium monolayer is realized via a one-fold N–Pd bond. In such an arrangement, one palladium atom is located directly above the nitrogen atom with a N–Pd distance of ~2.09 Å whereas the other two palladium atoms in each unit cell do not directly interact with the SAM. In the following, the two Pd species are distinguished with the former type denoted by Pd_b and the latter by Pd_n, respectively.

We will first consider a single H_2O molecule within the $(\sqrt{3}\times\sqrt{3})$R30° unit cell to elucidate the interaction between a water monomer and the palladium layer of the Au/Mpy/Pd complex. This corresponds to a water coverage (Θ_{H_2O}) of 1/3 of a monolayer (ML) in which individual H_2O molecules are relatively isolated from each other and do not form intermolecular hydrogen bonds. In the second step we add another H_2O molecule to the layer thus increasing Θ_{H_2O} to 2/3 ML. As a consequence of the higher density, the water molecules form a hydrogen-bonded ice-like bilayer structure which is well-known from theoretical studies of water layers on close-packed hexagonal transition metal surfaces [18,19]. In this structure, every second H_2O molecule is in a parallel configuration with respect to the metal surface, forming bonds via the oxygen atom to one metal atom, while the other set of H_2O molecules are oriented with one hydrogen atom pointing either down or up, depending on the specific metal substrate.

Structure of water on the Au/Mpy/Pd junction

Two types of water orientation were considered as the starting geometry of the structure optimization of a single H_2O molecule on the Au/Mpy/Pd surface. First, we set the initial condition for the adsorption geometry of a H_2O monomer on bulk Pd(111), in which the oxygen atom is at the top site 2.28 Å above the surface with the O–H bonds oriented parallel to the surface [18]. The top site of both types of palladium atoms Pd_b and Pd_n was considered as the starting adsorption position. In addition, an initial water structure with one O–H bond oriented towards a palladium atom (H_{down} structure) was also used in the structure optimization since this structural motive is present in water bilayers on metal surfaces [18,19].

Only one stable position with an isolated H_2O molecule located at the top site of the Pd_b atom was found within the Au/Mpy/Pd/H_2O complex. The optimized structure is depicted in Figure 1. The geometry parameters of the most stable configurations together with the corresponding adsorption energies are listed in Table 1. The energy gain ($-E_{ads}$) upon adsorption of a single

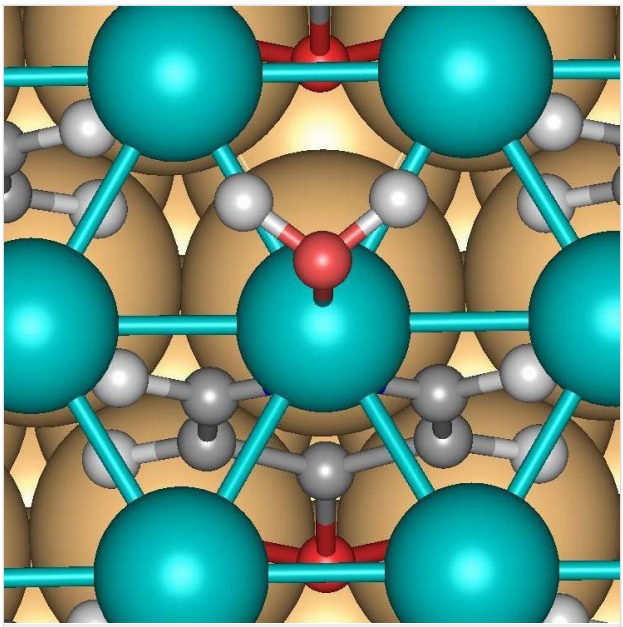

Figure 1: Top view of the optimized structure of a single H_2O molecule on the palladium monolayer of the $(\sqrt{3}\times\sqrt{3})$R30° Au/Mpy/Pd complex.

Table 1: Optimized geometry parameters and adsorption energies of a H_2O monomer and a H_2O hexagonal bilayer on a Au/Mpy/Pd contact within a $(\sqrt{3}\times\sqrt{3})$R30° geometry. The O–Pd_b value refers to the water molecule bound via the O atom to Pd, and the H–Pd_n distance is given for the H_{down} atom in the water bilayer. E_{ads} is the energy gain per H_2O molecule upon adsorption with respect to a H_2O molecule in the gas phase.

	distances Å			E_{ads} (eV)
	N–Pd_b	O–Pd_b	H–Pd_n	
Au/Mpy/Pd	2.09			
Au/Mpy/Pd/H_2O	2.01	2.12		−1.060
Au/Mpy/Pd/$(\sqrt{3}\times\sqrt{3})H_2O$	2.02	2.14	1.96	−0.837

H_2O molecule on the bare Au/Mpy/Pd system is about 1.060 eV indicating a rather strong interaction in contrast to the relatively weak interaction between H_2O and the (111) surfaces of transition metals [18,19]. Compared to water on bulk Pd(111), the O–Pd bond is shorter by about 0.12 Å. Interestingly, in this adsorption configuration the Pd_b atom is involved in two covalent bonds, to the H_2O molecule on the upper side through an O–Pd bond and to the Mpy-SAM through a N–Pd bond on the bottom side. Usually one would assume that the Pd atom that does not participate in the bonding to the SAM would show the stronger binding to additional adsorbates. Note that the N–Pd bond is only negligibly shortened with respect to the situation in the bare Au/Mpy/Pd complex. The water molecule assumes a flat configuration with the O–H bonds oriented parallel to the surface. The O–H bond is only slightly elongated by 0.02 Å and the H–O–H angle is negligibly reduced by 1.4° with respect to that for H_2O in the gas phase.

In order to check whether this is a consequence of the lowered coordination of the Pd atoms in the monolayer, or of the changes induced by the N–Pd_b interaction, we considered a free-standing palladium (111) monolayer using a (3 × 3) unit cell. Within this model, we first calculated the interaction of an isolated H_2O molecule with the bare monolayer ($Pd_{monolayer}$/H_2O), i.e., without any attached Mpy molecule. Interestingly enough, we obtained an adsorption energy of −0.34 eV with an O–Pd bond distance of 2.28 Å, which is similar to the situation for H_2O/Pd_{bulk} (111) [18], and this means that the water bonding to a free Pd(111) layer is weaker than that to a Pd layer deposited on the Mpy-SAM.

We extended the model by considering the additional adsorption of pyridine (Pyr) molecules on the other side of the Pd layer. This was motivated by the assumption that Pyr binds to Pd in the same way as Mpy since the sulfur head group of Mpy hardly affects the N–Pd contact. Upon the attachment of an up-right standing pyridine molecule to the Pd monolayer, with the water molecule adsorbed at the other side, the water adsorption energy was lowered to E_{ads} = −1.10 eV, i.e., the water binding became stronger, and the O–Pd_b distance decreased to 2.11 Å. Note that the optimized N–Pd bond length in this configuration is about 2.03 Å. This means that indeed the presence of a N–Pd_b bond leads to a stronger binding of water to the same Pd_b atom. The isolated H_2O molecule was also placed on top of the Pd_n atom neighboring the Pd_b atom that was involved in the interaction with the pyridine molecule. Surprisingly, this structure turned out to be unstable, and not even meta-stable, because of the strong attraction of the water molecule to the Pd_b atom.

In the next step we added a second water molecule on top of the Pd layer of the $(\sqrt{3}\times\sqrt{3})$R30° Au/Mpy/Pd structure to complete the ice-like water bilayer (H_2O_{hex}) and examined the interaction between this water bilayer and the Au/Mpy/Pd contact. The optimized geometry of this system is illustrated in Figure 2. There are two sets of H_2O molecules within the bilayer. In the optimized structure the first type of water molecule ($H_2O_{O–Pd}$) is located at the top site above the Pd_b atoms in a geometry similar to the one of a single H_2O molecule on Au/Mpy/Pd (Table 1). Both H atoms of this $H_2O_{O–Pd}$ molecule are involved in hydrogen bonds (H-bond) to two water molecules of the second type. In those H_2O molecules, only one hydrogen atom forms a H-bond to one $H_2O_{O–Pd}$ molecule, whereas the second H atom is directed towards one Pd_n atom with a Pd–H distance of 1.96 Å, corresponding to the H_{down} structure. Surprisingly, the H_{up} configuration is not stable on the Au/Mpy/Pd system. Consequently, there are three inequivalent Pd atoms within the monolayer: (i) The Pd_b atom directly interacting with the O atom of the H_2O molecule and the N atom of the Mpy molecule, respectively, (ii) the Pd_n atom interacting with the H atom of the second H_2O molecule, and (iii) the noninteracting Pd_n atom located in the middle of the hexagonal ring of the water bilayer.

The adsorption of H_2O molecules forming a H_2O_{hex} water bilayer on the Au/Mpy/Pd junction is less favorable than the adsorption of an isolated H_2O monomer (Table 1), by about ~0.22 eV per molecule. This is surprising since usually the attractive water–water interaction through intermolecular hydrogen bonds contributes significantly to the stability of

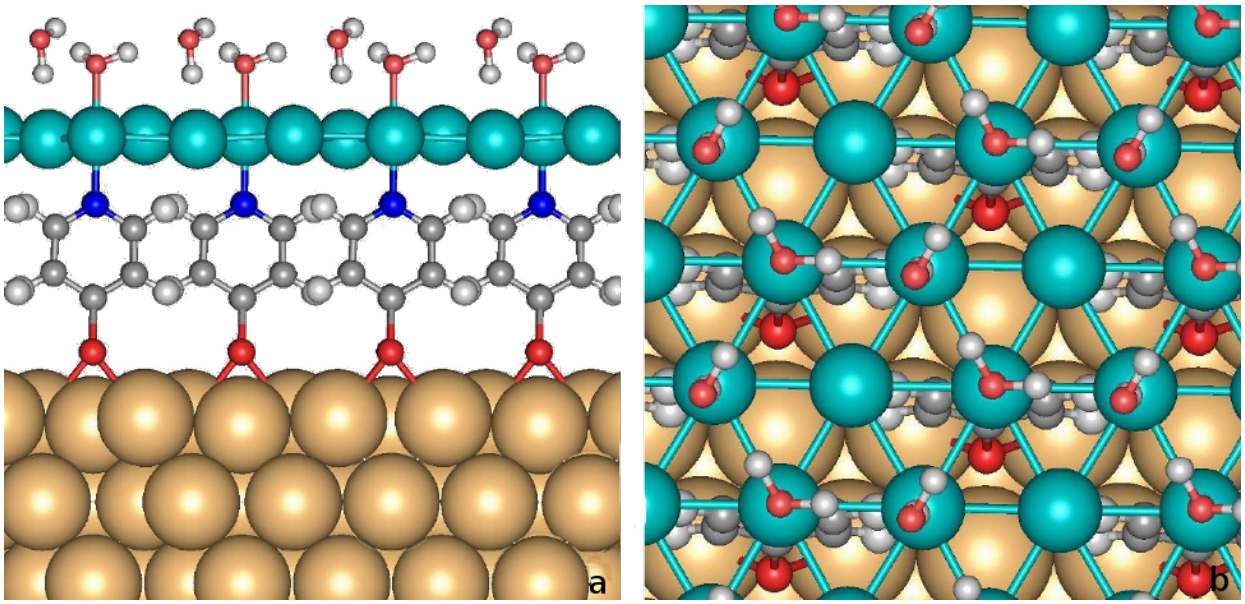

Figure 2: Side (a) and top (b) view of the optimized structure of water hexagonal bilayer on the palladium monolayer of $(\sqrt{3}\times\sqrt{3})$R30° Au/Mpy/Pd complex.

water layers on metal surfaces [16,18]. However, it has to be noted that there is no way to uniquely decompose the two contributions to the water adsorption energy since the strengths of the water–metal and the water–water bonding are not independent of one another [16]. Still, qualitative trends can be deduced when the adsorption energy of the water bilayer on the Au/Mpy/Pd complex is compared with the energy gain upon the formation of a free-standing water bilayer (i.e., without a metal substrate) in the geometry of the adsorbed H_2O_{hex} bilayer on the Au/Mpy/Pd complex. Note that the latter energy contribution is entirely due to the H-bond formation.

The energy gain upon the assembly of a free-standing relaxed water bilayer, within the used unit cell, amounts to ~0.37 eV per H_2O molecule. Using the geometry of the H_2O_{hex} bilayer on the Au/Mpy/Pd complex reduces the energy gain to ~0.20 eV as a consequence of the significant internal reorganization of the molecules in the bilayer upon the interaction with the Pd surface. Furthermore, in the bilayer not all water molecules are adsorbed in the optimal configuration as far as the water–metal bond is concerned, since only every second water molecules is bound via the oxygen atom to the metal. These two effects, reduced water–water attraction and non-optimal water adsorption configuration, together with a strong, dominating water metal bond, make the adsorption of isolated molecules energetically more favorable than the adsorption of the water bilayer, in contrast to bulk metal surfaces where the major contribution to E_{ads} appears to come from the intermolecular H-bonds [16,18].

Note furthermore that using a $(\sqrt{3}\times\sqrt{3})$R30° periodicity implies rather strict boundary conditions to the possible structures, e.g., it favors a hexagonal symmetry of the H_2O layers. In order to estimate the consequences of these geometry restrictions, we additionally considered a Pd monolayer using a (3 × 3) unit cell with three pyridine molecules placed at the positions corresponding to the $(\sqrt{3}\times\sqrt{3})$R30° structure, i.e., we considered a (3 × 3) Pyr/$Pd_{monolayer}$/H_2O_{hex} complex. By removing the pyridine molecules, the interaction between a pure $Pd_{monolayer}$ and a water bilayer was also examined.

We found no difference in the structural and energy parameters between the Pyr/$Pd_{monolayer}$/H_2O_{hex} and the Au/Mpy/Pd/H_2O_{hex} systems with respect to the water structure, i.e., E_{ads} = −0.85 eV and the O–Pd and H–Pd distances of 2.14 and 1.93 Å, respectively, remained basically unchanged. The H-bond contribution to E_{ads} is about −0.22 eV, similar to that in the $(\sqrt{3}\times\sqrt{3})$R30° unit cell. Upon removal of the Pyr molecules the H_2O layer became significantly relaxed. The O–Pd distance increased to 2.35 Å, but the Pd–H bond of 1.97 Å became only slightly elongated. Correspondingly, E_{ads} decreased to −0.51 eV, but, the energy of the H-bonds only changed by a small amount to −0.29 eV. Note that within the $Pd_{monolayer}$ / H_2O_{hex} structure the H_{up} water bilayer configuration turns out to be a local minimum, i.e., it becomes meta-stable, but it is still about 0.3 eV less stable than the H_{down} arrangement.

Apparently, the stronger binding between the water molecules and the palladium monolayer deposited on top of the SAM

compared to water on bulk metal substrates is due to the presence of the Mpy molecules binding to Pd from the bottom side. The fact that the palladium atoms in the (111) monolayer are less coordinated than the Pd atoms in a (111) surface apparently plays a minor role for the stability in the water complex. Ab initio molecular dynamics simulations showed that at room temperature the hexagonal water bilayer structure on bulk metal surfaces becomes disordered [19], but it may persist on the Au/Mpy/Pd junction because of the higher stability of the H_2O layer, which is not governed by intermolecular H-bond interactions. Still, it could strongly depend on the structure of the molecules in the SAM on which the Pd layer is deposited.

Note that so far we have only considered situations in which the lateral lattice constant of the Pd layer is dictated by the periodicity of the Au(111) substrate. However, it is fair to say that the Pd–Pd distance in the real system is not known, because in the scanning tunneling microscopy (STM) measurements the lateral distances could not be exactly calibrated [8]. It might well be that the Pd layer is not commensurate with the Au(111) substrate. A modified Pd–Pd spacing would of course influence the strength of the O–Pd bonds [28-30] and the H-bonds within the bilayer and thus affect the stability of the H_2O layer on the Pd monolayer. In order to check the effect of varying the Pd–Pd distance on the stability of the H_2O/Pd complex we changed the lateral constant of the (3 × 3) structure in a systematic fashion to cover Pd–Pd distances from 2.65 Å to 2.95 Å. The lower limit with a Pd–Pd distance of 2.65 Å corresponds to that for the optimized free-standing Pd monolayer [8], whereas the upper limit of 2.95 Å is the nearest-neighbor distance in bulk Au, which has been used in the calculations of the whole junction. The total adsorption energies together with the energy contribution coming from the H-bonds for the H_2O bilayer, either (i) free-standing (without a Pd monolayer), or (ii) interacting with the bare Pd monolayer, or (iii) interacting with the Pyr/Pd complex, are plotted in Figure 3.

The water adsorption energy E_{ads} in a bilayer on the Pyr/$Pd_{monolayer}$ complex decreases slightly with decreasing Pd–Pd distance, by about 0.06 eV per 0.1 Å. At the same time, the stabilization energy of the free-standing H_2O bilayer coming from the H-bonds increases by only about 0.015 eV per 0.1 Å, thus remaining almost constant in the range of the considered lattice constants.

Hence it is not surprising that in the Pyr/$Pd_{monolayer}$/H_2O_{hex} system the energy contribution coming from H-bonds remains practically constant, being about 0.2 eV smaller than the stabilization energy of the pure H_2O bilayer. This means that a change of E_{ads} upon a variation of the Pd–Pd lattice spacing is almost entirely due to the modification of the O–Pd interaction

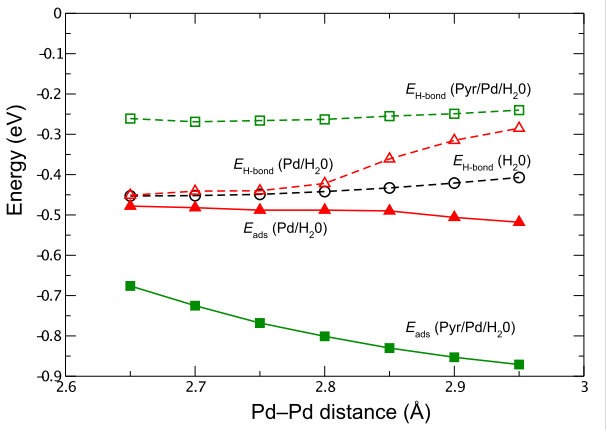

Figure 3: Adsorption energies E_{ads} of the water bilayer together with the contribution originating entirely from H-bonds E_{H-bond} obtained within a (3 × 3) unit cell as a function of the Pd–Pd distance from 2.65 Å to 2.95 Å, which are the nearest-neighbor distances in a free Pd monolayer and in bulk Au, respectively. The latter value has been used in the calculations of the full junction. Water in the bilayer structure is adsorbed on the (3 × 3) Pd monolayer without (Pd/H_2O) and in the presence of pyridine molecules attached to the bottom side of the Pd layer (Pyr/Pd/H_2O). The H-bond energy contribution of a free-standing H_2O bilayer (H_2O) without Pd was added as a reference.

strength. Since this dependence is also rather weak, there should only be a small influence of the Pd lattice spacing on the stability of the water bilayer on the Au/Mpy/Pd junction.

Electronic properties of the Au/Mpy/Pd/H_2O complex

The stabilization of the water adsorption on the Pd layer by the interaction with the underlying SAM is a rather surprising result, because usually one would assume that a higher coordination of the Pd atoms would lead to a smaller binding strength. In order to elucidate the nature of the N_{Mpy}–Pd_b–O_w bonding and its effect on the electronic structure of the Au/Mpy/Pd junction we determined the local density of states (LDOS) of the species involved in the complex formation, namely nitrogen, Mpy, oxygen, and palladium. The spectra of the various atoms are plotted in Figure 4.

As evident from Figure 4, the electronic structure of the Pd_b atom is considerably modified upon the formation of the N–Pd–O bonding complex compared to the LDOS of the non-interacting Pd_n. The latter LDOS is in fact rather close to that of a bare Pd monolayer (e.g., [8]). The Pd_b atom exhibits a significant reduction of the LDOS near the Fermi energy, whereas the small change of the LDOS of the Pd_n atom indicates that the effect of the N_{Mpy}–Pd_b–O_w bond is rather localized.

Figure 4 indicates furthermore that there is a hybridization between N_{Mpy}, O_w, and Pd_b states (marked by the arrows in Figure 4) leading to three separated peaks localized at −4.46,

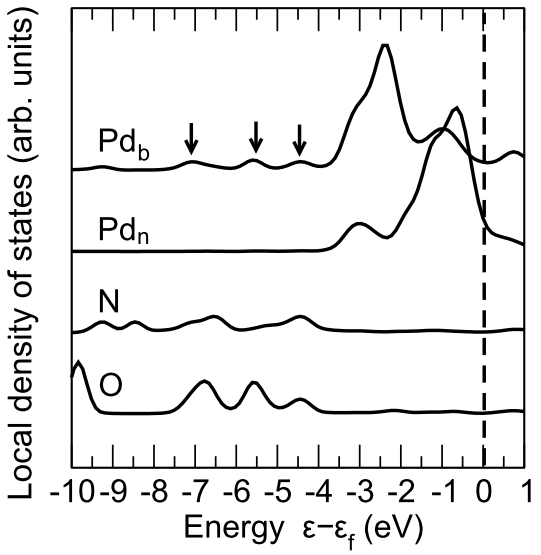

Figure 4: Local density of states (LDOS) of the Au/Mpy/Pd/H_2O complex at a water coverage of Θ_{H_2O} = 1/3 ML. Plotted, from the top, is the LDOS of the Pd_b atom bound to the nitrogen atom of 4-mercaptopyridine and the oxygen atom of the water molecule, of the Pd_n atom not interacting with any molecules, of the nitrogen atom (N) of the 4-mercaptopyridine molecule, and of the oxygen atom of the water molecule (O). The bonding states between Pd_b, N, and O atoms are marked with arrows.

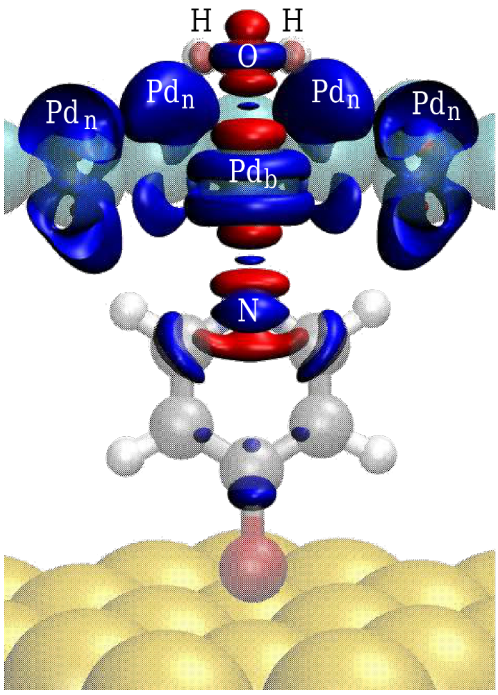

Figure 5: Charge density difference in an isodensity representation calculated as the difference between the charge density of the Au/Mpy/Pd/H_2O complex and the sum of the charge densities of the Au/Mpy, Pd, and H_2O subsystems. Blue and red surfaces depict the region of charge accumulation and depletion, respectively. The selected surfaces correspond to the charge isodensity of 0.016 *e*/Å^3 and −0.044 *e*/Å^3 encapsulating the total charge of 0.44 and −0.44 *e*, respectively.

−5.56, and −6.98 eV below E_f. As a further consequence, the Pd_b LDOS close to the Fermi level is reduced, and the maximum of the Pd_b LDOS is shifted to about −2.35 eV below E_f.

Such a strong change of the density of states also indicates a substantial charge transfer between the involved constituents. This is illustrated by the charge density difference isodensity surfaces shown in Figure 5, which correspond to the difference between the charge density of the interacting Au/Mpy/Pd/H_2O complex and the sum of the charge densities of the isolated Au/Mpy, Pd, and H_2O subsystems in the same configuration. There is a strong charge rearrangement along both the N–Pd_b and Pd_b–O bonds indicative of the covalent character of the bonds. The calculated patterns suggest a hybridization between the p_z orbitals of N_{Mpy} and O_w, and the d_{z^2} orbital of the Pd_b atoms upon the formation of the N_{Mpy}–Pd_b–O contact with *z* being the coordinate along the surface normal. However, the regions of the charge depletion are relatively localized in the region of the covalent bonds, and Figure 5 also reveals a diffuse charge accumulation around the non-bonding Pd_n atoms.

In order to get a more quantitative picture of the charge redistribution within the molecule/metal complex, we performed a Bader analysis [31,32]. To estimate the influence of water on the charge transfer we compare the results of the system without water (Au/Mpy/Pd) with the results for the system with adsorbed water (Au/Mpy/Pd/H_2O). The results are summarized in Table 2.

Table 2: Bader analysis of the total electronic charge depletion/accumulation in the Au slab, the 4-mercaptopyridine molecule, the palladium layer (in parenthesis: Charge localized on the Pd_b atom only), and the water layer (H_2O) within the Au/Mpy/Pd, Au/Mpy/Pd/H_2O, and Au/Mpy/Pd/$(\sqrt{3}\times\sqrt{3})H_2O$ complexes. The partial charge excess/deficiency, in electrons (*e*), is defined relative to the uncharged subsystems.

	Au	Mpy	Pd (Pd_b)	H_2O
Au/Mpy/Pd	+0.167	−0.230	+0.062 (+0.232)	
Au/Mpy/Pd/H_2O	+0.161	−0.268	+0.075 (+0.359)	+0.032
Au/Mpy/Pd/$(\sqrt{3}\times\sqrt{3})H_2O$	+0.158	−0.272	+0.130 (+0.354)	−0.016

In the bare Au/Mpy/Pd system without water adsorption, the Mpy molecular layer sandwiched between the Au substrate and the Pd monolayer becomes negatively charged. Consequently, there is an electron deficiency at both metal electrodes. This suggests a substantial polarization at both interfaces. The electrons are transferred from Au to Mpy along the two-fold coordinated S–Au bonds. This is completed by the additional electron transfer from Pd to Mpy via a single N–Pd_b bond. Closer inspection of the charge distribution within the Pd layer (note that the charge of the Pd_b atom is listed in parentheses in Table 2) reveals a substantial redistribution of the electron density between the Pd_b and Pd_n atoms. Although there is a charge deficiency of about 0.232 *e* on the Pd_b atom, the electron density on the two Pd_n atoms per unit cell is increased by 0.17 *e* clearly indicating an electron transfer from Pd_b to Pd_n.

Upon the adsorption of a single H_2O molecule on the Pd layer, the accumulation of electrons at the Mpy molecule further increases, but the electron depletion at the Au electrode remains practically unaltered. This means that the S–Au bond is hardly affected by the adsorption of water on the palladium layer. This is also reflected in the length of the S–Au bond, which does not change upon the water adsorption, remaining at 2.57 Å. The electron gain of Mpy due to the H_2O→Pd→Mpy charge transfer is accompanied by charge depletion on the H_2O molecule and a further polarization within the Pd layer through charge transfer from Pd_b to Pd_n. This inner polarization explains why a single H_2O molecule does not form a (meta-)stable structure on-top of the Pd_n atoms. The higher electron density at the Pd_n atoms increases the Pauli repulsion between the electron clouds of the closed-shell H_2O molecule and the Pd_n atoms. As a consequence, Pd_n atoms would not be covered by water molecules at low water coverage.

Although the character of the interaction between the oxygen atom of the H_2O molecule and the Pd_n atom is repulsive, the interaction between the hydrogen atom of the H_2O molecule and the Pd_n atom must be attractive since the H_2O bilayer on Au/Mpy/Pd is preferentially oriented in the H_{down} configuration with the hydrogen atoms pointing towards the Pd_b atoms thus forming Pd_n–H bonds. Since the electron screening of the hydrogen nucleus in the H_2O molecule is partially weakened due to the polarization of the O–H bond, the hydrogen atom can then bind to the additional electrons on the Pd_n atom. The electron density in fact shifts from the Pd_n atom to the H atoms of the water molecule, which is suggested by the increased electron deficiency within the whole Pd layer upon the deposition of the water bilayer. The charge at the Pd_b atom, however, remains the same compared to the case of the adsorption of a single water molecule on the Au/Mpy/Pd junction.

Finally, we compare the calculated total DOS of the palladium monolayer in the presence of various amounts of water with the experimental UPS spectrum of the palladium layer in the Au/Mpy/Pd system [8]. The DOS of the Pd monolayer in the Au/Mpy/Pd junction with Θ_{H_2O} = 0, 1/3 ML (isolated H_2O), and 2/3 ML (water bilayer) is plotted in Figure 6 together with the experimental spectrum adopted from [8]. The theoretical results should be compared to the calculated LDOS of the free-standing Pd monolayer plotted in [8]. The results can be summarized as follows: (i) Despite the strong interaction between water and the Au/Mpy/Pd complex, the presence of water induces only a negligible modification of the Pd LDOS compared to the bare Au/Mpy/Pd model; (ii) The LDOS of the Pd layer with the two different water coverages is basically equivalent; (iii) In strong contrast to the experimental spectrum none of the calculated LDOS shows a considerable reduction of the DOS near the Fermi energy.

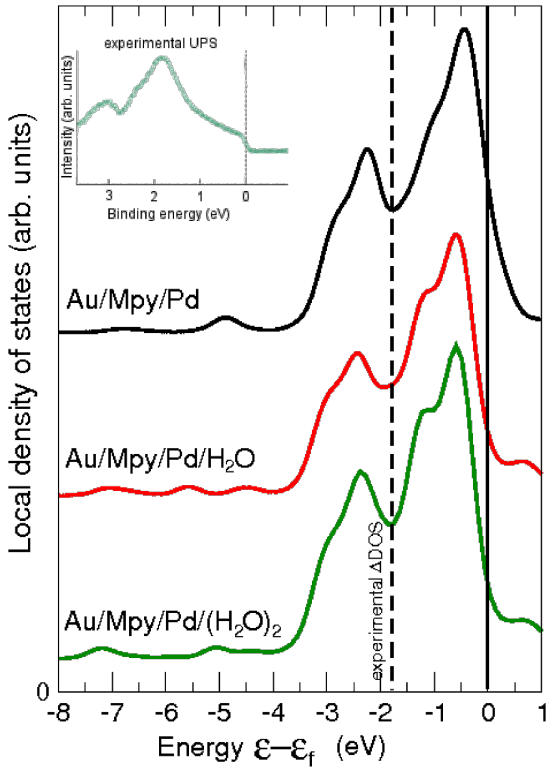

Figure 6: Local density of states of the Pd monolayer of the Au/Mpy/Pd system with and without water. Au/Mpy/Pd denotes bare the system without water, Au/Mpy/Pd/H_2O denotes an isolated H_2O molecule on the surface (Θ_{H_2O} = 1/3 ML), and Au/Mpy/Pd/$(H_2O)_2$ denotes a water hexagonal bilayer attached on the surface (Θ_{H_2O} = 2/3 ML). In the inset, the experimental UPS spectrum of the corresponding system is included (adopted from [8]).

It is in fact unsurprising that the LDOS of the Pd layer with the isolated H_2O molecule and with the H_2O bilayer structure are so similar, as the residual bond between the H atom of the H_2O molecule and the Pd atom is rather weak. Concerning the overall character of the spectra, qualitatively these are convoluted from the contributions of Pd_n and Pd_b atoms, which are present in the monolayer in a ratio of 2/1. This means that the Pd_n atoms which exhibit only a small downshift of the LDOS dominate the DOS of the whole Pd monolayer independent whether there is only a N–Pd_b bond (in the system without water) or a N–Pd_b–O bond (in the presence of water) since both bonding types affect the Pd monolayer only locally. Consequently, the adsorption of water cannot explain the observed downshift of the Pd DOS.

On the other hand, the rather stable water structures on the Au/Mpy/Pd junction might have a considerable impact on the adsorption of other species and directly influence the concentration of adsorbates on the Pd surface in equilibrium. As an alternative explanation, the adsorption of hydrogen atoms on the Pd layer might explain the observed UPS spectra since the presence of hydrogen on a Au/SAM/Pd junction can change the electronic structure of the Pd layer rather significantly, as shown in the case of the Au/ATP/Pd complex [12]. Work along this line is in progress.

Conclusions

We have investigated the geometric and electronic structure of a Au/Mpy/Pd junction upon the adsorption of water by first principles electronic structure calculations based on density functional theory. An isolated water molecule on the palladium monolayer of the Au/Mpy/Pd junction forms a relatively stable complex bonded through the oxygen atom of water to a single palladium atom. This bond is in fact stabilized through the N–Pd bond of the Pd layer with the underlying SAM leading to a much higher water adsorption energy on the Pd monolayer compared to bulk Pd(111). This stabilization is also present in an ice-like hexagonal water bilayer adsorbed in a $(\sqrt{3}\times\sqrt{3})$R30° structure on the Au/Mpy/Pd junction. This is caused by a strong polarization within the Pd monolayer induced by the Pd–N bond.

The formation of the N–Pd–O complex causes a significant modification of the local density of states of the Pd atom involved in this complex, resulting in a large decrease of the LDOS at the Fermi level. On the other hand, the LDOS of the other Pd atoms not interacting with the Mpy and the H_2O molecules is hardly changed. The overall DOS of the Pd layer is only weakly modified by the adsorption of water which thus can not explain the experimentally observed strong reduction of the DOS of the Pd layer in the junction at the Fermi energy.

Experimental

Self-consistent periodic DFT calculations were performed employing the Vienna ab initio simulation package (VASP) [33]. The exchange-correlation effects were described within the generalized gradient approximation using the Perdew–Burke–Ernzerhof (PBE) functional [34]. The interaction of the electrons with the ionic cores was treated with the projected augmented wave (PAW) method [35,36], and the Kohn–Sham one-electron valence states were expanded in a basis of plane waves with a cutoff energy of 400 eV. All calculations were spin-polarized since palladium in low-dimensional structures can become magnetic [37].

Most of the calculations are done for a $(\sqrt{3}\times\sqrt{3})$ surface unit cell. Within the supercell approach the Au(111) substrate was represented by slabs of five-layers, in which the two topmost layers were relaxed during the geometry optimization, while the rest of the gold atoms were kept fixed at the positions corresponding to the bulk Au crystal. The Au lattice spacing [d(Au–Au) = 2.95Å] was adopted from the equilibrium geometry of bulk Au calculated at the same level of the theory. To separate the Au slabs in the non-periodic direction along the surface normal a vacuum region of thickness 28 Å was inserted into the supercell. To carry out the Brillouin-zone integration, a Monkhorst–Pack [38] of 11 × 11 × 1 k-points were used.

The local density of states (LDOS) was calculated in order to interpret the experimental UPS spectra [8] of the palladium layer. To compare the experiment with the theoretical results we convoluted the calculated LDOS with a Gaussian of width 0.2 eV, thus taking into account the finite energy resolution of the experimental spectra as well as the generally observed broadening of spectroscopic features due to the finite life time of the photoionized states.

Acknowledgements

Financial support by the Deutsche Forschungsgemeinschaft (DFG) within SFB 569 is gratefully acknowledged. Computational resources have been provided by the bwGRiD project of the Federal State of Baden-Württemberg/Germany.

References

1. Baunach, T.; Ivanova, V.; Scherson, D. A.; Kolb, D. M. *Langmuir* **2004,** *20,* 2797. doi:10.1021/la035389t
2. Manolova, M.; Boyen, H.-G.; Kučera, J.; Groß, A.; Romanyuk, A.; Oelhafen, P.; Ivanova, V.; Kolb, D. M. *Adv. Mater.* **2009,** *21,* 320. doi:10.1002/adma.200801634
3. Eberle, F.; Kayser, M.; Kolb, D. M.; Saitner, M.; Boyen, H.-G.; D'Olieslaeger, M.; Mayer, D.; Wirth, A. *Langmuir* **2010,** *26,* 4738. doi:10.1021/la1000232

4. Eberle, F.; Metzler, M.; Kolb, D. M.; Saitner, M.; Wagner, P.; Boyen, H.-G. *ChemPhysChem* **2010,** *11,* 2951. doi:10.1002/cphc.201000309
5. Manolova, M.; Ivanova, V.; Kolb, D. M.; Boyen, H.-G.; Ziemann, P.; Büttner, M.; Romanyuk, A.; Oelhafen, P. *Surf. Sci.* **2005,** *590,* 146. doi:10.1016/j.susc.2005.06.005
6. Manolova, M.; Kayser, M.; Kolb, D. M.; Boyen, H.-G.; Ziemann, P.; Mayer, D.; Wirth, A. *Electrochim. Acta* **2007,** *52,* 2740. doi:10.1016/j.electacta.2006.08.038
7. Eberle, F.; Saitner, M.; Boyen, H.-G.; Kučera, J.; Groß, A.; Romanyuk, A.; Oelhafen, P.; D'Olieslaeger, M.; Manolova, M.; Kolb, D. M. *Angew. Chem., Int. Ed.* **2010,** *49,* 341. doi:10.1002/anie.200905339
8. Boyen, H.-G.; Ziemann, P.; Wiedwald, U.; Ivanova, V.; Kolb, D. M.; Sakong, S.; Groß, A.; Romanyuk, A.; Büttner, M.; Oelhafen, P. *Nat. Mater.* **2006,** *5,* 394. doi:10.1038/nmat1607
9. Ulusoy, I. S.; Scribano, Y.; Benoit, D. M.; Tschetschetkin, A.; Maurer, N.; Koslowski, B.; Ziemann, P. *Phys. Chem. Chem. Phys.* **2011,** *13,* 612. doi:10.1039/C0CP01289K
10. Keith, J. A.; Jacob, T. *Electrochim. Acta* **2010,** *55,* 8258. doi:10.1016/j.electacta.2010.04.027
11. Keith, J. A.; Jacob, T. *Chem.–Eur. J.* **2010,** *16,* 12381. doi:10.1002/chem.201001396
12. Kučera, J.; Groß, A. *Phys. Chem. Chem. Phys.* **2010,** *12,* 4423. doi:10.1039/b923700c
13. Henderson, M. A. *Surf. Sci. Rep.* **2002,** *46,* 1. doi:10.1016/S0167-5729(01)00020-6
14. Feibelman, P. J. *Science* **2002,** *295,* 99. doi:10.1126/science.1065483
15. Meng, S.; Xu, L. F.; Wang, E. G.; Gao, S. W. *Phys. Rev. Lett.* **2002,** *89,* 176104. doi:10.1103/PhysRevLett.89.176104
16. Roudgar, A.; Groß, A. *Chem. Phys. Lett.* **2005,** *409,* 157. doi:10.1016/j.cplett.2005.04.103
17. Roudgar, A.; Groß, A. *Surf. Sci.* **2005,** *597,* 42. doi:10.1016/j.susc.2004.02.040
18. Michaelides, A. *Appl. Phys. A* **2006,** *85,* 415. doi:10.1007/s00339-006-3695-9
19. Schnur, S.; Groß, A. *New J. Phys.* **2009,** *11,* 125003. doi:10.1088/1367-2630/11/12/125003
20. Carrasco, J.; Santra, B.; Klimeš, J.; Michaelides, A. *Phys. Rev. Lett.* **2011,** *106,* 026101. doi:10.1103/PhysRevLett.106.026101
21. Schnur, S.; Groß, A. *Catal. Today* **2011,** *165,* 129. doi:10.1016/j.cattod.2010.11.071
22. Cerdá, J.; Michaelides, A.; Bocquet, M.-L.; Feibelman, P. J.; Mitsui, T.; Rose, M.; Fomin, E.; Salmeron, M. *Phys. Rev. Lett.* **2004,** *93,* 116101. doi:10.1103/PhysRevLett.93.116101
23. Tatarkhanov, M.; Ogletree, D.; Rose, F.; Mitsui, T.; Fomin, E.; Maier, S.; Rose, M.; Cerdá, J.; Salmeron, M. *J. Am. Chem. Soc.* **2009,** *131,* 18425. doi:10.1021/ja907468m
24. Nie, S.; Feibelman, P.; Bartelt, N.; Thürmer, K. *Phys. Rev. Lett.* **2010,** *105,* 026102. doi:10.1103/PhysRevLett.105.026102
25. Michaelides, A.; Ranea, V. A.; de Andres, P. L.; King, D. A. *Phys. Rev. Lett.* **2003,** *90,* 216102. doi:10.1103/PhysRevLett.90.216102
26. Gohda, Y.; Schnur, S.; Groß, A. *Faraday Discuss.* **2009,** *140,* 233. doi:10.1039/b802270d
27. Kučera, J.; Groß, A. *Langmuir* **2008,** *24,* 13985. doi:10.1021/la802368j
28. Mavrikakis, M.; Hammer, B.; Nørskov, J. K. *Phys. Rev. Lett.* **1998,** *81,* 2819. doi:10.1103/PhysRevLett.81.2819
29. Groß, A. *Top. Catal.* **2006,** *37,* 29. doi:10.1007/s11244-006-0005-x
30. Groß, A. *J. Phys.: Condens. Matter* **2009,** *21,* 084205. doi:10.1088/0953-8984/21/8/084205
31. Bader, R. F. W. *Atoms in Molecules - A Quantum Theory;* Oxford University Press: Oxford, 1990.
32. Henkelman, G.; Arnaldsson, A. H.; Jónsson, H. *Comput. Mater. Sci.* **2006,** *36,* 354. doi:10.1016/j.commatsci.2005.04.010
33. Kresse, G.; Furthmüller, J. *Phys. Rev. B* **1996,** *54,* 11169. doi:10.1103/PhysRevB.54.11169
34. Perdew, J. P.; Burke, K.; Ernzerhof, M. *Phys. Rev. Lett.* **1996,** *77,* 3865. doi:10.1103/PhysRevLett.77.3865
35. Blöchl, P. E. *Phys. Rev. B* **1994,** *50,* 17953. doi:10.1103/PhysRevB.50.17953
36. Kresse, G.; Joubert, D. *Phys. Rev. B* **1999,** *59,* 1758. doi:10.1103/PhysRevB.59.1758
37. Groß, A. *Theoretical surface science – A microscopic perspective,* 2nd ed.; Springer: Berlin, 2009.
38. Monkhorst, H. J.; Pack, J. D. *Phys. Rev. B* **1976,** *13,* 5188. doi:10.1103/PhysRevB.13.5188

License and Terms

The definitive version of this article is the electronic one which can be found at: doi:10.3762/bjnano.2.44

Beilstein Journal of Nanotechnology

Simulation of bonding effects in HRTEM images of light element materials

Simon Kurasch*[1], Jannik C. Meyer[1,2], Daniela Künzel[3], Axel Groß[3] and Ute Kaiser[1]

Full Research Paper

Open Access

Address:
[1]Central Facility for Electron Microscopy, Group of Electron Microscopy of Materials Science, University of Ulm, 89081 Ulm, Germany, [2]New Address: University of Vienna, Department of Physics, 1090 Vienna, Austria and [3]Institute of Theoretical Chemistry, University of Ulm, 89069 Ulm, Germany

Email:
Simon Kurasch* - simon.kurasch@uni-ulm.de

* Corresponding author

Keywords:
chemical bonding; DFT; graphene; HRTEM

Beilstein J. Nanotechnol. **2011,** *2,* 394–404.
doi:10.3762/bjnano.2.45

Received: 18 April 2011
Accepted: 17 June 2011
Published: 19 July 2011

This article is part of the Thematic Series "Organic–inorganic nanosystems".

Guest Editor: P. Ziemann

Abstract

The accuracy of multislice high-resolution transmission electron microscopy (HRTEM) simulation can be improved by calculating the scattering potential using density functional theory (DFT) [1,2]. This approach accounts for the fact that electrons in the specimen are redistributed according to their local chemical environment. This influences the scattering process and alters the absolute and relative contrast in the final image. For light element materials with well defined geometry, such as graphene and hexagonal boron nitride monolayers, the DFT based simulation scheme turned out to be necessary to prevent misinterpretation of weak signals, such as the identification of nitrogen substitutions in a graphene network. Furthermore, this implies that the HRTEM image does not only contain structural information (atom positions and atomic numbers). Instead, information on the electron charge distribution can be gained in addition.

In order to produce meaningful results, the new input parameters need to be chosen carefully. Here we present details of the simulation process and discuss the influence of the main parameters on the final result. Furthermore we apply the simulation scheme to three model systems: A single atom boron and a single atom oxygen substitution in graphene and an oxygen adatom on graphene.

Introduction

Conventional HRTEM image simulation so far neglects all kinds of interatomic interactions within the specimen by calculating the total specimen potential as a superposition of isolated atom potentials [3]. It is generally known that the state of an atom is, of course, influenced by its environment and hence techniques that are more sensitive to changes in the electronic

state, such as electron energy loss spectroscopy [4] or scanning tunneling microscopy [5], make use of advanced simulation methods to model the specimen.

In 1997, Gemming and Möbus performed ab-initio HRTEM simulations of ionic crystals and justified the use of conventional image simulation [1]. About ten years later, and after enormous improvement in electron optics and the resolution of the TEM by means of aberration correction [6,7], Deng et al. [2,8] performed DFT based HRTEM calculations for bulk oxides and found that chemical bonding should be detectable and in practice is hindered only by the poor specimen quality obtained by ion-beam thinning. Furthermore they pointed out that it is possible to study charge transfer by other techniques such as convergent beam electron diffraction [9,10] but all methods available can only offer global information as they observe the charge distribution in reciprocal space. In contrast, the observation of the same effect in real space using HRTEM would result in local information, which would open new frontiers for electron microscopy [2,11].

Previous studies were focused on bulk oxides, because they are known to have strong ionic bonds. Our target materials, in contrast, are two dimensional crystals such as graphene and hexagonal boron nitride as they offer an outstanding specimen quality that has not been achieved for bulk materials so far: Their thickness is perfectly defined (one atomic layer) and it is possible to find areas without defects and without amorphous top and bottom layers. Furthermore both of our target materials are built from exclusively light elements where strong bonding effects can be expected because most of their electrons are valence electrons. Another important factor for the experimental detection of these effects in HRTEM is that the contrast of boron, carbon, nitrogen and oxygen is almost identical under our imaging conditions [12] (shown by the black curve in Figure 1). Hence even small contrast variations are relatively easy to detect.

Due to these improvements in specimen quality, for the first time, we were able to measure the influence of charge redistribution on the HRTEM image contrast experimentally for two different materials, namely nitrogen doped graphene and single-layer hexagonal boron nitride [13]. This result has two important implications: First, chemical bonding gives small corrections to the atomic contrast in the TEM, which has to be kept in mind whenever weak signals are analyzed. Second, and probably more importantly, the HRTEM image is not only governed by structural information but also contains information about the electronic state of the specimen. This allows the study of the electron charge distribution in point defects and other nanoscaled objects that can not be accessed by diffraction experiments.

Here we give detailed information on the DFT based simulation used in [13] and explain the analysis for three model systems: A single atom boron and a single atom oxygen substitution in graphene and an oxygen adatom on graphene.

Experimental

Modeling the HRTEM image formation

High resolution TEM image simulation can be separated in three main parts: First the interaction between the incident elec-

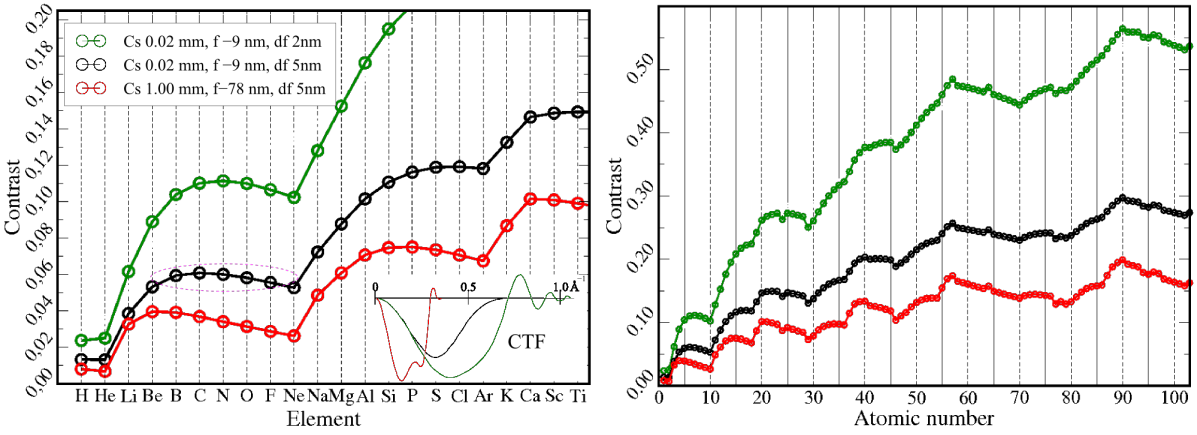

Figure 1: Analysis of atomic contrast for different TEM conditions at 80 kV obtained using a code of E. Kirkland [4]. The red curve corresponds to an uncorrected microscope and the black one to a state of the art C_s corrected microscope. The green curve is obtained when, in addition to C_s correction, the focus spread is reduced. This results in better resolution and can be achieved by a monochromator or a C_s corrector (inelastic scattering is neglected). The phase contrast transfer functions for the different microscopes and corresponding values of spherical aberration C_s, defocus *f* and focus spread *df* are shown in the inset. Importantly, one can find combinations of elements (such as B, C, N, O, marked by the dashed circle), where the neutral-atom contrast differences are very small and hence may potentially be dominated by bonding effects.

tron wave and the specimen is modeled and the specimen exit wave is obtained. Afterwards the specimen exit wave becomes the ”object” for the imaging system of the electron microscope, which produces the image intensity impinging on the recording medium [14]. Finally, the characteristics of the detector are taken into account [15].

The interaction with the specimen is described by a very simple scattering process where the incident high energy electron is scattered by the combined Coulomb potential of all atomic nuclei and electrons within the specimen. Mathematically one has to solve a relativistic version of the Schrödinger Equation 1, where $\Psi(\vec{x})$ is the wave function of the electron at position $\vec{x}$, m is the relativistic mass of the electron and $V_s(\vec{x})$ is the specimen potential.

$$\left[-\frac{h}{2m}\nabla^2 - eV_s(\vec{x})\right]\Psi(\vec{x}) = E\Psi(\vec{x}) \tag{1}$$

In the limit of high energy electrons, backscattering can be neglected and Equation 1 can be solved using the multislice algorithm. In this study we focus on single layer materials of light elements. Hence the exit wave can be calculated (in a single-slice approximation) by Equation 2, where σ is the interaction parameter and V_z is the projected specimen potential [3]. In addition, for these structures and our imaging conditions, it turned out that the linear image approximation (Equation 3) is justified, as found by comparison of the result with the standard calculation. The amplitude spectrum of the wave in the imaging plane $\psi_{image}(q_x, q_y)$ can be derived from the Fourier space specimen exit wave $\psi_{ex}(q_x, q_y)$ by multiplication with the objective lens phase factor function $\exp[i\chi(q_x, q_y)]$, where $\chi(q_x, q_y)$ depends on the defocus Δf, spherical aberration C_s and higher order aberrations [14]. The exact expression of $\chi(q_x, q_y)$ can be found in [16]. Because the structures studied here are weak scatterers, the linear imaging condition is justified and, for an incident plane wave, the final image intensity is given by Equation 5 [14].

$$\begin{aligned}\Psi_{ex}(x,y) &= \exp\left[i\sigma\int_{-\infty}^{+\infty} V_s(x,y,z)\,dz\right]\Psi_{in} \\ &= \exp\left[i\sigma V_z(x,y)\right]\Psi_{in}(x,y)\end{aligned} \tag{2}$$

$$\approx \left(1 - i\sigma V_z(x,y)\right)\Psi_{in}(x,y) \tag{3}$$

$$\Psi_{image}(q_x,q_y) = \exp\left[i\chi(q_x,q_y)\right]\Psi_{ex}(q_x,q_y) \tag{4}$$

$$I_{image}(x,y) = 1 + 2\sigma \mathrm{FT}^{-1}\left[\sin\left(\chi(q_x,q_y)\right)\cdot \mathrm{FT}\left[V_z(x,y)\right]\right] \tag{5}$$

Of course this is a very simple model of the real scattering process, which neglects all kinds of inelastic processes by assuming that the state of the specimen is not at all influenced by the presence of the high energy electrons. Nevertheless, it is well established for HRTEM simulation and in this work we use exactly the same framework (with all its limitations) but focus on a very fundamental question: How do we obtain the scattering potential? The standard approach is to calculate the total specimen potential as a superposition of isolated atom potentials, which have been calculated previously for each element by solving the quantum many body problem for all electrons and the nuclei of a single atom. One example are the potentials published by Doyle and Turner in 1968 [17]. Their paper was based on atomic potentials obtained by relativistic Hartree–Fock self-consistent field calculations performed by Coulthard in 1967 [18], where the main assumption was that the atomic charge distribution is spherically symmetric.

A more accurate way is to include electronic interactions between atoms in the specimen by DFT. In this way, ionic atoms with non-spherical electron distributions can be modeled without any a priori knowledge.

How to obtain DFT potentials

The DFT calculation was performed in two steps: First we performed a structure optimization of an initial atomic configuration by using the very fast and efficient pseudopotential DFT code VASP [19]. Unfortunately it was not possible to extract the total electrostatic potential directly from the pseudopotential calculation as it only offers the self consistent valence charge density but the total charge density is needed. Hence, in a second step, we used the relaxed structure to set up an all electron DFT calculation, and therefore we used the WIEN2k [20] DFT software. Furthermore, WIEN2k has the significant advantage that, besides offering access to the total electron charge density and corresponding X-ray scattering factors, in addition, the calculation of the total Coulomb potential (including all electrons and nuclei within the unit cell) is already implemented. Deng and Marks [8] used the X-ray scattering factors, while our method directly makes use of the available potential file.

A very important cross-check is to compare the WIEN2k potential to other potentials used in HRTEM simulations. This is easy to achieve, because the starting point for the DFT calculation (before the first iteration cycle) is also built up from isolated atom potentials, and the subsequent iteration process, searching

for a self-consistent field (SCF) solution, acts as a minor perturbation to the initial potential. In Figure 2 we compare the initial WIEN2k potential of a single carbon atom to Kirkland [3] and Doyle–Turner [17] isolated atom potentials. The WIEN2k potential was obtained by putting a single carbon atom into a 10 Å × 10 Å × 10 Å unit cell and calculating a linescan of the electrostatic potential with a resolution of 250 points per Angstrom (ppÅ). Far from the core, the WIEN2k potential approaches a non-zero constant value. In order to obtain the usual normalization, the potential was shifted (i.e., smallest value was set to zero).

The 3D unit-cell potential is stored in the file case.vcoul and WIEN2k comes with utility software (lapw5 and lapw5c) to extract linescans and 2D slices from this file. Hence a point grid of the 3D potential can be extracted by combining subsequently calculated 2D slices using the wien2venus script written by Masao Arai [21]. Difficulties arise from the fact that the potential is divergent near the positions of the atomic nuclei but equidistant discretization is performed. Furthermore the total number of sampling points is rather limited due to limited computer time. Usually this sampling problem is overcome by smoothing the analytical 3D potential before the discretization is performed and, in this way, a much smaller sampling rate can be used (typically 10 ppÅ). In Figure 2 this smoothing can be seen very well in the case of the Doyle–Turner potential, which is not divergent near the nucleus. However, in practice this was not possible here because we can only access the WIEN2k potential via the utility software.

We analyzed the sampling error in more detail by comparing the dependence of the projected potential from the position of the sampling point at a constant sampling rate of 30 ppÅ in the z-direction (parallel to the incident beam), which turned out to be a realistic compromise, but a much higher rate in the perpendicular direction. After projection along the z-direction, this results in the projected potential printed in green in Figure 3. From this it is possible to study the error that is made when this function is discretized using a smaller number of sampling points.

The blue boxes in Figure 3 indicate the mean value within one pixel at a resolution of 30 ppÅ, which corresponds to the ideal value within this quadrant. Hence the deviation from the top of the blue box indicates the sampling error. Interestingly, for 30 ppÅ, the sampling error is significant only for the center pixel and is caused by a single value in the 3D potential. We use a very simple method to handle this problem: Whenever a value in the 3D potential is higher than some cutoff value, we change this value to the highest value in the neighboring pixels. In this way the obtained projected potential value of the central pixel is in the range of the ideal value within a factor of three, instead of being off by up to two orders of magnitude (compare red and green curves in Figure 3). This very crude approach can be used, because the fraction of the intensity that interacts with this part of the potential remains negligibly small.

In order to be more flexible, we modified the wien2venus script: First, we included the possibility to shift the slicing volume with respect to the DFT unit cell. In this way it is possible to avoid sampling points very close to the nuclei. Second, it is now possible to slice sub-volumes. This can be used to speed up the calculation, because several sub-volumes can be sliced at the same time and vacuum regions can be skipped. The modified version of the script can be found in the Supporting Information (Supporting Information File 2).

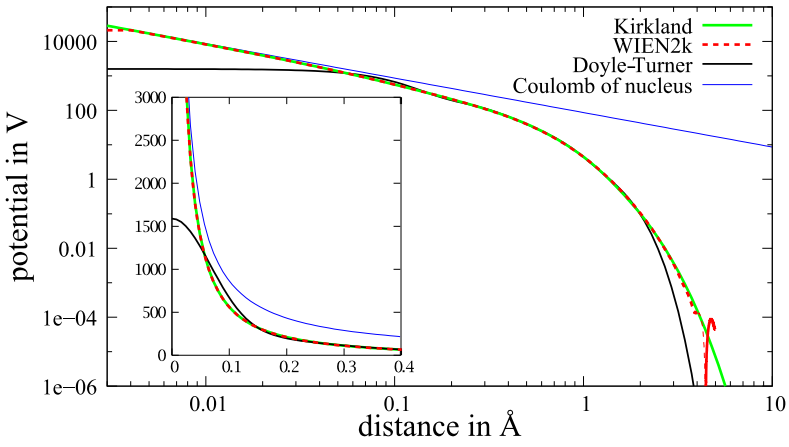

Figure 2: WIEN2k starting potential (red) compared to Doyle–Turner (black) and Kirkland (green) potentials. The blue line corresponds to the unscreened Coulomb potential of a carbon core. The WIEN2k potential linescan has a resolution of 250 ppÅ and was normalized in such a way that the smallest value is equal to zero. The WIEN2k and Kirkland potential show very good agreement.

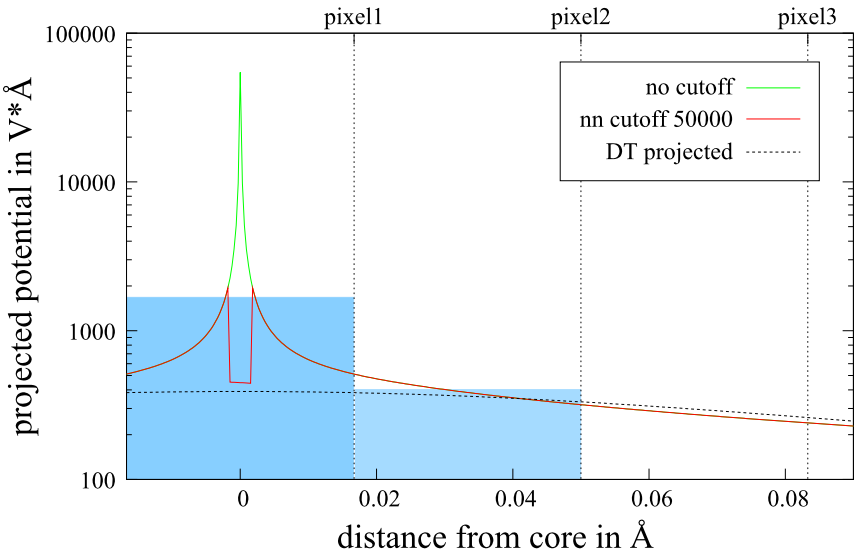

Figure 3: Projected potential near the core at very high resolution (green line). The blue boxes indicate the mean value of the green line at a resolution of 30 ppÅ. That means that the top value of these boxes corresponds to the "true" projected potential of the corresponding volume element. The red line is obtained using nearest neighbor cutoff. For comparison, the projected Doyle–Turner potential is plotted as a dashed black line.

Once an accurate 3D potential is obtained and renormalized it can be used for TEM image simulation. Thereby each direction of the incident beam can be modeled by rotating the 3D potential using linear interpolation algorithms.

Influence of DFT parameters

In order to set up meaningful DFT calculations, it is always necessary to do convergence tests of the main parameters such as k-points and basis set size [22]. Usually the convergence is tested with respect to the total energy and the electric field gradients. This was done using ideal graphene as a test structure. Interestingly, we find that the main quantity that we are interested in, i.e., the projected electrostatic potential, is not very sensitive to the DFT input parameters: The absolute differences between the DFT and IAM potentials are in the range of 10–30% where the influence of the DFT parameters is smaller than 1.5% (for details see Supporting Information File 1).

Example calculation

As we expect bonding effects to be strongest in exclusively light element materials, we applied this simulation scheme to different types of defects in graphene. The single atom substitutions, where one carbon position is occupied by another atomic species, turned out to be the ones that can be most easily accessed experimentally because the graphene structure remains almost undisturbed. Hence, bonding effects can easily be separated from structural changes by analyzing the deviations from the regular lattice contrast. For vacancies and adatoms the contrast analysis is much more difficult, due to changes in both, structural and electronic configuration. Nevertheless, the influence of chemical bonding on the final TEM image can be detected for all of them.

Boron and oxygen substitution in graphene

The structure models obtained from the VASP relaxation are shown in Figure 4. Details on the relaxation process can be found in the supplementary information of [13].

The WIEN2k calculation for the boron substitution was performed using the generalized gradient approximation (GGA) for the description of the exchange-correlation effects [23] with the following set of technical parameters: Separation energy −5.5 Ry, 6 × 6 × 1 k-points, RKMAX = 7 and GMAX = 12. For the calculations including oxygen atoms, the parameters were modified to: −6 Ry, 4 × 4 × 1 k-points, RKMAX = 8 and GMAX = 16. Both calculations were performed in a spin-polarized fashion, and the linearization energies were set automatically.

The effect of charge redistribution due to chemical bonding can be studied by comparing the initial charge density (before the first iteration cycle, labeled IAM) and the self-consistent charge density after the WIEN2k calculation has converged (labeled DFT). The same is done for the potentials. This approach has the advantage that subsequent processing steps, such as the TEM image simulation, influence the quantities obtained by IAM and DFT in exactly the same fashion. The only difference is that the latter includes chemical bonding while the former does not.

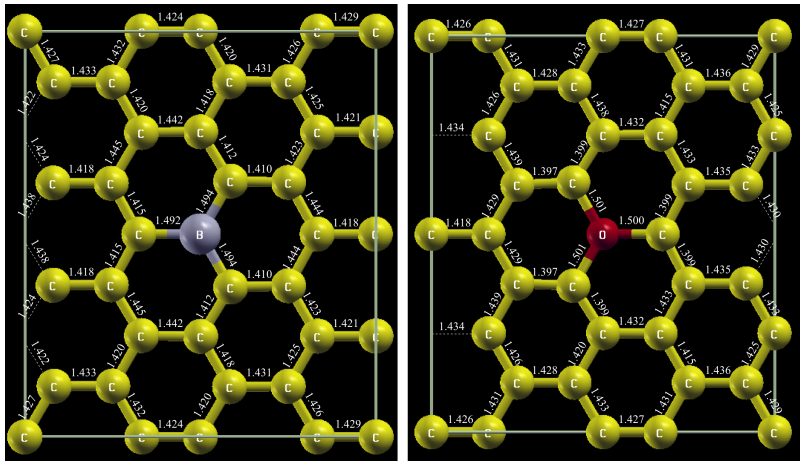

Figure 4: Relaxed structure model of boron and oxygen substitution in graphene. Bond lengths are given in Å.

The 3D potentials were sliced with a resolution of 30 ppÅ, normalized and projected along the *z*-direction using a cutoff of −50 kV, as described above. The same was done for the all-electron charge density (stored in the file clmsum) where the renormalization and the cutoff was skipped.

In Figure 5 we analyze the difference in the charge density. In the difference images (panel c and h) the sp^2 hybridization of the graphene lattice is clearly visible by the dark contrast between the carbon atoms meaning that the charge density of the bonded configuration is increased in this area. Interestingly,

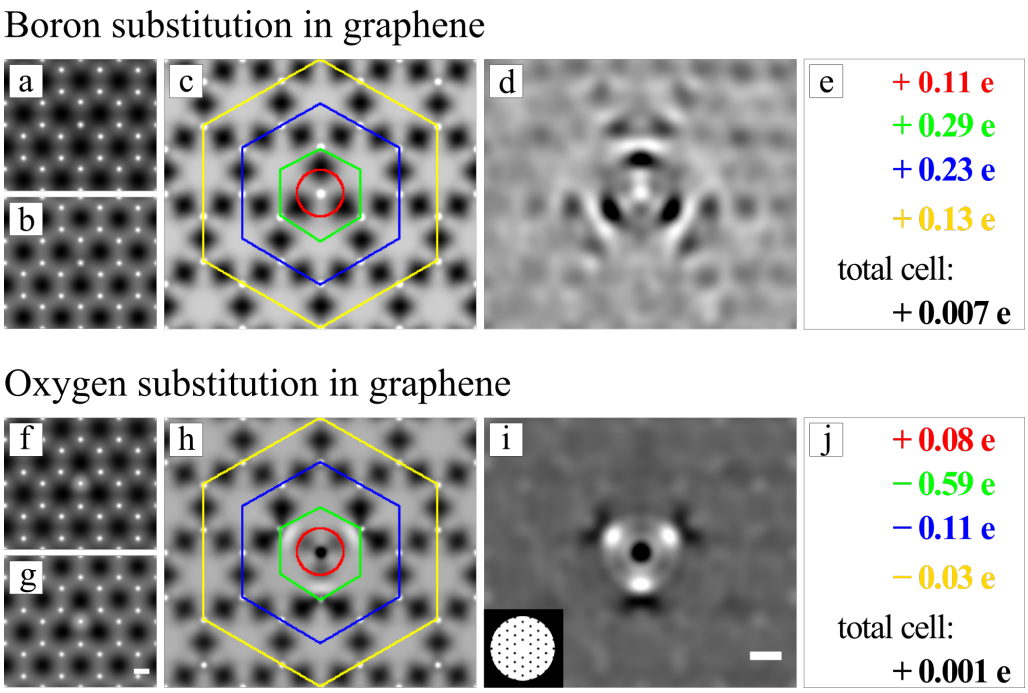

Figure 5: Analysis of the projected electron charge density of the boron (top) and oxygen substitution in graphene (bottom line). a) and b) show the projected charge density of the boron substitution for the neutral and bonded configuration respectively. c) shows the absolute difference between a) and b) where dark contrast corresponds to an increased electron density in the bonded configuration. This difference is integrated over the indicated areas and the values are given in e), where positive values correspond to an increased number of electrons in this area due to bonding. The diameter of the red ring is exactly half of the distance between the substitution and the neighboring carbon atoms and the green hexagon is exactly at the position of the neighboring carbons. The changes in the electron charge density, introduced by the substitution atom can be seen best in d), which is obtained after the periodic component of c) is removed by a Fourier filter, which is shown as inset in i). f)–j) show exactly the same analysis for the oxygen substitution. Scale bars are 1 Å.

for the boron as well as for the oxygen substitution we find big differences in the charge density at the three neighboring carbon atoms, whereas the substitution atom itself remains almost neutral. After removing the periodic signal from the difference images, using a Fourier filter (panel d and i), a dipole shaped rearrangement of the electrons at the carbon atoms next to the substitution is detected. Comparing the boron and oxygen case we find that the polarization of the carbon atoms is almost exactly opposite: The electron density in the area surrounding the boron atom (green hexagon) is increased, while for the oxygen atom it is decreased. This should result in a decrease of the boron potential due to stronger shielding of the core potential and reduced contrast in the TEM image. For oxygen, on the other hand, we expect to have a stronger signal in the TEM image due to weaker shielding.

This is exactly what we find when analyzing the projected potentials. Dark contrast in the filtered difference images in Figure 6 corresponds to a decreased projected potential in the bonded configuration. The increase of the oxygen and the decrease of the boron potential (compared to the IAM) is clearly visible. Besides these obvious differences two more subtle conclusions can be drawn from the potential analysis. First, we find that, also for the potential, the difference is not sharply located at the position of the substitution atom but instead spreads over further atomic distances. This results in low frequency information about the defect. The transfer of this information can be enhanced in the TEM by working at higher defocus. Second, for both cases the total potential is decreased by about 15% (see total change in panel e and j of Figure 6). This change in the mean inner potential is well known and was previously studied for semi-conducting materials by Schowalter et al. [24]. For ideal graphene we find a difference in the mean inner potential of 15.5%. Interestingly this results in an overall loss of contrast in the final TEM image of approximately 8%. However, this is only a minor contribution to the Stobbs factor [25], which is in the range of 50–80% and is used to fit simulated and experimental TEM image intensities.

After analyzing the DFT results we now want to study how the charge redistribution influences the observed contrast in the final TEM image, which is obtained by applying Equation 5. This calculation was performed for two different values of defocus: Scherzer defocus $f_1 = -9$ nm and $f_2 = -18$ nm, where the graphene lattice reflection is in the second extremum of the CTF. The former is the standard condition for high resolution TEM, whereas the latter offers better transfer of low spatial frequencies resulting in enhanced contrast of the substitution

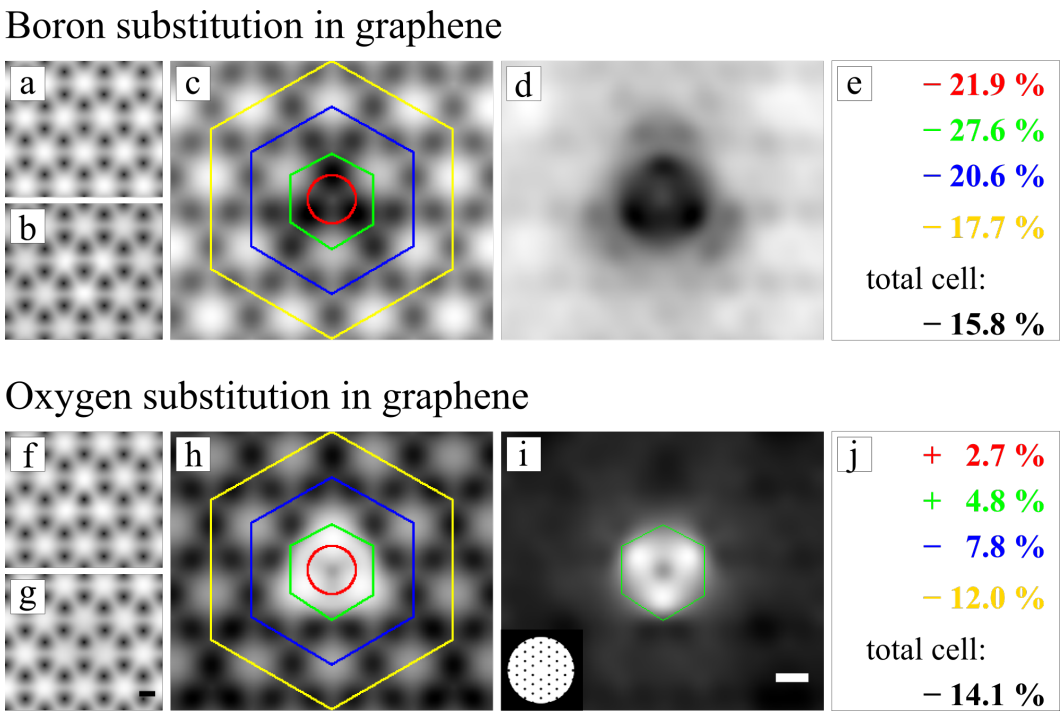

Figure 6: Analysis of the projected potential of the boron (top) and oxygen substitution in graphene (bottom line). a) and b) show the projected potential of IAM and DFT in logarithmic scaling, where the absolute difference image c) is displayed on a linear greyscale. Dark contrast in c) and d) corresponds to a decrease in the projected potential in the bonded configuration due to stronger shielding of the nuclear potential by electrons. The changes of the potential inside the marked areas in c) are given in e). Because the total potential is changing it is easier to compare relative differences. f)–j) show exactly the same analysis for the oxygen substitution. Scale bars are 1 Å.

defects. The other parameters were: High tension 80 kV and spherical aberration C_s = 0.02 mm. Higher order aberrations were not taken into account in this study.

The resulting micrographs for the boron substitution are shown in Figure 7. From this we see that the chemical bonding results in weaker contrast of the boron atom. This simplifies the detection of the substitution atom already at Scherzer defocus because the contrast difference between boron and the carbon atoms of the graphene lattice is increased from 5% for neutral atoms (IAM) to 9% in the bonded configuration (DFT). According to the DFT result this difference should be further pronounced by working at higher defocus, which is shown in the lower part of Figure 7.

For the oxygen substitution, shown in Figure 8, we find similar relative contrast changes but reach opposite conclusions, because the polarization of the carbons in the DFT calculation

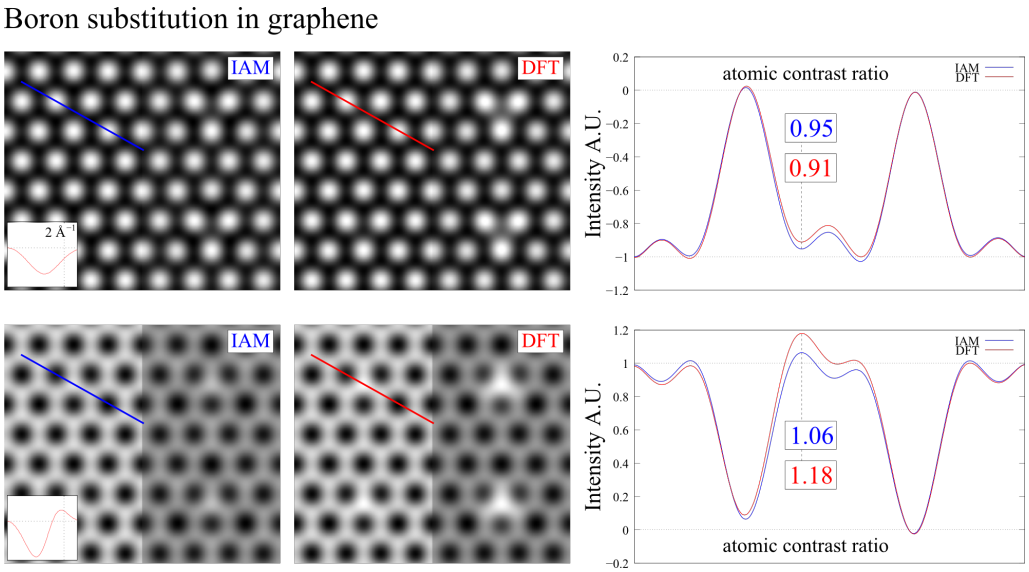

Figure 7: TEM image simulation of boron substitution in graphene for an electron energy of 80 keV. The upper images are for Scherzer defocus f_1 = −9 nm and the lower images are for f_2 = −18 nm. The contrast of the graphene lattice was normalized in all micrographs. This simplifies the comparison between the neutral and the bonded configuration.

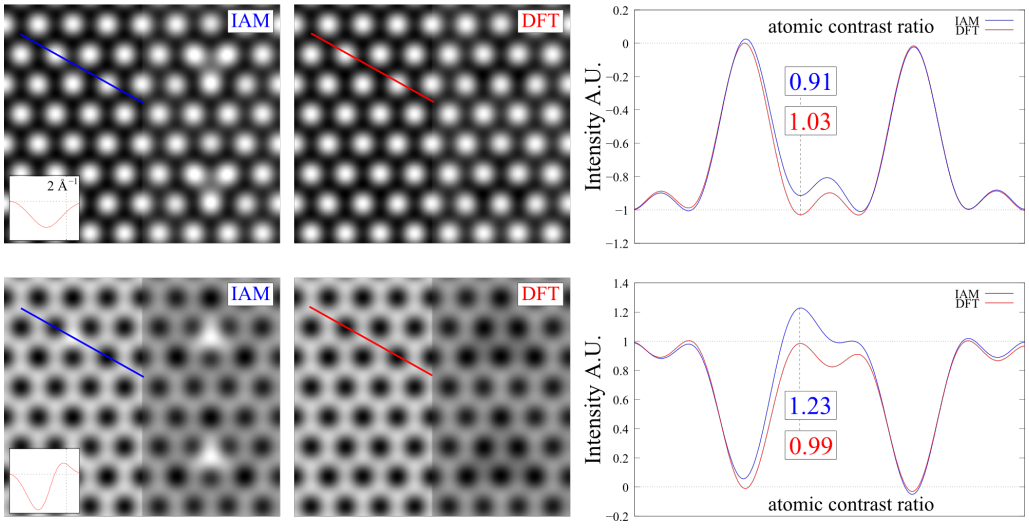

Figure 8: TEM image simulation of oxygen substitution in graphene for the same conditions used in Figure 7.

prevents the detection of the oxygen atom in the carbon network, whereas this should be possible according to the IAM result. This may be the reason why we did not detect residual oxygen atoms in reduced graphene oxide [26].

Oxygen adatom on graphene

The relaxation process resulted in an oxygen atom located at the bridge position between two carbons. The two carbon atoms are bent out of plane by approximately 0.4 Å. The C–C bond is stretched to 1.52 Å and the C–O distance is 1.47 Å, which is in good agreement with previously reported structures [27].

From analysis of the 3d densities, we found a very interesting charge redistribution in the out-of-plane directions, as can be seen in Figure 9. However, this direction cannot be accessed in a viewing direction orthogonal to the graphene plane.

The TEM simulation for normal incidence of the electron beam is shown in Figure 10. Again, the charge transfer around the oxygen atom would be very difficult to detect in a Scherzer defocus image. However, it might be discernable, if the lower spatial frequencies are included in the image. Under the assumption that the oxygen adatom remains stable enough under the electron beam to obtain a sufficient high signal to noise ratio, this might be achievable by applying higher defocus (see second row in Figure 10) or a phase plate (see third row in Figure 10).

Conclusion

We presented a practical method to include chemical bonding in the HRTEM image simulation process using DFT based scattering potentials recently applied in [13]. Hence, an all-electron calculation was set up based on a previously relaxed atomic configuration. As we have shown the WIEN2k software is well suited for this task as the initial potential is in good agreement with commonly used scattering potentials and the subsequent iteration process acts as a relatively minor perturbation. The potential itself is not very sensitive to the DFT input parameters. However, as the electrostatic potential is divergent at the position of the atomic nuclei, care has to be taken during the discretization process. We found that a sampling rate of 30 ppÅ in combination with a cutoff method produced reasonably accurate results. This 3d potential can subsequently be used for multislice TEM simulation, however this was not necessary for the single layer materials studied here. The influence of chemical bonding can be analyzed by comparing the IAM charge density, corresponding potential and TEM image with those obtained from the DFT calculation.

This analysis was demonstrated for the substitutions of a single boron and a single oxygen atom in graphene as well as for an oxygen adatom on graphene. The relative changes are very similar to the ones we found previously for the single atom nitrogen substitution [13], where we were able to validate the advantage of the DFT calculation over the isolated atom model experimentally. For the oxygen substitution we find exactly the same situation as for the nitrogen defect: The electron charge density in the area surrounding the substitution is decreased due to polarization of the neighboring carbons, resulting in weaker shielding of the core potential and increased TEM contrast of the substitution atom. For boron the situation is exactly the inverse. However, the implication on the final TEM image

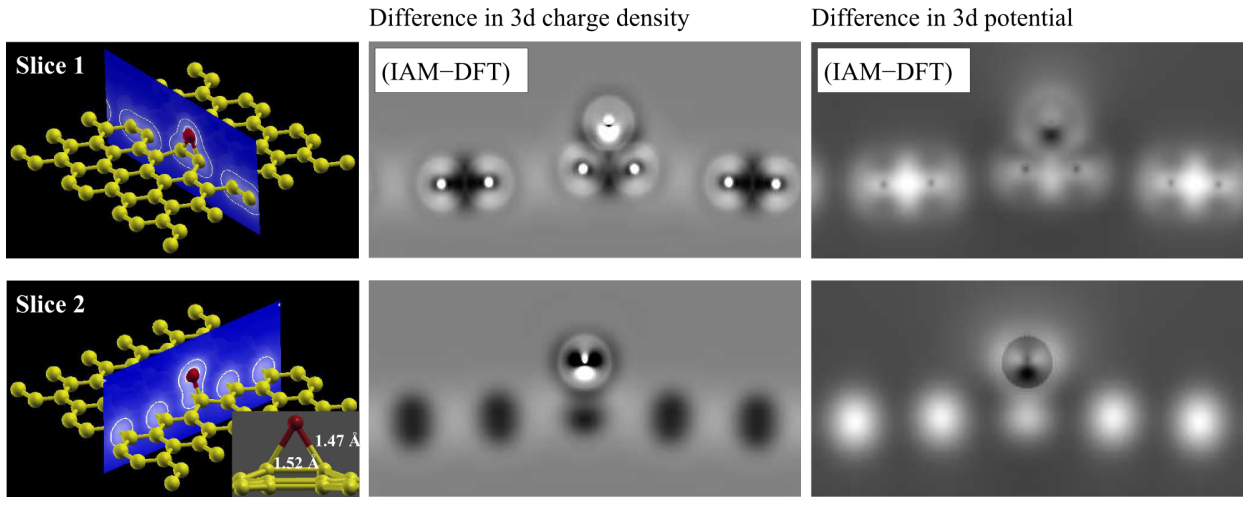

Figure 9: Difference between the 3d electron charge density (center column) and the 3d electrostatic potential (right column) between IAM and DFT for an oxygen adatom on graphene. The top row is for armchair and the bottom row for zig-zag direction. An increase in electron charge density (potential) due to chemical bonding appears as dark (bright) contrast in the difference image.

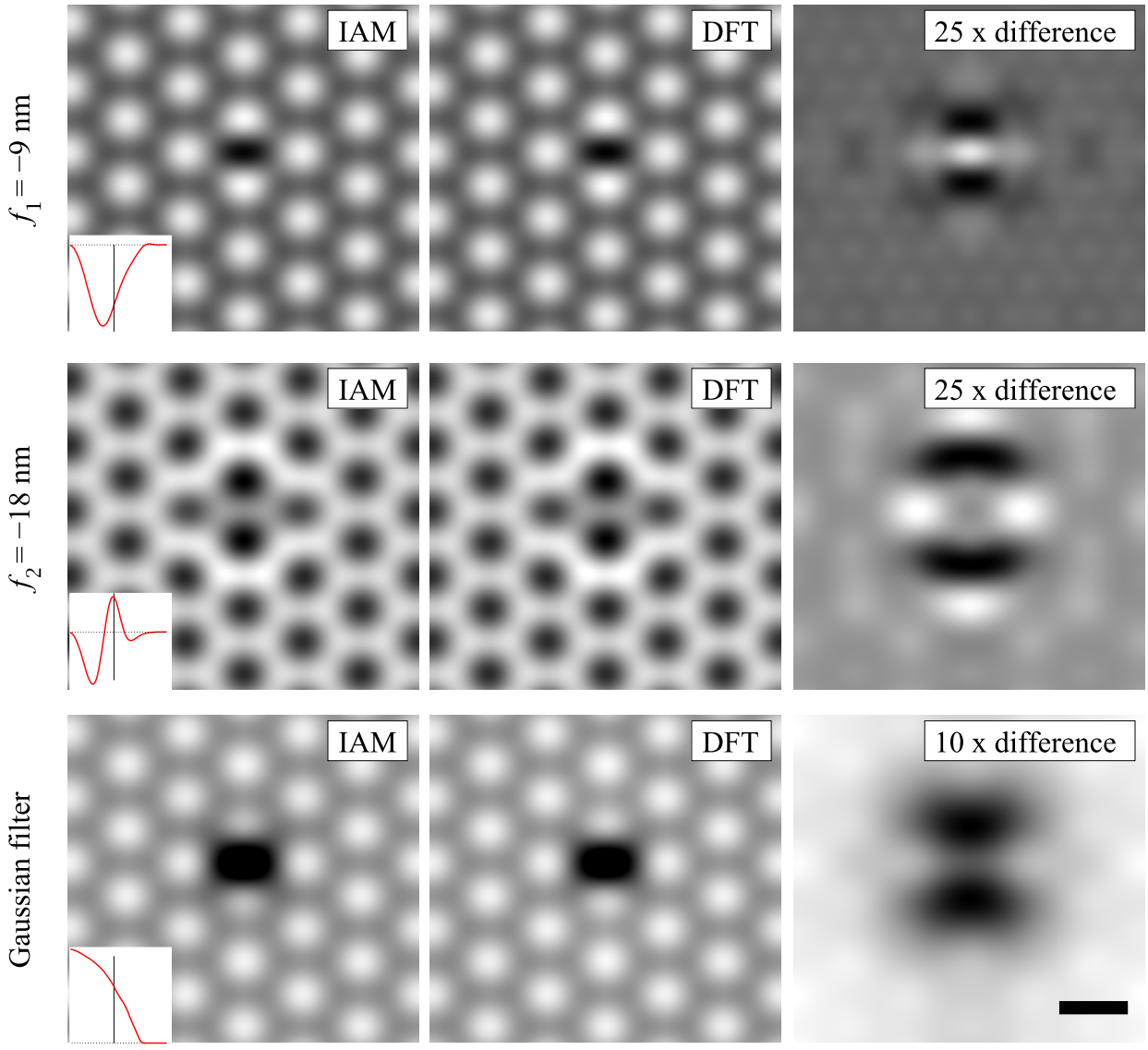

Figure 10: TEM image simulation of an oxygen adatom on graphene for 80 kV. The first row is for Scherzer conditions f_1 = −9 nm and the second row is for higher defocus f_2 = −18 nm. The third row results from applying a low pass filter to the projected potential (1.8 Å Gaussian blur). For each case the inset shows the CTF where the position of the 2.13 $Å^{-1}$ graphene reflex is marked by the black line. For direct comparison, the micrographs, resulting from IAM and DFT, were normalized to the contrast of the graphene lattice and all images within one row are shown on the same grey scale. Therefore the difference images were multiplied by the factor given in the inset. Most interesting, at better transfer of low spatial frequencies, the bonding signal is strongly enhanced. Scale bar is 2.5 Å.

is not very intuitive because it depends on the absolute potential values: For nitrogen, the increase of the contrast due to charging enables the detection whereas for oxygen this increase disables the detection. On the contrary, the decrease of the boron contrast simplifies the detection because the relative contrast difference to the carbon lattice is increased from 5% in the neutral to 9% in the bonded configuration, where only the latter is significantly above the experimental accuracy of 3% [13].

We conclude that chemical bonding must be included in comparative HRTEM image simulations whenever very small signals are analyzed. Here we want to emphasize that the key requirement for this kind of analysis is the well defined specimen geometry rather than the single layer thickness of the model systems used in this study. Earlier calculations showed that, whenever a high enough experimental accuracy is achieved, bonding effects should be detectable for a wide variety of materials [2,8]. This offers the possibility to gain

experimental insight into the electronic charge distribution of the specimen at the atomic scale by HRTEM.

Supporting Information

Supporting Information File 1

WIEN2k convergence tests for ideal graphene
[http://www.beilstein-journals.org/bjnano/content/supplementary/2190-4286-2-45-S1.pdf]

Supporting Information File 2

Program to get 3D WIEN2k potentials (Phyton script, rename to .py).
[http://www.beilstein-journals.org/bjnano/content/supplementary/2190-4286-2-45-S2.txt]

Acknowledgements

We gratefully acknowledge financial support by the German Research Foundation (DFG) within research project SFB 569 “Hierarchic Structure Formation and Function of Organic-Inorganic Nanosystems” as well as DFG and the Ministry of Science, Research and the Arts (MWK) of the state Baden-Württemberg within the Sub-Angstrom Low-Voltage Electron Microscopy project (SALVE).

References

1. Gemming, T.; Möbus, G.; Exner, M.; Ernst, F.; Rühle, M. *J. Microsc.* **1998,** *190,* 89–98. doi:10.1046/j.1365-2818.1998.3110863.x
2. Deng, B.; Marks, L. D. *Acta Crystallogr., Sect. A* **2006,** *62,* 208–216. doi:10.1107/S010876730601004X
3. Kirkland, E. J. *Advanced Computing in Electron Microscopy;* Plenum Press: New York and London, 1998.
4. Hébert, C. *Micron* **2007,** *38,* 12–28. doi:10.1016/j.micron.2006.03.010
5. Hofer, W. A. *A Guide to simulation of STM images and spectra from first principles*: bSKAN 3.6; www.liv.ac.uk/~whofer/stm/bskan_guide.pdf, 2005.
6. Rose, H. *Optik* **1990,** *85,* 19–24.
7. Haider, M.; Rose, H.; Uhlemann, S.; Kabius, B.; Urban, K. J. *Electron Microsc.* **1998,** *47,* 395–405.
8. Deng, B.; Marks, L. D.; Rondinelli, J. M. *Ultramicroscopy* **2007,** *107,* 374–381. doi:10.1016/j.ultramic.2006.10.001
9. Zhu, Y.; Wu, L.; Tafto, J. *Microsc. Microanal.* **2003,** *9,* 442–456. doi:10.1017/S143192760303037X
10. Zuo, J. M.; Spence, J. C. H.; O’Keeffe, M. *Phys. Rev. Lett.* **1988,** *61,* 353–356. doi:10.1103/PhysRevLett.61.353
11. Ciston, J.; Kim, J.; Haigh, S.; Kirkland, A.; Marks, L. *Ultramicroscopy* **2010**. doi:10.1016/j.ultramic.2010.12.003
12. Meyer, J. C.; Chuvilin, A.; Algara-Siller, G.; Biskupek, J.; Kaiser, U. *Nano Lett.* **2009,** *9,* 2683–2689. doi:10.1021/nl9011497
13. Meyer, J. C.; Kurasch, S.; Park, H. J.; Skakalova, V.; Künzel, D.; Groß, A.; Chuvilin, A.; Algara-Siller, G.; Roth, S.; Iwasaki, T.; Starke, U.; Smet, J. H.; Kaiser, U. *Nat. Mater.* **2011,** *10,* 209–215. doi:10.1038/nmat2941
14. O’Keefe, M. A. *Ultramicroscopy* **1992,** *47,* 282–297. doi:10.1016/0304-3991(92)90203-V
15. Thust, A. *Phys. Rev. Lett.* **2009,** *102,* 220801. doi:10.1103/PhysRevLett.102.220801
16. Lehmann, M.; Lichte, H. *Microsc. Microanal.* **2002,** *8,* 447–466.
17. Doyle, P. A.; Turner, P. S. *Acta Crystallogr., Sect. A* **1968,** *24,* 390–397. doi:10.1107/S0567739468000756
18. Coulthard, M. A. *Proc. Phys. Soc., London* **1967,** *91,* 44–49. doi:10.1088/0370-1328/91/1/309
19. Kresse, G.; Furthmüller, J. *Phys. Rev. B* **1996,** *54,* 11169–11186. doi:10.1103/PhysRevB.54.11169
20. Blaha, P.; Schwarz, K.; Madsen, G. K. H.; Kvasnicka, D.; Luitz, J. *An Augmented Plane Wave + Local Orbitals Program for Calculating Crystal Properties;* WIEN2k; Karlheinz Schwarz, Techn. Universitat Wien: Wien, Austria, 2001.
21. Arai, M. wien2venus.py. http://www.nims.go.jp/cmsc/staff/arai/wien/venus.html.
22. Cottenier, S. *Density Functional Theory, the family of (L)APW-methods: a step-by-step introduction;* Instituut voor Kern- en Stralingsfysica, K. U. Leuven: Leuven, Belgium, 2002.
23. Perdew, J.; Burke, K.; Ernzerhof, M. *Phys. Rev. Lett.* **1996,** *77,* 3865–3868.
24. Schowalter, M.; Lamoen, D.; Rosenauer, A.; Kruse, P.; Gerthsen, D. *Appl. Phys. Lett.* **2004,** *85,* 4938–4940. doi:10.1063/1.1823598
25. Hÿtch, M. J.; Stobbs, W. M. *Ultramicroscopy* **1994,** *53,* 191–203. doi:10.1016/0304-3991(94)90034-5
26. Gómez-Navarro, C.; Meyer, J. C.; Sundaram, R. S.; Chuvilin, A.; Kurasch, S.; Burghard, M.; Kern, K.; Kaiser, U. *Nano Lett.* **2010,** *10,* 1144–1148. doi:10.1021/nl9031617
27. Yan, J.-A.; Chou, M. Y. *Phys. Rev. B* **2010,** *82,* 125403. doi:10.1103/PhysRevB.82.125403

License and Terms

Beilstein Journal of Nanotechnology

Septipyridines as conformationally controlled substitutes for inaccessible bis(terpyridine)-derived oligopyridines in two-dimensional self-assembly

Daniel Caterbow[1], Daniela Künzel[2], Michael G. Mavros[1], Axel Groß[2], Katharina Landfester[3] and Ulrich Ziener[*1]

Full Research Paper

Open Access

Address:
[1]Institute of Organic Chemistry III/Macromolecular Chemistry, [2]Institute of Theoretical Chemistry, University of Ulm, Albert-Einstein-Allee 11, D-89081 Ulm, Germany and [3]Max Planck Institute for Polymer Research, Ackermannweg 10, D-55128 Mainz, Germany

Email:
Ulrich Ziener[*] - ulrich.ziener@uni-ulm.de

* Corresponding author

Keywords:
oligopyridines; self-assembled monolayer; STM

Beilstein J. Nanotechnol. **2011,** *2,* 405–415.
doi:10.3762/bjnano.2.46

Received: 17 April 2011
Accepted: 07 June 2011
Published: 26 July 2011

This article is part of the Thematic Series "Organic–inorganic nanosystems".

Guest Editor: P. Ziemann

Abstract

The position of the peripheral nitrogen atoms in bis(terpyridine)-derived oligopyridines (BTPs) has a strong impact on their self-assembly behavior at the liquid/HOPG (highly oriented pyrolytic graphite) interface. The intermolecular hydrogen bonding interactions in these peripheral pyridine units show specific 2D structures for each BTP isomer. From nine possible constitutional isomers only four have been described in the literature. The synthesis and self-assembling behavior of an additional isomer is presented here, but the remaining four members of the series are synthetically inaccessible. The self-assembling properties of three of the missing four BTP isomers can be mimicked by making use of the energetically preferred N–C–C–N transoid conformation between 2,2'-bipyridine subunits in a new class of so-called septipyridines. The structures are investigated by scanning tunneling microscopy (STM) and a combination of force-field and first-principles electronic structure calculations.

Introduction

Two-dimensional molecular self-assembly is a common approach to build up surface-supported nanostructures [1,2]. Appropriately-directed intermolecular interactions are required to guarantee nearly perfect ordering of these monolayers. Hydrogen bonding interactions serve this purpose: They are directed, of intermediate strength, and adjustable [3,4]. The bis(terpyridine)-derived oligopyridines (BTPs), are large polyaromatic molecules with C_{2v} symmetry, are well established compounds, and are known to self-assemble [5] at the liquid/HOPG [6-11] and at the gas/solid interface [12-14]. Self-assembly also occurs under electrochemical conditions [15], and the molecules assemble into a broad variety of two-dimen-

sional (2D) structures based on weak intermolecular C–H···N hydrogen bonds. Due to the directionality of the hydrogen bonds, the relative orientation of the peripheral pyridine rings has a strong impact on the 2D structure; in contrast, the substrate has a minor influence on the pattern formation [12]. Besides the preset constitution of each BTP molecule, different conformations are possible, which might subsequently lead to different monolayer structures. The influence of the conformation of adlayer molecules on the 2D structures formed is described in several examples in the literature. Most often, flexible substituents on more rigid core units lead to different conformers, which self-assemble in different 2D structures as shown, e.g., for porphyrin [16], phthalocyanine [17], and quinacridone derivatives [18], N,N-diphenyl oxalic amide [19], bithiophene–fluorenone conjugated oligomers [20], a 2,6-di(acetylamino)pyridine substituted conjugated module [21], and a molecular hexapod having a benzene core and six oligo(*p*-phenylene vinylene) legs [22]. The conformers can have an impact on the expression or suppression of chirality of the supramolecular structures [23-25], and sometimes extrinsic factors, such as the presence of guest molecules [26,27], or the pH value [28,29], trigger the formation of certain self-assembled conformers. It is known that for 2,2'-bipyridine, the transoid conformation of the N–C–C–N unit is preferred because of dipole–dipole interactions [30].

Due to the C_{2v} symmetry of the BTP molecules, nine constitutional isomers are possible by varying the connection between the four peripheral and the two central pyridine moieties (Figure 1). Until now, four compounds of this series have been described in the literature, including details of their 2D self-assembly [6,7]. The various isomers with their different peripheral pyridine ring orientations originate from the orientation of the pyridine rings in the different diazachalcone precursor molecules.

Here we present the synthesis of a fifth BTP isomer, 2,2'-BTP (**5**), and its self-assembly properties at the liquid/HOPG inter-

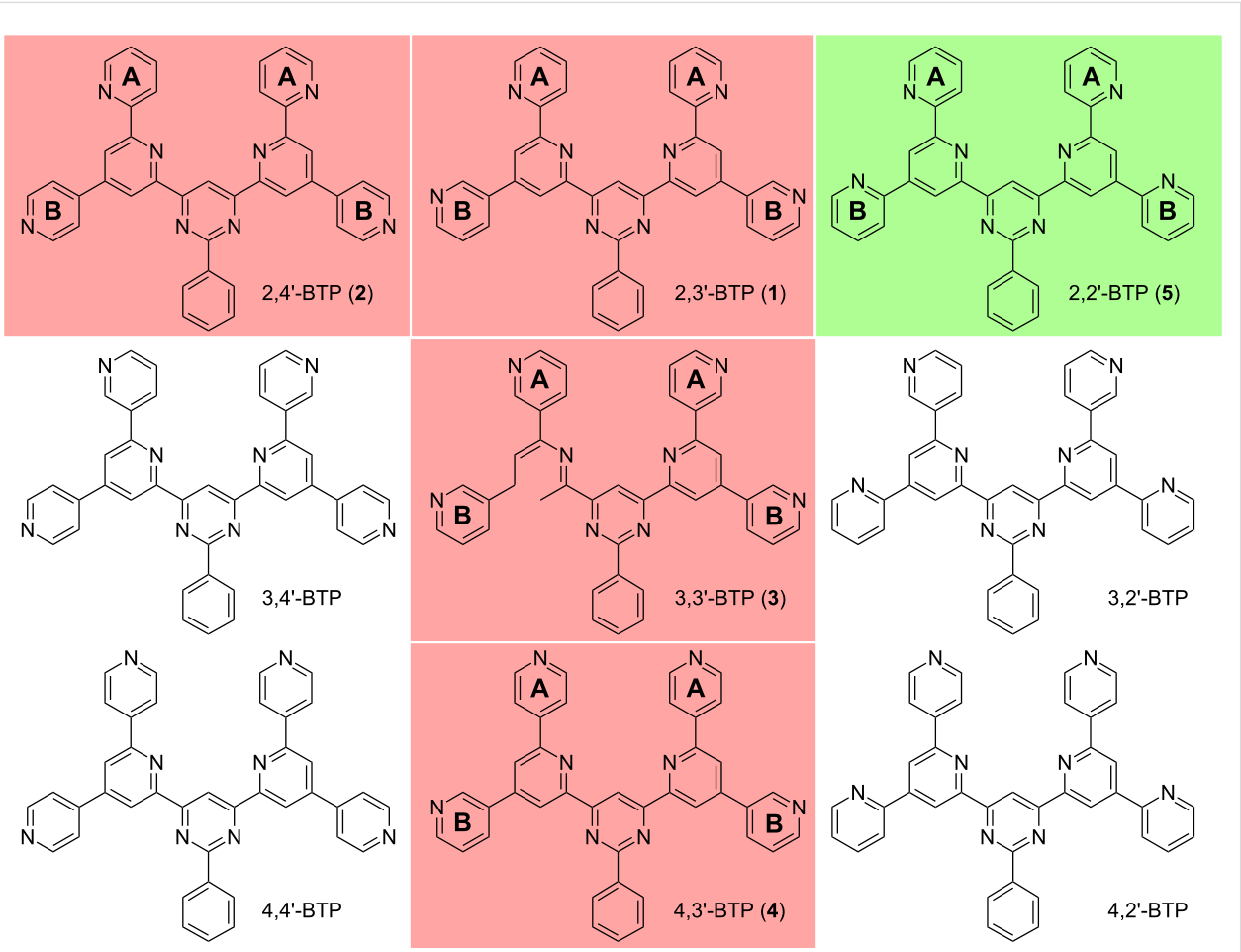

Figure 1: Nine possible constitutional BTP isomers with the four already described in literature (in red) [6,7] and the one newly synthesized as described in this paper (in green).

face. Additionally, a new class of oligopyridines comprising seven pyridine units and one phenyl substituent, the so-called phenylseptipyridines (PhSpPy), is presented. The PhSpPys display the same symmetry, shape, and size as the BTPs and can be regarded as substitutes for the inaccessible BTPs in terms of their 2D self-assembly behavior as shown by STM.

Results and Discussion

Synthesis

The synthesis of the BTPs is based on a double ring-closure reaction corresponding to the Kröhnke synthesis (Scheme 1) [31]. One component is the bipyridine-substituted unsaturated ketone (diazachalcone). The binding sites of the pyridine rings determine the orientation of the peripheral nitrogen atoms in the final BTPs. The diazachalcones were obtained from the condensation between the corresponding pyridylaldehyde and the acetylpyridine. Unfortunately, the only diazachalcones accessible are those that are derived from 2-acetylpyridine and/or 3-pyridylcarbaldehyde. We attribute this finding to the electron withdrawing effect of the pyridine rings, which is most pronounced in the *ortho*-position; this effect stabilizes the carbanion of the 2-acetylpyridine more effectively than the carbanions derived from the two other isomers. The unsuccessful trials to obtain the missing diazachalcones delivered mainly the double aldol adducts; the presence of these products suggests high reactivity of the aldehyde, which facilitates the attack of a second acetyl compound instead of elimination of water, a key step in the condensation leading to the formation of the BTP compounds. Thus, only the least reactive aldehydes, namely the *meta*-isomers, led to the desired diazachalcones. Consequently, by the reaction of 2,2'-diazachalcone (**6**) with the bis(pyridinium) salt (**7**), a fifth bis(terpyridine)-derived oligopyridine, 2,2'-BTP (**5**), could be added to the already known four isomers (**1**–**4**).

The known BTP isomers show a large variety of self-assembled 2D structures [7]. It is expected that the four missing isomers should also form interesting 2D structures; however, since they are synthetically inaccessible, a new molecular design is required to mimic the structure of the BTPs in order to study the 2D self-assembly properties of the missing isomers. The essential factors, which determine the self-assembled structure of the known BTPs are the intermolecular C–H···N hydrogen bonds, which are governed by the relative orientation of the peripheral pyridine rings. Thus, we seek C_{2v}-symmetric oligopyridines with 3,4'-, 3,2'-, 4,4'-, and 4,2'-orientation of the nitrogen atoms, with the first number indicating the connection of the A pyridine rings and the second the B pyridine rings (see Figure 1). The corresponding required diazachalcones are not synthetically available, but the 4,3'-, 2,3'-, and 2,4'-diazachalcones (**8**–**10**) are. As the BTPs in the 2D structures are essentially coplanar, they adopt the transoid N–C–C–N conformation between the pyrimidine and the central pyridine units, similarly known for 2,2'-bipyridine [30]. If the core unit of the BTPs is exchanged for a pyridine moiety, the opposite conformation should be preferably formed. Finally, the corresponding phenylseptipyridines prepared from the available 2,4'-, 2,3'-, 2,2'-, 3,3'-, and 4,3'-diazachalcones (**6, 8**–**11**) should adopt the same conformation as the 4,2'-, 3,2'-, 2,2'-, 3,3'-, and 3,4'-BTPs (Figure 2).

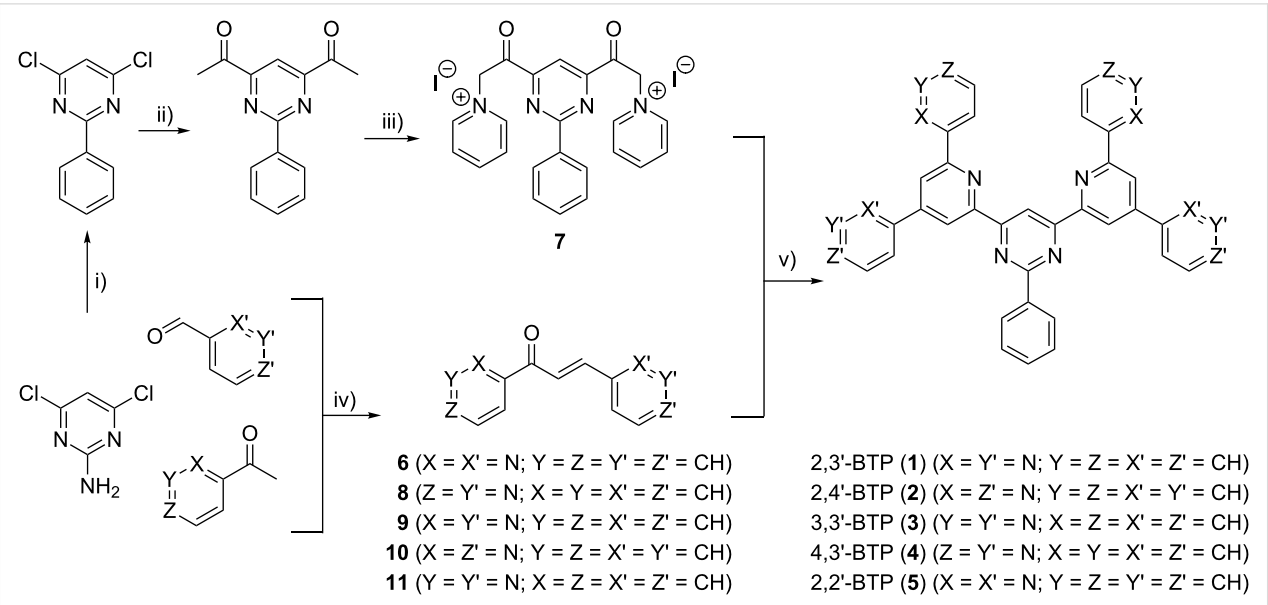

Scheme 1: Synthetic pathway to BTPs (**1**–**5**). i) Cu_2O, isoamylnitrite, benzene, 100 °C, 3 h; ii) (1-ethoxy)-vinyl-tributylstannane, $Pd(PPh_3)_4$, DMF, 20 h reflux, acetone, HCl; iii) iodine, pyridine, 100 °C, 4 h; iv) MeOH, NaOH; v) NH_4OAc, MeOH reflux.

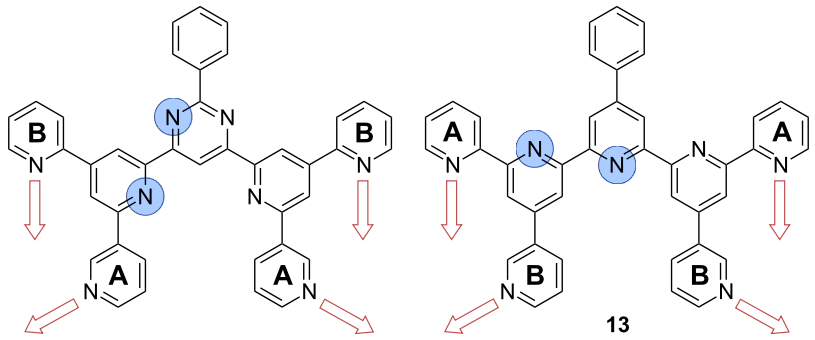

Figure 2: The synthetically unavailable 3,2'-BTP (left), which is representative of the other inaccessible BTPs, is hypothetically derived from the unavailable 3,2'-diazachalcone. The corresponding 2,3'-PhSpPy (**13**) (right), derived from the available 2,3'-diazachalcone, should adopt the transoid N–C–C–N conformation [30] in the coplanar adsorbed state and thus the same orientation of the peripheral pyridine units.

The synthesis of these phenylseptipyridines, which follows the same reaction scheme as for the BTPs, is presented in Scheme 2. The required phenylpyridine bis(pyridinium iodine) salt is synthesized analogously to the corresponding pyrimidine compound. In this way, five new PhSpPys (2,4'-, 2,3'-, 2,2'-, 3,3'-, and 4,3'-PhSpPy) (**12**–**16**) were be obtained in mediocre yield but with high purity.

STM and calculations

The self-assembly properties of the newly-synthesized oligopyridines in 1,2,4-trichlorobenzene (TCB) solution were investigated at the HOPG/liquid interface and compared to the already known BTPs. The 2D structure of 2,2'-BTP (**5**) can be seen in Figure 3. A square pattern of dark spots surrounded by bright areas with a unit cell of $a = 3.0 \pm 0.2$ nm, $b = 3.0 \pm 0.2$ nm, and an angle $\angle_{a,b} = 91 \pm 2°$ is observed. A closer look at the bright areas reveals small bright spots, which we attribute to the single (hetero)aromatic rings. The submolecular resolution allows for the suggestion of a tentative model. Self-assembly can be explained by the presence of intermolecular hydrogen bonds, which is already known from the previous BTPs [7]. Interestingly, comparison of the unit cell of self-assembled 2,2'-BTP (**5**) with the unit cell of 2,4'-BTP (**2**) shows almost identical data ($a = b = 3.1$ nm $\pm$ 0.2, $\angle_{a,b} = 90 \pm 1°$) [6,7]. The structural agreement can be understood by taking a closer look at the molecular structures of both compounds. Here, it can be seen that the exchange of the *para*-connected pyridine ring in 2,4'-BTP (**2**) by the *ortho*-connection in 2,2'-BTP (**5**) maintains the hydrogen bonding pattern and thus leads to the corresponding 2D structure (Figure 4). No further polymorph could be found for 2,2'-BTP (**5**) at the HOPG/TCB solution interface.

To further support the experimental results, force field calculations of the square symmetric adsorbate layers of 2,4'-BTP (**2**) and 2,2'-BTP (**5**) were performed. The results of these calculations underline their structural similarities: For both isomers,

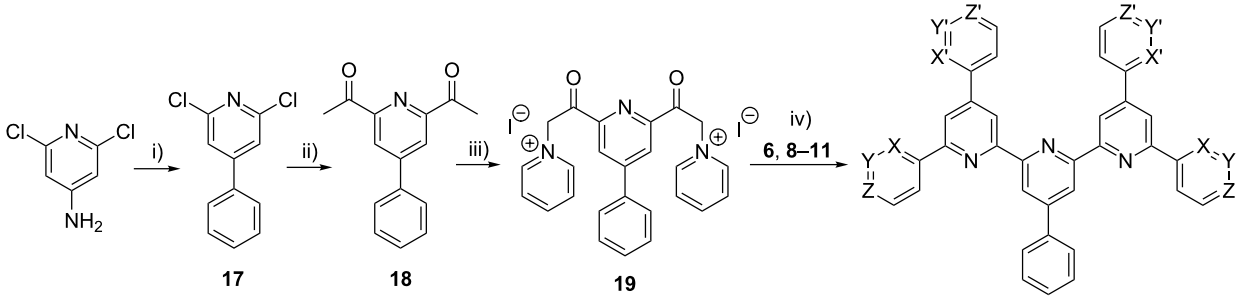

2,4'-PhSpPy (**12**) (X = Z' = N; Y = Z = X' = Y' = CH)
2,3'-PhSpPy (**13**) (X = Y' = N; Y = Z = X' = Z' = CH)
2,2'-PhSpPy (**14**) (X = X' = N; Y = Z = Y' = Z' = CH)
3,3'-PhSpPy (**15**) (Y = Y' = N; X = Z = X' = Z' = CH)
4,3'-PhSpPy (**16**) (Z = Y' = N; X = Y = X' = Z' = CH)

Scheme 2: Synthetic pathway to PhSpPys (**12**–**16**). i) Cu_2O, isoamylnitrite, benzene, 100 °C, 3 h; ii) (1-ethoxy)-vinyl-tributylstannane, $Pd(PPh_3)_4$, DMF, 20 h reflux, acetone, HCl; iii) iodine, pyridine, 100 °C, 4 h; iv) NH_4OAc, MeOH reflux.

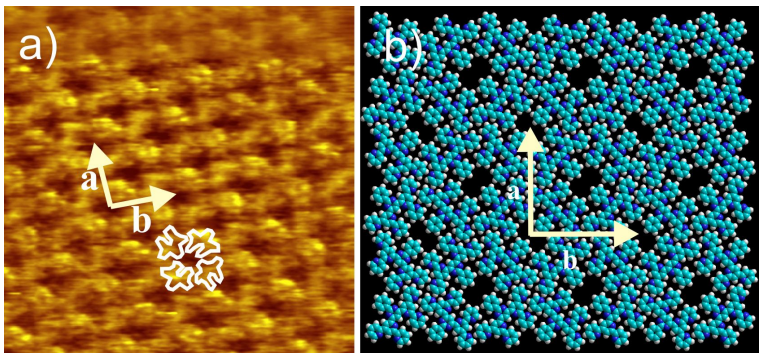

Figure 3: a) 15 × 15 nm^2 STM image (I_{set} = 14 pA, V_{set} = −0.64 V) of 2,2'-BTP (**5**) at the HOPG/TCB interface [a = 3.0 ± 0.2 nm, b = 3.0 ± 0.2 nm, $\angle_{a,b}$ = 91 ± 2°] with four overlaid molecules; b) model of the 2,2'-BTP (**5**) square pattern.

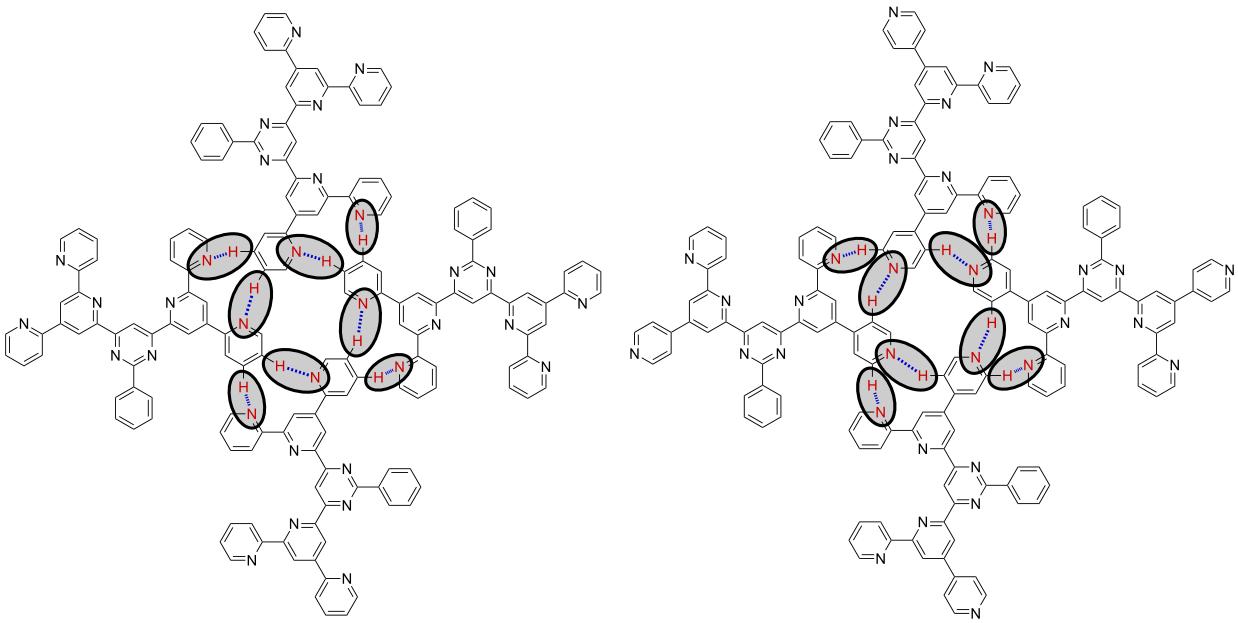

Figure 4: Hydrogen bonding motif of 2,2'-BTP (**5**) (left) and of 2,4'-BTP (**2**) [6,7] (right) found experimentally; the hydrogen bonds are marked by ovals.

the BTP molecules arrange in a similar fashion (Figure 5), forming intermolecular hydrogen bonds at comparable positions. In addition, the lattice constants of the relaxed network differ by less than 1%. For 2,4'-BTP (**2**), the Compass-optimized [32] lattice constant is 3.23 nm, and it is 3.26 nm for 2,2'-BTP (**5**).

Despite the similarity of the calculated structures, small differences were found in the energies of the hydrogen bonds. In the 2,4'-BTP (**2**) network, hydrogen bonds of −37.2 kJ mol^{-1} per molecule in the unit cell were obtained from the Compass [32] optimization. For 2,2'-BTP, a slightly weaker intermolecular bonding of −23.9 kJ mol^{-1} per molecule was calculated.

As the self-assembly of the oligopyridines is dominated by the orientation of the peripheral nitrogen atoms, 2,2'- (**14**) and 3,3'-PhSpPy (**15**) should display the 2D structures corresponding to 2,2'- (**5**) and 3,3'-BTP (**3**), respectively.

Although the resolution of the STM image is significantly lower than for 2,2'-BTP (**5**) (Figure 3) a square symmetric structure for 2,2'-PhSpPy (**14**) at the HOPG/TCB solution interface can be detected (Figure 6), just as for 2,2'-BTP (**5**). The unit cell dimensions (a = 3.0 ± 0.1 nm, b = 3.0 ± 0.1 nm, $\angle_{a,b}$ = 92 ± 3°) are essentially identical to those of the 2D structures of 2,2'-BTP (**5**) and 2,4'-BTP (**2**) (see above). Based on these observations, it is likely that a corresponding intermolecular

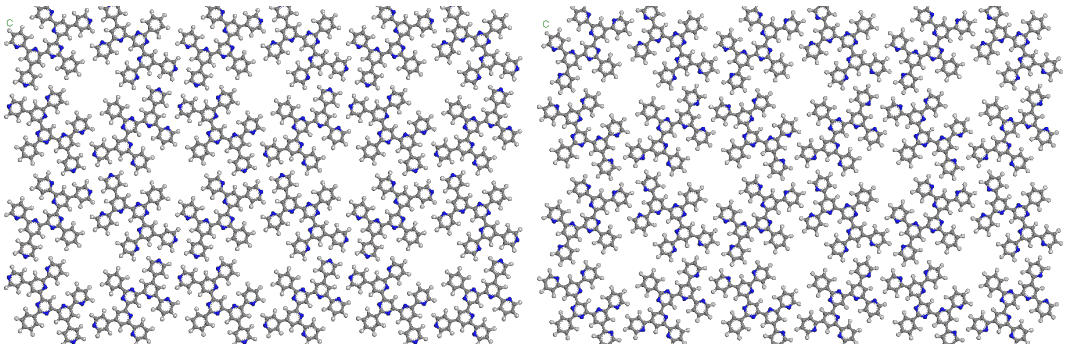

Figure 5: Adsorbate structures of 2,4'-BTP (**2**) (left) and 2,2'-BTP (**5**) (right) in the square symmetric structure, optimized with the Compass [32] force field.

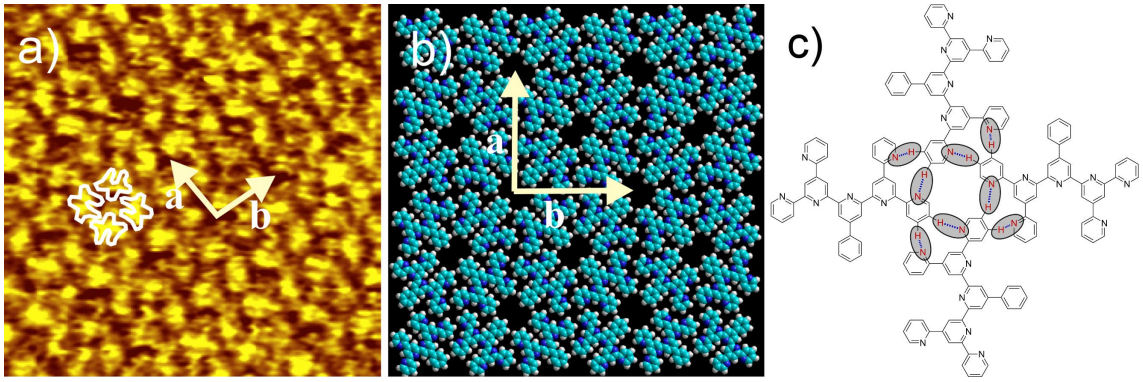

Figure 6: a) 15 × 15 nm^2 STM image (I_{set} = 3.41 nA, V_{set} = −660 mV) of 2,2'-PhSpPy (**14**) at the HOPG/TCB interface [a = 3.0 ± 0.1 nm, b = 3.0 ± 0.1 nm, $\angle_{a,b}$ = 92 ± 3°] with four overlaid molecules; b) model of the 2,2'-PhSpPy (**14**) square pattern; c) hydrogen bonding motif of 2,2'-PhSpPy (**14**); the hydrogen bonds are marked by ovals.

hydrogen bonding pattern gives rise to the square packing motif (Figure 6).

3,3'-BTP (**3**) is known to show four different 2D structures at the HOPG/TCB solution interface depending on the concentration: Three linear packing patterns and one hexagonal pattern [7,9]. For 3,3'-PhSpPy (**15**) only one 2D structure could be found with no dependence on the concentration, that is, a lamellar pattern with unit cell parameters of a = 2.7 ± 0.2 nm, b = 1.6 ± 0.2 nm, $\angle_{a,b}$ = 77 ± 2° (Figure 7 and Figure S1).

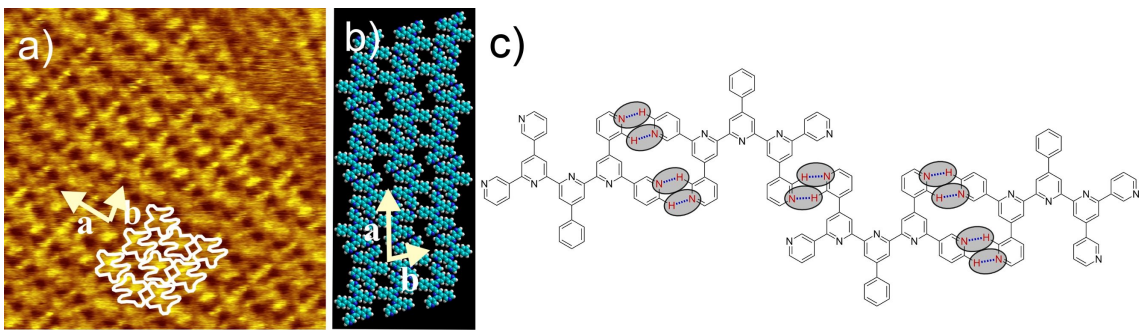

Figure 7: a) 15 × 15 nm^2 STM image (I_{set} = 14.5 pA, V_{set} = −610 mV) of 3,3'-PhSpPy (**15**) at the HOPG/TCB interface [a = 2.7 ± 0.2 nm, b = 1.6 ± 0.2 nm, $\angle_{a,b}$ = 77 ± 2°] overlaid with nine molecules; b) model of the 3,3'-PhSpPy (**15**) lamellar pattern; c) hydrogen bonding motif of 3,3'-PhSpPy (**15**); the hydrogen bonds are marked by ovals.

Those parameters correspond well to the data for a linear polymorph of 3,3'-BTP (**3**) (LinI, a = 2.9 ± 0.2 nm, b = 1.6 ± 0.2 nm, $\angle_{a,b}$ = 78 ± 1°) [7]. Interestingly, for 3,3'-BTP (**3**) the most densely packed structure was much more abundant than LinI, whereas for 3,3'-PhSpPy (**15**) the corresponding densely packed 2D assembly could not be found.

With density functional theory calculations, we can show that BTPs and corresponding PhSpPys both possess similar electronic structure. As an example, Figure 8 shows electronic properties for 3,3'-BTP (**3**) and the corresponding 3,3'-PhSpPy (**15**).

The electrostatic potential maps indeed illustrate the similarity of the two different oligopyridines. In both cases, an accumulation of negative charge on the peripheral nitrogen atoms can be observed, whereas the rest of the molecule shows no charge accumulation. While the molecules are very similar, a closer look at the frontier orbitals reveals key differences. In both isomers, the HOMO and LUMO are mainly localized on the backbone pyridine and the pyridines directly connected to it. In the 3,3'-PhSpPy (**15**) molecule, the HOMO extends to the backbone phenyl group, whereas in 3,3'-BTP (**3**) one of the peripheral pyridyl groups contributes to the HOMO. Only for 3,3'-BTP (**15**) an extension of the LUMO to the peripheral pyridines was observed.

The HOMO level is at an energy of −24.31 kJ mol^{-1} for 3,3'-BTP (**3**) and −23.83 kJ mol^{-1} for 3,3'-PhSpPy (**15**). The LUMO levels are at −9.46 kJ mol^{-1} and −8.59 kJ mol^{-1} for 3,3'-BTP (**3**) and 3,3'-PhSpPy (**15**), respectively. Still, it has to be noted that the accuracy of density functional theory for unoccupied states and HOMO–LUMO gaps is rather limited.

Even though there are slight differences in the simulated HOMO and LUMO orbitals, several calculated orbitals must be overlaid for comparison with experimental STM images [33]. With a finite range of orbitals contributing to an STM image, less importance is attributed to the differences in the single orbitals. As Figure 8 shows, the simulated STM images for 3,3'-BTP (**3**) and 3,3'-PhSpPy (**15**) are very similar: Only the phenyl ring, which is not affected by the intermolecular hydrogen bonding, shows any difference.

The similarity of the formed 2D structures of both the BTPs and the corresponding PhSpPys supports the hypothesis that the position of the nitrogen atoms in the central aromatic moiety plays only a minor role for pattern formation, and that the orientation of the peripheral pyridine nitrogen atoms is critical. Thus, we assume that the structures that are formed by the remaining three PhSpPys, with different peripheral pyridine ring orientations, can be seen as substitutes for the structures of the missing BTPs.

All three PhSpPys show lamellar 2D structures at the HOPG/TCB solution interface and only one assembly could be found for each compound.

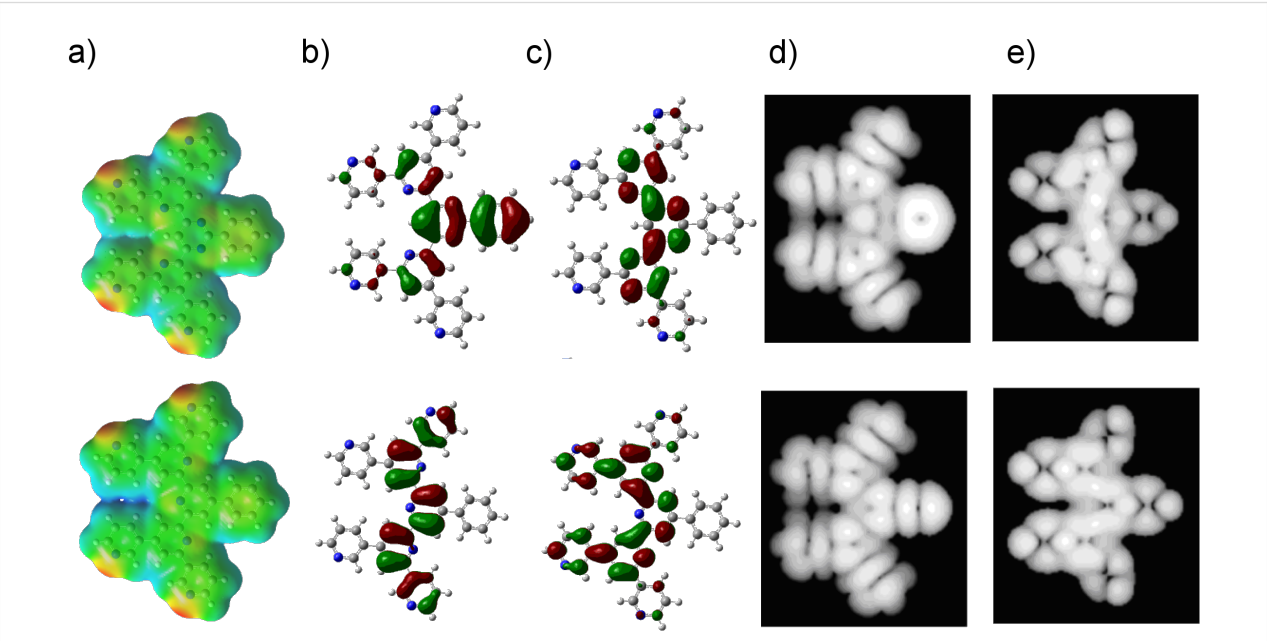

Figure 8: Electronic properties for 3,3'-BTP (**3**) (top) and 3,3'-PhSpPy (**15**) (bottom). (a) Electrostatic potential, (b) HOMO, (c) LUMO, and simulated STM images of (d) occupied and (e) unoccupied orbitals. The energy levels of LUMO and HOMO for 3,3'-BTP (**3**) are −9.46 kJ mol^{-1} and −24.31 kJ mol^{-1} , respectively, and for 3,3'-PhSpPy (**15**) −8.59 kJ mol^{-1} and −23.83 kJ mol^{-1}, respectively.

2,3'-PhSpPy (**13**) self-assembles into an almost rectangular structure (a = 2.8 ± 0.1 nm, b = 1.5 ± 0.1 nm, $\angle_{a,b}$ = 93 ± 2°), where the bright lamellae are clearly separated by slightly elongated dark spots (Figure 9 and Figure S1). In the bright areas, a substructure can be observed, which leads to a tentative model with pairs of PhSpPy molecules pointing with their "legs" to each other and assembled in rows (lamellae). There are intra- and interpair interactions based on single and double intermolecular hydrogen bonds between neighboring *ortho*-connected pyridine rings. There are no hydrogen bonding interactions between the rows. A further conformational arrangement could be imagined where the peripheral 3-pyridyl units point with both N-atoms in the opposite direction at the expense of attracting C–H···N interactions and forming a repulsive N···N interaction. An estimation of the interactions based on C–H···N double bond and single bond dimers [7] yields −36.5 kJ mol^{-1} for the conformation shown in Figure 9 and −29.5 kJ mol^{-1} for the alternative conformation, thus clearly favoring the first one.

A similar 2D structure is found for 4,3'-PhSpPy (**16**) displaying a unit cell with a = 2.8 ± 0.2 nm, b = 1.7 ± 0.2 nm, and $\angle_{a,b}$ = 93 ± 3° (Figure 10). We suggest a model with the corresponding intermolecular interactions as for 2,3'-PhSpPy (**13**), i.e., the *ortho*-connected pyridine rings seem to dominate the packing pattern. An energetic estimation, corresponding to the considerations above, makes an alternative conformation with both nitrogen atoms of the 3-pyridyl rings pointing in the opposite direction unlikely.

2,4'-PhSpPy (**12**) displays a more dense 2D structure than the previous oligopyridines expressed by rows of bright spots leading to a unit cell with a = 2.4 ± 0.2 nm, b = 1.5 ± 0.2 nm, and $\angle_{a,b}$ = 77 ± 2° (Figure 11). The resolution of the STM image does not allow a direct assignment of the molecules to the contrast. Thus, we suggest a tentative model, which shows reasonable hydrogen bonding interactions primarily between the peripheral *para*-connected pyridine units. The model implies dense packing, such that the phenyl rings cannot be coplanar. Rather, they must stand upright, stabilizing the packing by van der Waals interactions. This arrangement might be the reason for the relatively high electron density which is seen as the bright spots in Figure 11a.

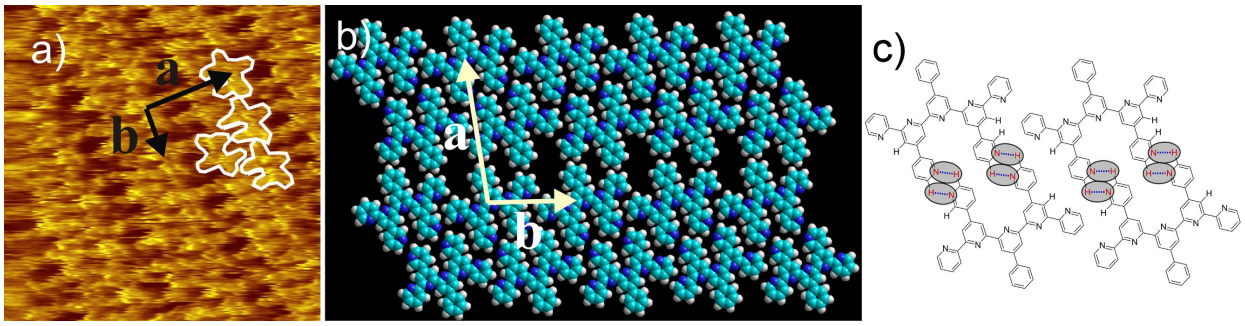

Figure 9: a) 16 × 16 nm^2 STM image (I_{set} = 2.1 nA, V_{set} = −0.60 V) of 2,3'-PhSpPy (**13**) at the HOPG/TCB interface [a = 2.8 ± 0.1 nm, b = 1.5 ± 0.1 nm, $\angle_{a,b}$ = 93 ± 2°] with four overlaid molecules; b) model of the 2,3'-PhSpPy (**13**) lamellar pattern; c) hydrogen bonding motif of 2,3'-PhSpPy (**13**); the hydrogen bonds are marked by ovals.

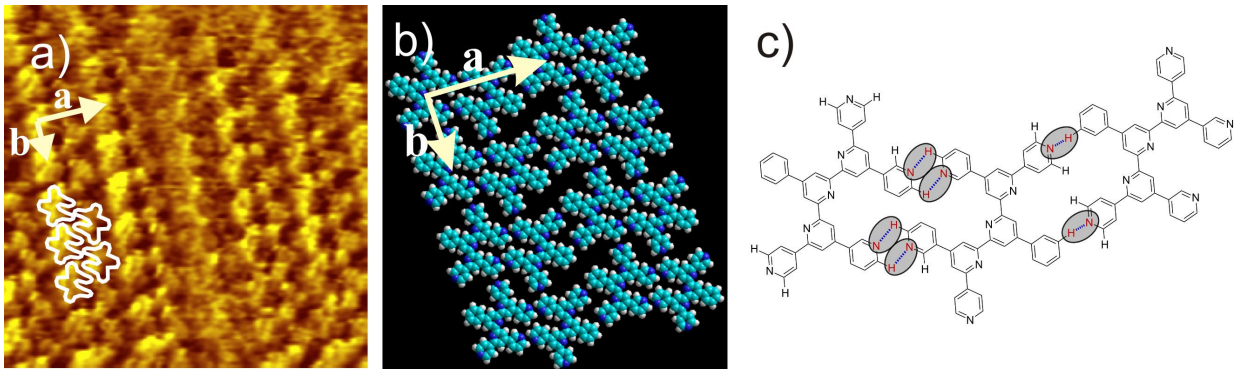

Figure 10: a) 15 × 15 nm^2 STM image (I_{set} = 2.51 nA, V_{set} = −600 mV) of 4,3'-PhSpPy (**16**) at the HOPG/TCB interface [a = 2.8 ± 0.2 nm, b = 1.7 ± 0.2 nm, $\angle_{a,b}$ = 93 ± 3°] with five overlaid molecules; b) model of the 4,3'-PhSpPy (**16**) lamellar pattern; c) hydrogen bonding motif of 4,3'-PhSpPy (**16**); the hydrogen bonds are marked by ovals.

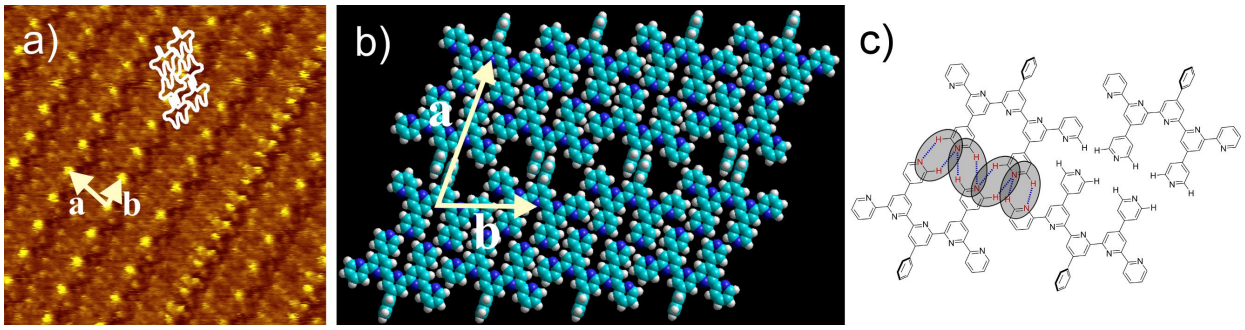

Figure 11: a) 15 × 15 nm^2 STM image (I_{set} = 23.5 pA, V_{set} = −580 mV) of 2,4'-PhSpPy (**12**) at the HOPG/TCB interface [a = 2.4 ± 0.2 nm, b = 1.5 ± 0.2 nm, $\angle_{a,b}$ = 77 ± 2°] with six overlaid molecules; b) model of the 2,4'-PhSpPy (**12**) lamellar pattern; c) hydrogen bonding motif of 2,4'-PhSpPy (**12**); the hydrogen bonds are marked by ovals.

Conclusion

The series of nine possible isomeric bis(terpyridine)-derived oligopyridines (BTPs) was extended by one further member, 2,2'-BTP (**5**). The still missing four isomers were synthetically not accessible, so the class of phenylseptipyridines (PhSpPys) was introduced, which differ from the BTPs only in the central aromatic moiety. The hypothesis that the backbone system of the oligopyridine does not affect 2D self-assembly at the HOPG/solution interface if the orientation of the peripheral nitrogen atoms in the BTPs and the PhSpPys stays the same, was supported by comparing the STM images of the pairs 2,2'-BTP (**5**)/2,2'-PhSpPy (**14**) and 3,3'-BTP (**3**)/3,3'-PhSpPy (**15**). DFT calculations carried out for additional support showed that the electronic structures of each PhSpPy and its corresponding BTP are similar, so a greatly differing behavior is not expected. Although only a single 2D structure was found at the HOPG/liquid interface for each of the new compounds we cannot exclude the possibility of further (pseudo)polymorphs such as is the case for the BTPs, especially for 3,3'-BTP [7,9]. Further experiments with varying concentration and/or different solvents are required to elucidate this issue.

Three new peripheral orientations of the nitrogen atoms in the pyridine rings were obtained using the PhSpPy isomers: 2,3'-PhSpPy (**13**), 3,3'-PhSpPy (**15**), and 4,3'-PhSpPy (**16**). These compounds correspond to three unavailable BTPs because of the inaccessibility of the corresponding three diazachalcone precursors. All of the resulting 2D structures showed lamellar patterns, which are stabilized by the expected hydrogen bonding interactions. Thus, the presented substitution strategy successfully allowed for the near completion of the series, with just one isomer (4,4'-BTP) missing. Such 2D assemblies broaden the understanding of structure formation toward 2D crystal engineering: Additionally, they may act as templates for the creation of hybrid nanostructures, which are under investigation.

Experimental

Scanning tunneling microscopy

STM measurements were carried out under ambient conditions with a low-current RHK 1000 control system. Before the desired measurements the tip was tested by imaging the HOPG surface. These HOPG measurements were used for internal calibration. Then 2 µL solutions of the respective oligopyridine with a concentration of 0.04 mg mL^{-1} (4,3'-PhSpPy (**16**)), 0.05 mg mL^{-1} (2,3'-PhSpPy (**13**) and 3,3'-PhSpPy (**15**)), and 0.20 mg mL^{-1} (2,2'-BTP (**5**), 2,2'-PhSpPy (**14**), and 2,4'-PhSpPy (**12**)) in TCB were prepared. All images presented were obtained in constant current mode using a Pt/Ir (90/10) tip, which was mechanically sharpened. The bias was applied to the tip. The raw STM images were smoothed and the heights were compensated with the program XPMPro2.0.0.8™ (RHK). Some images were Fourier transformed and filtered. The errors given for the unit cells were determined by averaging over several unit cells. The models for the monolayers are constructed with the help of the program Hyperchem (version 7.01, 2002, Hypercube, Inc.) and implemented MM+ force field. The single molecules were positioned manually in van der Waals contact with van der Waals radii for the H–H contacts of 82.5 pm, as given by the program.

Calculations

Gaussian 03 [34] density functional theory calculations were carried out with the B3YLP/6-311G [35,36] method. Electrostatic potentials were mapped onto a constant electron density surface. For the simulated STM images, a simple Tersoff–Hamann [37] approach was used. Orbitals in a given energy range close to the frontier orbitals were added and the resulting density was plotted. The orbitals were generated with Gaussian 03 from geometries that were obtained from relaxation of planar systems. For the addition and visualization steps, a homemade python script was used. Force field results were obtained from geometry optimizations of oligopyridine layers

carried out with the Compass [32] force field as implemented in the Accelrys Materials Studio program package.

Supporting Information

Supporting information describes the synthesis, purification and characterization data of all substances given in this article and some magnified STM images of selected compounds.

Supporting Information File 1

Experimental details.
[http://www.beilstein-journals.org/bjnano/content/supplementary/2190-4286-2-46-S1.pdf]

Acknowledgements

We thank the German Science Foundation ("Deutsche Forschungsgemeinschaft") for financial support within the framework of the Collaborative Research Center 569 ("Sonderforschungsbereich") at the University of Ulm.

References

1. De Feyter, S.; De Schryver, F. C. *Chem. Soc. Rev.* **2003,** *32,* 139–150. doi:10.1039/b206566p
2. De Feyter, S.; De Schryver, F. C. *J. Phys. Chem. B* **2005,** *109,* 4290–4302. doi:10.1021/jp045298k
3. Desiraju, G. R. *Acc. Chem. Res.* **2002,** *35,* 565–573. doi:10.1021/ar010054t
4. Desiraju, G. R. *Chem. Commun.* **2005,** 2995–3001. doi:10.1039/b504372g
5. Ziener, U. *J. Phys. Chem. B* **2008,** *112,* 14698–14717. doi:10.1021/jp805846d
6. Ziener, U.; Lehn, J.-M.; Mourran, A.; Möller, M. *Chem.–Eur. J.* **2002,** *8,* 951–957. doi:10.1002/1521-3765(20020215)8:4<951::AID-CHEM951>3.0.CO;2-9
7. Meier, C.; Ziener, U.; Landfester, K.; Weihrich, P. *J. Phys. Chem. B* **2005,** *109,* 21015–21027. doi:10.1021/jp054271d
8. Meier, C.; Landfester, K.; Künzel, D.; Markert, T.; Ziener, U.; Groß, A. *Angew. Chem. Int. Ed.* **2008,** *47,* 3821–3825. doi:10.1002/anie.200705527
Angew. Chem. **2008,** *120,* 3881–3885.
9. Meier, C.; Roos, M.; Künzel, D.; Breitruck, A.; Hoster, H. E.; Landfester, K.; Groß, A.; Behm, R. J.; Ziener, U. *J. Phys. Chem. C* **2010,** *114,* 1268–1277. doi:10.1021/jp910029z
10. Meier, C.; Landfester, K.; Ziener, U. *J. Phys. Chem. C* **2008,** *112,* 15236–15240. doi:10.1021/jp804235a
11. Ruben, M.; Ziener, U.; Lehn, J.-M.; Ksenofontov, V.; Gütlich, P.; Vaughan, G. B. M. *Chem.–Eur. J.* **2005,** *11,* 94–100. doi:10.1002/chem.200400584
12. Hoster, H. E.; Roos, M.; Breitruck, A.; Meier, C.; Waldmann, T.; Tonigold, K.; Ziener, U.; Landfester, K.; Behm, R. J. *Langmuir* **2007,** *23,* 11570–11579. doi:10.1021/la701382n
13. Breitruck, A.; Hoster, H. E.; Meier, C.; Ziener, U.; Behm, R. J. *Surf. Sci.* **2007,** *601,* 4200–4205. doi:10.1016/j.susc.2007.04.173
14. Roos, M.; Hoster, H. E.; Breitruck, A.; Behm, R. J. *Phys. Chem. Chem. Phys.* **2007,** *9,* 5672–5679. doi:10.1039/b708578h
15. Dai, Y.; Meier, C.; Ziener, U.; Landfester, K.; Täubert, C.; Kolb, D. M. *Langmuir* **2007,** *23,* 11058–11062. doi:10.1021/la701479r
16. Buchner, F.; Comanici, K.; Jux, N.; Steinruck, H. P.; Marbach, H. *J. Phys. Chem. C* **2007,** *111,* 13531–13538. doi:10.1021/jp074448z
17. Samuely, T.; Liu, S. X.; Wintjes, N.; Haas, M.; Decurtins, S.; Jung, T. A.; Stöhr, M. *J. Phys. Chem. C* **2008,** *112,* 6139–6144. doi:10.1021/jp710887g
18. Yang, X.; Wang, J.; Zhang, X.; Wang, Z.; Wang, Y. *Langmuir* **2007,** *23,* 1287–1291. doi:10.1021/la0624034
19. Klappenberger, F.; Canas-Ventura, M. E.; Clair, S.; Pons, S.; Schlickum, U.; Qu, Z.-R.; Strunskus, T.; Comisso, A.; Wöll, C.; Brune, H.; Kern, K.; Vita, A. D.; Ruben, M.; Barth, J. V. *ChemPhysChem* **2008,** *9,* 2522–2530. doi:10.1002/cphc.200800590
20. Linares, M.; Scifo, L.; Demadrille, R.; Brocorens, P.; Beljonne, D.; Lazzaroni, R.; Grevin, B. *J. Phys. Chem. C* **2008,** *112,* 6850–6859. doi:10.1021/jp711047x
21. Matena, M.; Llanes-Pallas, A.; Enache, M.; Jung, T.; Wouters, J.; Champagne, B.; Stöhr, M.; Bonifazi, D. *Chem. Commun.* **2009,** 3525–3527. doi:10.1039/b902120e
22. Xu, H.; Minoia, A.; Tomovic, Z.; Lazzaroni, R.; Meijer, E. W.; Schenning, A. P. H. J.; De Feyter, S. *ACS Nano* **2009,** *3,* 1016–1024. doi:10.1021/nn900131k
23. Donovan, P.; Robin, A.; Dyer, M. S.; Persson, M.; Raval, R. *Chem.–Eur. J.* **2010,** *16,* 11641–11652. doi:10.1002/chem.201001776
24. Zhang, J.; Gesquiere, A.; Sieffert, M.; Klapper, M.; Müllen, K.; De Schryver, F. C.; De Feyter, S. *Nano Lett.* **2005,** *5,* 1395–1398. doi:10.1021/nl050717q
25. Knudsen, M. M.; Kalashnyk, N.; Masini, F.; Cramer, J. R.; Laegsgaard, E.; Besenbacher, F.; Linderoth, T. R.; Gothelf, K. V. *J. Am. Chem. Soc.* **2011,** *133,* 4896–4905. doi:10.1021/ja110052n
26. Bonifazi, D.; Kiebele, A.; Stöhr, M.; Cheng, F.; Jung, T.; Diederich, F.; Spillmann, H. *Adv. Funct. Mater.* **2007,** *17,* 1051–1062. doi:10.1002/adfm.200600586
27. Shen, Y.-T.; Guan, L.; Zhu, X.-Y.; Zeng, Q.-D.; Wang, C. *J. Am. Chem. Soc.* **2009,** *131,* 6174–6180. doi:10.1021/ja808434n
28. Scherer, L. J.; Merz, L.; Constable, E. C.; Housecroft, C. E.; Neuburger, M.; Hermann, B. A. *J. Am. Chem. Soc.* **2005,** *127,* 4033–4041. doi:10.1021/ja043638+
29. Nishiyama, K.; Tsuchiyama, M.; Kubo, A.; Seriu, H.; Miyazaki, S.; Yoshimoto, S.; Taniguchi, I. *Phys. Chem. Chem. Phys.* **2008,** *10,* 6935–6939. doi:10.1039/b810777g
30. Howard, S. T. *J. Am. Chem. Soc.* **1996,** *118,* 10269–10274. doi:10.1021/ja960932w
31. Kröhnke, F. *Synthesis* **1976,** *1,* 1–24. doi:10.1055/s-1976-23941
32. Sun, H. *J. Phys. Chem. B* **1998,** *102,* 7338–7364. doi:10.1021/jp980939v
33. Künzel, D.; Markert, T.; Groß, A.; Benoit, D. *Phys. Chem. Chem. Phys.* **2009,** *11,* 8867–8878. doi:10.1039/b907443k
34. *Gaussian 03,* Revision D.1 ed.; Gaussian, Inc.: Wallingford, CT, 2004.
35. Becke, A. D. *J. Chem. Phys.* **1993,** *98,* 5648–5652. doi:10.1063/1.464913
36. McLean, A. D.; Chandler, G. S. *J. Chem. Phys.* **1980,** *72,* 5639. doi:10.1063/1.438980
37. Tersoff, J.; Hamann, D. R. *Phys. Rev. B: Condens. Matter Mater. Phys.* **1985,** *31,* 805–813. doi:10.1103/PhysRevB.31.805

Beilstein Journal of Nanotechnology

Charge transfer through single molecule contacts: How reliable are rate descriptions?

Denis Kast*, L. Kecke and J. Ankerhold

Full Research Paper

Open Access

Address:
Universität Ulm, Institut für Theoretische Physik, Albert-Einstein-Allee 11, 89069 Ulm, Germany

Email:
Denis Kast* - denis.kast@uni-ulm.de

* Corresponding author

Keywords:
inelastic charge transfer; molecular contacts; nonequilibrium distributions; numerical simulations; rate equations

Beilstein J. Nanotechnol. **2011,** *2,* 416–426.
doi:10.3762/bjnano.2.47

Received: 18 April 2011
Accepted: 06 July 2011
Published: 03 August 2011

This article is part of the Thematic Series "Organic–inorganic nanosystems".

Guest Editor: P. Ziemann

Abstract

Background: The trend for the fabrication of electrical circuits with nanoscale dimensions has led to impressive progress in the field of molecular electronics in the last decade. However, a theoretical description of molecular contacts as the building blocks of future devices is challenging, as it has to combine the properties of Fermi liquids in the leads with charge and phonon degrees of freedom on the molecule. Outside of ab initio schemes for specific set-ups, generic models reveal the characteristics of transport processes. Particularly appealing are descriptions based on transfer rates successfully used in other contexts such as mesoscopic physics and intramolecular electron transfer. However, a detailed analysis of this scheme in comparison with numerically exact solutions is still elusive.

Results: We show that a formulation in terms of transfer rates provides a quantitatively accurate description even in domains of parameter space where strictly it is expected to fail, e.g., at lower temperatures. Typically, intramolecular phonons are distributed according to a voltage driven steady state that can only roughly be captured by a thermal distribution with an effective elevated temperature (heating). An extension of a master equation for the charge–phonon complex, to effectively include the impact of off-diagonal elements of the reduced density matrix, provides very accurate solutions even for stronger electron–phonon coupling.

Conclusion: Rate descriptions and master equations offer a versatile model to describe and understand charge transfer processes through molecular junctions. Such methods are computationally orders of magnitude less expensive than elaborate numerical simulations that, however, provide exact solutions as benchmarks. Adjustable parameters obtained, e.g., from ab initio calculations allow for the treatment of various realizations. Even though not as rigorously formulated as, e.g., nonequilibrium Green's function methods, they are conceptually simpler, more flexible for extensions, and from a practical point of view provide accurate results as long as strong quantum correlations do not modify the properties of the relevant subunits substantially.

Introduction

Electrical devices on the nanoscale have received substantial interest in the last decade [1]. Impressive progress has been achieved in contacting single molecules or molecular aggregates with conducting or even superconducting metallic leads [2,3]. The objective is to exploit nonlinear transport properties of molecular junctions as the elementary units for a future molecular electronics. While the initial experiments were operated at room temperature, low temperatures down to the millikelvin range, the typical regime for devices in mesoscopic solid state physics, are also accessible (see, e.g., [4-6]). This allows for detailed studies of phenomena such as inelastic charge transfer due to molecular vibrations [7-9], voltage driven conformational changes of the molecular backbone [10], Kondo physics [11], and Andreev reflections [6], to name but a few.

These developments have been accompanied by efforts to advance theoretical approaches in order to obtain an understanding of general physical processes on the one hand and to arrive at a tool to quantitatively describe and predict experimental data. For this purpose, basically two strategies have been followed. One is based on ab initio schemes that have been successfully employed for isolated molecular structures, such as, e.g., density functional theory (DFT). Combining DFT with nonequilibrium Green's functions (NEGF) allows us to capture essential properties of junctions with specific molecular structures and geometries [2,3,12,13]. This provides insight into the electronic formations of contacted molecules and gives at least qualitatively correct results for currents and differential conductances. However, a quantitative description at the level of accuracy known from conventional mesoscopic devices still seems to be out of reach. Furthermore, these methods are not able to capture phenomena resulting from strong correlations effects, such as Kondo resonances.

Thus, an alternative route, mainly inspired by solid state methodologies, starts with simplified models that are assumed to cover the relevant physical features. The intention then is to reveal fundamental processes characteristic for molecular electronics that give a qualitative description of observations from realistic samples, but provide also the basis for a proper design of molecular junctions to exploit these processes. Information about specific molecular set-ups appears merely in the form of parameters which offer a large degree of flexibility. In general, to attack the respective many body problems, perturbative schemes have been applied, the most powerful of which are nonequilibrium Green's functions [14,15]. However, conceptually simpler, easier to implement, and often better at revealing the physics, are treatments in terms of master or rate equations. Being approximations to the NEGF frame in certain ranges of parameters space, they sometimes lack the strictness of perturbation series, but have been extensively employed for mesoscopic devices [16] and quantitatively often provide solutions of at least similar accuracy. Roughly speaking, these schemes apply as long as quantum correlations between relevant subunits of the full compound are sufficiently weak [15]. Physically, it places charge transfer through molecular contacts in the context of inelastic charge transfer through ultrasmall metallic contacts (dynamical Coulomb blockade [17]) and in the context of solvent or vibronic mediated intramolecular charge transfer (Marcus theory) [18-20].

While rate descriptions have been developed in a variety of formulations before [21-28], the performance of such a framework in comparison with numerically exact solutions has not yet been addressed. The reason for this is simple: A numerical method that provides numerically exact data in most ranges of parameters space (temperature, coupling strength, etc.) has only very recently been successfully implemented in the form of a diagrammatic Monte Carlo approach [29]. Path integral Monte Carlo methods have been used previously for intramolecular charge transfer in complex aggregates [18,19] in a variety of situations, including correlated [30] and externally driven transfer [31] and, of particular relevance to the present work, transfer in the presence of prominent phonon modes [32].

The goal of the present work is to study a simple yet highly nontrivial set-up, namely, a molecular contact with a single molecular level coupled to a prominent vibronic mode (phonon) which itself may or may not be embedded in a bosonic heat bath. We develop rate descriptions of various complexity, place them into the context of NEGF, and compare them with exact solutions. The essence of this study is, astonishingly enough, that rate theory provides quantitatively accurate results for mean currents over a very broad range of parameter space, even in domains where they are not expected to be reliable.

Results and Discussion

In subsection 1 we define the model and the basic ingredients for a perturbative treatment. A formulation which closely follows the $P(E)$ theory for dynamical Coulomb blockade is discussed in subsection 2. Nonequilibrium effects in the stationary phonon distribution are analyzed in subsection 3 based on a dynamical formulation of charge and phonon degrees of freedom. The presence of a secondary bath is incorporated in subsection 4 together with an improved treatment of the molecule–lead coupling, which is exact for vanishing electron–phonon interaction. The comparison with numerically exact data and a detailed discussion is given in subsection 5.

1 Model

We start with the minimal model of a molecular contact consisting of a single electronic level (dot) coupled to fermionic reservoirs, where a prominent internal molecular phonon mode interacting with the excess charge is described by a harmonic degree of freedom (Figure 1) [15,33,34].

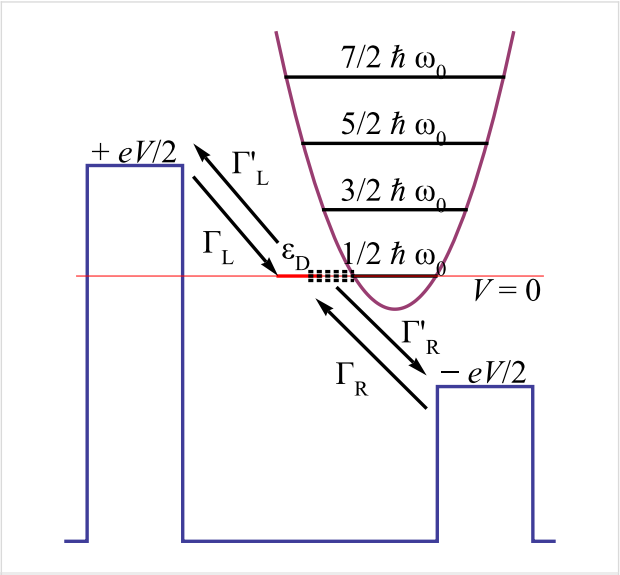

Figure 1: Single charge transfer through a molecular contact consisting of a single electronic level coupled to a harmonic phonon mode and contacted to metallic leads. Forward (no prime) and backward (with prime) rates are the basic ingredients for the approximate treatment, see text for details.

Neglecting spin degrees of freedom the total compound Hamiltonian is thus described by

$$\begin{aligned} H &= H_{\mathrm{L/R}} + H_{\mathrm{T}} + H_{\mathrm{D}} + H_{\mathrm{D,Ph}} + H_{\mathrm{Ph}} \\ &= \sum_{\alpha=\mathrm{L,R};\,\mathrm{k}} \varepsilon_{\mathrm{k},\alpha} c^{\dagger}_{\mathrm{k},\alpha} c_{\mathrm{k},\alpha} + \sum_{\alpha=\mathrm{L,R};\,\mathrm{k}} \left(T_{\mathrm{k},\alpha} c^{\dagger}_{\mathrm{k},\alpha} d + h.c.\right) \\ &\quad + \varepsilon_{\mathrm{D}} d^{\dagger} d + \frac{p_0^2}{2m} + \frac{m\omega_0^2}{2}\left(x_0 + l_0 d^{\dagger} d\right)^2 \end{aligned} \tag{1}$$

Here, the $T_{\mathrm{k},\alpha}$ denote tunnel couplings between dot level and reservoir α and $l_0 = M_0\sqrt{2/\hbar\omega_0^3 m}$ contains the coupling M_0 between excess charge and phonon mode. An external voltage V across the contact is applied symmetrically around the Fermi level such that $\varepsilon_{\mathrm{k},\alpha} = \varepsilon_0(k) + \mu_\alpha$, with the bare electronic dispersion relation $\varepsilon_0(k)$ and chemical potentials $\mu_{\mathrm{L}} = +eV/2$, $\mu_{\mathrm{R}} = -eV/2$. Below, this model will be extended further to include the embedding of the prominent mode into a large reservoir of residual molecular and/or solvent degrees of freedom acting as a heat bath. Qualitatively, since the dot occupation $d^{\dagger}d$ can only take the values $q = 0$ or 1, the sub-unit $H_{\mathrm{D}} + H_{\mathrm{D,Ph}} + H_{\mathrm{Ph}}$ describes a two state system coupled to a harmonic mode (spin–boson model [20]). Depending on the charge state of the dot the phonon mode is subject to potentials $V_{\mathrm{q}}(x_0) = (m\omega_0^2/2)(x_0 + l_0 q)^2$. Now, the presence of the leads acts (for finite voltages) as an external driving force alternately charging ($q = 1$) and discharging ($q = 0$) the dot, thus switching alternately between V_0 and V_1 for the phonon mode. The classical energy needed to reorganize the phonon is the so-called reorganization energy $\Lambda = V_1(0) - V_0(0) = M_0^2/\hbar\omega_0$. Quantum mechanically, the phonon mode may also tunnel through the energy barrier located around $x_0 = -l_0/2$ separating the minima of $V_{0,1}$.

It is convenient to work with dressed electronic states on the dot and thus to apply a polaron transformation generating the shift l_0 in the oscillator coordinate associated with a charge transfer process, i.e.,

$$U = \exp\left(-i\frac{p_0 l_0}{\hbar} d^{\dagger} d\right) \tag{2}$$

with momentum operator $p_0 = i\sqrt{\hbar m\omega_0/2}\,(b_0^{\dagger} - b_0)$ where $b_0^{\dagger}$ and b_0 are creation and annihilation operators of the phonon mode, respectively. We mention in passing that complementary to the situation here, the theory of dynamical Coulomb blockade in ultrasmall metallic contacts is based on a transformation which generates a shift in momentum (charge) rather than position [17]. Now, the electron–phonon interaction is completely absorbed in the tunnel part of the Hamiltonian, thus capturing the cooperative effect of charge tunneling onto the dot and photon excitation in the molecule, i.e., $H = H_{\mathrm{L/R}} + H_{\mathrm{D}} + \tilde{H}_{\mathrm{Ph}} + \tilde{H}_{\mathrm{T}}$ with

$$\begin{aligned} \tilde{H}_{\mathrm{Ph}} &= \hbar\omega_0\left(b_0^{\dagger} b_0 + \frac{1}{2}\right) \\ \tilde{H}_{\mathrm{T}} &= \sum_{\alpha=\mathrm{L,R};\,\mathrm{k}} T_{\mathrm{k},\alpha} c^{\dagger}_{\mathrm{k},\alpha} d\,\exp\left(\frac{i}{\hbar} p_0 l_0\right) + h.c. \end{aligned} \tag{3}$$

Single charge tunneling through the device can be formally and exactly captured under weak conditions (e.g., instantaneous equilibration in the leads during charge transfer) within the Meir–Wingreen formulation based on nonequilibrium Green's functions [14,15]. For the current–voltage characteristics one finds

$$\begin{aligned} I(V) = \frac{4e}{\hbar}\int d\varepsilon\ \frac{\Sigma_{\mathrm{L}}\Sigma_{\mathrm{R}}}{\Sigma_{\mathrm{L}} + \Sigma_{\mathrm{R}}}\left[f_\beta\left(\varepsilon - \frac{eV}{2}\right) - f_\beta\left(\varepsilon + \frac{eV}{2}\right)\right] \\ \times\left[iG^{>}(\varepsilon) - iG^{<}(\varepsilon)\right] \end{aligned} \tag{4}$$

with energy dependent lead self-energies $\sum_\alpha(\varepsilon) = 2\pi\sum_k|T_{k,\alpha}|^2\delta(\varepsilon - \varepsilon_k)$ and with the Fourier transforms of the time dependent Green's functions $G^<(t) = i\langle d^\dagger d(t)\rangle$ and $G^>(t) = -i\langle d(t)d^\dagger\rangle$. Upon applying the polaron transformation (Equation 2), one has

$$G^<(t) = i\left\langle d^\dagger \mathrm{e}^{-\frac{i}{\hbar}\mathrm{p}_0\mathrm{l}_0}\,\mathrm{e}^{\frac{i}{\hbar}\mathrm{p}_0(t)\mathrm{l}_0}\,d(t)\right\rangle$$
$$G^>(t) = -i\left\langle \mathrm{e}^{\frac{i}{\hbar}\mathrm{p}_0(t)\mathrm{l}_0}\,d(t)d^\dagger\,\mathrm{e}^{-\frac{i}{\hbar}\mathrm{p}_0\mathrm{l}_0}\right\rangle, \qquad (5)$$

where all expectation values are calculated with the full Hamiltonian (Equation 3). Of course, for $T_{k,\alpha} \to 0$, the Green's functions factorize as, e.g., $G^<(t) \to i\langle d^\dagger d(t)\rangle_D \exp[J(t)]$ with the phonon correlation

$$\mathrm{e}^{J(t)} = \left\langle \mathrm{e}^{-\frac{i}{\hbar}p_0 l_0}\,\mathrm{e}^{\frac{i}{\hbar}p_0(t)l_0}\right\rangle_{\mathrm{Ph}} \qquad (6)$$

into expectation values with respect to the dot (D) and the phonon (Ph), respectively. Any finite tunnel coupling induces correlations that in analytical treatments can only be incorporated perturbatively. There, the proper approximative scheme depends on the range of parameter space one considers. Generally speaking, there are four relevant energy scales $\sum_{L/R}$, M_0, k_BT, and $\hbar\omega_0$ of the problem corresponding to three independent dimensionless parameters, e.g.,

$$m_0 = \frac{M_0}{\hbar\omega_0},\ \theta = \omega_0\hbar\beta,\ \sigma = \frac{\Sigma_L + \Sigma_R}{\hbar\omega_0}. \qquad (7)$$

In the following we are interested in the low temperature domain $\theta > 1$ where thermal broadening of phonon levels is small such that discrete steps appear in the *I–V* characteristics. Qualitatively, seen from the dynamics of the phonon mode, two regimes can be distinguished according to the adiabaticity parameter $\sum/\hbar\omega_0 = \sigma$: For $\sigma < 1$ the phonon wave packet fulfills, on a *given surface* V_0 or V_1, multiple oscillations before a charge transfer process occurs. The electron carries excess energy due to the finite voltage, and this energy may be absorbed by the phonon to promote reorganization to the new conformation (in the classical case the reorganization energy Λ). In the language of intramolecular charge transfer this scenario corresponds to the diabatic regime with well-defined surfaces V_q. In the opposite regime $\sigma > 1$ charge transfer is fast such that the phonon may undergo multiple switchings *between the surfaces* $V_{0,1}$. This is the adiabatic regime. In this latter range the impact of the adiabaticity on the diabatic ground state wave functions is weak for $m_0 < 1$ when the distance of the diabatic surfaces is small compared to the widths of the ground states. For $m_0 > 1$ in both regimes electron transfer is accompanied by phonon tunneling through energy barriers separating the minima of adiabatic or diabatic surfaces. The dynamics of the total compound are then determined by voltage driven, collective tunneling processes. Master equation approaches to be investigated below, rely on the assumption that both sub-units, charge degree of freedom and phonon mode preserve their bare physical properties even in the case of finite coupling m_0. Hence, since the model (Equation 1) can be solved exactly in the limits $m_0 = 0$ and $\sigma = 0$ and following the above discussion, we expect them to capture the essential physics quantitatively in the domain $m_0 < 1$ and for all ratios σ. We note that recently the strong coupling limit including the current statistics has been addressed as well [35,36].

2 Rate approach I

The simplest perturbative approach considers the cooperative effect of electron tunneling and phonon excitation in terms of Fermi's golden rule for the tunneling part $\tilde{H}_T$. For this purpose one derives transition rates for sequential transfer according to Figure 1. A straightforward calculation for energy independent self-energies $\sum_{L/R}$ (wide band limit) gives the forward rate onto the dot from the left lead

$$\Gamma_L(V,\varepsilon_D) = \frac{\Sigma_L}{\hbar}\int d\varepsilon\, f_\beta\left(\varepsilon - \frac{eV}{2}\right)P_0(\varepsilon - \varepsilon_D), \qquad (8)$$

where $f_\beta(\varepsilon)$ is the Fermi distribution. Inelastic tunneling associated with energy emission/absorption of phonons is captured by the Fourier transform of the phonon–phonon correlation $\exp[J(t)]$ leading to

$$P_0(\varepsilon) = \mathrm{e}^{-\rho_a-\rho_e}\sum_{k,l}\frac{\rho_a^k\rho_e^l}{k!l!}\delta\left[\varepsilon - \hbar\omega_0(l-k)\right] \qquad (9)$$

with $\rho_{a/e} = (m_0^2/2)\left[\coth(\theta/2) \mp 1\right]$ denoting the mean values for single phonon absorption (a) and emission (e). The exponentials in the prefactor contain the dimensionless reorganization energy $m_0^2 = \Lambda/\hbar\omega_0$. Apparently, inelastic charge transfer includes the exchange of multiple phonon quanta according to a Poissonian distribution. Further, one has the detailed balance relation $P_0(-\varepsilon) = \mathrm{e}^{-\beta\varepsilon}P_0(\varepsilon)$. For vanishing phonon–electron coupling $m_0 \to 0$ only the elastic peak survives, thus $P_0(\varepsilon) \to \delta(\varepsilon)$. We note again the close analogy to the $P(E)$ theory for dynamical Coulomb blockade [17]. Moreover, golden rule rates

for intramolecular electron transfer between donor and acceptor sites coupled to a single phonon mode are of the same form with the notable difference, of course, that in this case one has a discrete density of states for both sites [20,22]. The fundamental assumption underlying the golden rule treatment is that equilibration of the phonon mode occurs much faster than charge transfer. In the last two cases this is typically guaranteed by the presence of a macroscopic heat bath (secondary bath) strongly coupled to the prominent phonon mode. Here, the fermionic reservoirs in the leads impose phonon relaxation due to charge transfer only. Thus, for finite voltage the steady state is always a nonequilibrium state that can only roughly be described by a thermal distribution of the bare phonon system (see below). One way to remedy this problem is to introduce a phonon–secondary bath interaction as well (see below in subsection 4). The remaining transition rates easily follow due to symmetry

$$\begin{aligned}\Gamma_{\mathrm{R}}(V,\varepsilon_{\mathrm{D}}) &= \frac{\Sigma_{\mathrm{R}}}{\Sigma_{\mathrm{L}}}\Gamma_{\mathrm{L}}(V,-\varepsilon_{\mathrm{D}}),\\ \Gamma'_{\mathrm{R}}(V,\varepsilon_{\mathrm{D}}) &= \frac{\Sigma_{\mathrm{R}}}{\Sigma_{\mathrm{L}}}\Gamma_{\mathrm{L}}(-V,\varepsilon_{\mathrm{D}}),\\ \Gamma'_{\mathrm{L}}(V,\varepsilon_{\mathrm{D}}) &= \Gamma_{\mathrm{L}}(-V,-\varepsilon_{\mathrm{D}}).\end{aligned} \tag{10}$$

Now, summing up forward and backward events, the dot population follows from

$$\frac{d\hat{p}_{\mathrm{dot}}}{dt} = -\Gamma_{\mathrm{tot},0}\,\hat{p}_{\mathrm{dot}} + \Gamma_{\mathrm{d}} \tag{11}$$

with the total rate $\Gamma_{\mathrm{tot},0} = \Gamma_{\mathrm{L}} + \Gamma_{\mathrm{R}} + \Gamma'_{\mathrm{L}} + \Gamma'_{\mathrm{R}}$ and the rate for transfer towards the dot $\Gamma_{\mathrm{D}} = \Gamma_{\mathrm{L}} + \Gamma'_{\mathrm{R}}$ obtained according to Equation 8. Note that for vanishing electron–phonon coupling $M_0 = 0$ one has $\hbar\Gamma_{\mathrm{tot},0}(M_0 = 0) = \sum_{\mathrm{L}} + \sum_{\mathrm{R}}$. The steady state distribution $\hat{p}_{\mathrm{dot}} \to p_{\mathrm{dot}} = \Gamma_{\mathrm{D}}/\Gamma_{\mathrm{tot},0}$ is approached with relaxation rate $\Gamma_{\mathrm{tot},0}$. For a symmetric situation $\sum_{\mathrm{L}} = \sum_{\mathrm{R}}$ with $\varepsilon_{\mathrm{D}} = 0$ one shows that $p_{\mathrm{dot}} = 1/2$ independent of the voltage, while asymmetric cases lead to voltage dependent stationary populations. The steady state current is given by $I(V) = (e/2)[(\Gamma_{\mathrm{L}} - \Gamma'_{\mathrm{R}})(1 - p_{\mathrm{dot}}) - (\Gamma'_{\mathrm{L}} - \Gamma_{\mathrm{R}})p_{\mathrm{dot}}]$ such that

$$I(V) = e\frac{\Gamma_{\mathrm{L}}\Gamma_{\mathrm{R}} - \Gamma'_{\mathrm{L}}\Gamma'_{\mathrm{R}}}{\Gamma_{\mathrm{tot},0}}. \tag{12}$$

A transparent expression is obtained for $\varepsilon_{\mathrm{D}} = 0$, namely,

$$I(V) = \frac{e}{\hbar}\frac{\Sigma_{\mathrm{L}}\Sigma_{\mathrm{R}}}{\Sigma_{\mathrm{L}} + \Sigma_{\mathrm{R}}}\int d\varepsilon\left[f_\beta\left(\varepsilon - \frac{eV}{2}\right) - f_\beta\left(\varepsilon + \frac{eV}{2}\right)\right]P_0(\varepsilon). \tag{13}$$

Despite its deficiencies mentioned above, the golden rule treatment provides already a qualitative insight into the transport characteristics. Typical results are shown in Figure 2.

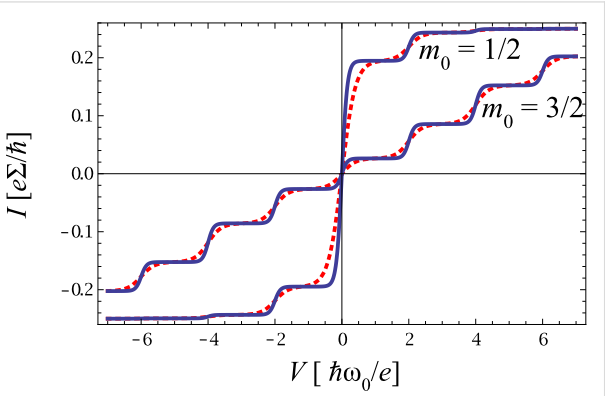

Figure 2: *I–V*-characteristics for symmetric coupling $\sum_{\mathrm{L}} = \sum_{\mathrm{R}}$ and for varying electron–phonon coupling m_0 at inverse temperature $\theta = 25$ (solid) and $\theta = 10$ (dashed).

The I–V curves display the expected steps at $eV = 2n\hbar\omega_0, n \in \mathbb{Z}$. Each time the voltage $eV/2$ exceeds multiples of $\hbar\omega_0$ new transport channels open associated with the excitation of one additional phonon. For higher temperatures the steps are smeared out by thermal fluctuations. The range of validity of this description follows from the fact that a factorizing assumption for the electron–phonon correlation *and* an instantaneous equilibration of the phonon mode after a charge transfer has been used, which means that $\sigma < 1$ and $m_0 < 1$. The latter constraint guarantees that conformational changes of the phonon distribution remain small.

There are now three ways to go beyond this golden rule approximation. With respect to the phonon mode, one way is to explicitly account for the nonequilibrium dynamics, another is to introduce a direct interaction with a secondary heat bath in order to induce sufficiently fast equilibration. With respect to the dot degree of freedom one can exploit the fact that for vanishing charge–phonon coupling the model can be solved exactly.

3 Master equation for nonequilibrated phonons

To derive an equation of motion for the combined dynamics of charge and phonon degrees of freedom, one starts from a Liouville–von Neumann equation for the full polaron transformed compound (Equation 3). Then, applying a Born–Markov type of approximation with respect to the tunnel coupling to the fermionic reservoirs, one arrives at a Redfield-type equation for the reduced density matrix of the dot–phonon system [15]. An additional rotating wave approximation (RWA) separates the

dynamics of diagonal (populations) and off-diagonal (coherences) elements of the reduced density. Denoting with $\hat{P}_q^n$ the probability to find q charges on the dot (here, for single charge transfer $q = 0,1$) and the phonon in its n-th eigenstate, one has

$$\frac{d\hat{P}_q^n(t)}{dt} = -\frac{1}{h}\sum_{\alpha=L,R;\,k}|f_{n,k}|^2 \times \Sigma_\alpha\left[f_\beta\left(E_{kn}^{q,\alpha}\right)\hat{P}_q^n - f_\beta\left(-E_{kn}^{q,\alpha}\right)\hat{P}_{q+\nu_q}^k\right] \quad (14)$$

with $\nu_0 = 1$, $\nu_1 = -1$ and energies $E_{kn}^{q,\alpha} = \hbar\omega_0(k-n)+\nu_q(\mu_\alpha+\varepsilon_D)$. The matrix elements of the phonon shift operator $f_{n,k} = \langle n|\exp(ip_0l_0/\hbar)|k\rangle$ read

$$f_{n,k} = e^{-m_0^2/2}\frac{(-m_0)^{|n-k|}}{(n-k)!}\left(\prod_{l=\min(n,k+1)}^{\max(n,k)} l\right)^{\frac{1}{2}} \times {}_1F_1\left(\max(n,k)+1,|n-k|+1,-m_0^2\right), \quad (15)$$

where ${}_1F_1$ denotes a hypergeometric function. The underlying assumptions of this formulation require weak dot–lead coupling $\sigma < 1$ and sufficiently elevated temperatures $\sigma\theta < 1$ for a Markov approximation to be valid. Although we will see below when comparing low temperature results with numerically exact solutions that this seems to be only a weak constraint.

The calculation of the steady state distribution $P_q^n = \lim_{t\to\infty}\hat{P}_q^n(t)$ reduces to a standard matrix inversion. One can show that for a symmetric system with $\varepsilon_D = 0$, $\Sigma_L = \Sigma_R$ one has $P_0^n = P_1^n$. A typical example for the mean phonon number $\langle n\rangle = \sum_{q,n} nP_q^n$ is depicted in Figure 3. The curve is well approximated by a/m_0 with $a \approx 0.7$. Apparently, $\langle n\rangle$ diverges for $m_0 \to 0$ since then P_0^n and P_1^n approach constants independent of the phonon number. Upon closer inspection one finds that excitation is more likely than absorption, i.e., $f(n,n+1) > f(n,n-1)$, for all $0 \le n \le N_0(m_0)$ where $N_0(m_0)$ increases with decreasing m_0. The opposite is true for $n > N_0(m_0)$ such that in a steady state, depending on the voltage, the tendency is to have higher excited phonon states occupied by smaller couplings m_0. In particular, for strong coupling transitions $n \to n+k, k \ge 0$ are blocked at small n.

A convenient strategy to include nonequilibrium effects in the phonon distribution, sometimes used in the interpretation of experimental data, is the introduction of an effective temperature T_{eff}. This way one could return to the simpler modeling of the previous section. However, the procedure to identify $P_0^n + P_1^n \approx P_\beta^n = \exp(-\beta_{eff}\hbar\omega_0 n)/[1-\exp(-\beta_{eff}\hbar\omega_0)]$ is not reliable, as Figure 4 reveals. While it clearly shows the general tendency of a substantial heating of the phonon degree of freedom induced by the electron transfer, the profile of a thermal distribution strongly differs from the actual steady state distribution.

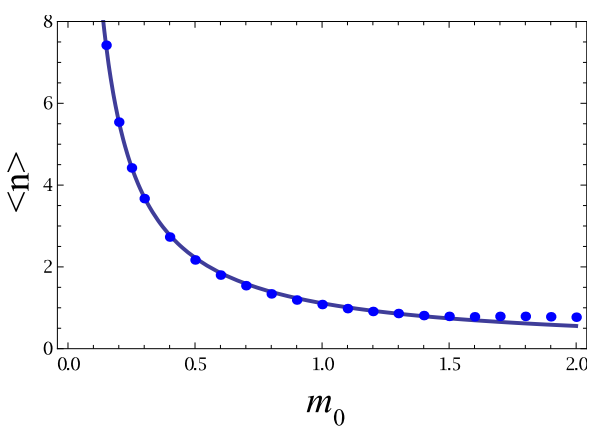

Figure 3: Mean phonon number in nonequilibrium for $eV = 3\hbar\omega_0$ and versus the electron–phonon coupling m_0.

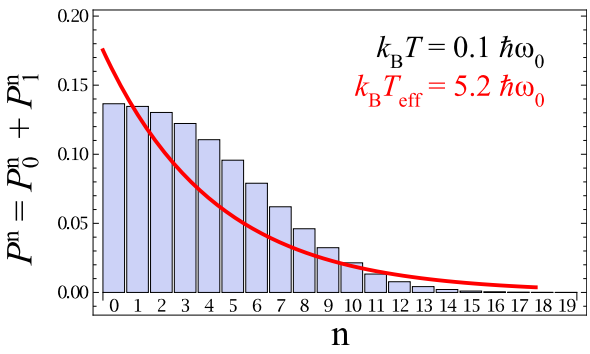

Figure 4: Phonon number distribution in nonequilibrium for $eV = 5\hbar\omega_0$, $m_0 = 0.5$ and $k_BT/\hbar\omega_0 = 0.1$ (histogram). The solid line depicts a fit to a Boltzmann distribution. See text for details.

Nonequilibrated phonons leave their signatures also in the I–V curves as compared to equilibrated ones. The net current through the contact follows from the summing up of the transfer rates from/onto the dot according to Equation 14, hence,

$$I(V) = \frac{e}{2\hbar}\sum_{n,k}|f_{n,k}|^2 \times\left\{\left[\Sigma_L f_\beta(E_{nk}^{0,L}) - \Sigma_R f_\beta(E_{nk}^{0,R})\right]P_0^n - \left[\Sigma_L f_\beta(E_{nk}^{1,L}) - \Sigma_R f_\beta(E_{nk}^{1,R})\right]P_1^n\right\}. \quad (16)$$

Figure 5 shows that deviations are negligible for low voltages in the regime around the first resonant step ($|eV/2| < \hbar\omega_0$), where at sufficiently low temperatures only the ground state participates such that the steady state distribution coincides with the thermal one. For larger voltages deviations occur with the tendency that for smaller couplings m_0 the nonequilibrated current is always smaller than the equilibrated one ($I_{non} < I_{eq}$), while the opposite scenario ($I_{non} > I_{eq}$) is observed for larger m_0. At sufficiently large voltages, one always has $I_{non} < I_{eq}$. This behavior results from the combination of two ingredients, namely, the phonon distributions P_q^n and the Franck–Condon overlaps $|f_{n,k}|^2$. To see this in detail, let us consider a fixed voltage. Then, on the one hand, for smaller m_0 the steady state distribution is broad (cf. Figure 3), such that, due to normalization, less weight is carried by lower lying states compared to a thermal distribution at low temperatures; on the other hand, for $m_0 < 1$ the overlaps $|f_{n,k}|^2$ favor contributions from low lying states in the current (16), which is thus smaller than I_{eq}. For increasing electron–phonon coupling $m_0 > 1$, the overlaps $|f_{n,k}|^2$ tend to include broader ranges of phonon states also covered by P_q^n, compared to those of low temperature thermal states. A voltage dependence arises since with increasing voltage higher lying phonon states participate in the dynamics supporting the scenario for smaller couplings. Interestingly, as already noted in [23] the overlaps $|f_{n,k}|^2$ may vanish for certain combinations of n,m depending on m_0 due to interferences of phonon eigenfunctions localized on different diabatic surfaces V_q, where $q = 0,1$.

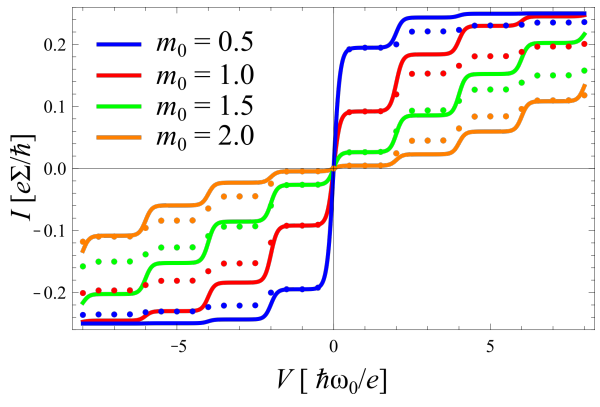

Figure 5: *I–V*-characteristics for equilibrated (solid) and nonequilibrated (dotted) phonon distributions according to Equation 13 and Equation 16, respectively.

4 Rate approach II

The assumption of a thermally distributed phonon degree of freedom during the transport can be physically justified only if this mode interacts directly and sufficiently strongly with an additional heat bath (secondary bath) realized, e.g., by residual molecular modes. Here we will generalize the formulation of subsection 2 to a situation where the secondary bath is characterized by Gaussian fluctuations. Its corresponding modes can thus effectively be represented by a quasi-continuum of harmonic oscillators for which the phonon correlation function (Equation 6) can be calculated easily

$$J(t) = \int_0^\infty \frac{d\omega}{\pi}\frac{I(\omega)}{\omega^2}\left[\coth\left(\frac{\omega\hbar\beta}{2}\right)[\cos(\omega t)-1] - i\sin(\omega t)\right]. \quad (17)$$

Here the spectral density $I(\omega)$ now describes the combined distribution of the prominent mode and its secondary bath. It is thus proportional to the imaginary part of the dynamic susceptibility of a damped harmonic oscillator [20]. For a purely ohmic distribution of bath modes, one has

$$I(\omega) = 2m_0^2\omega_0^3\frac{\gamma\omega}{(\omega^2-\omega_0^2)^2+\gamma^2\omega^2}, \quad (18)$$

where γ denotes the coupling between phonon mode and bath. The Fourier transform of exp(*J*) reads at finite temperatures

$$P_\gamma(\varepsilon) = \mathrm{e}^{-\rho_\gamma}\delta(\varepsilon) + \frac{\mathrm{e}^{-\rho_\gamma}}{\pi}\Re\sum_{(k,l)\neq(0,0)}\frac{\rho_{\gamma,a}^k}{k!}\frac{\rho_{\gamma,e}^l}{l!}\frac{i}{\varepsilon+\hbar\Omega k-\hbar\Omega^* l} \quad (19)$$

with the frequency Ω given by $\Omega = \omega_0\xi + i\gamma/2$ and $\rho_{\gamma,a}(\Omega) = (m_0^2/2\xi\Omega^2)[\coth(\beta\hbar\Omega/2)-1]$ where the parameter ξ is $\xi = \sqrt{1-\gamma^2/4\omega_0^2}$. Further, $\rho_{\gamma,e}(\Omega) = -\rho_{\gamma,e}(\Omega^*)$ (* means complex conjugation) and $\rho_\gamma = \Re[\rho_{\gamma,a} + \rho_{\gamma,e}]/2$. In the above expression, contributions from the Matsubara frequencies in Equation 17 have been neglected, since they are only relevant in the regime $\gamma\hbar\beta >> 2\pi$, which is not studied here. Apparently, the coupling to the bosonic bath effectively induces a broadening of the dot levels $\hbar\gamma(k+l)/2$ compared to the purely elastic case (Equation 9). In the low temperature regime, where for equilibrated phonons absorption (related to *k*) is negligible, the widths grow proportionally to *l*. The presence of the secondary bath drives the prominent phonon mode towards thermal equilibrium with a rate proportional to this broadening. Hence, if the time scale for thermal relaxation is sufficiently smaller than the time scale for charge transfer, i.e., $1/\tau_l \equiv (\sum_L + \sum_R)/\gamma << 1$, the assumption of an equilibrated phonon mode is justified and the golden rule formulation (Equation 13) can be used with $P_0(\varepsilon) \to P_\gamma(\varepsilon)$. However, this argument no longer applies in the overdamped situation $\gamma/\omega_0 >> 1$, where the phonon mode exhibits a sluggish thermalization on the time scale γ/ω_0^2, which may easily exceed τ_l.

As already mentioned above, for vanishing charge–phonon coupling $m_0 = 0$, the model (Equation 3) can be solved exactly for all orders in the lead–dot coupling [15]. In the frame of a rate description, one observes that in this limit the dot population (Equation 11) decays proportionally to $(\sum_L + \sum_R)$. The golden rule version of the theory neglects this broadening in Equation 13 since it is associated with higher order contributions to the current (Equation 13). Now, recalling that $P_0(\varepsilon)$ reduces to a delta function for $m_0 \to 0$, this finite lifetime of the electronic dot level is included for *all orders* by performing the time integral in the Fourier transform with $\varepsilon \to \varepsilon - i(\sum_L + \sum_R)/2 \equiv \varepsilon - i\Gamma_{tot}(M_0 = 0)/2$ [see Equation 11]. In fact, this way one reproduces the *exact* solution (one electronic level coupled to leads with energy independent couplings), i.e., its exact spectral function. To be specific, let us restrict ourselves for the remainder of this discussion to the symmetric situation $\sum_L = \sum_R \equiv \sum/2$, and $\varepsilon_D = 0$. Then, in the presence of the phonon mode ($m_0 \neq 0$) the corresponding function $P_0^{\Sigma}(\varepsilon)$ follows from Equation 9 by replacing the delta function by $i/[\varepsilon + \hbar\omega(k - l) + i\sum/2]$. Again following the idea of a rate treatment, an improved version of this result accounting for higher order electron–phonon correlations is obtained through the decay rate $\Gamma_{tot,0}(M_0 \neq 0)$, instead of the bare dot level width $\sum/\hbar \equiv \Gamma_{tot,0}(M_0 = 0)$. Equivalently, one replaces $i/[\varepsilon + \hbar\omega(k - l) + i\sum/2] \to i/[\varepsilon + \hbar\omega(k - l) + i\Gamma_{tot,0}/2]$ to arrive at an improved $P_l^{\Sigma}(\varepsilon)$. We note that within a Green's function approach, and upon approximating the corresponding equations of motion, a similar result has been found in [15,33], with the difference though that instead of $\Gamma_{tot,0}$ an imaginary part of a phonon state-dependent self-energy $\Sigma''_{k,l}$ appears. One can show that the $\Gamma_{tot,0}$ appearing here within a rate scheme is related to a thermally averaged P_l^{Σ}.

Now, an additional secondary bath can be introduced as above by combining Equation 19 with P_l^{Σ}, leading eventually to

$$P_{\gamma,l}^{\Sigma}(\varepsilon) = \frac{e^{-\rho_\gamma}}{\pi} \times \Re\left\{ \sum_{(k,l)\geq(0,0)} \frac{\rho_{\gamma,a}^{k}}{k!} \frac{\rho_{\gamma,e}^{l}}{l!} \times \frac{i}{\varepsilon + h\Omega k - h\Omega^{*} l + ih\Gamma_{tot,0}/2} \right\}. \quad (20)$$

The width of the electronic dot level is thus voltage dependent and approaches the bare width from below for large voltages, that is $\lim_{V\to\infty}\Gamma_{tot,0}(V) = \sum/\hbar$. The range of validity of this scheme is the following: It applies to all couplings σ in the domain where the electron–phonon coupling is weak $m_0 < 1$. In particular, second order processes in σ capture cotunneling processes. For $m_0 > 1$ charge transfer is strongly suppressed and the phonon dynamics still occurs on diabatic surfaces for $\sigma << 1$ so that we expect the approach to cover this range as well.

5 Comparison with numerically exact results

A numerically exact treatment of the nonequilibrium dynamics of the model considered here is a formidable task. The number of formulations which allow simulations in nonperturbative ranges of parameter space is very limited. Among them is a recently developed diagrammatic Monte Carlo approach (diagMC) based on a numerical evaluation of the full Dyson series, which, in contrast to numerical renormalization group (NRG) methods [37], covers the full temperature range. For calculations of single charge transfer, results have been obtained with and without the presence of a secondary bath interacting with the dot phonon mode.

We note that computationally these simulations are very demanding as for each parameter set and a given voltage the stationary current for the *I*–*V* curve needs to be extracted from the saturated value of the time dependent current $I(t)$ for longer times. Typical simulation times are on the order of several days to weeks, depending on the parameter range. In contrast, rate treatments require minimal computational effort and can be done within minutes. Here, we compare numerically exact findings with those gained from the various types of rate/master equations discussed above.

We start with the scenario where the coupling to a secondary bath is dropped ($\gamma = 0$) to reveal the impact of nonequilibrium effects in the phonon mode. The formulation for an equilibrated phonon is based on Equation 13 with P_0 replaced by $P_{\gamma,l}^{\Sigma}$ in Equation 20, while the steady state phonon distribution is obtained from the stationary solutions to Equation 14. In the latter approach the intrinsic broadening of the dot electronic level due to coupling to the lead is introduced in the following way: One first determines via Equation 14 a steady state distribution P_q^n. This result is used for an effective self-energy contribution (total decay rate) for nonequilibrated phonons, i.e.,

$$\Gamma_{tot,neq}(V) = \frac{\Sigma}{\hbar} \sum_{\alpha=L,R;\, n,k,q} |f_{n,k}|^2 \, P_q^n f_\beta\left(E_{nk}^{\alpha}\right), \quad (21)$$

where $E_{nk}^{\alpha} = \hbar\omega_0(n-k) + \mu_\alpha$. We note in passing that $\lim_{V\to\infty}\Gamma_{tot,neq}(V) = \sum/\hbar \equiv \Gamma_{tot}(M_0 = 0)$. Subsequently, an im-

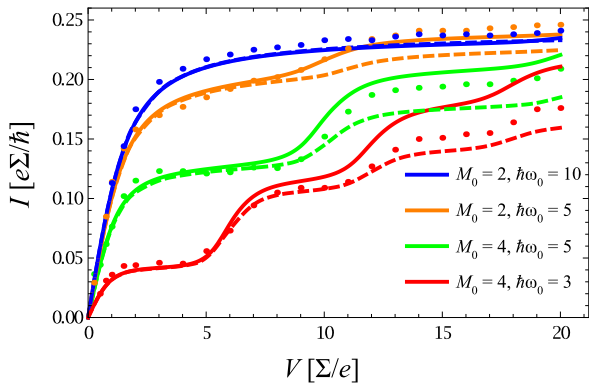

Figure 6: *I–V* characteristics according to approximate models based on equilibrated phonons (solid) and nonequilibrated phonons (dashed) together with exact DQMC data (dots) for $k_BT/\Sigma = 0.2$ and without coupling to a secondary bath ($\gamma = 0$). All quantities are scaled with respect to the dot–lead coupling Σ.

proved result for the steady state phonon distribution at a given voltage is evaluated working again with Equation 14, but using the replacement:

$$f_\beta\left(\hbar\omega_0(k-l)\mp\frac{eV}{2}\right)\rightarrow \int\frac{d\varepsilon}{2\pi}f_\beta\left(\varepsilon\mp\frac{eV}{2}\right)\frac{\hbar\Gamma_{\mathrm{tot,neq}}}{[\varepsilon-\hbar\omega_0(k-l)]^2+\hbar^2\Gamma^2_{\mathrm{tot,neq}}/4}. \quad (22)$$

Of course, for $\Sigma \rightarrow 0$ the standard Fermi distribution is regained. The corresponding steady state phonon distribution eventually provides the current according to Equation 16 with the same replacement (Equation 22) in this expression. The procedure relies on weak electron–phonon coupling $m_0 < 1$ and in principle also requires sufficiently elevated temperatures.

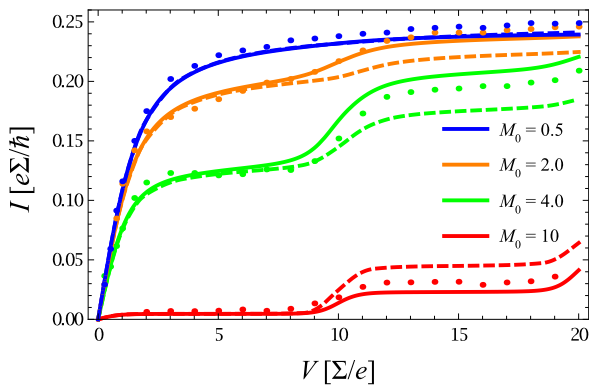

Figure 7: As Figure 6 but for fixed $\hbar\omega_0/\Sigma = 5$ and varying electron–phonon coupling.

Results are shown in Figure 6 together with corresponding diagMC data for various coupling strengths m_0. Interestingly, the equilibrated model describes the exact data very accurately from weak up to moderate electron–phonon coupling $m_0 \approx 1$, while deviations appear for stronger couplings $m_0 \gtrsim 1$ and voltages beyond the first plateau $eV > 2\hbar\omega_0$. For $m_0 > 1$ nonequilibrium effects are stronger and the corresponding master equation (Equation 14) gives a better description of higher order resonant steps. Moreover, as already addressed above, even in this low temperature domain the approximate description provides quantitatively reliable results.

In Figure 7 the frequency of the phonon mode is fixed and only the electron–phonon coupling is tuned over a wider range. For strong coupling (here $m_0 = 2$) the equilibrated (nonequilibrated) model predicts a smaller (larger) current than the exact one in contrast to the situation for smaller m_0. This phenomenon directly results from what has been said above in subsection 3: For stronger coupling the Franck–Condon overlaps favor higher lying phonon states that are suppressed by a thermal distribution.

After all, the approximate models give not only a qualitatively correct picture of the exact *I–V* curves, but even provide a reasonable quantitative description in this low temperature domain.

In a next step the coupling to a secondary bath is turned on ($\gamma \neq 0$) enforcing equilibration of the phonon mode, see Equation 20. The expectation is that in this case departures from the equilibrated model are reduced. In Figure 8 data are shown for a ratio $m_0 = 4/5$, where deviations occur at larger voltages, as observed in the previous figures. Obviously, due to the damping of the phonon mode the resonant steps are smeared out with increasing γ. However, the approximate model predicts this

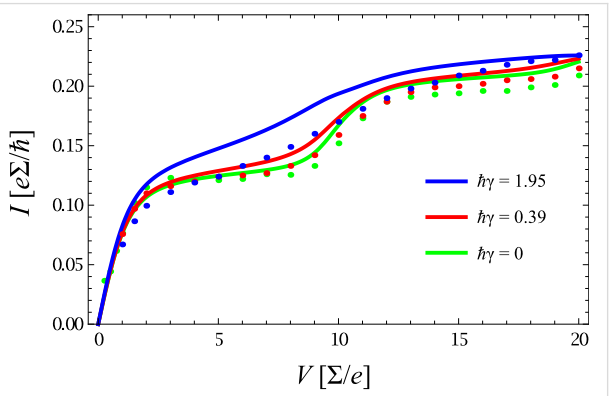

Figure 8: *I–V* characteristics in presence of a secondary heat bath interacting with the phonon with various coupling constants γ. Shown are approximate results (solid) using Equation 20 and diagMC data (dots); energies are scaled with Σ. Other parameters are $k_BT/\Sigma = 0.2$, $m_0 = 4/5$, $\sigma = 0.2$.

effect to be more pronounced as compared to the exact data, particularly for stronger coupling $\hbar\gamma/\sum > 1$, while still $\gamma/\omega_0 < 1$. In fact, in the limit of very large coupling only the $k = l = 0$ contribution to Equation 20 survives, such that at zero temperature one arrives at

$$\lim_{\gamma\to\infty} I(V) = I_\infty \frac{2}{\pi}\arctan\left(\frac{eV}{\hbar\Gamma_{\mathrm{tot},0}(V)}\right) \qquad (23)$$

with the current at large voltages $I_\infty = e\sum/4\hbar$ and $\Gamma_{\mathrm{tot},0}(V) \leq \sum/\hbar$, where equality is approached for $V \to \infty$. It seems that a broadened equilibrium distribution of the phonon, induced by the secondary bath according to Equation 20, overestimates the broadening of individual levels. Since the approach is exact in the limit $m_0 \to 0$, the deviations appearing in Figure 8 are due to intimate electron–phonon/secondary bath correlations not captured by the rate approach. In the overdamped regime, i.e., $\gamma/\omega_0 > 1$, the dynamics of the phonon mode slow down and may become almost static on the time scale of the charge transfer. In this adiabatic regime an extended version of the master equation (Equation 14) is not trivial since the conventional eigenstate representation becomes meaningless. It would be better then to switch to phase-space coordinates and develop a formulation based on a Fokker–Planck or Smoluchowski equation for the phonon. This will be the subject of future research.

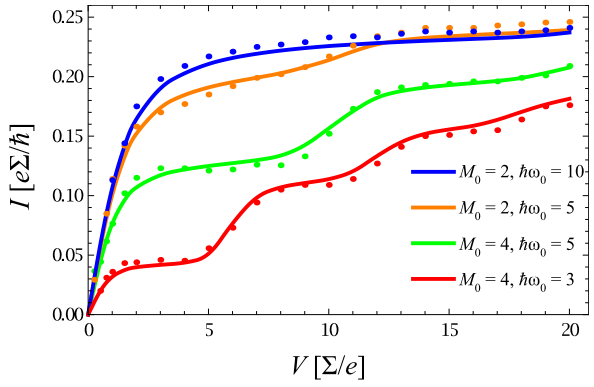

Figure 9: As Figure 6, but for nonequilibrated phonons based on an extended master equation (solid) in comparison to exact diagMC data (dots).

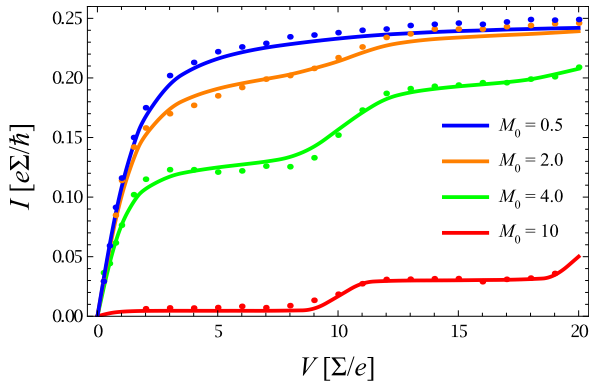

Figure 10: As Figure 7, but for nonequilibrated phonons based on an extended master equation (solid) in comparison to exact diagMC data (dots).

The essence of this comparison is that, as anticipated from physical arguments already in subsection 1, a rate description does indeed provide quantitatively accurate results in the regime of weak to moderate electron–phonon coupling $m_0 < 1$ and for all σ. Deviations that occur for larger values of m_0 can partially be explained by nonequilibrium distributions in the phonon distribution, where, however, the master equation approach seems to overestimate this effect. In order to obtain some insight into the nature of this deficiency, a minimal approach consists of extending Equation 14 with Equation 22, a mechanism that enforces relaxation to thermal equilibrium with a single rate constant Γ_0 that serves as a fitting parameter. Accordingly, the respective time evolution equation for $P_{\mathrm{q}}^{\mathrm{n}}(t)$ receives an additional term $-\Gamma_0[P_{\mathrm{q}}^{\mathrm{n}}(t) - P_{\beta}^{\mathrm{n}}]$ with the Boltzmann distribution for the bare phonon degree of freedom P_{β}^{n}. Corresponding results for the same parameter range as in Figure 6 and Figure 7 are shown in Figure 9 and Figure 10 including comparison with the exact diagMC data. There, the *same* equilibration rate $\hbar\Gamma_0/\sum = 0.25$ is used for *all* parameter sets. Astonishingly, this procedure provides excellent agreement over the full voltage range. It improves results particularly in the range of moderate to stronger electron phonon coupling, but has only minor impact for $m_0 < 1$. The indication is thus that electron–phonon correlations neglected in the original form of the master equation have effectively the tendency to support faster thermalization of the phonon. Indeed, preliminary results with a generalized master equation, where the coupling between diagonal (populations) and off-diagonal (coherences) elements of the reduced charge–phonon density matrix is retained (no RWA approximation), indicate that this coupling leads to an enhanced phonon–lead interaction and thus to enhanced phonon equilibration.

Acknowledgements

We thank L. Mühlbacher for helpful discussions and for providing numerical data from [29]. Financial support was provided by the SFB569, the Baden-Württemberg Stiftung, and the German-Israeli Foundation (GIF).

References

1. Goser, K.; Glösekötter, P.; Dienstuhl, J. *Nanoelectronics and Nanosystems: From Transistors to Molecular and Quantum Devices;* Springer: Berlin, 2004.

2. Cuniberti, G.; Fagas, G.; Richter, K., Eds. *Introducing Molecular Electronics;* Springer: Berlin, 2005.
3. Cuevas, J.; Scheer, E. *Molecular Electronics–An Introduction to Theory and Experiment;* World Scientific: Singapore, 2010.
4. Reichert, J.; Ochs, R.; Beckmann, D.; Weber, H. B.; Mayor, M.; von Löhneysen, H. *Phys. Rev. Lett.* **2002,** *88,* 176804. doi:10.1103/PhysRevLett.88.176804
5. Ruben, M.; Landa, A.; Lörtscher, E.; Riel, H.; Mayor, M.; Görls, H.; Weber, H. B.; Arnold, A.; Evers, F. *Org. Synth.* **2008,** *4,* 2229.
6. Pillet, J.-D.; Quay, C.; Morfin, P.; Bena, C.; Levy Yeyati, A.; Joyez, P. *Nat. Phys.* **2010,** *6,* 965. doi:10.1038/nphys1811
7. Park, H.; Park, J.; Lim, A. K. L.; Anderson, E. H.; Alivisatos, A. P.; McEuen, P. L. *Nature* **2000,** *407,* 57. doi:10.1038/35024031
8. Song, H.; Kim, Y.; Jang, Y. H.; Jeong, H.; Reed, M. A.; Lee, T. *Nature* **2009,** *462,* 1039. doi:10.1038/nature08639
9. Secker, D.; Wagner, S.; Ballmann, S.; Härtle, R.; Thoss, M.; Weber, H. B. *Phys. Rev. Lett.* **2011,** *106,* 136807. doi:10.1103/PhysRevLett.106.136807
10. Venkataraman, L.; Klare, J. E.; Nuckolls, C.; Hybertsen, M. S.; Steigerwald, M. L. *Nature* **2006,** *442,* 904. doi:10.1038/nature05037
11. Fernandez-Torrente, I.; Franke, K. J.; Pascual, J. I. *Phys. Rev. Lett.* **2008,** *101,* 217203. doi:10.1103/PhysRevLett.101.217203
12. Xue, Y.; Datta, S.; Ratner, M. A. *Chem. Phys.* **2002,** *281,* 151. doi:10.1016/S0301-0104(02)00446-9
13. Damle, P.; Ghosh, A. W.; Datta, S. *Chem. Phys.* **2002,** *281,* 171. doi:10.1016/S0301-0104(02)00496-2
14. Meir, Y.; Wingreen, N. S. *Phys. Rev. Lett.* **1992,** *68,* 2512. doi:10.1103/PhysRevLett.68.2512
15. Mitra, A.; Aleiner, I.; Millis, A. J. *Phys. Rev. B* **2004,** *69,* 245302. doi:10.1103/PhysRevB.69.245302
16. Gurvitz, S. A. *Phys. Rev. B* **1998,** *57,* 6602. doi:10.1103/PhysRevB.57.6602
17. Ingold, G.-L.; Nazarov, Y. V. Charge Tunneling Rates in Ultrasmall Junctions. In *Single Charge Tunneling;* Grabert, H.; Devoret, M., Eds.; Plenum Press: New York, 1992; pp 21–107.
18. Mühlbacher, L.; Ankerhold, J.; Escher, J. C. *J. Chem. Phys.* **2004,** *121,* 12696. doi:10.1063/1.1815293
19. Mühlbacher, L.; Ankerhold, J. *J. Chem. Phys.* **2005,** *122,* 184715. doi:10.1063/1.1896355
20. Weiss, U. *Quantum Open Systems;* World Scientific: Singapore, 2008.
21. Segal, D.; Nitzan, A.; Davis, W. B.; Wasielewski, M. R.; Ratner, M. A. *J. Phys. Chem. B* **2000,** *104,* 3817. doi:10.1021/jp993260f
22. Nitzan, A. *Annu. Rev. Phys. Chem.* **2001,** *52,* 681. doi:10.1146/annurev.physchem.52.1.681
23. Koch, J.; von Oppen, F. *Phys. Rev. Lett.* **2005,** *94,* 206804. doi:10.1103/PhysRevLett.94.206804
24. Donarini, A.; Grifoni, M.; Richter, K. *Phys. Rev. Lett.* **2006,** *97,* 166801. doi:10.1103/PhysRevLett.97.166801
25. Leijnse, M.; Wegewijs, R. *Phys. Rev. B* **2008,** *78,* 235424. doi:10.1103/PhysRevB.78.235424
26. Timm, C. *Phys. Rev. B* **2008,** *77,* 195416. doi:10.1103/PhysRevB.77.195416
27. Hübener, H.; Brandes, T. *Phys. Rev. B* **2009,** *80,* 155437. doi:10.1103/PhysRevB.80.155437
28. Härtle, R.; Thoss, M. *Phys. Rev. B* **2011,** *83,* 115414. doi:10.1103/PhysRevB.83.115414
29. Mühlbacher, L.; Rabani, E. *Phys. Rev. Lett.* **2008,** *100,* 176403. doi:10.1103/PhysRevLett.100.176403
30. Mühlbacher, L.; Ankerhold, J.; Komnik, A. *Phys. Rev. Lett.* **2005,** *95,* 220404. doi:10.1103/PhysRevLett.95.220404
31. Mühlbacher, L.; Ankerhold, J. *New J. Phys.* **2009,** *11,* 035001. doi:10.1088/1367-2630/11/3/035001
32. Escher, J. C.; Ankerhold, J. *Phys. Rev. A* **2011,** *83,* 032122. doi:10.1103/PhysRevA.83.032122
33. Flensberg, K. *Phys. Rev. B* **2003,** *68,* 205323. doi:10.1103/PhysRevB.68.205323
34. Egger, R.; Gogolin, A. O. *Phys. Rev. B* **2008,** *77,* 113405. doi:10.1103/PhysRevB.77.113405
35. Maier, S.; Schmidt, T. L.; Komnik, A. *Phys. Rev. B* **2011,** *83,* 085401. doi:10.1103/PhysRevB.83.085401
36. Schmidt, T. L.; Komnik, A. *Phys. Rev. B* **2009,** *80,* 041307. doi:10.1103/PhysRevB.80.041307
37. Bulla, R.; Costi, T. A.; Pruschke, T. *Rev. Mod. Phys.* **2008,** *80,* 395. doi:10.1103/RevModPhys.80.395

License and Terms

Beilstein Journal of Nanotechnology

Towards a scalable and accurate quantum approach for describing vibrations of molecule–metal interfaces

David M. Benoit[*1,2], Bruno Madebene[3], Inga Ulusoy[4], Luis Mancera[5], Yohann Scribano[6] and Sergey Chulkov[1]

Full Research Paper

Open Access

Address:
[1]Nachwuchsgruppe Theorie – SFB 569, Albert-Einstein-Allee 11, University of Ulm, D-89081 Ulm, Germany, [2]Department of Chemistry, The University of Hull, Cottingham Road, Kingston upon Hull HU6 7RX, United Kingdom, [3]L.A.D.I.R Boite 49, Bat F74, Université Pierre et Marie Curie, 4 Place Jussieu, F-75252 Paris, France, [4]Technische Universität München, Theoretical Chemistry, Lichtenbergstr. 4, D-85747 Garching, Germany, [5]Theoretical Chemistry, Albert-Einstein-Allee 11, University of Ulm, D-89081 Ulm, Germany and [6]Laboratoire Interdisciplinaire Carnot de Bourgogne,UMR 5209 CNRS – Université de Bourgogne, 9 av. A. Savary, BP 47870, F-21078 Dijon Cedex, France

Email:
David M. Benoit[*] - david.benoit@uni-ulm.de

* Corresponding author

Keywords:
computational scaling; grid computing; molecule–metal interactions; periodic density functional theory; vibrational theory

Beilstein J. Nanotechnol. **2011,** *2,* 427–447.
doi:10.3762/bjnano.2.48

Received: 19 April 2011
Accepted: 14 July 2011
Published: 10 August 2011

This article is part of the Thematic Series "Organic–inorganic nanosystems".

Guest Editor: P. Ziemann

Abstract

We present a theoretical framework for the computation of anharmonic vibrational frequencies for large systems, with a particular focus on determining adsorbate frequencies from first principles. We give a detailed account of our local implementation of the vibrational self-consistent field approach and its correlation corrections. We show that our approach is both robust, accurate and can be easily deployed on computational grids in order to provide an efficient computational tool. We also present results on the vibrational spectrum of hydrogen fluoride on pyrene, on the thiophene molecule in the gas phase, and on small neutral gold clusters.

Introduction

The study of molecular vibrations has been a topic of continued interest in chemistry for over a century, starting with the work of William Coblenz in 1905. The main driving force behind these studies has been the correlation that exists between molecular structure and observed vibrational transition frequencies. Thus, a measured vibrational frequency depends directly on the

strength of the bonds present in the molecule and on the mass of its atoms. Moreover, particular bonding patterns can give rise to specific collective motions of parts of the molecule; the corresponding oscillation frequencies of this set of atoms are usually known as group frequencies and are characteristic of a particular structural motif.

In heterogeneous catalysis, for example, the shift of the adsorbate vibrational frequencies allows us to follow the progress of surface reactions and provides important information on the bond strength and location of the adsorbate. A typical example is carbon monoxide, which can be used as a surface probe, as the C=O stretch frequency is very sensitive to the adsorption site of the molecule. This property was identified very early on, and was used by Yang and Garland [1] to investigate, for example, the binding mode of a CO molecule deposited on supported rhodium films and to suggest possible mechanisms for hydrogenation and oxidation reactions on this type of metal surface.

A recent development for vibrational spectroscopy in the field of surface characterisation is the use of scanning tunnelling microscopy (STM) to record single-molecule spectra. This relies on the technique of inelastic electron tunnelling spectroscopy (IETS), developed in the mid-1960s [2], and performs measurements on a single molecule using an STM tip as a contact instead of a macroscopic metal/oxide layer. There are a number of studies (see [3] for a review) that have shown the flexibility of the combination of STM with IETS for the investigation of single adsorbates on the nanoscale. Recently, our group was able to demonstrate that, with an appropriate anharmonic model of the vibrational structure, STM–IETS can be used to determine the adsorption geometry of a 4-mercaptopyridine molecule on the Au(111) surface [4]. This study confirmed that a coordination of the sulfur atoms by two gold atoms (bridge site or defect site) is likely to be the preferred binding mode for the adsorbate. This is in agreement with other theoretical predictions [5].

This paper describes our efforts over the past few years in developing scalable techniques for the computation of anharmonic vibrational frequencies of large systems, with a particular focus on the interface between organic molecules and metal surfaces. Such systems are of significant interest in the field of nanotechnology as they are the building blocks of functionalised interfaces and are also related to catalysis processes. The interface between the molecular world and the condensed phase is still relatively poorly understood, and the vibrations of adsorbed molecules provide us with information on their surface binding strength and on the dynamic processes that occur at the interface.

Our aim is to further the understanding of adsorbate vibrations by developing a set of techniques that render their accurate prediction possible at modest computational cost. We show that a systematic approach to the description of anharmonic vibrational structure, based on the vibrational self-consistent field (VSCF) method and its correlated variants, combined with an accurate yet scalable description of the underlying potential energy landscape, leads to a flexible way of describing these systems.

This paper is organised as follows: First, we give a brief introduction to the global theoretical framework used for our implementation. We then describe the details of our local implementation of the direct-VSCF technique, followed by a detailed account of our efforts to speed up vibrational correlation corrections for large systems. Next, we introduce a distributed approach for the computation of the necessary potential energy surfaces (PES). We finish the paper with two new developments: The frequencies of the thiophene molecule are calculated from a PES constructed with periodic density functional theory (DFT), and an assessment of DFT for the description of properties of small neutral gold clusters is given. We conclude this paper with an outlook on future work in the field of theoretical descriptions of vibrational spectra of adsorbed molecules.

Results and Discussion

Theoretical framework

The theoretical description of molecular vibrations is remarkably simple. In its most basic formulation, the harmonic approximation can successfully describe a very large number of observations. This has been shown in the excellent monograph by Wilson Jr., Decius and Cross [6], in which they demonstrated a straightforward procedure to obtain harmonic vibrational frequencies for any given molecule. The success enjoyed by the harmonic approximation over the years, combined with its relative simplicity, has made it a de facto standard for the prediction of vibrational frequencies.

From a theoretical point of view, the accuracy of the data obtained from high resolution spectra provides an ideal opportunity to validate the interaction models used to describe the observed molecule, be they empirical force fields or quantum chemical Hamiltonians, as vibrational spectra probe bond strengths directly. Unfortunately, standard vibrational theory is often powerless to explain the subtle changes observed in the vibrational spectrum when a molecule undergoes a conformational change or is adsorbed on a surface. Indeed, the harmonic approximation can only go so far, as it mainly considers infinitesimal displacements from the equilibrium structure and does not truly explore the local energy landscape

of a flexible molecule. This approximation usually results in a severe overestimation of experimental frequencies by up to 200–300 cm^{-1} for single stretching frequencies.

As an alternative to the harmonic approximation, two methods for computing anharmonic spectra are of particular interest: Molecular dynamics and the vibrational self-consistent field (VSCF) approach. Both techniques can go beyond the harmonic approximation, and provide a solid basis for the interpretation of complex vibrational experiments.

The first method offers a fully classical approach to anharmonic corrections that can easily include solvation (or more generally environment effects) and finite temperature effects. This latter aspect can be important in the case of conformationally flexible molecules. Due to its conceptual simplicity and the ready availability of reliable empirical force fields (or forces computed ab initio), molecular dynamics is currently the most popular method for determining anharmonic frequencies of large systems (see [7] for an overview of some applications for biological systems). However, given its classical nature, this technique cannot account consistently for quantisation effects such as Fermi resonances, overtones or combined excitations.

In contrast, VSCF-based methods provide a fully quantum mechanical picture of anharmonicity in molecular systems and, as such, are able to account for resonance phenomena, combination bands and vibrational overtones in a hierarchical and consistent manner. While temperature effects can be included using a statistical mechanics framework, these are usually neglected, and thus the approach is better suited to the description of low temperature vibrational spectra, such as those obtained in supersonic jet expansions or in ultrahigh-vacuum environments.

In most implementations of VSCF-based approaches, the required resolution of the vibrational Schrödinger equation means that it remains a time-consuming process. This is due to the necessity to first construct a potential energy surface (PES), which is then used to compute the vibrational Hamiltonian. The PES can also be generated directly from ab initio programs (direct-VSCF), thus leading to a straightforward route from electronic structure theory to a measurable vibrational spectrum, within the Born–Oppenheimer approximation.

This paper focuses on VSCF-based techniques and describes our local implementation, PVSCF, that aims to reduce the computational cost of the direct-VSCF method for large and interfacial systems. In order to render this approach suitable for large systems, two main aspects of the technique need to be considered: The generation of the PES and the vibrational computation itself.

Expressing the potential energy surface

In order to obtain a manageable and compact description of the multi-dimensional PES for large systems, it is desirable to use an approach that has a physical underpinning and whose accuracy can be improved systematically. Rabitz et al. [8,9] showed that a many-body decomposition leads to a convenient hierarchical representation of the PES. In their approach, the PES is expanded in a series of one-dimensional terms, two-dimensional couplings, three-dimensional couplings, etc. This expansion guarantees convergence, as a $3N_a - 6$ dimensional expansion describes the complete PES for a problem consisting of N_a atoms in the case of an isolated molecule. Note that other representations, such as polynomial expansions, do not necessarily possess such well defined multi-dimensional convergence properties. For large systems, Gerber et al. [10] have shown that a truncation of the expansion to two-dimensional (2-D) couplings built on the normal modes of the system is sufficiently accurate for most applications. This considerably reduces the computational effort of generating PES for the description of vibrational properties of large systems. Another advantage (which will become clearer later) of this type of representation is that it is isomorphic with electronic structure theory, where all interactions are two-body interactions. The direct method suggested by Gerber et al. [10] reduces the computation of the global PES for a given system to that of a local part of the energy landscape located around the energy minimum and expanded in a series of 1-D and 2-D cuts, calculated point-by-point through ab initio techniques. Thus, in this method, the speed at which the PES can be computed is directly related to the number of mode–mode couplings taken into account and to the amount of computing power allocated to the ab initio calculation of each grid point. However, the latter constitutes one of the main computational bottlenecks of the technique for large systems.

Accelerating anharmonic vibrational calculations

Several years ago [11], we formulated the concept of the fast-VSCF technique and demonstrated that the computationally expensive stages of direct-VSCF calculations, namely the computation of mode–mode coupling potentials using ab initio techniques, can be efficiently pre-screened using fast and approximate electronic structure methods. Indeed, for any given molecular system, we showed that the coupling pattern is mainly defined by the chemical nature of the molecule and the choice of coordinate system for the normal-mode expansion (see [12] for details of the influence of coordinate systems on VSCF calculations). Thus, any level of electronic structure

theory can be used to obtain a qualitative assessment of the strength of mode–mode coupling, as long as this level offers a reasonable description of the potential energy surface. This concept opens the way to a two-level approach to the determination of couplings that we have called the fast-VSCF method. Other groups have further developed such a multi-level approach in order to compute different parts of the PES through a set of electronic structure calculations of decreasing accuracy [13,14] and have achieved reasonable accuracy for small to medium-sized molecules.

The fast-VSCF technique uses the fact that there are preferred channels along which vibrational modes interact with each other and that these channels dominate the vibrational dynamics of the system. This is particularly manifest when a molecule contains similar functional groups, such as C–H bonds or C=O groups, that necessarily interact with one another for symmetry reasons (vibrations of identical functional groups should couple together even if it is only through Fermi resonances). Once these channels have been identified, it is possible to construct an approximate representation of the vibrational Hamiltonian that contains only these important interactions, and the resulting reduced-dimension model leads to a very reasonable description of the molecular vibrations. This approach bears similarities to some of the semi-empirical techniques used in electronic structure theory, such as the complete neglect of differential overlap (CNDO) approach of Pople et al. [15], but it mainly originates from considerations of the usage of locality in large-scale electronic structure methods (so called order-N approaches). Indeed, the idea of restricting the calculation to a local environment (often defined as nearest-neighbour interactions) is the major tenet of a large number of linear-scaling electronic structure methodologies, and in fast-VSCF we limit the treatment of vibrational correlation to a "local" group of modes. The delocalised nature of rectilinear normal modes usually renders a direct prediction of nearest-neighbour interactions difficult. There have been attempts at using criteria based on localisation techniques to determine the importance of a given mode–mode pair using only normal modes [16]. This approach relies on the assumption that two strongly coupled modes are likely to move the same atoms while two weakly coupled ones are not, and has so far shown moderate success at predicting all strong couplings of the systems investigated.

Unfortunately, generic non-trivial rules for determining the preferred channels of a given molecule have so far proved elusive, but we are pursuing research in this direction. Thus, for a practical implementation, the fast-VSCF approach usually requires an initial qualitative exploration of the PES of the system, albeit at a low level of theory.

By greatly reducing the time spent on the PES calculation, the fast-VSCF approach enables the investigation of larger systems, which would have otherwise been out of the reach of a standard direct-VSCF calculation. In particular, we have shown [11] that correlation-corrected fast-VSCF (fast-VMP2) achieves increases in speed of up to 80 times that of standard direct-VMP2 calculations on the systems studied.

Fast-VSCF is a technique that was initially built to accelerate PES calculations, but it also confers a particular structure on the vibrational Hamiltonian (rendering it sparser) that can be further exploited in the vibrational correlation treatment to construct efficient algorithms, as will be shown later in the paper.

Our local VSCF implementation

Our aim is to develop a program to compute accurate vibrational frequencies of polyatomic system in the gas phase, condensed phase and at interfaces. We start by assuming that the Born–Oppenheimer approximation is valid, and thus we first need to compute the PES of the system and then we consider the nuclear motion by solving the vibrational Schrödinger equation on the PES obtained.

Our implementation choices have been guided by the following requirements:

- The program should be an external code that could be interfaced with any given ab initio electronic structure code to ensure maximum flexibility during the construction of the PES. This enables us to change ab initio package according to the availability of electronic structures methods or performance of the implemented algorithms. This capability is a necessity for the investigation of large systems as the many packages that implement efficient density functional theory (DFT) are still in development and change on a regular basis.
- Scalability of the vibrational approach means that the program should be able to run on many cores (i.e., parallel code). Computationally speaking, the PES construction remains the most demanding part of the calculation as we typically need on the order of 10^6 points for large systems. However, this is a highly parallel task given that the various grid points are practically independent and we will discuss our strategy for scalable PES computation later in the paper. Finally, once the PES is computed, the vibrational treatment can become the limiting factor for systems containing a large number of modes. Thus there is a necessity for the development a vibrational treatment that may be parallelized for such cases.

- Ideally, the program should use the ab initio energy grid points themselves and avoid fitting the PES to a functional form. This ensures that the accuracy of the PES is preserved throughout the calculation.
- Finally, not only do we need the energy of the vibrational ground state of the system but also that of its vibrationally excited states in order to compute fundamental frequencies and overtones or combination bands. We also require a representation of the vibrational wave function in order to be able to compute vibrationally averaged geometries for a given state or in order to compute infrared transition intensities.

The core part of our program is built around a solver for 1-D radial vibrational Schrödinger equations of the kind:

$$\left\{-\frac{1}{2}\sum_{j=1}^{N}\frac{\partial^2}{\partial Q_j^2}+V^j\left(Q_j\right)\right\}\varphi_{n_j}^{(\mathbf{n})}\left(Q_j\right)=\varepsilon_{n_j}^{(\mathbf{n})}\varphi_{n_j}^{(\mathbf{n})}\left(Q_j\right) \quad (1)$$

where Q_j is usually a mass-weighted normal coordinate of the system, $V^j(Q_j)$ is a generic 1-D potential, $V^j(Q_j)$ is the single-mode wave function, $\varphi_{n_j}^{(\mathbf{n})}(Q_j)$ the corresponding eigenenergy and $(\mathbf{n}) = \{v_1,v_2,\ldots,v_n\}$ represents the excitation quanta for each vibrational mode. This routine must be fast, accurate and flexible enough to treat any kind of 1-D potential. After evaluating a number of approaches based on different basis sets for construction of the Hamiltonian representation (particle-in-a-box eigenfunctions, gaussian functions, harmonic oscillator eigenfunctions, delta functions), we solve Equation 1 using the Fourier grid Hamiltonian (FGH) approach proposed by Balint-Kurti and Martson [17,18]. This approach is fast and robust enough to accommodate any kind of potential that is likely to occur during the vibrational calculation (potential with one or several minima, periodic or aperiodic potential), and it gives the eigenvalues and the eigenfunctions as the results. The wave functions obtained are also easily integrable, as they are based on delta functions. The limiting part of the calculation is the diagonalisation of an $N_g \times N_g$ matrix, where N_g is the number of grid points (which must be even in this approach). We use mathematical libraries (Lapack) to ensure the scalability of the approach.

There are two possible points of failure in our technique, one is using too few or an odd number of grid points and the other is an insufficient exploration of the 1-D potential. The number of points, N_g, can be fixed by the user in our implementation but the default value of N_g = 128 is usually sufficient for most applications, and convergence with respect to N_g is easily checked. This leads to a relatively small computational burden on the diagonalisation routines. As the potential energy is usually computed ab initio on a grid that is sparser than N_g, the 1-D PES is interpolated using a cubic spline procedure (Numerical Recipes [19], modified by M. Lewerenz) in order to obtain the values on the N_g grid points. By default, the limits of the interpolated grid are those of the 1-D ab initio PES grid. The issue of insufficient exploration of the potential is more difficult to resolve, but we have implemented additional options to check the validity of the PES range: Basic linear extrapolation using energies derived from the limits of the potential, or usage of an infinite wall potential at the limits. In practice, if the first seven eigenvalues and wave functions do not change when extrapolating the potential, the initial potential range was large enough.

Diagonal (1-D) calculation

This is the first step beyond the harmonic approximation and a flow-chart diagram of our routine is shown in Figure 1. In this part, the 1-D vibrational Schrödinger equation for each mode is solved with the FGH subroutine and the potential obtained from 1-D PES cuts along each mode. The anharmonic frequencies are then obtained by simply subtracting the ground state energy from the first excited state energy for each vibrational mode. This leads to improved vibrational frequencies compared to the harmonic approximation, but even though these diagonal frequencies reflect the main anharmonic contributions, they do not include any vibrational correlation between modes. For many-mode systems, the diagonal approximation is not sufficient to obtain realistic vibrational frequencies but the solutions obtained at this stage can be improved through the VSCF procedure outlined below.

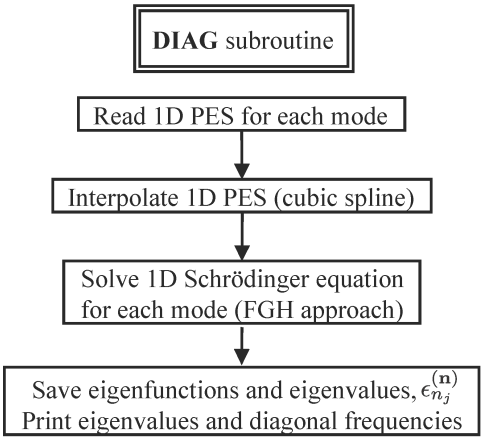

Figure 1: Flow-chart diagram of the computer code used to compute diagonal frequencies.

VSCF procedure

The main idea is to use an effective mean-field 1-D potential, $V_{eff}^{j}(Q_j)$, along each mode, instead of the diagonal potential, in order to take into account the vibrational coupling between modes:

$$V^{j}(Q_j) = V_{\text{eff}}^{j}\left(Q_j\right) = \left\langle \prod_{i\neq j} \varphi_{n_j}^{(\mathbf{n})} \middle| V(\mathbf{Q}) \middle| \prod_{i\neq j} \varphi_{n_j}^{(\mathbf{n})} \right\rangle \qquad (2)$$

where $V(\mathbf{Q})$ is the full potential energy surface of the N-dimensional problem and contains all the coupling terms of the potential energy operator. The main computational difficulty in solving Equation 1 at this stage comes from the evaluation of the multi-dimensional integral needed to compute the mean-field potential. To overcome this difficulty, Jung and Gerber [20] suggested using the following n-body representation of the potential energy surface:

$$\begin{aligned} V(\mathbf{Q}) = &\sum_{j=1}^{N} V_j^{(1)}\left(Q_j\right) + \sum_{i=1}^{N}\sum_{j>i}^{N} V_{ij}^{(2)}\left(Q_i,Q_j\right) \\ &+ \sum_{i=1}^{N}\sum_{j>i}^{N}\sum_{k>j}^{N} V_{ijk}^{(3)}\left(Q_i,Q_j,Q_k\right) + \ldots \end{aligned} \qquad (3)$$

For rectilinear normal-mode coordinates, Chaban et al. [10] have shown that a pairwise approximation (i.e., including up to $V_{ij}^{(2)}(Q_i,Q_j)$) for $V(\mathbf{Q})$ is sufficient to give reasonable vibrational frequencies for large molecular systems. This does not imply that higher-order couplings (three or more mode couplings) can always be safely ignored, as Bounouar and Scheurer [21] have shown that neglecting 3-D couplings can lead to artefacts for some systems. In such cases, an internal or (more generally) a curvilinear coordinate representation of the PES leads to a much more accurate description of mode–mode couplings (see [21] and [12], for example), and the error introduced by neglecting 3-D couplings and above can thus be strongly reduced. Yet the a priori definition of a suitably de-coupled set of coordinates for periodic systems remains a complex issue. We are currently investigating optimum decoupling techniques for such systems in our laboratory. In the present study, however, we use a rectilinear 2-mode representation of the PES, despite its limitations, as this simplifies the calculation of the matrix elements involving the potential operator, such that they require only two-dimensional integrals at most. Moreover, in order to speed up the calculations on parallel computers, we make use of the OpenMP library to distribute the integral calculations to many processors.

For a given vibrational state $(\mathbf{n}) = \{\nu_1,\nu_2,\ldots,\nu_n\}$, we can compute an initial $V_{eff}^{j}(Q_j)$ for each mode j, using the vibrational wave functions obtained from the diagonal calculations subroutine and the 2-D PES cut. This effective potential is then used to solve the 1-D Schrödinger equation for each mode. This leads to new eigenvalues and eigenfunctions that can be used to build the state wave function. Note that, in the VSCF approach, we use a separable product of normal coordinate functions to represent the total wave function:

$$\Psi_n(\mathbf{Q}) = \prod_{j=1}^{N} \varphi_{n_j}^{(\mathbf{n})}\left(Q_j\right) \qquad (4)$$

We can then use the new state wave function to compute a new $V_{eff}^{j}(Q_j)$ for each mode, and solve again the 1-D Schrödinger equation for each mode. This sequence of operations is performed until convergence of the total SCF energy:

$$E_{\mathbf{n}} = \sum_{j=1}^{N} \varepsilon_{n_j}^{(\mathbf{n})} - (N-1)\left\langle \prod_{j=1}^{N} \varphi_{n_j}^{(\mathbf{n})} \middle| V(\mathbf{Q}) \middle| \prod_{j=1}^{N} \varphi_{n_j}^{(\mathbf{n})} \right\rangle \qquad (5)$$

In order to ensure a stable wave function for the subsequent correlation treatment, we also monitor convergence of the effective potential. Our implementation of the VSCF procedure for a given state is shown in Figure 2.

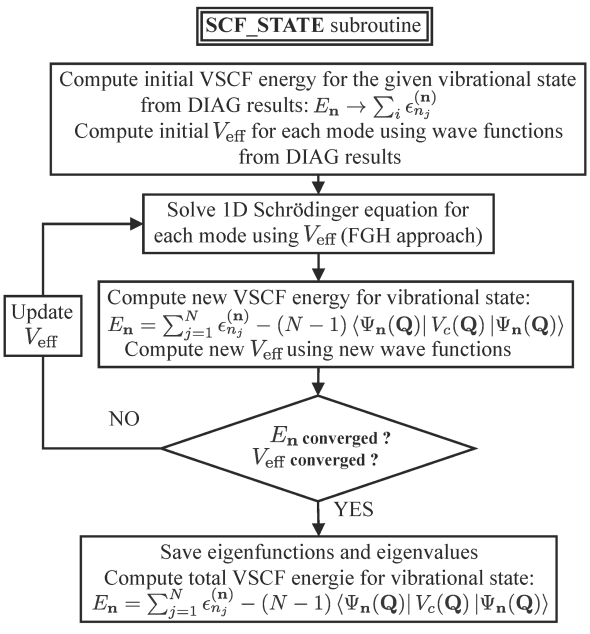

Figure 2: Flow-chart diagram of the computer code used to compute the VSCF state energy.

Although the convergence of the VSCF procedure is usually surprisingly smooth, in some cases convergence problems can occur. These often originate from the use of an inadequate coordinate system (e.g., rectilinear coordinates to describe a torsional motion, see also [12]), or from the limitation of the PES expansion to second order. In order to try and remedy convergence problems when a change of coordinate or a higher-order expansion are not possible, we implemented the following two techniques in our code:

- One possibility is to slow down the change in the effective potential by using a density mixing scheme. Compute the new effective potential by adding some of the effective potential obtained during the previous iteration, such as Equation 6, where b is a real number between 0 and 1, given by the user.

$$V^j_{\text{eff}}\left(Q_j\right) = (1-b)\left[V^j_{\text{eff}}\left(Q_j\right)\right]_{\text{old}} + b\left[V^j_{\text{eff}}\left(Q_j\right)\right]_{\text{new}} \quad (6)$$

- The second option is to scale down the second-order terms of the PES. This automatically decreases the coupling between modes and usually improves convergence. Such a scaling procedure is also implemented in the VSCF part of the GAMESS-US [22] suite of ab inito programs. One advantage of the technique is that it is known to converge in the limit of zero scaling factor (diagonal situation) and the coupling can be "switched on" progressively to include more coupling. However, this approach must be used with caution, as it changes the potential energy surface to force convergence, and, without further corrections at the correlated level of theory, leads to an inadequate result for the VSCF approach when compared to the fully coupled system.

Finally, the main algorithm used to compute VSCF frequencies is shown in Figure 3. Once the diagonal solutions have been computed, the program reads in the 2-D PES cuts and interpolates them using a bicubic interpolation algorithm [23]. The

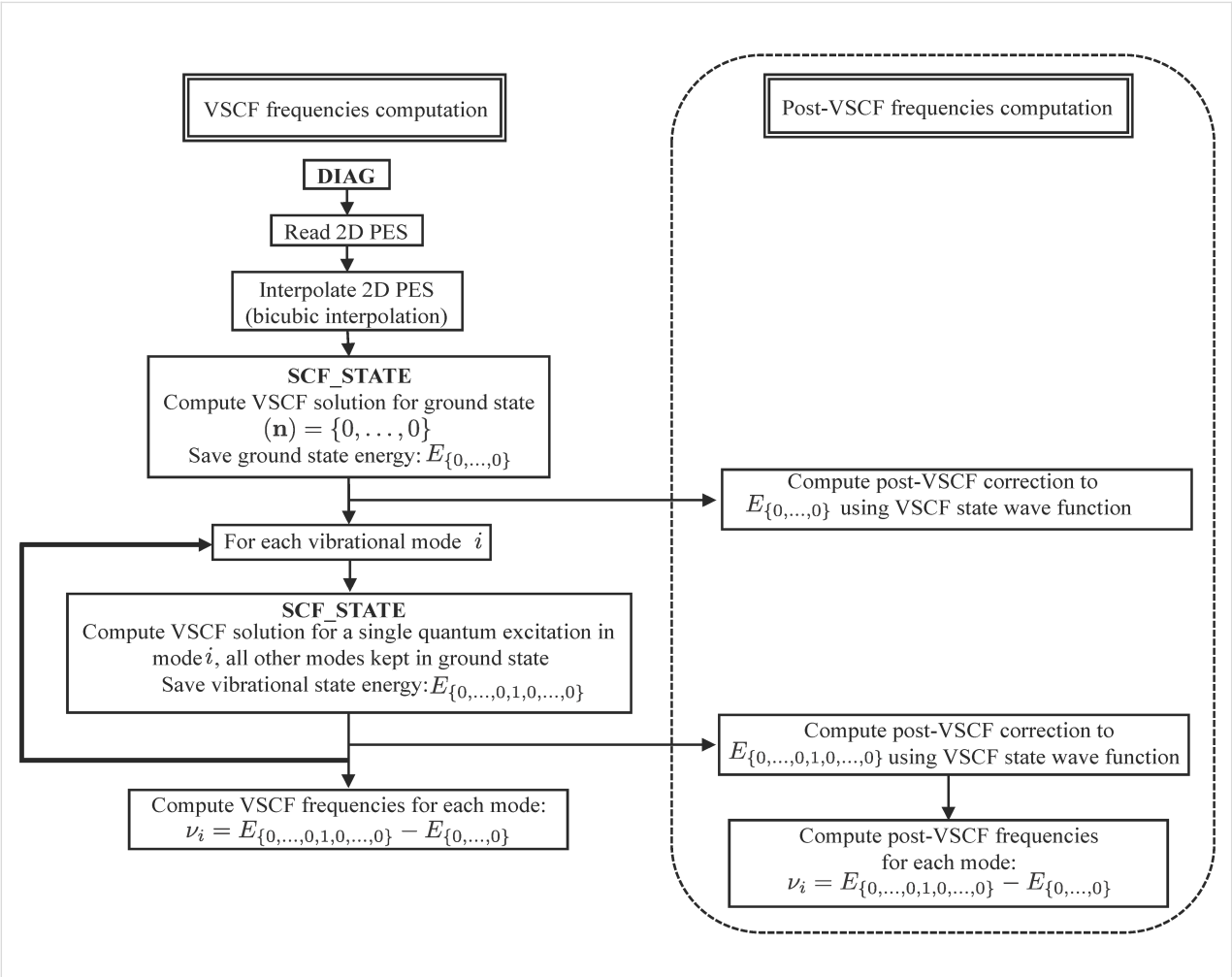

Figure 3: Flow-chart diagram of the computer code used to compute the VSCF and post-VSCF frequencies (dotted part of the diagram).

VSCF energy is then computed first for the ground state {0,…,0} and then for all necessary singly excited vibrational states, {0,…,0,1,0,…, 0}. The anharmonic frequencies are finally computed by a simple subtraction of the relevant vibrational state VSCF energies:

$$\nu_i = E_{\{0,...,0,1,0,...,0\}} - E_{\{0,...,0\}} \quad (7)$$

Note that all state energies can be corrected (right part of the flow chart) to include vibrational correlation using a range of post-VSCF methods described in the next section, and the corresponding corrected frequencies are simply calculated in the same way as Equation 7.

Improvement of the vibrational mean field approach

Vibrational Configuration Interaction: The VSCF/VCI approach

The vibrational mean field scheme is well adapted if the intermodal coupling potential is very weak. However, in most cases this condition is not fulfilled and the results of the SCF approach need correcting for mode–mode interactions. There are several ways to include vibrational correlation contribution, and, due to the analogy between VSCF and standard electronic structure theory, these corrections are usually expressed in a formalism based on the electronic Hartree–Fock method. Over the years, a number of groups have developed correction techniques such as the Vibrational Coupled Cluster (VCC) [24-26], Vibrational Multi-configurational SCF (VMCSCF) [27], Vibrational Mean Field Configuration Interaction (VMFCI [28,29]), Vibrational Configuration Interaction (VCI) [30-32] or the MP2-based methods [33,34], to name a few. This last set of approaches is very attractive for large systems as perturbative techniques usually do not require the solution of an eigenvalue problem. The most common perturbation correction is based on the Møller–Plesset formalism and is usually limited to second order of theory (although the use of higher orders has been carefully examined by Christiansen [24]). However, this approach is explicitly pertubative and thus assumes that the intermodal coupling is weak. This limitation has motivated the development of other methods. In our computer code PVSCF, we have mainly implemented the VMP2 (perturbative) and the vibrational configuration interaction scheme VCI (variational method). These two methods use the results of a preliminary VSCF calculation to compute the correlation correction. In this section, we will focus on the variational approach. The principal task of this approach is to diagonalise the following Hamiltonian:

$$\hat{H} = \hat{H}_0 + \Delta V(\mathbf{Q}) \quad (8)$$

where $\hat{H}_0$ is the vibrational mean field Hamiltonian computed in the VSCF step and ΔV the difference between the true N-dimensional potential operator (in our case limited to 2-mode representation (2MR) contributions) and the full mean field potential operator,

$$\Delta V(\mathbf{Q}) = \sum_{i=1}^{N}\sum_{j>i} V_{ij}^{(2)}(Q_i, Q_j) - \sum_i V_{\text{eff}}^{i}(Q_i) \quad (9)$$

Our implementation in PVSCF is made in a very flexible way. Before giving more details we will present the principal idea of this technique. Since the VSCF configuration is not sufficient to reproduce the anharmonic coupling between modes, we build a virtual basis set that can be used to express the full Hamiltonian by exciting the mean field modal basis. This provides a large number of virtual configurations based on the initial VSCF state, and the Hamiltonian is then diagonalised in this virtual basis (VCI basis). The initial VSCF step can be considered as a preconditioning scheme and gives a more physical vibrational basis than does a basis of uncoupled harmonic oscillators. The size of the virtual configuration basis set $\tilde{B}$ can be controlled by a threshold parameter that limits the excitation of each quanta and/or the sum of quanta over all vibrational modes. The term "virtual" indicates that all excited modal wave functions were computed from a single reference configuration, optimised with the VSCF technique. If the size of the VCI basis is reasonable (size up to around 10,000 elements), the Hamiltonian matrix can be directly diagonalised using routines from standard scientific libraries (e.g., Lapack). Nevertheless, despite the use of thresholds in order to reduce the number of virtual configurations, the VCI basis can very easily grow to a significant size for large systems and become impossible to diagonalise without further treatment.

As our implementation is aimed at large molecular and interfacial systems, we have then implemented an iterative diagonalisation solver based on the Davidson algorithm [35-37], which is well adapted when we have a good zeroth-order hamiltonian (in our case the mean field one). Moreover, as we are usually only interested in the bottom part of the vibrational spectrum, a full diagonalisation of the Hamiltonian matrix is not necessary. This method was firstly applied to this type of vibrational problem by Handy and coworkers [38] and is very well adapted for sparse matrices. The principle of the Davidson algorithm is presented below in Table 1.

Table 1: Davidson scheme used to converge a specific state $\left\{E_{ref}, \mathbf{v}_{ref}^{(p)}\right\}$. The $\mathbf{v}_{ref}^{(p)}$ eigenvector is expressed as the VSCF reference state plus the contribution of the excited virtual configurations.

(0) Initialisation (p = 1)	Define an initial vector $\mathbf{u}_0$ as the VSCF reference state.
(1) Diagonalisation	Diagonalise **H** in the $\{\mathbf{u}_0, \ldots, \mathbf{u}_{p-1}\}$ basis set $\rightarrow \left\{E_m^{(p)}, \mathbf{v}_m^{(p)}\right\}$ solutions
(2) Convergence	Form residual $\mathbf{q} = \left(\mathbf{H} - E_{ref}^{(p)}\right)\mathbf{v}_{ref}^{(p)}$; if $\lvert\mathbf{q}\rvert \le \varepsilon$ exit.
(3) Preconditioning	Precondition with the zero-order VSCF Hamiltonian $\mathbf{H}_0$ $\bar{\mathbf{q}} = \left(E_{ref}^{(p)} - \mathbf{H}_0\right)^{-1}\mathbf{q}$.
(4) Orthonormalisation	Define a new vector $\mathbf{u}_p$ orthogonal to the previous ones $\mathbf{e} = \left\{1 - \sum_{m=0}^{p-1} \lvert\mathbf{u}_m >< \mathbf{u}_m\rvert\right\}\bar{\mathbf{q}}$ and normalize $\mathbf{u}_p = \mathbf{e}/\lvert\mathbf{e}\rvert$.
(5) Loop $p := p + 1$, back to (1)	

Extension of VSCF/VCI for large systems

Direct Davidson diagonalisation

An initial strategy for large systems is to use the Davidson algorithm and store the pre-computed Hamiltonian matrix, expressed in the virtual configuration basis, in the main memory. The action of the Hamiltonian is then obtained through a matrix vector product $\mathbf{H} \cdot \mathbf{v}$ where the size of the matrix is $M \times M$, where M is the length of the initial seed vector $\mathbf{v}$. However, storing the full Hamiltonian in the main memory can be prohibitive and is not always possible in practice when we consider systems of several tens of modes. For these situations, we have the option of computing the action of the Hamiltonian on the seed vector on the fly, and each matrix element H_{ij} is then computed only when necessary, thus avoiding large memory requirements. In practice, this approach is suitable for large systems and circumvents the problems of memory requirements but at the detriment of computational speed.

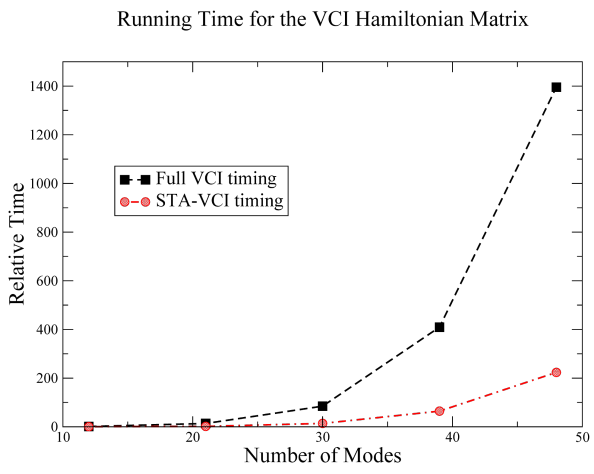

Figure 4: Representative timing for the construction of the Hamiltonian VCI matrix for a series of aliphatic alcohols (methanol to pentanol), for both standard VCI (Full VCI) and STA–VCI methods. All timings are relative to methanol using the standard VCI method.

A reduced-coupling approach for large mode systems

A different technique is implemented in PVSCF for the evaluation of the potential matrix elements of the VCI matrix. In order to reduce the timing cost of those elements, we use a number of reduced-coupling approaches. One of them is the single-to-all (STA) approach which leads to a significantly reduced computational scaling for large systems [39,40]. Indeed, only the two-mode potential coupling terms involving active modes ($N_{\tilde{A}}$) with themselves or with inactive ones ($N_{\tilde{I}}$) are used and thus the number of necessary terms in two-mode representation of the potential is highly reduced,

$$V(\mathbf{Q}) = \sum_{j=i}^{N_{\tilde{A}}} V_i^{(1)}\left(Q_i^{\tilde{A}}\right) + \sum_{j=1}^{N_{\tilde{I}}} V_j^{(1)}\left(Q_j^{\tilde{I}}\right) + \sum_{i=1}^{N_{\tilde{A}}}\sum_{j>i}^{N_{\tilde{A}}} V_{ij}^{(2)}\left(Q_i^{\tilde{A}}, Q_j^{\tilde{A}}\right) + \sum_{i=1}^{N_{\tilde{A}}}\sum_{j=1}^{N_{\tilde{I}}} V_{ij}^{(2)}\left(Q_i^{\tilde{A}}, Q_j^{\tilde{I}}\right) \quad (10)$$

This method improves the relative timing of calculations of the vibrational configuration interactions, since the computation of the VCI matrix elements are much less demanding. This type of speed-up is shown in Figure 4.

Moreover, our approach generates a sparser VCI matrix representation (Figure 5) that is better adapted to the Davidson algorithm. The STA–VCI approach allows the computation of

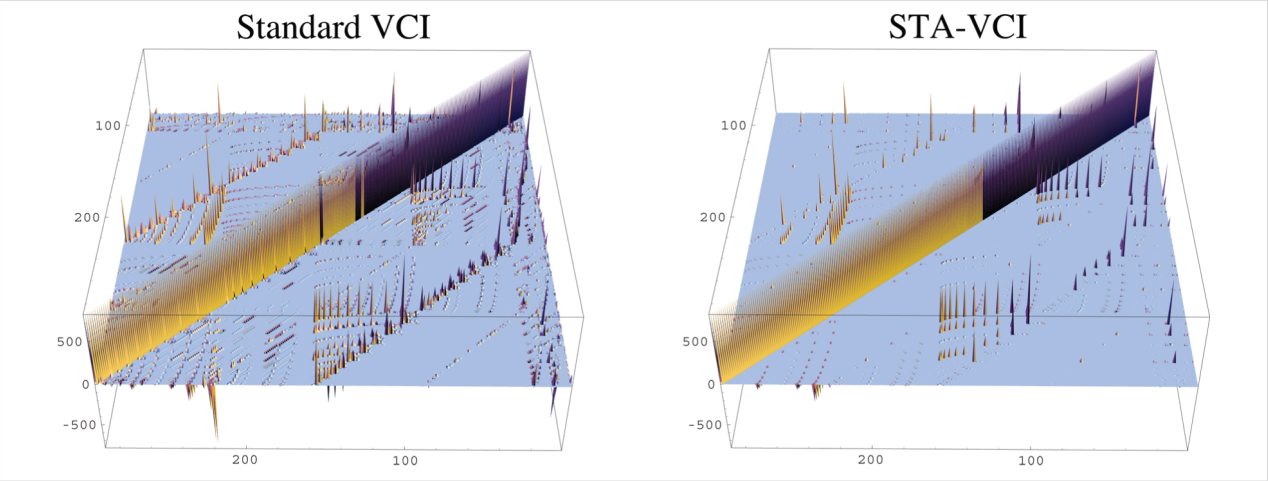

Figure 5: Graphical representation of the VCI matrix elements for a standard VCI and a STA–VCI calculation on methanol using the same basis. For the STA–VCI method, the OH-stretch mode is coupled to all other modes ($N_{\tilde{A}}$ = 1). Note the difference in the occurrence of off-diagonal elements between standard VCI and STA–VCI.

anharmonic frequencies with a low computational cost for the potential energy surface since only a subset of the intermodal coupling is computed.

Applications

The methods presented above allow us to treat large molecular systems and have been used to compute the OH-stretch frequency of benzoic acid (system with 39 modes) [40], for example. Our method can also be applied to larger systems and the STA approach was used to compute the anharmonic stretch frequency of hydrogen fluoride adsorbed on pyrene (Figure 6), a model system for the adsorption of HF on graphite.

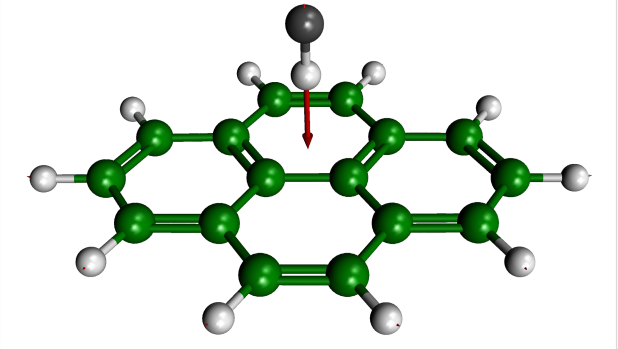

Figure 6: Hydrogen fluoride adsorbed on a pyrene molecule. The arrow represents the HF stretching mode.

The potential energy surface (mode–mode representation) is computed at a moderate ab initio cost (MP2/SBK level of theory). This system is challenging as it contains 78 modes and the weak π–hydrogen bond requires correlated electronic structure methods. The computed harmonic frequency for the stretching mode of HF adsorbed on pyrene is 3661 cm^{-1} which is −112 cm^{-1} away from that of the free HF molecule, ω(HF) = 3773 cm^{-1} at this level of theory. At the VSCF/VCI level of vibrational theory and using the STA approach we obtain 3477 cm^{-1} which corresponds to a shift of −135 cm^{-1} from the gas-phase molecule stretch frequency, ν(HF) = 3612 cm^{-1} from the 1-D vibrational solutions. To the best of our knowledge the HF-stretch frequency of hydrogen fluoride on pyrene has not been measured, however the spectrum of HF–benzene (a much smaller, yet similar system) has been measured by Andrews et al. [41]. The observed HF-stretch frequency is 3795 cm^{-1} in an argon matrix, which corresponds to a shift of −166 cm^{-1} compared to the vibrational stretch of free HF in a gas phase as reported by Herzberg [42] [ν(HF) = 3961 cm^{-1}].

We see that both harmonic and anharmonic calculations show the correct trend, i.e., a red shift of the HF frequency caused by the weak interaction with an aromatic compound. We note, however, that including anharmonicity causes almost a 20% change compared to the harmonic value and that the anharmonic results are in closer agreement with experiment (19% deviation), albeit performed on a related system. By comparing the experimental, free, HF-stretch frequency to our anharmonic results, it is obvious that the curvature of the MP2/SBK PES is much too shallow. Nevertheless, we are mainly interested in the effect of anharmonicity on the vibrational frequencies of adsorbed systems and thus focus on the vibrational shift, where this systematic error can be expected to compensate. Interestingly, scaling the vibrational harmonic frequencies – as is commonly done in a number of studies – does not improve much the prediction of the frequency shift at the harmonic level. Indeed, if we use the experimental HF-stretch frequency to compute a scaling factor [ν(HF,exp)/ω(HF) = 1.050], we obtain only a very modest improvement of the shift value (−118 cm^{-1})

which is still 30% away from the experiment. This can be compared to the anharmonic prediction of the shift, which does not use any scaling factor. Thus, we note that, for a PES computed at the same level of ab initio theory, the predictive power of the harmonic approximation for adsorption-induced vibrational shifts remains rather limited compared to an anharmonic calculation. This is mainly due to the nature of the harmonic model, that is the assumption of a quadratic shape of the PES at the minimum, which is inadequate for adsorbed molecules as their energetics can be markedly affected by the presence of a surface.

Iterative perturbative screening of the configuration space

When we consider large molecules, the main drawback of variational calculations is the rapid growth in the number of basis functions necessary in the VCI space. As the size of the molecule increases, the number of normal modes increases and so does the number of possible virtual excitations that can be performed to generate the VCI basis. Thus, even with an efficient VCI implementation, both the computational effort and the storage requirements grow rapidly for large systems, which severely limits the application of the VSCF/VCI scheme to large systems. Such a drawback is not confined to our implementation; in general, the principal difficulty in the development of any given variational method suitable for large molecular systems is the exponential growth in the size of the vibrational basis with the number of atoms.

We therefore implemented a different kind of VCI approach that overcomes these issues, and adapted the variation–perturbation method proposed by Pouchan and Zaki [43] to our STA–VSCF/VCI code. This method was originally proposed by Malrieu and co-workers for electronic structure theory [44], and later inspired a number of vibrational studies (see Brodersen and Lolck [45], for example). The implementation of Pouchan et al. uses a virtual basis set based on a product of harmonic oscillator wave functions and thus the number of configurations necessary to cover the active space is quite large for extended anharmonic systems. Our implementation uses VSCF step as a method to efficiently reduce the size of the configuration space.

The main idea of this approach is based on the separation of the full virtual configurational basis set $\tilde{B}$ into:

$$\tilde{B} = \tilde{P} \oplus \tilde{Q}$$

where $\tilde{P}$ is the active configuration subspace used to perform VCI calculations, and $\tilde{Q}$ is the subspace that contains virtual configurations, which do not contribute much to the true VCI eigenstate. This is based on the observation that, for most VCI calculations, the converged solutions usually only use about 1% of the relatively large virtual excitation basis set. This implies that there are a number of "preferred" excitations for a particular vibrational state and that the remaining excitations have a very limited impact on the solution. We use a perturbative preselection of the virtual states in order to capture the essential excitations, followed by a variational VCI in the preselected excitation space. The method then uses the new VCI solution as a reference to perform a new screening of the excitations and adds the relevant ones to the VCI space accordingly. This iterative multi-reference perturbative selection technique (VCIPSI) manages to keep the variational space manageably small (well below 2000 configurations in practice) and practically removes the VCI stage from the observed scaling.

Once the convergence of the $\tilde{P}$ space is reached, we suggested that the effect of the remaining neglected configurations left over in the $\tilde{Q}$ space can be easily accounted for by perturbation theory. We add a MP2 perturbative correction to the last eigenstate energies obtained by diagonalisation of the Hamiltonian in the converged active space $\tilde{P}$. This perturbative correction, computed with the converged non-active space $\tilde{Q}$ and the final eigenvalue, is called VCIPSI–PT2.

This new approach, combined with the STA technique in order to reduce the number of underlying ab initio calculations needed to compute the PES, provides a dramatic time saving and a much reduced memory usage compared to traditional approaches. This method had enabled us to compute the OH-stretch frequency of benzoic acid nearly 10 times faster than the standard VCI approach, with comparable accuracy [46]. Our results show that there is excellent agreement between the vibrational frequency computed using the STA–VSCF/VCI approach and the STA–VCIPSI–PT2 technique. The new VCIPSI algorithm reduces the memory footprint by a factor close to 200 for the STA–VCIPSI–PT2 method compared to VCI. Moreover, the total time taken by the VCIPSI calculation is reduced by a factor of seven compared to standard VSCF/VCI. These two observations demonstrate the efficiency of the STA–VCIPSI method for the treatment of molecular systems with a large number of normal modes.

Our implementation is very scalable and allows the investigation of larger systems such as an adsorbed 4-mercaptopyridine molecule on an Au(111) surface, using the partial Hessian method described in more details in the next section. The results obtained are in a good agreement with experiment [4] and allow the identification of possible adsorption sites for 4-mercaptopyridine using vibrational data alone, thus leading to a new type of structure determination for adsorbed organic molecules.

Description of adsorbate vibrations

Before performing an anharmonic calculation for adsorbed molecules on a surface, we need to determine the normal mode vectors of the system. This can be a computationally demanding task for large systems, and the normal mode analysis of adsorbates can be efficiently carried out using the partial Hessian technique [47] instead. Here, the Hessian matrix is split into two parts, one part is calculated explicitly while the matrix elements of the other part are set to zero. The full $3N_a$-dimensional space is divided into an "active" and an "inactive" subspace. One set of atoms is allowed to move while the other set is kept frozen during the Hessian calculation. The Hessian matrix, **H**, is organised such that the active and the inactive atoms each form one block on the diagonal, and the off-diagonal elements contain the coupling terms between active and inactive atoms:

$$\mathbf{H}_{full} = \begin{pmatrix} \mathbf{A} & \mathbf{AS} \\ \mathbf{SA} & \mathbf{S} \end{pmatrix} \tag{11}$$

where sub-matrix **A** contains only the force constants of the active part of the system (fragment *A*), usually made up of the adsorbate but which might also include a few surface atoms. Sub-matrix **S** in Equation 11 is usually set to zero to account for the inactive substrate (remaining atoms of the surface, fragment *S*). Sub-matrix **A** is then the only matrix needing diagonalisation, yielding $3N_A$ normal modes and frequencies, where N_A is the number of active atoms.

The partial Hessian technique reduces the number of dimensions of the system and focuses on a part of interest. It is justified only if fragment *S* is heavy compared to fragment *A*, which is the case in surface calculations where fragment *A* contains mostly the adsorbate atoms and *S* a large proportion of surface atoms; or more generally, if the modes examined are localised in one part of the system. In general, the eigenvectors and eigenvalues of the partial Hessian will converge towards the eigenvectors and eigenvalues of the full Hessian as the number of inactive atoms decreases (with an increasing coupling between the two fragments included in the Hessian).

We will illustrate this rapid convergence behaviour for the harmonic frequencies of 4-mercaptopyridine (mpy) adsorbed on Au(111) (Figure 7) for different sizes of the partial Hessian matrix. The largest active system, mpy-ads-5, contains five gold atoms (the two gold atoms directly bonded to the sulfur atom, and the gold atoms which are bonded to both the first two gold atoms), thus yielding 48 normal modes. The next size down, mpy-ads-2, contains two gold atoms, both connected to the sulfur atom, giving 39 normal modes. Finally, mpy-ads-0 is a minimal model that does not include any gold atoms in the partial Hessian matrix (33 modes).

The calculations were carried out using the Vasp [48] program and projector augmented wave (PAW) pseudo potentials [49] optimized for the Perdew–Burke–Ernzerhof (PBE) [50] exchange-correlation functional. A 3 × 3 surface unit cell was used, with a vacuum layer ≈17.5 Å thick, and three layers of Au atoms. The plane-wave cutoff was set to 400 eV, and the cutoff for the augmentation charges to 450 eV. The Brillouin zone was sampled using 25 k-points.

The harmonic frequencies, ω_i, obtained for each model are shown in Table 2. We observe that the three models are virtually identical for all modes down to $\omega = 395\ cm^{-1}$. Two of the Hessians were chosen to contain Au atoms in order to enable a possible coupling between surface modes and the adsorbate, while in mpy-ads-0 this coupling is excluded from the start. From the point of view of the definition of a partial Hessian, the smaller mpy-ads-0 model is better justified, as the active fragment is much lighter than the inactive fragment. However, since adsorbate modes are usually localised on the adsorbate rather than on the surface, the inclusion of Au atoms in the active region should only have a limited effect. This is also supported by Table 2: Only the low frequencies of mpy-ads-5 and mpy-ads-0 differ by more than a wavenumber, thus showing

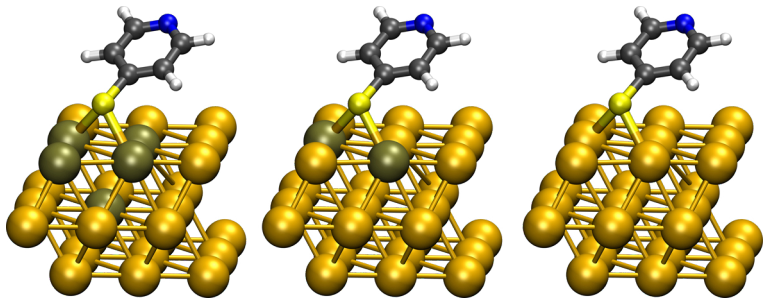

Figure 7: Active atoms for the partial Hessian: 4-Mercaptopyridine adsorbate plus different number of Au atoms, indicated by a darker color; **left**: mpy-ads-5, **middle**: mpy-ads-2, **right**: mpy-ads-0.

Table 2: Harmonic frequencies for mpy-ads-5, mpy-ads-2 and mpy-ads-0 (PBE/PAW); in parentheses deviation of mpy-ads-2 and mpy-ads-0 with respect to mpy-ads-5; in cm^{-1}. Mode numbers from mpy-ads-5. Assignment of normal mode vibrations: ν – stretching, δ – in-plane bending, γ – out-of-plane bending, ρ – rocking, χ – wagging, τ – twisting.

mode no.	mpy-ads-5	mpy-ads-2	mpy-ads-0	normal mode
48	3121	3121 (0)	3121 (0)	ν(CH)
47	3121	3121 (0)	3121 (0)	ν(CH)
46	3084	3084 (0)	3084 (0)	ν(CH)
45	3081	3081 (0)	3081 (0)	ν(CH)
44	1544	1544 (0)	1544 (0)	δ(HCC,HCN), ν(CC)
43	1532	1532 (0)	1532 (0)	δ(HCC,CCC), ν(CC,CN)
42	1451	1451 (0)	1451 (0)	δ(HCC,HCN), ν(CC,CN)
41	1389	1389 (0)	1389 (0)	δ(HCC,HCN), ν(CC)
40	1305	1305 (0)	1305 (0)	δ(HCC,HCN,SCC)
39	1274	1274 (0)	1274 (0)	δ(HCC,SCC), ν(CN)
38	1211	1211 (0)	1211 (0)	δ(HCC,HCN,CCC)
37	1074	1074 (0)	1074 (0)	δ(HCC,CCC,CNC), ν(SC)
36	1073	1073 (0)	1073 (0)	δ(HCC,CCC)
35	1058	1058 (0)	1058 (0)	δ(CCC,CNC), ν(SC)
34	972	972 (0)	972 (0)	δ(CCC,CNC)
33	961	961 (0)	961 (0)	τ(HCC)
32	944	944 (0)	944 (0)	τ(HCC)
31	838	838 (0)	838 (0)	χ(HCC)
30	787	787 (0)	787 (0)	χ(HCC)
29	720	720 (0)	720 (0)	χ(CCC,CNC)
28	679	679 (0)	679 (0)	δ(CCC,CNC), ν(SC)
27	652	652 (0)	652 (0)	δ(CCC,SCC)
26	484	484 (0)	484 (0)	γ(SCC)
25	395	395 (0)	394 (−1)	δ(AuSC), ring pulsation
24	357	357 (0)	357 (0)	ρ(HCC,CNC)
23	304	304 (0)	303 (−1)	δ(AuSAu,AuSC,SCC)
22	234	234 (0)	228 (−6)	δ(AuSC), ν(AuS), ring deformation
21	150	150 (0)	140 (−10)	δ(AuSC), ring deformation
20	129	129 (0)	117 (−12)	δ(AuSAu)
19	96	—	—	Au lattice
18	88	—	—	Au lattice
17	87	—	—	Au lattice
16	87	—	—	Au lattice
15	81	—	—	Au lattice
14	80	—	—	Au lattice
13	76	78 (2)	64 (−12)	frustrated rotation
12	72	—	—	Au lattice
11	70	70 (0)	—	Au lattice
10	66	69 (3)	—	Au lattice
9	65	65 (0)	—	Au lattice
8	61	63 (2)	—	Au lattice
7	60	—	—	Au lattice
6	56	53 (3)	—	Au lattice
5	50	52 (2)	—	ring pulsation, ν(CC)
4	46	—	—	Au lattice
3	33	33 (0)	33 (0)	frustrated rotation
2	24	24 (0)	25 (1)	frustrated translation
1	17	18 (1)	19 (2)	frustrated rotation

that the high-frequency adsorbate modes converge very quickly with the number of active atoms. However, one should be careful when choosing the computationally cheaper mpy-ads-0 model for an anharmonic treatment of molecule–surface vibrations. Indeed, this reduced-dimension model does not contain any degrees of freedom on the surface atoms and therefore no vibrational coupling is possible between the adsorbate atoms and the surface. This is particularly important for surfaces made of lighter atoms, e.g., carbon-based or silicon-based materials, where the coupling between adsorbate and surface is expected to be much larger. Note that in this case, the main assumption of the partial Hessian formalism (effectively that the surface has an infinite mass) is no longer guaranteed and rigorous convergence tests should be performed.

Scalable generation of potential energy surfaces

The main issue is to find a PES representation that is scalable and computationally manageable for large systems on the order of 50 atoms or more. Given that the number of degrees of freedom increases sharply with the size of the system, it is necessary to follow a systematic approach. Such an approach enables an automatic construction of the PES and provides a way of increasing PES accuracy by including higher order n-body terms in the potential expansion. In general, the 1-D terms are the largest contributors to the PES, followed by the 2-D terms that add couplings between the degrees of freedom. These coupling terms typically contribute significantly less than the 1-D terms but have important implications for vibrational resonances and energy transfer. The 3-D and higher terms add smaller corrections to the PES that are only required for a very high accuracy description. Note that the presence in the PES of terms greater than second order invalidates the direct isomorphism with electronic structure theory and often requires a different methodology.

The computational bottleneck of the direct-VSCF/VMP/VCI methods is the generation of accurate PES. With the fast algorithms introduced earlier, it is possible to significantly reduce the computational demands by taking into account only strong couplings. In the next section we discuss two PES generation schemes that both use delocalised computational resources. The first one is more suited to small scale calculations on a single computer cluster, while the second approach enables PVSCF to take advantage of multiple clusters at remote locations through grid computing.

Computational task farming

The potential energy surface required for the direct-VSCF calculation is calculated on a grid of points. The atoms are displaced along the normal mode vectors in steps whose size depends on the vibrational frequency of the mode considered. The total energy is then calculated at each of these n_{grid} grid points. Thus, a large number of single-point total energy (SPE) calculations are necessary for the construction of the PES. All of these SPE calculations are performed by an electronic structure program and are independent of each other and can thus be computed simultaneously using many processors. Our calculations were run on the bwGRiD [51] cluster at the university of Ulm, Germany, with unix scripts handling the job submission. All SPE calculations are submitted to the queueing system in bundles of maximum-job-number calculations, so that the queueing system handles the task distribution. On the bwGRiD cluster, each node has eight processors, such that eight calculations are performed in each job.

Without the automatisation and parallelisation of the PES construction, direct-VSCF calculations for interfacial systems of the size mentioned earlier would be computationally inaccessible. For example, the 4-mpy/Au(111) system with adsorbate at a bridge position contains 39 normal modes (if the Au atoms which are directly connected to the sulfur atom are included in the partial Hessian analysis). For this PES, n_{grid} = 16,624 SPE calculations are necessary for the 1-D PES, and 189,696 SPE calculations are required for the 2-D PES (39 × 38/2 mode–mode couplings, each of them using 16 × 16 grid points). The computational effort for the parallel calculation is no longer so heavily dependent on the system size, but more on the computation time for one SPE calculation.

Grid interface

Even after restricting the PES to include only the strong couplings, for a large system the number of SPE calculations remains quite large, usually between 10^3 and 10^6. The same problem also occurs during construction of the Hessian matrix: The number of displacements, which can be estimated as $6n_{\text{active}}(3n_{\text{active}} + 1)$, grows very rapidly with the number of active atoms, n_{active}. In both cases, the amount of processing time (wall time) can be reduced through parallel computing, the obvious technique being to distribute serial tasks across available computing cores. This method can be easily implemented and yields directly to a linear scaling approach, however, in order to use computational resources efficiently, some important questions need to be considered.

First, some queueing systems on grid resources distribute jobs on each node, and not to each core, such that we need to start several serial jobs on each node simultaneously, in order to optimise computational power use. Unfortunately, the different jobs, which run on the same node, may take different computational time. This situation happens very often, because during the PES generation the displacements far from the equilibrium

position usually require a longer iteration cycle to achieve convergence. It is also very hard to predict how many nodes and cores may be expected, due to different priority policies for each grid location. Thus, we need a balancing mechanism, which allows us to load all cores on all available nodes evenly. The solution involves implementing a distribution system that submits the grid points dynamically to each location. Instead of submitting a batch script, we submit a special universal executable script (UES) that connects to an SQL database, gets the next free grid point, related files and appropriate external executable script (EES), and runs EES on the particular node and core. This additional EES provides a way to extend functionality dynamically and to run a few different jobs using several ab initio programs simultaneously. Because we want to be able to run jobs on different clusters, grids and individual nodes with different kinds of processors and under various operating systems, all scripts have to be cross-platform. In our implementation of UES, we have chosen the perl language, as it has pure MySQL and PostgreSQL database interfaces that do not use dynamic libraries written in other languages. This is a critical point given that usually MySQL/pSQL client programs and libraries are not installed on the computational nodes. Moreover, perl provides a command line option to specify the locations of non-standard modules, which makes the installation procedure simple and flexible.

Second, due to the unreliable nature of distributed computing across various locations, some results can go missing for various reasons. In order to avoid missing points, we need an intelligent system to recognise and react to various failures, such as when a node goes down, job killed by queueing system or abnormally terminated due to convergence problems, network or SQL server troubles, and so on. Such a system was implemented in two stages: After the calculation of a grid point, the EES parses the output file and looks for results. It then sends the results to UES and returns an exit code. Depending on this code, the results will be uploaded back into the database, or the current point or even all points within a project may be marked as erroneous and will be no longer considered. Moreover, if there are no results during a specified period of time, it is assumed that something went wrong and the grid point will be resubmitted.

In summary, the grid-based PES construction process is composed of the following steps (Figure 8):

1. Generate the set of grid points and upload them to the database. Upload the EES designed specifically to perform the total energy calculation, along with dependent files, such as templates, external basis sets, restart files, etc.
2. Submit batch scripts using PBS, SGI or any other batch system, which will start one UES for each CPU, and/or start UES manually on the local workstation.
3. After UES is started, it downloads the EES and corresponding files once for each grid location, then gets the first available grid point, runs EES and provides it with the geometry of the system at the selected grid point. The EES reads the geometries, produces a valid input file from a template file, runs the particular ab initio program, parses the results and sends it back to UES or returns an appropriate error code. After termination of EES, UES returns results to the database or marks the grid point as defective and tries to download the geometry of the next grid point. This step is repeated until no more points are available.
4. Retrieving constructed PES and the list of non-converged points from the database.

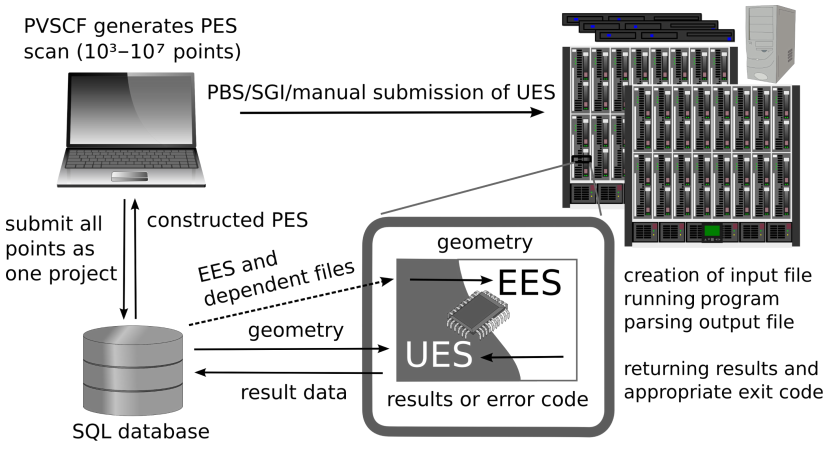

Figure 8: Diagrammatic representation of the grid interface.

Periodic density functional theory for molecular PES

In this section, we examine the accuracy provided by periodic density functional codes and their suitability for the construction of PES for anharmonic calculations. The use of periodic DFT codes is desirable for two reasons: A treatment of periodicity is a necessity for the correct description of molecule–metal interfaces, and periodic DFT codes are usually more efficient than standard molecular codes for large systems. Our group [4] and others [52] have shown that, provided the potential energy surface satisfies the periodicity conditions, the Γ-approximation provides an adequate description of the vibrations in periodic systems. If we focus mainly on the vibrational spectrum of adsorbed molecules, the description of surface phonons (which would require a periodic vibrational approach) is of lesser interest and a Γ-point representation leads to a realistic calculation. Moreover, in-phase vibrations (i.e., at the Γ-point) usually correspond to the most intense transitions observed in linear optical spectroscopy. We focus here on the thiophene molecule as it is a sizeable system of 21 vibrational modes (or 210 mode–mode couplings), and it has been shown to form self-assembled monolayers on gold surfaces [53] and as such is a system of relevance to surface science. This molecule is big enough to be a chemically meaningful system, but also small enough that it can be used as a benchmark system to compare DFT with ab initio calculations.

The optimal geometry of thiophene in the gas phase was obtained using Møller–Plesset perturbation theory (MP2) with TZVPP basis set (GAMESS-US [22]) and density functional theory (DFT) with the various functionals and TZVPP (GAMESS-US) or MOLOPT-TZV2P basis sets (CP2K [54]). For the CP2K calculations, the cell size is 10 × 10 × 14 $Å^3$ and the periodic solver is used with a 400 eV density cutoff. Pseudo potentials are used for all atoms and are optimised for the respective functionals (e.g., GTH-PBE for PBE), except for sulfur for which the GTH-BLYP pseudo potential was used instead of GTH-HCTH120, due to the lack of GTH-HCTH120 parameters for the sulfur atom. The GTH-BLYP pseudo potential was selected as it gives the best optimal structure.

The calculated geometrical parameters are compared to experimental ones in Table 3. According to the root-mean-square (RMS) deviation values for distances and angles, the PBE and HCTH120 functionals (CP2K) give the best overall agreement. Our ab initio reference method, MP2/TZVPP, gives results of similar quality to PBE.

The calculated anharmonic vibrational frequencies of thiophene in the gas phase are shown in Table 4, with PES computed using each of these three levels of electronic structure theory. We use the assignment of fundamental transitions by Rico and coworkers [55]. The vibrational calculations are performed using VSCF/VCI in curvilinear coordinates [12] on an equidistant grid with 16 points. We allow up to seven excitation quanta in the VCI basis. In spite of the fact that PBE gives a very good result for the geometry of thiophene, its performance for the prediction of anharmonic frequencies is very poor for this molecule. This is particularly evident for the stretching frequencies and seems to indicate that the atoms are too weakly bound with this functional. A similar behaviour was also observed by Handy and coworkers [56]. In contrast to PBE, the HCTH120 anharmonic frequencies slightly underestimate the experimental values but overall show a very good agreement

Table 3: Calculated and experimental molecular geometry of thiophene in the gas phase.

	DFT (GAMESS-US)		DFT (CP2K)					
mode	B3LYP	HCTH120	BLYP	BP86	PBE	HCTH120	MP2	Exp. [57]
r(C–S), Å	1.728	1.723	1.726	1.722	1.712	1.714	1.717	1.714(0)
r(C=C), Å	1.364	1.369	1.375	1.374	1.376	1.375	1.377	1.369(6)
r(C–C), Å	1.424	1.421	1.427	1.424	1.424	1.422	1.415	1.424(3)
r(=C–H), Å	1.077	1.079	1.081	1.084	1.085	1.082	1.075	1.077(6)
r(–C–H), Å	1.080	1.083	1.084	1.084	1.088	1.084	1.078	1.080(5)
α(CSC), °	91.6	91.9	91.8	92.1	92.2	92.3	92.1	92.1(7)
α(SCC), °	111.5	111.4	111.3	111.4	111.4	111.4	111.4	111(.47)
α(CCC), °	112.7	112.7	112.7	112.6	112.5	112.5	112.6	112(.45)
α(SCH), °	120.1	120.0	120.1	120.1	120.0	120.0	120.6	119(.85)
α(CCH), °	124.0	124.1	123.9	124.1	124.2	124.1	124.4	124.2(7)
RMSD, 10^{-3} Å	6.8	4.5	6.4	5.2	5.6	3.6	5.7	0.0
RMSD, °	0.32	0.20	0.29	0.16	0.08	0.12	0.35	0.00

Table 4: Anharmonic frequencies of the fundamental vibrational modes of thiophene in the gas phase (in cm^{-1}). The mode assignment convention is: ν – stretching, δ – bending, τ – twisting. The subscript "a" denotes an antisymmetric mode. The CH-stretching and CH-bending modes are labelled according to their irreducible symmetry representation in C_{2v}.

	DFT					DFT			
mode	PBE	HCTH120	MP2	Exp. [58]	mode	PBE	HCTH120	MP2	Exp. [58]
τ(C=C–S–C)	410	451	459	452	δ(CH)a_1	1016	1071	1094	1082
τ(C=C–C=C)	521	552	575	564	δ(CH)b_2	1017	1088	1095	1085
δ(CSC)	554	608	612	609	δ(CH)b_2	1174	1239	1266	1256
	637	652	676	683	δ(CH)a_1	1285	1351	1346	1364
	677	694	727	712	ν(C–C)	1329	1422	1427	1410
ν_a(SC)	693	760	755	754	ν_a(C–C)	1422	1502	1485	1510
ν(ring)	777	828	849	840	ν(CH)b_2	2877	3038	3122	3087
ν(SC)	805	846	854	866	ν(CH)a_1	2931	3060	3141	3097
δ(ring) + ν_a(SC)	807	864	879	873	ν(CH)b_2	2919	3103	3174	3125
	839	875	893	900	ν(CH)a_1	2972	3103	3178	3126
	982	1040	1047	1036					
					RMSD	99	20	23	0

with the experimental data. The situation is slightly worse at the MP2/TZVPP level due mainly to an overestimation of the strength of single bond stretching.

Our results show that a good agreement between predicted and experimental geometry does not guarantee a reliable prediction of the anharmonic vibrational frequencies. The PBE functional is very popular in surface science and solid state physics but we show that its description of the cohesion between atoms can be an issue for the description of molecular vibrations. While MP2-based calculation of the PES has been shown in the past to lead to reliable anharmonic frequencies for molecular systems [59], perturbation theory remains computationally expensive for periodic systems. We observe that HCTH120 seems to be a much cheaper alternative to MP2 periodic systems, and that it provides a better description of the vibrational properties than the ubiquitous PBE functional. However, the HCTH family of functionals do not satisfy the uniform electron gas limit and were mainly parameterised for molecular systems [60].

Assessing metal–metal bonds through anharmonic calculations

The description of binding forces in metals is still a topical issue, where density functional theory has so far been very successful. Indeed, the complexity of transition metal bonding, potentially involving a number of degenerate electronic states, appears to be easily described by gradient-corrected functionals such as PBE. In order to further investigate the suitability of some currently used density functionals for the description of gold–gold interactions, we compare our results for the geometries and binding energies of the Au_2–Au_{10} clusters to the reported theoretical and experimental results from other authors. We also give a brief outlook of our study of the harmonic and anharmonic vibrational frequencies for these gold clusters, as vibrational properties are directly connected to the curvature of the potential energy landscape and thus provide important information on the overall quality of the PES.

In order to obtain local minimum energy structures, we use the Nelder and Mead version of the Simplex method [61,62], together with five different empirical models: The Murrell–Mottram potential [63] with the parameters used by Wilson and Johnston [64], the Sutton–Chen potential [65], the Gupta potential [66] with the parametrisation defined by Cleri and Rosato [67], the Glue model as developed by Ercolessi et al. [68], and the Voter–Chen version of the embedded atom model (EAM) [69-71]. In order to reproduce planar structures using these potentials, geometrical constraints are introduced. Planar structures have already been predicted by high level theory to be the global minima for the smallest clusters. The size of planar-to-nonplanar transition in gold clusters varies between $n = 7$ and $n = 15$, depending on the DFT approach used. Our DFT calculations are carried out using a plane-wave basis set with relativistic ultra-soft Vanderbilt (VDB) pseudo potentials [72]. We perform plane-wave DFT calculations using the CPMD code (version 3.11.1) [73]. We use the Perdew–Burke–Ernzerhof PBE [50] functional and other functionals such as BP86 [74,75], BLYP [74,76] and LDA [77]. We use periodic boundary conditions and a cubic supercell of $(15\ Å)^3$ to avoid strong interactions between neighbouring clus-

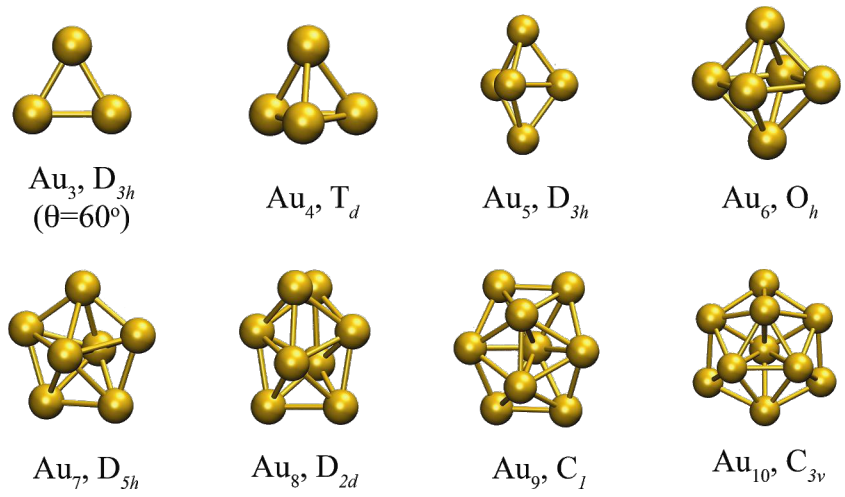

Figure 9: Global minimum energy structures for Au_3–Au_{10} clusters obtained for empirical potentials, along with their symmetry point group.

ters and a plane-wave energy cutoff of 30 Ry (408 eV). Additionally, we optimise a selected set of structures up to Au_7, using the MP2 method. These calculations are carried out using the SBKJC(1*f*) basis set [78,79]. Geometry optimisations were performed using GAMESS-US code [22], but only on a selected set of structures. In contrast to most DFT calculations, in which planar structures are predicted as the global minimum even for sizes above $n = 10$, MP2 predicts the first non-planar minimum energy structure at a size of $n = 7$ [78,80].

We use our fast-VSCF/VCI [11,40] technique to compute the anharmonic frequencies of the lowest DFT energy minima for each size. The global minimum energy structures obtained with the empirical potentials are shown in Figure 9. All of them are non-planar except for the trivial cases, Au_2 and Au_3. The global minimum energy structures obtained using PBE/VDB, which are all planar, are shown in Figure 10.

The binding energies for the non-planar empirical global minimum structures are shown in Figure 11 (left). Among the empirical potentials studied, the experimental binding energy of the gold dimer is best reproduced by the Voter–Chen potential. This empirical potential also provides the best prediction for the bond length and is also the most suitable potential to reproduce

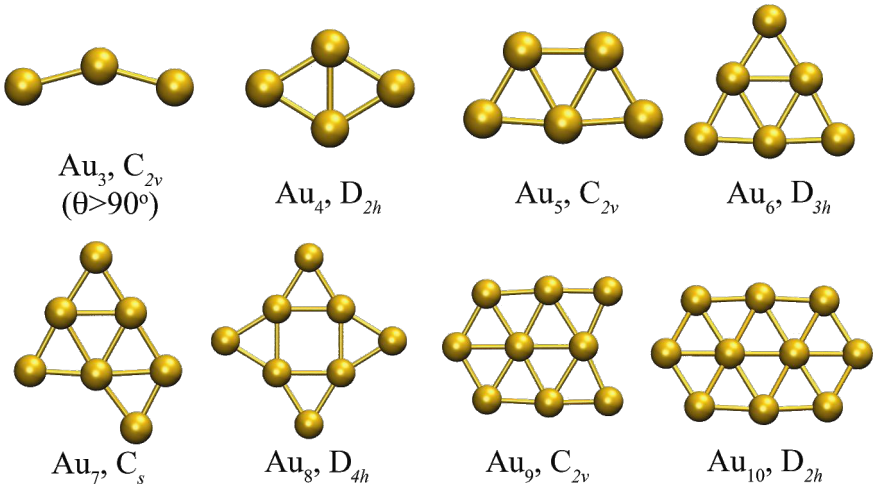

Figure 10: Global minimum energy structures for Au_3–Au_{10} clusters obtained for PBE/VDB, along with their symmetry point group. Structures with equivalent but not identical geometry can be obtained from the empirical potentials by including constraints.

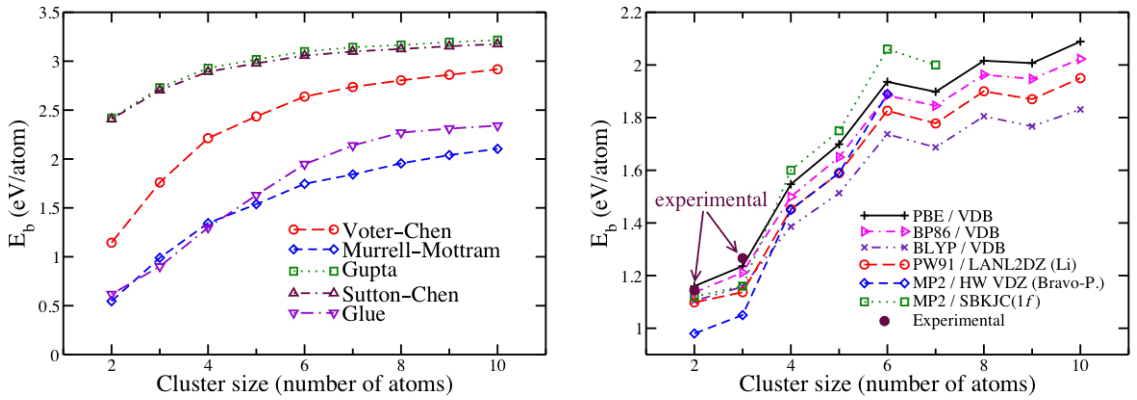

Figure 11: Left: Binding energies calculated for Au_2–Au_{10} clusters using different empirical potentials. The values correspond to the global minimum energy structures, which are always non-planar (except for Au_2 and Au_3). Right: Binding energies obtained using DFT and MP2 calculations, compared to DFT values reported by Li [81], to MP2 values reported by Bravo-Perez [82], and to experimental values reported by Bishea and Morse [83,84]. All structures are planar (MP2 global minimum energy structure for Au_7 is non-planar, but here we show the value corresponding to the planar structure). For Au_3, the structure reported by Bravo–Perez is the equilateral triangle.

the features of the high-level PBE/VDB potential energy surfaces. It is therefore used to pre-scan PES in the fast-VSCF method. The right part of Figure 11 shows a plot of the binding energies for the various DFT approaches and MP2/SBKJC(1*f*), compared to energy values reported in other studies and to available experimental values.

We find that PBE/VDB reproduces best the experimental binding energies of Au_2 and Au_3, as well as the bond length of Au_2. Experimental binding energies for larger clusters have not been reported. The calculated energies using PBE/VDB are in close agreement with the values reported by Li et al. [81] using the PW91 functional [85] with a LANL2DZ basis (~0.1 eV on average). Better agreement is found with binding energies reported by Xiao et al. [86], who used the PW91 functional with the projector augmented wave (PAW) method (differences of ~0.01 eV/atom). We assume that, for each cluster size, the characteristics of the vibrational spectrum are determined only by the global minimum energy structure. This assumption is valid for small clusters but, as size increases, the presence of near degenerate minima is likely to give rise to extra transitions due to other isomers. The Voter–Chen version of the embedded-atom model is used to prescan the PES for the fast-VSCF/VCI calculations.

For the gold dimer, the computed harmonic frequency using PBE/VDB is $\omega = 176.2$ cm^{-1}, and the anharmonic frequency is $\nu = 175.3$ cm^{-1}. These values are ~8% lower than the experimental frequencies, $\omega = 190.9$ cm^{-1} and $\nu = 190.1$ cm^{-1}, respectively [83]. Nevertheless, the calculated anharmonic frequency is 0.9 cm^{-1} lower than the calculated harmonic frequency, almost the same difference as that between the experimental values.

A comparison of the RMS deviation between the harmonic and anharmonic frequencies (Table 5) shows that the anharmonicity for all the small clusters studied is around ~1.0 cm^{-1}. Even if gold clusters do not show large overall vibrational anharmonicity, some specific vibrational transitions show large relative anharmonicity. The modes exhibiting larger anharmonicity are generally associated with bending motions of the molecule. We also note that vibrational anharmonicity does not affect the planarity of the Au_7 cluster.

Table 5: Differences between anharmonic (ν) and harmonic (ω) frequencies for the global minima of bare planar clusters Au_2 to Au_{10} obtained using PBE/VDB, in cm^{-1}. The anharmonic results are obtained from fast-VSCF/VCI calculations for clusters with size and from standard VSCF/VCI calculations for the smaller clusters. For each cluster, we report the difference for the highest frequency mode (ν_{max}) in the cluster, the maximum difference (MAXD), and the rms deviation for all normal modes (RMSD).

Cluster size	ν – ω		
n	ν_{max}	MAXD	RMSD
2	−0.9	−0.9	0.9
3	−1.1	1.6	1.2
4	−1.8	−1.8	0.9
5	−1.2	−2.1	1.1
6	−0.8	−1.6	0.6
7	0.8	0.8	0.4
8	0.0	−2.6	0.8
9	−0.7	−2.0	0.6
10	−1.1	−1.2	0.5

Conclusion

In this paper we have shown that a careful implementation of the direct vibrational self-consistent field method enables us to

investigate the quantum vibrational properties of extended systems. Our physically intuitive picture of "preferential" communication channels between normal modes provides a fast and accurate way of performing these calculations, at a fraction of the computational cost of the standard approaches. This new perspective opens the door to novel ways of obtaining accurate anharmonic spectra directly from ab initio or density functional theory data, thus making a direct link between theory and experiment. We believe that the techniques we have developed lay the foundations for a rigorous description of the vibrational spectra of complex systems beyond the harmonic approximation, and provide a very promising tool for future investigations of vibrational, bound states in large systems. The applications presented enabled us to assess the quality of the standard electronic structure techniques against experimental results and revealed the strengths and weaknesses of certain types of exchange and correlation functionals. Setting such a benchmark provides a way of systematically improving and cross-checking the description of inter-atomic interactions, which is a necessary building block for the theoretical description of nanostructures.

Acknowledgements

This work was supported by a generous grant ("SFB-569/TP-N1") from the Deutsche Forschungsgemeinschaft (DFG).

References

1. Yang, A. C.; Garland, C. W. *J. Phys. Chem.* **1957,** *61,* 1504–1512. doi:10.1021/j150557a013
2. Jaklevic, R. C.; Lambe, J. *Phys. Rev. Lett.* **1966,** *17,* 1139–1140. doi:10.1103/PhysRevLett.17.1139
3. Ho, W. *J. Chem. Phys.* **2002,** *117,* 11033. doi:10.1063/1.1521153
4. Ulusoy, I. S.; Scribano, Y.; Benoit, D. M.; Tschetschetkin, A.; Maurer, N.; Koslowski, B.; Ziemann, P. *Phys. Chem. Chem. Phys.* **2011,** *13,* 612–618. doi:10.1039/C0CP01289K
5. Kučera, J.; Gross, A. *Langmuir* **2008,** *24,* 13985–13992. doi:10.1021/la802368j
6. Wilson, J. E. B.; Decius, J. C.; Cross, P. C. *Molecular Vibrations;* Dover Publications: New York, 1980.
7. Gaigeot, M.-P. *Phys. Chem. Chem. Phys.* **2010,** *12,* 3336–3359. doi:10.1039/B924048A
8. Rabitz, H.; Aliş, Ö. F.; Shorter, J.; Shim, K. *Comput. Phys. Commun.* **1999,** *117,* 11–20. doi:10.1016/S0010-4655(98)00152-0
9. Rabitz, H.; Aliş, Ö. F. *J. Math. Chem.* **1999,** *25,* 197–233. doi:10.1023/A:1019188517934
10. Chaban, G. M.; Jung, J. O.; Gerber, R. B. *J. Chem. Phys.* **1999,** *111,* 1823. doi:10.1023/A:1019188517934
11. Benoit, D. M. *J. Chem. Phys.* **2004,** *120,* 562. doi:10.1063/1.1631817
12. Scribano, Y.; Lauvergnat, D. M.; Benoit, D. M. *J. Chem. Phys.* **2010,** *133,* 094103. doi:10.1063/1.3476468
13. Hrenar, T.; Werner, H.-J.; Rauhut, G. *Phys. Chem. Chem. Phys.* **2005,** *7,* 3123–3125. doi:10.1039/b508779a
14. Yagi, K.; Hirata, S.; Hirao, K. *Theor. Chem. Acc.* **2007,** *118,* 681–691. doi:10.1007/s00214-007-0363-x
15. Pople, J. A.; Segal, G. A. *J. Chem. Phys.* **1965,** *43,* S136. doi:10.1063/1.1701476
16. Pele, L.; Gerber, R. B. *J. Chem. Phys.* **2008,** *128,* 165105. doi:10.1063/1.2909558
17. Martson, C. C.; Balint-Kurti, G. G. *J. Chem. Phys.* **1989,** *91,* 3571. doi:10.1063/1.456888
18. Balint-Kurti, G. G.; Ward, C. L.; Marston, C. C. *Comput. Phys. Commun.* **1991,** *67,* 285. doi:10.1016/0010-4655(91)90023-E
19. Press, W. H.; Teukolsky, S. A.; Vetterling, W. T.; Flannery, B. P. *Numerical Recipes in C: The Art of Scientific Computing,* 2nd ed.; Cambridge University Press: New York, 1992.
20. Jung, J. O.; Gerber, R. B. *J. Chem. Phys.* **1996,** *105,* 10332. doi:10.1063/1.472960
21. Bounouar, M.; Scheurer, C. *Chem. Phys.* **2008,** *347,* 194–207. doi:10.1016/j.chemphys.2007.12.002
22. Schmidt, M. W.; Baldridge, K. K.; Boatz, J. A.; Elbert, S. T.; Gordon, M. S.; Jensen, J. H.; Koseki, S.; Matsunaga, N.; Nguyen, K. A.; Su, S.; Windus, T. L.; Dupuis, M.; Montgomery, J. J. A. *J. Comput. Chem.* **1993,** *14,* 1347–1363. doi:10.1002/jcc.540141112
23. Akima, H. *ACM T. Math. Software* **1996,** *22,* 357–361. doi:10.1145/232826.232854
24. Christiansen, O. J. *Chem. Phys.* **2003,** *119,* 5773. doi:10.1063/1.1601593
25. Christiansen, O. J. *Chem. Phys.* **2004,** *120,* 2149. doi:10.1063/1.1637579
26. Christiansen, O.; Luis, J. M. *Int. J. Quantum Chem.* **2005,** *104,* 667–680. doi:10.1002/qua.20615
27. Heislbetz, S.; Rauhut, G. *J. Chem. Phys.* **2010,** *132,* 124102. doi:10.1063/1.3364861
28. Cassam-Chenaï, P.; Liévin, J. *J. Comput. Chem.* **2006,** *27,* 627–640. doi:10.1002/jcc.20374
29. Cassam-Chenaï, P.; Scribano, Y.; Liévin, J. *Chem. Phys. Lett.* **2008,** *466,* 16–20. doi:10.1016/j.cplett.2008.10.025
30. Bowman, J. M. *J. Chem. Phys.* **1978,** *68,* 608. doi:10.1063/1.435782
31. Bowman, J. M.; Christoffel, K.; Tobin, F. *J. Phys. Chem.* **1979,** *83,* 905–912. doi:10.1021/j100471a005
32. Bowman, J. M. *Acc. Chem. Res.* **1986,** *19,* 202–208. doi:10.1021/ar00127a002
33. Norris, L. S.; Ratner, M. A.; Roitberg, A. E.; Gerber, R. B. *J. Chem. Phys.* **1996,** *105,* 11261. doi:10.1063/1.472922
34. Yagi, K.; Hirata, S.; Hirao, K. *Phys. Chem. Chem. Phys.* **2008,** *10,* 1781–1788. doi:10.1039/b719093j
35. Davidson, E. R. *J. Comput. Phys.* **1975,** *17,* 87–94. doi:10.1016/0021-9991(75)90065-0
36. Davidson, E. R. *Comput. Phys. Commun.* **1989,** *53,* 49–60. doi:10.1016/0010-4655(89)90147-1
37. Murray, C. W.; Racine, S. C.; Davidson, E. R. *J. Comput. Phys.* **1992,** *103,* 382–389. doi:10.1016/0021-9991(92)90409-R
38. Carter, S.; Bowman, J. M.; Handy, N. C. *Theor. Chem. Acc.* **1998,** *100,* 191–198. doi:10.1007/s002140050379
39. Benoit, D. M. *J. Chem. Phys.* **2006,** *125,* 244110. doi:10.1063/1.2423006
40. Scribano, Y.; Benoit, D. M. *J. Chem. Phys.* **2007,** *127,* 164118. doi:10.1063/1.2798104
41. Andrews, L.; Johnson, G. L.; Davis, S. R. *J. Phys. Chem.* **1985,** *89,* 1706–1709. doi:10.1021/j100255a034
42. Huber, K. P.; Herzberg, G. *Molecular Spectra and Molecular Structure IV. Constants of Diatomic Molecules;* Van Nostrand Reinhold: New York, 1979.

43. Pouchan, C.; Zaki, K. *J. Chem. Phys.* **1997,** *107,* 342. doi:10.1063/1.474395
44. Huron, B.; Malrieu, J. P.; Rancurel, P. *J. Chem. Phys.* **1973,** *58,* 5745. doi:10.1063/1.1679199
45. Brodersen, S.; Lolck, J.-E. *J. Mol. Spectrosc.* **1987,** *126,* 405–426. doi:10.1016/0022-2852(87)90246-3
46. Scribano, Y.; Benoit, D. M. *Chem. Phys. Lett.* **2008,** *458,* 384–387. doi:10.1016/j.cplett.2008.05.001
47. Head, J. D. *Int. J. Quantum Chem.* **1997,** *65,* 827–828. doi:10.1002/(SICI)1097-461X(1997)65:5<827::AID-QUA47>3.0.CO;2-U
48. Kresse, G.; Hafner, J. *Phys. Rev. B* **1993,** *47,* 558–561. doi:10.1103/PhysRevB.47.558
49. Kresse, G.; Joubert, D. *Phys. Rev. B* **1999,** *59,* 1758–1775. doi:10.1103/PhysRevB.59.1758
50. Perdew, J. P.; Burke, K.; Ernzerhof, M. *Phys. Rev. Lett.* **1996,** *77,* 3865–3868. doi:10.1103/PhysRevLett.77.3865
51. BwGRiD, member of the German D-Grid initiative, funded by the Ministry for Education and Research (Bundesministerium für Bildung und Forschung) and the Ministry for Science, Research and Arts Baden-Württemberg (Ministerium für Wissenschaft, Forschung und Kunst Baden-Württemberg). http://www.bw-grid.de
52. Keçeli, M.; Hirata, S.; Yagi, K. *J. Chem. Phys.* **2010,** *133,* 034110. doi:10.1063/1.3462238
53. Matsuura, T.; Nakajima, M.; Shimoyama, Y. *Jpn. J. Appl. Phys.* **2001,** *40,* 6945–6950. doi:10.1143/JJAP.40.6945
54. *CP2K,* version 2.0.0 (Development Version); 2007.
55. Rico, M.; Orza, J.; Morcillo, J. *Spectrochim. Acta* **1965,** *21,* 689–719. doi:10.1016/0371-1951(65)80026-1
56. Cohen, A. J.; Handy, N. C. *Chem. Phys. Lett.* **2000,** *316,* 160–166. doi:10.1016/S0009-2614(99)01273-7
57. Bak, B.; Christensen, D.; Hansen-Nygaard, L.; Rastrup-Andersen, J. *J. Mol. Spectrosc.* **1961,** *7,* 58–63. doi:10.1016/0022-2852(61)90341-1
58. Klots, T. D.; Chirico, R. D.; Steele, W. V. *Spectrochim. Acta, Part A* **1994,** *50,* 765–795. doi:10.1016/0584-8539(94)80014-6
59. Benoit, D. M. *J. Chem. Phys.* **2008,** *129,* 234304. doi:10.1063/1.3040427
60. Kurth, S.; Perdew, J. P.; Blaha, P. *Int. J. Quantum Chem.* **1999,** *75,* 889–909. doi:10.1002/(SICI)1097-461X(1999)75:4/5<889::AID-QUA54>3.0.CO;2-8
61. Nelder, J. A.; Mead, R. *The Computer Journal* **1965,** *7,* 308–313. doi:10.1093/comjnl/7.4.308
62. Lagarias, J. C.; Reeds, J. A.; Wright, M. H.; Wright, P. E. *SIAM J. Optim.* **1998,** *9,* 112–147. doi:10.1137/S1052623496303470
63. Murrell, J. N.; Mottram, R. *Mol. Phys.* **1990,** *69,* 571–585. doi:10.1080/00268979000100411
64. Wilson, N. T.; Johnston, R. L. *Eur. Phys. J. D* **2000,** *12,* 161–169. doi:10.1007/s100530070053
65. Sutton, A. P.; Chen, J. *Philos. Mag. Lett.* **1990,** *61,* 139–146. doi:10.1080/09500839008206493
66. Gupta, R. P. *Phys. Rev. B* **1981,** *23,* 6265–6270. doi:10.1103/PhysRevB.23.6265
67. Cleri, F.; Rosato, V. *Phys. Rev. B* **1993,** *48,* 22–33. doi:10.1103/PhysRevB.48.22
68. Ercolessi, F.; Parrinello, M.; Tosatti, E. *Philos. Mag. A* **1988,** *58,* 213–226. doi:10.1080/01418618808205184
69. Voter, A. F. Embedded atom method potentials for seven FCC metals: Ni, Pd, Pt, Cu, Ag, Au, and Al, 1993. Los Alamos technical report no. LA-UR 93-3901, Unclassified.
70. Voter, A. F.; Chen, S. P. *Mater. Res. Soc. Symp. Proc.* **1986,** *82,* 175. doi:10.1557/PROC-82-175
71. Voter, A. F. The embedded-atom method. In *Intermetallic compounds;* Westbrook, J. H.; Fleischer, R. L., Eds.; Wiley, 1994; Vol. 1. Chapter 4.
72. Vanderbilt, D. *Phys. Rev. B* **1990,** *41,* 7892–7895. doi:10.1103/PhysRevB.41.7892
73. *CPMD;* Copyright IBM Corp 1990–2008, Copyright MPI für Festkörperforschung Stuttgart,1997–2001, 2008.
74. Becke, A. D. *Phys. Rev. A* **1988,** *38,* 3098–3100. doi:10.1103/PhysRevA.38.3098
75. Perdew, J. P. *Phys. Rev. B* **1986,** *33,* 8822–8824. doi:10.1103/PhysRevB.33.8822
76. Lee, C.; Yang, W.; Parr, R. G. *Phys. Rev. B* **1988,** *37,* 785–789. doi:10.1103/PhysRevB.37.785
77. Perdew, J. P.; Zunger, A. *Phys. Rev. B* **1981,** *23,* 5048–5079. doi:10.1103/PhysRevB.23.5048
78. Olson, R. M.; Varganov, S.; Gordon, M. S.; Metiu, H.; Chretien, S.; Piecuch, P.; Kowalski, K.; Kucharski, S. A.; Musial, M. *J. Am. Chem. Soc.* **2005,** *127,* 1049–1052. doi:10.1021/ja040197l
79. Olson, R. M.; Gordon, M. S. *J. Chem. Phys.* **2007,** *126,* 214310. doi:10.1063/1.2743005
80. Hermann, A.; Krawczyk, R. P.; Lein, M.; Schwerdtfeger, P.; Hamilton, I. P.; Stewart, J. J. P. *Phys. Rev. A* **2007,** *76,* 013202. doi:10.1103/PhysRevA.76.013202
81. Li, X.-B.; Wang, H.-Y.; Yang, X.-D.; Zhu, Z.-H.; Tang, Y.-J. *J. Chem. Phys.* **2007,** *126,* 084505. doi:10.1063/1.2434779
82. Bravo-Pérez, G.; Garzón, I.; Novaro, O. *THEOCHEM* **1999,** *493,* 225–231. doi:10.1016/S0166-1280(99)00243-2
83. Bishea, G. A.; Morse, M. D. *J. Chem. Phys.* **1991,** *95,* 5646. doi:10.1063/1.461639
84. Bishea, G. A.; Morse, M. D. *J. Chem. Phys.* **1991,** *95,* 8779. doi:10.1063/1.461213
85. Perdew, J. P.; Chevary, J. A.; Vosko, S. H.; Jackson, K. A.; Pederson, M. R.; Singh, D. J.; Fiolhais, C. *Phys. Rev. B* **1992,** *46,* 6671–6687. doi:10.1103/PhysRevB.46.6671
86. Xiao, L.; Tollberg, B.; Hu, X.; Wang, L. *J. Chem. Phys.* **2006,** *124,* 114309. doi:10.1063/1.2179419

License and Terms

Beilstein Journal of Nanotechnology

Plasmonic nanostructures fabricated using nanosphere-lithography, soft-lithography and plasma etching

Manuel R. Gonçalves*[1], Taron Makaryan[1], Fabian Enderle[2], Stefan Wiedemann[2], Alfred Plettl[2], Othmar Marti[1] and Paul Ziemann[2]

Full Research Paper

Open Access

Address:
[1]Ulm University, Institute of Experimental Physics, Albert-Einstein-Allee 11, 89069 Ulm, Germany and [2]Ulm University, Institute of Solid State Physics, Albert-Einstein-Allee 11, 89069 Ulm, Germany

Email:
Manuel R. Gonçalves* - manuel.goncalves@uni-ulm.de

* Corresponding author

Keywords:
nanosphere-lithography; near-field enhancement; plasma etching; soft-lithography; surface plasmons

Beilstein J. Nanotechnol. **2011,** *2,* 448–458.
doi:10.3762/bjnano.2.49

Received: 19 April 2011
Accepted: 26 July 2011
Published: 16 August 2011

This article is part of the Thematic Series "Organic–inorganic nanosystems".

Guest Editor: P. Ziemann

Abstract

We present two routes for the fabrication of plasmonic structures based on nanosphere lithography templates. One route makes use of soft-lithography to obtain arrays of epoxy resin hemispheres, which, in a second step, can be coated by metal films. The second uses the hexagonal array of triangular structures, obtained by evaporation of a metal film on top of colloidal crystals, as a mask for reactive ion etching (RIE) of the substrate. In this way, the triangular patterns of the mask are transferred to the substrate through etched triangular pillars. Making an epoxy resin cast of the pillars, coated with metal films, allows us to invert the structure and obtain arrays of triangular holes within the metal. Both fabrication methods illustrate the preparation of large arrays of nanocavities within metal films at low cost.

Gold films of different thicknesses were evaporated on top of hemispherical structures of epoxy resin with different radii, and the reflectance and transmittance were measured for optical wavelengths. Experimental results show that the reflectivity of coated hemispheres is lower than that of coated polystyrene spheres of the same size, for certain wavelength bands. The spectral position of these bands correlates with the size of the hemispheres. In contrast, etched structures on quartz coated with gold films exhibit low reflectance and transmittance values for all wavelengths measured. Low transmittance and reflectance indicate high absorbance, which can be utilized in experiments requiring light confinement.

Introduction

Classical electromagnetic theories describing optical transmission through small apertures [1,2] do not take into account the role of surface plasmons on metal films. In contrast to the predictions of these theories, enhanced optical transmission (EOT) was found for arrays of holes in metal films [3]. The transmission enhancements were attributed to the surface plasmons excited in the array [4]. This discovery triggered extensive research on nanostructures that support surface plasmons, namely, nanocavities on metal films, arrays of interacting metal particles and gratings. The coupling between light and localized surface plasmons on metal nanostructures that have been favorably tailored leads to a variety of effects, such as optical resonances [5-10], near-field enhancements [11-14], enhanced scattering [15], enhanced transmission [3,4,16-24], and plasmonic whispering gallery modes [25-27]. Some of these effects have been explored in applications such as surface enhanced Raman spectroscopy (SERS) [28-31] and, more recently, in studies of fluorescence lifetime [32,33] and the enhancement of the Purcell rate [34] (achieved mainly by confinement of light in small mode volumes rather than by very large Q-values of the resonances).

The strong sensitivity of these effects to the shape and size of the structures means that we require good reproducibility in the fabrication technique and good knowledge of the optical properties. However, some applications demand structures of extended size. Thus, the optimization of fabrication methods is intimately linked with the optical function of the structures.

Current techniques for the fabrication of plasmonic cavities include electrochemical growth combined with nanosphere lithography [25,35], electron-beam lithography [36], etching techniques [37-40] and focused ion beam milling [41-43]. The techniques based on electron beam lithography and focused ion beam milling allow us to obtain structures of arbitrary shape and two-dimensional profile, but they are size limited and time consuming.

Applications outside of sensing are also envisaged. Plasmonic resonators can not only confine light but can also enhance scattering at their resonances. This effect has been exploited in solar cells, for example, enhanced scattering by arrays of silver nanoparticles permits a thickness reduction of Si solar cells without compromising the intrinsic energy conversion efficiency [44-46]. Applications of this kind require large area nanostructured surfaces. Thus only methods allowing large scale lithography/patterning are appropriate for this purpose. E-beam lithography and FIB based nanofabrication would be prohibitively expensive.

The most common fabrication technique using arrays of polystyrene (PS) or silica beads is based on the evaporation of metal films on top of the spheres. This technique is called nanosphere lithography and the patterns obtained on the substrate are often referred to as Fischer's projection patterns [47]. Nanosphere lithography can serve as a large scale fabrication method and the lattice constant of the resulting structures can be changed by adequate choice of the diameter of the beads [35,48]. The standard shape of the projected pattern is triangular, but etching techniques have been used to obtain other shapes [49].

EOT was investigated from polystyrene or silica spheres coated by metal films [50-53]. The interstices of the coated beads form an array of triangular holes on a corrugated surface. The details of the pattern projected on the substrate have no significant effect on the optical transmission according to calculations [51]. However, plasmonic structures fabricated by nanosphere lithography can also be used for other purposes.

Soft lithography [54] is an alternative technique for nano- and micro-fabrication involving the inverse replication of a mold with the aid of elastomeric polymers. It can be reliably scaled down to sizes of ~100 nm. Nanoimprint lithography [55,56] is another alternative technique in which a pattern is formed on top of a substrate by pressing a mold against a thin resist film, followed by reactive ion etching (RIE) of the patterned substrate. This allows patterning of reproducible structures up to a few tens of nanometers. However, instead of casting the resist for preparation of the mask for RIE, high ordered arrays of PS spheres can be used directly.

With this in mind, we propose two fabrication routes to obtain periodic structures comprising arrays of nanocavities in metal films. Both techniques are suitable for large scale fabrication. The optical properties of these structures can be exploited in applications requiring strong confinement of light.

Results and Discussion

The fabrication techniques comprise several steps, including preparation of colloidal crystal templates, metal evaporation and one or more casting steps. The most important steps for the fabrication of metal coated hemispheres are presented in Figure 1. The main steps in the etching of quartz substrates, patterned with hexagonal arrays of Cr triangular particles to obtain arrays of triangular mesas or triangular holes, are depicted in Figure 4.

The topography of the structures at different stages of fabrication was characterized by atomic force microscopy (AFM) (Figure 2, Figure 5 and Figure 7) and by SEM (Figure 6). The

optical measurements performed on coated hemispheres, polystyrene (PS) spheres and on coated arrays of pillars are discussed in the next two subsections.

Coated hemispheres

Figure 1 shows schematically the fabrication of hemispheres coated by a metal film. After the preparation of a PS 2D colloidal crystal and two casting steps, the resulting structures were metal coated by physical vapor deposition. In Figure 2, AFM images of coated beads and coated hemispheres are shown. For further details on the fabrication, see the Experimental section.

Reflectance and transmittance measurements on coated spheres and hemispheres of the same size permit a comparison of the resonances and their spectral positions. While in the case of coated spheres there are interstices serving as transmission holes, in the case of hemispheres there are no regularly spaced holes. Thus, on thin gold films only low transmission can be expected. However, the coated hemispheres can be seen as a two-dimensional grating with deep "valleys".

Significant differences were observed for the reflectance measured on comparing gold coated PS spheres to hemispheres, within the size range of 400 nm to 1100 nm (Figure 3). The array of spheres exhibited low reflectance bands corresponding to wavelengths of around 700 nm (for 400 nm diameter) and 800 nm (for 500 nm). In contrast, there were no such low reflectance bands for coated hemispheres. The low reflectance band between 400 nm and 500 nm wavelengths (on the 400 nm and 500 nm diameter coated spheres) broadens for spheres of large size. The first peak appearing at around 570 nm (for 900 nm spheres) was shifted to higher wavelengths with increasing sphere diameter.

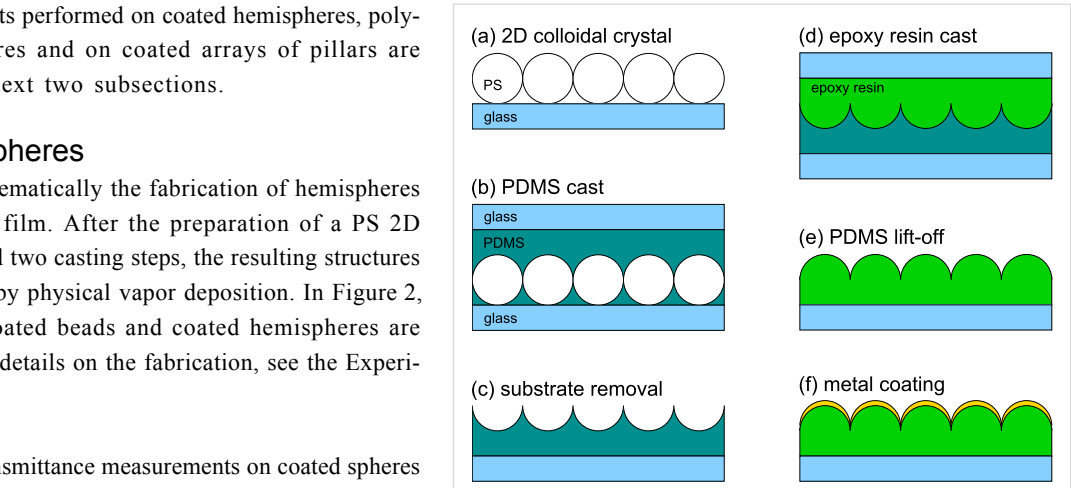

Figure 1: Fabrication of arrays of metal film coated hemispheres. Main steps: (a) Preparation of 2D colloidal crystal; (b) cast of polydimethylsiloxane (PDMS); (c) detachment of substrate; (d) cast with epoxy resin; (e) PDMS detachment and (f) metal coating by physical vapor deposition.

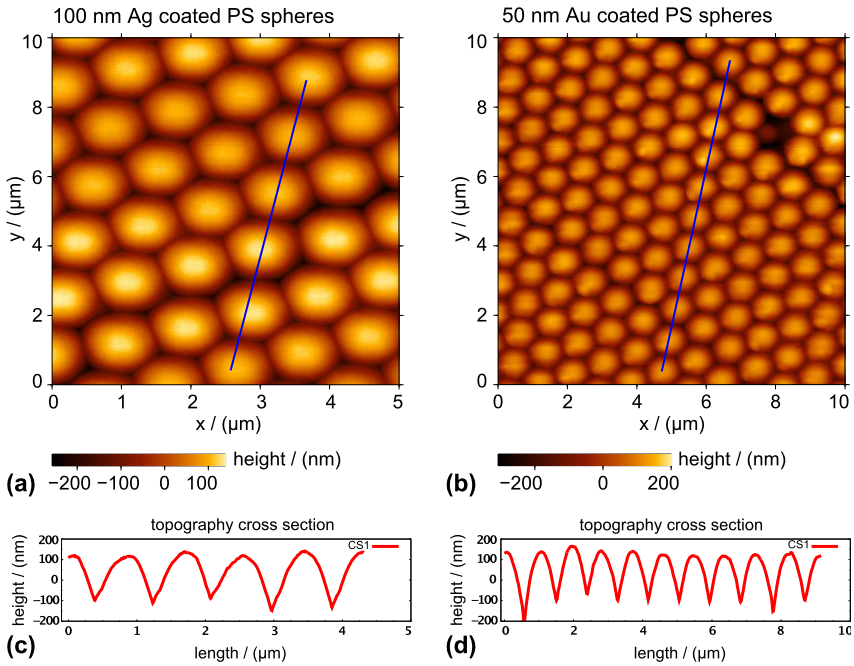

Figure 2: AFM topography images of coated beads (a) and coated hemispheres (b), both fabricated using PS spheres of 1 µm diameter. The plots of (c) and (d) are cross sections of lines marked in the topography images.

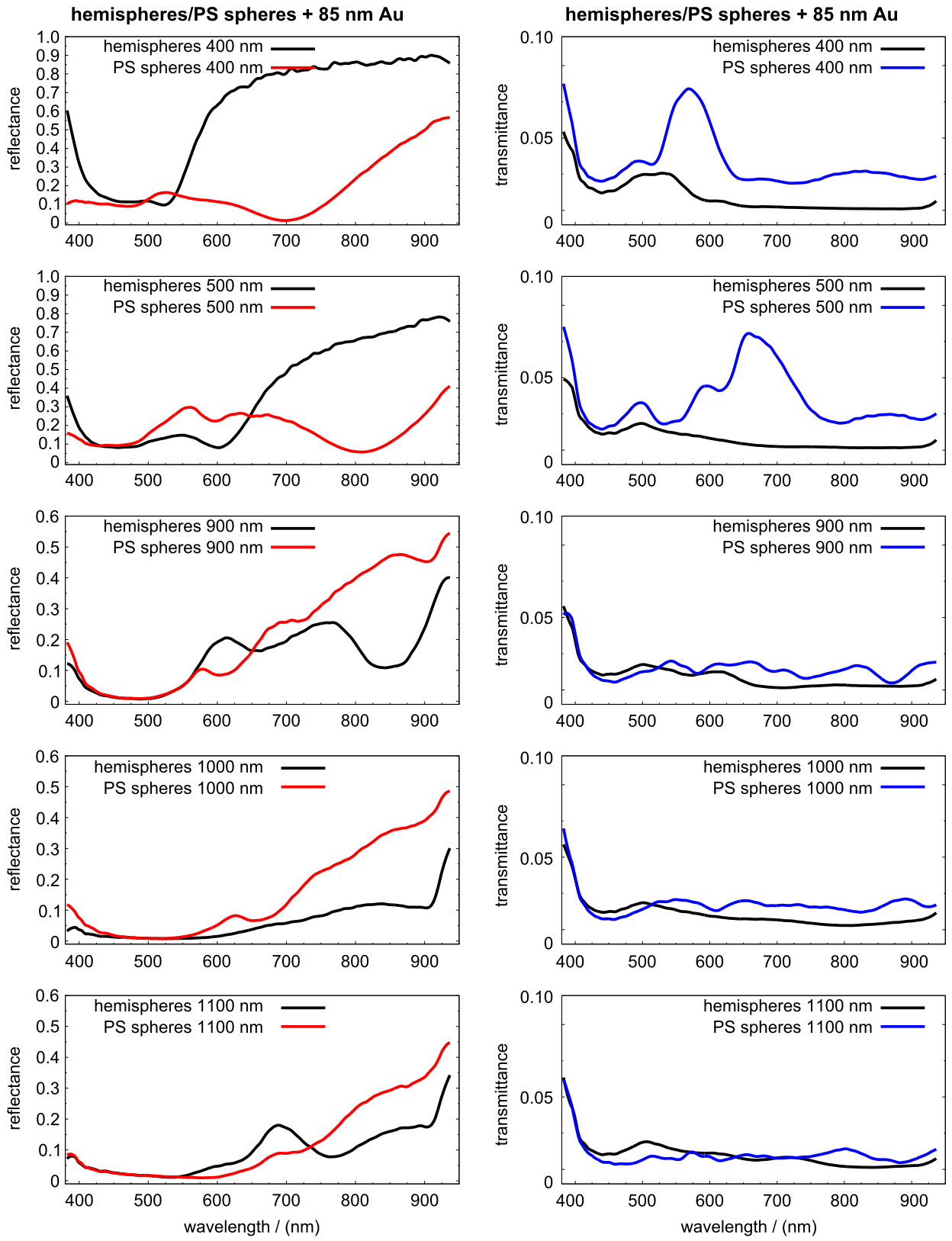

Figure 3: Reflectance (left) and transmittance (right) obtained at vertical illumination with an objective of *NA* = 0.25. The diameter of the PS spheres or hemispheres is indicated in the legend of each spectrum. The thickness of the gold film is approximately 85 nm.

Hemispheres of 400 nm diameter coated with 85 nm Au exhibited a lower reflectance than that of the coated spheres of around 525 nm diameter. This was more evident for 500 nm diameter hemispheres, where the band of low reflectance extended from 500 nm to 650 nm. Simultaneously, the transmittance of coated hemispheres, mainly those of 400 nm and 500 nm diameter, was clearly below that of the coated spheres. In contrast, the transmittance spectra of the coated spheres showed resonances at $\lambda \approx 570$ nm (for 400 nm spheres) and at $\lambda \approx 670$ nm (for 500 nm spheres).

Larger hemispheres (with diameters of 900 nm and 1100 nm) presented more complex optical spectra, with bands of both higher and lower reflectance compared to those of the spheres. The zeroth-order reflectance of 1100 nm hemispheres was, in general, lower than that of the spheres with the same diameter. The transmittance for the last three diameters was similar for both structures. However, the coated hemispheres generally transmitted less light than the coated spheres. Some of our transmittance results can be compared with the results from experiments performed with silver coated spheres of different sizes [51]. The transmission spectrum of PS spheres of 390 nm diameter, coated with 75 nm Ag, presented a similar spectral resonance to that of 400 nm spheres coated with 85 nm Au, but the peak was shifted to a lower wavelength. In general, samples of Ag coated spheres exhibited higher transmittance than Au coated ones. The position of the highest transmittance found in PS spheres of 400 nm and 500 nm was shifted to higher wavelengths. The highest transmittance for spheres of larger diameter (900 nm and above) is expected to be found at wavelengths above 1000 nm.

The low reflectance bands of Au coated hemispheres and their simultaneous low transmittance indicate a high absorbance, at least for 400 nm and 500 nm hemispheres. Under illumination at normal incidence no diffraction occurred for wavelengths smaller than the diameter of the hemispheres. An increase in diffraction intensity in some or all diffraction orders, at the expense of the zeroth-order reflectance, cannot be excluded for the three largest diameters. However, the shift to higher wavelengths of the low reflectance bands for the larger structures cannot be explained exclusively by diffraction effects. In particular, for the 900 nm hemispheres there is a band, around 600 nm, where the reflectance was larger than that for the sample with coated spheres. For the 1000 nm hemispheres the reflectance remained always below the corresponding value for the coated spheres.

According to some reports, both total absorption [57] and omnidirectional absorption [58] can occur on nanostructured metal surfaces at certain wavelengths. Indeed, we found spectral bands of very low reflectance and low transmittance for 400 nm and 500 nm diameter PS spheres coated with gold, at around $\lambda = 700$ nm and $\lambda = 800$ nm, respectively. Therefore in these bands the absorbance must be quite large.

Triangular mesas and holes

The main steps for the fabrication of arrays of quartz triangular mesas and arrays of triangular holes, obtained by epoxy resin cast, are presented in Figure 4. In order to produce the masks for reactive ion etching, a film of chromium was evaporated on top of the PS beads. The mask obtained was in the form of a hexagonal array of triangular structures. Measurements of the topography by atomic force microscopy (WITec Alpha 300 AFM in AC mode) typically gave larger thickness values than those given by the quartz crystal balance; Figure 5 shows an example of such a measurement. Some protrusions and isolated clusters seen in the AFM image are due to residual polymer material or other chemical species that were not completely removed by the cleaning process.

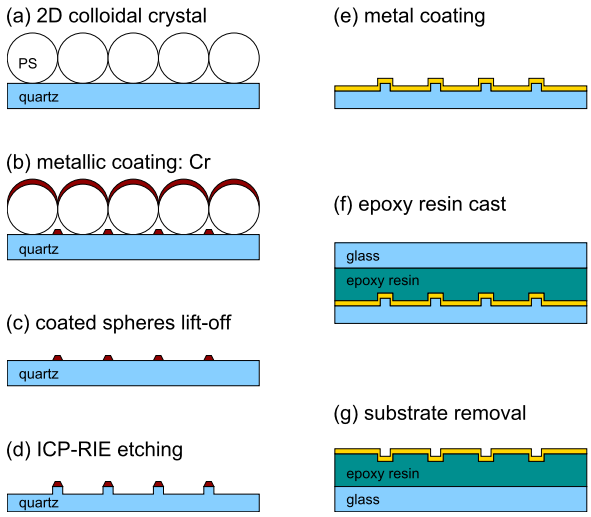

Figure 4: Fabrication steps for arrays of triangular mesas etched in quartz and arrays of holes in metal films, prepared by casting with epoxy resin: (a) Preparation of 2D colloidal crystal; (b) Cr coating; (c) PS spheres lift-off; (d) RIE; (e) metal coating (PVD) (f) epoxy resin cast; (g) substrate removal.

Scanning electron micrographs of samples of etched quartz, fabricated from Cr masks of 3 μm and 1 μm size, are presented in Figure 6. The left image shows triangular mesas replicating the shape of the Cr mask, and also some isolated pillars within the etched substrate area. The reason why the pillars were formed has not yet been determined, but it may be due to residual contaminants on the quartz surface. Deep etched structures (500 nm) exhibited rough side walls near the triangular Cr pattern (Figure 6a). Increasing the thickness of the Cr film

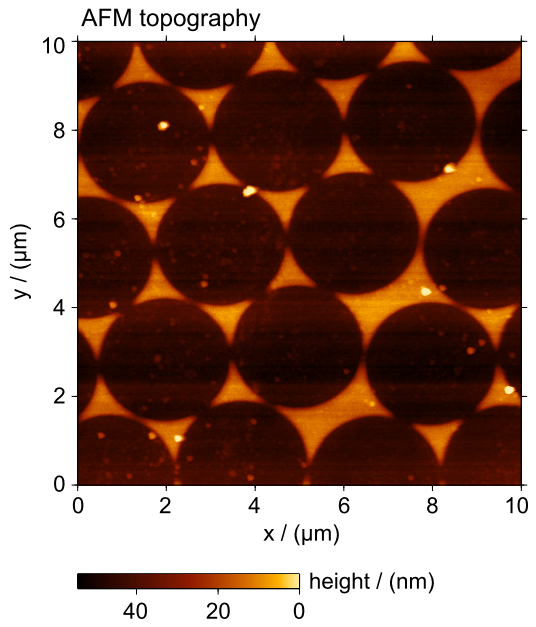

Figure 5: Topography image of a projection pattern of Cr on quartz. The height of the pattern is 30 nm. Small particles scattered on the surface are chemical species that were not completely removed during the spheres lift-off.

produced patterns that were not terminated by vertical sidewalls but instead with tails. Thus, the roughness can be explained by progressive erosion of the Cr tails during the RIE. On thinner Cr films (18 nm) the side walls of the etched pattern were smoother and more vertical (Figure 6b).

In order to avoid problems associated with the formation of the small isolated pillars within the otherwise flat area, an additional ion bombardment step had to be implemented. For this purpose, Ar^+ sputter cleaning (3.5 µA/cm^2, 3 kV, at a grazing angle of 10°) for typically 20 min proved to be suitable, as demonstrated in the right electron microscopy image of Figure 6. Compared to etched samples without this Ar^+ cleaning step, the amount of random pillars and roughness is strongly reduced.

Subsequently, the RIE the Cr masks were removed by wet etching. The surface of etched quartz is hydrophilic. This is not a limitation for the metal coating but does, however, impede the detachment of the casting polymers. Indeed, cured epoxy resin cast directly onto etched quartz could not be removed. One might expect that aliphatic silane molecules would bond covalently to silicon oxide, forming a hydrophobic surface. However, no significant change was observed after dipping the sample in silane solution, and epoxy resin cast on that sample could still not be detached. For the preparation of an anti-adhesive coating the same plasma etching system was used. By plasma polymerization of the process gas CHF_3, a fluorocarbon film was deposited on the previously prepared quartz substrate. This technique delivers layers of excellent conformity, and of very low surface energy, to the subjacent structure [59,60]. Furthermore, this coating technique works on most substrates, e.g., silicon, glass, metals, or any on passivation layer on the pillars. In all cases, the thickness of the anti-adhesive layers is in range of 5 nm to 10 nm. These additional layers allow detachment of the cured epoxy resin cast on top of etched quartz, or on top of metal films that then remain bound with the cast material. Figure 7 presents two AFM topography images of samples fabricated from 3 µm and 400 nm PS beads, respectively, with evaporation of 180 nm of Au and a cast of epoxy resin. The resulting structures have triangular holes within the gold films that were detached together with the epoxy resin. Even for the sample using 400 nm beads, where the average side of the triangular particles is of the order of 130 nm, deep triangular holes are obtained. The roughness at the edge of the triangles, caused by the pillar shaped defects previously mentioned, is still

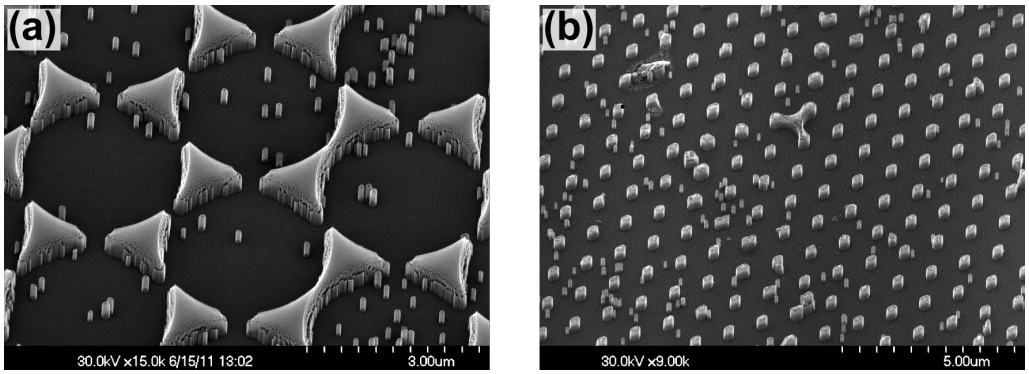

Figure 6: SEM micrographs of arrays of triangular mesas etched into the quartz substrate. Spheres of 3 µm diameter (a) and 1 µm (b) were used for the production of the Cr mask. The pattern of the etched mesas in the right image was obtained from a Cr deposition over a double layer of spheres. The depth of the quartz structures was (a) 500 nm and (b) 300 nm. The thickness of the Cr film of the mask was (a) 30 nm and (b) 18 nm.

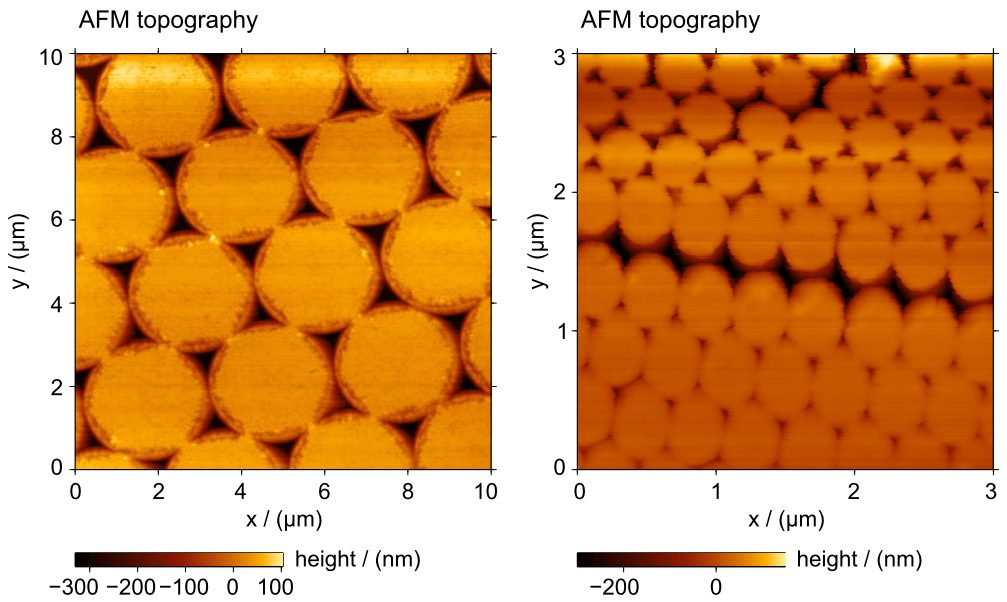

Figure 7: Arrays of triangular holes in 180 nm thick gold film. Monolayer colloidal crystals of 3 µm (left) and 400 nm (right) PS spheres were used as templates for the fabrication. The progressive degradation of quality in the topography of the right image is due to the reduction of the tip radius of the cantilever during scanning.

reflected in the topography of the gold film (Figure 7 left). Our preliminary results, in experiments employing colloidal crystals of PS beads, of 3 µm, 1 µm and 400 nm diameter, as templates for the etching masks, demonstrate that it is possible to tailor well-defined quartz mesas and deep triangular holes. Large scale fabrication is guaranteed by the size of the template. In Figure 7, AFM topography images of two of the samples after the detachment step are shown revealing sharp corners and edges of the holes within the gold film.

The roughness at the edges of the particles after the etching process, due to residual contaminants on the surface of the quartz, remains a problem. Preliminary sputtering with Ar^+ ions improved the quality of the samples, as demonstrated by SEM studies. The samples studied with AFM were not sputtered with Ar^+ ions. The high aspect ratio of some small defects (20 nm width and 500 nm height), found between the triangular mesas, indicates that it is possible to fabricate triangular cross-sectioned structures with a much higher aspect ratio. The gold evaporation was performed at a fixed angle, but full coating of the etched mesas is possible if the sample is rotated during the metal evaporation. By this way, shadows and hence pinholes in the metal film are less prone to occur.

Reflectance and transmittance spectra, of 115 nm Au films evaporated on top of structures etched on quartz, are presented in Figure 8. These films were not evaporated vertically but instead using a rotation stage with a rotation axis making an

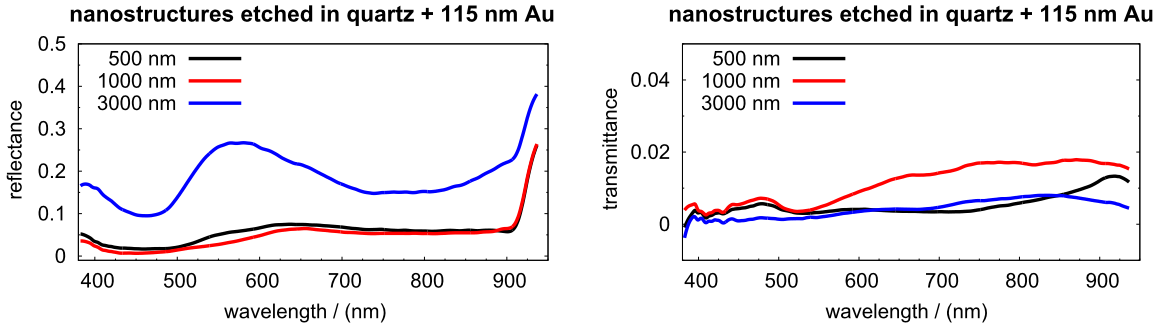

Figure 8: Reflectance (left) and transmittance (right) of triangular nanostructures etched in quartz and coated with 115 nm of gold. The diameter of the PS spheres used for the fabrication of the Cr masks is indicated in each spectrum.

angle of 15° to the vertical. The samples were rotated during the evaporation to avoid shadows at the etched structures. However, the rotation leads to a different thickness of the film on the top of the mesas compared to on their lateral walls.

Compared to hemispheres, fabricated from spheres of the same size, the gold films evaporated on the etched quartz exhibited low reflectance and very low transmittance. The reflectance decreased with increasing pattern diameter. For 500 nm patterns no diffraction is expected for $\lambda > 500$ nm. Therefore, most of the light was absorbed. Investigations of gratings and small cavities of various shapes have demonstrated strong light confinement [10,61-65]. Thus, etched structures with sharp edges, coated by gold films are suitable to confine light. The confinement efficiency and the plasmonic mode dispersion, leading to the highest near-field enhancements, need to be investigated in more depth.

Conclusion

Two novel methods of fabrication of plasmonic structures were introduced, based on nanosphere lithography, combining soft lithography and reactive ion etching techniques. The first permits the preparation of large arrays of hemispheres, using PS beads as templates. The second allows either the fabrication of high aspect ratio triangular mesas or, alternatively, arrays of deep holes obtained by making a polymer cast of the protrusions. The fabrication of arrays of hemispheres is relatively simple and lends itself to large scale fabrication (up to several cm^2). PS spheres of micrometer size down to a few hundreds of nanometers can be used. However, mainly due to the low Young's modulus of PDMS used in the fabrication of the stamp, deformed hemispheres may occur for very small PS beads. The zeroth-order reflectance and transmittance of gold films evaporated onto the hemispheres was measured. The low reflectance bands found on coated hemispheres, when compared to coated PS spheres of the same size, indicate an enhanced absorbance, which may be due to light confinement effects. Films of other materials and heterogeneous metal–insulator–metal films, of great importance in plasmonics, may be prepared in the future as well. For a better understanding, however, simulations are necessary to elucidate how light confinement occurs at the "valleys" and for which specific wavelengths. Furthermore, additional experimental methods, such as scattering-SNOM and fluorescent lifetime imaging, could provide information about local field enhancements.

The second fabrication route, involving RIE of quartz, constitutes an alternative nanofabrication method for plasmonic structures based on arrays of quartz mesas and arrays of holes in metal films. In this case the experimental aim is the preparation of large nanostructures for light confinement and, eventually, enhanced optical transmission based applications. The first transmittance and reflectance measurements indicate a strong absorbance at optical wavelengths. Here, calculations of near-fields of the prepared structures are necessary to quantify the efficiency of light confinement for various geometries. Furthermore, angular resolved reflectance spectroscopy is required as a function of the angle of incidence to confirm directional effects.

Experimental

Two-dimensional colloidal crystals

Colloidal suspensions of polystyrene (PS) beads of different sizes, in water, were purchased from Thermo Scientific. Sizes of 400 nm, 500 nm, 900 nm, 1000 nm, 1100 nm and 3 μm diameter were used. The suspensions conform the NIST Standards and have sharp size distributions of 1.0% to 2.5%. According to the supplier some proprietary surfactants may be added to the suspension. Volumes of 1 mL were centrifuged until full sedimentation of the beads was achieved. After removal of the liquid, the same volume of MilliQ water was added and the sediment beads resuspended. The process was repeated three times in order to remove surfactants of the suspension, which prevent the aggregation of the beads, but limit the quality and size of the two-dimensional colloidal crystals. Glass cover slides of 20×20 mm^2 and quartz glass of the same size, but of 1 mm thickness (used for the fabrication of samples etched by RIE) were used as substrates. Each substrate was cleaned by sonication in methyl ethyl ketone (MEK) and isopropanol, and dried by nitrogen jet. The surfaces of the samples were submitted to an air plasma at primary vacuum for 10 s, in order to improve the wetting properties of the surface. Suspension volumes of 15 to 55 μL, depending on the size of the beads, were put on top of substrates and the samples were put inside an acrylic glass container of 1.25 cm^3 volume. The cold sides of two Peltier elements were attached to the upper and lower sides of the sample container. By applying adequate currents the rate of evaporation was reduced and the crystallization of the beads occurred, mostly forming monolayers with areal extents up to 1 cm^2. The number of vacancies and dislocations of the colloidal crystal increased as the size of the beads decreased. For beads of 3 μm size, single crystals of several mm^2 were usually obtained. The evaporation of the water and full crystallization takes up to 6 h.

Epoxy resin hemispheres

Polydimethylsiloxane (PDMS) from Dow Chemical was prepared using the elastomer and curing agent in a ratio of 10:1. The two components were mixed and air bubbles were removed by submitting the liquid to primary vacuum for 15 min. The cast of polymer beads was achieved by filling a cylindrical ring on

top of the two-dimensional colloidal crystal. This limited the flow of the PDMS to the wall of the ring. The epoxy resin was cured in an oven at 35 °C for 24 h. The substrate with beads was then detached from the PDMS stamp. PS beads remaining in the PDMS were dissolved by sonication in MEK. The second cast process with epoxy resin was performed on top of the PDMS stamp (Figure 1d). Commercial epoxy resin of high transparency was used. Air bubbles were removed in vacuum, as for PDMS. A small droplet of the liquid was put on top of the PDMS and covered by a glass cover slide. The curing took 12 h at 20 °C. Afterwards the cover slide was detached from the PDMS stamp. The topography of the epoxy resin surface was a replica of the original colloidal array. Between the hemispheres there were "valleys" of approximately one beads radius in depth (Figure 1e).

Nanostructures etched on quartz

The masks for the patterns to be etched on quartz by RIE were fabricated by nanosphere lithography and evaporation of Cr films of 5 to 15 nm thickness. The Cr coated spheres were removed by three sonications in MEK, and rinsing in MilliQ water and isopropanol. This cleaning is crucial, as chemical species adsorbed on the surface influence the anisotropic etching of quartz (Figure 5). The anisotropic RIE (using ICP-RIE Oxford Plasmanlab 80 Plus) process was applied to transfer the Cr pattern onto the quartz substrate [39,40]. The etching process uses a side wall passivation similar to the Bosch process [38], but works with a mixture of CHF_3 and CF_4 in a ratio of 10:1, at a working pressure of 10 mTorr. The DC bias of the etcher was set to −96 V during the process, resulting in an etching rate of approximately 4 nm/min. The same plasma etching system was used for coating of etched quartz with the anti-ahesive film. The Cr masks were removed with a commercial etching solution (Chrome Etch 1 from SOTRAMCHEM Technic, France).

Metal coating

Gold films were deposited by physical vapor deposition (PVD), from tungsten boats, at a rate of 1 to 2 Å/s under a vacuum of 10^{-6} to 10^{-5} mbar. The thickness of the film and the evaporation rate was monitored using a quartz crystal balance. The evaporation was performed with the sample holder vertically opposite the boat. This minimizes the risk of shadows on the hemispheres. However, the thickness of the film between the hemispheres was thinner than that on top due to the smaller projected area (Figure 1f). Films thicker than 50 nm were deposited in two or more evaporations. In each evaporation, the samples were rotated by 180° to avoid shadows. For example, Au films of 85 nm were evaporated in two steps: 50 nm + 35 nm. Films of 180 nm thickness were obtained in two steps: 80 nm + 100 nm. Figure 2 presents examples of PS coated spheres and hemispheres of the same diameter. The cast reproduced the topography of two-dimensional crystal very well. Distortions of the spherical shape only occurred for small spheres (400 nm).

Optical characterization

The zeroth-order reflectance and transmittance of Au coated samples of different sizes were investigated. A WITec AlphaSNOM microscope was used for illumination and collection of the reflected light from the sample. For the illumination of samples and light collection, objectives of low numerical aperture (Nikon 10×, $NA = 0.25$) were used. The aperture angle was 15°, which restricts the detection to the zeroth-order diffraction. The illumination light source was a halogen lamp (Ocean Optics) of spectral range between 400 nm and 1000 nm. The microscope has a hot-mirror in the optical path that reflects light of wavelengths above 950 nm. The reflected light was coupled into a monochromator (Acton Research SpectraPro 300i) using a multi-mode optical fiber and detected by a liquid nitrogen cooled CCD (Princeton Instruments). Integration times of 1 s with 10 accumulations were used for each spectrum. Spectra were normalized against the reference.

Acknowledgements

We thank M. Asbach and D. Han for assistance in sample preparation, and H.-D. Kerpes for technical assistance on the PVD system. This work was supported by the collaborative research center SFB-569 (Projects C10 and G2) of the German Science Foundation (DFG).

References

1. Bethe, H. A. *Phys. Rev.* **1944,** *66,* 163. doi:10.1103/PhysRev.66.163
2. Bouwkamp, C. J. *Rep. Prog. Phys.* **1954,** *17,* 35. doi:10.1088/0034-4885/17/1/302
3. Ebbesen, T. W.; Lezec, H. J.; Ghaemi, H. F.; Thio, T.; Wolff, P. A. *Nature* **1998,** *391,* 667. doi:10.1038/35570
4. Ghaemi, H. F.; Thio, T.; Grupp, D. E.; Ebbesen, T. W.; Lezec, H. J. *Phys. Rev. B* **1998,** *58,* 6779. doi:10.1103/PhysRevB.58.6779
5. Wood, R. W. *Philos. Mag. (1798–1977)* **1902,** 4–396.
6. Raether, H. In *Surface Plasmons on Smooth, Rough Surfaces, on Gratings;* Höhler, G., Ed.; Springer Tracts in Modern Physics, Vol. 111; Springer Verlag: Berlin, 1988.
7. Watts, R. A.; Preist, T. W.; Sambles, J. R. *Phys. Rev. Lett.* **1997,** *79,* 3978. doi:10.1103/PhysRevLett.79.3978
8. Kitson, S. C.; Barnes, W. L.; Sambles, J. R. *Phys. Rev. Lett.* **1996,** *77,* 2670. doi:10.1103/PhysRevLett.77.2670
9. Hooper, I. R.; Sambles, J. R. *Phys. Rev. B* **2003,** *67,* 235404. doi:10.1103/PhysRevB.67.235404
10. Chen, Z.; Hooper, I. R.; Sambles, J. R. *Phys. Rev. B* **2008,** *77,* 161405(R). doi:10.1103/PhysRevB.77.161405
11. Glass, N. E.; Maradudin, A. A.; Celli, V. *J. Opt. Soc. Am.* **1983,** *73,* 1240. doi:10.1364/JOSA.73.001240
12. García-Vidal, F. J.; Pendry, J. B. *Phys. Rev. Lett.* **1996,** *77,* 1163. doi:10.1103/PhysRevLett.77.1163

13. Sobnack, M. B.; Tan, W. C.; Wanstall, N. P.; Preist, T. W.; Sambles, J. R. *Phys. Rev. Lett.* **1998,** *80,* 5667. doi:10.1103/PhysRevLett.80.5667
14. Popov, E.; Nevière, M.; Wenger, J.; Lenne, P.-F.; Rigneault, H.; Chaumet, P.; Bonod, N.; Dintinger, J.; Ebbesen, T. *J. Opt. Soc. Am. A* **2006,** *23,* 2342. doi:10.1364/JOSAA.23.002342
15. García de Abajo, F. J. *Rev. Mod. Phys.* **2007,** *79,* 1267. doi:10.1103/RevModPhys.79.1267
16. Porto, J. A.; García-Vidal, F. J.; Pendry, J. B. *Phys. Rev. Lett.* **1999,** *83,* 2845. doi:10.1103/PhysRevLett.83.2845
17. Popov, E.; Nevière, M.; Enoch, S.; Reinisch, R. *Phys. Rev. B* **2000,** *62,* 16100. doi:10.1103/PhysRevB.62.16100
18. Martín-Moreno, L.; García-Vidal, F. J.; Lezec, H. J.; Pellerin, K. M.; Thio, T.; Pendry, J. B.; Ebbesen, T. W. *Phys. Rev. Lett.* **2001,** *86,* 1114. doi:10.1103/PhysRevLett.86.1114
19. Cao, Q.; Lalanne, P. *Phys. Rev. Lett.* **2002,** *88,* 057403. doi:10.1103/PhysRevLett.88.057403
20. Degiron, A.; Lezec, H. J.; Barnes, W. L.; Ebbesen, T. W. *Appl. Phys. Lett.* **2002,** *81,* 4327. doi:10.1063/1.1526162
21. van der Molen, K. L.; Segerink, F. B.; van Hulst, N. F.; Kuipers, L. *Appl. Phys. Lett.* **2004,** *85,* 4316. doi:10.1063/1.1815379
22. Klein Koerkamp, K. J.; Enoch, S.; Segerink, F. B.; van Hulst, N. F.; Kuipers, L. *Phys. Rev. Lett.* **2004,** *92,* 183901. doi:10.1103/PhysRevLett.92.183901
23. Garcia-Vidal, F. J.; Martin-Moreno, L.; Ebbesen, T. W.; Kuipers, L. *Rev. Mod. Phys.* **2010,** *82,* 729. doi:10.1103/RevModPhys.82.729
24. Rodrigo, S. G.; Mahboud, O.; Degiron, A.; Genet, C.; García-Vidal, F. J.; Martín-Moreno, L.; Ebbesen, T. W. *Opt. Express* **2010,** *18,* 23691. doi:10.1364/OE.18.023691
25. Coyle, S.; Netti, M. C.; Baumberg, J. J.; Ghanem, M. A.; Birkin, P. R.; Bartlett, P. N.; Whittaker, D. M. *Phys. Rev. Lett.* **2001,** *87,* 176801. doi:10.1103/PhysRevLett.87.176801
26. Cole, R. M.; Baumberg, J. J.; Garcia de Abajo, F. J.; Mahajan, S.; Abdelsalam, M.; Bartlett, P. N. *Nano Lett.* **2007,** *7,* 2094. doi:10.1021/nl0710506
27. Vesseur, E. J. R.; García de Abajo, F. J.; Polman, A. *Nano Lett.* **2009,** *9,* 3147. doi:10.1021/nl9012826
28. Fleischmann, M.; Hendra, P.; McQuillan, A. *Chem. Phys. Lett.* **1974,** *26,* 163. doi:10.1016/0009-2614(74)85388-1
29. Moskovits, M. *Rev. Mod. Phys.* **1985,** *57,* 783. doi:10.1103/RevModPhys.57.783
30. Baumberg, J. J.; Kelf, T. A.; Sugawara, Y.; Cintra, S.; Abdelsalam, M. E.; Bartlett, P. N.; Russell, A. E. *Nano Lett.* **2005,** *5,* 2262. doi:10.1021/nl051618f
31. Maier, S. A. *Opt. Express* **2006,** *14,* 1957. doi:10.1364/OE.14.001957
32. Rigneault, H.; Capoulade, J.; Dintinger, J.; Wenger, J.; Bonod, N.; Popov, E.; Ebbesen, T. W.; Lenne, P.-F. *Phys. Rev. Lett.* **2005,** *95,* 117401. doi:10.1103/PhysRevLett.95.117401
33. Bär, S.; Chizhik, A.; Gutbrod, R.; Schleifenbaum, F.; Chizhik, A.; Meixner, A. J. *Anal. Bioanal. Chem.* **2010,** *396,* 3. doi:10.1007/s00216-009-3227-5
34. Vesseur, E. J. R.; García de Abajo, F. J.; Polman, A. *Phys. Rev. B* **2010,** *82,* 165419. doi:10.1103/PhysRevB.82.165419
35. Hulteen, J. C.; Treichel, D. A.; Smith, M. T.; Duval, M. L.; Jensen, T. R.; Duyne, R. P. V. *J. Phys. Chem. B* **1999,** *103,* 3854. doi:10.1021/jp9904771
36. Ditlbacher, H.; Krenn, J. R.; Schider, G.; Leitner, A.; Aussenegg, F. R. *Appl. Phys. Lett.* **2002,** *81,* 1762. doi:10.1063/1.1506018
37. Matthias, S.; Müller, F.; Jamois, C.; Wehrspohn, R. B.; Gösele, U. *Adv. Mater. (Weinheim, Ger.)* **2004,** *16,* 2166. doi:10.1002/adma.200400436
38. Laerme, F.; Schilp, A.; Funk, K.; Offenberg, M. Bosch deep silicon etching: improving uniformity and etch rate for advanced MEMS applications. *Twelfth IEEE International Conference on Micro Electro Mechanical Systems;* IEEE Publishing: New York, 1999; pp 211–216.
39. Brieger, S.; Dubbers, O.; Fricker, S.; Manzke, A.; Pfahler, C.; Plettl, A.; Ziemann, P. *Nanotechnology* **2006,** *17,* 4991. doi:10.1088/0957-4484/17/19/036
40. Manzke, A.; Pfahler, C.; Dubbers, O.; Plettl, A.; Ziemann, P.; Crespy, D.; Schreiber, E.; Ziener, U.; Landfester, K. *Adv. Mater. (Weinheim, Ger.)* **2007,** *19,* 1337. doi:10.1002/adma.200601945
41. Vasile, M. J.; Niu, Z.; Nassar, R.; Zhang, W.; Liu, S. *J. Vac. Sci. Technol., B: Microelectron. Nanometer Struct.–Process., Meas., Phenom.* **1997,** *15,* 2350. doi:10.1116/1.589644
42. Hofmann, C. E.; Vesseur, E. J. R.; Sweatlock, L. A.; Lezec, H. J.; de Abajo, F. J. G.; Polman, A.; Atwater, H. A. *Nano Lett.* **2007,** *7,* 3612. doi:10.1021/nl071789f
43. Nagpal, P.; Lindquist, N. C.; Oh, S.-H.; Norris, D. J. *Science* **2009,** *325,* 594. doi:10.1126/science.1174655
44. Ferry, V. E.; Verschuuren, M. A.; Li, H. B. T.; Schropp, R. E. I.; Atwater, H. A.; Polman, A. *Appl. Phys. Lett.* **2009,** *95,* 183503. doi:10.1063/1.3256187
45. Ferry, V. E.; Verschuuren, M. A.; Li, H. B. T.; Verhagen, E.; Walters, R. J.; Schropp, R. E. I.; Atwater, H. A.; Polman, A. *Opt. Express* **2010,** *18,* A237. doi:10.1364/OE.18.00A237
46. Atwater, H. A.; Polman, A. *Nat. Mater.* **2010,** *9,* 205. doi:10.1038/nmat2629
47. Fischer, U. C.; Zingsheim, H. P. *J. Vac. Sci. Technol. (N. Y., NY, U. S.)* **1981,** *19,* 881. doi:10.1116/1.571227
48. Haynes, C. L.; Duyne, R. P. V. *J. Phys. Chem. B* **2001,** *105,* 5599. doi:10.1021/jp010657m
49. Tan, B. J. Y.; Sow, C. H.; Koh, T. S.; Chin, K. C.; Wee, A. T. S.; Ong, C. K. *J. Phys. Chem. B* **2005,** *109,* 11100. doi:10.1021/jp045172n
50. Farcau, C.; Astilean, S. *J. Opt. A: Pure Appl. Opt.* **2007,** *9,* S345. doi:10.1088/1464-4258/9/9/S10
51. Landström, L.; Brodoceanu, D.; Bäuerle, D.; García-Vidal, F. J.; Rodrigo, S. G.; Martín-Moreno, L. *Opt. Express* **2009,** *17,* 761. doi:10.1364/OE.17.000761
52. Ding, B.; Pemble, M. E.; Korovin, A. V.; Peschel, U.; Romanov, S. G. *Phys. Rev. B* **2010,** *82,* 035119. doi:10.1103/PhysRevB.82.035119
53. Ding, B.; Pemble, M. E.; Korovin, A. V.; Peschel, U.; Romanov, S. G. *Appl. Phys. A* **2011,** *103,* 889. doi:10.1007/s00339-011-6251-1
54. Xia, Y.; Whitesides, G. M. *Angew. Chem., Int. Ed.* **1998,** *37,* 550. doi:10.1002/(SICI)1521-3773(19980316)37:5<550::AID-ANIE550>3.0.CO;2-G
55. Chou, S. Y.; Krauss, P. R.; Renstrom, P. J. *J. Vac. Sci. Technol., B: Microelectron. Nanometer Struct.–Process., Meas., Phenom.* **1996,** *14,* 4129. doi:10.1116/1.588605
56. Guo, L. J. *Adv. Mater. (Weinheim, Ger.)* **2007,** *19,* 495. doi:10.1002/adma.200600882
57. Popov, E.; Enoch, S.; Bonod, N. *Opt. Express* **2009,** *17,* 6770. doi:10.1364/OE.17.006770
58. Teperik, T. V.; García de Abajo, F. J.; Borisov, A. G.; Abdelsalam, M.; Bartlett, P. N.; Sugawara, Y.; Baumberg, J. J. *Nat. Photonics* **2008,** *2,* 299. doi:10.1038/nphoton.2008.76

59. Yanev, V.; Krischok, S.; Opitz, A.; Wurmus, H.; Schaefer, J.; Schwesinger, N.; Ahmed, S.-I.-U. *Surf. Sci.* **2004,** *566–568,* 1229. doi:10.1016/j.susc.2004.06.096
60. Yanev, V. Erzeugung, Charakterisierung und Strukturierung von Fluorcarbon-Plasmapolymeren für den Einsatz in der Mikrosystemtechnik. Ph.D. Thesis, Technische Universität Illmenau, 2004.
61. Miyazaki, H. T.; Kurokawa, Y. *Phys. Rev. Lett.* **2006,** *96,* 097401. doi:10.1103/PhysRevLett.96.097401
62. Miyazaki, H.; Kurokawa, Y. *IEEE J. Sel. Top. Quantum Electron.* **2008,** *14,* 1565. doi:10.1109/JSTQE.2008.931107
63. Perchec, J. L.; Quémerais, P.; Barbara, A.; Lopéz-Ríos, T. *Phys. Rev. Lett.* **2008,** *100,* 066408. doi:10.1103/PhysRevLett.100.066408
64. Kuttge, M.; García de Abajo, F. J.; Polman, A. *Opt. Express* **2009,** *17,* 10385. doi:10.1364/OE.17.010385
65. Huang, F. M.; Wilding, D.; Speed, J. D.; Russell, A. E.; Bartlett, P. N.; Baumberg, J. J. *Nano Lett.* **2011,** *11,* 1221. doi:10.1021/nl104214c

License and Terms

Beilstein Journal of Nanotechnology

Platinum nanoparticles from size adjusted functional colloidal particles generated by a seeded emulsion polymerization process

Nicolas Vogel[1], Ulrich Ziener[2], Achim Manzke[3], Alfred Plettl[3], Paul Ziemann[3], Johannes Biskupek[4], Clemens K. Weiss[1] and Katharina Landfester[*1]

Full Research Paper

Open Access

Address:
[1]Max Planck Institute for Polymer Research, Ackermannweg 10, 55128 Mainz, Germany, [2]Department of Organic Chemistry III, University of Ulm, Albert-Einstein-Allee 11, 89081 Ulm, Germany, [3]Department of Solid State Physics, University of Ulm, Albert-Einstein-Allee 11, 89081 Ulm, Germany and [4]Central Facility of Electron Microscopy, University of Ulm, Albert-Einstein-Allee 11, 89081 Ulm, Germany

Email:
Nicolas Vogel - vogel@mpip-mainz.mpg.de; Ulrich Ziener - ulrich.ziener@uni-ulm.de; Achim Manzke - achim.manzke@uni-ulm.de; Alfred Plettl - alfred.plettl@uni-ulm.de; Paul Ziemann - paul.ziemann@uni-ulm.de; Johannes Biskupek - johannes.biskupek@uni-ulm.de; Clemens K. Weiss - weiss@mpip-mainz.mpg.de; Katharina Landfester* - landfester@mpip-mainz.mpg.de

* Corresponding author

Keywords:
colloid lithography; functional colloids; miniemulsion polymerization; nanoparticles; seeded emulsion polymerization

Beilstein J. Nanotechnol. **2011,** *2,* 459–472.
doi:10.3762/bjnano.2.50

Received: 18 April 2011
Accepted: 30 July 2011
Published: 18 August 2011

This article is part of the Thematic Series "Organic–inorganic nanosystems".

Editor-in-Chief: T. Schimmel

Abstract

The benefits of miniemulsion and emulsion polymerization are combined in a seeded emulsion polymerization process with functional seed particles synthesized by miniemulsion polymerization. A systematic study on the influence of different reaction parameters on the reaction pathway is conducted, including variations of the amount of monomer fed, the ratio of initiator to monomer and the choice of surfactant and composition of the continuous phase. Critical parameters affecting the control of the reaction are determined. If carefully controlled, the seeded emulsion polymerization with functional seed particles yields monodisperse particles with adjustable size and functionalities. Size-adjusted platinum-acetylacetonate containing latex particles with identical seed particles and varied shell thicknesses are used to produce arrays of highly ordered platinum nanoparticles with different interparticle distances but identical particle sizes. For that, a self-assembled monolayer of functional colloids is prepared on a solid substrate and subsequently treated by oxygen plasma processing in order to remove the organic constituents. This step, however, leads to a saturated state of a residual mix of materials. In order to determine parameters influencing this saturation state, the type of surfactant,

the amount of precursor loading and the size of the colloids are varied. By short annealing at high temperatures platinum nanoparticles are generated from the saturated state particles. Typically, the present fabrication method delivers a maximum interparticle distance of about 260 nm for well-defined crystalline platinum nanoparticles limited by deformation processes due to softening of the organic material during the plasma applications.

Introduction

Uniform colloidal particles have attracted attention from various research fields for their ability to crystallize in highly symmetric arrangements. Two-dimensional crystals, commonly referred to as colloidal monolayers, are widely used for lithographic processes to create metal nanostructures in a cheap and highly parallel fashion [1]. As it is not a light-based process, the diffraction limit is conveniently circumvented and nanostructures with dimensions of only several tens of nanometers are created with remarkable ease. While the conventional process, leading to triangular shaped particle arrays, has long been established [2,3], research is focused on the creation of more sophisticated structures [4], including embedded objects [5,6], rings [7], discs [8] and crescent shaped particles [9,10].

While the majority of work on lithographic applications deals with plain colloidal particles, the incorporation of functionalities leads to different structural designs. In particular, the incorporation of metal complexes into polymer particles assembled into 2D crystals has recently been used as a non-conventional lithography approach to construct highly symmetrical arrays of metal nanoparticles (NPs) with dimensions of only several nanometers [11,12]. In contrast to conventional colloidal lithography, this approach employs the functional colloids as sacrificial carriers, rather than, e.g., being used as masks for metal evaporation. The size of the resulting metal NPs is determined by the quantity of complex in the precursor loaded colloids. Their adjustable size defines the interparticle distance of the NPs, and simultaneous loading with two metal complexes gives access to the fabrication of alloy NPs.

A number of different synthetic approaches for colloidal particles is known in literature, most prominently emulsion and miniemulsion polymerization. Although both yield polymeric colloidal particles, they differ both in reaction mechanism as well as in the properties of the resulting particles. Surfactant-free emulsion polymerization is a diffusion controlled process that is praised for excellent monodispersity and precise control of the particle size [13-15]. However, problems arise when the incorporation of functionalities (e.g., co-monomers, dyes, metal complexes) is required, as the different diffusion coefficients of monomer and functional molecule complicate the incorporation. Quantitative incorporation, for example, to create a precise stoichiometry of several different molecules within a latex particle, is thus impeded by emulsion polymerization [16].

Miniemulsion polymerization on the contrary is a powerful tool for the synthesis of highly functional polymeric nanoparticles [17-20]. Here, the monomer droplets are preformed by ultrasonication and critically stabilized against coagulation by the addition of surfactants. Ostwald ripening, the mechanism that leads to formation of bigger particles at the expense of smaller ones due to the higher Laplace pressure of the latter, is prevented by addition of a co-stabilizer. This component, highly insoluble in the continuous phase, creates an osmotic pressure in the droplets and, thus, acts as a counterforce to the Laplace pressure. Hence, no effective diffusion takes place during the polymerization, and functional molecules can be incorporated in defined amounts. The only requirement for the incorporation is a higher solubility of the functional molecule in the monomer droplets as compared to the continuous phase. As many different monomers can be used, and both direct (oil-in-water) and indirect (water-in-oil) processes are accessible, solubility is not a significant limitation for the majority of molecules. In recent years, the incorporation of functionalities into polymeric particles was thoroughly explored and includes fluorescent molecules [21], metal complexes [16], pigments [22], quantum dots [11] and magnetic particles [23].

In this article, we report on studies undertaken to determine process parameters for the creation of advanced colloidal monolayer architectures. A seeded emulsion polymerization process was applied and used to combine the benefits of both emulsion and miniemulsion polymerization. Using a miniemulsion polymerization process, functional seed particles were synthesized. Subsequent application of an emulsion-like polymerization in the presence of seed particles allowed the control of the size and polydispersity of such functional latex particles. Subsequently, these particles could then be crystallized into functional 2-D or 3-D colloidal crystals. As an application, we demonstrate, in subsection 2 of the Results and Discussion, the use of platinum containing spheres in an etching process leading to arrays of platinum NPs with controlled interparticle distances [11,12].

Results and Discussion

1 Adjustment of colloidal size by a seeded emulsion polymerization process

In order to combine the advantages of both miniemulsion- and emulsion polymerization to create monodisperse functional colloidal particles with precisely adjustable sizes, a seeded

emulsion polymerization process was adopted and the influence of principal reaction parameters on the resulting particles was investigated. Scheme 1 shows the mechanism of the seeded emulsion polymerization process. Latex particles loaded with platinum acetylacetonate as a model compound for a functional molecule, were prepared by a conventional miniemulsion polymerization process [24]. The reaction parameters are specified in the Experimental section. The process resulted in polystyrene latex particles with a size of 167 ± 14 nm and a platinum acetylacetonate load of 1 wt %. They were used as seed particles for the investigations that are presented in the following. A representative scanning electron microscopy (SEM) image of the particles is shown in Figure 1b (see below).

All seeded emulsion polymerization reactions were executed as follows. A dispersion of 0.1 wt % of seed particles with 0.01 wt % of sodium dodecylsulfate (SDS, relative to the amount of water used) was heated to 75 °C. Ammonium peroxodisulfate, (APS, $(NH_4)_2S_2O_8$), used as initiator, was dissolved in a small amount of ultra-pure water and added to the dispersion. Styrene, as monomer, was added to the solution using a syringe pump with a flow rate of 1 $mL \cdot h^{-1}$. The solution was stirred for 24 h at 80 °C under an argon atmosphere. After completion, the resulting particles were dialyzed in order to remove the unreacted initiator and monomer. Previously, it has been shown by inductively coupled plasma optical emission spectrometry (ICP-OES) that a seeded emulsion polymerization process does not change the amount of platinum acetylacetonate in the particle [24].

1.1 Polymerization mechanism and factors influencing secondary nucleation

For the detailed investigation of the influences of the different reaction parameters, it is essential to examine the reaction mechanism in detail. The focus of the present study lies in tuning the reaction in such a way as to avoid secondary nucleation. Secondary nucleated particles are colloids newly formed in the course of the reaction, similar to the formation of latex particles in a conventional emulsion polymerization [25,26]. Given that the seeded emulsion polymerization is applied to adjust the size of the final functional colloidal particles, secondary nucleation must be prevented in order to guarantee that all particles bear the desired functionality.

Scheme 1 gives a simplified picture of the processes involved. After injection, the monomer diffuses through the water phase to the hydrophobic seed particles, which thus represent a monomer rich area. The initiator thermally decomposes to form radicals in the water phase. These start to polymerize monomer molecules that are present in the aqueous phase, to form oligoradicals $IM_i\cdot$. Due to the ionic head group introduced by the persulfate radical, the oligoradicals remain water soluble until they reach a critical chain length $IM_j\cdot$, upon which they become insoluble in water [26,27]. For styrene, this length was found to

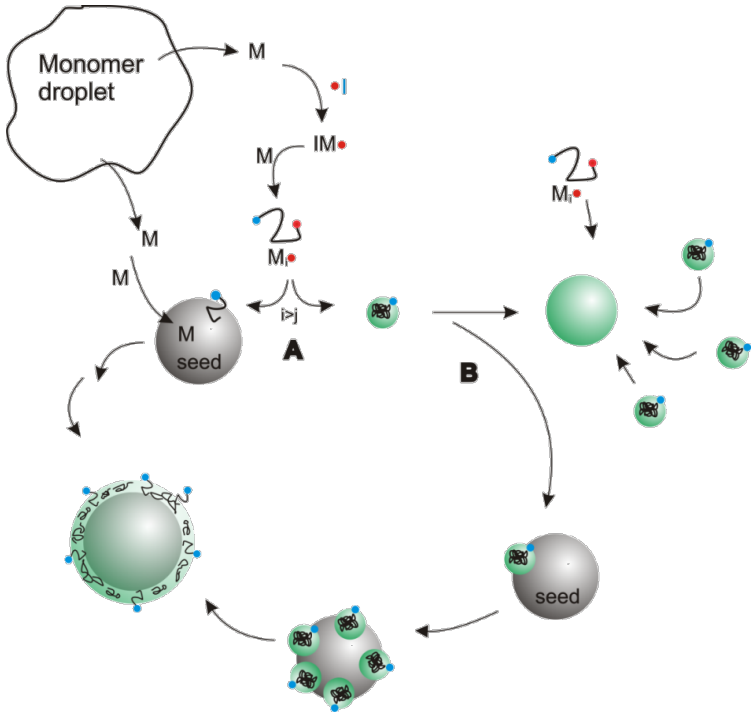

Scheme 1: Simplified model of a seeded emulsion polymerization process to clarify the desired reaction pathway.

be five monomer units [27,28]. The fate of the water soluble oligoradical and, thus, the development of the reaction, is determined by the question of whether or not it enters a seed particle before reaching the critical chain length. This point is marked as A in Scheme 1. Entering a seed particle gives the radical access to the monomer reservoir present in the particle, where it subsequently polymerizes, resulting in a size-increased seed particle (Scheme 1, left side). Assuming the oligoradical does not meet a seed particle before adding the last monomer unit necessary to exceed the critical chain length, the chain becomes insoluble in the water phase and forms a particle nucleus by a coil-to-globule transition (this pathway of the reaction is shown on the right side of the scheme) [25,27,29]. This particle nucleus itself is not stable as it features only one charge from the initiator. Stabilization can be achieved by two different pathways, marked with a B in Scheme 1. First, the particle nucleus can attach to a seed particle, where it will eventually be completely incorporated over the course of reaction due to more diffusion of monomers to the particle. In this case, no secondary particle will appear in the final dispersion [25,26]. On the other hand, several particle nuclei can cluster together to form a stable particle when the charge density on their surface becomes sufficiently high [25,27,29]. This particle, termed the secondary particle (shown in green color) now participates in the reaction as a new seed particle. In order to avoid secondary nucleation forming unwanted, plain particles without a metal precursor, the latter pathway needs to be avoided. Several factors influence the course of the reaction: Predominantly the seed concentration and the concentration of surfactant added to the reaction. Furthermore, the initiator concentration and the composition of the continuous phase important for determining the fate of the radicals as well as of the particle nuclei. Various studies have been published, especially on the role of seed particle concentration [30,31]. It was found that concentrations above 10^{14} particles per litre are sufficient to avoid the formation of particle nuclei [30]. Therefore, for all reactions performed, the seed particle concentration was fixed to 2.65×10^{14} particles per litre and the effect of the other reaction parameters was investigated.

Furthermore, in all cases styrene was added dropwise, very slowly at a rate of 1 $mL \cdot h^{-1}$. This ensured that the monomer was directly consumed once it appeared in the reaction mixtures ('monomer starved condition') [32] and no monomer reservoir was present that might steer the reaction pathway towards secondary nucleation in a classical emulsion polymerization way.

Seed particles containing platinum-acetylacetonate were used in all experiments in order to establish a procedure to tune, systematically, the size of the functional colloidal particles. Metal-complex containing polymer latexes are promising materials for a nonconventional lithography approach to produce ordered arrays of platinum nanoparticles [11]. Here, it is of particular importance that no secondary particles are generated, as otherwise, in the finally obtained array of Pt nanoparticles, some of them would be randomly missing, hence deteriorating the desired order.

1.2 Variation of the amount of monomer added

In a first set of experiments, the amount of monomer added was varied while all other parameters remained constant. These experiments were aimed at the investigation of the available size range for the seeded emulsion polymerization. The amount of monomer added is described as the normalized quantity *monomer excess* and describes the mass of styrene added relative to the total mass of seed particles ($m_{styrene}/m_{seed}$). Please note that the total amount of initiator was unchanged, leading to a constant initiator concentration in the water phase, but drastically changing the ratio of initiator to monomer added. Table 1 presents the reaction details, Figure 1 shows the dependency of the amount of monomer added on the resulting particle size.

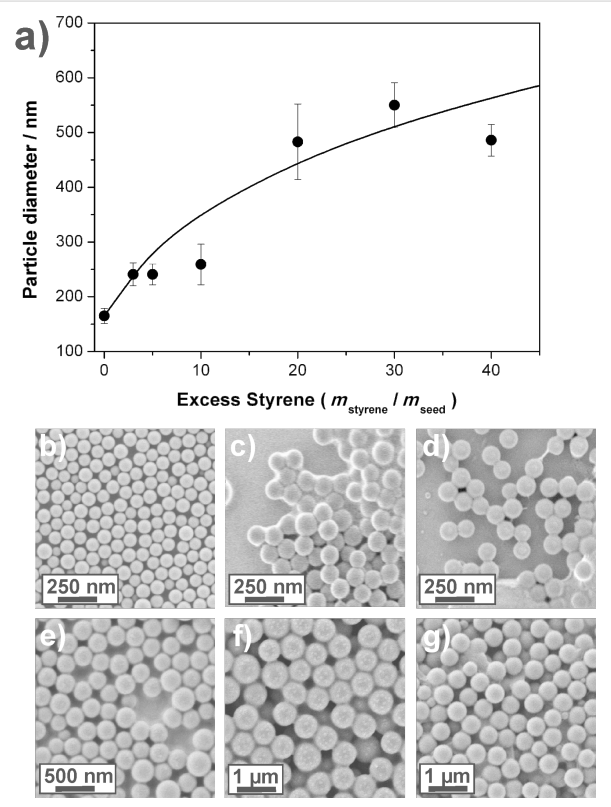

Figure 1: Variation of the amount of monomer added to control the resulting size in the seeded emulsion polymerization process. a) Styrene excess versus size of the resulting particles. The solid curve in the diagram indicates the theoretical expectation, assuming 100% conversion of the excess monomer added (diameter ~ $(excess)^{1/3}$).; b–g) SEM images of the resulting particles: b) seed particles as produced by a miniemulsion process; c) 3-fold excess of styrene; d) 5-fold excess; e) 10-fold excess; f) 30-fold excess; g) 40-fold excess.

Table 1: Reaction details for the set of experiments shown in Figure 1.

styrene added		H_2O	N_{seed} (wt %)	[I]	[I]/[M] ratio	[I]/[H_2O] ratio	SDS conc.	diameter SEM (theory)
$m_{styrene}/m_{seed}$	/mg	/g	/L^{-1}	/mg	/%	/%	/wt % of H_2O	/nm
3	150	50	2.65×10^{14} (0.1)	250	166.7	0.5	0.01 (5 mg)	241 ± 21 (238)
5	250	50	2.65×10^{14} (0.1)	250	100.0	0.5	0.01 (5 mg)	241 ± 19 (282)
10	500	50	2.65×10^{14} (0.1)	250	50.0	0.5	0.01 (5 mg)	255 ± 37 (355)
20	1000	50	2.65×10^{14} (0.1)	250	25.0	0.5	0.01 (5 mg)	483 ± 68 (448)
30	1500	50	2.65×10^{14} (0.1)	250	16.7	0.5	0.01 (5 mg)	550 ± 41 (513)
40	2000	50	2.65×10^{14} (0.1)	250	12.5	0.5	0.01 (5 mg)	488 ± 28[a] (564)
50	2500	50	2.65×10^{14} (0.1)	250	10.0	0.5	0.01 (5 mg)	multimodal (608)
100	5000	50	2.65×10^{14} (0.1)	250	5.0	0.5	0.01 (5 mg)	multimodal (766)

[a]appearance of secondary nucleated particles.

The solid curve in panel a) of Figure 1 indicates the theoretically expected size of the colloids assuming full conversion of the monomer in the seed particles, leading to the relation: Diameter ~ (excess)$^{1/3}$. The experimentally found colloidal diameters follow the relation reasonably well up to a monomer excess of approximately 30. For higher amounts (<50-fold excess) of monomer added, secondary particles appear leading to a reduction in size of the primary, seeded particles. Even higher monomer amounts (≥50-fold excess) lead to multimodal size distributions indicating uncontrolled reactions with secondary nucleation as the primary reaction pathway [30]. SEM images of the differently produced particles are shown in Figure 1b–g. Compared to the seed particles (Figure 1b), the size enhanced particles exhibit a higher homogeneity. From the present set of experiments one concludes that particles with diameters up to at least 500 nm can be synthesized in a single reaction, a number that relates to an almost 40-fold increase in volume. Larger diameters of seeded colloids could not be achieved as the present reaction pathway appears to break down with higher monomer excesses: Secondary nucleation or instable dispersions are the result.

As all reactions produced an increase of particle size, it can be stated that the initiator concentration in the aqueous phase was high enough to provide enough radicals for a successful polymerization. However, with the initiator concentration being constant in the aqueous phase, we face the unfavourable situation of having an enormous amount of initiator relative to the amount of monomer added for small monomer excesses. Hence, the degree of polymerization is low, and oligomers are formed that reside in the aqueous phase. These oligomers are seen in the SEM images in Figure 1c and Figure 1d as an undefined film covering the colloidal particles, appearing as bright seams. In the following section, the influence of the initiator concentration is discussed in more detail. In general, the molecular weight of the polymer is of minor importance for colloidal synthesis as long as the degree of polymerization is high enough to ensure that the polymeric chains will be found inside the particle.

1.3 Variation of the initiator to monomer ratio [I]/[M]

Next, the influence of the initiator concentration on the course of the reaction was investigated. In contrast to normal bulk polymerizations, not only is the amount of initiator relative to the monomer important, but also the concentration in the water phase has to be taken into account, as initiation and the first propagation steps take place in the continuous phase. Therefore, the amount of initiator needed is generally higher compared to bulk polymerizations. Figure 2 presents the effect of the initiator concentration on the resulting particle sizes for styrene excesses of 5 (Figure 2a) and 20 (Figure 2b), respectively. The parameters used for the reactions are summarized in Table 2. Dotted lines are inserted into the diagrams to indicate the original size of the seed particles as well as the maximum theoretical size. Both sets of reactions show that lower initiator amounts (1–5% relative to the monomer added) do not induce an increase in size, as the concentration of initiator in the water phase is insufficient to induce polymerization processes. For the optimum initiator concentration for the seeded reactions, as determined for 5-fold and 20-fold monomer excess, we estimate values between 10 and 25 wt % relative to the monomer. At higher quantities of initiator, the resulting particle sizes decrease (cf. Figure 2a) as a result of insufficient polymerization leading to oligomers that remain in the water phase, as seen by the films covering the particles in the SEM micrographs. As shown in previous experiments, the most suitable values for the initiator concentration are not exclusively determined by the amount of added monomer but also by the concentration of radicals in the water phase. Hence, it can be expected that for higher monomer excesses, smaller values for the initiator to monomer ratio will be sufficient to induce polymerization.

Table 2: Reaction details for the set of experiments shown in Figure 2.

styrene added		H_2O	N_{seed} (wt %)	[I]	[I]/[M] ratio	[I]/[H_2O] ratio	SDS conc.	diameter SEM (theory)
$m_{styrene}/m_{seed}$	/mg	/g	/L^{-1}	/mg	/%	/%	/wt % of H_2O	/nm
5	250	50	2.65×10^{14} (0.1)	2.5	1	0.005	0.01 (5 mg)	167 ± 13 (282)
5	250	50	2.65×10^{14} (0.1)	12.5	5	0.025	0.01 (5 mg)	169 ± 14 (282)
5	250	50	2.65×10^{14} (0.1)	25	10	0.05	0.01 (5 mg)	250 ± 14 (282)
5	250	50	2.65×10^{14} (0.1)	62.5	25	0.125	0.01 (5 mg)	261 ± 20 (282)
5	250	50	2.65×10^{14} (0.1)	250	100	0.5	0.01 (5 mg)	241 ± 19 (282)
20	1000	50	2.65×10^{14} (0.1)	10	1	0.02	0.01 (5 mg)	175 ± 16 (448)
20	1000	50	2.65×10^{14} (0.1)	50	5	0.1	0.01 (5 mg)	215 ± 18 (448)
20	1000	50	2.65×10^{14} (0.1)	100	10	0.2	0.01 (5 mg)	336 ± 24 (448)
20	1000	50	2.65×10^{14} (0.1)	250	25	0.5	0.01 (5 mg)	483 ± 68 (448)

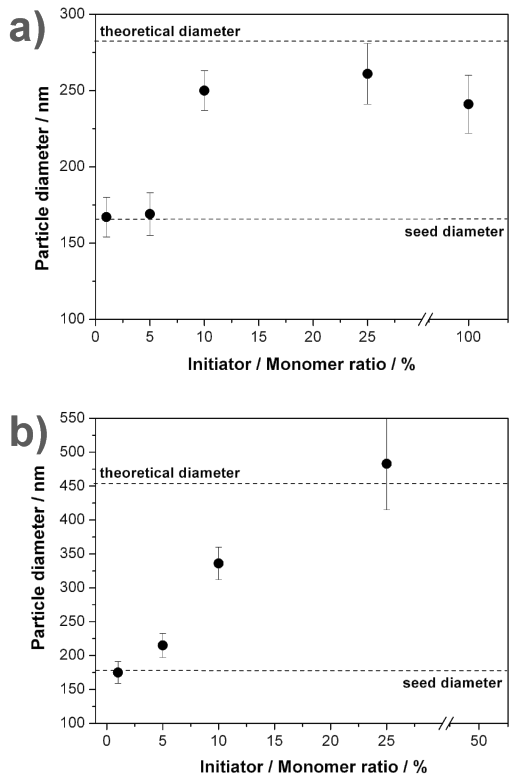

Figure 2: Variation of the amount of initiator relative to the amount of added monomer. The dotted lines are guides to the eye and represent the diameter of the seed particles used in the reaction as well as the theoretical diameter reached for 100% conversion of the additional monomer. a) Reactions with 5-fold excess of styrene with respect to the mass of seed particles. b) Reactions with 20-fold excess of styrene with respect to the mass of seed particles.

1.4 Variation of surfactant type and concentration

It is to be expected that the type and amount of surfactant added to stabilize the seeded particles should have a significant influence on the reaction pathway [33]. This becomes clear when considering that the surfactant not only stabilizes the growing seed particles but can also adsorb to and stabilize undesirable nucleated secondary particles. Thus, it is expected that the amount of surfactant should be minimized to that concentration necessary to yield a stable emulsion. Figure 3 and Table 3 present the experimental data for reactions performed with varying surfactant type and concentrations. As a test system, the reaction with a styrene excess of 100 was chosen as this led to multimodal size distributions in previous experiments (Figure 3a shows the result of the standard reaction). Obviously, the amount of SDS added in the standard recipe is insufficient to induce stable reaction conditions. Hence, the SDS concentra-

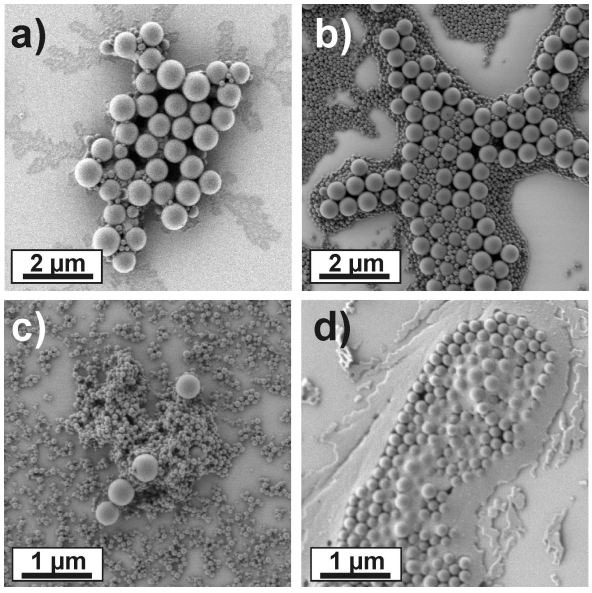

Figure 3: Effect of different concentrations and types of surfactants applied to stabilize the particles in the process. All concentrations given are relative to the weight of the water phase. a) 0.01 wt % SDS. b) 0.05 wt % SDS. c) 0.1 wt % SDS. d) 0.1 wt % Lutensol AT50.

Table 3: Reaction details for the set of experiments shown in Figure 3.

styrene added		H_2O	N_{seed} (wt %)	[I]	surfactant	surfactant conc.
$m_{styrene}/m_{seed}$	/mg	/g	/L^{-1}	/mg		/wt % of H_2O
100	250	50	2.65×10^{14} (0.1)	250	SDS	0.01 (5 mg)
100	250	50	2.65×10^{14} (0.1)	250	SDS	0.05 (25 mg)
100	250	50	2.65×10^{14} (0.1)	250	SDS	0.1 (50 mg)
100	250	50	2.65×10^{14} (0.1)	250	Lutensol AT50	0.1 (50 mg)

tion in the continuous phase was increased from 0.01 wt % up to 0.1 wt %. All SDS concentrations were below the critical value for micelle formation (cmc). Such concentrations are used in conventional emulsion polymerization and lead to particles nucleated in monomer swollen micelles [13]. Figure 3b and c show representative SEM micrographs of the resulting dispersions. For both cases, massive secondary nucleation took place, leading to bimodal size distributions. In the first case (0.05 wt % SDS), the size enhanced seed particles feature an excellent monodispersity and have a size of approximately 600 nm, indicating a more stable course of reaction. In contrast, higher amounts of SDS stabilize the particle nuclei more efficiently and induce massive secondary nucleation. With a SDS concentration of 0.1 wt %, almost all of the monomer added is converted into secondary particles, thus resembling a conventional emulsion polymerization. Only a minor fraction of size enhanced seed particles is found (Figure 3c). Changing the type of surfactant from the anionic SDS to the non-ionic Lutensol AT50 compromised the reaction stability. As depicted in Figure 3d, the reaction did not lead to a successful conversion of the monomer to size enhanced particles. Instead, the seed particles only marginally grew in size, and most of the monomer added was found as a polymeric film covering the complete surface. This is not surprising as non-ionic surfactants are known to stabilize colloids less efficiently than charged ones. Thus, significantly larger amounts of non-ionic surfactants are usually needed to stabilize droplets or particles.

Summarizing these experiments, it can be stated that the amount and type of surfactant crucially influences the reaction pathway. Surfactant has to be added in order to stabilize the growing particles. However, the concentration should be as small as possible. Otherwise, secondary nucleation becomes the primary reaction pathway. As a consequence, the direct conversion of small seed particles to very large ones, above approximately 600 nm, was impeded. From a technological point of view, seeded particles with larger particles have to be synthesized in a step-wise manner, using consecutive seeding reactions. The secondary particles appearing from the reaction with 0.05 wt % SDS could be also successfully removed by centrifugation.

1.5 Variation of continuous phase composition

The continuous phase has an important influence on the reaction pathway as well. The monomer added has to diffuse through the continuous phase in order to reach the seed particles. Polymerization initiation takes place in the continuous phase and its properties are important for both stabilization of seed particles and nucleation of secondary particles over the course of the reaction. Additionally, both diffusion and solubility of the monomer are affected drastically by compositional changes in the continuous phase. In order to investigate these effects, systematic variations of the continuous phase were performed. Figure 4 and Table 4 show the properties of the resulting dispersions and the reaction details, respectively.

First, sodium chloride was added to the continuous phase. The presence of salt affects the stability of colloidal particles as the extension of the electrical double layer of ionic surfactants present at the colloid interface is reduced by the counter ions of the salt. Naturally, this is undesirable for the seed particles. However, it may be that the stability of newly formed secondary particles is reduced as well. Assuming that a secondary particle is composed of a certain number of collapsed chains in order to be stable, the corresponding coagulation of such chains may be suppressed by the addition of small amounts of salt and, thus, the concentration of secondary particles may be strongly reduced without compromising the stability of the seed particles. The experimental data (Figure 4a) seem to support this idea. While very small amounts of sodium chloride (0.05 wt %) did not affect the polymerization, the addition of 0.1 wt % of NaCl induced an increase in final particle size almost to the theoretical value. NaCl concentrations beyond this value interfered with electrostatic stabilization and led to irregularly shaped particles and partial aggregation.

Next, ethanol was added to the continuous phase. In that case, the stability of the latex particles was not crucially affected as only a maximum of 20 wt % of ethanol was added. It was expected that ethanol addition would increase the solubility of styrene in the continuous phase. Moreover, the oligoradical

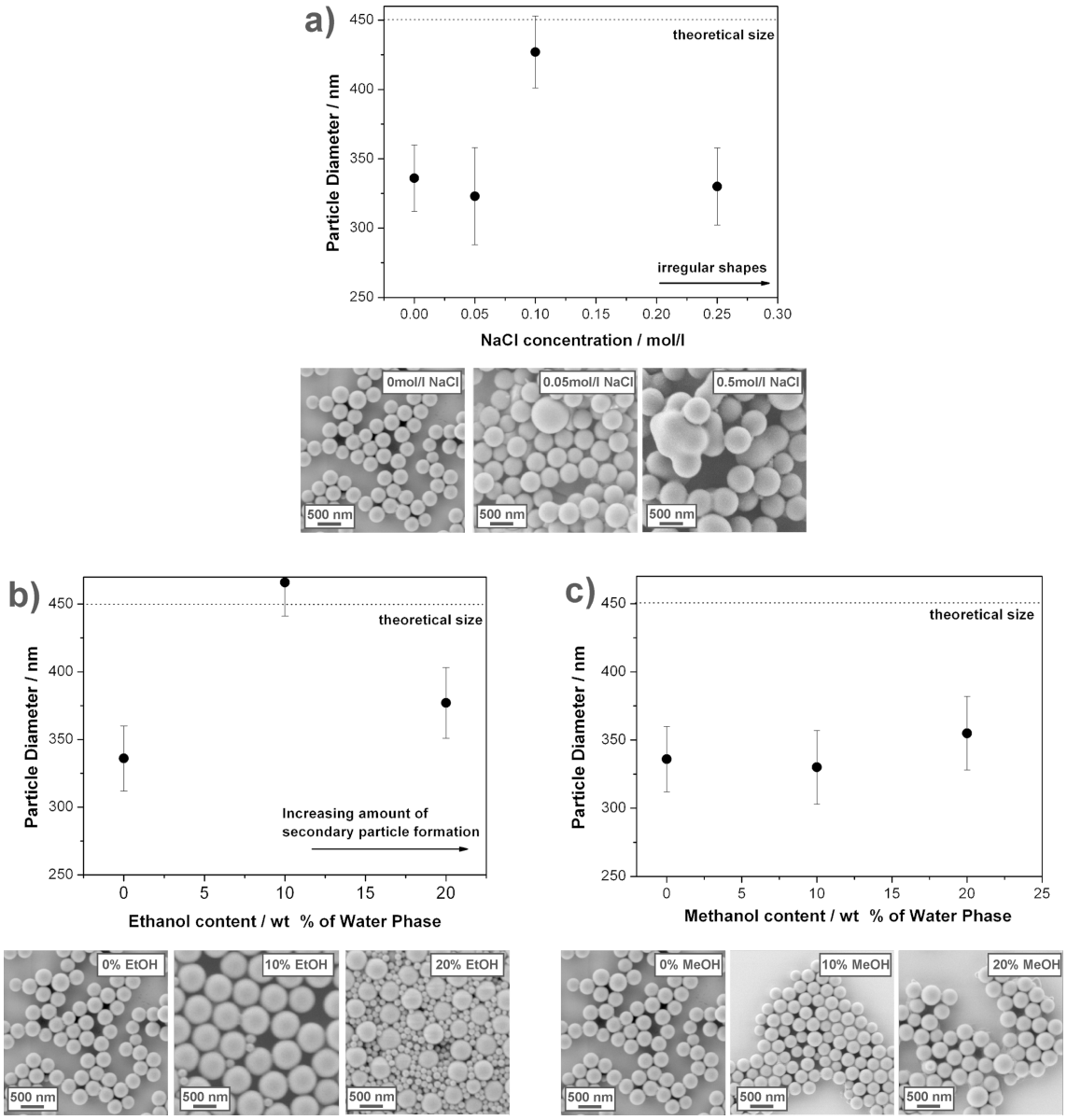

Figure 4: Effects of the composition of the continuous phase on the seeded polymerization reactions. The dotted lines in the diagrams represent the theoretical size of the colloids assuming full conversion of the added monomer. Representative SEM images are shown below the different diagrams. a) Addition of sodium chloride to the continuous water phase. b) Addition of ethanol to the water phase. c) Addition of methanol to the continuous water phase.

Table 4: Reaction details for the set of experiments shown in Figure 4.

styrene added		H_2O	N_{seed} (wt %)	[I]	SDS conc.	addition cont. phase	diameter SEM (theory)
$m_{styrene}/m_{seed}$	/mg	/g	/L^{-1}	/mg	/wt % of H_2O		/nm
20	1000	50	2.65×10^{14} (0.1)	100	0.01 (5 mg)	—	336 ± 24 (448)
20	1000	50	2.65×10^{14} (0.1)	100	0.01 (5 mg)	60 mg NaCl (0.05 mol·L^{-1})	323 ± 35(448)
20	1000	50	2.65×10^{14} (0.1)	100	0.01 (5 mg)	120 mg NaCl (0.1 mol·L^{-1})	427 ± 26 (448)
20	1000	50	2.65×10^{14} (0.1)	100	0.01 (5 mg)	300 mg NaCl (0.5 mol·L^{-1})	330 ± 28 (448)
20	1000	50	2.65×10^{14} (0.1)	100	0.01 (5 mg)	600 mg NaCl (0.5 mol·L^{-1})	irreg. shapes (448)

Table 4: Reaction details for the set of experiments shown in Figure 4. (continued)

20	1000	45	2.65×10^{14} (0.1)	100	0.01 (5 mg)	5 mg EtOH (10 wt %)	463 ± 25[a] (448)
20	1000	40	2.65×10^{14} (0.1)	100	0.01 (5 mg)	10 mg EtOH (20%)	377 ± 26[a] (448)
20	1000	45	2.65×10^{14} (0.1)	100	0.01 (5 mg)	5 mg MeOH (10%)	330 ± 27 (448)
20	1000	40	2.65×10^{14} (0.1)	100	0.01 (5 mg)	10 mg MeOH (20%)	355 ± 27 (448)

[a]secondary particle formation observed.

formed would have a different solubility in ethanol-containing water as well, leading to an increase of the critical chain length IM_j·.

The experimental results, shown in Figure 3b show the following characteristics. First, small amounts of ethanol (10 wt %) induce well-growing seed particles that feature a final size close to the theoretical expected value. A minor amount of secondary particles is visible. Increasing the ethanol content induces a drop in the final diameter close to the value measured for particles synthesized in pure water. Additionally, the amount of secondary particles drastically increases. It is worth mentioning that the particles from reactions with ethanol generally feature a higher monodispersity than the particles prepared in pure water.

Finally, methanol was added to the continuous phase as well (Figure 3c), however, no influence on the reaction was detected, even for a methanol content of 20 wt %. Furthermore, all obtained dispersions closely resembled each other with respect to final size and homogeneity. This may be attributed to the fact that methanol does not act as a solvent for polystyrene.

2 Generation of platinum nanoparticles

Colloidal spheres, as prepared by the above described seeding process, were applied for the fabrication of well-ordered Pt NPs of controlled size and interparticle distance on solid substrates. Since the starting size of the colloidal spheres determines the finally obtained interparticle distance of the Pt NPs, the presently introduced novel seeding procedure to tailor that size plays an essential role.

The starting situation and the final state of this fabrication process on a silicon wafer are demonstrated in Figure 5. After depositing a single layer of the precursor loaded colloids on top of Si substrates, their size is reduced by exposure to an isotropic oxygen plasma (see Experimental section). In this way, one arrives at a continuous and laterally homogeneous reduction of the particle diameters while the original particle positions are strictly preserved. The reduction rate of this etching process, imposed by the isotropic plasma, monotonically decreases and finally becomes zero. The corresponding saturation diameters are, however, much larger than what is implied for a pure Pt particle from the amount of metal present within a colloidal sphere. An additional subsequent short annealing in oxygen at 1100 °C (see Experimental section) and cooling down in nitrogen gas-flow is needed to finally obtain well-defined crystalline Pt NPs.

2.1 Oxygen plasma exposure: Dependency of the saturation state on different parameters

The plasma procedure was optimized and then performed by default according to the recipe described in the Experimental

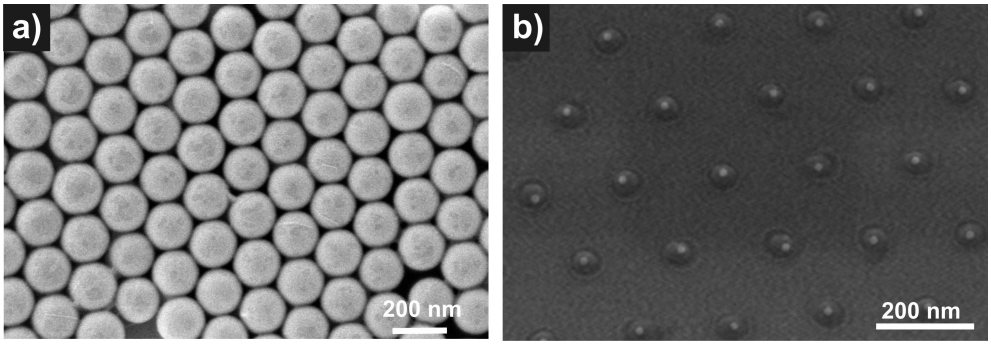

Figure 5: A non-conventional lithographic process is used to produce arrays of Pt NPs from platinum-acetylacetonate containing polymer particles on top of a Si wafer. a) Colloidal monolayer formed by drop casting of seeded colloid particles. b) Arrays of Pt NPs produced by plasma-assisted removal of the organic material and subsequent thermal annealing.

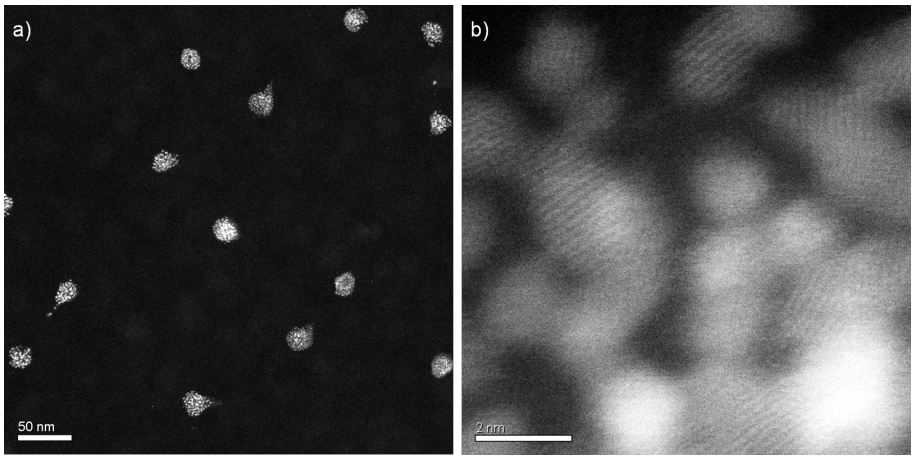

Figure 6: Pt-precursor loaded PS colloids on a Si_3N_4 membrane in the saturated state after exposure to isotropic oxygen plasma for 25 min. a) The diameters of the lumps average out to 35 nm. b) Magnified HRSTEM image of one of the particles demonstrates that they consist of an agglomeration of ca. 1–2 nm Pt-rich crystallites.

part. Varying the process parameters is possible within certain limits without influencing the results given below. In the saturated state as obtained by plasma etching, the small lumps forming the hexagonal arrangements always consist of independently nucleated small crystalline particles, which are still embedded in a residual matrix (see the high resolution scanning transmission electron microscope (HRSTEM) images in Figure 6). Some of the particles are not spherical, because they were tilted towards one side during plasma treatment [34]. As proven by X-ray photoelectron spectroscopy (XPS), the lumps always contain PtO_2. In this state also sodium and sulfur was detected when SDS was used as surfactant. Similar observations for Pt NPs produced from precursor-loaded colloids, prepared with emulsion or miniemulsion polymerization, have already been reported but were not investigated in detail at the time [11,12]. In order to determine the parameters influencing the saturation state, we varied the type of surfactant, the amount of precursor loading and the size of the colloids. The results are discussed in the subsequent sections.

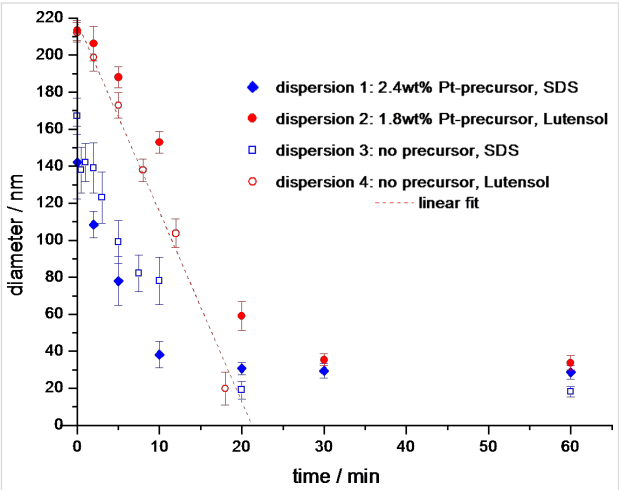

Figure 7: Diameter of Pt-precursor loaded or unloaded PS particles prepared with the surfactants SDS or Lutensol AT50 versus oxygen plasma exposure time. Only particles without Pt-precursor and synthesized with Lutensol AT50 can be removed without residues from the surface (dispersion 4). For all other particles the diameter monotonically decreases and finally approaches a saturation diameter (see also Figure 8).

2.1.1 Platinum precursor and surfactant

Based on the observation that the saturated state after etching contains tiny platinum oxide crystallites, it is reasonable to assume that the precursor-complex platinum acetylacetonate has an influence on the saturation. Therefore, colloids were investigated that were prepared by emulsion polymerization with or without the precursor complex, and with SDS or Lutensol AT50 as surfactant. In contrast to SDS, which contains sodium and sulfur, Lutensol AT50 only consists of carbon, oxygen and hydrogen, which are likely to be transformed into volatile products during plasma treatment. The according etching behaviour of the various cases is summarized in Figure 7.

First, the effect of the surfactant on the plasma assisted size reduction was investigated. For dispersion 1 and 3 the ionic surfactant SDS, and for dispersions 2 and 4 the non-ionic Lutensol AT50, were used. It turned out that for dispersions 1 to 3, containing either Pt precursor or SDS or both, oxygen plasma etching leads to a saturation of the particle diameter (Figure 8). In contrast, colloids of dispersion 4 which did not contain Pt precursor and were synthesized with Lutensol AT50, could be completely removed under identical etching conditions, as proved by HRSEM (Figure 7, linear fit). In summary, the Pt precursor within the colloids as well as the surfactant SDS inter-

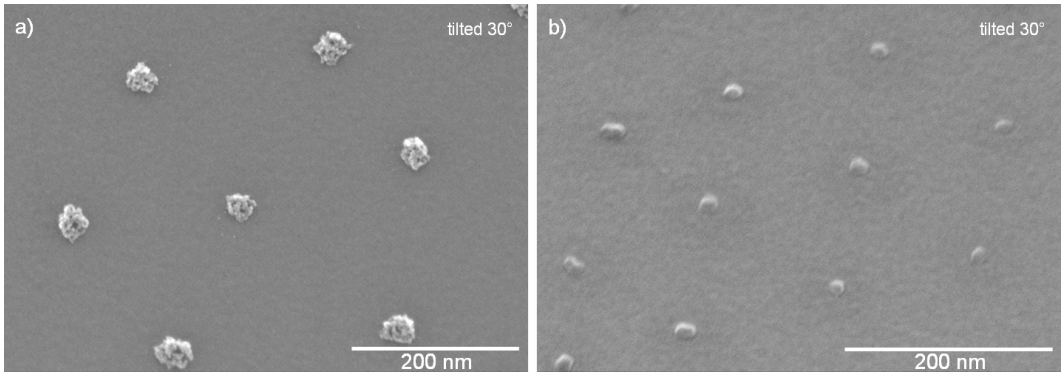

Figure 8: HRSEM images of particles in the saturated state after 60 min isotropic oxygen plasma treatment. a) Loaded with Pt-precursor and synthesized with the surfactant Lutensol AT50 and b) unloaded but synthesized by using SDS (dispersion 2 and 3 of Figure 7).

feres with the etching process and, thus, leads to the saturated state. As they are not present in dispersion 4, non-volatile components such as metals (Pt, Na) and/or sulfur were responsible for saturation. However, currently one cannot exclude further factors contributing to the appearance of the saturated state.

2.1.2 Amount of platinum precursor

In order to analyze the effect of Pt-precursor concentration within the colloids on the saturation diameter after oxygen plasma exposure, a set of three colloidal dispersions, synthesized by surfactant free emulsion polymerization (for details see [12]), were investigated. Here, the loading of the colloids with platinum acetylacetonate was varied from (1 wt %, to 2 wt % and 4 wt %) relative to the monomer while keeping all other parameters constant. After deposition of the initially 175 nm sized colloids onto Si substrates and reducing their size in oxygen plasma, diameters of 27 ± 2, 41 ± 3 and 45 ± 2 nm were found for the corresponding saturated states. Obviously, the total amount of Pt precursor strongly influences the saturation diameter: The higher the precursor content the larger the diameter of the saturated lumps. A simple model may account for this observation. Assuming a homogeneous distribution of Pt precursor within the initial colloids, isotropic etching will reduce the colloidal size by removing volatile species shell-by-shell, whereas the non-volatile constituents such as the Pt will remain on top of the residual particle, which, in this way, will be increasingly protected from further etching. Calculating the total amount of Pt originally present within a shell thickness defined by the difference of the initial radius of the colloid and its value in the saturated state after etching, one arrives at an equivalent Pt layer thickness of around 3 to 4 Å (Pt lattice parameter a_{Pt} = 3.92 Å).

A similar result was obtained for Pt-precursor loaded polymethylmethacrylate (PMMA) particles [35]. This suggests that the saturated etching state is obtained whenever the non-volatile Pt produced by the etching approximately forms a protective closed layer around the residual particle. However, the HRSTEM image of Figure 6 does not reveal such a closed film of Pt or PtO_2 around the lumps. Thus, a more sophisticated model including the role of the SDS component is needed. But the described "monolayer"-result at least delivers a useful empirical rule to predict the size of the saturated particles.

2.1.3 Size of the colloids

With the method of the miniemulsion polymerization described in subsection 1, seed particles of 165 ± 14 nm with a loading of 4 wt % Pt precursor (with respect to the monomer) were synthesized in a first step. Subsequently, the particles were enhanced in size by seeded emulsion polymerization, such that they all had identical loading but variable size. Exemplarily, here colloids with diameters of 256 ± 9, 423 ± 19 and 594 ± 48 nm were investigated in detail with respect to their post-etching saturation diameter. The corresponding diameters of the lumps after the plasma treatment were 40, 55 and 97 nm (for details of the size determination see the Experimental section).

It should be noted, however, that the shape of the resulting lumps differs drastically. For the smallest particles, a round, closed shape of the lumps was obtained after the plasma treatment (Figure 9a). The bigger particles exhibited a porous nonspherical shape, as illustrated in Figure 9b. This transition in shape is caused by softening of the colloidal particles during the plasma procedure and, as a consequence, spreading of particle material on the substrate [34]. This leads to a laterally extended lump which is too large to allow agglomeration into a single metal particle during the annealing process. In detail, elements such as sodium and sulfur are removed by annealing, and the platinum oxide is decomposed into platinum as revealed by XPS. Finally, the platinum agglomerates into one NP, sometimes still exhibiting a granular substructure. During the cool-

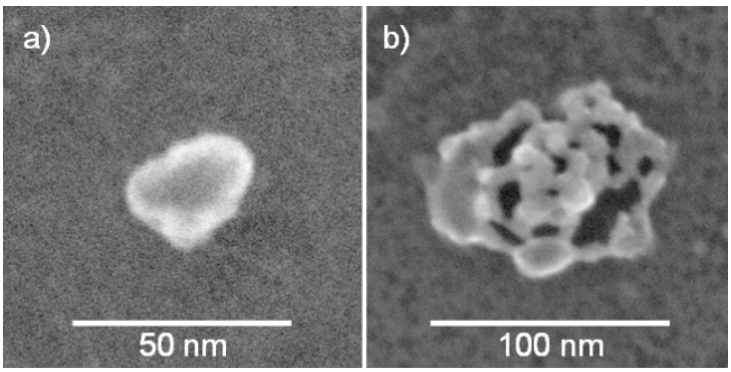

Figure 9: Saturated states after plasma etching: a) Closed surface of a seeded 256 nm particle and b) porous shape of a seeded 594 nm particle, both with a 165 nm precursor-filled core.

down process in nitrogen the Pt NPs remain stable in the metallic state. The experimental observation that exclusively colloids with initial diameters below 260 nm could be transformed into single NPs by annealing, whereas bigger colloids ended in the granular structure [12], appears to be a serious limit of the colloidal technique.

In summary, the size of the etch-induced lumps is dependent on the initial size of the colloids. A full understanding is hindered by the fact that different initial parameters are interrelated. For example, the initial surface as well as total concentration of surfactant could be different for various colloidal diameters. Furthermore, the contact area of particle and substrate is clearly dependent on the initial size of the colloid. Finally, the distribution of the Pt precursor inside the colloidal particle may also play an important role.

To clarify this last point, TEM and EDX (energy dispersive X-ray spectroscopy) investigations on seed and size enhanced seeded colloids were performed. However, due to the limited element specific sensitivity of these techniques and the small Pt content in the NPs, respectively, it was not possible to resolve any gradients in the distribution of the Pt complex inside the seeded colloids. Nevertheless, it was possible to exclude agglomerates of Pt precursors inside or on the surface of the colloids. It is worth mentioning, that Pt precursor loaded PMMA particles show similar etching-induced saturation behaviour as for loaded PS particles. In both cases, a homogenous diffusion of the Pt precursor during the seeded emulsion polymerization cannot be safely excluded at the moment.

Conclusion

In this contribution, we applied miniemulsion polymerization to produce metal-complex containing polystyrene particles as a model compound for a functional latex particle. A seeded emulsion polymerization process to increase the size and monodispersity of the particles was investigated. Finally, as an application of the newly developed process, the preparation of platinum nanoparticle arrays was demonstrated exhibiting high homogeneity and lateral order. For this purpose, a plasma-assisted removal of the organic material of the colloids was applied.

The following conclusions regarding experimental conditions of the seeded emulsion polymerization reactions and Pt-particle generation processes can be drawn from the experiments performed.

1) It is possible to synthesize functional colloidal particles with a diameter up to 600 nm in one step. Larger diameters have to be synthesized in a step-by-step fashion.

2) The initiator concentration has to be high in order to induce polymerization and not only depends on the amount of monomer added, but also on the amount of the continuous phase. The best results were achieved using 10–25 wt % APS relative to the added monomer.

3) The choice and concentration of the surfactant is critical for a successful reaction. SDS as an anionic surfactant proved to be superior to Lutensol AT50 as non-ionic surfactant. High surfactant concentrations lead to more homogeneous particles but, eventually, favour secondary nucleation. Therefore, the surfactant concentration ought to be as small as possible in order to stabilize the dispersion without inducing secondary nucleation.

4) The composition of the continuous phase also influences the reaction. Small amounts of added salt lead to final particle sizes

reaching the theoretical diameter, whereas higher salt amounts deteriorate the stability of the dispersion. Ethanol may be added to improve the monodispersivity of the samples. However, care has to be taken as secondary nucleation seems to be favoured as well.

5) The precursor platinum acetylacetonate inside the PS colloids and the surfactant SDS causes saturation of the particle diameter during the oxygen plasma induced etching.

6) The diameter of the particles in the saturated state depends on the total amount of Pt precursor inside the PS particles as well as on the initial size of the colloids.

7) The interparticle distance is presently limited to about 260 nm.

Experimental

Miniemulsion polymerization

Hexadecane (250 mg), 2,2'-Azobis(2-methylbutyronitril) (V59, 100 mg) and platinum(II) acetylacetonate (60 mg) were dissolved in monomer (6 g) under continuous stirring. To this phase, a mixture of water (milliQ quality) and SDS (60 mg) was added. After stirring for one hour at 1800 rpm and at room temperature, miniemulsification was achieved by ultrasonication of the mixture under ice-cooling for 120 s with a 1/2" tip at 90% amplitude, following a 10 s pulse-10 s break-protocol (Branson digital sonifier 450-D, Dietzenbach, Germany). Subsequently, the mixture was heated to 72 °C and polymerized for 12 h under gentle continuous stirring. After cooling to room temperature, the colloidal dispersion was filtered and extensively dialysed (Visking tubes, MWCO 14.000 g/mol, Carl Roth, Karlsruhe, Germany) until the conductivity of the water phase after dialysis was similar to that for deionized water.

Seeded polymerization

The protocol given here can be considered the standard protocol. All reactions deviating from this protocol are specified in the main text. A dispersion of 0.1 wt % of seed particles with 0.01 wt % of SDS (relative to the amount of water used) was heated to 75 °C. Ammonium peroxodisulfate, (APS, $(NH_4)_2S_2O_8$), and 10–15% of the monomer added was dissolved in a small amount of ultra-pure water and added to the dispersion. Styrene as monomer was added to the solution using a syringe pump with a flow rate of 1 $mL \cdot h^{-1}$. The amount of monomer was varied to obtain different sizes of the resulting seeded particles. The reaction was stirred for 24 h at 80 °C under an argon atmosphere. After completion, the final dispersion was dialysed extensively.

Plasma assisted combustion of the colloidal particles to produce nanoparticle arrays

The plasma was delivered by a commercially available etching machine (Oxford Plasmalab 80 Plus RIE) with an inductively coupled plasma source (ICP). The colloids were etched by an isotropic oxygen plasma [11,12].

Annealing

After finishing the plasma treatment, the particles were annealed at 1100 °C in a commercially available lamp furnace (UniTemp RTP-1200-100) in an oxygen atmosphere at 1 mbar for 10 min and cooled down in a nitrogen gas-flow to RT.

Sample Characterization

Scanning electron microscope images of the colloidal particles were recorded on a Gemini 1530 microscope (Carl Zeiss AG, Oberkochen, Germany).

High resolution SEM images were taken on a Hitachi S5200 with an acceleration voltage of 30 kV guaranteeing a resolution of 0.5 nm.

TEM was carried out using a FEI Titan 80-300 (FEI, Eindhoven, Netherlands) operating at 300 kV in the scanning mode (STEM). The images were acquired using a mass sensitive high annular dark-field detector (HAADF, type Fischione) resulting in a resolution of < 0.135 nm.

Images were evaluated by the use of the program ImageJ. The diameters of the particles in the saturation state were determined as follows: First the outer rim of the particles was defined, then it was assumed that the total area inside this rim equals the projected area of a round particle, and hence the diameter was calculated.

Acknowledgements

N.V. acknowledges funding from the Materials Science in Mainz (MAINZ) graduate school. The support by Deutsche Forschungsgemeinschaft (DFG) within the Cooperative Research Center SFB 569 (project G2) as well as by Baden-Württemberg-Stiftung is gratefully acknowledged. We thank Thomas Diemant for the XPS measurements, and Elena Kobitskaya for the synthesis of dispersions.

References

1. Zhang, J.; Li, Y.; Zhang, X.; Yang, B. *Adv. Mater.* **2010,** *22,* 4249–4269. doi:10.1002/adma.201000755
2. Fischer, U. C.; Zingsheim, H. P. *J. Vac. Sci. Technol.* **1981,** *19,* 881–885. doi:10.1116/1.571227
3. Hulteen, J. C.; Van Duyne, R. P. *J. Vac. Sci. Technol., A* **1995,** *13,* 1553–1558. doi:10.1116/1.579726

4. Vogel, N.; de Viguerie, L.; Jonas, U.; Weiss, C. K.; Landfester, K. *Adv. Funct. Mater.*, in press. doi:10.1002/adfm.201100414
5. Vogel, N.; Jung, M.; Retsch, M.; Jonas, U.; Knoll, W.; Köper, I. *Small* **2009,** *5,* 821–825. doi:10.1002/smll.200801583
6. Vogel, N.; Jung, M.; Bocchio, N. L.; Retsch, M.; Kreiter, M.; Köper, I. *Small* **2010,** *6,* 104–109. doi:10.1002/smll.200900497
7. Aizpurua, J.; Hanarp, P.; Sutherland, D. S.; Käll, M.; Bryant, G. W.; García de Abajo, F. J. *Phys. Rev. Lett.* **2003,** *90,* 057401. doi:10.1103/PhysRevLett.90.057401
8. Hanarp, P.; Käll, M.; Sutherland, D. S. *J. Phys. Chem. B* **2003,** *107,* 5768–5772. doi:10.1021/jp027562k
9. Retsch, M.; Tamm, M.; Bocchio, N. L.; Horn, N.; Förch, R.; Jonas, U.; Kreiter, M. *Small* **2009,** *5,* 2105–2110. doi:10.1002/smll.200900162
10. Vogel, N.; Fischer, J.; Mohammadi, R.; Retsch, M.; Butt, H.-J.; Landfester, K.; Weiss, C. K.; Kreiter, M. *Nano Lett.* **2011,** *11,* 446–454. doi:10.1021/nl103120s
11. Manzke, A.; Pfahler, C.; Dubbers, O.; Plettl, A.; Ziemann, P.; Crespy, D.; Schreiber, E.; Ziener, U.; Landfester, K. *Adv. Mater.* **2007,** *19,* 1337–1341. doi:10.1002/adma.200601945
12. Manzke, A.; Vogel, N.; Weiss, C. K.; Ziener, U.; Plettl, A.; Landfester, K.; Ziemann, P. *Nanoscale* **2011,** *3,* 2523–2528. doi:10.1039/c1nr10169b
13. Harkins, W. D. *J. Am. Chem. Soc.* **1947,** *69,* 1428–1444. doi:10.1021/ja01198a053
14. Goodwin, J. W.; Hearn, J.; Ho, C. C.; Ottewill, R. H. *Colloid Polym. Sci.* **1974,** *252,* 464–471. doi:10.1007/BF01554752
15. Egen, M.; Zentel, R. *Macromol. Chem. Phys.* **2004,** *205,* 1479–1488. doi:10.1002/macp.200400087
16. Schreiber, E.; Ziener, U.; Manzke, A.; Plettl, A.; Ziemann, P.; Landfester, K. *Chem. Mater.* **2009,** *21,* 1750–1760. doi:10.1021/cm802796y
17. Landfester, K. *Macromol. Rapid Commun.* **2001,** *22,* 896–936. doi:10.1002/1521-3927(20010801)22:12<896::AID-MARC896>3.0.CO;2-R
18. Landfester, K. *Annu. Rev. Mater. Res.* **2006,** *36,* 231–279. doi:10.1146/annurev.matsci.36.032905.091025
19. Landfester, K. *Angew. Chem., Int. Ed.* **2009,** *48,* 4488–4507. doi:10.1002/anie.200900723
20. Landfester, K.; Weiss, C. K. *Adv. Polym. Sci.* **2010,** *229,* 1–49. doi:10.1007/12_2009_43
21. Lorenz, S.; Hauser, C. P.; Autenrieth, B.; Weiss, C. K.; Landfester, K.; Mailänder, V. *Macromol. Biosci.* **2010,** *10,* 1034–1042. doi:10.1002/mabi.201000099
22. Tiarks, F.; Landfester, K.; Antonietti, M. *Macromol. Chem. Phys.* **2001,** *202,* 51–60. doi:10.1002/1521-3935(20010101)202:1<51::AID-MACP51>3.0.CO;2-J
23. Holzapfel, V.; Lorenz, M.; Weiss, C. K.; Schrezenmeier, H.; Landfester, K.; Mailänder, V. *J. Phys.: Condens. Matter* **2006,** *18,* S2581–S2594. doi:10.1088/0953-8984/18/38/S04
24. Vogel, N.; Hauser, C. P.; Schuller, K.; Landfester, K.; Weiss, C. K. *Macromol. Chem. Phys.* **2010,** *211,* 1355–1368. doi:10.1002/macp.201000036
25. Hansen, F. K.; Ugelstad, J. *J. Polym. Sci., Polym. Chem. Ed.* **1978,** *16,* 1953–1979. doi:10.1002/pol.1978.170160814
26. Hansen, F. K.; Ugelstad, J. *J. Polym. Sci., Polym. Chem. Ed.* **1979,** *17,* 3033–3045. doi:10.1002/pol.1979.170171001
27. Coen, E. M.; Gilbert, R. G.; Morrison, B. R.; Leube, H.; Peach, S. *Polymer* **1998,** *39,* 7099–7112. doi:10.1016/S0032-3861(98)00255-9
28. Maxwell, I. A.; Morrison, B. R.; Napper, D. H.; Gilbert, R. G. *Macromolecules* **1991,** *24,* 1629–1640. doi:10.1021/ma00007a028
29. Morrison, B. R.; Gilbert, R. G. *Macromol. Symp.* **1995,** *92,* 13–30. doi:10.1002/masy.19950920104
30. Jiang, S.; Sudol, E. D.; Dimonie, V. L.; El-Aasser, M. S. *J. Appl. Polym. Sci.* **2008,** *108,* 4096–4107. doi:10.1002/app.28027
31. Chern, C.-S.; Chen, T.-J.; Wu, S.-Y.; Chu, T.-B.; Huang, C.-F. *J. Macromol. Sci., Part A: Pure Appl. Chem.* **1997,** *34,* 1221–1236. doi:10.1080/10601329708009381
32. Jönsson, J. E.; Hassander, H.; Törnell, B. *Macromolecules* **1994,** *27,* 1932–1937. doi:10.1021/ma00085a042
33. Castelvetro, V.; De Vita, C.; Giannini, G.; Giaiacopi, S. *J. Appl. Polym. Sci.* **2006,** *102,* 3083–3094. doi:10.1002/app.23717
34. Plettl, A.; Enderle, F.; Saitner, M.; Manzke, A.; Pfahler, C.; Wiedemann, S.; Ziemann, P. *Adv. Funct. Mater.* **2009,** *19,* 3279–3284. doi:10.1002/adfm.200900907
35. Schüler, B. Strukturierte Deposition von Kolloiden mittels DUV-Lithographie. Diploma thesis, University Ulm, Germany, 2009; pp 1–93.

License and Terms

Beilstein Journal of Nanotechnology

Nanoscaled alloy formation from self-assembled elemental Co nanoparticles on top of Pt films

Luyang Han[1], Ulf Wiedwald[*1], Johannes Biskupek[2], Kai Fauth[3], Ute Kaiser[2] and Paul Ziemann[1]

Full Research Paper

Open Access

Address:
[1]Institut für Festkörperphysik, Universität Ulm, Albert-Einstein-Allee 11, 89069 Ulm, Germany, [2]Materialwissenschaftliche Elektronenmikroskopie, Universität Ulm, Albert-Einstein-Allee 11, 89069 Ulm, Germany, and [3]Experimentelle Physik IV, Universität Würzburg, Am Hubland, 97074 Würzburg, Germany

Email:
Ulf Wiedwald[*] - ulf.wiedwald@uni-ulm.de

* Corresponding author

Keywords:
alloy; Co; CoPt; epitaxy; HRTEM; magnetometry; nanoparticles; Pt; XMCD

Beilstein J. Nanotechnol. **2011,** *2,* 473–485.
doi:10.3762/bjnano.2.51

Received: 01 June 2011
Accepted: 31 July 2011
Published: 23 August 2011

This article is part of the Thematic Series "Organic–inorganic nanosystems".

Associate Editor: P. Leiderer

Abstract

The thermally activated formation of nanoscale CoPt alloys was investigated, after deposition of self-assembled Co nanoparticles on textured Pt(111) and epitaxial Pt(100) films on MgO(100) and $SrTiO_3$(100) substrates, respectively. For this purpose, metallic Co nanoparticles (diameter 7 nm) were prepared with a spacing of 100 nm by deposition of precursor-loaded reverse micelles, subsequent plasma etching and reduction on flat Pt surfaces. The samples were then annealed at successively higher temperatures under a H_2 atmosphere, and the resulting variations of their structure, morphology and magnetic properties were characterized. We observed pronounced differences in the diffusion and alloying of Co nanoparticles on Pt films with different orientations and microstructures. On textured Pt(111) films exhibiting grain sizes (20–30 nm) smaller than the particle spacing (100 nm), the formation of local nanoalloys at the surface is strongly suppressed and Co incorporation into the film via grain boundaries is favoured. In contrast, due to the absence of grain boundaries on high quality epitaxial Pt(100) films with micron-sized grains, local alloying at the film surface was established. Signatures of alloy formation were evident from magnetic investigations. Upon annealing to temperatures up to 380 °C, we found an increase both of the coercive field and of the Co orbital magnetic moment, indicating the formation of a CoPt phase with strongly increased magnetic anisotropy compared to pure Co. At higher temperatures, however, the Co atoms diffuse into a nearby surface region where Pt-rich compounds are formed, as shown by element-specific microscopy.

Introduction

Magnetic nanoparticles (NPs), with narrow distributions of their size and mutual spacing, offer a high potential with respect to both, fundamental and applied studies [1-4]. Although a broad palette of methods has been established for the preparation of such NPs, if additionally their deposition onto a specific substrate in the form of *ordered* arrays over reasonably large areas is required, then the number of applicable fabrication recipes dramatically decreases. Focusing on NP sizes below 15 nm and

excluding purely sequential procedures such as those based on scanning probe microscopy techniques [5], one is left with processes relying on the self-assembly of colloids or micelles [6-8]. In the context of magnetic NPs, two prominent examples, both dealing with the preparation of magnetically attractive FePt NPs, which successfully demonstrated fulfillment of the above requirements were presented by Sun et al. applying colloidal chemistry [9] and Ethirajan et al. using micellar methods [10]. Due to the higher variability of the micellar approach with respect to the interparticle distance, this technique has been continually improved and also extended to CoPt NPs as summarized in a recent publication [11]. Despite these successful attempts at fabricating arrays of the specific binary alloy NPs FePt and CoPt, from empirical evidence it appears much easier to prepare elemental NPs along these approaches, as judged from the sheer number of different magnetic or non-magnetic NPs reported. This leads to the simple idea of deposition of an ordered array of elemental NPs onto a metallic film in a first step, and the subsequent reaction of these primary NPs with the subjacent film by temperature-driven alloying. In the case of a reasonable separation of primary NPs, a local binary alloy might form on the nanoscale and maintain the initial particle center-to-center distance. Besides giving insight into nanoalloy formation, such experiments also open the perspective to locally create more complex systems by depositing the NPs on top of pre-alloyed binary or ternary films. Pertinent questions regarding such an approach are: To what extent can the resulting alloy really be confined on the nanoscale; can the orientation of the finally obtained local alloy be controlled by the primary orientation of the film; and how do the resulting phases compare to equilibrium phase diagrams [12]. This last point is closely related to the property changes of the alloy particles considered, in the context of catalysis, such as a narrowing of miscibility gaps upon size reduction [13].

In this paper, the basic idea outlined above is tested by the deposition of hexagonally ordered arrays of Co NPs on top of textured and epitaxial Pt films. Similarly to the previous research interest in FePt equiatomic alloys in the chemically ordered $L1_0$ phase, our interest in this system is motivated by the magnetic properties of CoPt alloys exhibiting very large magnetocrystalline anisotropy energy density (MAE) and, directly related to that, a high value of the coercive field H_C in the direction of the easy axis of magnetization. However, as it has been reported previously, laterally extended CoPt alloy systems may form $CoPt_3$ as well [14]. At this composition the MAE is significantly lower than for CoPt in the $L1_0$ phase.

The Co volume fraction in our specimens typically amounts to few parts per thousand or less. Therefore, a thorough structural characterization of the alloy formation with standard laboratory equipment is not practical. Instead, we probe the magnetic signatures of alloy formation by X-ray absorption spectroscopy and SQUID magnetometry. The excellent sensitivity of SQUID magnetometers can be exploited, at suitably selected temperatures, to detect the magnetic response corresponding to the Co particles and nanoscale alloys. X-ray magnetic circular dichroism (XMCD) derives its sensitivity from being both element specific and surface sensitive. It is therefore ideally suited for the kind of specimens studied here. In addition to the information contained in (both, SQUID and XMCD) hysteresis loops, we obtain spectroscopic signatures of the average magnetocrystalline anisotropy through the determination of the orbital contribution μ_L to the Co magnetic moments [15]. Notable differences of this quantity are known between Co and CoPt alloys [16,17], owing to both Co–Pt hybridisation and atomic structure.

Results and Discussion

The thermal reaction of metallic NPs with a subjacent metallic film demands the following experimental sequence: 1) Deposition of a thin metal film A exhibiting high quality with respect to grain size, orientation and roughness. 2) Placement of metallic NPs of type B on top of film A. 3) Thermal reaction of A and B and the characterization of the resulting local alloy. In this paper we report the experimental details and results for the specific case of Co NPs on top of Pt(111)/MgO(100) and Pt(100)/$SrTiO_3$(100). (For the sake of clarity and brevity, $SrTiO_3$(100) is renamed STO(100) in the following).

Pt films on MgO(100) and STO(100)

Due to the attractive catalytic properties of Pt on top of ceramic supports, much work has been dedicated to the identification of active sites on its surface. For this purpose the controlled growth of Pt films on various single crystalline metal oxides, such as MgO(100) or STO(100), is advantageous. On the resulting epitaxial films, for instance, kink and step sites, with their selective catalytic activities, can be distinguished [13]. Pt films have typically been prepared by sputtering. With regards to the deposition on MgO(100) and STO(100), it is generally agreed that high quality epitaxial Pt(100) films can be obtained with elevated substrate temperature T_S during deposition. At T_S = 600 °C epitaxial growth was obtained on MgO(100) or STO(100) substrates [18-20], whereas deposition at ambient temperature led to textured growth of Pt films. Pulsed laser deposition (PLD) produced a similar result for the Pt orientation on MgO(100), at $T_S \geq 600$ °C [21]. The same authors also found a three-dimensional mosaic like island growth under these conditions. In the present study this observation is confirmed by our own PLD experiments performed at T_S = 600 °C. For sputtering as well as for PLD a switching of the Pt orientation towards (111) orientation has been demonstrated

upon lowering of the deposition temperature. This is corroborated by our own PLD experiments. Furthermore, as revealed by AFM measurements, such (111) oriented Pt films exhibit significantly lower roughness on the micron length scale (typical RMS values of 1–2 nm) enabling homogeneous deposition of NPs over the entire sample surface. Despite the island growth mode of Pt(100) when deposited at elevated temperature and the resulting increased roughness (cf. Figure 2), each single island has an almost atomically flat surface (RMS roughness of 0.3 nm).

In the preparation of such Pt films, the following PLD conditions were used: An ArF excimer laser (193 nm, pulse duration 20 ns, 10 Hz repetition frequency) served as the light source for hitting the polycrystalline Pt target. The ablated Pt material was collected on 10 × 5 mm^2 MgO(100) or STO(100) substrates fixed at a distance of 30 mm from the target. To reduce particulate formation, the target was rotated as well as periodically tilted during the ablation process. To allow calibration of the deposition rate, a movable quartz crystal monitor can be placed at exactly the substrate position. More details on the PLD apparatus, including its UHV chamber, are given in [22,23]. By monitoring the deposition rate as a function of the laser power, an ablation threshold of 2.5 J/cm^2 was determined for Pt. Standard deposition was performed at 5 J/cm^2 resulting in a Pt deposition rate of 1 nm/min.

Standard X-ray diffraction (XRD) diffractograms (Cu Kα radiation, λ = 0.15418 nm) from Pt films deposited on MgO(100) at ambient temperature (nominal thickness 15 nm) and on STO(100) at 600 °C (nominal thickness 40 nm), are presented in Figure 1a. Besides the MgO(200) substrate peak, the diffractogram of the film deposited at ambient temperature exclusively reveals the Pt(111) peak as expected. The rocking curve on the Pt(111) peak has a full width at half maximum (FWHM) of 14.4° indicating a rather poor degree of (111) orientation.

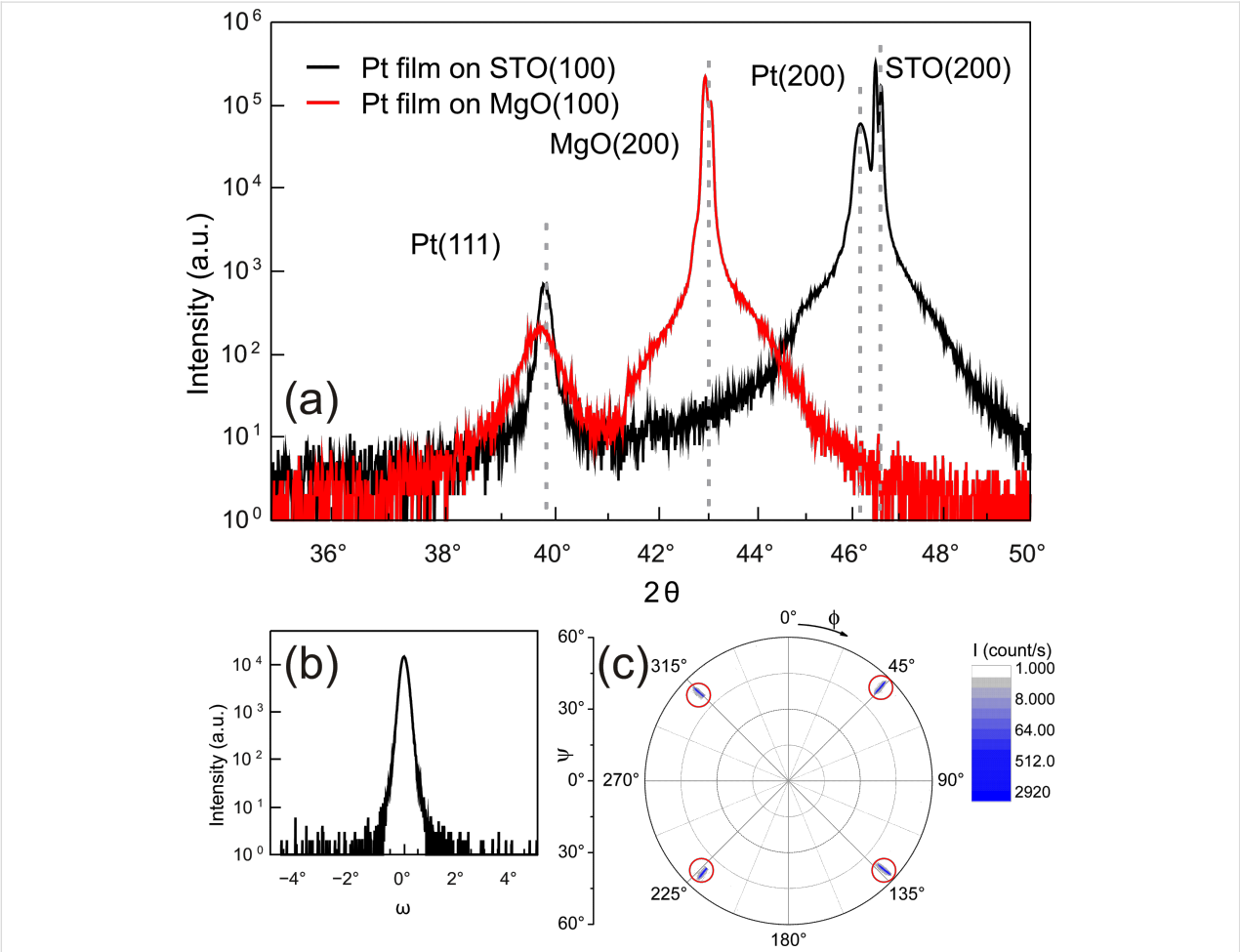

Figure 1: (a) XRD of Pt films on STO(100) and MgO(100) in Bragg–Brentano geometry. The diffractograms clearly show the two different orientations of Pt films when deposited on MgO(100) at ambient temperature or STO(100) at 600 °C. Panel (b) shows the rocking curve on the Pt(200) peak of Pt/STO(100). Panel (c) displays the Pt/STO(100) pole figure measured on the Pt(111) peak position. Diffraction peaks are highlighted by red circles. Details are given in the text.

Pole figure scans reveal a practically random in-plane orientation of the Pt(111) film on MgO(100) deposited at ambient temperature (not shown). The grain size was estimated using Scherrer's formula to be about 16 nm, which is in good agreement with the nominal film thickness. For comparison, the in-plane dimension of the grains is about 20–30 nm, as determined from scanning electron microscopy (SEM) images (cf. Figure 2a). XRD from the Pt film on STO(100) deposited at 600 °C reveals two orientations: First, the Pt(111) orientation is present but with a much larger grain size as indicated by the sharper peak. More important is the observation of the Pt(200) peak slightly above 46° having a much higher diffraction intensity. Evaluation of the intensity ratio of the Pt(200) and Pt(111) peaks yields $I_{(200)}/I_{(111)} = 86$ and, moreover, using tabulated powder diffraction intensities, one finds an intensity ratio of $I_{(200)}/I_{(111)} = 0.53$ for Pt powder. Thus, the Pt film deposited at elevated temperature has predominantly the Pt(100) orientation on STO(100). Qualitatively similar results were also obtained for Pt films on MgO(100) when deposited above 600 °C (not shown), albeit with a lesser degree of Pt(100) orientation. Figure 1b presents the rocking curve on the Pt(200) peak of the Pt film on STO(100). The small rocking width of FWHM = 0.29° indicates a high degree of orientation of the film. To test possible epitaxy of this film a pole figure was measured at the Pt(111) peak position ($2\theta = 39.8°$) by scanning both the in-plane angle Φ and the tilting angle ψ. Figure 1c presents the result in a polar plot. Four (111) peaks are observed at $\psi = 54.7°$ and $\Phi = 45°$, 135°, 225°, and 315°. Note that a slit aperture was used here to reduce the acquisition time, leading to a broadening of the diffractogram in ψ direction. From the above diffraction peaks and the known orientation of the STO substrates we find a cube-on-cube growth of the Pt film on the STO(100) with orientations Pt(100)||STO(100) and Pt[010]||STO[010].

Co nanoparticles on Pt films

The preparation of metal NPs is based on spherical reverse micelles formed by the diblock copolymer poly(styrene)[*m*]-*block*-poly(2-vinylpyridine)[*n*] (PS[*m*]-*b*-P2VP[*n*]) in toluene (*m*, *n* indicate the number of monomers for each block, and, thus, determine the size of the resulting micelles). In this case, the hydrophobic PS forms the outer corona of the micelles and the hydrophilic P2VP their core. To this core, metal precursors can be selectively bonded, and thus the micelles serve as carriers for these precursors, during their own self-assembly, when deposited onto a substrate. The standard way to accomplish such a deposition is optimized dip coating, which leads to a single monolayer of hexagonally ordered micelles. In the next step, the organic constituents are completely removed by exposure to oxygen plasma, while simultaneously the precursor material is nucleated into a metal or metal oxide NP, without losing the original hexagonal ordering. In case of oxide NPs, an additional treatment in hydrogen plasma finally delivers the desired hexagonally ordered array of metal oxide NPs. More details on this fabrication process can be found in [11,24,25].

For the preparation of Co NPs for the present study, PS[1779]-*b*-P2VP[857] diblock copolymers were employed in combination with anhydrous $CoCl_2$ as precursor at a loading rate of $L_{Co} = 0.5$ (L_{Co} is defined as the ratio of ligated Co within the micellar core to the total number of pyridine moieties). The two parameters L_{Co} and $(n + m)$, together with the substrate velocity during dip coating (15 mm/min), determine the particle size and interparticle distance. In the present study, these parameters were fixed as given above resulting in Co NPs with diameters of about 7 nm and mutual separation of 100 nm. More details on the specific preparation and chemical control of the final NP arrays are presented in reference [11].

It should be noted that, although the fabrication is highly reproducible for a given micellar solution, separately prepared solutions from the same commercial copolymer may nevertheless deliver a different size distribution of the formed micelles, despite filtering. For that reason, in the present study samples were prepared in parallel from a single solution in order to guarantee arrays of NPs with reproducible size and spacing, before starting the various annealing experiments. All NP arrays were examined by SEM to determine the interparticle distance, lateral diameter and degree of hexagonal order. In the following we describe NPs as being "in the as-prepared state", meaning that a 10 min reduction process was applied, in hydrogen plasma at 10^{-1} mbar at T = 200–250 °C, to reliably restore the pure metallic state after the inevitable ex-situ transfer. Similarly, the thermal reaction of the Co NPs with the subjacent Pt film was induced by heating to a given temperature for 30 min in the presence of 10^{-4} mbar H_2 to avoid any oxidation.

The results corresponding to the above experimental steps are described below. The SEM image (Hitachi S5200) in Figure 2a shows the in-plane grains of a typical Pt(111) film, with an average size of approximately 20–30 nm and a RMS roughness below 2 nm as determined by AFM. On top of the Pt(111) film Co NPs can be observed. Note that strong image filtering was applied here to better visualize the NPs on the Pt(111) film, and the lower left section shows part of the original SEM image. Figure 2b illustrates the arrangement of Co NPs on top of a 50 nm epitaxial Pt(100) film. Co NPs form hexagonal arrays on the micron-sized islands. The islands are single crystalline (cf. Figure 1) flat surfaces, with only a few atomic steps, and a RMS roughness of 0.3 nm (AFM). The darker areas consist of smaller Pt grains at a reduced height compared to the islands. The films, however, are continuous at the film–substrate interface and pos-

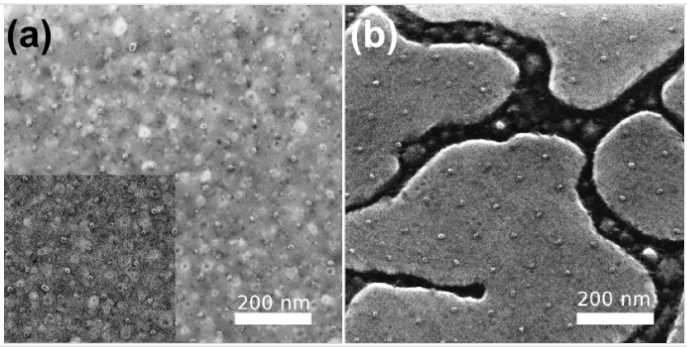

Figure 2: SEM images of Co NPs on Pt(111)/MgO(100) and Pt(100)/STO(100) are displayed in panels (a) and (b), respectively. Co particles are oxidized due to ex-situ transport. For better contrast of NPs three quarters of panel (a) is strongly filtered while in the lower left quarter the original SEM image is displayed.

sess metallic conductivity. The fraction of height-reduced areas depends on the film thickness and is below 10% for nominally 50 nm Pt(100) films.

Effects of annealing on Co nanoparticles on Pt(111) films

AFM measurements were performed on Co NPs on Pt(111) to corroborate changes of the vertical height of the Co NPs, as well as to monitor the effect of increasing temperatures on this height. Here, the same sample was successively annealed at increasing temperature under a H_2 atmosphere at 10^{-4} mbar. AFM measurements were performed ex situ, consequently the NPs oxidized in the ambient air. After inspection the specimen was reduced in hydrogen plasma before the next annealing step was applied. This procedure guarantees that the NPs as well as the film are always metallic during the annealing process. Due to the limited in-plane resolution of AFM, particle sizes are characterized by the maximum height with respect to substrate plane. Such height distributions obtained for the as-prepared NPs, as well as after annealing at 400 °C and 500 °C, are given in Figure 3. Each annealing step resulted in a reduction of the average particle height. This decrease may arise from different processes, such as deformation due to increased substrate wetting, loss of Co atoms due to evaporation and bulk diffusion, or a combination of these processes. While the possibility of metal NPs wetting the metal substrate [26] is not excluded in this study, the TEM investigation (see below) clearly reveals a spherical particle shape before annealing and subsequent vanishing of particles after annealing (cf. Figure 7), favoring the model of Co atom loss. To estimate the degree of Co atom loss, we calculate the corresponding metallic NP diameters by assuming the formation of CoO with a lower density of 6.44 g/cm^3 compared to the density of metallic Co, at 8.90 g/cm^3, in the bulk. Assuming spherical particles, this estimate leads to mean heights of pure Co NPs of 7.0 nm, 6.5 nm, and 6.0 nm in the as-prepared state and after annealing at an annealing temperature T_A = 400 °C and T_A = 500 °C, respectively. The mean height reduction from 7 nm to 6 nm yields a 37% loss of Co from the NPs after annealing at 500 °C for 30 min.

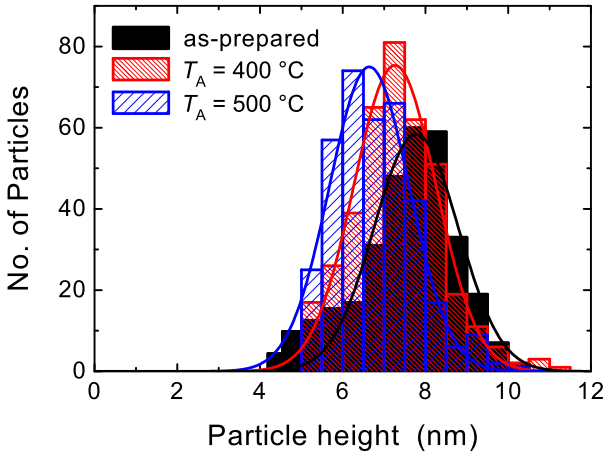

Figure 3: AFM height distributions of Co NPs on Pt(111)/MgO(100) in the as-prepared state and after annealing at T_A = 400 °C and 500 °C for 30 min. Additionally, the Gaussian fits to the measured size distributions are shown. Note that the particles are oxidized when examined ex-situ by AFM.

Consequently, a significant amount of the NP material is no longer discernable by AFM. A simple explanation attributing this decreasing particle size to thermal evaporation caused by vapor pressure enhancement due to the reduced size of the NPs is, however, unlikely for 7 nm Co NPs at an T_A below 500 °C. To further clarify the processes involved, we additionally carried out a surface and element specific characterization of the specimen by in-situ X-ray photoelectron spectroscopy (XPS). These data (not shown) clearly demonstrate that the intensity ratio of the Co 2p peaks with respect to the Pt 4f peaks decreases by about 40% after annealing at 500 °C, compared to the as-prepared state. This change is in good agreement with the results from AFM inspection above. Since XPS samples the

surface region of the Pt film, including the Co NPs, we can conclude that the observed "AFM loss" cannot be attributed to Co atoms still remaining within the probing depth of XPS, which is restricted by a photoelectron mean free path of about 1.6 nm [27]. Rather, diffusion along the large number of grain boundaries in the Pt(111) film on MgO(100) is expected. On Pt(100) films with micron-sized, atomically-flat surfaces this diffusion channel does not exist for most of the NPs, thus markedly different diffusion and alloying behavior is expected. An additional AFM inspection of the Co NPs on Pt(100) after annealing at 500 °C for 30 min (not shown) yielded an average particle height of 5.4 nm, which is significantly smaller than the finding on the Pt(111) film (cf. Figure 3). By ex-situ AFM measurements, however, we cannot distinguish different modes of diffusion on Pt(100) and Pt(111) films. In the context of the following magnetic measurements and HRTEM investigations, this point is discussed in more detail.

Magnetic properties of Co NPs on Pt(100) and Pt(111) films

Co $L_{3,2}$ XMCD measurements were made on specimens of the deposited Co NPs on both textured Pt(111) and epitaxial Pt(100) films, as function of annealing temperature. The investigations were performed at the bending magnet beamline PM3 of BESSY II synchrotron radiation facility at the Helmholtz-Center Berlin, Germany. Throughout all steps of the specimen investigation, ultrahigh vacuum conditions were maintained, except for the annealing steps carried out in a H_2 atmosphere at 10^{-4} mbar. All XMCD measurements were taken at low temperature (T ≈ 12 K) and at normal incidence of the circularly polarized X-rays (p ≈ 0.93), by recording the sample drain current (total electron yield, TEY) as a function of photon energy. External fields of up to $\mu_0 H = \pm 3$ T were available. Spectra and hysteresis loops were recorded and evaluated by methods described previously [11,28-30]. The insert to Figure 4a displays a typical pair of XAS energy scans, obtained in applied fields of $\mu_0 H = \pm 1$ T, sufficient to achieve magnetic saturation. While the Co $L_{3,2}$ resonances as well as the magnetic dichroism are clearly visible, we note that even the resonant Co signal amounts to only a fraction (≈1%) of the strong TEY background (≈170 pA) generated in the Pt film. In addition, because the background is curved, a quantitative determination of the (spin and orbital) magnetic moments from the XMCD sum rules is problematic. We will therefore resort to the more robust procedure of evaluating the ratio of the orbital magnetic moment to the effective spin magnetic moment μ_L/μ_S^{eff}, where the effective spin moment $\mu_S^{eff} = \mu_S + 7\,\mu_T$ contains two contributions: The spin moment μ_S, as well as the magnetic dipole moment μ_T, which relates to the anisotropy of the spin density distribution. As the magnetic dipole term may be quite significant in CoPt systems due to the structural anisotropy in the chemically ordered $L1_0$ phase [31], only μ_S^{eff} will be discussed for the NPs in this study.

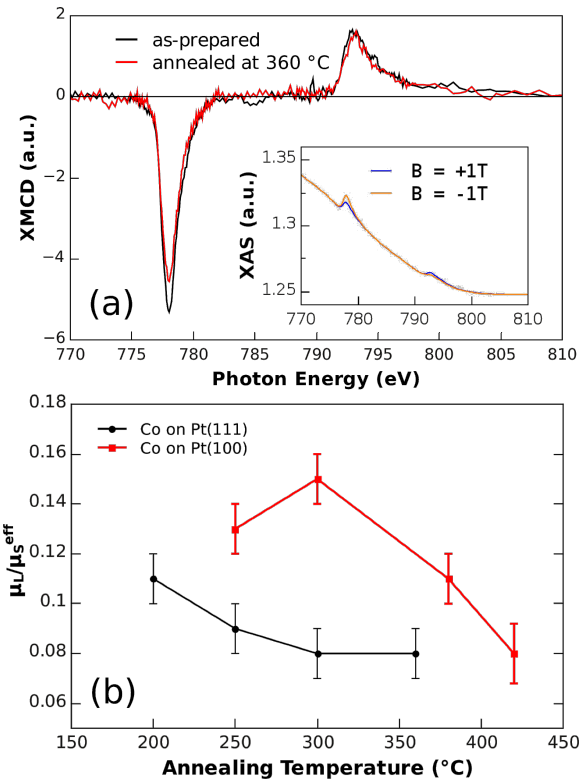

Figure 4: Panel (a) shows XMCD difference spectra for Co NPs on Pt(111) in the as-prepared state and after annealing at 360 °C for 30 min (final state). The inset displays the absorption spectra for external fields of $\mu_0 H = \pm 1$T in the as-prepared state. Panel (b) presents the resulting ratios of orbital-to-spin moments for Co NPs on Pt(111) and Pt(100) films as a function of annealing temperature T_A (holding time 30 min). The lines are given as guides to the eye.

Figure 4a compares two XMCD difference spectra, i.e., the difference in the X-ray absorption spectra, for antiparallel external fields (here $\mu_0 H = \pm 1$ T) collinear to the incident X-ray beam, of Co NPs deposited on Pt(111) in the as-prepared state and after annealing at $T = 360$ °C for 30 min. Both spectra are scaled to the same L_2 dichroic amplitude at about ≈794 eV. This scaling facilitates the comparison of the orbital magnetic moment, which now correlates with the resulting L_3 dichroic intensity. Details are discussed further, below.

For Co NPs on Pt(111) films, XMCD spectra were measured for as-prepared and annealed samples. Increasing annealing temperatures (250 °C, 300 °C, 360 °C) were used, with the samples held for 30 min at each temperature. The results reveal a monotonic, small decrease of μ_L/μ_S^{eff} for increasing annealing temperatures approaching $\mu_L/\mu_S^{eff} = 0.08$ at T_A = 300 °C and above (Figure 4b). Although the comparison to isotropically averaged values of $\mu_L/\mu_S^{eff} = 0.095$ for Co [32],

μ_L/μ_S^{eff} = 0.09 CoPt [16], and μ_L/μ_S^{eff} = 0.15 for $CoPt_3$ [17] in bulk samples or thin films is generally useful, one has to consider that these values may vary due to size effects in NPs, such as enhanced surface moments. Thus, we restrict ourselves to the direct comparison of annealing effects on Pt(111) and Pt(100) films. On Pt(111), huge orbital moments, as observed for Co adatoms on Pt(111) single crystals [33], were not found. Moreover, the AFM size distribution discussed above (cf. Figure 3) only showed a slight reduction of the metal particle height from about 7 nm to 6.5 nm after annealing at T_A = 400 °C. Our finding, by XPS, of a simultaneously reduced Co content after annealing suggests that Co atoms diffuse away from the surface along grain boundaries at elevated temperature. Thus, we speculate that after annealing the size-reduced NPs on Pt(111) remain in a pure Co, or at least Co-rich, phase having a rather low orbital moment. Nevertheless, we note that Co atoms generally possess larger spin moments in CoPt alloys (1.76 μ_B per atom for $L1_0$ ordered CoPt alloy [16] and 1.60 μ_B per atom for $L1_2$ ordered $CoPt_3$ alloy [17]) compared to pure Co (1.55 μ_B per atom [28]). Thus, an increase of the spin moment of up to 15% can be expected. Surface alloy formation therefore might additionally contribute to the reduction of the ratio μ_L/μ_S^{eff}.

For Co particles deposited onto the large islands of the epitaxial Pt(100) film (cf. Figure 2b) the situation is quite different. Starting from μ_L/μ_S^{eff} = 0.13 we found an initial increase to μ_L/μ_S^{eff} = 0.15 after annealing at 300 °C for 30 min. At higher annealing temperatures μ_L/μ_S^{eff} decreased, and after annealing at T_A = 420 °C a similar value to that for the Co NPs on Pt(111) was observed. Although alloying results in slightly increased spin moments, pointing to lower ratios μ_L/μ_S^{eff}, the initial increase in our experiments can only be explained by a faster growth of the orbital moment upon annealing. Such rising orbital moments signal alloy formation on the Pt(100) surface.

If such an alloy formation preserves the (100) starting orientation of the film, one expects the easy axis of magnetization and, thus, the largest orbital moment of resulting chemically ordered CoPt thin films [16] or Co/Pt multilayers [34] to be perpendicular to the Pt atomic layers. Indeed, within the error bars, the observed maximum of μ_L/μ_S^{eff} = 0.15 is found rising towards the expectations for both, ordered CoPt (μ_L/μ_S^{eff} = 0.16) and $CoPt_3$ alloys (μ_L/μ_S^{eff} = 0.19) in the easy axis of magnetization, corroborating the idea of alloy formation at these intermediate annealing temperatures. Such a finding is comparable to results from ultrathin Co films deposited on Pt(100) [35] and Pt(111) [36] single crystal surfaces, where alloying occurs between 300 °C to 400 °C. An alignment of the easy axis of magnetization should, however, be visible in the hysteresis loops discussed below.

Obviously, two competing effects play a decisive role in the present study, i.e., diffusion and the formation of local surface alloys. Insight into the progress of these processes can be provided by the measurement of hysteresis loops after the various annealing steps. In Figure 5 element specific XMCD hysteresis loops, measured along the surface normal, are displayed for two temperatures of the annealing series.

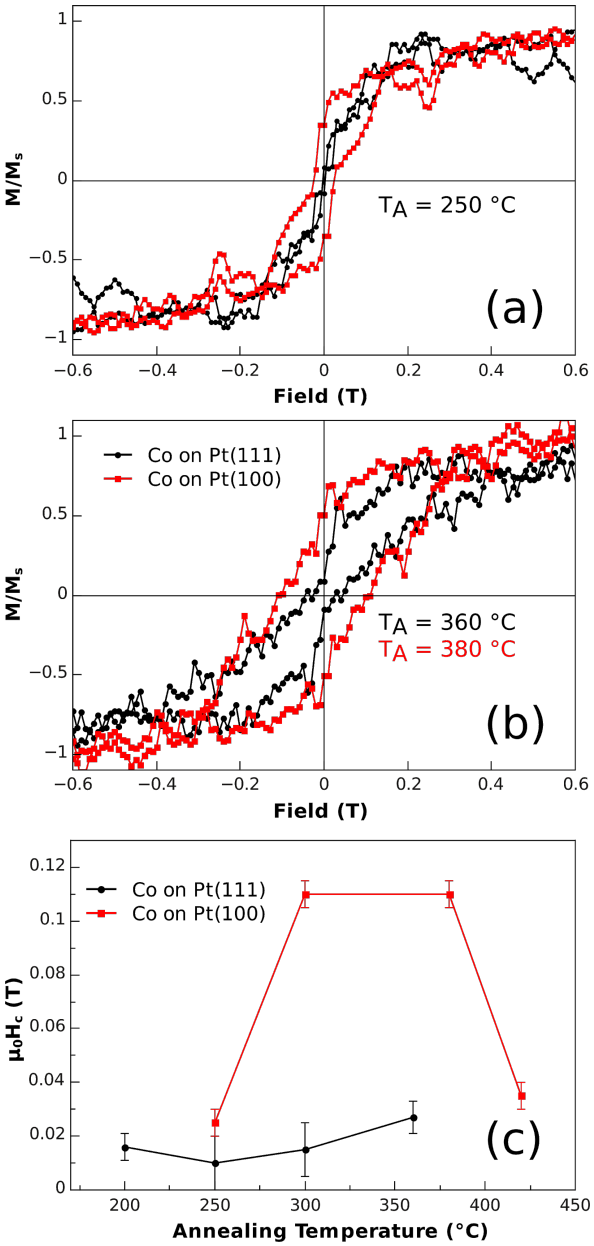

Figure 5: Element specific XMCD hysteresis loops measured at the Co L_3 maximum dichroic signal at T = 12 K and out-of-plane geometry for Co NPs on Pt(100) and Pt(111) films after annealing at (a) T_A = 250 °C and (b) 360 °C on Pt(111) and 380 °C on Pt(100). Panel (c) shows the evolution of the coercive field as function of the annealing temperature (holding time at each T_A: 30 min). The lines are given as guides to the eye.

Although the hysteresis loops appear quite noisy due to the low volume fraction of magnetic material on the surface, the remnant magnetization, coercive fields and the shape of the hysteresis are sufficiently well defined to allow the confirmation of alloy formation for Co NPs on Pt(100) films.

After the first annealing step (T_A = 250 °C) a narrow hysteresis loop was observed with a coercive field of $\mu_0 H_C$ = 27 mT on Pt(100) films, while no clear opening was detected for Co NPs on Pt(111), within the experimental uncertainties. The largest difference of coercive fields was obtained after annealing in the interval T_A = 300–380 °C for 30 min, as can been seen in Figure 5c. Whereas for Co NPs on the Pt(111) film only a slight increase up to about $\mu_0 H_C$ = 27 mT was measured, the evolution of the coercive field on Pt(100) epitaxial films was more pronounced. For T_A = 300 °C it jumped to 110 mT, which is comparable to previous reports on $Co_{0.25}Pt_{0.75}$ films [37]. Thus, a significant difference for the two types of Pt films is observed, which parallels the changes of the ratio of orbital-to-spin moments discussed above. At still higher temperatures (T_A = 420 °C), however, the H_C enhancement is followed by a pronounced H_C reduction for Co NPs on Pt(100). Similarly, the two types of Pt films exhibit a clear difference in their remnant magnetization M_R. After annealing the Co NP on Pt(111) at 360 °C, M_R found at 12 K was rather low and hardly detectable due to the small signals, whereas after annealing Co NP on Pt(100) at 380 °C (Figure 5b) M_R was about $0.5 \cdot M_S$ (M_S: saturation magnetization). The higher the value of M_R, the larger the number of magnetic entities found aligned in the direction of measurement. For a preferred structural orientation of NPs with respect to the Pt(100) film, however, M_R is too low, it actually matches well the value for Stoner–Wohlfarth particles with random orientation of the anisotropy axis. Here one may speculate that much longer annealing times at an T_A of around 350 °C could lead to at least some structural orientation relative to the Pt(100) film [38]. In summary, the hysteresis loops in perpendicular orientation reveal no dramatic changes of coercive fields for the Co NPs on the Pt(111) film, whereas on the Pt(100) film $\mu_0 H_C$ = 110 mT is more than twice as large as the value found for metallic Co nanoparticles of comparable size after application of a similar sample treatment [39]. This finding additionally confirms the lateral spread of Co atoms.

Additional in-plane hysteresis loops were measured by SQUID magnetometry for 7 nm Co NPs on Pt(111) films after different annealing steps. Note that each hysteresis loop was measured on a separate sample to exclude any effect of the thin SiO cover layer used for preservation in ambient conditions after in-situ annealing. Contrary to XMCD, SQUID magnetometry measures the total magnetic moment of the sample, i.e., the NPs, the paramagnetic Pt film, the SiO protective layer and the diamagnetic MgO(100) substrate. Usually the magnetic response of the support easily overwhelms the total magnetic moment of the tiny amount of ferromagnetic material in the NPs. In the present system one can benefit from the paramagnetic response of the Pt(111) film and paramagnetic impurities in MgO compensating the diamagnetic signal of the substrate. Since the diamagnetism of MgO is temperature independent and the paramagnetic signal follows Curie's law at low temperatures [40], compensation can be achieved at an appropriate temperature, which is experimentally determined to be around 29 K for our samples. As the non-ferromagnetic background was strongly reduced, a reasonable signal quality was obtained as shown in Figure 6a, after subtraction of a smaller slope arising from the sum of substrate and film contributions.

The in-plane hysteresis loops shown in Figure 6a after different annealing steps show almost no change. The coercive fields are around $\mu_0 H_C$ = 15 mT and the remanence amounts to $M_R/M_S \approx$ 25%. Both values are consistent with the corresponding normal incidence XMCD data (Figure 5). The similarity between the in-plane (SQUID) and out-of-plane (XMCD) hysteresis loops

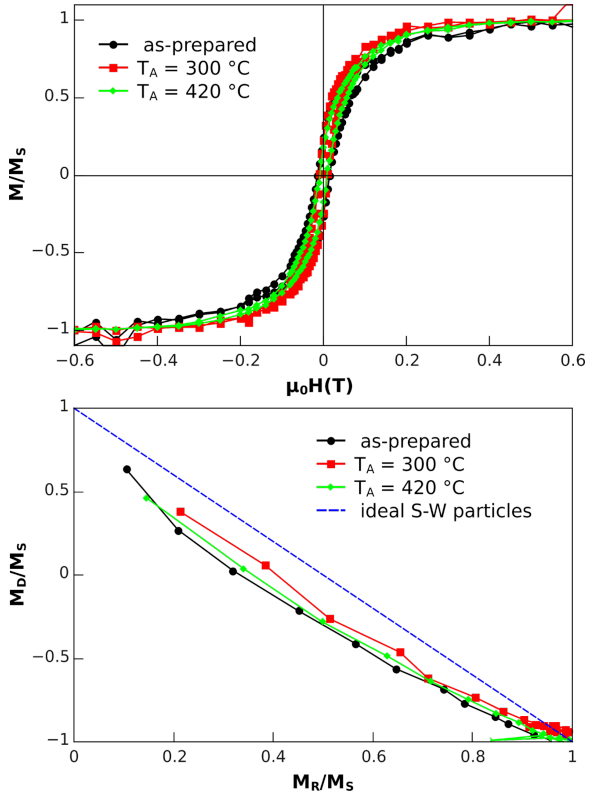

Figure 6: (a) In-plane hysteresis loops measured by SQUID magnetometry at T = 29 K, i.e., close to the compensation temperature of the diamagnetic MgO substrate and the paramagnetic Pt(111) film on top. In (b), the Henkel plots for three annealing steps are presented. The data of the as-prepared state was taken from [11]. Details are discussed in the text.

suggests that the Co NPs on Pt(111) are essentially magnetically isotropic and thus posses little MAE. Such finding confirms that CoPt alloys with high MAE have not been formed by the annealing of Co NPs on Pt(111). Additionally, DC-demagnetization (DCD) and isothermal remnant magnetization (IRM) [41,42] were measured for identical external magnetic fields, and the remnant magnetizations after DCD (M_D) and IRM (M_R) yielded the so-called Henkel plot [43] shown in Figure 6b. From this plot additional information relating to the possible magnetic interaction among NPs can be obtained. In the case of non-interacting ideal Stoner–Wohlfarth (S–W) NPs the corresponding Henkel plot is linear with a slope of −2, indicated by the dashed line in Figure 6b. Recently, we have shown that this linear behaviour is obtained for Co NPs on Si/SiO_2 substrates at T = 10 K with interparticle distances comparable to those in the present samples [11]. The experimental curves for different annealing temperatures closely resemble each other and all are found to be near to the Stoner–Wohlfarth line. The small deviation at intermediate demagnetization fields can be understood as the effect of thermal fluctuation at T = 29 K [41]. Such a finding implies that there is no significant dipolar or exchange coupling between neighbouring magnetic entities, and the annealing does not lead to agglomeration of Co atoms, although significant diffusion of Co atoms is expected.

HRTEM of Co NPs on Pt(100) films

Since the CoPt phases with high MAE were only formed by annealing on epitaxial Pt(100) films, we concentrated our HRTEM investigations on this system. For this study a MgO(100) substrate was used and the Pt film was deposited at 600 °C. Before the TEM investigation a protective layer of SiO_2 was deposited to prevent NP oxidation. TEM samples were prepared for cross section imaging by standard techniques, namely mechanical grinding and polishing followed by low angle Ar^+-ion etching. Bright-field TEM and aberration corrected HRTEM images were taken on a FEI Titan TEM equipped with a C_s imaging corrector. Scanning TEM and energy dispersive X-ray spectra (EDX) were acquired on a FEI Titan equipped with an HAADF-STEM detector and EDAX SiLi X-ray detector.

Typical bright field TEM images in the as-prepared state (T_A = 250 °C) and after annealing at 400 °C are shown in Figure 7. Apart from the MgO substrate and the Pt(100) film, the protective layer of SiO_2 is also visible. In the as-prepared state an isolated Co particle could be identified, as indicated by the red circle in the centre of the image. After annealing at 400 °C, however, particles could no longer be detected on the Pt film. This finding was confirmed on three samples at annealing temperatures of 400 °C and above.

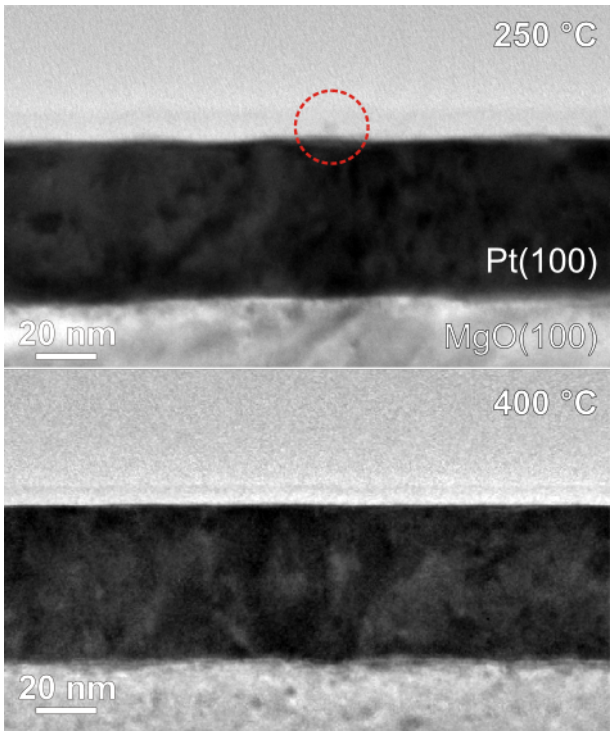

Figure 7: Bright field TEM images of Co NPs on Pt(100) films after annealing at T_A = 250 °C (as-prepared state) and T_A = 400 °C.

Additionally, HRTEM investigations were performed for Co NPs annealed at 500 °C, as shown in Figure 8. The structure indicated by the arrows clearly demonstrates alloy formation

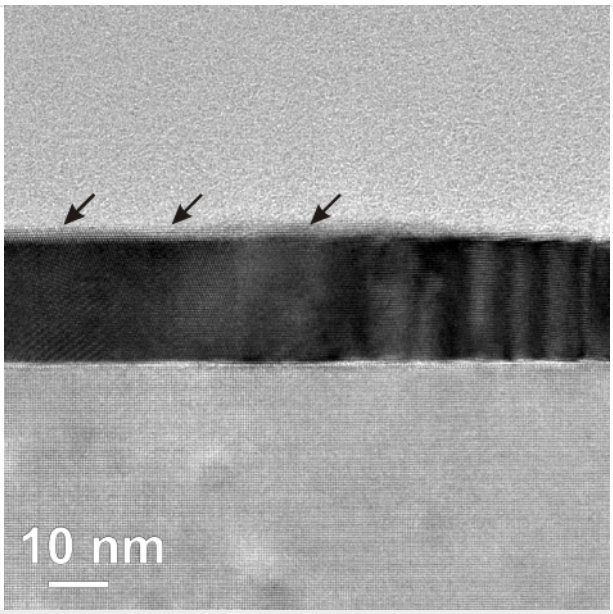

Figure 8: HRTEM image of annealed Co NPs on Pt(100) film after T_A = 500 °C for 30 min. The arrows indicate a thin surface layer of Pt-rich Co_xPt_{1-x} alloy on top of the Pt (seen by the weaker absorption contrast). Note that this sample has not been covered by any protective layer.

along the Pt surface. Such structures have typical thickness of 2–3 nm and lateral spread of 30–40 nm. The lighter contrast of such structures indicates that their constituents contain elements with lower atomic number than Pt. This result suggests that the observed structures are local alloys formed by lateral diffusion of Co atoms from the originally spherical Co NPs and simultaneous alloying with the Pt film underneath. Assuming the 7 nm Co NPs are completely transformed into the $Co_{50}Pt_{50}$ phase, the resulting volume of the alloy is expected to be about 300 nm^3 per Co NP. This estimated volume is far too low to account for the observed dimensions of the alloy structure revealed by HRTEM. Thus, the formation of a much more Pt-rich phase is suggested by these images. This conclusion is also consistent with the magnetic investigations indicating that, after annealing above 400 °C on Pt(100) films, the MAE decreases and ratio of orbital-to-spin moment approaches the value of a disordered Pt-rich Co_xPt_{1-x} alloy.

Although only a chemically disordered Co_xPt_{1-x} alloy is observed in this sample, an important feature of such a local alloying process can be recognized: The alloy formed at the surface has the same crystalline orientation as the Pt film underneath, as shown in Figure 8. Such an epitaxial relation is potentially very useful for the alignment of the magnetic easy axis if the local alloy has high magneto-crystalline anisotropy energy.

The formation of local alloys is further confirmed by scanning TEM analysis with EDX on the same sample as in Figure 8. The left panel of Figure 9 shows an overview image of the sample, where the bright stripe corresponds to the Pt thin film due to the elemental contrast (contrast scales with Z^2) of the HAADF-STEM detector. Locally resolved EDX-STEM analysis (1 nm scan width, beam diameter ~0.5 nm) was performed in the area indicated by the red box, and the corresponding Pt, Co and O elemental maps are shown on the right. It is evident from the Co elemental map that the Co atoms are distributed along the Pt surface, giving the direct proof of Co surface diffusion. The large agglomeration with higher Co concentration in the center likely corresponds to the initial position of one Co NP. A combined elemental map is also given by mapping Pt, Co, O signals to red, green and blue channels, respectively. Apart from the Pt film (red region) and the residual of the Co NP (green island in the center), the yellow region at the film surface consists of both, Co and Pt. This can be interpreted as the region of alloy formation. It is worthwhile noting that a small concentration of oxygen can also be identified, which essentially follows the distribution of Co atoms. Since this sample has not been covered by any protective layer due to the requirements of the EDX-STEM analysis, oxidation of Co is expected. The EDX-STEM analysis is an additional confirmation of the lateral spread of Co atoms.

Conclusion

We investigated the thermally driven diffusion and formation of local alloys starting from self-organized metallic Co NPs deposited on top of Pt(100) and Pt(111) films. For this purpose

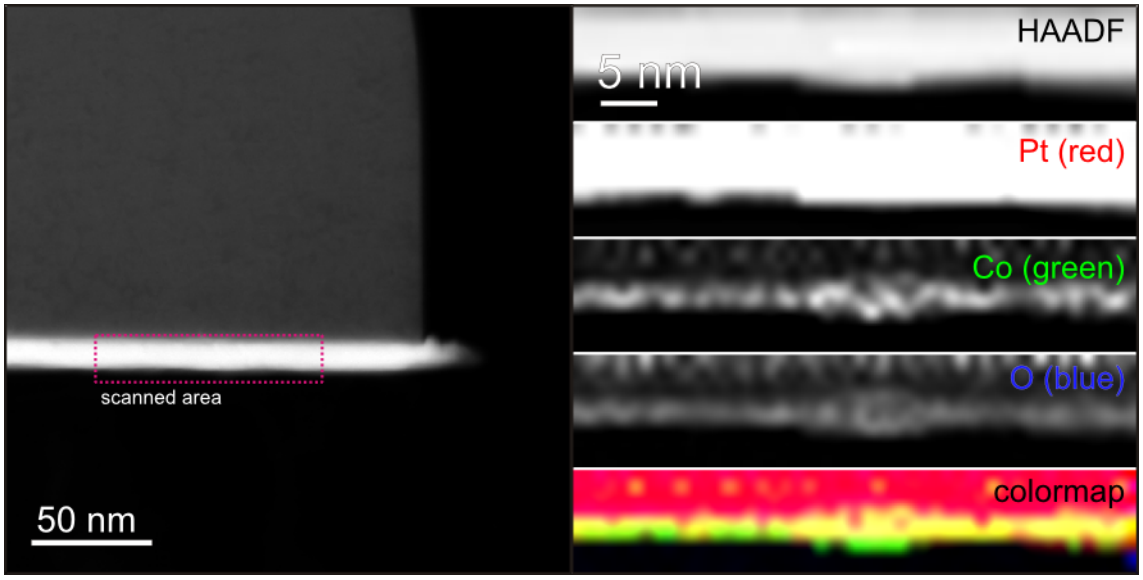

Figure 9: The left image shows the high angle annular dark-field (HAADF) image of the sample shown in Figure 8 using scanning TEM. EDX scanning TEM analysis of the selected area is shown on the right for Pt, Co, and O. A color map is reconstructed by using Pt as red color channel, Co as green color channel, and O as blue color channel. The yellow region at the film surface consists of both, Co and Pt and, thus, indicates alloy formation.

Pt films with (100) and (111) orientations were prepared on MgO(100) and STO(100) substrates by pulsed laser deposition. When deposited at elevated temperature (600 °C and above) epitaxial growth was achieved on STO(100) and MgO(100) with micron-sized atomically flat islands. When the deposition temperature was held at ambient temperature the Pt films exhibited a (111) structure with a lateral grain size of 20–30 nm as estimated by SEM. On these two types of films metallic Co particles (diameter 7 nm) were prepared by a micellar approach and reactive plasma etching, resulting in interparticle distances of about 100 nm. These well separated NPs serve here as local Co reservoirs on the nanoscale. By annealing experiments at various temperatures up to 500 °C, the alloy formation was characterized by various techniques (SEM, AFM, TEM, XPS, XMCD and SQUID magnetometry). All annealing experiments were performed in the pure metallic state, thus excluding any effects of (partial) oxidation of Co NPs and Pt films. In a first survey of local alloy formation we investigated the remaining Co particle height on Pt(111) films by AFM after different annealing steps. Here, a decreasing particle diameter, from 7 nm to 6 nm, was observed after annealing at T_A = 500 °C for 30 min. This loss of Co material, however, is attributed to diffusion of Co atoms into the subjacent Pt film, as suggested by XPS.

Since the magnetism of metallic Co and various CoPt alloys is known to change strongly due to the huge variations of MAE, and sufficient sensitivity is guaranteed compared to standard structure investigations (e.g., XRD), we investigated the magnetic properties by XMCD and SQUID magnetometry on both Pt(100) and Pt(111) films. On the latter, annealing led to a decreasing ratio of orbital-to-effective spin moment μ_L/μ_S^{eff}. Moreover, no drastic changes of the coercive field were found perpendicular to the film plane. Additional in-plane measurements by SQUID magnetometry suggest that the shrinking NPs essentially remain in a low anisotropy phase, presumably as pure Co NPs on the surface and Co atoms diffusing along grain boundaries facing a Pt-rich environment. Moreover, magnetic coupling of NPs can be excluded as shown by Henkel plots.

On the Pt(100) epitaxial films a completely different behavior has been observed up to intermediate annealing temperature T_A = 380 °C. In this regime, both μ_L/μ_S^{eff} and the coercive field rise to values exceeding the expectations for pure Co NPs. This finding indicates formation of local Co_xPt_{1-x} alloys. The exact phase, however, cannot be determined on the basis of our data. At higher T_A the magnetic indicators μ_L/μ_S^{eff} and H_C start decreasing, probably matching the experiments on the Pt(111) film at slightly higher T_A values. The local distribution of Co atoms after annealing at T_A = 500 °C was imaged by HRTEM and EDX-STEM. At this temperature the observed volume of the Co–Pt solid state reaction is much larger than the initial volume of Co NPs. Although a quantitative statement is not possible here, we can conclude that a Pt-rich Co_xPt_{1-x} phase has been formed.

The results above lead to the conclusions displayed in Figure 10 for the two systems under investigation. Annealing of Co NPs on Pt(111) films gives rise to surface diffusion of Co atoms. The microstructure of the film consisting of rather small grains (20–30 nm), however, lets the diffusing atoms easily find grain boundaries in the Pt film. It is well-known that the grain boundaries act as fast diffusion channels. Thus the grain boundaries in the Pt(111) film effectively remove Co atoms from the surface. The limited Co surface concentration implies that only disordered Co_xPt_{1-x} phases with low MAE can be formed in the bulk. As a result, the film microstructure hinders the formation of ordered CoPt alloy with high MAE.

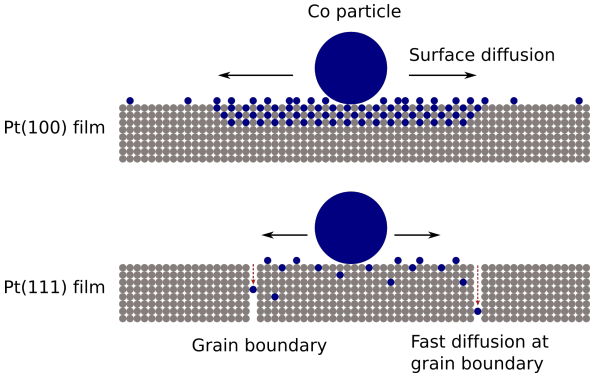

Figure 10: Proposed model of local alloying and diffusion of Co NPs on Pt films. Details are discussed in the text.

On epitaxial Pt(100) films with micron-sized islands having high structural quality, diffusion along grain boundaries plays a minor role. Consequently, a higher concentration of Co surface atoms can be established in the vicinity of the as-prepared Co NPs, and alloying spreading from the initial NP location becomes possible. At intermediate T_A the observations strongly suggest a phase with enhanced MAE, as indicated in Figure 10. However, for the chosen T_A and 30 min annealing time, the detailed composition of this phase cannot unequivocally be determined. Annealing at higher temperature leads to further diffusion of Co into the Pt film. Due to the locally reduced Co concentration, Pt-rich alloys are formed. Nevertheless, the epitaxial orientation of the alloyed region can be clearly identified.

The above findings motivate further investigations at intermediate annealing temperatures for longer periods of time. Under these conditions a local alloy close to $Co_{50}Pt_{50}$ with high MAE

may form. Additionally, the epitaxial relation to the Pt(100) film underneath could serve as a template to completely align the easy axis of magnetization of the alloy phase perpendicular to the sample plane. Such experiments are currently under way.

Acknowledgements

We would like to thank our former and current students Stefan Nau (Univ. Basel), Dr. Moritz Trautvetter and Felix Häring for the preparation of Pt films. We acknowledge Prof. Dr. Paul Walther for access to the SEM and Sabine Grötzinger for TEM sample preparation. We are grateful to Dr. B. Rellinghaus of IFW Dresden for granting access to the EDX-STEM TEM system. Beamline support by Dr. Thorsten Kachel and Helmut Pfau at beamline PM-3 of Bessy II synchrotron facility at the Helmholtz Center Berlin, Germany is gratefully acknowledged. This work has been supported by the Deutsche Forschungsgemeinschaft (DFG) through SFB 569 and the Baden-Württemberg Stiftung through Kompetenznetz Funktionelle Nanostrukturen.

References

1. Schmid, G., Ed. *Nanoparticles;* Wiley-VCH: Weinheim, 2004. doi:10.1002/3527602399
2. Brèchignac, C.; Houdy, Ph.; Lahmani, M., Eds. *Nanomaterials and Nanochemistry;* Springer: Berlin, Heidelberg, New York, 2007.
3. Lu, A.-H.; Salabas, E. L.; Schüth, F. *Angew. Chem., Int. Ed.* **2007,** *46,* 1222. doi:10.1002/anie.200602866
4. Goesmann, H.; Feldmann, C. *Angew. Chem., Int. Ed.* **2010,** *49,* 1362. doi:10.1002/anie.200903053
5. Köhler, M.; Fritzsche, W. *Nanotechnology: An Introduction to Nanostructuring Techniques;* Wiley-VCH: Weinheim, 2007.
6. Kästle, G.; Boyen, H.-G.; Weigl, F.; Lengl, G.; Herzog, T.; Ziemann, P.; Riethmüller, S.; Mayer, O.; Hartmann, C.; Spatz, J. P.; Möller, M.; Ozawa, M.; Banhart, F.; Garnier, M. G.; Oelhafen, P. *Adv. Funct. Mater.* **2003,** *13,* 853. doi:10.1002/adfm.200304332
7. Krishnamoorthy, S.; Hinderling, C.; Heinzelmann, H. *Mater. Today* **2006,** *9,* 40. doi:10.1016/S1369-7021(06)71621-2
8. Shevchenko, E. V.; Talapin, D. V.; Rogach, A. L.; Kornowski, A.; Haase, M.; Weller, H. *J. Am. Chem. Soc.* **2002,** *124,* 11480. doi:10.1021/ja025976l
9. Sun, S.; Murray, C. B.; Weller, D.; Folks, L.; Moser, A. *Science* **2000,** *287,* 1989. doi:10.1126/science.287.5460.1989
10. Ethirajan, A.; Wiedwald, U.; Boyen, H.-G.; Kern, B.; Han, L.; Klimmer, A.; Weigl, F.; Kästle, G.; Ziemann, P.; Fauth, K.; Cai, J.; Behm, R. J.; Romanyuk, A.; Oelhafen, P.; Walther, P.; Biskupek, J.; Kaiser, U. *Adv. Mater.* **2007,** *19,* 406. doi:10.1002/adma.200601759
11. Wiedwald, U.; Han, L.; Biskupek, J.; Kaiser, U.; Ziemann, P. *Beilstein J. Nanotechnol.* **2010,** *1,* 24. doi:10.3762/bjnano.1.5
12. Honolka, J.; Lee, T. Y.; Kuhnke, K.; Enders, A.; Skomski, R.; Bornemann, S.; Mankovsky, S.; Minar, J.; Staunton, J.; Ebert, H.; Hessler, M.; Fauth, K.; Schütz, G.; Buchsbaum, A.; Schmid, M.; Varga, P.; Kern, K. *Phys. Rev. Lett.* **2009,** *102,* 067207. doi:10.1103/PhysRevLett.102.067207
13. Li, Y.; Somorjai, G. A. *Nano Lett.* **2010,** *10,* 2289. doi:10.1021/nl101807g
14. Chen, Y. J.; Hwang, E. J.; Shem, C. S. *J. Appl. Phys.* **2008,** *103,* 07B516. doi:10.1063/1.2836409
15. Bruno, P. *Phys. Rev. B* **1989,** *39,* 865. doi:10.1103/PhysRevB.39.865
16. Grange, W.; Galanakis, I.; Alouani, M.; Maret, M.; Kappler, J.-P.; Rogalev, A. *Phys. Rev. B* **2000,** *62,* 1157. doi:10.1103/PhysRevB.62.1157
17. Grange, W.; Maret, M.; Kappler, J.-P.; Vogel, J.; Fontaine, A.; Pétroff, F.; Krill, G.; Rogalev, A.; Goulon, J.; Finazzi, M.; Brookes, N. B. *Phys. Rev. B* **1998,** *58,* 6298. doi:10.1103/PhysRevB.58.6298
18. McIntyre, P. C.; Maggiore, C. J.; Nastasi, M. *Acta Mater.* **1997,** *45,* 869. doi:10.1016/S1359-6454(96)00182-6
19. Xu, X. M.; Liu, J.; Yuan, Z.; Weaver, J.; Chen, C. L.; Li, Y. R.; Gao, H.; Shi, N. *Appl. Phys. Lett.* **2008,** *92,* 102102. doi:10.1063/1.2890844
20. Balestrino, G.; Martellucci, S.; Medaglia, P. G.; Paoletti, A.; Tebano, A.; Tucciarone, A. *Microsyst. Technol.* **1999,** *6,* 37. doi:10.1007/s005420050172
21. Scavia, G.; Agostinelli, E.; Laureti, S.; Varvaro, G.; Paci, B.; Generosi, A.; Rossi Albertini, V.; Kaciulis, S.; Mezzi, A. *J. Phys. Chem. B* **2006,** *110,* 5529. doi:10.1021/jp0554644
22. Krieger, M.; Plettl, A.; Steiner, R.; Boyen, H.-G.; Ziemann, P. *Appl. Phys. A* **2004,** *78,* 327. doi:10.1007/s00339-003-2353-8
23. Trautvetter, M.; Wiedwald, U.; Paul, H.; Minkow, A.; Ziemann, P. *Appl. Phys. A* **2011,** *102,* 725. doi:10.1007/s00339-010-5972-x
24. Bansmann, J.; Kielbassa, S.; Hoster, H.; Weigl, F.; Boyen, H. G.; Wiedwald, U.; Ziemann, P.; Behm, R. J. *Langmuir* **2007,** *23,* 10150. doi:10.1021/la7012304
25. Boyen, H.-G.; Kästle, G.; Zürn, K.; Herzog, T.; Weigl, F.; Ziemann, P.; Mayer, O.; Jerome, C.; Spatz, J. P.; Möller, M.; Garnier, M. G.; Oelhafen, P. *Adv. Funct. Mater.* **2003,** *13,* 359. doi:10.1002/adfm.200304319
26. Kleibert, A.; Bulut, F.; Gebhardt, R. K.; Rosellen, W.; Sudfeld, D.; Passig, J.; Bansmann, J.; Meiwes-Broer, K. H.; Getzlaff, M. *J. Phys.: Condens. Matter* **2008,** *20,* 445005. doi:10.1088/0953-8984/20/44/445005
27. Gries, W. H. *Surf. Interface Anal.* **1996,** *24,* 38. doi:10.1002/(SICI)1096-9918(199601)24:1<38::AID-SIA84>3.0.CO;2-H
28. Chen, C. T.; Idzerda, Y. U.; Lin, H.-J.; Smith, N. V.; Meigs, G.; Chaban, E.; Ho, G. H.; Pellegrin, E.; Sette, F. *Phys. Rev. Lett.* **1995,** *75,* 152. doi:10.1103/PhysRevLett.75.152
29. Fauth, K. *Appl. Phys. Lett.* **2004,** *85,* 3271. doi:10.1063/1.1804600
30. Goering, E.; Fuss, A.; Weber, W.; Will, J.; Schütz, G. *J. Appl. Phys.* **2000,** *88,* 5920. doi:10.1063/1.1308095
31. Galanakis, I.; Alouani, M.; Dreyssé, H. *J. Magn. Magn. Mater.* **2002,** *27,* 242–245. doi:10.1016/S0304-8853(01)01179-9
32. O'Brien, W. L.; Tonner, B. P. *Phys. Rev. B* **1994,** *50,* 12672. doi:10.1103/PhysRevB.50.12672
33. Gambardella, P.; Rusponi, S.; Veronese, M.; Dhesi, S. S.; Grazioli, C.; Dallmeyer, A.; Cabria, I.; Zeller, R.; Dederichs, P. H.; Kern, K.; Carbone, C.; Brune, H. *Science* **2003,** *300,* 1130. doi:10.1126/science.1082857
34. Zeper, W. B.; van Kesteren, H. W.; Jacobs, B. A. J.; Spruit, J. H. M.; Garcia, P. F. *J. Appl. Phys.* **1991,** *70,* 2264. doi:10.1063/1.349419
35. Pan, M.; He, K.; Zhang, L.; Jia, J.; Xue, Q.; Kim, W.; Qiu, Z. Q. *J. Vac. Sci. Technol., A* **2005,** *23,* 790. doi:10.1116/1.1885025
36. Ferrer, S.; Alvarez, J.; Lundgren, E.; Torrelles, X.; Fajardo, P.; Boscherini, F. *Phys. Rev. B* **1997,** *56,* 9848. doi:10.1103/PhysRevB.56.9848
37. Shapiro, A. L.; Rooney, P. W.; Tran, M. Q.; Hellman, F.; Ring, K. M.; Kavanagh, K. L.; Rellinghaus, B.; Weller, D. *Phys. Rev. B* **1999,** *60,* 12826. doi:10.1103/PhysRevB.60.12826

38. Boeglin, C.; Carriere, B.; Deville, J. P.; Heackmann, O.; Leroux, C.; Panissod, P. *Surf. Sci.* **1989,** *211–212,* 767. doi:10.1016/0039-6028(89)90839-X
39. Wiedwald, U.; Fauth, K.; Heßler, M.; Boyen, H.-G.; Weigl, F.; Hilgendorff, M.; Giersig, M.; Schütz, G.; Ziemann, P.; Farle, M. *ChemPhysChem* **2005,** *6,* 2522. doi:10.1002/cphc.200500148
40. Marzke, R. F.; Glaunsinger, W. S.; Bayard, M. *Solid State Commun.* **1976,** *18,* 1025. doi:10.1016/0038-1098(76)91231-X
41. Garcia-Otero, J.; Porto, M.; Rivas, J. *J. Appl. Phys.* **2000,** *87,* 7376. doi:10.1063/1.372996
42. Harrell, J. W.; Wang, S.; Nikles, D. E.; Chen, M. *Appl. Phys. Lett.* **2001,** *79,* 4393. doi:10.1063/1.1427751
43. Henkel, O. *Phys. Status Solidi* **1964,** *7,* 919. doi:10.1002/pssb.19640070320

License and Terms

Beilstein Journal of Nanotechnology

Inorganic–organic hybrid materials through post-synthesis modification: Impact of the treatment with azides on the mesopore structure

Miriam Keppeler[1], Jürgen Holzbock[1], Johanna Akbarzadeh[2], Herwig Peterlik[2] and Nicola Hüsing[*1,3]

Full Research Paper

Open Access

Address:
[1]Inorganic Chemistry I, Ulm University, Albert-Einstein Allee 11, D-89081 Ulm, Germany, [2]Faculty of Physics, University of Vienna, Strudlhofgasse 4, A-1090 Vienna, Austria, and [3]Materials Chemistry, Paris-Lodron University Salzburg, Hellbrunner Str. 34, A-5020 Salzburg, Austria

Email:
Nicola Hüsing* - nicola.huesing@sbg.ac.at

* Corresponding author

Keywords:
inorganic–organic hybrid materials; mesoporous materials; nucleophilic substitution; silica; sol–gel chemistry

Beilstein J. Nanotechnol. **2011,** *2,* 486–498.
doi:10.3762/bjnano.2.52

Received: 18 April 2011
Accepted: 13 July 2011
Published: 26 August 2011

This article is part of the Thematic Series "Organic–inorganic nanosystems".

Guest Editor: P. Ziemann

Abstract

Hybrid, hierarchically organized, monolithic silica gels, comprising periodically arranged mesopores and a cellular macroscopic network, have been prepared through a co-condensation reaction of tetrakis(2-hydroxyethyl)orthosilicate with chloromethyl-trimethoxysilane or 3-(chloropropyl)-triethoxysilane. Subsequent conversion of the chloro groups into azido groups, by nucleophilic substitution with NaN_3 in *N*,*N*-dimethylformamide, was conducted upon preservation of the monolithic structure. However, treatment with NaN_3 had a strong influence on the structure in the mesoporous regime, with changes such as an increase of mesopore diameter, pore volume and lattice constants, as well as a concomitant decrease of the pore wall thickness, as confirmed by small angle X-ray scattering, transmission electron microscopy, and nitrogen sorption analysis. Similar effects were observed for unmodified silica gels by simple ageing in azide-containing media, whether a relatively small or a sterically demanding counter ion (Na^+ or $(H_3C)_4N^+$) was used. The structural modification did not seem to depend greatly on whether an organic aprotic solvent (*N*,*N*-dimethylformamide, 1,1,3,3-tetramethylurea, 1,3-dimethyl-2-imidazolidinone) or a protic solvent that can form hydrogen bonds, such as water, was used.

Introduction

Inorganic–organic hybrid materials with tailored porosity on several length scales are of interest for a variety of applications, such as separation, adsorption, catalysis, energy storage, etc., due to the benefits arising from each pore size regime, e.g., rapid mass transport through macropores combined with selectivity provided by meso- or micropores. This is especially true

for materials with uniform pore size distributions in the mesoporous (2–50 nm) and/or macroporous regime (>50 nm) [1-3].

A powerful tool in the preparation of stable, mesoscopically organized materials that are characterized by narrow mesopore size distributions, high specific surface areas and large pore volumes, is the application of cooperative self-assembly processes between supramolecular aggregates of organic molecules, oligomers or polymers and inorganic species such as alkoxysilanes for silica-based materials [4-12]. Since the first presentation by Kresge and Beck in 1992, these so-called M41S-materials have attracted great attention and their formation mechanism as well as the parameters influencing the textural properties have been well investigated [4,5]. It is well-known that the manipulation of the dimensions and the state of aggregation of the supramolecular aggregates will directly influence the structural properties of the resulting inorganic porous material, and research efforts are devoted to the control of the structural properties through the synthesis conditions. For ordered mesoporous materials, whose syntheses are based on block copolymers such ethylene oxide $(EO)_x$–propylene oxide $(PO)_y$–ethylene oxide $(EO)_x$, this can be achieved by variation of the length of the EO or PO blocks, by increasing the synthesis temperature or by the addition of inorganic salts [6,9,13]. Currently, progress in the synthesis protocols even allows for the preparation of different macroscopic morphologies such as powders, coatings, fibres, or monoliths.

Monoliths are of special interest for functional devices, e.g., as chromatography columns, or catalytic reactors. However, to allow mass transport with a minimal pressure build-up the presence of a macroporous network is indispensable. Such a second level of porosity in mesoporous silica monoliths can be introduced by several synthetic approaches: Dual templating with sacrificial templates, phase separation processes (e.g., based on polymers), or the application of diol/polyol-modified silanes [1-3,14-18].

Nakanishi and Lindén relied on polymerization-induced phase separation during sol–gel processing to form monolithic bodies with a hierarchical organisation of the pore structure at the meso- and macroscopic length scale [16,17]. The materials obtained were characterized by interconnected porosity on several length scales. The macropore diameter was controlled through PEO–siloxane interactions, whereas the mesopore diameter was governed by the presence of the surfactant, e.g., cetyltrimethylammonium bromide or a poly(ethylene oxide)-based polymer. In our group, silicon diolates in the presence of surfactants were applied for the preparation of monolithic gels (silica and inorganic–organic hybrid networks) with a cellular network built up of macropores of about 2 μm diameter and periodically arranged mesopores of 7 nm [18]. Each of these strategies allows for a high level of control over macropore/mesopore size distribution, surface area, etc.

It is well known that ageing of silica gels in different environments or in hydrothermal conditions has a pronounced influence on the final gel structure [19,20]. Ageing at 100 °C in an autoclave yields mesoporous silica gels with larger pore sizes and pore volumes compared to gels aged in ethanol at room temperature due to promoted dissolution and reprecipitation processes [20]. Processes such as syneresis, Ostwald ripening, etc., are facilitated and accelerated with increasing temperature and pressure. The same is true for gels with periodically arranged mesopores or even mesostructured cellular foams [21].

Structural arrangements can be quite pronounced depending on the conditions of the post-treatment. One example is the so-called pseudomorphic transformation, in alkaline solutions and hydrothermal conditions, from amorphous mesoporous materials to well-organized mesoporous structures [22,23].

Many silica gels are functionalized by organic groups specific for their eventual applications. Typical examples are the hydrophobization with methyl or phenyl groups, and even functional groups such as polymerizable moieties or metal-coordinating groups can be introduced [24]. These groups are typically incorporated either by post-synthetic grafting processes or by co-condensation reactions of different alkoxysilanes. The impact of these synthesis steps on the final pore structure is quite well investigated [25]. In post-synthetic functionalization procedures, a porous matrix with the desired pore size, pore connectivity, surface area, etc., is prepared prior to the modification step and the organic moieties are made to react with the surface silanol groups in a second step. For this approach, it is assumed that structural changes are minimal [25]. For the co-condensation approach, in which tetraalkoxysilanes $[Si(OR)_4]$ are condensed to form an inorganic network in the presence of organically substituted tri-alkoxysilanes $[R'–Si(OR)_3]$, network formation and thus structural features such as pore size, connectivity, etc., are strongly influenced by the presence of the organosilane [25].

These organo-functionalized silica gels can be further modified by chemical reactions with more complex functional groups; recent examples include Cu(I)-catalyzed 1,3-dipolar cycloadditions, also termed Click reactions, on silica surfaces involving alkynes and azide functionalities [26-28]. Reviewing the literature on this topic reveals that most of the examples of postsynthesis surface chemical reactions are concerned with the successful chemical conversion, but the structure of the modified materials is in many cases not characterized in great detail.

In a recent work, we have shown that prior to the Click reaction, the conversion from chloro to azido functionalities in silica monoliths is possible, but that this reaction concomitantly occurs with major structural changes [29].

The present work focuses on the influence of these surface functionalization reactions on the structural properties of preformed silica gels. The first section describes the nucleophilic substitution of hierarchically organized SiO_2–$(CH_2)_{1,3}$–Cl gels to give the corresponding SiO_2–$(CH_2)_{1,3}$–N_3 gels in a saturated NaN_3/DMF solution, with special focus on the structural changes of the silica backbone. In a second section the influence of different solvents and counter ions is discussed for unmodified hierarchically organized SiO_2 gels as reference samples.

Results and Discussion

Nucleophilic substitution of chloro- by azido groups on the silica surface

Nucleophilic substitution of chloroalkyl-modified silica monoliths to azide-containing monoliths (SiO_2–$(CH_2)_{1,3}$–Cl → SiO_2–$(CH_2)_{1,3}$–N_3) was conducted in a saturated solution of NaN_3 in DMF on monolithic silica gels that had been treated with trimethylchlorosilane (Figure 1). During the course of this reaction, the macroscopic morphology of the monoliths was retained, and no significant influence on the macroporous network was observed. The gels had been treated with trimethylchlorosilane to remove reactive silanol groups and facilitate drying of the monoliths.

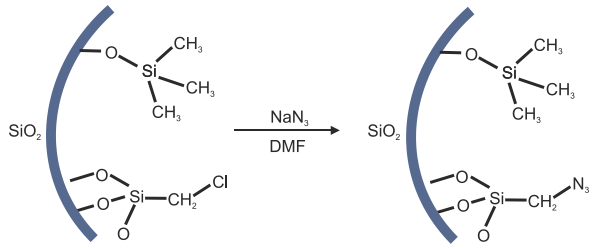

Figure 1: Schematic description of the nucleophilic substitution reaction for chloromethyl-modified silica pore surfaces.

Gels modified with chloromethyl groups (CMTMS) or chloropropyl groups (CPES) were subjected to the azide solutions. The number of azide groups per nm^2 was evaluated according to a previously published method and was found to be in the range of 0.7 nm^{-2} (3.0 mmol CMTMS), 1.2 nm^{-2} (4.5 mmol CMTMS), 1.3 nm^{-2} (6.0 mmol CMTMS) and 0.7 nm^{-2} (3.0 mmol CPES) at a reaction temperature of 60 °C [29]. The presence of the newly inserted azide functionalities was also confirmed by IR–ATR spectroscopy. This type of reaction has previously been reviewed for a variety of different silica surfaces, however, the influence of the reaction on the structural properties of the material has been mostly neglected [30].

This influence of the nucleophilic substitution on the porous structure of the meso/macroporous monoliths, with special emphasis on the long range hexagonal ordering of the mesopores, was evaluated by nitrogen sorption and small angle X-ray scattering (SAXS) analyses. Figure 2 shows the nitrogen adsorption/desorption isotherms at 77 K for modified silica gels before and after nucleophilic substitution (SiO_2–$(CH_2)_{1,3}$–Cl → SiO_2–$(CH_2)_{1,3}$–N_3). The isotherms for the chloroalkyl-containing precursor materials are of type IV with H2 hysteresis loops according to the classification of Sing et al. [31], whereas the same samples after conversion of the chlorides into azides display hysteresis loops of H1 type indicating a narrow distribution of pores. In addition, the isotherms for SiO_2–$(CH_2)_{1,3}$–N_3 exhibit stretching along the volume axis, adsorption and desorption isotherms display a sharper capillary condensation step and the relative pressure of the pore filling is shifted to larger values compared to the corresponding SiO_2–$(CH_2)_{1,3}$–Cl. These variations in the hysteresis loops indicate an increase in the pore diameter and still a narrow pore size distribution for SiO_2–$(CH_2)_{1,3}$–N_3.

The H2 type hysteresis loops obtained for SiO_2–$(CH_2)_{1,3}$–Cl suggest rather complex pore structures with interconnected pores of different size and shape, e.g., spherical mesopores interconnected by smaller windows or large pore channels with undulating walls are possible. The pore sizes calculated from the desorption branch of the isotherm, applying the Barrett–Joyner–Halenda (BJH) model, are in the range of 3.5–4.7 nm for all samples. However, for pore diameters smaller than 5 nm (in our case presumably given by the small interconnecting windows; see Table 1, $D_{BJH,Des}$) the relative pressure at which desorption occurs is strongly influenced by fluid cavitations and instability of the meniscus [32]. In addition, the BJH model is based on the Kelvin equation, which describes the relationship between the relative vapour pressure in equilibrium and the radius of curvature of the meniscus [33]. Since a stable fluid meniscus with a given radius of curvature cannot be guaranteed for the desorption process in all systems, and the risk of obtaining physically meaningless results exists, the adsorption branch was also used to calculate the pore size distribution. This is not the case for the azido-functionalized samples (SiO_2–$(CH_2)_{1,3}$–N_3) with pore sizes larger than 5.4 nm for all samples. Here, the calculation using the desorption isotherm is favoured, since desorption processes are thermodynamically more stable compared to the corresponding adsorption processes.

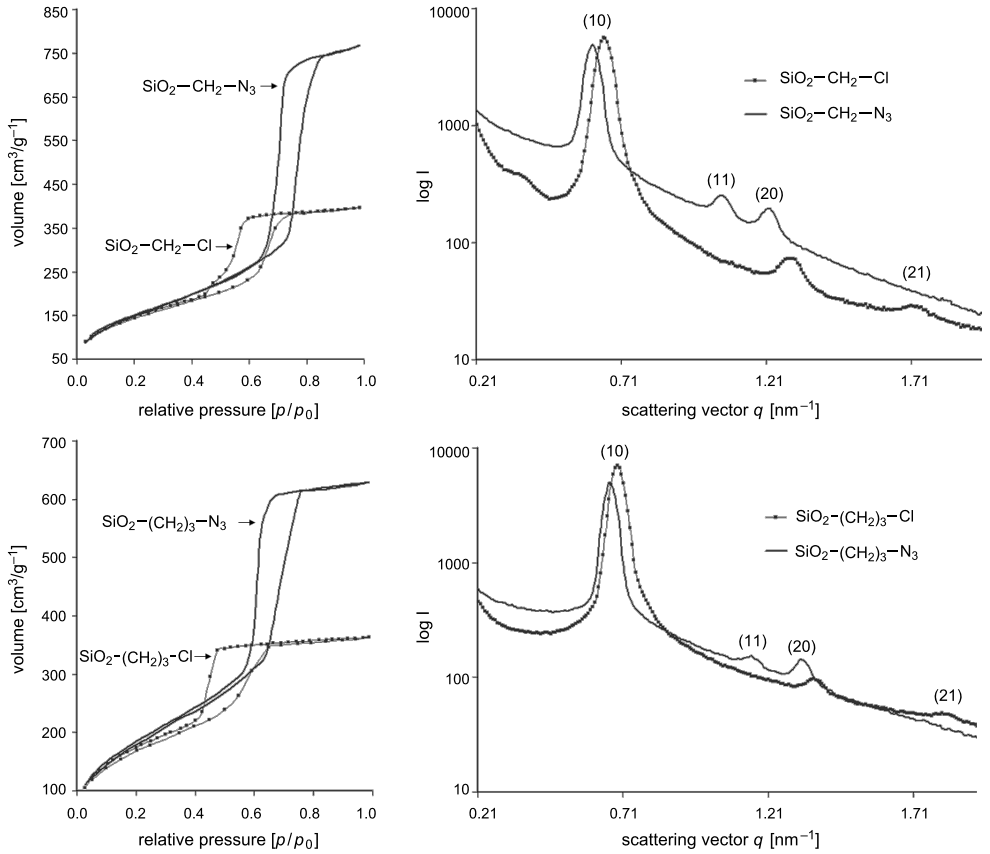

Figure 2: Nitrogen sorption isotherms (taken at 77 K, left) and SAXS patterns (right) of SiO_2–$(CH_2)_n$–Cl and SiO_2–$(CH_2)_n$–N_3 gels after nucleophilic substitution in a saturated DMF/NaN_3 solution at 60 °C. n = 1 (top): Prepared from a silica precursor solution containing 4.5 mmol CMTMS; n = 3 (bottom): Prepared from a silica precursor solution containing 3.0 mmol CPES.

Table 1 gives all pore sizes as calculated from the adsorption and desorption isotherms. As expected, the calculation from the adsorption isotherm led to larger pore diameters for all samples with differences in the desorption pore size in the range of 1.7 to 2.4 nm for the methyl-spacer samples (n = 1), and in the range of 1.0 to 1.3 nm for the propyl-spacer samples (n = 3). Regardless of which sorption branch was applied for the calculation, a significant enlargement in the mesopore diameter after nucleophilic substitution in the range of 2.7 to 3.7 nm for methyl-spacer samples and in the range of 1.5 to 1.9 nm for propyl-spacer samples was observed. For instance, the chloromethyl-modified sample (3.0 mmol CMTMS) showed a pore diameter $D_{BJH,Ads}$ of 5.54 nm prior to nucleophilic substitution and after conversion into the azides an increase to $D_{BJH,Ads}$ = 9.17 nm was detected. The larger amount of nitrogen adsorbed at relative pressures above p/p_0 = 0.3 indi-

Table 1: Structural characteristics of SiO_2–$(CH_2)_{1,3}$–Cl compared to corresponding SiO_2–$(CH_2)_{1,3}$–N_3, obtained from nitrogen sorption analysis at 77 K.

	S_{BET}[a] [m² g⁻¹]		C_{BET}		V_{max} [cm³ g⁻¹]		$D_{BJH,Des}$ [nm][b]		$D_{BJH,Ads}$ [nm][c]	
	SiO_2–Cl	SiO_2–N_3	SiO_2–Cl	SiO_2–N_3	SiO_2–Cl	SiO_2–N_3	SiO_2–Cl	SiO_2–N_3	SiO_2–Cl	SiO_2–N_3
3.0 mmol CMTMS	566	513	80.0	56.7	347.5	650.2	3.69	6.74	5.54	9.17
4.5 mmol CMTMS	529	556	64.7	66.7	397.2	768.2	4.68	7.34	6.36	9.12
6.0 mmol CMTMS	445	563	56.3	55.4	325.7	768.5	3.70	7.33	5.48	9.13
3.0 mmol CPES	611	664	74.8	55.7	363.0	630.0	3.50	5.37	4.82	6.34

[a]Calculated by using the Brunauer–Emmett–Teller (BET) model. [b]Calculated from the desorption isotherm by using the BJH model. [c]Calculated from the adsorption isotherm by using the BJH model.

cates a dramatic increase of the specific pore volumes (V_{max} and V_{meso}) after nucleophilic substitution, but relatively constant specific surface areas were observed from the pressure range p/p_0 = 0.05–0.30). V_{max} and V_{meso} followed the same trend and showed only slight deviations in their values, thus only V_{max} is discussed in the course of this work. The difference in V_{max} between samples before and after nucleophilic substitution was in the range of 300 to 440 $cm^3\ g^{-1}$ for methyl-spacer samples and in the range of 270 $cm^3\ g^{-1}$ for propyl-spacer samples (Table 1).

The decreasing *C*-value, indicative of the adsorbent–adsorbate interactions, for gels prepared from a silica-precursor solution containing 3.0–6.0 mmol CMTMS follows the trend expected for gels with increasing coverage of the silica surface with organic groups. For nitrogen sorption on non-modified silica materials, the C_{BET} values are typically in the range 80–150 [34].

Figure 2 also shows the SAXS patterns for the modified silica gels before and after nucleophilic substitution of the chlorides into azides (SiO_2–$(CH_2)_{1,3}$–Cl → SiO_2–$(CH_2)_{1,3}$–N_3). For all samples, higher order reflections were found, indicating long range ordering of the pore system. SiO_2–$(CH_2)_{1,3}$–N_3 exhibited the characteristic Bragg reflection sequence for a 2-D hexagonal ordering of $1 : 3^{1/2} : 2 : 7^{1/2}$… and the reflections were indexed to the (10)-, (11)- and (20)-crystallographic planes [35]. A comparison with SAXS patterns of the corresponding SiO_2–$(CH_2)_{1,3}$–Cl precursor material clearly indicates mesostructural changes during the process of nucleophilic substitution. Both, SiO_2–$(CH_2)_{1,3}$–Cl as well as SiO_2–$(CH_2)_{1,3}$–N_3 showed typical diffraction patterns for a 2-D hexagonal ordering of the pores. However, the relative intensities of the reflections were different for the chloroalkyl-modified silica gels compared to the corresponding azido-modified gels. The intensity of the (11)-reflection was reduced (almost to zero) compared to the corresponding azidoalkyl-modified silica gels. Furthermore, an additional higher order reflection was found for the chloroalkyl-modified precursor material that can be indexed to the (21)-crystallographic plane.

The differences in the reflection intensities before and after nucleophilic substitution (Figure 2) are attributed to the different form factors arising from differences in the respective pore wall thicknesses and pore diameters. One approach to describe these intensities is a two-phase model (pore and silica), where the form factor can be analytically solved (for more details see Supporting Information File 1 and [36]). This model has been previously used to determine the pore diameter and pore-wall thickness of surface functionalized silica gel monoliths [37].

Another approach is based on the reconstruction of the electron densities from a Fourier series and the appropriate choice of the phases [38,39]. This has been experimentally and theoretically used to model the electron density across the pore for modified and unmodified MCM-41 and SBA-15 materials [11,40] (for detailed information on SAXS data evaluation, see Supporting Information File 1).

The best solution for the three observed reflections in our case was −+−, which differs to the phase shift from −−++ for the first four coefficients for the SBA 15 material observed by Flodström et al. or −++− for the MCM 41 material [11,40]. This could be due to the variations in the synthesis conditions of the different materials.

As an example, in Figure 3, the electron density reconstructions are shown for the SiO_2–CH_2–Cl and SiO_2–CH_2–N_3 gels, with SiO_2–CH_2–Cl exhibiting a smaller pore with a steeper slope of

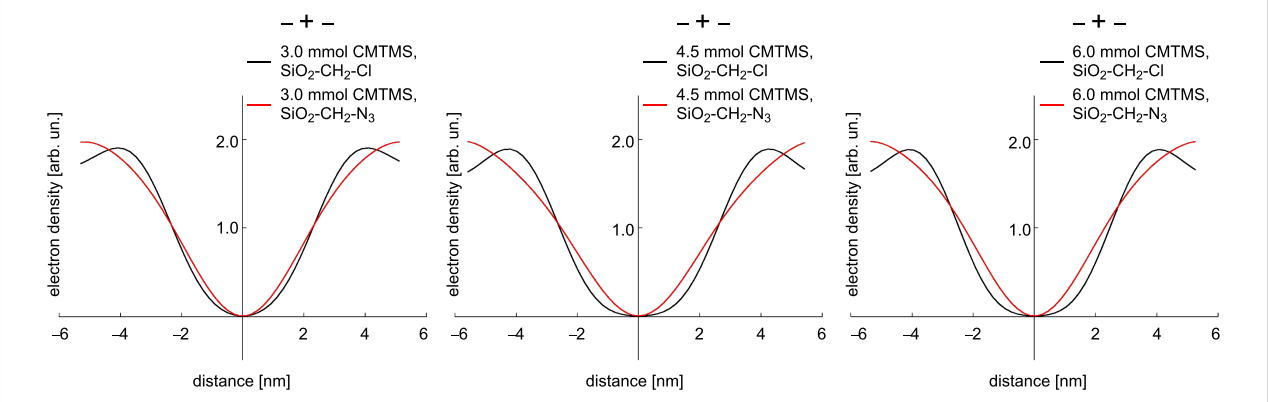

Figure 3: Electron density reconstructions for modified silica gels (SiO_2–CH_2–Cl and SiO_2–CH_2–N_3) that have been prepared from a silica precursor solution containing 3.0 (left), 4.5 (middle) and 6.0 (right) mmol CMTMS. The electron density of SiO_2–CH_2–Cl corresponds to a sharper interface, whereas the broader distribution of SiO_2–CH_2–N_3 indicates a higher surface roughness due to the nucleophilic substitution.

the electron densities, whereas the corresponding substituted gel (SiO_2–CH_2–N_3) has a broader distribution, which indicates a larger pore with a higher surface roughness.

One would expect the electron density to converge to a constant value within the silica phase. Unfortunately, due to the limited number of peaks available for the reconstruction, the resolution was limited [38,39]. A large constant region would require the sum of a large number of Fourier coefficients, i.e., a large number of diffraction peaks, which are not available for our type of materials. Thus this is an inevitable inherent weakness of the model.

The change in the ratio of the silica wall thickness to the pore diameter, during the nucleophilic substitution process, was also evidenced by nitrogen sorption analysis. An increase in pore diameter was observed (Table 1), while simultaneously a reduction of the pore wall thickness was detected for SiO_2–$(CH_2)_{1,3}$–N_3 compared to SiO_2–$(CH_2)_{1,3}$–Cl (Table 2).

In the SAXS experiments, this led to the striking appearance of the (11)-reflection and the disappearance of the (21)-reflection. However, whereas sorption analysis indicated a strong decrease of the pore wall thickness, this effect was much less pronounced for the SAXS measurements. One possible explanation could be an additional surface roughness of the pores, which is also in coincidence with the electron density reconstruction (Figure 3). The model description in SAXS (see Supporting Information File 1) as a two-phase material, i.e., cylindrical pores of identical radius embedded in a silica matrix, leads to the measurement of a mean radius and averages out any differences in the radii or effects from surface inhomogeneities or roughness along the length or cross section of the pore. The radius obtained from SAXS could then lie intermediate between the radius obtained in the BJH analysis, from the adsorption branch and that from the desorption branch, as shown in Figure 4. In the desorption branch, the BJH analysis is restricted, by the presence of small pores or surface roughness, to give the smallest pore size (Figure 4).

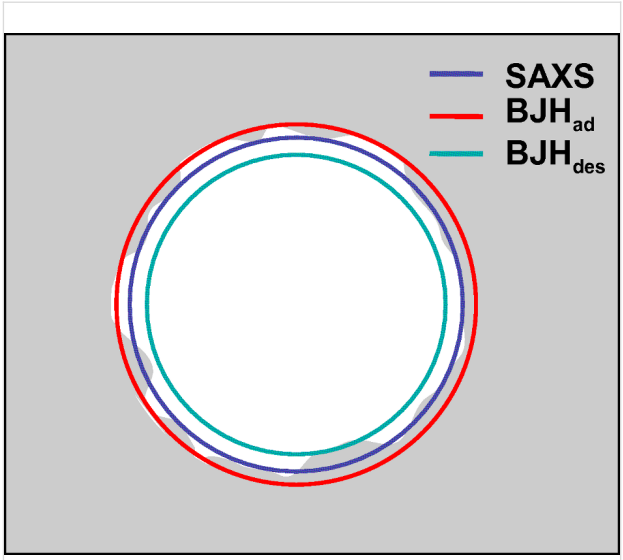

Figure 4: SAXS averages the surface inhomogeneities to a mean radius in the two-phase model and leads therefore to a slightly larger diameter than the nitrogen sorption analysis (desorption branch).

Not only did the reflection intensity change during nucleophilic substitution, but also the relative position of the scattering vector $q_{(hk)}$ shifted to smaller values (Table 3), indicating an increase of the repeating unit distance. For instance, the chloromethyl-modified sample (4.5 mmol CMTMS) showed a shift of the scattering vector $q_{(10)}$ from 0.65 to 0.61 nm^{-1} after conversion of the chlorides into the azides, corresponding to an increase of the $d_{(10)}$-spacing from 9.66 nm to 10.26 nm. The $d_{(10)}$-spacing was used to calculated the lattice constant, which was also found to increase during nucleophilic substitution (Table 3). For example, the chloromethyl-modified sample showed an increase in the lattice constant from 11.15 nm to 11.85 nm during nucleophilic substitution.

Table 2: Comparison of the structural characteristics of SiO_2–$(CH_2)_{1,3}$–Cl and the corresponding SiO_2–$(CH_2)_{1,3}$–N_3.

	mean pore diameter ± 0.3[a] [nm]		mean wall thickness ± 0.3[a] [nm]		t_{Des}[b] [nm]		t_{Ads}[c] [nm]	
	SiO_2–Cl	SiO_2–N_3	SiO_2–Cl	SiO_2–N_3	SiO_2–Cl	SiO_2–N_3	SiO_2–Cl	SiO_2–N_3
3.0 mmol CMTMS	6.60	7.85	4.00	3.15	6.92	4.22	5.07	1.79
4.5 mmol CMTMS	7.05	8.75	4.15	3.25	6.52	4.51	4.84	2.73
6.0 mmol CMTMS	6.65	8.10	4.05	3.15	7.02	3.87	5.24	2.07
3.0 mmol CPES	6.50	7.70	4.00	3.30	7.00	5.59	5.68	4.62

[a]Mean pore diameter and wall thickness calculated from the peak intensities using a two-phase model with an analytical approach. [b]Wall thickness, calculated by: Lattice constant a − $D_{BJH,Des}$. [c]Wall thickness, calculated by: Lattice parameter a − $D_{BJH,Ads}$.

Table 3: Structural properties of SiO_2–$(CH_2)_{1,3}$–Cl compared to corresponding SiO_2–$(CH_2)_{1,3}$–N_3 obtained from SAXS analysis.

	$q_{(10)}$[a] [nm^{-1}]		$d_{(10)}$[a] [nm]		a[b] [nm]	
	SiO_2–Cl	SiO_2–N_3	SiO_2–Cl	SiO_2–N_3	SiO_2–Cl	SiO_2–N_3
3.0 mmol CMTMS	0.69	0.66	9.17	9.51	10.58	10.98
4.5 mmol CMTMS	0.65	0.61	9.66	10.26	11.15	11.85
6.0 mmol CMTMS	0.68	0.65	9.26	9.72	10.69	11.23
3.0 mmol CPES	0.69	0.67	9.10	9.45	10.50	10.91

[a]Calculated from SAXS measurements, $q_{(10)} = 4\pi/\lambda \cdot \sin\Theta$, $d_{(10)}$ calculated by the Bragg equation. [b]Lattice constant, calculated by $2d_{(10)}/(3)^{1/2}$.

The structural parameters obtained from nitrogen sorption and SAXS analyses suggest a process of mesostructural changes during conversion of SiO_2–$(CH_2)_{1,3}$–Cl into the corresponding SiO_2–$(CH_2)_{1,3}$–N_3. Figure 5 shows schematically a hexagonally organized porous material with cell parameters a, wall thickness t, repeating unit distance d_{10} and pore diameter D as obtained from nitrogen sorption.

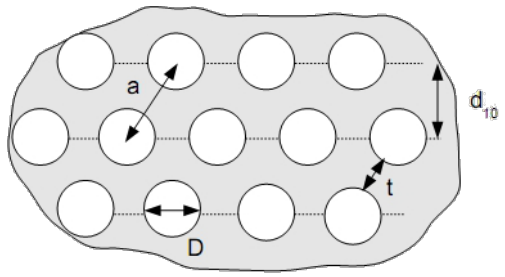

Figure 5: Schematic representation of a hexagonally organized pore system with the characteristic sizes. A similar arrangement is found for the samples by SAXS and transmission electron microscopy (TEM) analyses.

Based on the nitrogen sorption and SAXS analysis, the following trends were observed during nucleophilic substitution: The mesopore diameter and maximal pore volume drastically increased, while the lattice constant showed only a small enlargement with a simultaneous decrease in pore wall thickness. The ratio of pore wall thickness to pore diameter decreased to such an extent, that the new electron density (phase shift of Fourier coefficients) involved a significant change in the reflection intensity. We assume that the reduction in pore wall thickness with a simultaneous increase in pore diameter can not simply be explained by dissolution processes of silica, because the lattice constants also increased during the nucleophilic substitution. Simple ageing of unmodified mesoscopically organized silica gels in azide-containing media allows us to demonstrate that the observed effects are not due to the inserted azide-functionalities, which are covalently attached to the silica surface, but rather to an exposure of a mesostructured silica matrix to azide ions, as presented vide infra.

Ageing of unmodified silica gels in azide-containing media

From the results obtained above for the chloroalkyl-modified silica gels, the cause of the structural changes cannot be identified clearly and without ambiguity. Therefore, the reaction conditions were changed step by step to isolate the influence of temperature, solvent, anion-cation pair and solvent-azide compositions to identify the critical parameter. Pure (not organically modified) silica gels were kept for 3 d at 60 °C (identical conditions as for the nucleophilic substitution described above) in solutions of NaN_3 in different solvents ranging from *N*,*N*-dimethylformamide (DMF), 1,1,3,3-tetramethylurea (TMU), 1,3-dimethyl-2-imidazolidinone (DMI) to H_2O. Reference samples were kept for 3 d at 60 °C in the respective solvents without azide and pure silica gels were aged at that temperature. In addition, sodium azide was changed to tetramethylammoniumazide ($(H_3C)_4NN_3$, TMAA). All gels were aged, treated with trimethylchlorosilane and dried. The structural characteristics of untreated, reference and silica gels that were exposed to the different reaction conditions were again determined by nitrogen sorption and SAXS analyses. Note that the untreated silica, reference silica and azide-treated silica gels originated from the same monolithic silica piece, which was divided into three parts. Figure 6 shows the nitrogen adsorption/desorption isotherms taken at 77 K for gels treated in DMF and DMI; detailed information on gels in H_2O and TMU is given in Supporting Information File 1.

All isotherms are of type IV with H1 hysteresis loops according to the classification of Sing et al. [33]. The reference samples that were heat treated in the various solvents showed higher pore volumes compared to untreated silica gels, but this effect was clearly intensified by the addition of NaN_3, as demonstrated by the stretching of the hysteresis loops along the

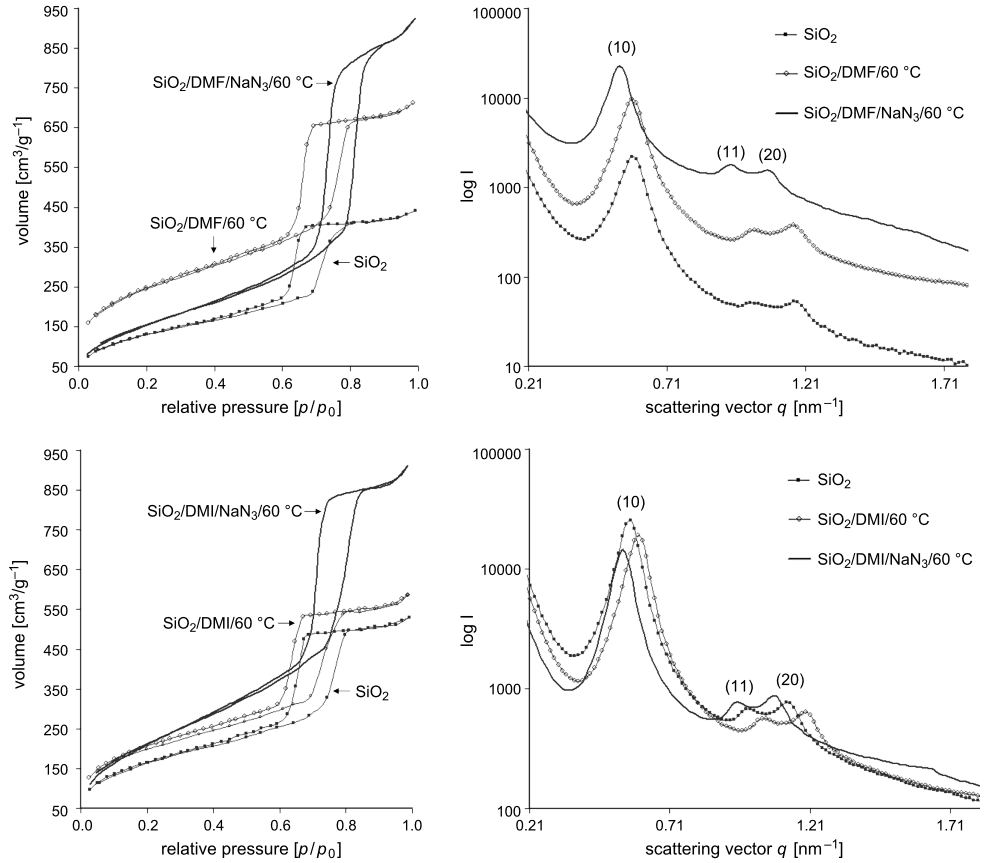

Figure 6: Nitrogen isotherms and SAXS patterns of untreated silica gels, reference silica gels (solvent/60 °C) and azide-treated silica gels (solvent/NaN_3/60 °C) in different solvents: DMF (top) and DMI (bottom).

volume axis. Furthermore, the addition of NaN_3 led to a shift of the relative pressure of the pore filling, by capillary condensation, to higher values. Pore diameters were significantly increased by the treatment with azide-containing solvents (Table 4). Differences in pore diameters for the various samples calculated from the adsorption isotherm in the BJH model were 4.05 nm (DMF/NaN_3); 4.21 nm (TMU/NaN_3); 2.20 nm (DMI/NaN_3) and 2.25 nm (H_2O/NaN_3). The analogous calculation

Table 4: Structural characteristics of untreated silica, reference silica (solvent/60 °C) and azide-treated silica gels (solvent/NaN_3/60 °C) from nitrogen sorption analysis at 77 K, solvents: DMF and DMI; azide: NaN_3 and TMAA.

	S_{BET}[a] [m² g⁻¹]	C_{BET}	V_{max} [cm³ g⁻¹]	$D_{BJH,Des}$[b] [nm]	$D_{BJH,Ads}$[c] [nm]
SiO_2	477	62.6	441.9	5.75	7.51
SiO_2/DMF	876	103.3	712.7	6.27	9.24
SiO_2/DMF/NaN_3	592	42.2	924.8	8.01	11.56
SiO_2	607	54.1	529.6	6.21	9.35
SiO_2/ DMI	712	110.6	586.1	5.73	7.54
SiO_2/DMI/NaN_3	803	47.6	913.0	7.34	11.55
SiO_2	627	62.0	554.4	6.23	9.21
SiO_2/DMF	906	93.0	759.4	6.74	9.18
SiO_2/DMF/TMAA	657	50.2	856.6	7.33	11.63

[a]Calculated in the BET model. [b]Calculated from the desorption isotherm in the BJH model. [c]Calculated from the adsorption isotherm in the BJH model.

Table 5: Structural properties as obtained from SAXS analysis of untreated silica, reference silica (solvent/60 °C) and azide-treated silica gels (solvent/NaN_3 or TMAA/60 °C), solvents: DMF and DMI.

	$q_{(10)}$[a] [nm^{-1}]	$d_{(10)}$[a] [nm]	a[b] [nm]	t_{Des}[c] [nm]	t_{Ads}[d] [nm]	mean pore diameter[e] ± 0.2 [nm]	mean wall thickness[e] ± 0.2 [nm]
SiO_2	0.59	10.73	12.39	6.68	4.92	8.60	3.80
SiO_2/DMF	0.58	10.77	12.44	6.16	3.19	8.52	3.98
SiO_2/DMF/NaN_3	0.54	11.68	13.49	5.40	1.85	10.05	3.40
SiO_2	0.56	11.13	12.85	6.53	3.39	8.60	4.20
SiO_2/ DMI	0.60	10.55	12.18	6.40	4.59	8.15	4.05
SiO_2/DMI/NaN_3	0.54	11.60	13.39	6.07	1.86	9.20	4.20
SiO_2	0.57	11.04	12.75	6.52	3.54	8.70	4.10
SiO_2/DMF	0.61	10.27	11.86	5.12	2.68	8.15	3.85
SiO_2/DMF/TMAA	0.55	11.33	13.08	5.75	1.45	9.75	3.55

[a]Calculated from SAXS measurements, $q_{(10)} = (4\pi/\lambda)\sin\Theta$, $d_{(10)}$ calculated by the Bragg equation. [b]Lattice constant, calculated by $2d_{(10)}/(3)^{1/2}$. [c]Wall thickness, calculated by: Lattice parameter a − $D_{BJH,Des}$. [d]Wall thickness, calculated by: Lattice parameter a − $D_{BJH,Ads}$. [e]Mean pore diameter and wall thickness calculated from the peak intensities (SAXS) using a two-phase model with an analytical approach.

from the desorption branch led to smaller, but still significant, values for the increase in the pore diameter, i.e., 2.26 nm (DMF/NaN_3); 1.77 nm (TMU/NaN_3); 1.13 nm (DMI/NaN_3) and 1.84 nm (H_2O/NaN_3).

Interestingly, the specific surface area S_{BET} dramatically increased from 477 m^2 g^{-1} to 876 m^2 g^{-1} by treatment of silica gels with pure DMF, whereas by treatment with DMF/NaN_3 the S_{BET} value only slightly increased from 477 m^2 g^{-1} to 592 m^2 g^{-1}. For the series with DMF this behaviour was reproduced for several samples (Table 4). The sample series with TMU and H_2O showed the same behaviour, whereas for the series with DMI the sample with additional NaN_3 exhibited the highest surface area (Table 4, and Supporting Information File 1).

Higher order reflections were found in the SAXS patterns for every sample, with the characteristic sequence for a 2-D hexagonal ordering of $1 : 3^{1/2} : 2 : 7^{1/2}$… [35]. As noted before for the series with SiO_2–$(CH_2)_{1,3}$–Cl and SiO_2–$(CH_2)_{1,3}$–N_3, a variation in ratio of the radius of the high electron density region (that is the silica wall) to the inner pore volume was indicated by changes in relative reflection intensities. However, for the unmodified silica gels, neither untreated silica, reference silica nor azide-treated silica displayed the (21)-reflection or disappearance of the (11)-reflection as was seen for SiO_2–$(CH_2)_{1,3}$–Cl or SiO_2–$(CH_2)_{1,3}$–N_3. This is also reflected in the electron density reconstruction (Figure 2, and Supporting Information File 1). We assume that this is due to differences in the electron density and pore wall thicknesses for unmodified silica compared to silica modified with organic functionalities covalently attached to the silica walls.

After treatment with solvent/NaN_3 at 60 °C the relative positions of the scattering vectors $q_{(hk)}$ shifted to smaller values (Table 5, and Supporting Information File 1) indicating an increase of the repeating unit distances. This was accompanied by an increase in the lattice constants, with a = 13.49 nm for samples that have been treated in DMF with the addition of NaN_3, and a = 13.44 nm for the respective TMU and a = 13.39 nm for DMI samples. With H_2O/NaN_3 a slightly smaller lattice constant of 13.22 nm was observed (Supporting Information File 1).

With DMF, TMU and DMI we deliberately chose aprotic solvents that would not solvate the azide ions. This is important when azides are made to react by nucleophilic substitution, since assuming a bimolecular mechanism (S_N2), the rate constant will be increased by a unsolvated, and therefore not stabilized, nucleophilic agent. This is in agreement with the fact that when methanol was used as the solvent for the nucleophilic substitution, the yield was much lower. However, the results from the series of gels treated in H_2O clearly demonstrate that the effect on the mesostructure is due to the azide ions, independent of the coordination environment of the azide.

Substitution of NaN_3 by $(H_3C)_4NN_3$ (tetramethylammonium-azide, TMAA) led to similar effects on the mesostructure as mentioned above. An unmodified silica gel was kept for 3 d at 60 °C in a solution of TMAA in DMF. A reference sample was kept for 3 d at 60 °C in DMF. The structural characteristics of untreated silica, reference silica and silica gels that were exposed to DMF/TMAA (all originating from the same gel monolith) were again determined by nitrogen sorption and SAXS analyses.

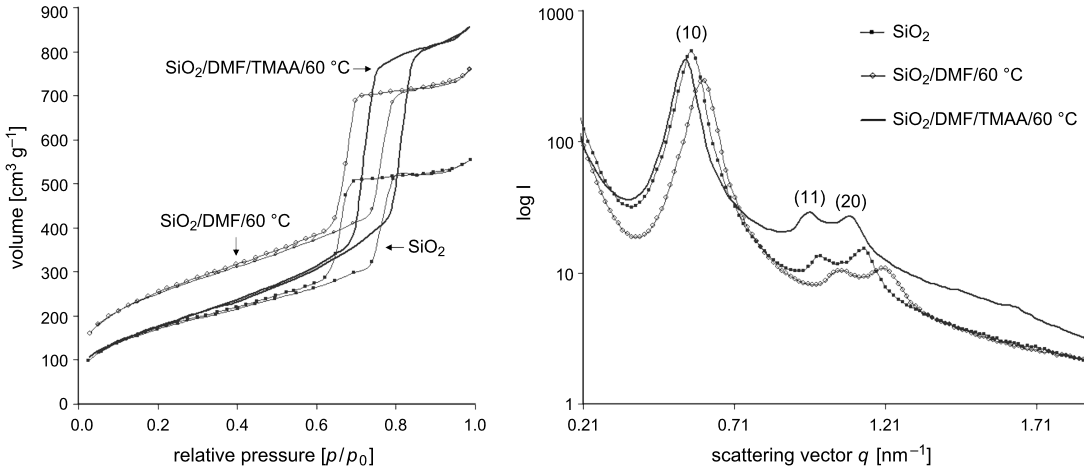

Figure 7: Nitrogen isotherms at 77 K and SAXS patterns of untreated silica, reference silica (DMF/60 °C) and azide-treated silica gels (DMF/TMAA/60 °C).

Figure 7 shows the nitrogen sorption isotherms and SAXS patterns. As observed previously for NaN_3, the addition of TMAA leads to a shift of the relative pressure of the capillary condensation step to larger values, indicating an increase in mesopore diameter. Calculation from the desorption isotherm in the BJH model indicated an increase in the pore diameter from 6.23 to 7.33 nm, and calculation from the adsorption isotherm indicated an increase from 9.21 nm to 11.63 nm (Table 4). The specific surface area S_{BET} showed the same behaviour as for the series with DMF/NaN_3 (Table 4). By treatment with pure DMF, a dramatic increase from 627 m^2 g^{-1} to 906 m^2 g^{-1} was observed, whereas by addition of the azide the S_{BET} value remained almost constant.

Higher order reflections with the same characteristic sequence for a 2-D hexagonal ordering of $1 : 3^{1/2} : 2 : 7^{1/2}$… were found. As observed for the series before, exposure to the azide compound led to a shift of positions for the scattering vectors $q_{(hk)}$ to smaller values, indicating an increase of the repeating unit distance. In addition to that, an increase in the lattice constant was detected. A value of 13.08 nm was found for the sample that was treated with DMF and addition of TMAA in comparison to 12.75 nm for the untreated sample.

Exposure of silica gels to TMAA led to the same mesostructural effects as observed for NaN_3. Therefore, substitution of a relatively small counter ion (Na^+) by a sterically demanding counter ion ($(H_3C)_4N^+$) did not change the observed effects of azides on mesoscopically organized silica gels.

Conclusion

In summary, it was shown that a simple nucleophilic substitution reaction of chloroalkyl-functionalities on a silica surface to azidoalkyl-functionalities had an unexpected and drastic effect on the mesoporous structure. For such co-condensed silica samples with chloroalkyl-functionalities on the surface, an increase in the mesopore diameter, pore volumes (V_{max} and V_{meso}) and lattice constant with a simultaneous decrease in pore wall thickness was observed upon nucleophilic substitution in NaN_3 and DMF. Interestingly no influence on the macroscopic morphology (monoliths) and macroporous network was observed. In principle the same structural changes, albeit less pronounced, were observed for pure silica gels that have been treated in the presence of azide ions.

Further studies have shown that the structural changes can be related to the presence of the azide ions and are not due to the higher processing temperatures, counter ions or solvent molecules, as has been tested for *N*,*N*-dimethylformamide, 1,1,3,3-tetramethylurea, 1,3-dimethyl-2-imidazolidinone and water as the solvent, as well as tetramethylammonium cations as the counter ion.

Therefore, exposure to an azide-containing medium can be seen as a new postsynthetic approach to influence the mesostructural properties of highly porous silica gels.

Experimental

Materials: Tetraethylorthosilicate (TEOS, Fluka), 3-(chloropropyl)-triethoxysilane (CPES, Aldrich), chloromethyltrimethoxysilane (CMTMS, Wacker Chemie AG), and trimethylchlorosilane (TMCS, Merck) were used without further purification. Ethylene glycol (EG, Aldrich) was purified by drying with Na_2SO_4 and distillation from Mg. Pluronic P123 (M_{av} = 5800), $EO_{20}PO_{70}EO_{20}$ (BASF) was applied without purification. For preparation of saturated azide solutions,

sodium azide (Merck), tetramethylammoniumchloride (TMAC, Alfa Aesar) and tetramethylammoniumazide (TMAA, synthesized as described below), *N*,*N*-dimethylformamide (DMF, VWR), 1,3-dimethyl-2-imidazolidinone (DMI, Aldrich) and 1,1,3,3-tetramethylurea (TMU, Aldrich), were used without further purification.

Preparation of hierarchically organized silica gels: Tetrakis(2-hydroxyethyl)orthosilicate (EGMS) was synthesized according to Brandhuber et al. [41,42]. Hierarchically organized silica gels were prepared by condensation of EGMS in an aqueous reaction mixture containing P123 as the structure-directing agent and hydrochloric acid as the catalyst, according to a percentage by weight ratio of SiO_2/P123/1M HCl : 18/30/70 wt %. The reaction mixture was homogenized for 1 min using a vortex stirrer to obtain a viscous white mixture, which was allowed to gel in a closed PP cylinder at 40 °C. The gels were kept at the same temperature for 7 d after gelation for ageing. Immersion of the wet gels in a solution of 10 wt % of trimethylchlorosilane (TMCS) in petroleum ether (PE) for 24 h and washing with PE and ethanol according to [37] resulted in complete expulsion of Pluronic P123, water and glycol.

Preparation of chloroalkyl-modified silica gels: Chloroalkyl-modified silica gels were prepared according to [29] by a co-condensation of EGMS and CMTMS or CPES in various molar ratios of EGMS:CMTMS = 9:1; 6.75:1 and 4.5:1. EGMS and CPES were used in a molar ratio of 9:1. The exact compositions can be found in Table 6. The gels were kept at the same temperature for 7 d after gelation for ageing. The wet gels were immersed in a solution of 10 wt % of trimethylchlorosilane (TMCS) in petroleum ether (PE) for 24 h to react with the free silanol groups, and washed by repeated immersion and storage of the whole monoliths into PE (three times within 24 h) and ethanol (five times within 48 h).

Nucleophilic substitution: The wet chloroalkyl-modified silica gels were immersed into a saturated solution of NaN_3 in DMF at 60 °C, kept for 3 d and subsequently purified by repeated immersion in water (five times within 24 h) and ethanol (three times within 48 h) to remove unchanged NaN_3. Drying of the wet silica gels was performed by simple evaporation of the solvent under reduced pressure at 60 °C.

Ageing of the silica gels in azide-containing media: Azide solutions of NaN_3 in DMF or TMU were prepared by heating under reflux for 8 h at 80 °C followed by decantation from residual sediment at room temperature. A solution of NaN_3 (0.1 g) in DMI (40 mL) was refluxed for 8 h at 80 °C, resulting in a transparent solution. A solution of NaN_3 (0.1 g) in H_2O (40 mL) was prepared at room temperature, resulting in a transparent solution. A solution of TMAA in DMF was prepared by mixing 0.78 g TMAC (0.78 g) and NaN_3 (0.46 g) in DMF (70 mL) followed by refluxing for 8 h at 80 °C and filtration. The wet silica gels were immersed into the azide solutions at 60 °C and kept for 3 d. Purification and drying of the wet gels was performed as describe above.

Characterization: The azide functionalities were detected by ATR–FT-IR spectroscopy using a Bruker Tensor 27. The density of the azides on the surface was calculated by the specific surface area (S_{BET}) and the percentage of nitrogen, which was determined by elemental analysis of nitrogen using an ELEMENTAR Varino, according to:

$$\rho(\text{azide}) = \frac{m_N \cdot N_A}{M_N \cdot 300 \cdot S_{BET} \cdot 10^{18}}$$

where m_N is the mass of nitrogen in 100 g of the silica gel, N_A is Avogadro's constant, M_N is the molar mass of nitrogen and S_{BET} is the specific surface area according to the Brunauer–Emmett–Teller (BET) model.

Adsorption/desorption isotherms of nitrogen at 77 K were obtained with a NOVA 4000e (Quantachrome). Prior to analysis the samples were degassed at 60 °C for 3 h. The specific surface area was evaluated using sorption data in a relative pressure range of 0.05–0.30 with a five-point-analysis

Table 6: Starting composition for chloroalkyl-modified mesostructured silica gels.

EGMS		chloroalkyltrialkoxysilane			template	
SiO_2 content [%][a]	amount [g]	organo-functional silane	amount [mL]	amount [mmol]	P123 [g]	1M HCl [g]
21.8	8.20	—	—	—	3	7
21.8	7.38	CMTMS	0.38	3.0	3	7
21.3	7.10	CMTMS	0.57	4.5	3	7
21.3	6.82	CMTMS	0.78	6.0	3	7
21.8	7.35	CPES	0.72	3.0	3	7

[a]Determined by TG analysis.

according to the BET model. Small angle X-ray scattering (SAXS) experiments were performed either with a Bruker Nano-Star or a Bruker Nano-Star (turbospeed solution) and a 2-D position sensitive detector (HiStar or Vantec 2000). Both instruments are equipped with a pinhole generator, where the X-ray beam is collimated and monochromatized by crossed Göbel mirrors.

The pore-to-pore distances of the mesoporous structures were obtained from the first Bragg peak, the $d_{(10)}$ reflection. The lattice constant a was calculated by $2d_{(10)}/(3)^{1/2}$. The pore diameter and the pore wall thickness were calculated from the peak intensities using a two-phase model with an analytical approach [36,37] or alternatively from an electron density reconstruction with the appropriate choice of phases for hexagonal structures [11,37,38].

For comparison, the pore size was obtained from the Barrett–Joyner–Halenda (BJH) model from the de- and adsorption branch of the isotherm and the pore wall thickness derived from the pore-to-pore distance from the SAXS measurements and subtraction of the corresponding pore diameter from the BJH model.

Supporting Information

Supporting Information features a detailed description on the evaluation of SAXS data, as well as extensive measurement data on unmodified silica gels.

Supporting Information File 1

Evaluation of the SAXS data and measurements of unmodified gels.
[http://www.beilstein-journals.org/bjnano/content/supplementary/2190-4286-2-52-S1.pdf]

Acknowledgements

We acknowledge the financial support of the Deutsche Forschungsgemeinschaft DFG within the collaborative research network SFB 569 and the Austrian Science Fund FWF (DACH project I449). We thank the Wacker Chemie AG for providing chemicals. M. Lindén is gratefully acknowledged for helpful discussions, and we thank D. Mannes for the small angle X-ray scattering measurements, C. Egger for the nitrogen sorption measurements and M. Lang for the elemental analyses.

References

1. Colombo, P.; Vakifahmetoglu, C.; Costacurta, S. *J. Mater. Sci.* **2010,** *45,* 5425–5455. doi:10.1007/s10853-010-4708-9
2. Schüth, F.; Sing, K. S. W.; Weitkamp, J., Eds. *Handbook of Porous Solids;* Wiley-VCH: Weinheim, Germany, 2002.
3. Ahmed, A.; Clowes, R.; Myers, P.; Zhang, H. *J. Mater. Chem.* **2011,** *21,* 5753–5763. doi:10.1039/c0jm02664f
4. Kresge, C. T.; Leonowicz, M. E.; Roth, W. J.; Vartuli, J. C.; Beck, J. S. *Nature* **1992,** *359,* 710–712. doi:10.1038/359710a0
5. Beck, J. S.; Vartuli, J. C.; Roth, W. J.; Leonowicz, M. E.; Kresge, C. T.; Schmitt, K. D.; Chu, C. T. W.; Olson, D. H.; Sheppard, E. W.; McCullen, S. B.; Higgins, J. B.; Schlenker, J. L. *J. Am. Chem. Soc.* **1992,** *114,* 10834–10843. doi:10.1021/ja00053a020
6. Galarneau, A.; Cambon, H.; Di Renzo, F.; Fajula, F. *Langmuir* **2001,** *17,* 8328–8335. doi:10.1021/la0105477
7. Schüth, F. *Angew. Chem., Int. Ed.* **2003,** *42,* 3604–3622. doi:10.1002/anie.200300593
8. Alfredsson, V.; Keung, M.; Monnier, A.; Stucky, G.; Unger, K.; Schüth, F. *J. Chem. Soc., Chem. Commun.* **1994,** 921–922. doi:10.1039/C39940000921
9. Zhao, D.; Feng, J.; Huo, Q.; Melosh, N.; Fredrickson, G. H.; Chmelka, B. F.; Stucky, G. D. *Science* **1998,** *279,* 548–552. doi:10.1126/science.279.5350.548
10. Zhao, D.; Huo, Q.; Feng, J.; Chmelka, B. F.; Stucky, G. D. *J. Am. Chem. Soc.* **1998,** *120,* 6024–6036. doi:10.1021/ja974025i
11. Flodström, K.; Teixrira, C. V.; Amenitsch, H.; Alfredsson, V.; Lindén, M. *Langmuir* **2004,** *20,* 4885–4891. doi:10.1021/la049637c
12. Ryoo, R.; Ko, C. H.; Kruk, M.; Antochshuk, V.; Jaroniec, M. *J. Phys. Chem. B* **2000,** *104,* 11465–11471. doi:10.1021/jp002597a
13. Yu, C.; Tian, B.; Fan, J.; Stucky, G. D.; Zhao, D. *Chem. Commun.* **2001,** 2726–2727. doi:10.1039/b107640j
14. Sakatani, Y.; Boissiére, C.; Grosso, D.; Nicole, L.; Soler-Illia, G. J. A. A.; Sanchez, C. *Chem. Mater.* **2008,** *20,* 1049–1056. doi:10.1021/cm701986b
15. Sel, O.; Kuang, D. B.; Thommes, M.; Smarsly, B. *Langmuir* **2006,** *22,* 2311–2322. doi:10.1021/la0520841
16. Nakanishi, K.; Tanaka, N. *Acc. Chem. Res.* **2007,** *40,* 863–873. doi:10.1021/ar600034p
17. Smått, J.-H.; Schunk, S.; Lindén, M. *Chem. Mater.* **2003,** *15,* 2354–2361. doi:10.1021/cm0213422
18. Hartmann, S.; Brandhuber, D.; Hüsing, N. *Acc. Chem. Res.* **2007,** *40,* 885–894. doi:10.1021/ar6000318
19. Chou, K.; Lee, B. I. *J. Mater. Sci.* **1994,** *29,* 3565–3571. doi:10.1007/BF00352064
20. He, F.; Zhao, H. L.; Qu, X. H.; Zhang, C. J.; Qiu, W. H. J. *Mater. Process. Technol.* **2009,** *209,* 1621–1626. doi:10.1016/j.jmatprotec.2008.04.009
21. Li, Q.; Wu, Z.; Feng, D.; Tu, B.; Zhao, D. *J. Phys. Chem. C* **2010,** *114,* 5012–5019. doi:10.1021/jp9100784
22. Galarneau, A.; Iapichella, J.; Bonhomme, K.; Di Renzo, F.; Kooyman, P.; Terasaki, O. T.; Fajula, F. *Adv. Funct. Mater.* **2006,** *16,* 1657–1667. doi:10.1002/adfm.200500825
23. Galarneau, A.; Cambon, H.; Di Renzo, F.; Ryoo, R.; Choi, M.; Fajula, F. *New J. Chem.* **2003,** *27,* 73–79. doi:10.1039/b207378c
24. Bruhwiler, D. *Nanoscale* **2010,** *2,* 887–892. doi:10.1039/c0nr00039f
25. Sanchez, C.; Shea, K. J.; Kitagawa, S., Eds. Hybrid materials. *Chem. Soc. Rev.* **2011,** *40,* 453–1152. doi:10.1039/c1cs90002a
26. Ortega-Munoz, M.; Lopez-Jaramillo, J.; Hernandez-Mateo, F.; Santoyo-Gonzales, F. *Adv. Synth. Catal.* **2006,** *348,* 2410–2420. doi:10.1002/adsc.200600254
27. Guo, Z.; Lei, A.; Liang, X.; Xu, Q. *Chem. Commun.* **2006,** 4512–4514. doi:10.1039/b610733h

28. Guo, Z.; Lei, A.; Zhang, Y.; Xu, Q.; Xue, X.; Zhang, F.; Liang, X. *Chem. Commun.* **2007,** 2491–2493. doi:10.1039/b701831b
29. Keppeler, M.; Hüsing, N. *New J. Chem.* **2011,** *35,* 681–690. doi:10.1039/c0nj00645a
30. Haensch, C.; Hoeppener, S.; Schubert, U. S. *Chem. Soc. Rev.* **2010,** *39,* 2323–2334. doi:10.1039/b920491a
31. Sing, K. S. W.; Everett, D. H.; Haul, R. A. W.; Moscou, L.; Pierotti, R. A.; Rouquéol, J.; Siemieniewska, T. *Pure Appl. Chem.* **1985,** *57,* 603–619. doi:10.1351/pac198557040603
32. Kleitz, F.; Czuryszkiewicz, T.; Solovyov, L. A.; Lindén, M. *Chem. Mater.* **2006,** *18,* 5070–5079. doi:10.1021/cm061534n
33. Gregg, S. J.; Sing, K. S. W. *Adsorption, Surface Area and Porosity,* 2nd ed.; Academic Press: London, UK, 1982.
34. Rouquerol, F.; Rouquerol, J.; Sing, K. S. W. *Adsorption by powders & porous solids: principles, methodology and applications;* Academic Press: San Diego, CA, USA, 1999.
35. Soni, S. S.; Botons, G.; Bellour, M.; Narayanan, T.; Gibaud, A. *J. Phys. Chem. B* **2006,** *110,* 15157–15165. doi:10.1021/jp062159p
36. Jähnert, S.; Müter, D.; Prass, J.; Zickler, G. A.; Paris, O.; Findenegg, G. H. *J. Phys. Chem. C* **2009,** *113,* 15201–15210. doi:10.1021/jp8100392
37. Brandhuber, D.; Peterlik, H.; Hüsing, N. *J. Mater. Chem.* **2005,** *15,* 3896–3902. doi:10.1039/b505976c
38. Turner, D. C.; Gruner, S. M. *Biochemistry* **1992,** *31,* 1340–1355. doi:10.1021/bi00120a009
39. Harper, P. E.; Mannock, D. A.; Lewis, R. N. A. H.; McElhaney, R. N.; Gruner, S. M. *Biophys. J.* **2001,** *81,* 2693–2706. doi:10.1016/S0006-3495(01)75912-7
40. Beurroies, I.; Agren, P.; Buchel, G.; Rosenholm, J. B.; Amenitsch, H.; Denoyel, R.; Lindén, M. *J. Phys. Chem. B* **2006,** *110,* 16254–16260. doi:10.1021/jp053746y
41. Hüsing, N.; Brandhuber, D.; Torma, V.; Raab, C.; Peterlik, H.; Kulak, A. *Chem. Mater.* **2005,** *17,* 4262–4271. doi:10.1021/cm048483j
42. Hüsing, N.; Raab, C.; Torma, V.; Brandhuber, D.; Peterlik, H. *J. Mater. Chem.* **2005,** *15,* 1801–1806. doi:10.1039/b417675h

License and Terms

Beilstein Journal of Nanotechnology

Self-organizing bioinspired oligothiophene–oligopeptide hybrids

Alexey K. Shaytan*[1,2], Eva-Kathrin Schillinger[3], Elena Mena-Osteritz[3], Sylvia Schmid[3], Pavel G. Khalatur[1,4], Peter Bäuerle[3] and Alexei R. Khokhlov[1,5]

Review

Open Access

Address:
[1]Institute of Polymer Science, University of Ulm, Albert-Einstein-Allee 47, D-89069 Ulm, Germany, [2]Biology Department, Moscow State University, 119991 Moscow, Russia, [3]Institute of Organic Chemistry II and Advanced Materials, University of Ulm, Albert-Einstein-Allee 11, D-89081 Ulm, Germany, [4]Institute of Organoelement Compounds, Russian Academy of Science, 119991 Moscow, Russia and [5]Physics Department, Moscow State University, 119991 Moscow, Russia

Email:
Alexey K. Shaytan* - alexey.shaytan@uni-ulm.de

* Corresponding author

Keywords:
amyloid-like fibrils; bioinspired conjugates; molecular dynamics simulations; oligopeptides; oligothiophenes; self-assembly

Beilstein J. Nanotechnol. **2011,** *2,* 525–544.
doi:10.3762/bjnano.2.57

Received: 19 April 2011
Accepted: 17 August 2011
Published: 05 September 2011

This article is part of the Thematic Series "Organic–inorganic nanosystems".

Guest Editor: P. Ziemann

Abstract

In this minireview, we survey recent advances in the synthesis, characterization, and modeling of new oligothiophene–oligopeptide hybrids capable of forming nanostructured fibrillar aggregates in solution and on solid substrates. Compounds of this class are promising for applications because their self-assembly and stimuli-responsive properties, provided by the peptide moieties combined with the semiconducting properties of the thiophene blocks, can result in novel opportunities for the design of advanced smart materials. These bio-inspired molecular hybrids are experimentally shown to form stable fibrils as visualized by AFM and TEM. While the experimental evidence alone is not sufficient to reveal the exact molecular organization of the fibrils, theoretical approaches based on quantum chemistry calculations and large-scale atomistic molecular dynamics simulations are attempted in an effort to reveal the structure of the fibrils at the nanoscale. Based on the combined theoretical and experimental analysis, the most likely models of fibril formation and aggregation are suggested.

Introduction

Amyloid and amyloid-like fibrillar aggregates, formed by natural proteins or oligopeptides, have attracted much attention both due to their involvement in medical pathologies (such as Alzheimer's disease, Parkinson's disease, etc. [1-3]) and their possible applications as building blocks in nano- and biotechnology. Understanding the molecular details of peptide self-assembly into fibrillar aggregates has been a challenge owing to the large size, low solubility, and the noncrystalline and heterogeneous nature of the fibrils.

During the last decade, considerable progress in our understanding of the principles of fibril formation has been made

owing to numerous experimental and theoretical studies and, importantly, the resolution of peptide arrangements at the atomistic level by means of X-ray crystallography and solid-state NMR [4-6]. The outstanding ability of amyloidogenic peptides to self-assemble and form extremely stable and tough nanostructures has been realized, and thus they are now actively probed as building blocks for various nanotechnology applications by covalently binding them to synthetic moieties [7-10], and engineering fusion proteins [11] and colloidal particles [12,13]. However, we are still too far away to say that the complete picture of the fibril self-assembly is now available at the molecular, nano- and microscale levels.

In this area, the approach that is gaining more and more attention is the synthetic conjugation of peptides to other molecular compounds. Conjugates of synthetic and natural macromolecules are of great current interest because of their promising biomedical, microelectronic, and other advanced technological applications [7-10,14,15]. Covalent attachment of synthetic polymer blocks to amyloidogenic peptide sequences leads to a new class of block copolymers that can inherit typical properties of their constituents, e.g., enhanced performance characteristics, conductivity, biocompatibility, and high propensity for self-organization. In this respect, oligothiophene–oligopeptide conjugates are of particular interest. The conjugation of oligothiophenes and amyloidogenic peptides may result in new compounds that supplement the potentially semiconducting, optical, and electroluminescent properties of oligo- and polythiophenes with the self-assembling, specific binding, and stimuli responsive behavior of biological moieties, thus opening up opportunities for the design of smart materials at the nanoscale. An example of a hypothetical fibrillar aggregate structure, formed by a bithiophene covalently linked to peptide sequences, is illustrated in Figure 1d.

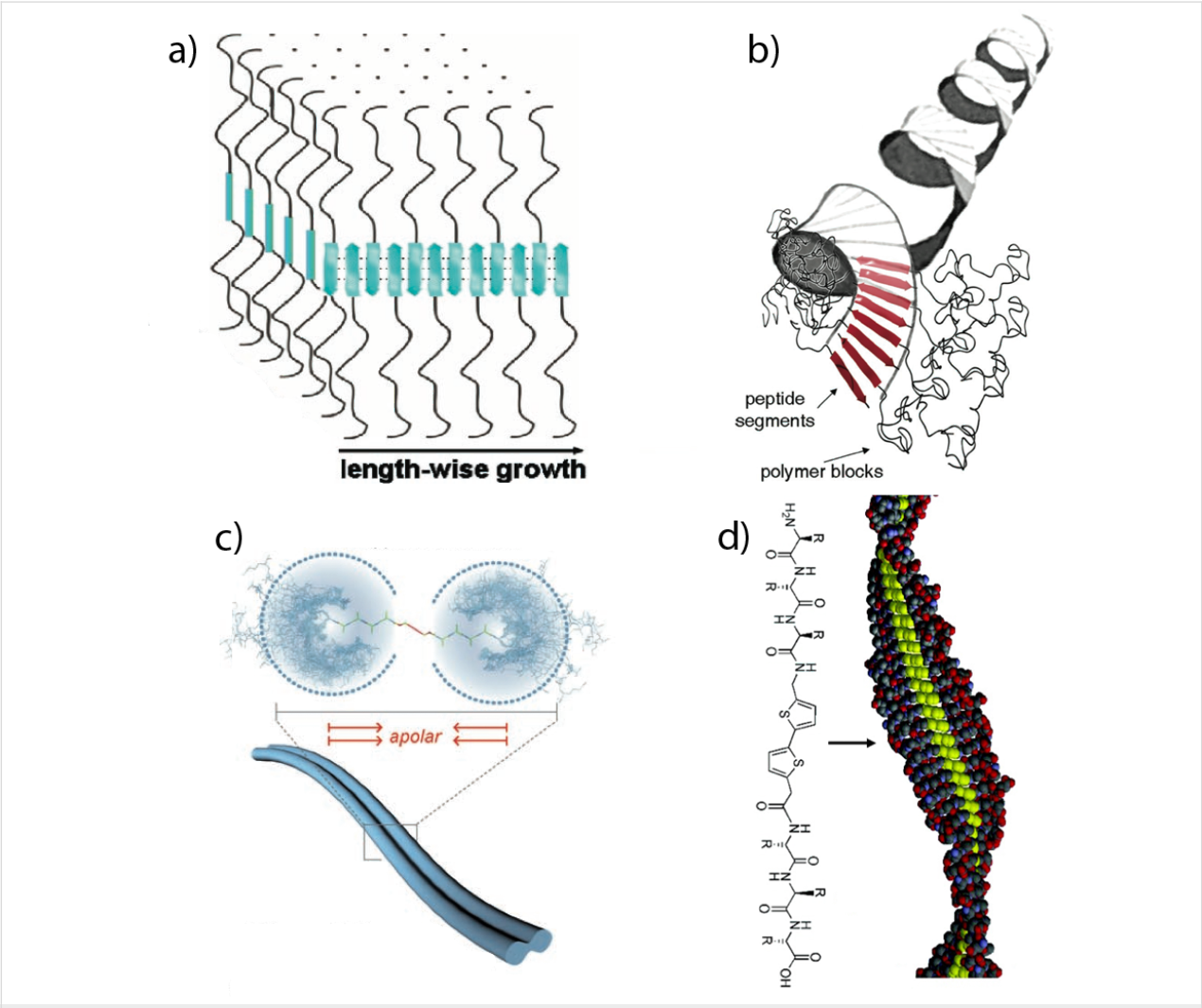

Figure 1: Various morphological organization examples of fibrillar aggregates that can be formed by polymer bioconjugates: (a) Wide planar tapes [18]; (b) helical superstructure [19]; (c) tapes with a dumb-bell shaped cross section [20]; (d) helical tapes with a thiophene block in the middle [21].

Several reviews [7-9,15] summarize the recent progress in the field of the chemistry of polymer bioconjugation in which the biconjugation with amyloidogenic peptides is one of the most frequently used techniques. The resulting interplay of intermolecular interactions is affected by both the synthetic and peptide parts, leading to an even greater structural polymorphism than observed in natural amyloid fibers, keeping in mind that synthetic chemistry provides more variability in the structure of the building blocks, including branched molecular topologies [16].

A number of hypothesized self-organized morphologies that may be adopted by various polymer bioconjugates are shown in Figure 1. Moreover, the interplay between different interactions may also suggest a dependence of the supramolecular organization on the external conditions, such as temperature, solvent quality, pH value, etc. [17].

While the chemical structure of the aggregating compounds is almost always known, and the fibrillar morphology at the submicrometer scale is resolved by electron or atomic force microscopy, the structure of the fibrils at the atomistic and nanoscales, including the packing of the single molecules, very often remains beyond the capabilities of experimental measurements to elucidate. In particular cases, it becomes possible to gain insight into the intrinsic structure of the fibrils, e.g., by means of X-ray diffraction when the corresponding microcrystals can be obtained, or when sufficient solid state NMR data is available. However, for the majority of compounds and moreover for polymer-bioconjugates, the available experimental evidence regarding the intermolecular interactions is in most cases limited to spectroscopic analysis (IR, UV–vis, CD spectroscopy) and diffraction patterns (X-ray, SAED) and thus the exact structural arrangement at the nanoscale and its connection to the morphology remains elusive.

The molecular simulation methods in this respect become an attractive tool to supplement and interpret the experimental data, because they can fill in the missing gaps in the understanding of the relationship between the structural arrangement and the fibrillar morphology. When 3-D atomistic structures of microcrystals or oligomeric aggregates are available they may be used to construct computational models of the fibrillar aggregates, and through the application of atomistic molecular dynamics (MD) simulations the structural data can be extended into the dynamic domain. Since microcrystals usually only provide the structures of the basic aggregation units, different arrangements of these units into the protofilaments and then fibers may be probed in computer simulations. However, when no initial 3-D structural data is available, the application of computer simulations may be less straightforward. In this case, it is necessary to predict or suggest various trial arrangements, construct the aggregates, and then test their characteristics against available experimental data. The latter approach has a much wider applicability in terms of studied compounds and potential applications for the rational computer-aided design of new macromolecular systems with specific properties.

In this minireview, we discuss the recent progress in the design, synthesis and in computer simulations of new oligothiophene–oligopeptide conjugates that can self-assemble to form nanoscale fibrillar aggregates. The main focus is on the experimental and theoretical results obtained in our group.

Review

Synthesis of oligothiophene–oligopeptide hybrids

The hybrid molecules discussed in this paper are bio-functionalized organic semiconductors. They represent either di- or monosubstituted conjugates with a quaterthiophene block and an oligopeptide block containing three repeat units of L-valine-L-threonine. These molecular hybrids – the A–B–A-type compound **1** [22] and the A–B-type compound **6** [23] – and their synthesis are presented in Scheme 1 and Scheme 2, respectively. The peptide blocks were equipped at the termini with

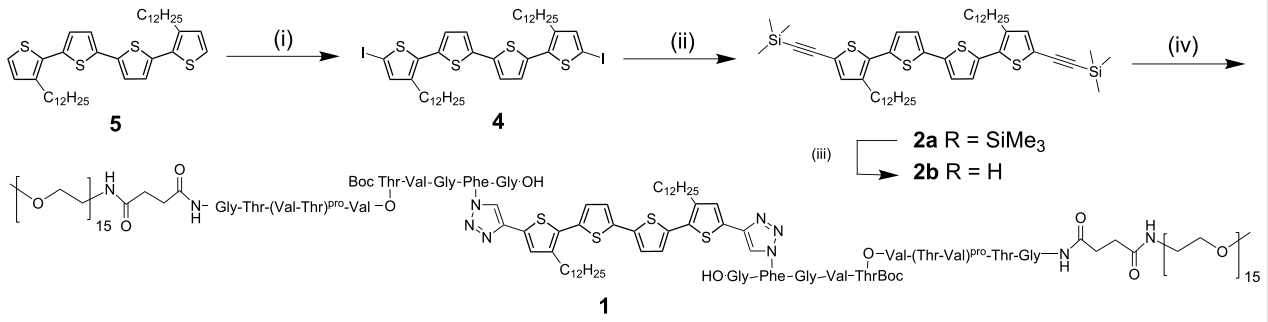

Scheme 1: Synthesis of quaterthiophene-β-sheet-peptide hybrid **1** [22]; (i) $Hg(II)OAc_2$, $CHCl_3$, 0 °C → r.t., 14 h; I_2, 0 °C → r.t., 6 h; (ii) Cu(I)I, TMSA, $Pd(PPh_3)_2Cl_2$, piperidine, 60 °C, 2 h; (iii) 6 equiv CsF, MeOH/THF, r.t., 2 h; (iv) 0.4 equiv $[Cu(CH_3CN)_4]PF_6$, 0.4 equiv Cu(0), DCM, r.t., 40 h.

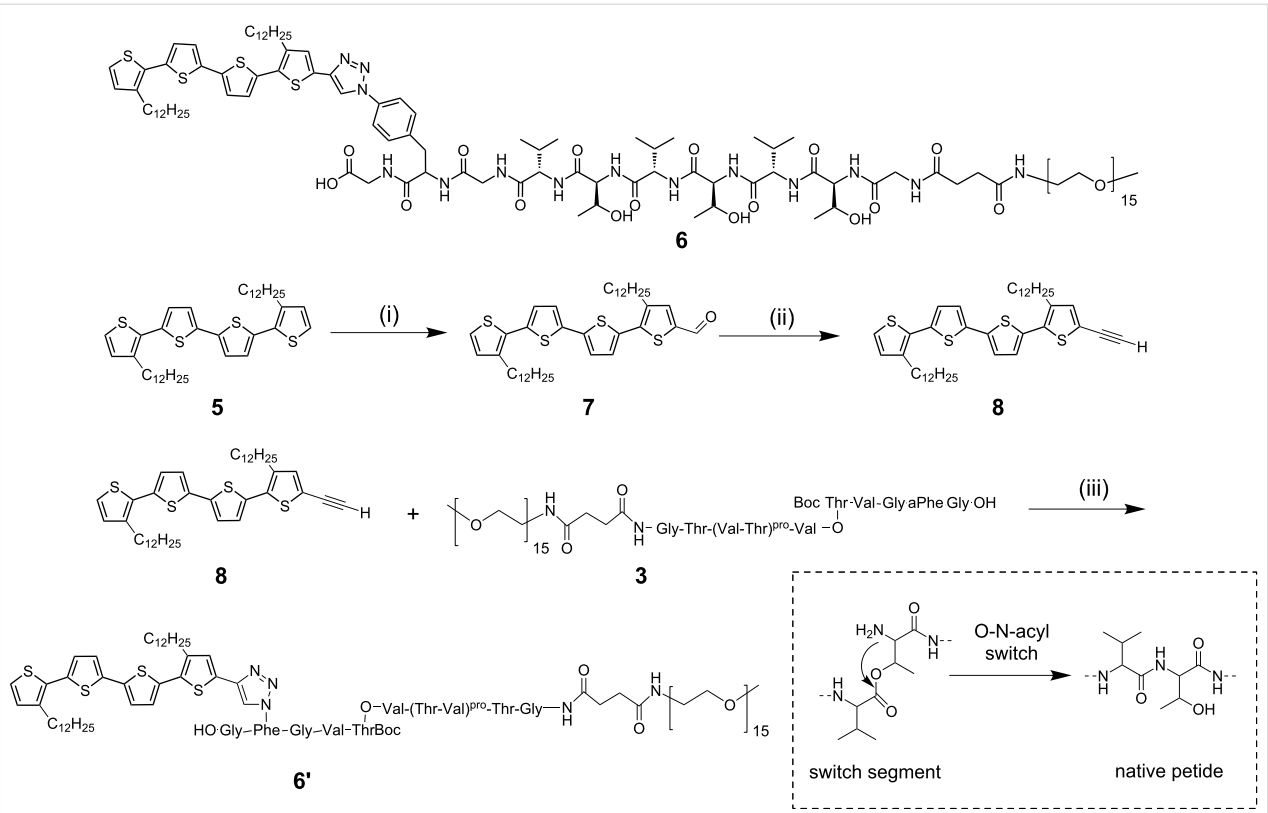

Scheme 2: Synthesis of quaterthiophene-β-sheet-peptide hybrid **6** [23]; (i) $POCl_3$, DMF, dichloroethane, reflux, 3 h; (ii) K_2CO_3, methanol/THF, r.t., overnight; (iii) 0.4 equiv $[Cu(CH_3CN)_4]PF_6$, 0.4 equiv Cu(0), DCM, r.t., 40 h. (Thr–Val)^{pro} refers to a pseudoprolien unit, (Val–O–Thr) refers to the switch segment (framed bottom right) , and aPhe stands for *p*-azido-Phe.

poly(ethylene oxide) (PEO) chain. Due to their amphiphilic character and the defined secondary structure of the biological moiety, hybrids **1** and **6** are expected to reveal interesting self-assembly behavior in solution and on solid substrates.

Symmetrically substituted didodecyl-quaterthiophene **5** was chosen as the basic building block (Scheme 1), representing a planar fully conjugated backbone with the ability to self-assemble at the liquid–solid interface into very regular lamellar structures [24]. The intermolecular forces involved are primary van der Waals interactions of the interdigitating long alkyl side chains. Furthermore, the planar conjugated thiophene backbone is well known to interact by π–π stacking to form larger crystalline structures. With respect to the peptide part, the L-valine-L-threonine $(Val–Thr)_3$ sequence effectively forms β-sheet secondary structures. Hybrids **1** and **6** were shielded laterally by poly(ethylene oxide) chains in order to enhance solubility and processability and to induce the formation of isolated fibrillar structures.

The synthesis of the semiconductor block, bisethynylated quaterthiophene **2b** and the final oligothiophene–peptide hybrid **1** is shown in Scheme 1: The diiodinated quaterthiophene **4** was synthesized from the corresponding parent compound **5** by iodination at the terminal α-positions, with mercury(II)acetate and elemental iodine in dry chloroform, to give compound **4** in 94% yield.

The remarkable tendency of these peptide blocks to form β-sheets enormously hinders the synthesis of the hybrids due to aggregation during reaction [16,25]. In order to overcome this problem, the aggregation tendency was temporarily suppressed through a synthetic strategy, which employs pseudoprolines ((Thr–Val)^{pro}) [26] and a switch ester segment [27] (Scheme 2). The pseudoprolines were inserted as a transient structure-disrupting protecting group for threonine and the switch ester segment as a temporary structural defect in the peptide block. Whereas the pseudoproline unit is removed during standard acidic deprotection conditions, the switch ester segment is preserved at low pH. Reestablishment of the native α-amide peptide backbone can be achieved by an increase in the pH to neutral or even slightly basic conditions.

The peptide segment was obtained by a semi-automated solid-phase supported peptide synthesis (SPPS) by sequential coupling of standard fluorenylmethoxycarbonyl (Fmoc)-

protected amino acids and the pseudoproline unit onto a preloaded TentaGel resin [27]. Incorporation of the Fmoc-protected azido-phenylalanine (aPhe) and the addition of the switch ester segment between valine (Val) and threonine (Thr) were accomplished by means of bench top coupling techniques [27]. An end-functionalized poly(ethylene oxide) block, containing 14 or 15 repeat units, was attached to the N-terminus of the supported peptide. Subsequent liberation of the peptide-PEO_{15} conjugate from the support, followed by precipitation, centrifugation and lyophilization, gave the fully protected peptide-PEO_{15} conjugate **3** in 61% yield (Scheme 2) [19].

The PEO–peptide–quaterthiophene hybrid (A–B) **6** was prepared analogously to the A–B–A-type hybrid **1** by the reaction of monoethynylated quaterthiophene **8** and protected peptide–PEO_{15} conjugate **3** [28] (Scheme 2). Ligation of freshly prepared **8** with the PEO-peptide conjugate **3** was accomplished by Cu(I)-catalyzed Huisgen cycloaddition.

Self-assembly of oligothiophene–oligopeptide hybrids

The self-assembly properties of the A–B–A-type molecules on surfaces were analyzed by means of atomic force microscopy (AFM) as a powerful tool to visualize superstructures in the nano- and micrometer regime [22,23]. The substrate employed was muscovite mica, and tapping mode was chosen for scanning.

For deprotection, the triblock oligothiophene–oligopeptide compound **1** (Scheme 1) was first treated with 30% trifluoro acetic acid (TFA) in dichloromethane. Under these acidic conditions, all protecting groups present in hybrid **1** (*t*-Boc, pseudoproline, *t*-butyl ester) are removed, except for the switch ester segment, which is preserved in the new form **1'**. Thus, molecule **1'** still exhibits a kink in the peptide backbone, as shown in Figure 2.

To investigate the self-assembly of **1'**, several solvents were employed, including water (pH ≈ 4–4.5), aqueous phosphate

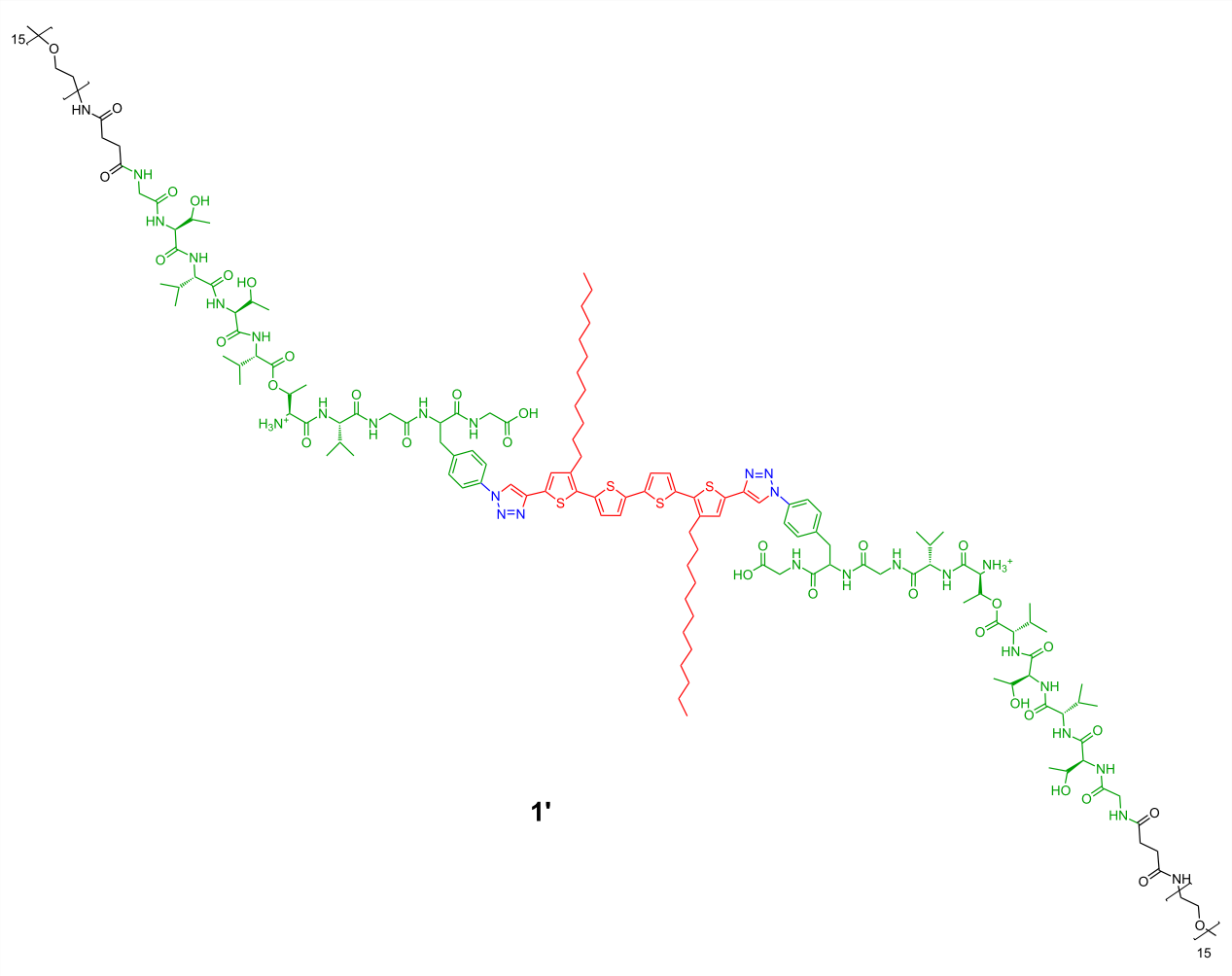

1'

Figure 2: The A–B–A-type hybrid **1** in the deprotected, but still kinked, form **1'**.

buffer (pH ≈ 6–6.5), and dichloromethane with two droplets of THF (pH ≈ 2). These attempts resulted in the formation of clusters or irregularly twisted short fibers of **1'** on the mica substrate.

Due to the hybrid nature of **1'**, two opposing intermolecular interactions could dominate the self-assembly process, namely H-bonding and π–π stacking. Thus, a solvent-guided strategy was employed in order to gain control over the self-assembly process. Deprotected, but still kinked, compound **1'** was dissolved in dichloromethane (a good solvent for the oligothiophene moiety), and to this solution methanol (non-solvent for the oligothiophene part) was added gradually through a syringe pump until a ratio of DCM/MeOH of 1:1 was reached (pH ≈ 5). The switch segments in the peptide moieties were still intact [19,27]. The solution was spin-coated on the mica substrate and well-defined microstructures were visualized by means of AFM (Figure 3).

The fibrillar structures exhibit single object widths of about 12 ± 1 nm (not tip corrected), with height maxima of 3 ± 0.4 nm, and lengths of up to several micrometers. The presence of these fibers was confirmed in our recent work [22] by means of transmission electron microscopy (TEM). The finding of helical self-assembled fibers for compound **1'** (Figure 3b) is rather surprising, since the efficiency of the switch ester segment in suppressing β-sheet formation had been demonstrated previously [19,25].

In order to re-establishing the native peptide backbone of **1**, 0.001 M sodium hydroxide dissolved in methanol was added to a solution of **1'** in dichloromethane. The AFM images (Figure 4) showed fibrous structures with lengths of up to 1–2 µm, heights of 2.4 ± 0.4 nm and widths of 11 ± 2 nm. The lack of helicity in the fibers (at least at our resolution capacity) indicated that in this state of the peptide the fibers do not possess a chiral substructure. This finding was confirmed by means of TEM [22].

The self-assembly of the unsymmetrical mono-β-sheet-peptide–oligothiophene hybrid **6** (Scheme 2) was investigated on mica substrates by AFM as well. For deprotection, this compound was treated with 30% trifluoro acetic acid (TFA) in dichloromethane. Under these acidic conditions, all protecting

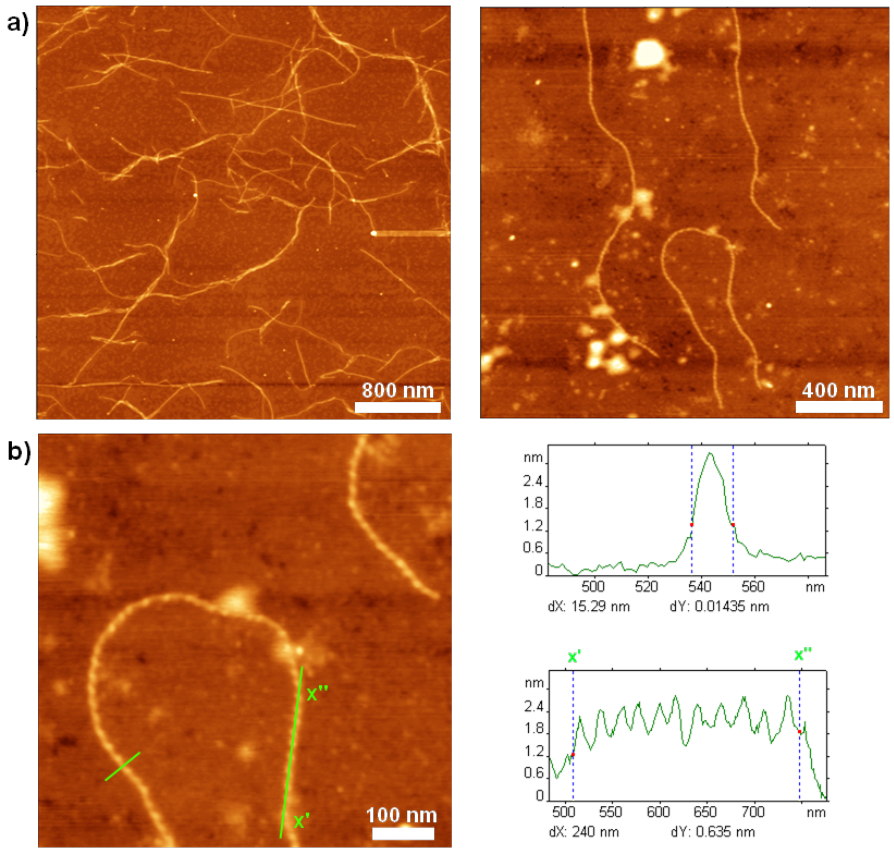

Figure 3: AFM height images of hybrid **1'** on mica from a 1:1 DCM/MeOH solution; a) left: Network of fibers after 2 d; right: Fibrillar features found after 2 h; b) left: Left-handed helical fiber, right: Cross section and height profile from the marked sections in 2b [22].

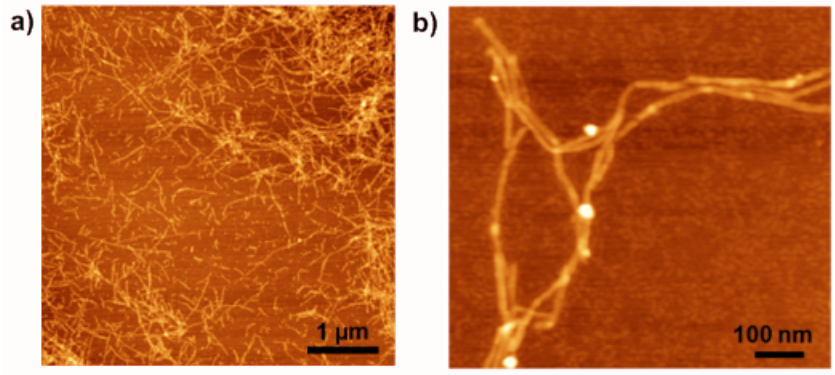

Figure 4: AFM images of the switched PEO–peptide–quaterthiophene–peptide–PEO compound **1** [22].

groups present in hybrid **6** are removed, except for the switch ester segment, which is preserved. Thus, the molecule **6'** still exhibits a kink in the peptide backbone (Figure 5).

Taking into account the experimental findings described before for the disubstituted A–B–A system **1'**, similar conditions were chosen for A–B system **6'**. The 1:1 DCM/MeOH solution of **6'**

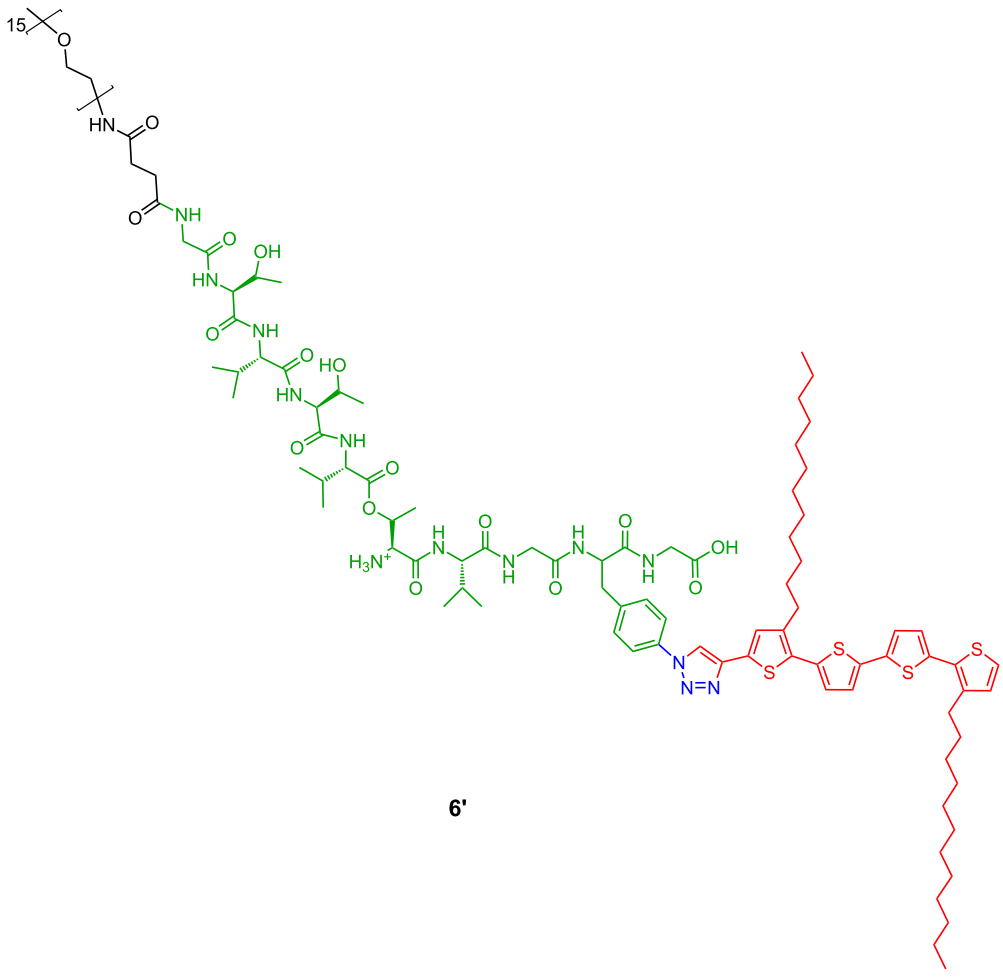

6'

Figure 5: A–B system **6'** in deprotected, but still kinked, form.

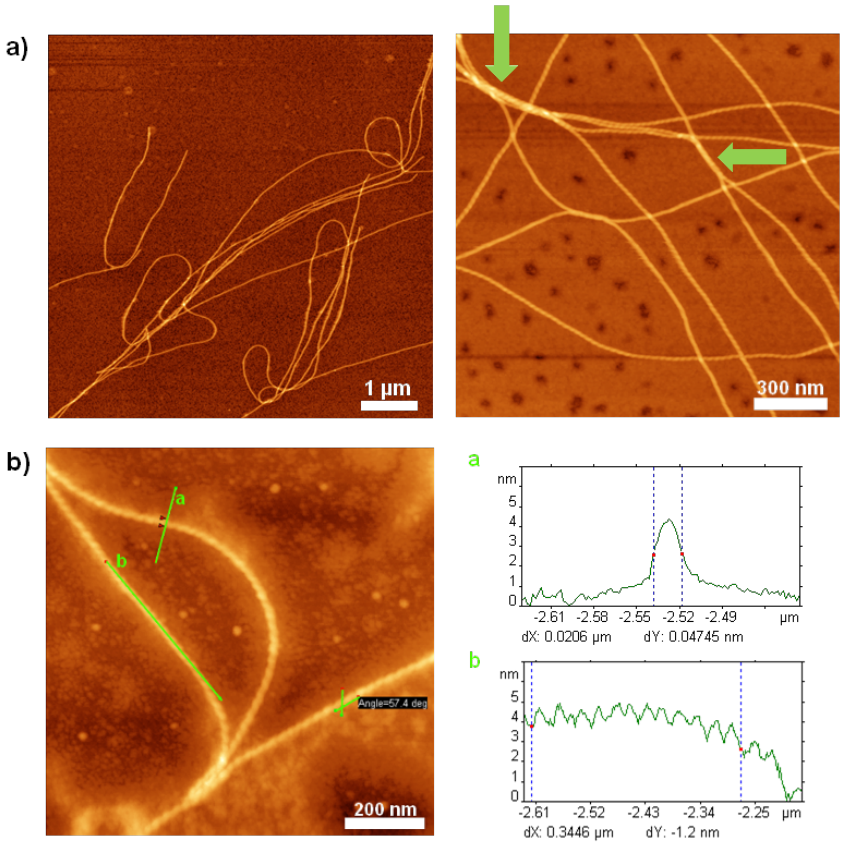

Figure 6: AFM height images of **6'** on mica from a 1:1 DCM/MeOH solution. a) left: Image of fibers obtained after 2 d; right: Zoom of fiber networks; green arrows: Contact points of individual fibers; b) left: Zoom of left-handed helical fibers; right: Cross section and height profile of helical fiber [22].

was established much faster than the one of **1'** in order to form the highly regular, exclusively left-handed, helical fibers, which can be observed in AFM (Figure 6).

The fibrillar structures show single object widths of about 20 ± 2 nm (AFM, not tip corrected), height maxima of 3.5 ± 0.4 nm, and lengths of up to several micrometers (Figure 6a, left). A tightly wound, strictly left-handed substructure was resolved for the fibers, possessing a pitch length of 25 ± 2 nm (Figure 6b, right). At several points, contact between the individual fibers can be seen (green arrows in Figure 6a, right) but there is no evidence for fiber intertwining to form multihelices.

Based on the results obtained from the symmetric system **1'**, the same controlled way of transferring the switch ester segment into native amide bonds was chosen for **6'**. The AFM investigations of **6** adsorbed onto the mica substrate revealed fibrous structures (Figure 7).

The pattern of the self-assembled fibers, though, does not correspond to a network but is instead more reminiscent of bundles or clusters of fibers (Figure 7a, left). Surrounding these larger areas of concentrated material, single fibers can be found (Figure 7a). At higher resolution it was shown that the "single" fibers consist of several smaller filaments aligned in parallel (Figure 7b), which explains the irregularly frayed appearance of the bigger fibers. The cross-section analysis reveals, as well, the structure of the filaments composing the bigger fiber (Figure 7b, middle). Especially in the close view images (Figure 7b, left: Height, right: Amplitude), it can clearly be seen that shorter fibrillar structures are also deposited as singular features on the mica surface. These features can be considered to represent single filaments that have not been self-assembled into the bigger structures ("fibers" or bundles).

Because of the composition of the bigger fibers from filaments, it was impossible to determine unambiguous values for the height and width of the bigger fibers or even bundles. For the bigger fibers, lengths between 1 and 2 µm and heights of 1 ± 0.2 nm were observed. Widths ranged mostly between 15 and 48 nm but also sporadic widths of up to ≈80 nm could be found. In order to gain more information on the smallest objects observed, the filaments seen in the background of the images were investigated with respect to their geometry as well. They

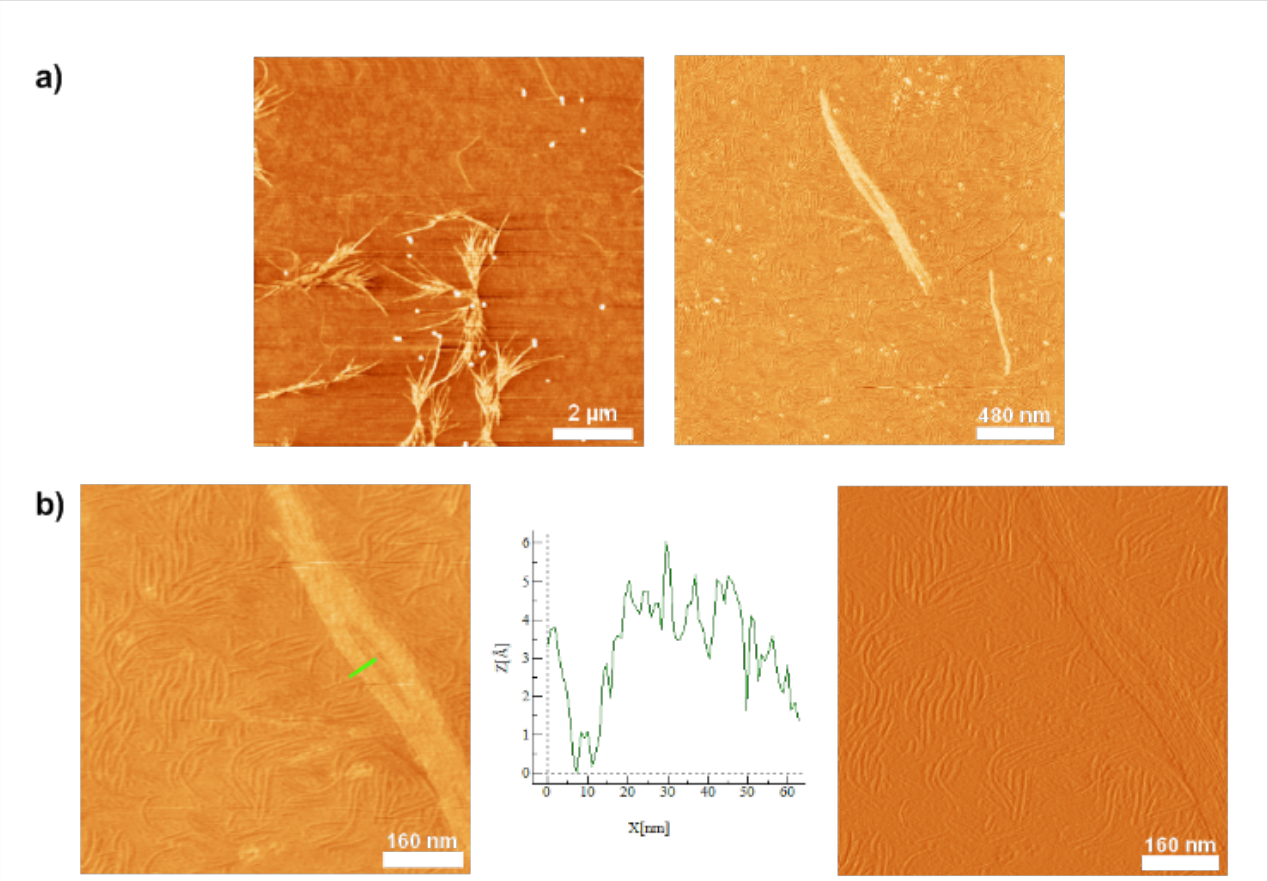

Figure 7: AFM height and amplitude images of fully switched PEO–peptide–quaterthiophene **6** on mica [23]. a) left: AFM height image obtained after 7 d; right: Zoom of single fiber; b) left: Height image of single fiber consisting of smaller filaments; middle: Cross section corresponding to the marked section in b), right: Amplitude image of b) left.

showed lengths of 100–200 nm, widths of 6–8 (±2) nm and heights of 0.4–0.7 (±0.2) nm.

Compared to the fibers obtained in the kinked state of the molecule, **6'** (Figure 6), the microstructures found for the fully stretched out peptide, **6**, seem to be, by far, less self-contained and persistent (Figure 7). Not only do they lack the left-handed helical superstructure observed for the latter, but also the filaments containing molecules **6** seem to be more prone to self-assemble into higher structures (fibers and bundles), whereas the helical fibers of the hybrid **6'**, are more insulated and do not seem to merge into any higher order (Figure 6). In addition, fibers from **6'** observed by AFM are much longer and well confined. These observations lead to the assumption that the mode of self-assembly of the individual molecules in their respective states, kinked **6'** and stretched **6**, differs profoundly. Whereas the kinked hybrids, **6'**, seem to self-assemble in such a way that the intermolecular noncovalent interacting forces are fully saturated, i.e., the formed microstructures do not make use of any unsaturated sites for, e.g., hydrogen bonding, the stretched out state of the peptide in **6** seems to form higher structures, in which unsaturated sites for intermolecular interactions may be present.

Models of molecular aggregates

Molecular models were developed and simulated on the basis of our experimental findings. Quantum chemical calculations based on the Austin Model 1 (AM1) level were performed on isolated, and bundles of, oligothiophene–oligopeptide molecules for the case of **1'**. The PEO units were omitted in the calculations for simplification. The models were constructed in vacuum.

Accounting for the unexpected formation of helical fibers in the kinked state of hybrid **1'**, as discussed in the previous section (see also [22]), we suggested the molecular models shown in Figure 8.

The symmetric optimized conformation of **1'** was employed as the basis for the development of a model. The slightly offset

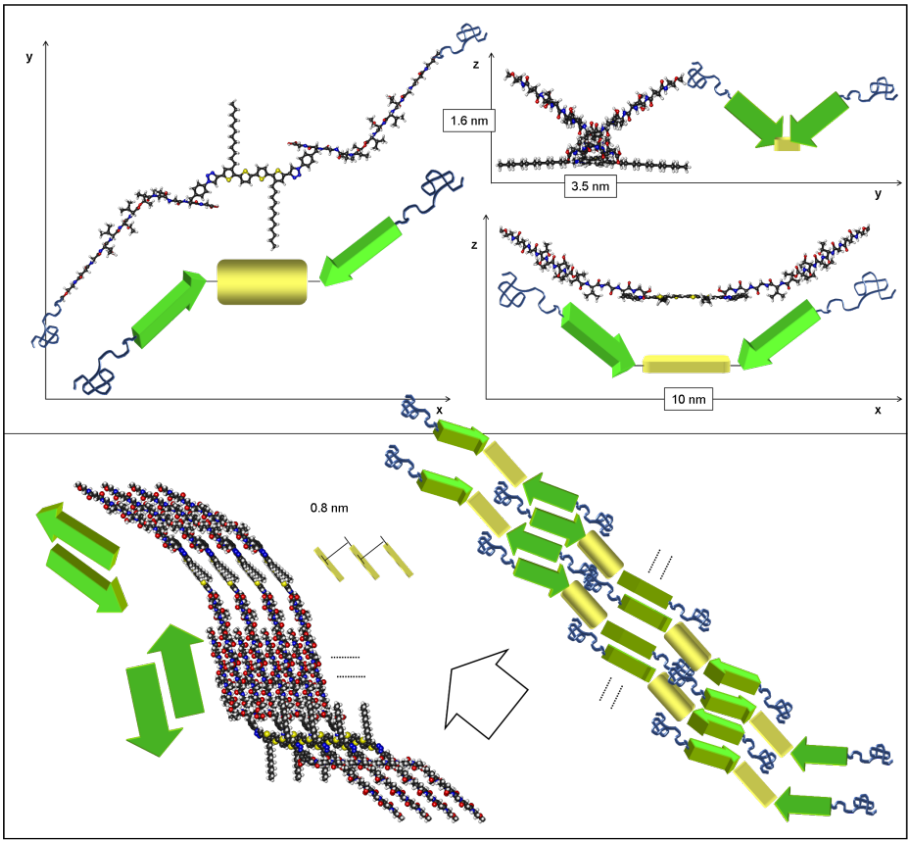

Figure 8: Calculated minimum energy conformation of oligothiophene–oligopeptide hybrid **1'** in the three Cartesian directions (top). Calculated model of an ensemble of eight molecules (bottom, left) as well as a model cartoon (bottom, right). White arrow shows the fiber growth direction [22].

packing of two **1'** molecules leads to 8 favorable H-bond interactions in each peptide part. Thus, the peptide strands interact in a favorable antiparallel fashion (green arrows in Figure 8). The oligothiophene backbones (yellow boxes in Figure 8) are separated by 8 Å, avoiding an efficient π–π interaction in the **1'** fibers. The voids in between the oligothiophenes can be filled by the nondepicted flexible PEO-chains (blue coils in Figure 8).

This model also accounts for an inherent left-handed superstructure of the formed fibers, arising from the function of the oligothiophene block as a rigid and preorientating spacer between the peptide arms of **1'**. In addition, the antiparallel arrangement of the peptide blocks stabilizes the fiber in a helical manner and is responsible for fiber growth. The height of the superstructures is predicted to be 3.2 nm, fitting well with the experimental values of 3 ± 0.4 nm. The calculated angle between the pitch and the fiber growth direction (45 ± 2°) corresponds well to the experimental finding (40 ± 5°). The model predicts three hybrids of **1'** to be needed for the completion of one loop, leading to a theoretical pitch length of 18 ± 1 nm, which is in agreement with the experimental finding from AFM images (20 ± 1 nm). The thicknesses of the fibers experimentally determined by AFM and TEM correspond to the lateral interaction of 8–12 molecules of **1'** in the theoretical model.

For the native state of the peptide moiety in hybrid **1**, the following model for the superstructure can be deduced from the stretched molecular geometry and by following the best packing taking into account the intermolecular interactions observed in the calculated model of **1'** (Figure 9).

The fibers observed in AFM and TEM do not display any helical superstructure. Hence, a flat arrangement of the single molecules in a β-sheet structure is most likely. The β-sheet structure itself was corroborated by IR spectroscopy and SAED (*d* spacing of 4.8 ± 0.1 Å). The calculated molecular length of **1** (without the flexible PEO chains) amounts to 10 nm, which fits very well with the experimentally observed widths of the fiber of 11 ± 2 nm (AFM). The height of the fibers observed on the mica was 2.4 ± 0.4 nm. It is known, that the height of a single layer β-sheet with this peptide sequence is 0.9 ± 0.1 nm, so a double layer structure of two β-sheets on top of each other is

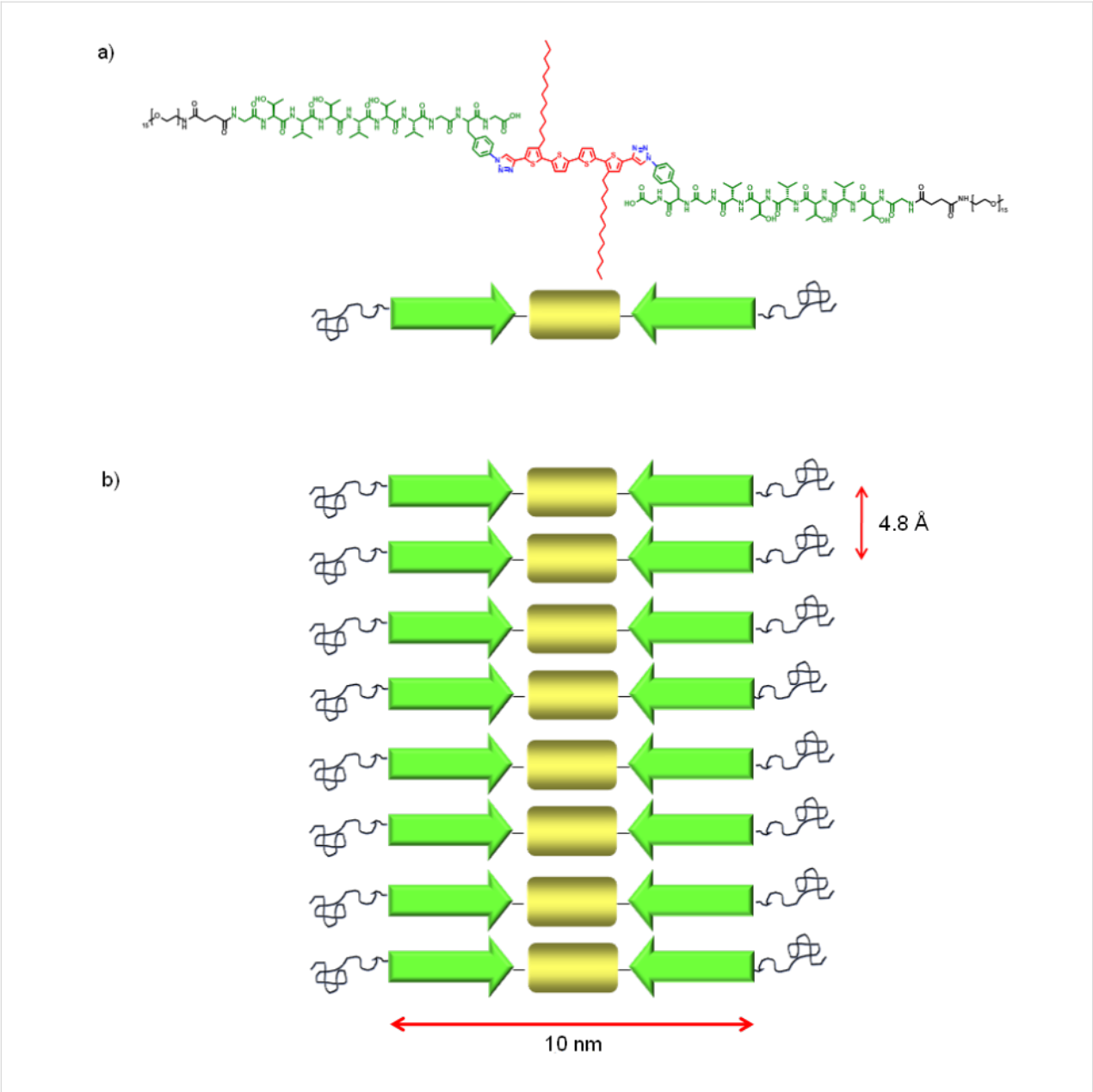

Figure 9: a) Schematic representation of hybrid **1**. Black coils: PEO chains, green arrow: Peptide strand; yellow box: Quaterthiophene; b) Model of parallel β-sheet superstructures of hybrid **1**.

assumed based on the data available. Such multilayer β-sheets are well known in literature and result from interactions of the hydrophilic or hydrophobic sides, respectively, of two β-sheets [20]. In such a manner, unfavorable interactions with the solvent can be prevented.

The model for the self-assembly of **6'** is depicted in Figure 10. The superstructure was deduced from the theoretically calculated molecular geometry of **6'** and by taking into account the knowledge of the intermolecular interactions of the thiophene moieties and the calculated model of **1'**.

The representation of the molecule's minimum energy conformation and its schematic representation is given by the same code as that used for the model of **1'** (yellow box: Quaterthiophene backbone; green arrow: Peptide segment; blue coils: PEO chains). When forming dimers from molecules of **6'** (kinked state), such as depicted in Figure 7b and c, an analog of hybrid **1'** (referring to the arrangement of the peptide arms with respect to the conjugated backbones) is obtained. Thus, such dimers should mimic the single molecules of the corresponding disubstituted hybrid **1'** with respect to the formation of inherently left-handed helical fibers (Figure 8, bottom panel). The driving

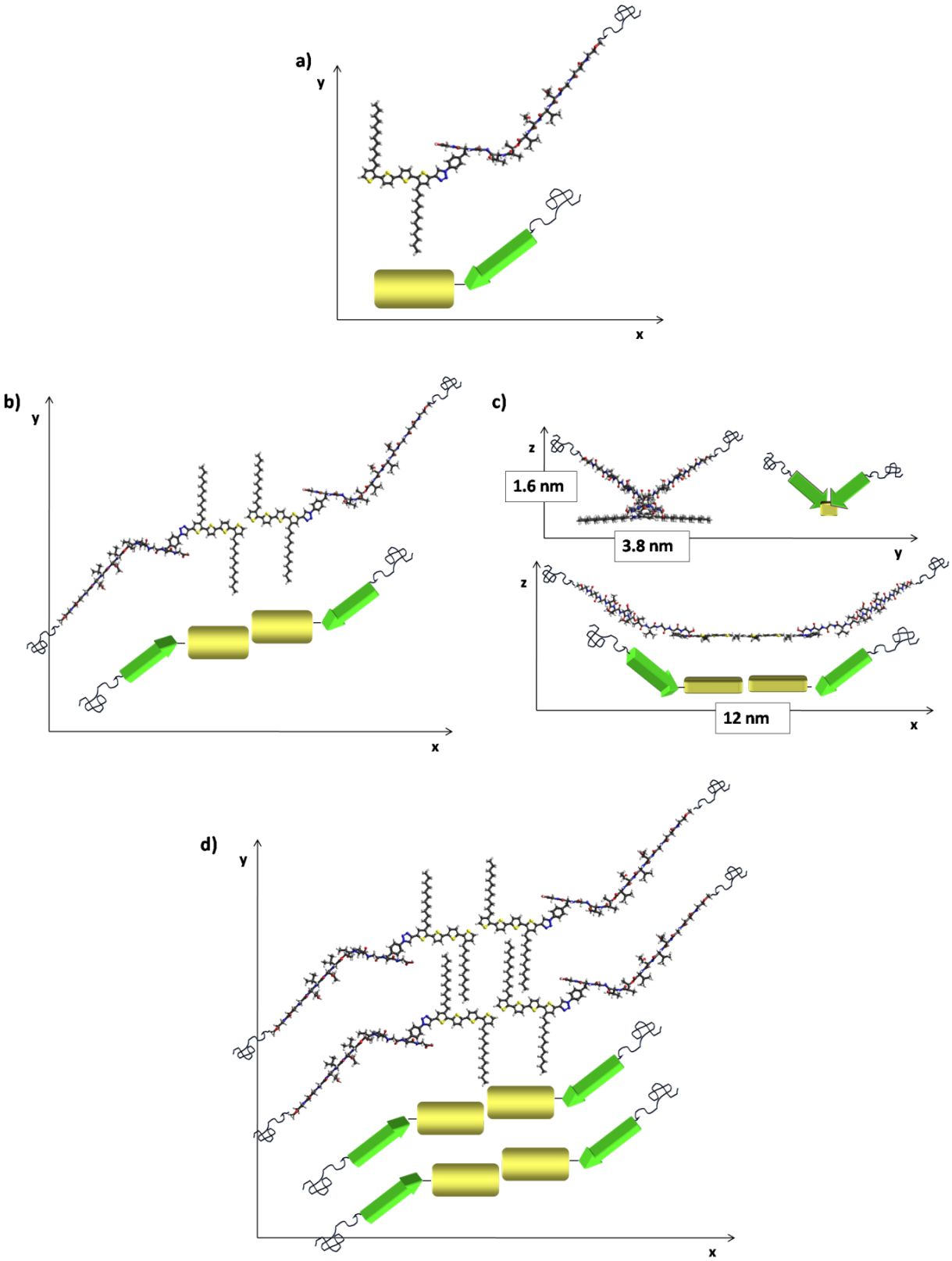

Figure 10: Model for the self-assembly of hybrid **6'**, based on the theoretically calculated conformation of **6'** and the model for hybrid **1'**; a) conformation of **6'**; b) and c) depiction of dimers of **6'** in the three Cartesian directions; c) proposed ensemble of four molecules of **6'**.

forces for the formation of such proposed dimers could be the compensation of dipole moments of the single molecules in addition to a favorable intermolecular interaction of hydrophilic (peptide–PEO) and hydrophobic (quaterthiophene) parts of the molecules.

Furthermore, the model revealed a separation of 8 Å between the quaterthiophene backbones of two adjacent dimers of **6'**, due to the antiparallel intermolecular interaction of their peptide arms, similar to the case of **1'** (Figure 8). In the case of the postulated formation of dimers of **6'**, however, favorable van der Waals interactions of the alkyl side chains are also involved (Figure 10d) [29]. Eventually, the voids in between laterally adjacent molecules can be filled by the PEO-chains due to their high degree of flexibility, as in the case of **1'**.

The dimensions of the left-handed helical fiber observed in AFM for hybrid **6'** would fit well with such a proposed model. The experimentally observed fibers of **6'** are wider than for hybrid **1'** (20 ± 2 nm versus 11 ± 2 nm). Thus, more dimers of **6'** interact laterally in the superstructure, possibly due to favorable van der Waals interactions of the alkyl chains, leading to a greater width of the fiber. The height of the fiber was experimentally determined to be 3.5 ± 0.4 nm for hybrid **6'**, which is comparable to the height determined for hybrid **1'** (3 ± 0.4 nm). Hence, also the observed angle between the pitch and the fiber growth direction, which was determined to be 55 ± 3° for **6'** as opposed to 45 ± 2° for **1'**, becomes comprehensible, since for a larger number of laterally interacting molecules, and a higher resulting width of the fiber, a more obtuse angle between the pitch and the fiber growth direction must result, if the same overall height of the fiber for **1'** and **6'** is to be maintained (Figure 8). Eventually, for hybrid **1'**, it was predicted that three hybrids are needed to complete one loop of the helical structure resulting in an experimental pitch length of 20 ± 1 nm (see above). The length of a single molecule of **1'** amounts to 10 nm, whereas the length of a dimer of **6'** is approximately 12 nm. Thus, the greater pitch length of **6'** (25 ± 2 nm) fits very well with the proposed model based on the assumption that also for **6'** three dimers are needed to complete one loop of the helix.

Atomistic molecular dynamics simulation

To further enhance our theoretical understanding of the principles governing the formation of the fibrillar structures from thiophene–peptide conjugates and to gain more insight into the structure and dynamical behavior of the aggregates at finite temperatures, a theoretical methodology based on classical mechanical force fields and molecular dynamics simulations was developed [23]. Although molecular models based on classical mechanics lack the level of precision in describing intermolecular interactions when compared to quantum chemistry models, they allow much higher levels of conformational space sampling, which are needed to reveal the optimal conformation of the aggregates and incorporate the entropic finite temperature effects, which may lead, for instance, to the twist of the fibrils induced by an increase in backbone dynamics [30]. Computer simulations provide an important opportunity to shed light on the possible supramolecular organization patterns, their stability and the governing interplay of intermolecular interactions. To the best of our knowledge, we were the first to apply the rational principles of structure prediction by means of conformation space search based on molecular mechanics, and subsequent MD simulations to study the peptide-directed, noncovalent assembly of thiophene-peptide hybrids [23,31-35].

However, even in classical MD simulations, the rate of conformational sampling is not enough to observe spontaneous formation of fibrillar aggregates; hence, a special computational methodology incorporating the available experimental evidence was developed.

As a starting point for the theoretical considerations of the experimentally observed nanofibers, the molecular structure of the molecule was constructed. Our theoretical research methodology consists of four main steps schematically depicted in Figure 11.

First, the available experimental data, including available X-ray structural data, for the arrangement of peptide moieties in biological amyloid-like fibrils was analyzed, and possible periodic arrangements of molecules consistent with experimental results were proposed. Second, an approach based on MD simulations was applied to obtain periodic molecular arrangements that correspond to the local free-energy minimum where all local degrees of freedom (torsion angles, side chain conformations, hydrogen bonds) achieve their optimal positions. Then, these optimal arrangements were used to construct long fibrillar aggregates, the dynamic and statistical behaviors of which were investigated by means of MD simulations. Finally, the results obtained from analysis of the simulations were compared with experimental data, which enables us to suggest the most likely molecular arrangement pattern that should be observed in the experiment.

We demonstrate this approach through the example of the A–B system **6** in the native state of the peptide. In principle both parts of this hybrid molecule (thiophene part and peptide part) may be capable of strong intermolecular interactions, thus leading to the formation of highly anisotropic structures such as nanofibers, nanorods, etc. However, the IR spectroscopic data for the compound under study revealed that the β-sheet struc-

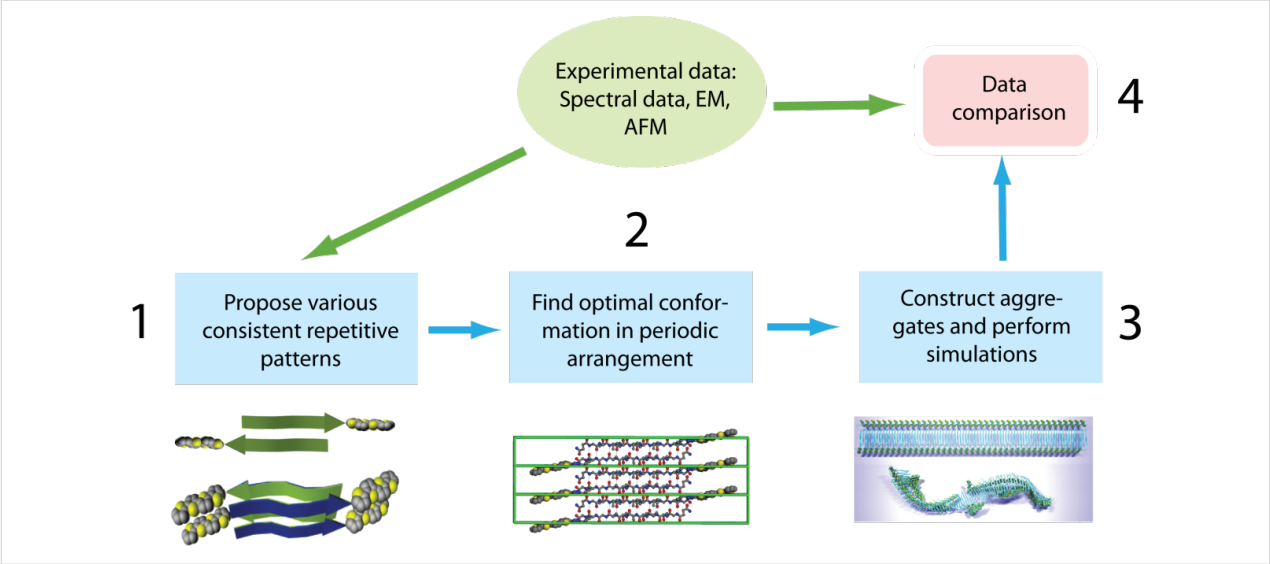

Figure 11: Theoretical analysis workflow (see text).

ture formation was at least involved in the self-assembly mechanism of our nanofibers. While the formation of fibers at the nanometer scale (especially amyloid-like fibers) from separate peptide moieties due to β-sheet aggregation is a common self-assembly mechanism, as discussed previously, it is natural to assume that similar peptide–peptide interactions play the structure-determining role during the aggregation of our hybrid compound and form the scaffold of the fibrils.

Relying on the basic ideas and our current understanding of amyloid fibril aggregation patterns [2,4,36], one can hypothesize that the basic arrangement pattern of peptides in the fibrils is either simply single layer β-sheets (as is sometimes seen for peptide polymer conjugates [19,20]) or double layer aggregates (as seen in many natural fibrils). One can propose two basic periodic arrangements of hybrid molecules in single layer tapes based on an either parallel or antiparallel organization of the peptide moieties in the β-sheets. Several other double layer arrangements are then derived from these single layer arrangements by stacking the β-sheets face-to-face in an aggregation manner similar to the cross-β-spine structure of amyloid fibrils (for more detail, see, e.g., [37]). Below we present the details of the periodic arrangement construction by using the combination of molecular alignment and MD simulations.

The construction of aggregates from single molecules can be done with the inclusion of subsequent minimization and relaxation steps as follows. First, the conformations of the initial molecules were adjusted: The peptide block is considered to be in the form of a β-strand engaged in either an ideal parallel or ideal antiparallel β-sheet; this is solely determined by the values of the dihedral ϕ and ψ angles of the peptide backbone, which are known to be $\phi = -119°$, $\psi = 113°$ for β-strands engaged in parallel β-sheets and $\phi = -139°$, $\psi = 135°$ for β-strands engaged in antiparallel β-sheets. The thiophene block, including the 4-azidophenyl-alanine side chain and alkyl chains, is considered to be in a planar, extended conformation corresponding to the local energy minimum. In order to construct a proper periodic arrangement that could be used as an elementary structure to construct long fibrils, a corresponding periodic unit cell that consists of two (for single-layer fibrils) or four (for double-layer fibrils) molecules was derived. The period implied by the unit cell along the fibrillar axis was set to be 4.8 Å per β-strand so as to correspond to that generally observed in amyloid fibrils (9.6 Å for two strands). As a first step, two molecules were arranged into two single-layered periodic structures with a parallel and an antiparallel arrangement of β-strands, the peptide segments in both cases were aligned in register so as to maximize the number of interstrand hydrogen bonds, which was monitored during the system arrangement (Figure 12). Energy minimization for such periodic single-layer systems (that can be regarded as infinitely long crystalline tapes) was then performed followed by a long relaxation MD run.

The single-layer periodic structures obtained were then used as building blocks to form various double-layer structures, that is, structures that contain a double-layer β-sheet as the main structural part. An efficient computational strategy for constructing these double-layer arrangements from the equilibrated single-layer dimers was used to mimic the “steric zipper” arrangement of the peptide part as observed in some microcrystals [37,38], followed by an extensive relaxation MD run allowing the molecules to adjust their periodic arrangement to the best local minimum of free energy.

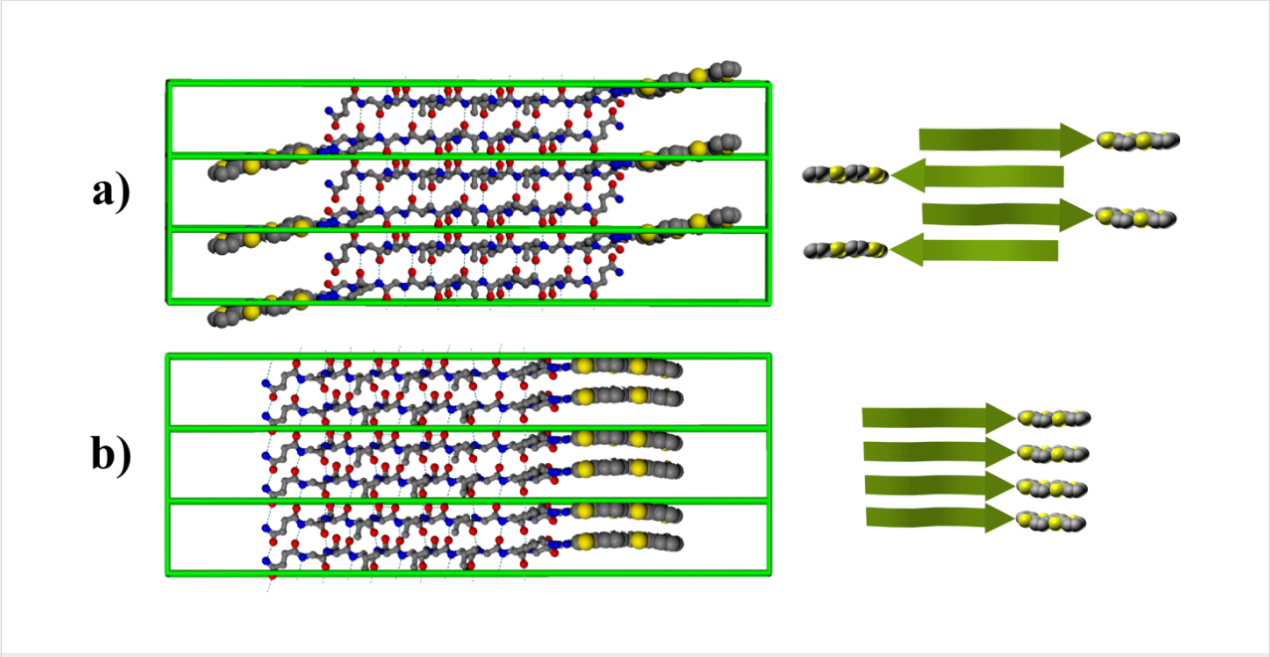

Figure 12: Constructed periodic crystalline cells for (a) antiparallel and (b) parallel arrangement of peptide strands in single-layer fibrils. Alkyl chains are not shown. Dashed lines represent the hydrogen bonds responsible for β-sheet formation. Right insets present the principal arrangement of peptide and thiophene moieties [23].

The double-layer arrangements were then created from the single layer arrangements. In principle, possible hypothetical double tape arrangements of the peptide core are depicted schematically in Figure 13.

There are in total eight principal arrangement possibilities. However, due to experimental evidence and basic physical principles, many of them may be left out from further consideration. It is worth noting that the alternating nature of $[Thr–Val]_3$ sequence exposes the hydrophilic threonine side chains from one side of the β-sheet and hydrophobic valine side chains from the other side. Thus one side of the β-sheet may be considered hydrophobic while the other hydrophilic. Assuming that the hydrophobic–hydrophilic interactions are one of the main

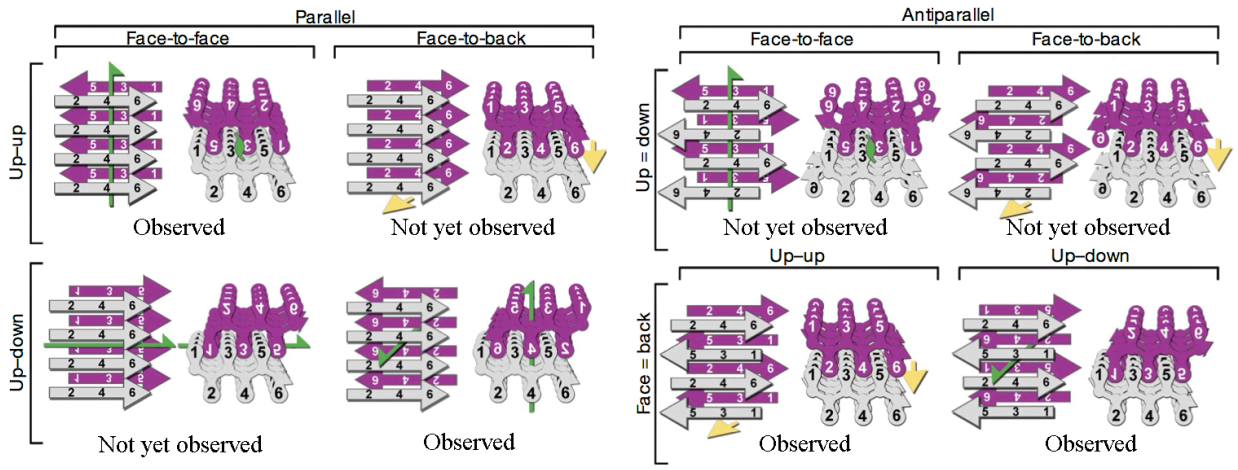

Figure 13: Possible options for the arrangement of β-sheets in a cross-β motif. Two identical sheets can be classified by the orientation of their faces (either “face-to-face” or “face-to- back”), the orientation of their strands (with both sheets having the same edge of the strand “up”, or one “up” and the other “down”), and whether the strands within the sheets are parallel or antiparallel. Both side views (left) and top views (right) show which of the six residues of the segment point into the zipper and which point outward. Green arrows show two-fold screw axes, and yellow arrows show translational symmetry. Below each class are listed protein segments that belong to that class. Reprinted by permission from Macmillan Publishers Ltd: Nature [37], copyright 2007.

driving forces, the structures with energetically unfavorable contacts of hydrophobic and hydrophilic moieties can be left out. This simple consideration already reduces the number of possible double-layer arrangements to the following three structures: The "face-to-face" antiparallel arrangement and two parallel face-to-face arrangements ("up-up" and "up-down" structures). The "up-down, face-to-face" parallel arrangement in turn is considered unlikely as (i) such a structural arrangement of β-strands is not observed experimentally to date for biological amyloid fibers, (ii) such an arrangement will not be favored by the interaction of dipole moments of the adjacent tapes, and (iii) moreover only one such arrangement is sterically allowed because of the bulkiness of the thiophene fragments of the hybrid molecule.

Each of the two remaining principal arrangements can be realized in two variants depending on which kind of faces (with exposed threonine or valine sidechains) are in contact. The resulting four arrangements are shown in Figure 14 (here and below they are denoted as I, II, III, and IV).

These structures were constructed as follows. First, the single-layer structure was replicated, turned 180° around the axis of the tape, and then adjusted in the lateral plane, so that the peptide segments of two single-layer fibrils would be approximately in register forming a "steric zipper" in the center of the fibril as seen in microcrystals of amyloidogenic peptides. Any overlap of molecular fragments that occurred (e.g., within alkyl-chains) was removed by small adjustments of the involved torsion angles, which would anyway reach their equilibrium values during the relaxation run. Since double-layers are considerably more complicated conformational assemblies, particularly with respect to the organization of the surfaces buried between the two β-sheets and the interaction of the side chains at these surfaces, a 10 ns MD relaxation run was performed for these periodic structures. During this run, a certain rearrangement of the side chain conformations between the β-sheets took place. The relative enthalpies of formation for these structures during the run were monitored, in order to track the system relaxation. The lowest relative enthalpy of formation was observed for structure III. Relative to structure III, structures I, II and IV have an additional enthalpy of formation of 11, 6 and 12 kcal/mol per molecule, respectively. Although this data set was obtained in vacuum simulations and the effect of solvent was neglected, it gives valuable quantitative data for the understanding of the hierarchy of interactions in such systems and is consistent with the supposition that hydrophilic interlayer contacts and an antiparallel arrangement of the β-sheets are the factors that lead to a gain in enthalpy of formation. However, in our case because of the specific geometry of the molecules, the aggregation pattern based on antiparallel β-sheets and hydrophilic interlayer contact (Figure 14, system IV) leads to the loss of close packing between the thiophene moieties and thus becomes energetically unfavorable.

Both obtained single-layer periodic arrangements and two of the double-layer structures with minimal enthalpy of formation (arrangements (II) and (III)) were used to construct long fibrils by replicating the periodic cell along the axis of the filament. For the selected systems, planar straight fibrils 80 β-strands in length (approximately 40 nm) were constructed and subjected to 10 ns MD simulations at $T = 300$ K. To this end, the LAMMPS simulation package [39], based on the domain decomposition strategy, was employed. The conformational evolution of the constructed aggregates during the simulations allows the study of the shape and morphology of the fibrils, as well as tracing the influence of the intermolecular arrangement on the conformation of the aggregates at the nanoscale. Comparative analysis of various fibrils (as well as comparison of the fibrils composed of hybrid molecules to those consisting only of

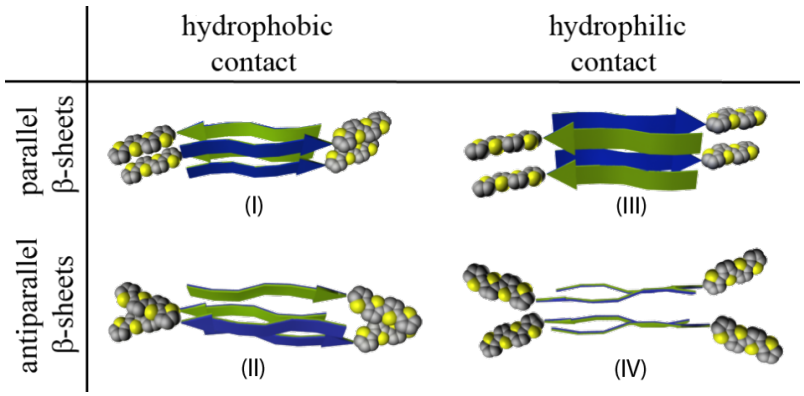

Figure 14: Schematic representations of constructed double-layer periodic arrangements from the hybrid molecule under study, classified by β-sheet orientation (parallel versus antiparallel) and the type of interlayer contact (hydrophobic versus hydrophilic) [23].

peptides) allows us to discuss the role of various intermolecular interactions in stability and behavior of the aggregates, as well as to compare their geometry and behavior to the experimentally observed characteristics.

Representative snapshots that describe the conformational evolution of different fibrillar arrangements are presented in Figure 15.

All the systems demonstrated their stability during the simulation run in the sense that all molecules preserved their relative positions in the aggregates with respect to their neighbors, however, certain conformational rearrangements both at the molecular level and at the nanoscale were observed. In all the cases, the β-sheet organization dominated the structure and remained the main scaffold for the fibril organization. A simulation time of 10 ns appeared to be enough to grasp the main characteristics of the fibril morphology and its evolution. As seen from Figure 15a and b, single layer fibrils are capable of a more pronounced conformational rearrangement than double layer fibrils, as the double-layer organization of the fibrils makes them stiffer and conformationally more stable. Further we will examine the evolution of different aggregate types.

The simulations of single layer fibrils based on the parallel arrangement of β-strands (Figure 15a), revealed that the fibril undergoes certain conformational changes during the evolution, however, it remains rather linear and axially rigid (Figure 15a2). The initially planar structure of the fibril undergoes certain twists with respect to its axis, while the conformation of the peptide backbone changes. As seen from Figure 15a2 the originally flat peptide sequences of the molecules have developed a kink by rotational rearrangement of the peptide backbone at the position of the glycine residue, which connects the $[Thr–Val]_3$ sequence with the rest of the molecule. Since glycine has no side chain, it does not hinder the rotation around C–N and C–O bonds of the peptide backbone and hence allows the observed flexibility. Meanwhile, the thiophene moieties of the molecules remain in closely packed alignment, thus forming a continuously organized axial structure with a left-handed twist. On the contrary, the single layer fibril based on the antiparallel arrangement of β-strands, which lacks much of the thiophene–thiophene interactions (since the spacing

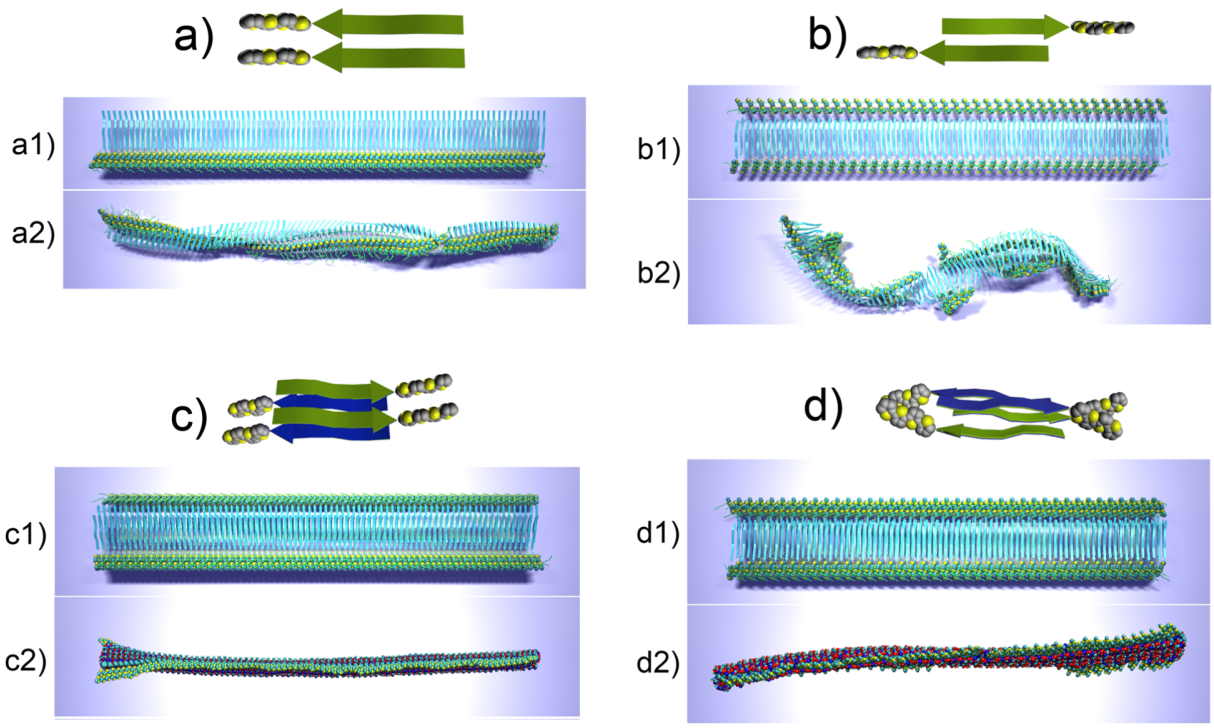

Figure 15: Snapshots of four different types of fibrils at the initial conformation (a1, b1, c1, d1) and after 10 ns of evolution (a2, b2, c2, d2). Peptide moieties are depicted with arrows, thiophene moiety using van der Waals spheres; images c2, c3, d2, d3 use van der Waals representation also for the peptide part for clarity [23].

between the thiophene segments is twice as large as in the case of the parallel arrangement), tends to curl to form a left-handed helical structure (Figure 15b). It should also be noted that the left-handed helix formed by a tape that has different types of faces (e.g., hydrophobic and hydrophilic face) may in principle exist in two conformations, that is, one where the hydrophobic side is directed to the inner compartment of the helix, and the reverse case. The variant of the helix curl should depend on the balance between the interactions of the side chains on each side of the tape with each other as well as with the solvent. Note that the fibril composed of the hybrid molecules (Figure 15b) tended to have the hydrophobic face of the tape at the inner part of the helix.

Contrary to the single layer fibrils, double layer fibrils result in almost planar tapes with a possible twist along the axis. The interactions between the adjacent single layer tapes strengthen the structure and molecular order by hydrogen bonds and steric interactions. However, the interactions also reduce the peptide flexibility, and thus do not favor additional peptide bending, which, e.g., led to the formation of kinks in the peptide backbones of single layer arrangements (Figure 15a). Moreover the stacking of two tapes with identical faces implies other "geometrical" considerations, such as suppression of helix formation, since each tape, if taken separately, would prefer to curl in the opposite direction to its neighbor, and thus the "curling" potential vanishes. The double tape fibril composed of parallel β-sheets stacked with hydrophilic faces (Figure 15c) remained surprisingly planar with only a small left-handed twist at one end of the fibril, which may be attributable to end effects.

Meanwhile the double tape arrangements based on antiparallel β-sheets (Figure 15d) formed a relatively planar, stable, left-handed twisted tape with an approximate twist of 30 degrees per 40 nm.

From the view point of various technological applications, the most important question concerns the arrangement of the conjugated thiophene moieties and the interplay between π−π stacking and β-sheet formation. As spacing between the molecules implied by the β-sheet structure corresponds to 4.8−5 Å, whereas the spacing between the planes of thiophene rings participating in π−π stacking interaction is estimated ideally to be around 3.3−3.5 Å [40,41], these interactions have competing behavior in terms of the periodicity implied during molecular aggregation. The analysis of histograms for the distribution of distances between the centers of mass of peptides and also between quaterthiophenes clearly reveals that the arrangement of the peptides into β-sheets dominates the periodicity implied for the aggregates for all types of simulated fibrils, thus meaning that the thiophene moieties have to adopt the periodic arrangement settled by the peptides. There are two possible variants of such behavior. In the case of a parallel arrangement of the β-strands, the thiophene moieties tilt synchronously, thus simultaneously preserving the high degree of ordering and fulfilling the periodicity restrictions implied by the β-sheets. In the case of the antiparallel arrangement, the proposed double layer fibril (Figure 15d) in principle has the same linear density of quaterthiophenes along the fibril as in the case of fibrils with parallel arrangement, because the thiophene moieties from different tapes come in contact to make a sort of "steric zipper" along each side of the double tape. However, in this case, the thiophene parts tend to lean towards one another to form dynamic clusters with gaps between them, which alleviate the differences between optimal inter-thiophene and inter-peptide distances.

The comparison of the conformational behavior (twisting or curling of the aggregates) of various simulated fibrillar aggregates and their spatial dimensions (cross section of 6−8 Å, heights of 1.4−1.8 Å (double layers)) with the available AFM data (Figure 7) suggests that the double layer arrangement based on parallel β-sheet organization (Figure 15c) fits well with the available experimental data and may be considered as the highly probable model for the actual aggregation pattern.

Conclusion

Combining synthetic and biological building blocks to form various types of biomimetic thiophene-based hybrid compounds offers a means to construct new ordered supramolecular nanostructures and soft materials through self-organization, and such structures may exhibit a rich polymorphism over nanometer length-scales. The design of such hybrid molecules is a unique strategy, which aims to create smart nanomaterials that combine the properties of both the synthetic and biological components. Applying such an approach in the chemistry of conjugated compounds leads to new organizational concepts at nanoscales for these technologically important molecules.

This minireview was focused on and limited to a summary of recent advances in the understanding the self-organization processes observed for oligothiophene–oligopeptide conjugates, which are capable of forming long fibrillar aggregates in solution and on substrates. In particular, we reported on the successful synthesis of new bio-substituted organic semiconductor compounds where the rigid quaterthiophene block is either di- or monosubstituted with peptide sequences that display a high propensity to form β-sheets. These molecular hybrids can spontaneously self-assemble into stable fibrillar aggregates as visualized by AFM and TEM. We presented data on both kinked and nonkinked states of the peptide chains and

found that the behavior of both symmetric (A–B–A) and asymmetric (A–B) hybrids in relation to the superstructure formation differs deeply, depending on the peptide conformation. These observations lead to the assumption that the mode of self-assembly of the individual molecules in their respective states, kinked and stretched, differs profoundly. Theoretical approaches based on quantum chemistry calculations and atomistic molecular dynamics (MD) simulations were attempted in order to reveal the possible intermolecular arrangements, their characteristic features, and to devise the possible arrangement models. Several models of the aggregation pattern of molecules for the A–B-and A–B–A-type conjugates were presented based on quantum chemical calculations. We have discussed a theoretical approach developed to study possible intermolecular arrangements and their characteristic features at finite temperature. This methodology incorporates available experimental data to suggest different variants of possible fibrillar nanostructures. These structural candidates were studied theoretically and their behavior was then cross-validated against available experimental evidence. Large-scale all-atom MD simulations for several proposed fibrillar models were also performed. They revealed the dependence of the fibrillar morphology on the intrinsic molecular organization of the fibrils. Using combined theoretical and experimental analysis, we have suggested the most likely models of fibril formation.

Future work should be aimed towards the development of new ways for the formation of semiconducting fiber-like supramolecular structures with mechanical properties mimicking those of natural materials such as silk or amyloid fibers. The idea is to obtain conductive materials with good mechanical strength and elasticity for various applications. Innovative methods such as computer simulations and combined multidisciplinary partnerships between chemists, physicists, and biochemists are required for the development and optimization of these bioinspired materials to provide fundamental understanding of their structural and charge transport properties.

Acknowledgements

We would like to thank Hans G. Börner and Jens Hentschel (Humboldt-University Berlin). Financial support from the Deutsche Forschungsgemeinschaft (SFB 569, project A11 "Self-organizing bioinspired oligothiophene/oligopeptide hybrids: A joint experimental and theoretical approach"), RFBR (projects 09-03-12033, 09-04-12146, 10-03-92003 and 10-04-01182), and FTOP “Research and scientific-pedagogical staff of innovational Russia” for 2009-2013 (government contract P475) is highly appreciated.

References

1. Chiti, F.; Dobson, C. M. *Annu. Rev. Biochem.* **2006,** *75,* 333–366. doi:10.1146/annurev.biochem.75.101304.123901
2. Makin, O. S.; Serpell, L. C. *FEBS J.* **2005,** *272,* 5950–5961. doi:10.1111/j.1742-4658.2005.05025.x
3. Rochet, J.-C.; Lansbury, P. T., Jr. *Curr. Opin. Struct. Biol.* **2000,** *10,* 60–68. doi:10.1016/S0959-440X(99)00049-4
4. Fändrich, M.; Meinhardt, J.; Grigorieff, N. *Prion* **2009,** *3,* 89–93. doi:10.4161/pri.3.2.8859
5. Kumar, S.; Udgaonkar, J. B. *Curr. Sci.* **2010,** *98,* 639–656.
6. Rambaran, R. N.; Serpell, L. C. *Prion* **2008,** *2,* 112–117. doi:10.4161/pri.2.3.7488
7. Börner, H. G. *Prog. Polym. Sci.* **2009,** *34,* 811–851. doi:10.1016/j.progpolymsci.2009.05.001
8. Börner, H. G.; Schlaad, H. *Soft Matter* **2007,** *3,* 394–408. doi:10.1039/b615985k
9. Lutz, J.-F.; Börner, H. G. *Prog. Polym. Sci.* **2008,** *33,* 1–39. doi:10.1016/j.progpolymsci.2007.07.005
10. Schlaad, H.; Antonietti, M. *Eur. Phys. J. E* **2003,** *10,* 17–23. doi:10.1140/epje/e2003-00004-3
11. Baldwin, A. J.; Bader, R.; Christodoulou, J.; MacPhee, C. E.; Dobson, C. M.; Barker, P. D. *J. Am. Chem. Soc.* **2006,** *128,* 2162–2163. doi:10.1021/ja0565673
12. Scheibel, T.; Parthasarathy, R.; Sawicki, G.; Lin, X.-M.; Jaeger, H.; Lindquist, S. L. *Proc. Natl. Acad. Sci. U. S. A.* **2003,** *100,* 4527–4532. doi:10.1073/pnas.0431081100
13. Reches, M.; Gazit, E. *Science* **2003,** *300,* 625–627. doi:10.1126/science.1082387
14. Hardy, J. G.; Scheibel, T. R. *Biochem. Soc. Trans.* **2009,** *37,* 677–681. doi:10.1042/BST0370677
15. Vandermeulen, G. W. M.; Klok, H.-A. *Macromol. Biosci.* **2004,** *4,* 383–398. doi:10.1002/mabi.200300079
16. Eckhardt, D.; Groenewolt, M.; Krause, E.; Börner, H. G. *Chem. Commun.* **2005,** 2814–2816. doi:10.1039/b503275j
17. Ikkala, O.; Brinke, G. *Chem. Commun.* **2004,** 2131–2137. doi:10.1039/B403983A
18. Hentschel, J.; Krause, E.; Börner, H. G. *J. Am. Chem. Soc.* **2006,** *128,* 7722–7723. doi:10.1021/ja060759w
19. Hentschel, J.; Börner, H. G. *J. Am. Chem. Soc.* **2006,** *128,* 14142–14149. doi:10.1021/ja0649872
20. Frauenrath, H.; Jahnke, E. *Chem.–Eur. J.* **2008,** *14,* 2942–2955. doi:10.1002/chem.200701325
21. Diegelmann, S. R.; Gorham, J. M.; Tovar, J. D. *J. Am. Chem. Soc.* **2008,** *130,* 13840–13841. doi:10.1021/ja805491d
22. Schillinger, E.-K.; Mena-Osteritz, E.; Hentschel, J.; Börner, H. G.; Bäuerle, P. *Adv. Mater.* **2009,** *21,* 1562–1567. doi:10.1002/adma.200803110
23. Shaytan, A. K.; Schillinger, E.-K.; Khalatur, P. G.; Mena-Osteritz, E.; Hentschel, J.; Börner, H. G.; Bäuerle, P.; Khokhlov, A. R. *ACS Nano* published ASAP. doi:10.1021/nn2011943
24. Azumi, R.; Götz, G.; Debaerdemaeker, T.; Bäuerle, P. *Chem.–Eur. J.* **2000,** *6,* 735–744. doi:10.1002/(SICI)1521-3765(20000218)6:4<735::AID-CHEM735>3.0.CO;2-A
25. Hentschel, J.; ten Cate, M. G. J.; Börner, H. G. *Macromolecules* **2007,** *40,* 9224–9232. doi:10.1021/ma071810z
26. Sohma, Y.; Sasaki, M.; Hayashi, Y.; Kimura, T.; Kiso, Y. *Chem. Commun.* **2004,** 124–125. doi:10.1039/B312129A

27. Mutter, M.; Chandravarkar, A.; Boyat, C.; Lopez, J.; Dos Santos, S.; Mandal, B.; Mimna, R.; Murat, K.; Patiny, L.; Saucède, L.; Tuchscherer, G. *Angew. Chem., Int. Ed.* **2004,** *43,* 4172–4178. doi:10.1002/anie.200454045
28. Schillinger, E.-K. Peptide- and Amino Acid-Directed Self-Assembly of Oligothiophenes. Ph.D. Thesis, University of Ulm, Ulm, Germany, 2010. http://vts.uni-ulm.de/docs/2010/7350/vts_7350_10424.pdf
29. Mena-Osteritz, E. *Adv. Mater.* **2002,** *14,* 609–616. doi:10.1002/1521-4095(20020418)14:8<609::AID-ADMA609>3.0.CO;2-7
30. Periole, X.; Rampioni, A.; Vendruscolo, M.; Mark, A. E. *J. Phys. Chem. B* **2009,** *113,* 1728–1737. doi:10.1021/jp8078259
31. Gus'kova, O. A.; Khalatur, P. G.; Bäuerle, P.; Khokhlov, A. R. *Chem. Phys. Lett.* **2008,** *461,* 64–70. doi:10.1016/j.cplett.2008.06.058
32. Gus'kova, O. A.; Khalatur, P. G.; Khokhlov, A. R. *Nanotechnologies in Russia* **2008,** *3,* 481–493. doi:10.1134/S1995078008070112
33. Gus'kova, O. A.; Khalatur, P. G.; Khokhlov, A. R. *Macromol. Theory Simul.* **2009,** *18,* 219–246. doi:10.1002/mats.200800090
34. Gus'kova, O. A.; Schillinger, E.; Khalatur, P. G.; Bäuerle, P.; Khokhlov, A. R. *Polym. Sci., Ser. A* **2009,** *51,* 430–445. doi:10.1134/S0965545X09040099
35. Shaytan, A. K.; Khokhlov, A. R.; Khalatur, P. G. *Soft Matter* **2010,** *6,* 1453–1461. doi:10.1039/b918562c
36. Tycko, R. *Curr. Opin. Struct. Biol.* **2004,** *14,* 96–103. doi:10.1016/j.sbi.2003.12.002
37. Sawaya, M. R.; Sambashivan, S.; Nelson, R.; Ivanova, M. I.; Sievers, S. A.; Apostol, M. I.; Thompson, M. J.; Balbirnie, M.; Wiltzius, J. J. W.; McFarlane, H. T.; Madsen, A. Ø.; Riekel, C.; Eisenberg, D. *Nature* **2007,** *447,* 453–457. doi:10.1038/nature05695
38. Nelson, R.; Sawaya, M. R.; Balbirnie, M.; Madsen, A. Ø.; Riekel, C.; Grothe, R.; Eisenberg, D. *Nature* **2005,** *435,* 773–778. doi:10.1038/nature03680
39. Plimpton, S. *J. Comput. Phys.* **1995,** *117,* 1–19. doi:10.1006/jcph.1995.1039
40. Rodríguez-Ropero, F.; Casanovas, J.; Alemán, C. *J. Comput. Chem.* **2008,** *29,* 69–78. doi:10.1002/jcc.20763
41. Tsuzuki, S.; Honda, K.; Azumi, R. *J. Am. Chem. Soc.* **2002,** *124,* 12200–12209. doi:10.1021/ja0204877

License and Terms

Beilstein Journal of Nanotechnology

Fabrication of multi-parametric platforms based on nanocone arrays for determination of cellular response

Lindarti Purwaningsih‡, Tobias Schoen‡, Tobias Wolfram, Claudia Pacholski and Joachim P. Spatz*

Full Research Paper

Open Access

Address:
Department of New Materials and Biosystems, Max Planck Institute for Intelligent Systems, Heisenbergstraße 3, 70569 Stuttgart, Germany

Email:
Joachim P. Spatz* - spatz@mf.mpg.de

* Corresponding author ‡ Equal contributors

Keywords:
block copolymer nanolithography; cell adhesion; nanostructures; surface chemistry; surface topography

Beilstein J. Nanotechnol. **2011,** *2,* 545–551.
doi:10.3762/bjnano.2.58

Received: 28 April 2011
Accepted: 02 August 2011
Published: 06 September 2011

This article is part of the Thematic Series "Organic–inorganic nanosystems".

Guest Editor: P. Ziemann

Abstract

Cellular response to both surface topography and surface chemistry has been studied for several years. However, most of the studies focus on only one of the two parameters and do not consider their possible synergistic effects. Here, we report on a fabrication method for nanostructured surfaces composed of highly ordered arrays of silica nanocones with gold tips. By using a combination of block copolymer nanolithography, electroless deposition, and reactive ion etching several parameters such as structure height and structure distance could easily be adjusted to the desired values. The gold tips allow for easy functionalization of the substrates through a thiol linker system. Improved neural cell adhesion can be obtained and is dependent on the nature of the nanocone surface, thus illustrating the influence of different surface topographies on the nanometer length scale, on a complex cellular behavior such as cell adhesion. Substrate and surface functionality are shown to last over several days, leading to the conclusion that the features of our substrates can also be used for longer term experiments. Finally, initial neural cell adhesion is found to be more prominent on substrates with short intercone distances, which is an important finding for research dealing with the reactions of neuron-like tissue in the immediate moments after direct contact with an implanted surface.

Introduction

Nanostructured materials for medical applications are intended to be in contact with human tissue and therefore to influence cell function by their surface topography as well as by their surface chemistry. Countless studies on cellular response to nanoscale topographies [1-4], chemical gradients [5,6], and combinations of both [7] have been conducted, which has led to

the accumulation of basic knowledge concerning cell morphology changes. However, long-term cellular response to nanostructures has not been understood due to the lack of material integrity. In addition, mainly standard microfabrication techniques including photolithography, wet etching, or reactive ion etching, as well as simple chemical approaches, have been employed for the fabrication of nanostructured materials neglecting the complexity of the biological aspects.

After tremendous work on cellular response to surface features in the micrometer range, such as grooves, ridges and wells, the research focus has shifted to the investigation of the potential of nanostructured materials for controlling cell–surface interactions [8]. For several years experimental studies on the influence of nanoscale topography on cell behavior have been largely obstructed by the lack of nanofabrication techniques to generate functional structures. Recent advances in nanofabrication techniques such as nanoimprint lithography (NIL) [9], nanosphere/colloidal lithography [10], dip pen lithography [11], e-beam lithography [12] have enabled and motivated biomaterial development. However, most of these methods have disadvantages such as high fabrication costs, lengthy preparation times, small-sized nanostructured areas (few square microns) or restricted chemical functionality due to the limited access to composite materials. In particular, the number of material surfaces that offer a tuneable parameter range is insufficient. In spite of the huge progress in material science, chemical and topographical surface gradients have mainly been investigated separately [13] neglecting composite materials such as semiconductor/metal structures [14-17]. Only a few attempts to study cell–surface interactions through topographical and chemical gradients have been reported to date [18]. Representative review articles on neuronal cell response to nanostructured surfaces have been published [19,20]. Despite the enormous effort made in this research area, intelligently designed materials are still required in order to control the interaction between cells and materials, and which can find applications in the fields of tissue engineering, implants, cell-based biosensors, and basic cell biology [21].

In this work, a multiparametric platform for the determination of cellular response has been fabricated by a combination of block copolymer micelle lithography (BCML), electroless deposition (ED) and reactive ion etching (RIE). The resulting highly ordered silica nanocone array with gold tips allows for the investigation of several parameters in cell studies at the same time, that is two- (distance) and three-dimensional (topography) aspects, as well as chemical and biological stimuli. Structures with feature sizes in a range of 50–250 nm for the nanoparticle spacing (i.e., the distance between etched nanostructures) and 10–500 nm for the structural height, can be easily achieved on large areas. Gold nanoparticles on top of the nanostructures allow for spatially resolved functionalization with a variety of biomolecules through simple thiol chemistry. A 3,3'-dithiobis(sulfosuccinimidylpropionate) (DTSSP) linker molecule was used to immobilize laminin, an extracellular matrix, multidomain, trimeric glycoprotein, on the differently structured substrates. Laminin is known to support neural cell adhesion, proliferation, and differentiation. The cell adhesion activity of human neuroblastoma cells (SHSY-5Y) was investigated on these substrates and correlated with topographical features of the nanocone arrays.

Results and Discussion

Scheme 1 shows the fabrication process for nanocone arrays with gold tips. First, arrays of gold nanoparticles were deposited on a glass surface by diblock copolymer micelle lithography (BCML); this is a versatile technique which allows for the generation of extended quasi-hexagonal arrays of metallic nanoparticles with tuneable interparticle distance (Scheme 1a). Briefly, a diblock copolymer (polystyrene-*block*-poly(2-vinylpyridine), PS-*b*-P2VP) was utilized as a nanoreactor for depositing metallic nanoparticles. A representative SEM image of an as-prepared gold nanoparticle array that should act as a mask upon subsequent reactive ion etching (RIE), is shown in Figure S1a (Supporting Information File 1). However, the small diameters of the gold nanoparticles (1–15 nm) are not sufficient to resist the harsh etching conditions required for the fabrication of the desired topography and chemical functionality (gold on top of the nanocones). To increase the size of the gold nanoparticles, electroless deposition (ED) was used (Scheme 1b) resulting in the generation of nanocone arrays with

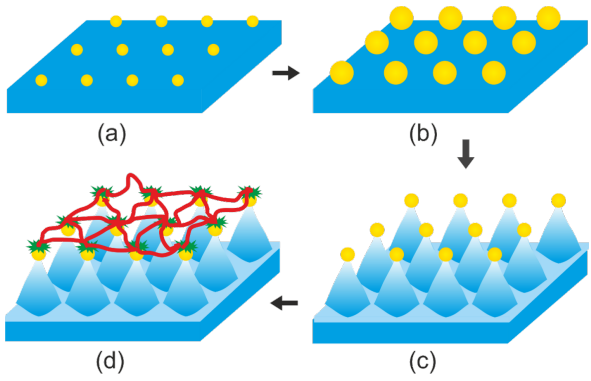

Scheme 1: Method used to fabricate silica nanocone arrays with gold functionalized tips. A quasi-hexagonally ordered gold nanoparticle array was deposited on a silica substrate by block copolymer nanolithography (a). Electroless deposition was employed to increase the size of the gold particles (b) before subsequent reactive ion etching was performed (c). The resulting nanostructures can be functionalized with biological active molecules at their gold tips through thiol chemistry. (d) Gold nanocone array whose gold tips have been functionalized with DTSSP and laminin.

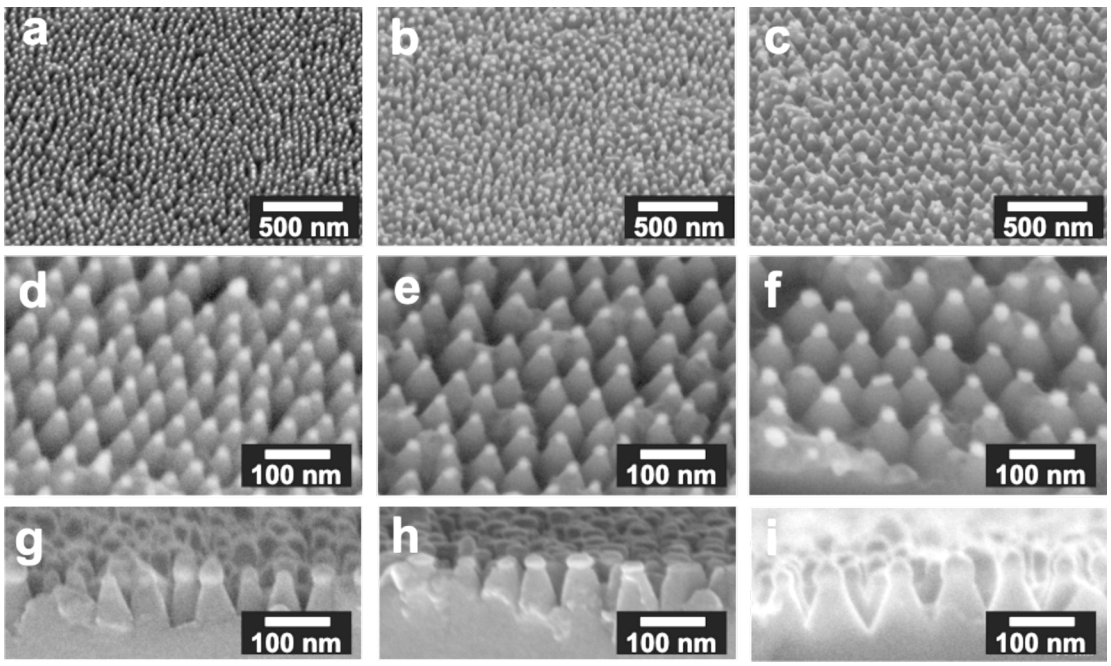

Figure 1: SEM images of the nanocone arrays with gold tips fabricated by a combination of BCML, electroless deposition, and RIE, from three different block copolymer solutions: (PS(501)-*b*-P2VP(323) (first column), PS(1056)-*b*-P2VP(495) (second column), and PS(5355)-*b*-P2VP(714) (third column)). The first row (a–c) shows SEM images of the nanocones taken at a 45° angle from the surface. The second row (d–f) depicts SEM images taken by using an ESB detector showing the compositional intensity differences between the gold particle and amorphous silicon oxide underneath. Finally, the last row (g–i) displays cross-sectional SEM images.

tuneable topographic features. Electroless deposition is an autocatalytic process that allows for the spatially resolved deposition of metal on to metal surfaces or colloids. Gold nanoparticle arrays with gold particle diameters of approximately 30–45 nm were prepared (Figure S1b). Finally, a reactive ion etching (RIE) process was employed to generate nanocone arrays (Scheme 1c). The etching process was controlled in such a way that gold particles remained on top of the nanocones, in order to provide easily accessible anchor points for biological molecules (Scheme 1d). As expected, the nanostructure height could be controlled by choosing the appropriate etching time. The shape of the etched nanoscale features depends on the etching gas composition as well as on the employed substrate material (glass or fused silica; data not shown).

Scanning electron microscopy (SEM) images of the fabricated nanocone arrays with gold tips are displayed in Figure 1 and Figure S1c,d (Supporting Information File 1). Three different diblock copolymers were used for the generation of gold nanoparticle arrays ((PS(501)-*b*-P2VP(323), polymer 501 (first column); PS(1056)-*b*-P2VP(495), polymer 1056 (second column); and PS(5355)-*b*-P2VP(714), polymer 5355 (third column)) in order to tune the interparticle and, consequently, the nanocone spacing, as well as the amount of potential binding sites available in every 1 μm^2 of the flat surface. Below, each polymer is abbreviated by its PS unit number. Low-magnification side-view SEM images (tilt angle: 45°) of the nanostructures are shown in the first row and confirm the quasi-hexagonal order of the array as well as the variation of the nanocone distance. The location of gold and SiO_2 in the nanostructures was visualized using an energy selective backscattered (ESB) detector, which gives nanoscale compositional information by contrast differences. Obviously, gold is mainly detected at the tips of the silica nanocones (Figure 1, second row). The height of the different nanostructures is similar and does not depend on the employed diblock copolymer but rather on the etching time (cross-sectional SEM images, third row).

Important parameters of the fabricated nanocone arrays with gold tips are summarized in Table 1. Relevant parameters such as the interparticle distance *d* and the radius of the gold particle *r* were directly extracted from SEM images or deduced by simple calculations (i.e., the number of gold nanoparticles in every 1 μm^2 surface). In order to obtain reliable data, at least three samples from every batch of the nanostructures were inspected with Inlens, SE2 and ESB detectors. An increase in gold nanoparticle size and interparticle/nanocone distance with increasing diblock copolymer chain length was observed. Consequently, a declining number of gold nanoparticles per μm^2 of the flat glass surface was obtained with increasing

Table 1: Measured (*r*, *R* and *d*) and calculated (*N*) dimensions of the nanocone arrays fabricated using three block copolymer solutions (PS(501)-*b*-P2VP(323), PS(1056)-*b*-P2VP(495), and PS(5355)-*b*-P2VP(714)).

	PS(501)-*b*-P2VP(323)	PS(1056)-*b*-P2VP(495)	PS(5355)-*b*-P2VP(714)
radius of the gold particle *r* (nm)	13 ± 2	14 ± 3	17 ± 3
radius of the base of the nanocone *R* (nm)	28 ± 5	36 ± 4	42 ± 7
distance between two nanocones *d* (nm)	65 ± 12	78 ± 16	105 ± 26
gold-nanoparticle projected surface density (μm^{-2}) after BCML (calculated value)	289 ± 106	189 ± 32	105 ± 20

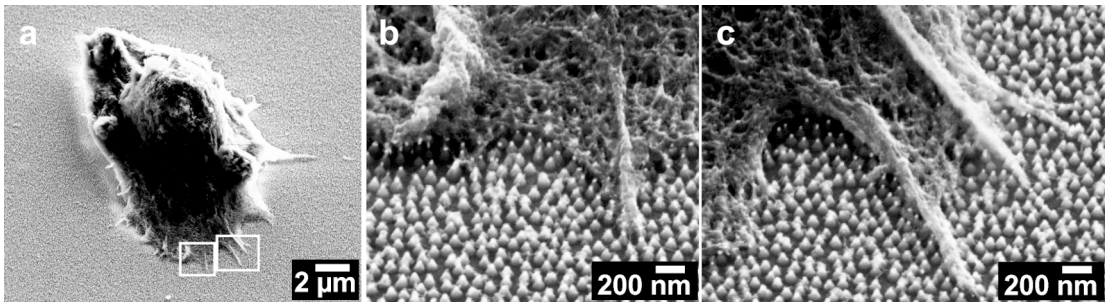

Figure 2: Scanning electron microscopy analysis (45° tilt) of adhering SHSY5Y human neuroblastoma cells. The figure shows a clear adhesion of cellular protrusions to the Au-tipped nanocones. Images were taken at different magnification with a SE2 detector.

diblock copolymer chain length. The structures had an average areal density of particles of 289 ± 106, 189 ± 32, and 105 ± 20 μm^{-2} for the substrates fabricated from polymer 501, polymer 1056 and polymer 5355, respectively.

Contact angle measurements were carried out prior to the surface functionalizations in order to determine the intrinsic hydrophobicity resulting from the nanostructure. Figure S2 (Supporting Information File 1) illustrates the contact angle measurements taken from nanocone arrays prepared from three different diblock copolymer chain lengths, before (first row) and after surface functionalization with DTSSP and laminin (second row). In general, the contact angles and therefore the hydrophobicities of the three fabricated nanostructures are quite similar before functionalization (~60°). Attaching biomolecules to the surfaces lowers the contact angle to values of approximately 20° proving that the hydrophobicity/hydrophilicity of the substrates is a constant parameter in the following cell experiments. The potential of the substrates to support neural cell adhesion was tested with SHSY5Y human neuroblastoma cells.

Figure 2 shows adhered SHSY5Y human neuroblastoma cells on top of the nanostructured arrays. The gold-tipped nanocones were biofunctionalized with laminin with DTSSP as a thiol-based linker between the gold tips and the protein. Laminin is a protein that mediates cell adhesion and provides a cell survival signal. It was covalently bound to the gold nanoparticles. The line between biofunctionalized nanocone arrays and nonfunctionalized glass is clearly visible in the phase contrast and scanning electron microscopy images (see Figure S3, Supporting Information File 1). The bare glass was completely passivated by silane–PEG2000 and showed little or no cell adhesion. The images shown were taken after 3 hours adhesion time and cells showed protrusion and spreading activity on all substrates.

Figure S4 (Supporting Information File 1) depicts single neural cells and their protrusions, as analyzed by scanning electron microscopy. The substrates were tilted at 45° to make the three dimensional pillar structures visible. For SEM analysis of neural cell adhesion, both Inlens- and SE2-detectors were used. The Inlens detector offers better insights to the cellular details and the SE2-detector gives a better resolution for the nanocone structures. The images show that cellular protrusions adhere on top of the nanocones and not in between. Gold that may have been sputtered back to the surface in small amounts did not lead to effective cell adhesion on the nonfunctionalized side of the substrate. The cell membrane and the cellular protrusions are in close proximity, which is important for the functional aspects of the substrates in possible applications as surfaces for neuroactive implants.

Figure 3 shows the quantitative analysis of SHSY5Y-cell adhesion to three different kinds of laminin-functionalized

substrate: A flat glass surface, a glass surface decorated with a gold nanoparticle array, and a glass surface structured with an array of gold-capped nanocones. The data shown were extracted from microscopy images taken after 24 hours adhesion time. The gold nanoparticle substrates showed more cell adhesion than did the pure glass surfaces but less cell adhesion than did the nanocone arrays with gold tips. The gold-capped nanocones display overall higher cell adhesion in comparison to flat gold particles or bare glass. Cellular adhesion was ~40% higher on gold-capped nanocones compared to flat gold nanoparticles. Comparison of cell adhesion on substrates fabricated from polymer 501, polymer 1056, and polymer 5355 reveals that cells plated on substrates generated from polymer 501 and polymer 1056 have similar adhesion activities, while cells on the substrates made from the 5355 polymer have slightly less cell adhesion activity in terms of cell numbers. Cellular adhesion is highly influenced by the protein density that is afforded to the cell by the substrate [22,23].

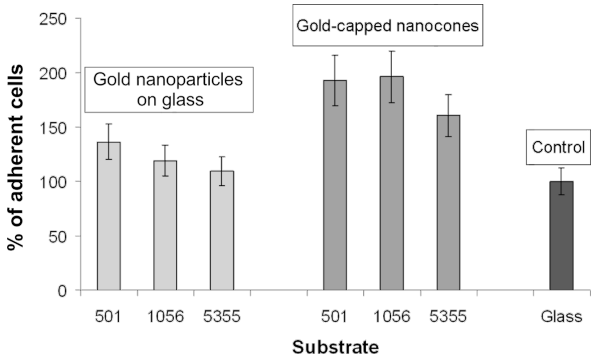

Figure 3: Percentage of adherent cells compared to cell adhesion on control surfaces (glass cover slip coated with laminin, value equals 100%). The nanocone arrays with gold tips show overall higher cell adhesion in comparison to gold nanoparticles on glass or bare glass. Cell adhesion on nanocones is approximately 40% higher compared to flat gold nanoparticles.

An increased ligand-to-ligand spacing results in an increased distance between the transmembrane proteins of the adherent cells, which in turn results in decreased cellular adhesion. Substrates obtained from polymer 501 and polymer 1056 have similar spacing compared to substrates made from polymer 5355 (Table 1) and thus exhibit similar cell adhesion activities. Our experiments showed that nanocone arrays with gold tips are a suitable tool for higher neural cell adhesion activity and therefore might be interesting as a surface structuring scheme for neuroimplants.

Experimental

Synthesis of gold nanoparticle arrays: The gold nanoparticle arrays are generated on SiO_2 surfaces by means of the BCML technique as described before [24-26]. Briefly, three different polystyrene(*x*)-*block*-poly(2-vinylpyridine)(*y*) block copolymers were employed: (PS(*x*)-*b*-P2VP(*y*)) with *x* and *y* being 501 and 323; 1056 and 495; and 5355 and 714 respectively, where *x* and *y* represent the number of theoretical repeat units of polystyrene and poly-vinylpyridine, respectively, as calculated by the initial monomer/initiator feed ratio. Except for the polymer solution of *x*, *y* = 501, 323 which was made to a concentration of 5 mg/mL and a loading of 0.4 (defined as $L = n$(metal precursor)/n(PS-*b*-P2VP)), the other polymer solutions were made to a concentration of 3 mg/mL and a loading of 0.4. The substrates were treated with hydrogen plasma in a PVA TePla plasma system (150 W, 0.4 mbar, and 45 minutes) in order to reduce the metal salts into the corresponding metals and as well as to remove the polymer matrix.

Gold nanoparticle enlargement by electroless deposition: The next step is to increase the size of the gold nanoparticles by a published method, known as light-assisted electroless deposition [27-29].

Reactive Ion Etching: Afterwards, an RIE process was applied to etch the SiO_2 layer. A Plasma Lab 80 Plus ICP-RIE system was used, with a mixture of CHF_3 and CF_4 gases (at a ratio of 10:1, respectively) at a total pressure of 10 mTorr, a temperature of 20 °C and an RF power of 30 W. The gold particles act as a "mask" for the etch resulting in conical structures with gold particles located at the top. The nanocone arrays with gold tips can later be coated with different molecules such as proteins or antibodies.

Cell culture and cell adhesion experiments: Cell culture maintenance for SHSY-5Y neuroblastoma cells was performed as described previously [24]. The substrates for cell adhesion experiments were passivated with silane–PEG2000 as described before [30] and then biofunctionalized with 10 µg/mL laminin-1 with a 25 mM solution of DTSSP (Pierce, USA) in PBS as a linker between gold and laminin. Laminin-coated glass cover slips (control) were fabricated by a standard protocol [31]. SHSY5Y human neuroblastoma cells were then incubated on the substrates for 3–24 h at 37 °C and 5% CO_2 at a cell density of 80,000 cells/mL. The cells were fixed with 4% para-formaldehyde and analyzed by phase contrast microscopy (Zeiss Axiovert 40 CFL microscope). The average cell counts per measured field with 10× magnification objective normalized to glass for each substrate, offer the possibility to directly compare each substrate and deduct its adhesion activity. After critical point drying (Baltec CPD 030 critical point dryer), the substrates were coated with carbon by means of a Med 020 Coating System (Leica Microsystems) and finally examined by scanning electron microscopy (Zeiss Gemini Ultra-55).

Supporting Information

Supporting Information features additional images and illustrations of the nano-arrays and the adhered cells.

Supporting Information File 1

Additional images and illustrations.
[http://www.beilstein-journals.org/bjnano/content/supplementary/2190-4286-2-58-S1.pdf]

Acknowledgements

We are grateful for the support by the Max Planck Society. The research leading to these results has received funding from the European Union Seventh Framework Programme (FP7/2007-2013) under grant agreement no. NMP3-SL-2009-229294 NanoCARD. JS is a Weston Visiting Professorship at the Weizmann Institute of Science, Israel.

References

1. Decuzzi, P.; Ferrari, M. *Biomaterials* **2010,** *31,* 173. doi:10.1016/j.biomaterials.2009.09.018
2. Brunetti, V.; Maiorano, G.; Rizzello, L.; Sorce, B.; Sabella, S.; Cingolani, R.; Pompa, P. P. *Proc. Natl. Acad. Sci. U. S. A.* **2010,** *107,* 6264. doi:10.1073/pnas.0914456107
3. Wilkinson, C. D. W.; Riehle, M.; Wood, M.; Gallagher, J.; Curtis, A. S. G. *Mater. Sci. Eng., C* **2002,** *19,* 263. doi:10.1016/S0928-4931(01)00396-4
4. Flemming, R. G.; Murphy, C. J.; Abrams, G. A.; Goodman, S. L.; Nealey, P. F. *Biomaterials* **1999,** *20,* 573. doi:10.1016/S0142-9612(98)00209-9
5. Arnold, M.; Cavalcanti-Adam, E. A.; Glass, R.; Blümmel, J.; Eck, W.; Kantlehner, M.; Kessler, H.; Spatz, J. P. *ChemPhysChem* **2004,** *5,* 383. doi:10.1002/cphc.200301014
6. Barry, J. J. A.; Howard, D.; Shakesheff, K. M.; Howdle, S. M.; Alexander, M. R. *Adv. Mater.* **2006,** *18,* 1406. doi:10.1002/adma.200502719
7. Yang, J.; Rose, F. R. A. J.; Gadegaard, N.; Alexander, M. R. *Adv. Mater.* **2009,** *21,* 300. doi:10.1002/adma.200801942
8. Stevens, M. M.; George, J. H. *Science* **2005,** *310,* 1135. doi:10.1126/science.1106587
9. Yim, E. K. F.; Reano, R. M.; Pang, S. W.; Yee, A. F.; Chen, C. S.; Leong, K. W. *Biomaterials* **2005,** *26,* 5405. doi:10.1016/j.biomaterials.2005.01.058
10. Dalby, M. J.; Gadegaard, N.; Tare, R.; Andar, A.; Riehle, M. O.; Herzyk, P.; Wilkinson, C. D. W.; Oreffo, R. O. C. *Nat. Mater.* **2007,** *6,* 997. doi:10.1038/nmat2013
11. Lee, K.-B.; Park, S.-J.; Mirkin, C. A.; Smith, J. C.; Mrksich, M. *Science* **2002,** *295,* 1702. doi:10.1126/science.1067172
12. Teixeira, A. I.; Nealey, P. F.; Murphy, C. J. *J. Biomed. Mater. Res., Part A* **2004,** *71A,* 369. doi:10.1002/jbm.a.30089
13. Lim, J. Y.; Donahue, H. J. *Tissue Eng.* **2007,** *13,* 1879. doi:10.1089/ten.2006.0154
14. Zhang, H.; Amro, N. A.; Disawal, S.; Elghanian, R.; Shile, R.; Fragala, J. *Small* **2007,** *3,* 81. doi:10.1002/smll.200600393
15. Hsu, C.-H.; Lo, H.-C.; Chen, C.-F.; Wu, C. T.; Hwang, J.-S.; Das, D.; Tsai, J.; Chen, L.-C.; Chen, K.-H. *Nano Lett.* **2004,** *4,* 471. doi:10.1021/nl049925t
16. Lewis, P. A.; Ahmed, H.; Sato, T. *J. Vac. Sci. Technol., B: Microelectron. Nanometer Struct.–Process., Meas., Phenom.* **1998,** *16,* 2938. doi:10.1116/1.590322
17. Ovchinnikov, V.; Malinin, A.; Novikov, S.; Tuovinen, C. *Phys. Scr.* **1999,** 263. doi:10.1238/Physica.Topical.079a00263
18. Richert, L.; Vetrone, F.; Yi, J. H.; Zalzal, S. F.; Wuest, J. D.; Rosei, F.; Nanci, A. *Adv. Mater.* **2008,** *20,* 1488. doi:10.1002/adma.200701428
19. Roach, P.; Parker, T.; Gadegaard, N.; Alexander, M. R. *Surf. Sci. Rep.* **2010,** *65,* 145. doi:10.1016/j.surfrep.2010.07.001
20. Khan, S.; Newaz, G. *J. Biomed. Mater. Res., Part A* **2010,** *93A,* 1209. doi:10.1002/jbm.a.32698
21. Price, R. L.; Haberstroh, K.; Webster, T. *Med. Biol. Eng. Comput.* **2003,** *41,* 372. doi:10.1007/BF02348445
22. Thelen, K.; Wolfram, T.; Maier, B.; Jährling, S.; Tinazli, A.; Piehler, J.; Spatz, J. P.; Pollerberg, G. E. *Soft Matter* **2007,** *3,* 1486. doi:10.1039/b707250c
23. Wolfram, T.; Spatz, J. P.; Burgess, R. W. *BMC Cell Biol.* **2008,** *9,* No. 64. doi:10.1186/1471-2121-9-64
24. Spatz, J. P.; Eibeck, P.; Mössmer, S.; Möller, M.; Kramarenko, E. Yu.; Khalatur, P. G.; Potemkin, I. I.; Khokhlov, A. R.; Winkler, R. G.; Reineker, P. *Macromolecules* **2000,** *33,* 150. doi:10.1021/ma990751p
25. Spatz, J. P.; Mössmer, S.; Hartmann, C.; Möller, M.; Herzog, T.; Krieger, M.; Boyen, H.-G.; Ziemann, P.; Kabius, B. *Langmuir* **2000,** *16,* 407. doi:10.1021/la990070n
26. Haupt, M.; Miller, S.; Glass, R.; Arnold, M.; Sauer, R.; Thonke, K.; Möller, M.; Spatz, J. P. *Adv. Mater.* **2003,** *15,* 829. doi:10.1002/adma.200304688
27. Tanahashi, I.; Tohda, T. *J. Am. Ceram. Soc.* **1996,** *79,* 796. doi:10.1111/j.1151-2916.1996.tb07948.x
28. Spatz, J. P.; Sheiko, S.; Möller, M.; Winkler, R. G.; Reineker, P.; Marti, O. *Langmuir* **1997,** *13,* 4699. doi:10.1021/la970311w
29. Lohmueller, T.; Bock, E.; Spatz, J. P. *Adv. Mater.* **2008,** *20,* 2297. doi:10.1002/adma.200702635
30. Blümmel, J.; Perschmann, N.; Aydin, D.; Drinjakovic, J.; Surrey, T.; Lopez-Garcia, M.; Kessler, H.; Spatz, J. P. *Biomaterials* **2007,** *28,* 4739. doi:10.1016/j.biomaterials.2007.07.038
31. Kucik, D. F.; Wu, C. Cell-adhesion assays. In *Cell Migration;* Guan, J.-L., Ed.; Methods in Molecular Biology, Vol. 294; Humana Press: Totowa, NJ, 2005; pp 43–54. doi:10.1385/1-59259-860-9:043

Beilstein Journal of Nanotechnology

Terthiophene on Au(111): A scanning tunneling microscopy and spectroscopy study

Berndt Koslowski*[1], Anna Tschetschetkin[1], Norbert Maurer[1], Elena Mena-Osteritz*[2], Peter Bäuerle[2] and Paul Ziemann[1]

Full Research Paper

Open Access

Address:
[1]Institut für Festkörperphysik, Albert-Einstein-Allee 11, 89081 Ulm, Germany and [2]Institut für Organische Chemie II und Neue Materialien, Albert-Einstein-Allee 11, 89081 Ulm, Germany

Email:
Berndt Koslowski* - berndt.koslowski@uni-ulm.de; Anna Tschetschetkin - anna.tschetschetkin@uni-ulm.de; Norbert Maurer - norbert.maurer@uni-ulm.de; Elena Mena-Osteritz* - elena.mena-osteritz@uni-ulm.de; Peter Bäuerle - peter.baeuerle@uni-ulm.de; Paul Ziemann - paul.ziemann@uni-ulm.de

* Corresponding author

Keywords:
Au(111); electronic density of states; STM; STS; terthiophene

Beilstein J. Nanotechnol. **2011,** *2,* 561–568.
doi:10.3762/bjnano.2.60

Received: 03 June 2011
Accepted: 25 August 2011
Published: 09 September 2011

This article is part of the Thematic Series "Organic–inorganic nanosystems".

Associate Editor: E. Meyer

Abstract

Terthiophene (3T) molecules adsorbed on herringbone (HB) reconstructed Au(111) surfaces in the low coverage regime were investigated by means of low-temperature scanning tunneling microscopy (STM) and spectroscopy (STS) under ultra-high vacuum conditions. The 3T molecules adsorb preferentially in fcc regions of the HB reconstruction with their longer axis oriented perpendicular to the soliton walls of the HB and at maximum mutual separation. The latter observation points to a repulsive interaction between molecules probably due to parallel electrical dipoles formed during adsorption. Constant-separation (*I*-*V*) and constant-current (*z*-*V*) STS clearly reveal the highest occupied (HOMO) and lowest unoccupied (LUMO) molecular orbitals, which are found at −1.2 eV and +2.3 eV, respectively. The HOMO–LUMO gap corresponds to that of a free molecule, indicating a rather weak interaction between 3T and Au(111). According to conductivity maps, the HOMO and LUMO are inhomogeneously distributed over the adsorbed 3T, with the HOMO being located at the ends of the linear molecule, and the LUMO symmetrically with respect to the longer axis of the molecule at the center of its flanks. Analysis of spectroscopic data reveals details of the contrast mechanism of 3T/Au(111) in STM. For that, the Shockley-like surface state of Au(111) plays an essential role and appears shifted outwards from the surface in the presence of the molecule. As a consequence, the molecule can be imaged even at a tunneling bias within its HOMO–LUMO gap. A more quantitative analysis of this detail resolves a previous discrepancy between the fairly small apparent STM height of 3T molecules (1.4–2.0 nm, depending on tunneling bias) and a corresponding larger value of 3.5 nm based on X-ray standing wave analysis. An additionally observed linear decrease of the differential tunneling barrier at positive bias when determined on top of a 3T molecule is compared to the bias independent barrier obtained on bare Au(111) surfaces. This striking difference of the barrier behavior with and without adsorbed molecules is interpreted as indicating an adsorption-induced dimensionality transition of the involved tunneling processes.

Introduction

Because of their expedient properties and their diversity, oligo- and polythiophenes are among the most investigated organic semiconductors. Especially, oligothiophenes are very promising candidates for molecular electronics and have been exploited to form organic field-effect transistors [1,2], optical switches [3], light emitting diodes [4], and solar cells [5-7]. To optimize the performance of such devices, the properties of the interface between the organic component and a metal electrode are of utmost importance. Essential parameters, such as the injection characteristics of charge carriers into the organic semiconductor or the temporal stability of a device function, critically depend on this interface behavior. As a consequence, the information on detailed adsorption geometries of a single molecule and on the morphology of extended molecular structures, as well as insight into the electronic structure of molecules on metal surfaces and their dynamic properties are of fundamental interest. All these basic issues can be addressed by scanning tunneling microscopy (STM) on a single-molecule scale. Additionally, quantum chemical properties of a thiophene molecule acting as a single-molecular wire have been investigated [8]. In that specific work, however, the molecule was just weakly coupled to the metal through a thin insulating layer, whereas strong coupling is desirable when contacting a molecular semiconductor to a metal electrode in order to obtain an efficient injection behavior.

Earlier investigations of thiophenes with STM were carried out on self-assembled monolayers (SAMs) mostly under ambient conditions or in the liquid environment of an electrochemical cell [9-11]. In the present contribution we analyze terthiophene (2,2':5',2"-terthiophene), 3T, as a representative of linear oligothiophenes being adsorbed on a Au(111) electrode within the low coverage regime (<1 monolayer (ML)), allowing us to study the interaction of molecules with the substrate on a single-molecule level. Specifically, the topographic and morphological properties of the molecules as well as of their arrays were studied by STM and the corresponding electronic properties by scanning tunneling spectroscopy (STS), both at low temperature to obtain the highest resolution possible. The results reveal many similarities to the corresponding experimental data obtained for 4-mercaptopyridine (4MPy) on Au(111) [12]. This suggests a common STM contrast mechanism for such molecules, at least on this surface. Finally, we discuss the differential barrier height. This not so commonly determined characteristic, describing the voltage dependent tunneling barrier, has been introduced recently in order to remove features of the tunneling tip from STS spectra, assuming the validity of the Wentzel–Kramers–Brillouin (WKB) approximation. Again, 3T and 4MPy on Au(111) exhibit a similar bias dependence of the barrier, which may be attributed to a different dimensionality of the tunneling process on the 2-dimensional surface state and on the localized state induced by the molecule.

Experimental

Commercially available gold films (typical thickness 250 nm, Arrandee, Germany) on glass were flame annealed in a butane flame to develop extended (111) facets. After introduction into ultra-high vacuum (UHV), these films were further annealed at temperatures up to 700 °C to remove contaminants from the surface. After a routine check of the gold surface by STM at low temperature ($p < 1 \times 10^{-10}$ mbar, $T \approx 5.5$ K) [13], the samples were quickly transferred to the preparation chamber under UHV conditions and, there, 0.2 to 0.7 monolayers (ML) of 3T (obtained from Sigma Aldrich and further purified) were deposited onto the gold film at a rate of about 0.01 nm/s from a home-built Knudsen-type cell. After deposition, the samples were immediately transferred back to the low-temperature STM. During the complete transfer and deposition process, the sample holder was kept well below room temperature. A rough estimate from the cooling curve gives $T_{sample} < -40$ °C at any time with molecules on the surface.

For tunneling, W tips were prepared by electrochemically etching of W wires and subsequent annealing of the tips at ~2000 °C in UHV. Finally, tips were conditioned by field emission and desorption at ~1 μA and <1000 V until they showed the expected topographic and spectroscopic STM/STS behavior on Au(111) and Nb(110).

Results and Discussion

Figure 1(a) shows a topographic image of about 0.2 ML of 3T on Au(111) several days after preparation. One recognizes the elongated molecules on top of a faint corrugation (~10 pm) given by the herringbone reconstruction (HB) of the gold surface (Au(111)-(22 × √3)). Presumably, due to the boundary conditions and strain in the Au film, the HB is straight and the length of the unit mesh may vary from 18 to 22. Whereas immediately after their deposition the 3T molecules are almost randomly distributed on the Au(111) surface, the distribution in Figure 1(a) clearly reveals that the HB serves as a template where (i) the 3T prefer the fcc regions (~93%); (ii) the 3T orient themselves perpendicular to the soliton walls of the HB and, at a lower probability, in multiples of 120° (<1 $\bar{1}$0> directions); and (iii) for a given coverage, the 3T apparently maximize their intermolecular distance (here: 2.4 nm). The observed preferential occupation of fcc areas within the HB reconstruction by the 3T translates into a higher binding energy of the molecules at these locations as compared to hcp areas. This is, at least qualitatively, corroborated by the fact that molecules from within hcp areas can be easily made to move by scanning the STM tip,

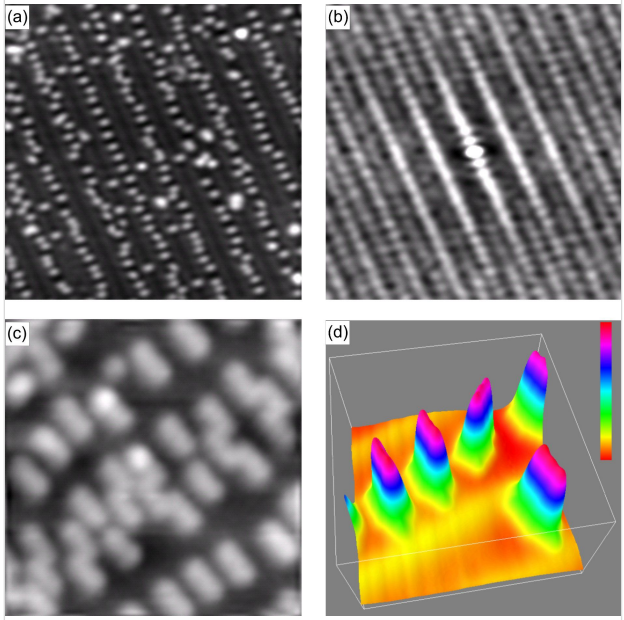

Figure 1: (a) Topographic image of ~0.2 ML of 3T on Au(111) (50 × 50 × 0.17 nm^3; I_{set} = 90 pA, V_t = −2.0 V); (b) autocorrelation of (a) indicating the abandonment of the hcp regions as well as the equidistant arrangement of the molecules; (c) topographic image of 3T/Au(111) at a coverage of 0.5 ML (7.7 × 7.7 × 0.2 nm^3; I_{set} = 70 pA, V_t = −1.5 V): 3T form armchair units made from 3 molecules in fcc regions; (d) close-up of a few 3T molecules in 3D representation (7.0 × 7.0 × 0.17 nm^3; I_{set} = 70 pA, V_t = −1.4 V). The molecules in the upper row reside in an fcc region.

or even made to jump onto the tip, whereas corresponding movements of molecules from fcc areas demand tunneling currents considerably higher than 100 pA and also a tunneling bias, V_t, close to the lowest unoccupied molecular orbital (LUMO) of 3T.

A preferential adsorption of the aromatic molecules in the fcc regions has also been observed for azobenzene [14], 1-nitronaphthalene [15,16], tetrathiafulvalene [17], and 9-aminoanthracene [18]. The tendency of the molecules to maximize the intermolecular distances may point to some charge transfer between molecule and substrate upon adsorption [17]; the resulting dipoles would be perpendicular to the surface and parallel to each other, and thus a repulsive interaction is expected. Both, the preferential occupation of fcc areas by the molecules as well as their equidistant chain-like arrangement are made even more clearly visible by the autocorrelation function of Figure 1(a) as presented in panel (b).

At higher coverage, 3T adsorbs increasingly in hcp regions. Concurrently, 3T aggregates are formed in fcc regions. These small aggregates are armchair structures which are perpendicularly aligned with the HB as seen in the center of Figure 1(c). These 3D aggregates, however, are not stable under STM conditions and their formation is in contrast to the observation of long range ordering of α-sexithiophene on Au(111) [19]. A possible reason could be the considerably weaker interaction of 3T with the substrate due to its shorter chain length.

The appearance of 3T/Au(111) is bias dependent in STM. In Figure 1 all molecules appear as elongated entities. In a close-up, Figure 1(d), one recognizes two faint constrictions (3–5 pm) in the molecules at the positions of the two bonds between the thiophene rings. At higher bias, the molecules appear more rounded in STM and become almost spherical at a bias of $V_t > +2.0$ eV. Figure 2(a) and Figure 2(b) summarize the bias dependent morphology of 3T. The molecular height is almost independent of bias, V_t, when $|V_t| < 1.5$ eV, with a value of 0.14 nm. For lower and higher values of V_t (< −1.5 eV or > 1.5 eV) the molecular height increases linearly although with different slopes (−0.16 nm/eV and 0.69 nm/eV in the two regimes given above, respectively). The length of the molecules is almost constant for $V_t < -1.2$ eV at 1.39 ± 0.07 nm and for $V_t > -1.2$ eV at 1.25 ± 0.01 nm (Figure 2(b)). Finally, also the molecular width is almost constant for $V_t < 1.5$ eV at 0.7 nm

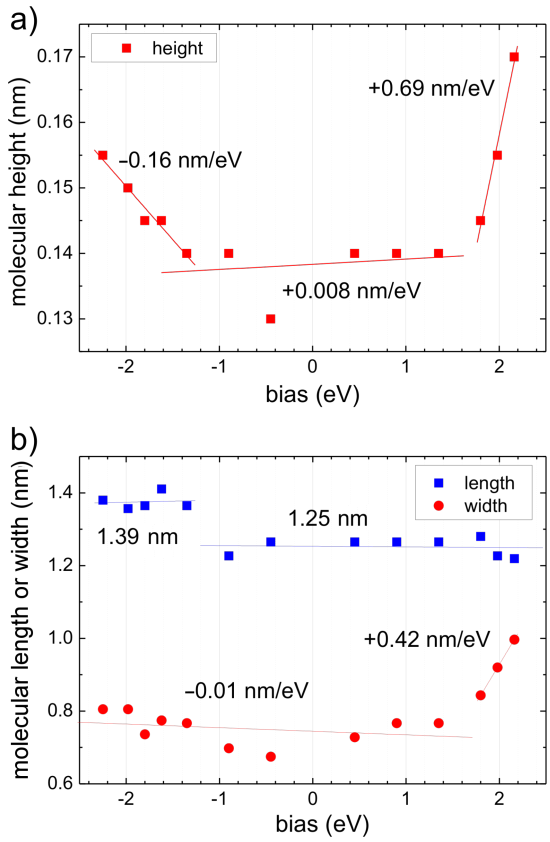

Figure 2: Apparent (a) molecular height, *h*, and (b) molecular length, *l*, and width, *w*, of 3T/Au(111). Solid straight lines indicate linear fits to sections of data discussed in the text; slopes/constant values are assigned to each.

and increases to approximately the molecular length at $V_t \approx 2.4$ eV. At low bias the size of 3T is slightly larger as compared to the geometric size of a free 3T molecule (1.26 nm × 0.47 nm), which can easily be explained by the finite radius of curvature of the tunneling tip. The height, however, is considerably smaller than expected. Kilian et al. measured the height of quaterthiophene on Ag(111) by X-ray standing waves and determined a separation of the molecules from the surface of 0.315 nm [20]. Such a considerable difference requires an explanation. Typically one would argue in STM that a change of the density of states (DOS) or the barrier height, Φ, above a molecule changes the tip–sample separation. However, the spatial distribution of the DOS may also change. We will discuss this in more detail later.

In order to understand the morphology of the 3T/Au(111) we performed STS. Since 3T is an extended object in STM, one must take into consideration that the STS results may depend on the specific location on a molecule where spectra are taken. Figure 3(a) displays *I*-*V* spectra recorded on the bare Au(111) (dashed red curve), at the end of the molecules (green curve, position 1 as indicated in the inset), and in the center of the molecular flank (blue curve, position 2 as indicated in the inset). The bare Au(111) shows the expected behavior with the Shockley surface state for $E > -0.5$ eV, the lower edge of the *L* gap at $E \approx -1$ eV, and the *d* bands for $E < -2$ eV. At the end of the molecule, the *I*-*V* curve is very similar to the curve on bare gold except for a pronounced peak of the conductivity at −1.3 eV, which is attributed to the HOMO of 3T/Au(111), and there is a minor but significant increase for $E > 2$ eV caused by the LUMO of 3T/Au(111). In the flanks, the *I*-*V* curve corresponds, to a good approximation, to 1/5 of the *I*-*V* curve measured on bare Au(111) with a pronounced increase for $V_t > 1.0$ eV which is due to the LUMO of the molecule.

To resolve the electronic structure in an extended energy range covering more of the *d* bands and the entire LUMO, we performed constant-current (*z*-*V*) spectroscopy, where the tunneling current is kept constant while the tip–sample separation, *z*, and the differential conductivity, $\partial_V I$, is recorded. As shown previously [12], a more appropriate quantity to compare to the DOS of the sample is the product $\partial_V I \times V_t$ since, when plotting versus V_t, the singularity of $\partial_V I$ at $V_t = 0$ is lifted.

Besides the features already mentioned above, these *z*-*V* spectra show additionally the upper edge of the *L* gap on the bare gold at $V_t \approx +3.7$ eV, and, most importantly, one finds a pronounced peak on the molecule, which we attribute to the LUMO of the molecule. In this representation (Figure 3(b)), the LUMO of a molecule in the fcc region of the HB can be nicely fit by a Lorentzian with the center at $V_t = +2.26$ eV and a width of 0.71 eV, which corresponds to a lifetime of electrons in the LUMO of ~0.5 fs.

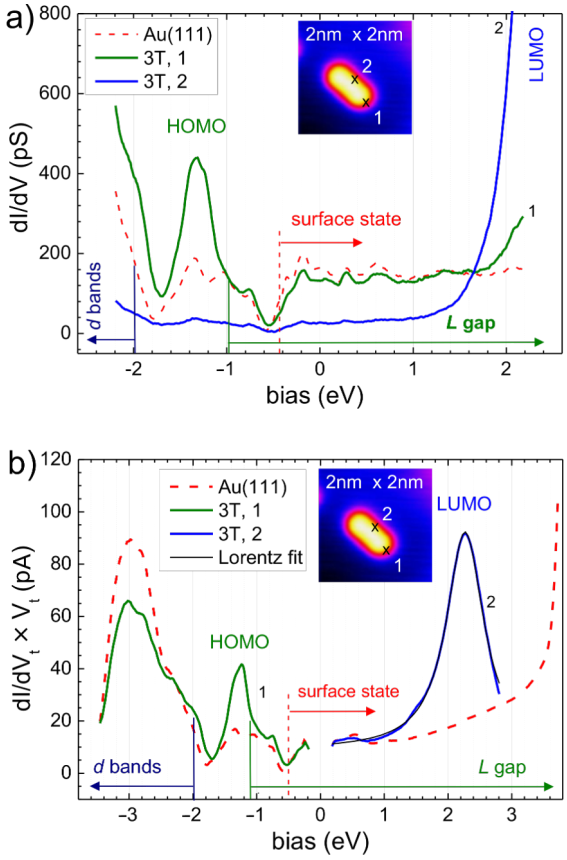

Figure 3: STS of 3T/Au(111): (a) constant-separation (*I*-*V*) spectra taken on the bare gold surface significantly far away from the molecule (red), taken at the center of the flanks (position 2 in the inset) (blue), and taken at an end of the molecule (position 1 in the inset) (green); the initial setpoint before disabling the feedback loop is approximately given by the intersection of the curves at (+1.6 eV, 150 pS); (b) constant-current (*z*-*V*) spectra (I_{set} = 29 pA) taken at the bare gold surface (red curves) and in the flanks (blue) or the ends (green) of the molecule to detect the LUMO and the HOMO, respectively. Also shown is a Lorentzian fitted (black curve) to the positive branch on the molecule (center 2.26 eV, width 0.71 eV corresponding to a lifetime of ~0.5 fs).

The spatial distribution of electronic states at an energy *E* can be imaged by measuring the conductivity of the tunneling junction simultaneously with topography at a given bias $V_t = E$ and a bias modulation at a frequency well above the cut-off frequency of the topographic feedback loop. Figure 4 displays the topography (left column, (a) and (e)) of a single molecule that was scanned twice, once with $V_t = -1.14$ eV close to the HOMO (upper row) and once with $V_t = +2.28$ eV close to the LUMO (lower row). The corresponding conductivity maps are shown in the second column of Figure 4 for the HOMO (Figure 4(b)) and for the LUMO (Figure 4(f)). The lateral drift is negligible resulting in a excellent reproducibility of the lateral

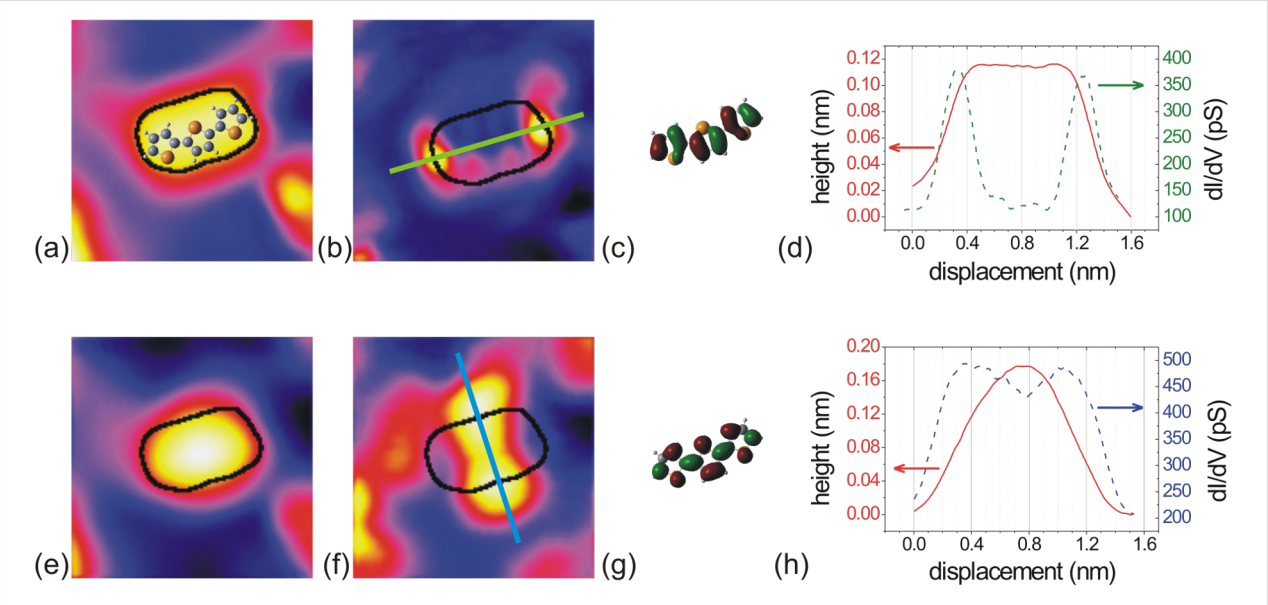

Figure 4: (a) and (e) shape of single 3T molecule on Au(111) (2 × 2 × 0.15) nm^3, (b) and (f) $\partial_V I$ maps showing the spatial distribution of the electron density of the HOMO (V_t = −1.14 eV, I_t = 56 pA for (a) and (b)) and the LUMO (V_t = 2.28 eV, I_t = 100pA for (e) and (f)), respectively. (d) and (h) show line profiles across the molecule in the topographies (a) and (e), together with the profile across the $\partial_V I$ maps (b) and (f), respectively. (c) and (g) represent the electron density for 3T of (c) the HOMO and (g) the LUMO, respectively, as calculated by the program "Gaussian03". Scales and the orientation of the molecule in (c) and (g) are approximately equal to (a) and (e).

position during consecutive scans. The contour of the topography (half height of the molecule, black line) is drawn in the $\partial_V I$ maps for better orientation and comparison. For clarity, we took also cross sections from topography and conductivity maps along the lines included in the conductivity maps. These profiles are displayed in Figure 4(d) and Figure 4(h). Accordingly, the main maxima of the HOMO are located exactly at the ends of the molecule with four additional minor maxima in between at the boundary of the molecule, two on each side. The LUMO is located exactly at the flanks of the molecule appearing like the wings of a butterfly. Consequently, the molecule appears slightly longer by ~0.14 nm at biases below –1.2 eV (Figure 2(b)), and it gets broader when approaching the bias corresponding to the LUMO, in accordance with the results shown in Figure 2. Relative to the long axis of the molecular contour, the minor maxima of the HOMO are typically very asymmetric while the LUMO appears symmetric relative to the same axis. Thus, the HOMO allows identification of the orientation of the 3T molecules. Comparison to a ball-and-stick model of the 3T molecule, as inserted in Figure 4(a), and to the HOMO–LUMO distributions of a free 3T as calculated by Gaussian03, and given in panels Figure 4(c) and Figure 4(g), respectively, suggests that the observed asymmetry can be attributed to the fact that the central sulfur atom does not contribute significantly to the HOMO of a free molecule, as opposed to its contribution to the LUMO. Thus, with respect to symmetry, the adsorbed 3T molecule shows some resemblance to the free molecule behavior. In closer detail, however, clear indications of the influence of adsorption are visible, such as the butterfly shape of the LUMO.

We return to the discussion of the contrast mechanism of 3T in STM. At low bias, as mentioned above, the 3T molecule appears to have a height of 0.125 nm in STM images while X-ray standing wave measurements suggest a separation of 0.315 nm between the nuclear planes of the gold surface and the molecule. To clarify this significant discrepancy from the STM's point of view, the differential barrier height defined by $\Phi_{diff} = (\partial_z \partial_V I/\partial_V I)^2$ [21] was determined. The differential barrier, Φ_{diff}, may be thought of as similar to the commonly used apparent barrier height defined by $\Phi_{app} = (\partial_z I/I)^2$, which is bias dependent. Due to differentiation, however, Φ_{diff} is much more sensitive to changes in the tunneling probability at the Fermi levels as compared to Φ_{app}. The corresponding results for Φ_{diff} measured on and away from the molecule are displayed in Figure 5. For the bare Au(111), Φ_{diff} is almost constant at Φ_{diff} = 4.8 eV over the complete bias range from −2 eV to +2 eV [22]. Though the absolute value of Φ_{diff} may vary from sample to sample within a range from 4 eV to 5 eV, the constancy of those values independent of the applied bias, V_t, is typical for Au(111) surfaces [12]. On the molecule, Φ_{diff} is slightly higher at low bias and decreases linearly for positive bias. Importantly, the barriers on and away from the molecule are not sufficiently different to change the tip-sample separation significantly in these two positions. Thus, barrier effects cannot be responsible for the above-mentioned height discrep-

ancy. Furthermore, since STS reveals that the electronic properties of 3T/Au(111) are almost identical to those of bare Au(111) (Figure 3) in the bias range −1 eV to +1.5 eV, one concludes that STM performed at low bias on 3T/Au(111) senses a Au surface state that is modified by the molecular adsorption. Assuming, similarly to the case of 4-mercaptopyridine (4MPy) on Au(111) [12], that the final tunneling state is simply the Au(111) surface state shifted outwards from the surface due to the presence of the molecule, this shift can be identified from the experimentally determined height of the 3T molecule at low bias (0.14 nm).

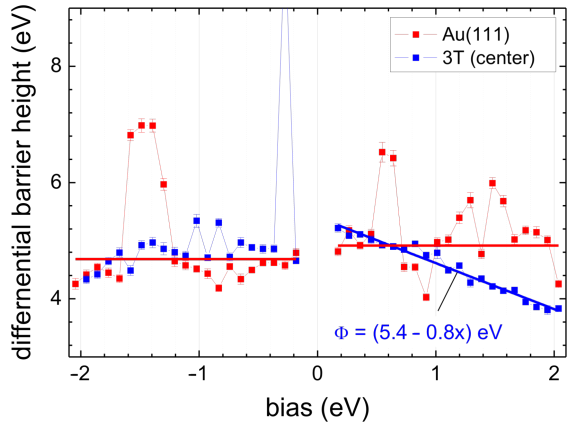

Figure 5: Differential barrier height $\Phi_{diff} = (\partial_z \partial_V I / \partial_V I)^2$ on (blue) and off (red) the 3T molecule. The straight lines are linear fits to the positive and negative branches, respectively (red: On Au(111); blue: In the center of 3T). The differential barrier of gold here is almost constant at $\Phi_{diff} \approx 4.8$ eV. The differential barrier on 3T drops off linearly for positive bias and is slightly greater at small bias compared to bare Au(111).

At a bias $V_t > 1.5$ eV the LUMO of the molecule contributes perceptibly to the density of states (DOS) and, to maintain the current setpoint under feedback, the tip must be withdrawn from the surface with increasing bias in accordance with the DOS of the LUMO, thus leading to an enhanced apparent height of the 3T molecule. For the LUMO energy, a molecular height of approximately $h_m \approx 0.2$ nm (Figure 2(a)) with respect to the surface state on the bare Au(111) is extrapolated. Combined with the expectation that the position of the undisturbed Au(111) surface state is approximately half a Fermi wavelength in front of the nuclear surface plane (0.15 nm), this adds up to an apparent molecular height, h_m, of about 0.35 nm in excellent agreement with the X-ray standing-wave experiment [20] and, thus, resolving the above discrepancy.

It is interesting to mention here, that, as in the case for 4MPy/Au(111), also 3T/Au(111) exhibits a linear dependence of Φ_{diff} for positive bias with a slope close to −1. This behavior is significantly different from the bias-independent barrier height on the bare Au(111) surface. As mentioned previously [12], such a linear bias dependence of the differential barrier as measured on the molecules is hard to understand within the three-dimensional WKB approximation, since, in that case, the parallel component of the energy E_p (perpendicular to the tunneling direction z) formally adds to the effective barrier (the transmission probability function changes from

$$T(E,V;z) = \exp\left(-\sqrt{\Phi + V_t/2 - E}\cdot z\right)$$

in one dimension to

$$T(E,V;z) = \exp\left(-\sqrt{\Phi + V_t/2 - E_z}\cdot z\right) = \exp\left(-\sqrt{\Phi + V_t/2 - E + E_p}\cdot z\right)$$

in three dimensions with $E = E_z + E_p$). At positive bias we may assume, for simplicity, that the states aligned with the upper Fermi level (tip) dominate the barrier measurement. Additionally, for 3T as well as for 4MPy on Au(111), the sample DOS does not influence the barrier measurement since it is constant [21] at least in the low bias range. Consequently, we may set $E = V_t$ and, hence, $E_p \approx -E/3$ to $E_p \approx -E/2$ to explain the measurement of Φ_{diff}. On the other hand, we attributed the involved sample states in that energy range to a modified surface state which means extending the 2D state into the 3rd dimension. We believe that the characteristic change in the behavior of Φ_{diff}, from being approximately constant on Au(111) to dropping off almost linearly on a molecule, is a manifestation of that change in dimensionality. However, presently there are still too many open questions as to the role of the tip (dispersion) and even whether there would be principal limits to the WKB approximation.

Conclusion

Low-temperature scanning tunneling microscopy and spectroscopies (STM, STS) under ultra-high vacuum conditions were applied to investigate the structural and electronic properties of terthiophene molecules (3T) adsorbed on Au(111) in the submonolayer regime. The data clearly revealed that the standard herringbone reconstruction (HB) of the Au(111) surface acts as a template, with 3T molecules preferentially adsorbed on its fcc regions in a perpendicular orientation with respect to the soliton walls of the HB. Adsorbed in this way, the 3T molecules exhibited almost identical interparticle distances pointing to repulsive intermolecular interactions, probably due to electrical dipoles formed by the adsorption. The lateral variation of the adsorption energy appeared to be relatively small allowing for tip-induced rotations and displacements of the molecules, depending on the tunneling current and the bias.

The shape of a single 3T molecule on Au(111) depended merely on the bias for values below +1.5 eV. For a bias above +1.5 eV,

the shape of the molecule was strongly influenced by tunneling into its LUMO. The STM height of the molecules was shown to have special significance. Emphasizing here the bias regime between HOMO and LUMO, the STM appearance of the 3T was found to be governed by a modified Shockley-like surface state of Au(111), which is shifted outwards from the gold surface in the presence of the molecule. Additionally, when adding the separation of the Shockley-like surface state from the nuclear plane of the Au surface atoms to the apparent STM height of the 3T molecules on Au(111) measured at a bias corresponding to the LUMO, one obtains a value for the molecule–surface separation close to that which was reported for X-ray standing-wave experiments.

The energetic positions of both, the HOMO and LUMO, could be precisely determined by constant-current STS resulting in values of −1.3 eV and +2.26 eV, respectively. While most data suggest a relatively weak interaction of 3T with the gold surface, the lateral distribution of the LUMO–HOMO is significantly different from the expectation based on calculated electron distributions of a free 3T molecule. While the LUMO is mostly located at the center of the flanks of the molecules, leading to a butterfly-like appearance of this distribution, the HOMO is located at the ends of the molecule and shows a clear asymmetry relative to the axis of the 3T molecules. Combining LUMO–HOMO STS data, thus, allows determination of the orientation of a 3T molecules on Au(111).

Finally, the differential barrier on and away from the 3T/Au(111) was determined and similar results were obtained as previously reported for 4-mercaptopyridine on Au(111). In both cases, the differential barrier shows a linear drop-off at positive bias as opposed to the practically bias-independent behavior on the bare Au(111) surface. Referring to the expected WKB behavior and combining with the presently reported results leads to an interpretation in terms of a dimensional crossover induced by performing STS on top of and through a 3T molecule.

Acknowledgements

We thank the Deutsche Forschungsgemeinschaft (DFG) for generous support within the Collaborative Research Center (SFB) 569 TP C5. The free program ‘ImageJ’ [23] was used to display images in 3D representation.

References

1. Horowitz, G.; Fichou, D.; Peng, X.; Xu, Z.; Garnier, F. *Solid State Commun.* **1989,** *72,* 381. doi:10.1016/0038-1098(89)90121-X
2. Horowitz, G.; Romdhane, S.; Bouchriha, H.; Delannoy, P.; Monge, J. L.; Kouki, F.; Valat, P. *Synth. Met.* **1997,** *90,* 187. doi:10.1016/S0379-6779(98)80005-2
3. Lap, D. V.; Grebner, D.; Rentsch, S. *J. Phys. Chem. A* **1997,** *101,* 107. doi:10.1021/jp961670n
4. Lang, P.; Hajlaoui, R.; Garnier, F.; Desbat, B.; Buffeteau, T.; Horowitz, G.; Yassar, A. *J. Phys. Chem.* **1995,** *99,* 5492. doi:10.1021/j100015a036
5. Bäuerle, P.; Mitschke, U.; Mena-Osteritz, E.; Sokolowski, M.; Mueller, D. C.; Meerholz, K.; Gross, M. S. *Proc. SPIE* **1998,** *3476,* 32. doi:10.1117/12.332636
6. Fischer, M. K. R.; López-Duarte, I.; Wienk, M. M.; Martínez-Díaz, M. V.; Janssen, R. A. J.; Bäuerle, P.; Torres, T. *J. Am. Chem. Soc.* **2009,** *131,* 8669. doi:10.1021/ja901537d
7. Schulze, K.; Uhrich, C.; Schüppel, R.; Leo, K.; Pfeiffer, M.; Brier, E.; Reinold, E.; Bäuerle, P. *Adv. Mater.* **2006,** *18,* 2872. doi:10.1002/adma.200600658
8. Repp, J.; Liljeroth, P.; Meyer, G. *Nat. Phys.* **2010,** *6,* 975. doi:10.1038/nphys1802
9. Stecher, R.; Drewnick, F.; Gompf, B. *Langmuir* **1999,** *15,* 6490. doi:10.1021/la990196k
10. Noh, J.; Ito, E.; Nakajima, K.; Kim, J.; Lee, H.; Hara, M. *J. Phys. Chem. B* **2002,** *106,* 7139. doi:10.1021/jp020482w
11. Glowatzki, H.; Duhm, S.; Braun, K.-F.; Rabe, J. P.; Koch, N. *Phys. Rev. B* **2007,** *76,* 125425. doi:10.1103/PhysRevB.76.125425
12. Koslowski, B.; Tschetschetkin, A.; Maurer, N.; Ziemann, P. *Phys. Chem. Chem. Phys.* **2011,** *13,* 4045. doi:10.1039/c0cp02162h
13. Koslowski, B.; Dietrich, Ch.; Tschetschetkin, A.; Ziemann, P. *Rev. Sci. Instrum.* **2006,** *77,* 063707. doi:10.1063/1.2213171
14. Kirakosian, A.; Comstock, M. J.; Cho, J.; Crommie, M. F. *Phys. Rev. B* **2005,** *71,* 113409. doi:10.1103/PhysRevB.71.113409
15. Böhringer, M.; Morgenstern, K.; Schneider, W.-D.; Berndt, R.; Mauri, F.; De Vita, A.; Car, R. *Phys. Rev. Lett.* **1999,** *83,* 324. doi:10.1103/PhysRevLett.83.324
16. Böhringer, M.; Morgenstern, K.; Schneider, W.-D.; Wühn, M.; Wöll, C.; Berndt, R. *Surf. Sci.* **2000,** *444,* 199. doi:10.1016/S0039-6028(99)01039-0
17. Fernandez-Torrente, I.; Monturet, S.; Franke, K. J.; Fraxedas, J.; Lorente, N.; Pascual, J. I. *Phys. Rev. Lett.* **2007,** *99,* 176103. doi:10.1103/PhysRevLett.99.176103
18. Lauffer, P.; Graupner, R.; Jung, A.; Hirsch, A.; Ley, L. *Surf. Sci.* **2007,** *601,* 5533. doi:10.1016/j.susc.2007.09.023
19. Kiel, M.; Duncker, K.; Hagendorf, C.; Widdra, W. *Phys. Rev. B* **2007,** *75,* 195439. doi:10.1103/PhysRevB.75.195439
20. Kilian, L.; Weigand, W.; Umbach, E.; Langner, A.; Sokolowski, M.; Meyerheim, H. L.; Maltor, H.; Cowie, B. C. C.; Lee, T.; Bäuerle, P. *Phys. Rev. B* **2002,** *66,* 754121. doi:10.1103/PhysRevB.66.075412
21. Koslowski, B.; Dietrich, C.; Tschetschetkin, A.; Ziemann, P. *Phys. Rev. B* **2007,** *75,* 035421. doi:10.1103/PhysRevB.75.035421
22. Unfortunately, the present experimental data taken on the bare Au(111) surface in the neighborhood of adsorbed 3T molecules appear quite noisy. This is not generally the case. However, we preferred to keep the noisy data taken close to but clearly off the 3T molecule, which had delivered the (blue) “on-top-of-the-molecule barrier”, rather than comparing to less noisy results taken at a completely different location or even on a different Au(111) sample.
23. *ImageJ;* U. S. National Institutes of Health: Bethesda, Maryland, USA, 2011, http://imagej.nih.gov/ij/.

Beilstein Journal of Nanotechnology

Surface induced self-organization of comb-like macromolecules

Konstantin I. Popov[1], Vladimir V. Palyulin[1,2], Martin Möller[3], Alexei R. Khokhlov[1,2] and Igor I. Potemkin[*1,2]

Full Research Paper

Open Access

Address:
[1]Physics Department, Moscow State University, Moscow 119991, Russian Federation, [2]Institute of Polymer Science, University of Ulm, 89069 Ulm, Germany and [3]Institute of Technical and Macromolecular Chemistry, RWTH Aachen and DWI at the RWTH Aachen e.V., 52056 Aachen, Germany

Email:
Igor I. Potemkin[*] - igor@polly.phys.msu.ru

* Corresponding author

Keywords:
comb copolymers; macromolecules; adsorption; self-organization

Beilstein J. Nanotechnol. **2011,** *2,* 569–584.
doi:10.3762/bjnano.2.61

Received: 13 May 2011
Accepted: 01 July 2011
Published: 12 September 2011

This article is part of the Thematic Series "Organic–inorganic nanosystems".

Guest Editor: P. Ziemann

Abstract

We present a review of the theoretical and experimental evidence for the peculiar properties of comb copolymers, demonstrating the uniqueness of these materials among other polymer architectures. These special properties include an increase in stiffness upon increasing side-chain length, the spontaneous curvature of adsorbed combs, rod–globule transition, and specific intramolecular self-assembly. We also propose a theory of chemically heterogeneous surface nanopattern formation in ultrathin films of comblike macromolecules containing two different types (A and B) of incompatible side chains (so-called binary combs). Side chains of the binary combs are strongly adsorbed on a surface and segregated with respect to the backbone. The thickness of surface domains formed by the B side chains is controlled by the interaction with the substrate. We predict the stability of direct and inverse disc-, torus- and stripelike nanostructures. Phase diagrams of the film are constructed.

Introduction

Recent advances in macromolecular synthesis allow precise control over structure and polydispersity of architecturally complex polymers [1-3]. Among these polymers are comb or brush copolymers, i.e., macromolecules which consist of a backbone and attached side chains [4,5]. Originally the interest in comb copolymers was motivated by the desire to achieve liquid-crystalline (LC) ordering of flexible linear macromolecules through the attachment of mesogene side chains and also to enhance the solubility of rigid conjugated polymers such as polyaniline [5-7]. Additional attention to brush copolymers was stimulated by their biological relevance – such an important class of biomolecules as proteoglycans has comblike structure. These

molecules are involved in cell signalling and cell surface protection as well as joint lubrication, lung clearance and cartilage stability, cellular matrix integrity [8-13]. Comb copolymers also have unusual viscoelastic properties (super-soft elastomers) [5,14], may form micelles as big as 300 nm [15] and have extremely interesting 2D conformational behavior in the adsorbed state [4]. Brush copolymers with diblock and triblock copolymers as side chains can be used for the creation of well defined organic nanotubes that are soluble in water [16,17].

There are three key methods for the synthesis of graft copolymers [1,5]. The first method involves grafting of previously prepared side chains onto the backbone (the so-called "grafting onto" method). Branch points are obtained by chemical modification of backbone units or by copolymerization with a monomer of the required functionality. The second approach involves the synthesis of active centers along the backbone (the synthesis of macroinitiators) and subsequent growth of side chains from these centers by polymerization (the so-called "grafting from" method). The third approach is termed macromonomer (or "grafting through" method). This method consists of two steps. In the first stage macromonomers (future side chains) are synthesized. Then the copolymerization of the macromonomers and the monomers forming the backbone takes place. Each strategy enables control of different parameters such as grafting density, chemical composition, polymerization degree of side chains and the backbone, polydispersity, etc. Achievement of the desired set of these parameters is quite a complicated task, e.g., due to the steric repulsion of side chains in the case of dense grafting. In some cases a combination of these methods may produce combs which would be otherwise unobtainable.

In this article we pursue two goals. In the first part we give an overview of the peculiar properties of comblike macromolecules, emphasizing the behavior of the macromolecules adsorbed on a surface. In the second part we propose a theory of self-organization of binary combs, i.e., macromolecules with incompatible side chains of types A and B, adsorbed on the surface.

Results and Discussion

Properties of comb copolymers

Stiffness of macromolecules

One of the most prominent properties of densely grafted comblike macromolecules is their high stiffness induced by strong intermolecular interactions of the side chains. It was suggested that this feature may lead to the creation of systems capable of LC ordering. Such ordering may appear in semidilute solutions of semiflexible polymers if the ratio of the persistence length λ to the diameter of the molecule D exceeds some threshold value, $\lambda/D > 10$ [18,19].

The last couple of years have seen a somewhat revolutionary change in the understanding of the basic properties of single polymer chains [20,21,23]. New theoretical approaches and modeling results indicated that correlations of tangent vectors along a polymer chain are described by a power law instead of exponential decay, even in theta solvent [21] and in the melt [22]. Previously, this fact was also established for chains in a good solvent [24,25]. These findings make the use of the persistence length meaningless as a quantity for the description of the local bending properties. The trajectory of comblike macromolecule (semiflexible cylindrical object) also follows a power law dependence, rather than exponential [23], and thus cannot be correctly described by the persistence length. At first glance, this may bring a two decades long discussion of the scaling properties of the persistence length of comb copolymers to a halt. However, all the inconsistencies are still relevant if as we remind ourselves that the discussion was actually devoted to the bending elasticity, which is described by the bending modulus and not by the persistence length. The latter characterizes orientational correlations in the case of their exponential decay and may not exist, while the bending modulus always does. Nonetheless, in this section we will use the term persistence length for convenience.

Starting with the computer simulation work in the mid 1960s [26], a few experimental and simulation papers, demonstrating the effect of stiffening of the comblike macromolecules with the increase of the side chain length and grafting density, appeared in the 1980s [27-29]. However, only after blob concept was introduced by De Gennes [30], were the first theoretical explanations presented, including a theory by Birshtein et al. [31]. According to this theory, deformation of a comb copolymer with bending less than the diameter of the molecule leads to jumping of the side chains, from concave to the convex side of the "persistence tube", and the elastic energy increases only when the radius of curvature becomes less than D. Hence, it was proposed that the persistence length is on the order of the diameter of the polymer and their ratio does not depend on either the length of the side chains or on their grafting density. Since the approach did not allow an estimation of the coefficients, it was impossible to devise any conclusions about LC ordering in these systems. An alternative theory was developed by Fredrickson [32]. The persistence length of the molecule was estimated by comparison of the free energies of rectilinear and curved brushes, and calculations led to the following result: $\lambda \sim \sigma^{17/8} M^{15/8}$, where M is the number of segments in the side chain and σ is the grafting density of the side chains, $\sigma < 1$. The expression for the diameter of the tube $D \sim \sigma^{1/4} M^{3/4}$ agreed with that obtained by Birshtein et al. Thus, $\lambda/D \sim \sigma^{15/8} M^{9/8}$ and was much higher than unity at $\sigma >> M^{-3/5}$, i.e., according to the theory of Fredrickson, nematic ordering is possible. Numerous

later theoretical and experimental works [33-43] have not reached a consensus over the scaling of the persistence length with the diameter of comb molecules, nor about the possibility of LC ordering (for detailed discussion, see another review [4]).

Notwithstanding the difficulties, all the studies indicated a substantial increase in the stiffness for the backbone and the side chains. For the discrepancies Binder et al. [23] offered two possible explanations. First, they may arise because of the use of the persistence length in the experiment, while the use of alternative measures of rigidity may lead to consistent results between modeling and experiment. Second, the scaling regime discussed by theoreticians is not attainable in experiments, because the length of the side chains is rather short (around 100 monomer units or less) [23,44,45]. As a conclusion of this section, we hope that further accurate studies and comparison of theory and experiment in light of new discoveries [20-23] may resolve an almost two decade old contradiction [31,32].

Combs with complex chemical structure

After revealing the properties of combs with homopolymer side chains, the next logical step is an increase in the complexity of the chemical structure of the system under consideration. If more than one type of monomer unit is introduced in the comb copolymer a whole range of questions arises, the most interesting being: What types of intramolecular aggregation may occur in solution? The case of a hydrophobic backbone with hydrophilic side chains has revealed quite interesting behavior [46-48]. Both scaling theory [46,47] and simulations [47,48] predicted that collapse of the main chain with increase of hydrophobicity in densely grafted combs would lead to formation of a necklace of intramolecular starlike micelles, with hydrophobic corelike domains connected by extended bridges and hydrophilic corona formed by the grafts (Figure 1). Scaling analysis reveals that the formation of finite-size intramolecular micelles happens only in a narrow range of interaction parameters near the transition point. A similar pearl-necklace structure was detected experimentally for core–shell cylindrical polymer brushes with a solvophobic inner (core) block and a solvophilic outer (shell) block in selective solvents [49].

Combs with two types of incompatible side chains (binary brushes) obviously represent quite intriguing objects due to the potential for intrachain segregation leading to Janus-like structure. Theoretical analysis, within the Flory–Huggins approach, of the intrachain segregation [50,51] demonstrated that, as the quality of the solvent worsens, segregation occurs at lower values of the parameter χ_{AB}. In the case of a poor solvent, the segregation condition $\chi_{AB}M \sim 1$ qualitatively corresponds to the spinodal conditions for microphase segregation in melts of diblock copolymers [52]. Calculation of the free energy for a comblike copolymer with complete segregation of side chains showed that a molecule can spontaneously curve. A simulation study [53] confirmed the existence of spontaneously curved conformations under certain conditions, but failed to find the regime of complete separation into two distinct domains.

Further studies were done by Binder et al. [44,45] for combs with high grafting density (bottle-brushes). They suggested that separation in comb copolymers with two types of side chains is a phase transition in a quasi one-dimensional object. Hence, an ordered state is impossible according to Landau theorem [54].

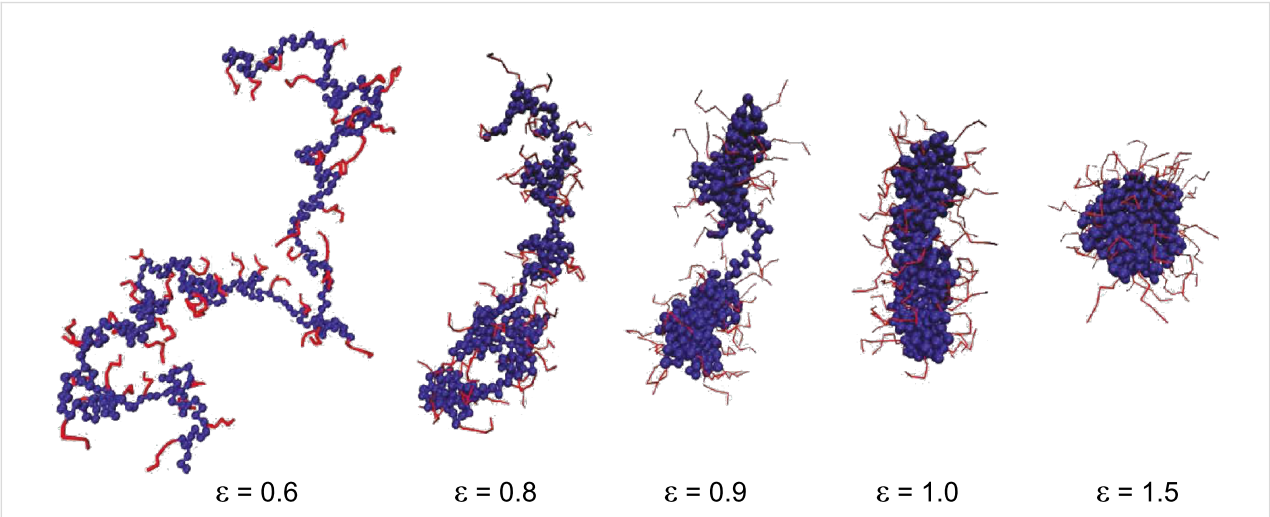

Figure 1: Illustration of the transition from a wormlike structure through a cylindrical micelle down to a spherical micelle, with decreasing solvent quality for the backbone. To make the structure of the backbone clearly visible, the side chains are only drawn as thin lines. Reprinted with permission from Kosovan, P.; Kuldova, J.; Limpouchova, Z.; Prochazka, K.; Zhulina, E. B.; Borisov, O. V. *Macromolecules* **2009,** *42,* 6748–6760. Copyright 2009 American Chemical Society.

In all the cases under consideration (poor, theta, and good solvents, and various forces of interaction between units of side chains of various types), correlations along the backbone rapidly decayed [45]. The extrapolation of the correlation length to $T \rightarrow 0$ showed that, even in this case, there was no long-range ordering. Moreover, Binder et al. mention that at finite M values, the cross section will look like a butterfly rather than a circle, as this ensures the smaller number of contacts between A and B units. Segregation will proceed according to the Janus cylinder type only if the energy of attraction between equivalent units is much higher than the energy of repulsion between units of different kinds. As in [53], it was shown that if the solvent is selective for A and B chains, spontaneous curvature of the molecule will occur.

Recent data obtained from off-lattice molecular dynamics simulations [55] suggest that pearl-necklace type separation is also possible in binary bottle-brushes. This type of separation induced by the decrease in the solvent strength was also predicted for combs with one type of side chain through scaling [56], self-consistent field theories [57] and computer simulations [58]. Such a structure was shown to be stable for intermediate and small values of grafting density.

Janus cylinders were experimentally obtained in a rather different way by dissolution of a microscopically separated polymer melt of triblock copolymers [59,60]. At first, a phase is obtained, where the middle block forms thin cylinders on the border between lamellae formed by the outer blocks. Subsequently, the chains in the middle block are cross-linked, and in the last stage, the melt is dissolved. Each comb in the solution consists of a backbone formed by cross-linked middle blocks, and end blocks remain in segregated state after dissolution.

Microphase separation

Microphase separation in block copolymer melts has attracted significant attention over the past several decades [61-64] because it produces a fascinating set of ordered nanostructures, which are envisioned to become a core solution of many applications [65,66]. At first, researchers concentrated on the detailed study of self-organization in melts of diblock copolymers [52,67,68]. Later on the interest in the search for novel morphologies shifted to the consideration of copolymers with complex architectures [69,70], nanoparticles imbedded in block copolymer matrices [71], etc.

Before the successful controlled synthesis of graft copolymers [1,2], microphase separation in combs was modelled by theoreticians mostly within the weak segregation theory (WST) approach [52,72]. Spinodals of microphase separation were calculated for melts of comb copolymer in which the backbone and the side chains were chemically different units [73]. It was shown that the transition from a homogeneous to an ordered state is determined by the parameters of the repeating unit, each unit consisting of a spacer between the adjacent branch points, and of the side chain. An increase in the number of these elements ceases to influence the spinodal curves after it exceeds about 20 units. The spinodals were constructed for two types of branching point distributions: Regular and random [74]. The authors found that spinodals of microphase separation for different distributions converge to different limiting curves while having the same chemical composition. A theory of microphase separation in melts of double comblike copolymers was developed in [75,76]. This kind of comb contains two different types of side chains attached to common branch points in a pairwise fashion (A and B side chains are attached to a common unit of the backbone). In [75], copolymers with a regular distribution of branch points were examined. The behavior of a spinodal as a function of the number of repeating units showed two characteristic types. For one combination of the parameters, abrupt changes in the wave vector characterizing the instability of the homogeneous state were discovered. These changes are specific for systems with two characteristic length scales corresponding to the lengths of the backbone and side chains. The existence of these abrupt changes implies that systems with two different scales can form periodic microstructures that are of great interest for potential applications. This so-called two-scale instability was discovered first in comb-coil copolymers [77,78] which consist of comb-like and linear blocks and represent an example of high architectural complexity for graft copolymers. The effect of the distribution of branch points of the side chains on the spinodals of microphase segregation in melts of double comb-like copolymers, was considered in terms of the weak segregation theory by comparison of regular, random and gradient distributions [76]. It was demonstrated that an increase in the nonuniformity of the distribution of the side chains widens the stability region of the microphases. Abrupt changes of the wave vector of the microstructure are also possible for the nonuniform distribution.

Liquid-crystalline side chains

Multiscale ordering, which was discussed in the previous subsection, can be achieved in a different way, namely through comb copolymers with liquid crystalline side chains (SCLC). The self-assembly of such copolymers with LC chains is different from that of their flexible counterparts, due to the combined possibility of microphase separation with LC ordering of stiff segments. For example, already linear rod–coil copolymers exhibit such non-trivial morphologies as arrowhead, zigzag, wavy lamellar and smectic bilayers [79,80]. For more details, see recent review [81]. LC phase transition temperatures were found to be close to the homopolymer case.

However, in several examples stabilization of liquid-crystalline and microphases influenced each other. Zhang and Hammond achieved the stabilization of the smectic phase by lamellar phase formation [82]. Influence of LC transition on microphase segregation was observed in [83] where the authors demonstrated that the transition from a body-centered cubic morphology to a hexagonal one was stimulated by an isotropic–nematic transition. In another case, a mixed lamellae/cylinder phase transformed into a pure lamellar one as a result of the loss of LC ordering [84].

The first theories to described the SCLC copolymers appeared in the 1980s, on the basis of lattice models [85,86], as a response to the achievements in synthesis [87]. Subsequently, a more rigorous approach, with inclusion of the Maier–Saupe form of interaction, was suggested by Warner and Wang [88]. Spinodals of the microphase separation of a SCLC copolymer with LC groups, attached to the backbone through the flexible spacers, were calculated in [89].

From a practical point of view coil–LC comb copolymers, i.e., copolymers which contain a coil block and a block with LC side chains (Figure 2), are more interesting than SCLC copolymers without a coil block. The main reason is simple: Microphase separation in the latter case between the backbone and the LC side chains is achievable, but the period of the microstructures is strongly limited by the length of the spacer between adjacent LC side chains. Coil-comb architecture allows better control of this parameter and the symmetry of the phases, and thus attracts more attention from both experimentalists [82,90-93] and theoreticians [94-96].

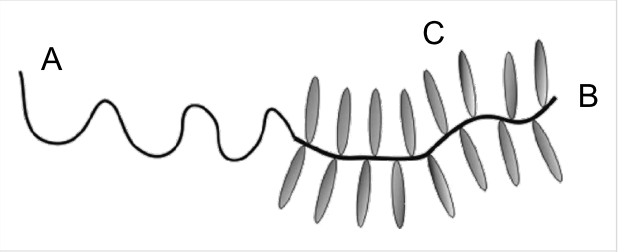

Figure 2: Schematic representation of coil–LC comb copolymer.

In the first of the theoretical publications concerning coil–LC comb copolymers [94], the authors plotted phase diagrams by comparison of the free energies of homogeneous, lamellar, cylindrical and spherical morphologies. The free energy was calculated by summation of the bending energy of the worm-like chain of the backbone, the Maier–Saupe contribution for LC ordering of side LC chains, the stretching energy of the amorphous block, the surface tension and the mixing Flory–Huggins contributions. Later studies [95,96] used SCFT and strong segregation theories. In particular, it was found that, for the probed parameter space, microphase separation is necessary in order to achieve the orientational ordering [95]. The structure of lamellar and cylindrical phases was considered in more detail in [96]. Stability regions of two different cylindrical and four different types of lamellar phases were found (Figure 3). Conditions for stability of each structure can be summarized as follows [96]:

1. Amorphous cylinders: Long macromolecules; high fraction of the B and C (LC) units; any values of the surface tension coefficients satisfying the strong segregation conditions.
2. Liquid crystalline cylinders: Long macromolecules; high fraction of the A units and small enough fraction of the liquid crystalline units; any values of the surface tension coefficients satisfying the strong segregation conditions.
3. A⊥B lamellae: Long macromolecules; the A block has to be a bit longer than the B block; small enough fraction of the liquid crystalline units; any values of the surface tension coefficients satisfying the strong segregation conditions.
4. BAB lamellae: Short enough macromolecules; high fraction of the A units; small enough fraction of the liquid crystalline units; high values of the surface tension coefficient γ_{AC}.
5. ABB lamellae: Short enough macromolecules; high fraction of the A units; high enough fraction of the liquid crystalline units.
6. ABA lamellae: Short enough macromolecules; high fraction of the A units; high fraction of the liquid crystalline units.

Theoretical predictions [96] were consistent with experimental results [93] for the transition between amorphous cylinders and A⊥B lamellar phases. In the experiment [93], wedge-shaped molecules with sulfonic group at the tip have been incorporated into a poly(2-vinylpyridine)-*block*-poly(ethylene oxide) (P2VP-*b*-PEO) diblock copolymer by proton transfer at different degrees of neutralization. Then scanning force microscopy (SFM) and X-ray studies were applied to assess the morphology. The agreement was found to be especially good for the diameters of cylindrical domains in the amorphous cylindrical phase, for different degrees of neutralization.

The evident tendency of researcher to study more complex systems is represented by the use of mean-field theory [97] to investigate diblock copolymers with both blocks containing mesogene groups. It was predicted that the lamellar phase has an unusual nonlinear soft elastic response due to the rotation of the LC groups.

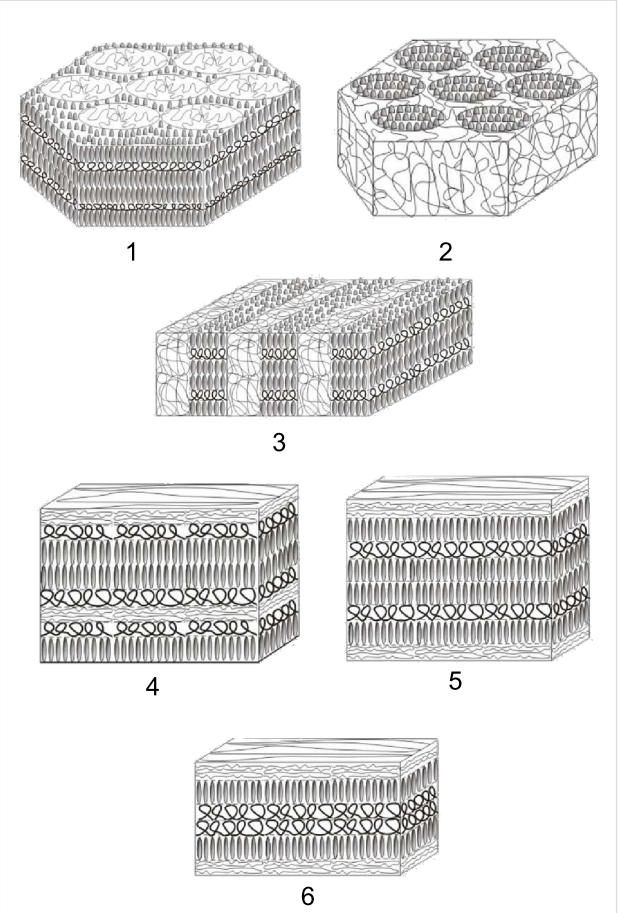

Figure 3: Stable morphologies in coil–LC comb copolymer melts.

Comblike macromolecules adsorbed on a flat surface

The physical behavior of adsorbed comb copolymers is much better understood, through the direct visualization of the molecules by SFM [98]. SFM allows the determination of the conformational characteristics such as contour length, comb width, backbone curvature, radius of gyration, etc. After adsorption the macromolecules can adopt many different conformations including globular, coil- and rod-like. The physical phenomena behind this complex behavior are described in the following few subsections.

Bending modulus

In comparison with the macromolecules in solution, strong adsorption makes most of the side chains two-dimensional (2D). This leads to a large stretching of the 2D chains, $D \sim M$, in contrast to a weaker exponent for the 3D case, $D \sim M^{3/4}$. Theoretical calculations for the 2D comb predicted a dependence of the bending modulus on the number of segments in the side chain as M^3, both for symmetric or asymmetric distributions of side chains relative to the backbone [99]. For combs made of polyhydroxyethyl methacrylate backbone ($N = 2150 \pm 100$) and PBA side chains (polymerization degree $n = (12 \pm 1)–(140 \pm 12)$) adsorbed from good solvent on mica, SFM results for the bending modulus are approximated by the exponents $\nu = 2.7 \pm 0.2$ [100], which is close to the theoretical prediction of 3. The difference between the experimental and theoretical results may be attributed to the incomplete adsorption of side chains: Part of the chains forms a 3D brush atop a 2D monolayer. Therefore, a "2.5"-dimensional model including two objects, a 2D monolayer and a 3D semi-cylinder, can be used to approximate the shape of the adsorbed brush. Within this model, the bending modulus of the adsorbed brush in a poor solvent can be approximated as follows [101]:

$$\kappa \propto \left(\frac{\varphi}{x}\right)^5 M^3 + \left(\frac{1-\varphi}{x}\right)^3 M \qquad (1)$$

where φ is the fraction of adsorbed chains and parameter $x \leq 1$ is the ratio of the brush length L to the contour length of the backbone aN. Parameters φ and x depend on the energy of attraction to the surface. Equation 1 shows that if the bending modulus is approximated solely by the power-law function $\kappa \sim aM^{\nu}$, then, depending on the strength of adsorption, the exponent will be in the range 2–3, in agreement with the above reported experimental value [100].

Interactions between the 2D side chains induce a very strong force, elongating the backbone. Furthermore, if the length of the side chains exceeds some threshold value, the brushes undergo self-scission because of the breaking of the covalent bonds in the main chain [100,102].

Spontaneous curvature

If the distribution of 2D side chains is "frozen" and asymmetric, then the comb molecule will form curved and snakelike conformations [99,103,104]: The higher the asymmetry, the bigger the curvature. It is surprising that if one allows the possibility of the side chains "jumping" from one side to the other, rectilinear conformation of the brush with symmetric distribution of the side chains will not be reconstructed, despite a penalty in the mixing entropy. It was found that the self-equilibration of 2D brushes results in their curvature [105-109]; the explanation was provided in the theoretical papers [107-109]. The free energy of the curved conformation is smaller due to the decrease in the extension of the side chains under their asymmetric distribution. On the convex side of the brush, the extension drops due to enlargement of accessible space, while on the concave side it decreases due to a reduction in the number of side chains. Further computer simulation [110] and theoretical [111] studies

confirmed the existence of the spontaneous curvature of adsorbed comb macromolecules. Similar results were obtained for brush membranes within the self-consistent field approximation [112]. In addition, all theories predict the existence of a small barrier for the bending free energy.

Rod–globule transition

Brush molecules adsorbed at the water/air surface with the Langmuir–Blodgett technique have shown an ability to undergo transition from straight (rodlike) to globular conformation [98,105,113]. For potential applications there exists the interesting possibility to govern this process either by lateral compression-expansion of the film [105] or by a change of the spreading parameter by admixing of an organic solvent [113]. The character of rod-to-globule transition depends on the length of the side chains: Discontinuous (first order) transition was observed and quantified for brushes with long side chains [105].

Recently, a series of works [114-118] has revealed a new way to change the conformation of brushes adsorbed on solid substrates. Relative changes in composition of water/ethanol vapors lead to reversible transformations from the extended to the compact globular conformation both for isolated molecules [114] and dense films [118].

Interesting results were obtained for the critical exponent ν of the end-to-end distance of the adsorbed brushes [117,118]. Adsorption of isolated combs of poly(butanoate-ethyl methacrilate)-*graft*-poly(n-butyl acrylate) were studied in [117]. Immediately after adsorption, a value of $\nu = 0.77$ was measured, which is close to the 2D statistics of a polymer chain with excluded volume interactions. This quantity dropped to 0.53 after a collapse–reexpansion cycle. The proposed explanation was the following: Initially after deposition from a good solvent the molecule adopts the conformation with a symmetric distribution of the side chains (left–right distribution), which is kinetically trapped. After transition to a globular state and reexpansion, the side chains have the possibility to rearrange thus forming an asymmetric distribution. The asymmetric distribution is thermodynamically more favorable [104] and leads to the snakelike structure with $\nu \sim 0.5$.

In the case of the dense brush monolayer, the exponent $\nu \sim 0.75$ practically does not change after the collapse–reexpansion cycles [118]. The monolayer was prepared by LB technique and transferred on mica. In the LB monolayer, each individual chain saves the conformation of the single 2D molecule, hence $\nu \sim 0.75$. After the collapse–reexpansion cycle, the exponent is slightly smaller, $\nu = 0.73$, but still larger than that for the isolated molecules. One possible explanation is the idea of "memory" of the intermediate conformation in the collapsed state. Another explanation takes into account the balance between the surface energy of 3D aggregate and the stretching free energy of combs in the film [118].

Tadpole conformation and the idea of a molecular motor

Quite an important parameter for the rod–globule transition is the grafting density of the side chains. A more densely grafted brush becomes globular much earlier upon an increase in the surface pressure. A good example is provided in experiments with a gradient in the grafting density along the backbone of the brush [119]. An increase in the surface pressure led to rod–globule transition at the end of the brush with a higher grafting density, thus leading to tadpole-like form of the comb molecules. This kind of molecule may serve as a molecular motor by analogy with the directional movement of diblock copolymers [120]. Computer simulations demonstrated that diblock copolymer adsorbed on a striped surface can shift preferentially in one direction if one of the blocks undergoes periodic collapse and readsorption [120]. In the case of combs, a difference in the desorption properties between the sparsely and densely grafted ends may have the same effect on the movement [4,120].

Nanostructures in monolayers of binary comb copolymers

Thin films of block copolymers have attracted considerable attention as a convenient material for the preparation of heterogeneous surfaces. The proximity of macroscopic phase boundaries affects the orientation of the nanodomains as well as the film structure. Parameters, which govern the orientation, are the interfacial energy of the boundaries [121,122] and the film thickness [123]. In the case of lamellae-forming symmetric diblock copolymers, the perpendicular orientation of the lamellae was found to be stable if the polymer had a high molar mass [123,124] or if none of the blocks had a strong affinity towards the substrate or the air [125]. Otherwise, the lamellae have a parallel orientation with respect to the substrate [125]. Many other factors such as an electric field [122], or competition between the non-lamellar bulk morphology and the affinity of the blocks to the surface [126], or chemically patterned substrates [127,128] may also have a strong influence on the orientation of the diblock copolymer domains.

A chemically heterogeneous surface pattern can reliably be generated from ultrathin films with thickness much smaller than the equilibrium period of the bulk morphology. For instance, this can be obtained by the adsorption of a polystyrene-*block*-poly(2,4-vinylpyridine) diblock copolymer (PS-*b*-P2,4VP) on mica from a non-selective dilute solution [129-133]. The P2,4VP-block is strongly adsorbed and forms approximately a

monolayer; the other (PS)-block is incompatible with the air, substrate and P2,4VP-block. In order to reduce the number of unfavorable contacts, PS aggregates into clusters which are stable over a very wide range of block lengths [134]. A different situation can be observed when the stickiness of one of the blocks is variable (for example, poly(ethylene oxide)-*block*-poly(2-vinylpyridine, PEO-*b*-P2VP)). Variation of the stickiness can result in surface nanopattern formation [135]. A theoretical study of ultrathin films of diblock copolymers with varying stickiness of one of the blocks shows that surface nanopatterns with disc-, stripe- and holelike structures can be obtained. If both blocks can be partially desorbed and one of them can spread atop the other block [136], a wider set of morphologies appears: Stripes, discs, holes, bilayers, substrate-phobic stripes and discs, etc. [136].

Binary comb copolymers comprising incompatible side chains of A and B types attached to a common backbone, may also be used as building blocks to form novel nanopatterns. In our previous work we demonstrated that the conformation of the adsorbed binary comb molecule has a controlled spontaneous curvature [137]. Thus, repulsion of the side chains of different type, on the one hand, and connectivity of the side chains by the backbone, on the other hand, lead to the formation of intramolecular structures. The goal of this section is to study the self-assembly of ultrathin films of binary comb copolymers within a strong segregation approach.

Model of ultrathin film of binary combs

As in [135], we study here a dry, ultrathin film of binary comb copolymers, which were obtained by adsorption of the blocks on a flat surface from a dilute solution. The usual procedure for the preparation of these films involves immersion of the substrate into the solution and pulling it out. Hence, we assume that the overall number of adsorbed macromolecules is constant, but the surface area is still larger than the total area covered with polymer segments. Thus we may analyze the thermodynamically stable morphologies through the variation of the spreading parameter (film area). Each brush molecule contains two types (A and B) of incompatible, flexible side chains. It was assumed that the sequence of grafting points of A and B chains is regularly alternating. Let us denote by N, M_A, and M_B the number of segments in the backbone, A and B side chains, respectively; $N,M_A,M_B >> 1$. It was assumed that the linear size of each segment of the brush is equal to a. We studied densely grafted combs, i.e., the side chains are attached to each segment of the backbone and their number is equal to N. The fraction of the side chains of type B is denoted by $\beta = N_B/N$, where N_B is the total number of side chains of type B. The side chains of type A are strongly adsorbed on the surface and form a layer of the thickness a. This allows us to consider the latter as a two dimensional object with densely packed units, as it minimizes the number of unfavorable contacts between A units and the air. The B chains are strongly incompatible with the A side chains and may adopt both the two-dimensional (adsorbed) conformation as well as partially desorbed ("shrunken") one. Adsorption and desorption of the B chains is controlled by the interactions with the substrate. The sum of contributions from the interfacial interactions and the entropic elasticity of the side chains determines whether the lateral segregation is possible. The following structures are involved in the analysis of thermodynamic stability (Figure 4): Disclike structure (a) and the structure of the inverse discs (e); hexagonally packed micelles with a toruslike core formed by partially desorbed B chains (b); parallel stripes (c); and hexagonally packed inverse toruslike "holes" formed by strongly adsorbed A chains in the matrix of partially desorbed B chains (d). The analysis is performed within the strong segregation approximation [68].

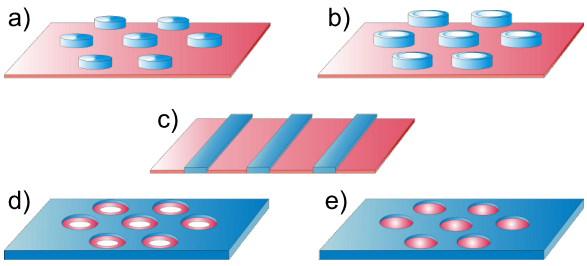

Figure 4: Schematic representation of some of the possible nanostructures formed by binary combs with strongly adsorbed A side chains (red) and partially desorbed B chains (blue): (a) Disc-shaped micelles ordered with the symmetry of a hexagonal lattice (HEX); (b) Torus-shaped micelles ordered with HEX symmetry; (c) parallel stripes; (d) Inverse torus-shaped micelles ordered with HEX symmetry; (e) inverse disc-shaped micelles ("holes") also ordered with HEX symmetry.

Discs

In the model of the disclike micelle, we assumed that the core is formed by the side chains of type B and has a disc shape of radius $\widetilde{R}$ and the thickness $\widetilde{h}$ (Figure 5). We studied the regime of weak desorption of the B chains where the end-to-end distance of them is considerably larger than the thickness of the core, $a \leq \widetilde{h} << \widetilde{R}$. Side chains of the A type are strongly adsorbed and form the shell of the micelle with outer radius $\widetilde{R}_A$ and thickness a.

The free energy of the micelle can be written as a sum of four contributions:

$$F_{disc} = F_{int} + F_{el}^{A} + F_{el}^{B} + F_{conf} \qquad (2)$$

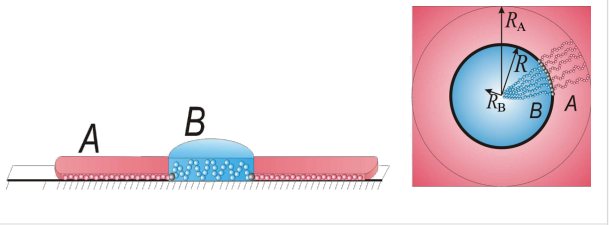

Figure 5: Schematic representation of the disc-shaped structure.

The first term, F_{int}, is the interfacial energy:

$$F_{\text{int}} = (\bar{\gamma}_{\text{As}} + \bar{\gamma}_{\text{Aa}})\pi(R_{\text{A}}^2 - R^2) + (\bar{\gamma}_{\text{Bs}} + \bar{\gamma}_{\text{Ba}})\pi R^2 + 2\pi R(\tilde{h} - a)\bar{\gamma}_{\text{Ba}} + 2\pi R a\bar{\gamma}_0(\sigma_0 - \pi R_{\text{A}}^2) \quad (3)$$

Here, $R = \tilde{R}/a$ and $R_{\text{A}} = \tilde{R}_{\text{A}}/a$. The first term in Equation 3 is the energy of interactions of the A side chains with the substrate and the air; $\bar{\gamma}_{\text{As}}$ and $\bar{\gamma}_{\text{Aa}}$ are the corresponding surface tension coefficients. The next two terms describe interactions of B chains with the substrate and the air. The last term in Equation 3 corresponds to the energy of the substrate/air surface; $\bar{\gamma}_0$ is the substrate/air surface tension coefficient; σ_0 is the area of the substrate divided by the number of micelles on the substrate. This contribution describes spreading of B chains on the surface: It is not a constant as it would be in the case of the fixed film area. Each micelle comprises Q macromolecules. The condition of the dense packing of monomer units in the core and in the shell of the micelle can be written as:

$$\pi R^2 h = QN_{\text{B}}M_{\text{B}}, \quad \pi(R_A^2 - R^2) = QN_{\text{A}}M_{\text{A}}, \quad 2\pi R = QN \quad (4)$$

Here, the volume per monomer unit is assumed to be equal to the cube of the segment length. The last condition corresponds to the fact that the backbone of each particular brush molecule is almost fully stretched. Using the above conditions, the interfacial energy per macromolecule (divided by a constant N) can be written in the following form:

$$\bar{F}_{\text{int}} = \frac{F_{\text{int}}}{k_{\text{b}}TQN} = \gamma_{\text{Ba}}(h-1) - \frac{2S_{\text{B}}M\beta}{(x+1)h} - \frac{2S_A Mx(1-\beta)}{(x+1)} + \frac{\gamma_0\sigma_0}{QNa^2} \quad (5)$$
$$= \gamma_{\text{Ba}}(h-1) - \frac{2S_{\text{B}}M\beta}{(x+1)h} + const.,$$

where $\gamma_{\text{ij}} = \bar{\gamma}_{\text{ij}}a^2/k_{\text{b}}T$ are the dimensionless surface tension coefficients; $x = M_{\text{A}}/M_{\text{B}}$, ($x \geq 1$), and $M = (M_{\text{A}} + M_{\text{B}})/2$. $S_{\text{A}} = (\gamma_0 - \gamma_{\text{Aa}} - \gamma_{\text{As}})$ and $S_{\text{B}} = (\gamma_0 - \gamma_{\text{Ba}} - \gamma_{\text{Bs}})$ are dimensionless spreading parameters, which control the stickiness of the side chains. In our case, S_{A} is fixed, positive and should be fairly large to provide a monomer thick layer for A chains. We considered only variation of the stickiness of B chains. In the system with a fixed number of chains, parameter $\sigma_0\gamma_0/NQ$ (the area of the substrate divided by the number of chains) is constant for all the nanostructures examined, and therefore, it can be omitted.

Now let us calculate the elastic free energy of the side chains (terms F_{el}^{A} and F_{el}^{B} in Equation 2) which can be calculated by analogy with [137]. For the shell (A chains) we supposed that all chains are equally stretched and their ends are located at the outer boundary (Figure 5). The elastic free energy can be written as:

$$\bar{F}_{\text{el}}^{\text{A}} = \frac{F_{\text{el}}^{\text{A}}}{k_{\text{b}}TQN} = \frac{(1-\beta)}{a}\int_R^{R_{\text{A}}} E(r)dr \quad , \quad (6)$$

where $E(r) = dr/ds$ is the local stretching of the side chain, which depends on radial coordinate r. The expression for $E(r)$ can be calculated using the differential form for the dense packing condition of the monomer units in the ring of width dr: $2\pi rdr = adsQN_A$. Therefore, taking into account the space filling condition Equation 4, we get:

$$\bar{F}_{\text{el}}^{\text{A}} = \frac{2(1-\beta)^2\beta M}{(x+1)h}\ln\left(1 - \frac{x(1-\beta)h}{\beta}\right) \quad (7)$$

To calculate the elastic free energy of B side chains, the radial distribution of the free ends has to be taken into account. This term can be approximated by the one obtained for the case of cylindrical micelles in the bulk [68]:

$$\bar{F}_{\text{el}}^{\text{B}} = \frac{\pi^2}{24}\frac{\beta R^2}{M_{\text{B}}} = \frac{\pi^2}{3}\frac{M\beta^3}{h^2} \quad (8)$$

Conformational entropy loss due to adsorption of the side chains comprises contributions from A and B units. The free energy of the B chains can be calculated as that of the chains placed in a slit of thickness h. Owing to the condition $R >> h$, we can use the so-called ground-state approximation [138], where the energy per monomer unit is the minimum eigenvalue λ of the differential equation:

$$\frac{a^2}{6}\frac{\partial^2\psi(x)}{\partial x^2}+\lambda\psi(x)=0$$
$$\frac{\partial\psi(x)}{\partial x}|_{x=\pm h/2}=0,-\frac{h}{2}\le x\le\frac{h}{2} \quad (9)$$

The boundary conditions are taken to satisfy the requirement of a constant density of monomer units inside the slits. The solution of Equation 9 has to be symmetric with respect to the coordinates origin (the middle of the slit), i.e., $\psi(x)=const.\cdot\cos\left(x\sqrt{6\lambda}/a\right)$. Thus, the confinement free energy per chain takes the following form:

$$\bar{F}^{\mathrm{B}}_{\mathrm{conf}}=\frac{F^{\mathrm{B}}_{\mathrm{conf}}}{k_{\mathrm{b}}TQN}=\frac{4\pi^2}{3}\frac{M\beta}{(x+1)h^2} \quad (10)$$

For A side chains the confinement free energy is constant for all the structures considered and therefore can be omitted. From Equation 5, Equation 7, Equation 8, and Equation 10, the total free energy of the disc-like micelle (per one molecule), Equation 2, can be written as:

$$\bar{F}_{\mathrm{disc}}=\frac{2(1-\beta)^2\beta M}{(x+1)h}\ln\left(1-\frac{x(1-\beta)h}{\beta}\right)+\frac{\pi^2}{3}\frac{M\beta^3}{(x+1)h^2}+\frac{4\pi^2}{3}\frac{M\beta}{(x+1)h^2}-\frac{2S_{\mathrm{B}}M\beta}{(x+1)h}+\gamma_{\mathrm{Ba}}(h-1). \quad (11)$$

The equilibrium value of the free energy is calculated by minimization with respect to the thickness h.

Tori

The toruslike micelle has a dense, torus-shaped core of thickness $\tilde{h}$ and of radii $\tilde{R}_{\mathrm{B}}$ and $\tilde{R}$ formed by the B side chains. A smoothed profile of the core can be approximated by a step-like shape (Figure 6) if the width of the torus, $\tilde{R}-\tilde{R}_{\mathrm{B}}$, is much larger than the thickness $\tilde{h}$. Strongly adsorbed A side chains occupy a ring of thickness a and of outer radius $\tilde{R}_{\mathrm{A}}$.

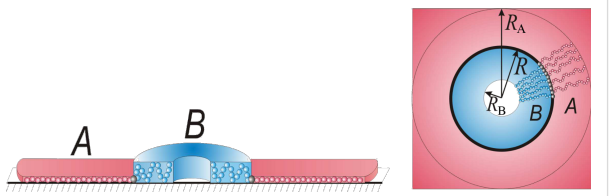

Figure 6: Schematic representation of torus-shaped structure.

The general form of the free energy can be described by Equation 2. In the case of torus-like micelles the condition for the dense packing of monomer units in the core and in the shell of the micelle can be written as:

$$\pi(R^2-R_{\mathrm{B}}^2)h=QN_{\mathrm{B}}M_{\mathrm{B}},\quad \pi(R_A^2-R^2)=QN_{\mathrm{A}}M_{\mathrm{A}},\quad 2\pi R=QN \quad (12)$$

Interaction contribution F_{int} takes the form:

$$\bar{F}_{\mathrm{int}}=\frac{F_{\mathrm{int}}}{k_{\mathrm{b}}TQN}=\gamma_{\mathrm{Ba}}(h-1)-\frac{2S_{\mathrm{B}}M\beta}{(x+1)h}+\gamma_{\mathrm{Ba}}h\sqrt{1-\frac{4M\beta}{(x+1)Rh}}-\frac{2S_{\mathrm{A}}Mx(1-\beta)}{(x+1)}+\frac{\gamma_0\sigma_0}{QNa^2}=\gamma_{\mathrm{Ba}}(h-1)-\frac{2S_{\mathrm{B}}M\beta}{(x+1)h}+\gamma_{\mathrm{Ba}}h\sqrt{1-\frac{4M\beta}{(x+1)Rh}}+const. \quad (13)$$

The elastic free energies of the core and the shell are calculated in a similar way to those of the disclike structure:

$$\bar{F}^{\mathrm{B}}_{\mathrm{el}}=-\frac{\beta^2}{2h}R\ln\left(1-\frac{4M\beta}{(x+1)hR}\right), \quad (14)$$

and

$$\bar{F}^{\mathrm{A}}_{\mathrm{el}}=\frac{(1-\beta)^2}{2}R\ln\left(1+\frac{4Mx(1-\beta)}{(x+1)R}\right), \quad (15)$$

where the conditions in Equation 12 are used.

The confinement free energy has the same form as for the case of discs. Hence the total free energy of the torus-like micelles can be written as

$$\bar{F}_{\mathrm{tor}}=\frac{(1-\beta)^2}{2}R\ln\left(1+\frac{4Mx(1-\beta)}{(x+1)R}\right)-\frac{\beta^2}{2h}R\ln\left(1-\frac{4M\beta}{(x+1)Rh}\right)+\frac{4\pi^2}{3}\frac{M\beta}{(x+1)h^2}-\frac{2S_{\mathrm{B}}M\beta}{(x+1)h}+\gamma_{\mathrm{Ba}}(h-1)+\gamma_{\mathrm{Ba}}h\sqrt{1-\frac{4M\beta}{(x+1)Rh}} \quad (16)$$

The equilibrium value is calculated by minimization with respect to the parameters R and h.

Stripes

If the value of the fraction of B side chains β increases, the torus-like structure becomes unfavorable and a stripes-like structure can be observed (Figure 7). The width of the A chains monolayer is $2(R_0 - R)$. The B stripes have width $2R$ and thickness h (condition $1 \leq h << R$ remains valid).

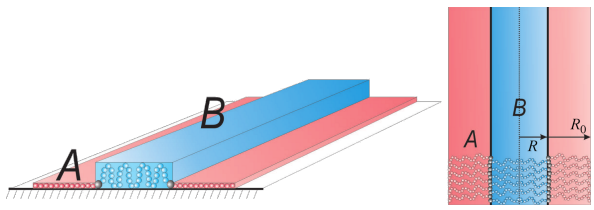

Figure 7: Schematic representation of a stripe-shaped structure.

For this structure the total free energy has the form:

$$\bar{F}_{\text{str}} = \frac{2\beta^3 M}{(x+1)h^2}\left(1+\frac{x(1-\beta)^3 h^2}{\beta^3}\right) + \frac{4\pi^2}{3}\frac{M\beta}{(x+1)h^2} - \frac{2S_B M\beta}{(x+1)h} + \gamma_{Ba}(h-1) \quad (17)$$

where the space-filling conditions are: $2LRh = QN_BM_B$ and $2L(R_0 - R) = QN_AM_A$, respectively. Here, $L \to \infty$ is the length of the stripes. The first term in Equation 17 is the elastic free energy of the side chains, $N_BR^2/M_B + N_A(R_0 - R)^2/M_A$. Other terms are written similarly to the case of torus shaped micelles.

We can find conditions for the transition to a monomer thick structure ($h = 1$) for the stripes:

$$S_B^{cr} \approx \frac{4\pi^2}{3} + 2\beta^2.$$

Thus, the completely two dimensional structure is stable if $S_B > S_B^{cr}$.

Inverse Tori

In the case of a large asymmetry of the binary combs forming the film ($N_B < N_A$), the inverse torus-shaped structure can be stable. Morphology of this structure is similar to that of the torus-shaped one, with the difference being that the inner part (core) of the micelles forms a monolayer of A type (Figure 8).

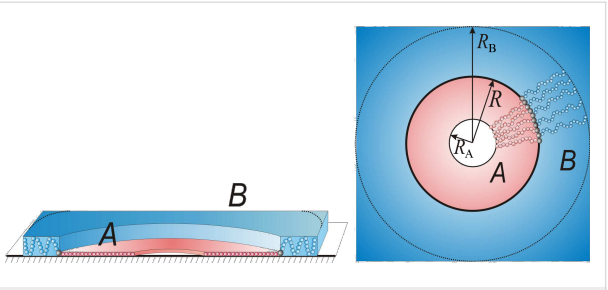

Figure 8: Schematic representation of an inverse torus-like structure.

Similarly to the free energy of the conventional torus, Equation 16, the free energy of the inverse torus takes the form:

$$\bar{F}_{\text{tor}} = \frac{\beta^2}{2h}R\ln\left(1+\frac{4M\beta}{(x+1)Rh}\right) - \frac{(1-\beta)^2}{2}R\ln\left(1-\frac{4Mx(1-\beta)}{(x+1)R}\right) + \frac{4\pi^2}{3}\frac{M\beta}{(x+1)h^2} - \frac{2S_BM\beta}{(x+1)h} + \gamma_{Ba}(h-1) + \gamma_{Aa}\sqrt{1-\frac{4Mx(1-\beta)}{(x+1)R}} \quad (18)$$

Holes

Finally, the last structure that can be observed in ultrathin film of the binary comb copolymers is the one inverse to the disk-like micelles (Figure 9). This structure is characterized by a disk-like, monomer thick core of the A side chains and by thickened corona of the B units.

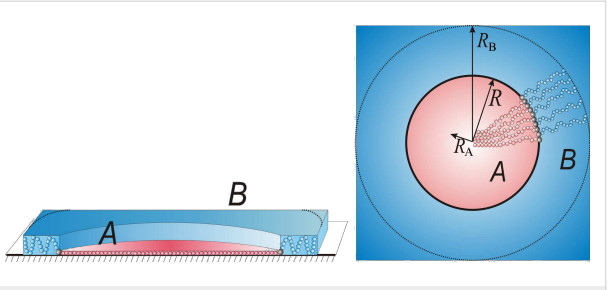

Figure 9: Schematic representation of "holes"

The free energy of the "holes" takes a form similar to the case of disks, Equation 11:

$$\bar{F}_{\text{hole}} = \frac{2(1-\beta)\beta^2 M}{(x+1)h}\ln\left(1-\frac{\beta}{x(1-\beta)h}\right) + \frac{\pi^2}{3}\frac{Mx(1-\beta)^3}{(x+1)} + \frac{4\pi^2}{3}\frac{M\beta}{(x+1)h^2} - \frac{2S_BM\beta}{(x+1)h} + \gamma_{Ba}(h-1) \quad (19)$$

Phase diagrams

Phase diagrams in terms of the fraction of B side chains, $\beta = N_B/N$, and of the spreading parameter, S_B, are depicted in Figure 10. Boundaries between different nanostructures are determined from the conditions of equality of the free energies. The nearly horizontal line, S_B^{cr}, distinguishes the "landscape" of the film. Above the line (high values of S_B), the film is completely flat consisting of 2D binary combs. Depending on interaction parameters, all analyzed morphologies can be stable. If β is small enough, a minor fraction of the B chains forms the core of the micelles in the film, i.e., disclike morphology. An increase of β may result in toruslike structure if the incompatibility of polymer B with the air (the surface tension coefficient γ_{Ba}) is low enough. Indeed, the inner surface (line) of the torus possesses extra (in comparison with the disc) energy, which destabilizes the structure at high values of γ_{Ba}. A further increase of β leads to the formation of a stripelike structure, which does not correspond to the symmetric composition β = 1/2. The reason for that is the value of the parameter $x = M_A/M_B = 2$ (Figure 10a–c). One needs a higher fraction of short B chains on one side of the backbone to "equilibrate" the excluded volume of long A chains on the other side. The inverse toruslike structure is also stable only at relatively small values of the surface tension coefficient γ_{Aa} (Figure 10a). Finally, if β is high enough, the A blocks form the core of the micelles in the film.

Prominent nanostructures with elevated B domains are stable at $S_B < S_B^{cr}$. Here all the boundaries are shifted towards higher values of β. This effect can be explained by partial desorption (shrinkage) of the B chains, which is accompanied by the decrease of their lateral stretching. Therefore, in order to stabilize a certain structure at low values of S_B, one needs to take molecules with higher β to increase the stretching of the B chains. Both direct and inverse toruslike structures disappear with the decrease of S_B at fixed values of γ_{Ba} and γ_{Aa}. This behavior is also related to the energy of the inner surface of the torus: Decreasing S_B thickens the torus and increases the

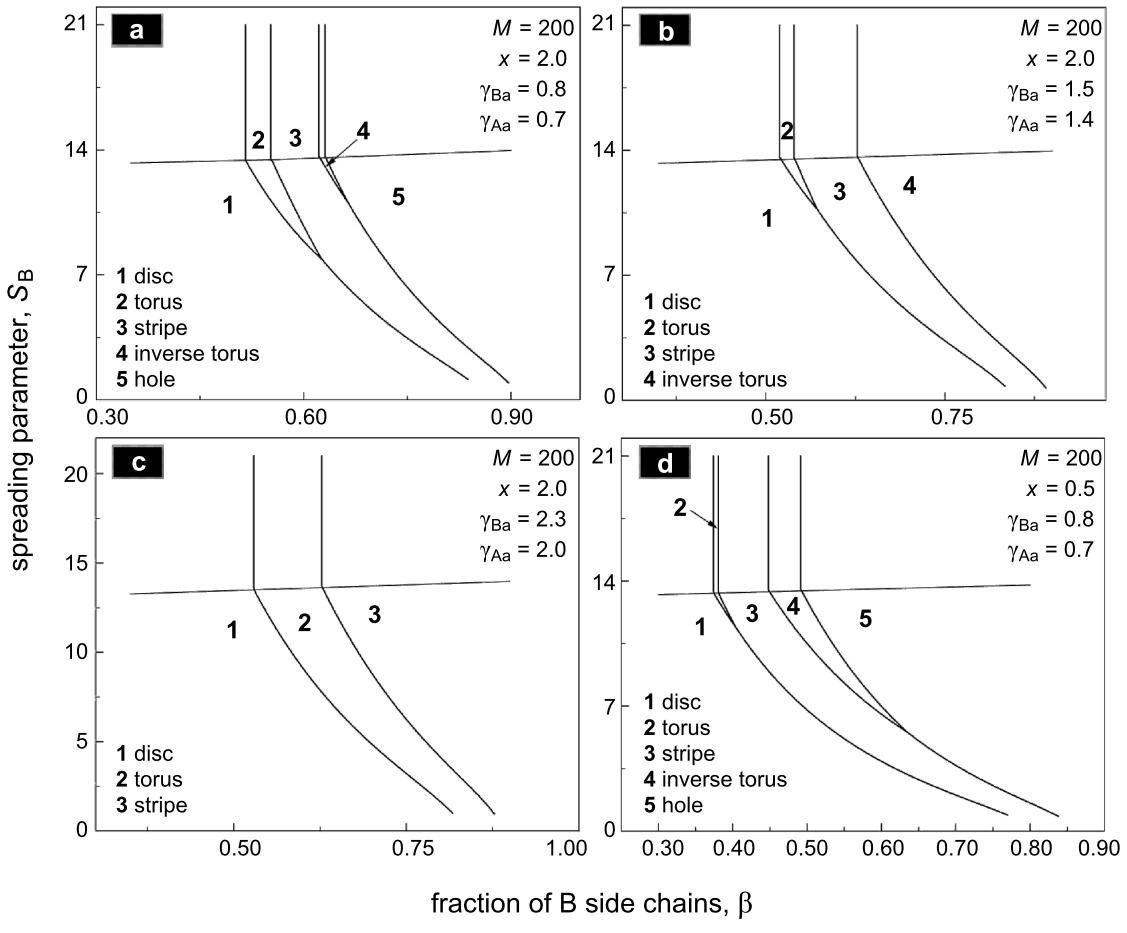

Figure 10: Phase diagram of the film in terms of the fraction of B side chains, $\beta = N_B/(N_A + N_B)$, and the spreading parameter S_B. The line $S_B = S_B^{cr}$ splits the regions of flat and prominent morphologies. The spreading parameter S_A satisfies the inequality $S_A > S_A^{cr}$ to ensure 2D conformation of A chains.

surface energy. The particular slope of the boundaries of the prominent morphologies allows us to conclude that the variation of the stickiness of one of the blocks in the film can lead to morphological transitions.

Changing of the parameter x from 2 to 0.5 (Figure 10a and Figure 10d) corresponds to the shortening of the A chains with respect to the B chains. In this case the whole phase diagram shifts towards lower values of β (one needs a smaller fraction of long side chains of B type to change the morphology).

Partial desorption of the B side chains influences not only the morphology but also the size and aggregation number of the micelles in the film (Figure 11). The increase in stretching of the B chains with S_B leads to a decrease in the value of the spontaneous curvature of each comblike molecule (the so-called energetic curvature [137]) and, hence, to the growth of the radius of the micelles (disc- or toruslike) and their aggregation number (Figure 11).

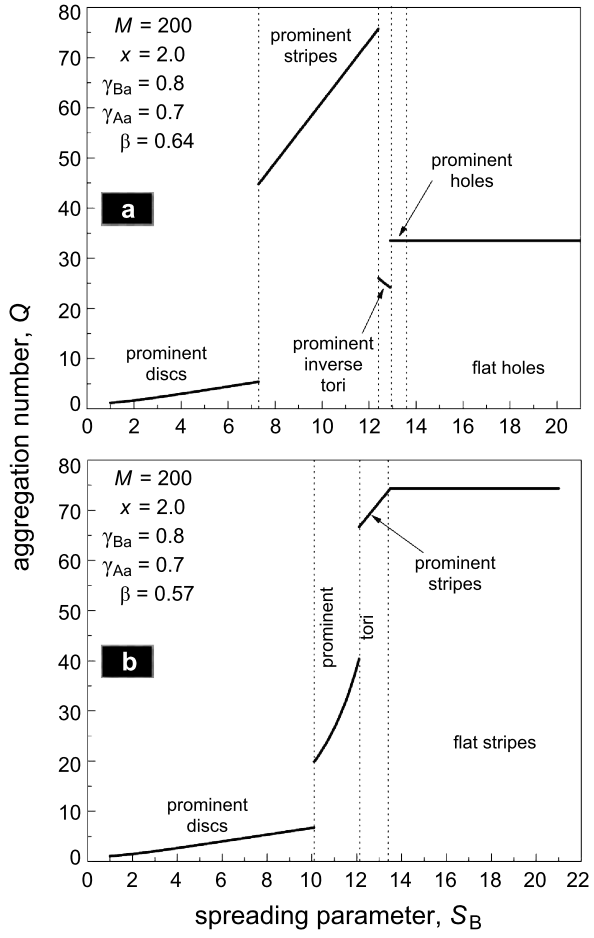

Figure 11: Aggregation number Q as a function of the spreading parameter S_B at different values of β: β = 0.64 (a) and 0.57 (b). The vertical lines split the regions of stability of various nanostructures.

Direct and inverse toruslike nanostructures are characteristic structures of the binary combs and they are absent in the films formed by diblock copolymers [135,136]. This feature is related to the form of "building blocks" in self-organized films. The ability to form spontaneous curvature on the level of individual comblike macromolecules predefines stability of the toruslike structures.

Conclusion

In conclusion, we can state that the improvement in procedures for the synthesis of comblike macromolecules makes it possible to prepare new classes of polymers with well-defined structures. In turn, this leads to the discovery of properties not typical of other types of molecules. Specifically, the effects of the strong extension of chains and the feasibility of controlling conformational properties on the surface are of indubitable interest for the creation of diverse molecular machines. Even though intensive studies of comblike polymers have been carried out for more than two decades, the question whether the conformational properties of such molecules in solution depend on structural parameters remains unsolved. However, considerable progress has been achieved in the study of polymers adsorbed on the surface.

At present, researchers have shifted their attention to comblike macromolecules of complex chemical structure. These systems are of the utmost interest for the discovery of new effects and for creating new materials.

Acknowledgements

Financial support of the Deutsche Forschungsgemeinschaft within the SFB 569, the Ministry of Education and Science (Russian Federation), and the Russian Foundation for Basic Research is gratefully acknowledged.

References

1. Hadjichristidis, N.; Pitsikalis, M.; Pispas, S.; Iatrou, H. *Chem. Rev.* **2001,** *101,* 3747–3792. doi:10.1021/cr9901337
2. Matyjaszewski, K.; Xia, J. *Chem. Rev.* **2001,** *101,* 2921–2990. doi:10.1021/cr940534g
3. Hadjichristidis, N.; Pitsikalis, M.; Iatrou, H. *Adv. Polym. Sci.* **2005,** *189,* 1–124. doi:10.1007/12_005
4. Potemkin, I. I.; Palyulin, V. V. *Polymer Science, Series A* **2009,** *51,* 123–149. doi:10.1134/S0965545X09020011
5. Sheiko, S. S.; Sumerlin, B. S.; Matyjaszewski, K. *Prog. Polym. Sci.* **2008,** *33,* 759–785. doi:10.1016/j.progpolymsci.2008.05.001
6. Ballauff, M. *Angew. Chem., Int. Ed.* **1989,** *28,* 253–267. doi:10.1002/anie.198902533
7. Hartikainen, J.; Lahtinen, M.; Torkkeli, M.; Serimaa, R.; Valkonen, J.; Rissanen, K.; Ikkala, O. *Macromolecules* **2001,** *34,* 7789–7795. doi:10.1021/ma010209c
8. Scott, J. E. *Biochemistry* **1996,** *35,* 8795–8799. doi:10.1021/bi960773t

9. Chen, L.; Yang, B. L.; Wu, Y.; Yee, A.; Yang, B. B. *Biochemistry* **2003,** *42,* 8332–8341. doi:10.1021/bi034335f
10. Kaneider, N. C.; Dunzendorfer, S.; Wiedermann, C. J. *Biochemistry* **2004,** *43,* 237–244. doi:10.1021/bi035295i
11. Bromberg, L. E.; Barr, D. P. *Biomacromolecules* **2000,** *1,* 325–334. doi:10.1021/bm005532m
12. Celli, J. P.; Turner, B. S.; Afdhal, N. H.; Ewoldt, R. H.; McKinley, G. H.; Bansil, R.; Erramilli, S. *Biomacromolecules* **2007,** *8,* 1580–1586. doi:10.1021/bm0609691
13. Galuschko, A.; Spirin, L.; Kreer, T.; Johner, A.; Pastorino, C.; Wittmer, J.; Baschnagel, J. *Langmuir* **2010,** *26,* 6418–6429. doi:10.1021/la904119c
14. Neugebauer, D.; Zhang, Y.; Pakula, T.; Sheiko, S. S.; Matyjaszewski, K. *Macromolecules* **2003,** *36,* 6746–6755. doi:10.1021/ma0345347
15. Neiser, M. W.; Muth, S.; Kolb, U.; Harris, J. R.; Okuda, J.; Schmidt, M. *Angew. Chem., Int. Ed.* **2004,** *43,* 3192–3195. doi:10.1002/anie.200353259
16. Huang, K.; Rzayev, J. *J. Am. Chem. Soc.* **2009,** *131,* 6880–6885. doi:10.1021/ja901936g
17. Müllner, M.; Yuan, J.; Weiss, S.; Walther, A.; Förtsch, M.; Drechsler, M.; Müller, A. H. E. *J. Am. Chem. Soc.* **2010,** *132,* 16587–16592. doi:10.1021/ja107132j
18. Onsager, L. *Ann. N. Y. Acad. Sci.* **1949,** *51,* 627. doi:10.1111/j.1749-6632.1949.tb27296.x
19. Khokhlov, A. R.; Semenov, A. N. *Physica A* **1981,** *108,* 546–556. doi:10.1016/0378-4371(81)90148-5
20. Wittmer, J. P.; Meyer, H.; Baschnagel, J.; Johner, A.; Obukhov, S.; Mattioni, L.; Müller, M.; Semenov, A. N. *Phys. Rev. Lett.* **2004,** *93,* 147801. doi:10.1103/PhysRevLett.93.147801
21. Shirvanyants, D.; Panyukov, S.; Liao, Q.; Rubinstein, M. *Macromolecules* **2008,** *41,* 1475–1485. doi:10.1021/ma071443r
22. Semenov, A. N. *Macromolecules* **2010,** *43,* 9139–9154. doi:10.1021/ma101465z
23. Hsu, H.-P.; Paul, W.; Binder, K. *Macromolecules* **2010,** *43,* 3094–3102. doi:10.1021/ma902715e
24. Schäfer, L.; Ostendorf, A.; Hager, J. *J. Phys. A: Math. Gen.* **1999,** *32,* 7875–7899. doi:10.1088/0305-4470/32/45/306
25. Schäfer, L.; Elsner, K. *Eur. Phys. J. E* **2004,** *13,* 225–237. doi:10.1140/epje/i2003-10071-1
26. Gallacher, L. V.; Windwer, S. *J. Chem. Phys.* **1966,** *44,* 1139–1148. doi:10.1063/1.1726799
27. McCrackin, F. L.; Mazur, J. *Macromolecules* **1981,** *14,* 1214–1220. doi:10.1021/ma50006a015
28. Magarik, S. Ya.; Pavlov, G. M.; Fomin, G. A. *Macromolecules* **1978,** *11,* 294–300. doi:10.1021/ma60062a003
29. Tsvetkov, V. N. *Rigid-chain polymers: hydrodynamic, optical properties in solution;* Consultants Bureau: New York, 1989.
30. de Gennes, P.-G. *Scaling concepts in polymer physics;* Cornell University Press: Ithaca, N. Y., 1979.
31. Birshtein, T. M.; Borisov, O. V.; Zhulina, Ye. B.; Khokhlov, A. R.; Yurasova, T. A. *Polym. Sci. USSR* **1987,** *29,* 1293–1300. doi:10.1016/0032-3950(87)90374-1
32. Fredrickson, G. H. *Macromolecules* **1993,** *26,* 2825–2831. doi:10.1021/ma00063a029
33. Wintermantel, M.; Schmidt, M.; Tsukahara, Y.; Kajiwara, K.; Kohjiya, S. *Macromol. Rapid Commun.* **1994,** *15,* 279–284. doi:10.1002/marc.1994.030150315
34. Yoshizaki, T.; Nitta, I.; Yamakawa, H. *Macromolecules* **1988,** *21,* 165–171. doi:10.1021/ma00179a033
35. Wintermantel, M.; Gerle, M.; Fischer, K.; Schmidt, M.; Wakaoka, I.; Urakawa, H.; Kajiwara, K.; Tsukahara, Y. *Macromolecules* **1996,** *29,* 978–983. doi:10.1021/ma950227s
36. Rathgeber, S.; Pakula, T.; Wilk, A.; Matyjaszewski, K.; Lee, H.-i.; Beers, K. L. *Polymer* **2006,** *47,* 7318–7327. doi:10.1016/j.polymer.2006.06.010
37. Zhang, B.; Gröhn, F.; Pedersen, J. S.; Fischer, K.; Schmidt, M. *Macromolecules* **2006,** *39,* 8440–8450. doi:10.1021/ma0613178
38. Terao, K.; Nakamura, Y.; Norisuye, T. *Macromolecules* **1999,** *32,* 711–716. doi:10.1021/ma9816517
39. Terao, K.; Hokajo, T.; Nakamura, Y.; Norisuye, T. *Macromolecules* **1999,** *32,* 3690–3694. doi:10.1021/ma990091o
40. Saariaho, M.; Subbotin, A.; Szleifer, I.; Ikkala, O.; ten Brinke, G. *Macromolecules* **1999,** *32,* 4439–4443. doi:10.1021/ma990307m
41. Saariaho, M.; Szleifer, I.; Ikkala, O.; ten Brinke, G. *Macromol. Theory Simul.* **1998,** *7,* 211–216. doi:10.1002/(SICI)1521-3919(19980301)7:2<211::AID-MATS211>3.0.CO;2-A
42. Rouault, Y.; Borisov, O. V. *Macromolecules* **1996,** *29,* 2605–2611. doi:10.1021/ma951126x
43. Feuz, L.; Leermakers, F. A. M.; Textor, M.; Borisov, O. *Macromolecules* **2005,** *38,* 8891–8901. doi:10.1021/ma050871z
44. Hsu, H.-P.; Paul, W.; Binder, K. *Europhys. Lett.* **2006,** *76,* 526–532. doi:10.1209/epl/i2006-10276-4
45. Hsu, H.-P.; Paul, W.; Binder, K. *Macromol. Theory Simul.* **2007,** *16,* 660–689. doi:10.1002/mats.200700031
46. Borisov, O. V.; Zhulina, E. B. *Macromolecules* **2005,** *38,* 2506–2514. doi:10.1021/ma047464s
47. Košovan, P.; Kuldova, J.; Limpouchova, Z.; Procházka, K.; Zhulina, E. B.; Borisov, O. V. *Macromolecules* **2009,** *42,* 6748–6760. doi:10.1021/ma900768p
48. Kramarenko, E. Yu.; Pevnaya, O. S.; Khokhlov, A. R. *J. Chem. Phys.* **2005,** *122,* 084902. doi:10.1063/1.1849160
49. Polotsky, A.; Charlaganov, M.; Xu, Y.; Leermakers, F. A. M.; Daoud, M.; Müller, A. H. E.; Dotera, T.; Borisov, O. *Macromolecules* **2008,** *41,* 4020–4028. doi:10.1021/ma800125q
50. Stepanyan, R.; Subbotin, A.; ten Brinke, G. *Macromolecules* **2002,** *35,* 5640–5648. doi:10.1021/ma011441l
51. Subbotin, A. V.; Semenov, A. N. *Polymer Science, Series A* **2007,** *49,* 1328–1357. doi:10.1134/S0965545X07120085
52. Leibler, L. *Macromolecules* **1980,** *13,* 1602–1617. doi:10.1021/ma60078a047
53. de Jong, J.; ten Brinke, G. *Macromol. Theory Simul.* **2004,** *13,* 318–327. doi:10.1002/mats.200300052
54. Landau, L. D.; Lifshitz, E. M. *Statistical Physics, Part I;* Pergamon Press: Oxford, 1980.
55. Theodorakis, P. E.; Paul, W.; Binder, K. *Europhys. Lett.* **2009,** *88,* 63002. doi:10.1209/0295-5075/88/63002
56. Sheiko, S. S.; Borisov, O. V.; Prokhorova, S. A.; Möller, M. *Eur. Phys. J. E* **2004,** *13,* 125–131. doi:10.1140/epje/e2004-00049-8
57. Polotsky, A.; Daoud, M.; Borisov, O.; Charlaganov, M.; Leermakers, F. A. M. *Int. J. Polym. Anal. Charact.* **2007,** *12,* 47–55. doi:10.1080/10236660601060151
58. Theodorakis, P. E.; Paul, W.; Binder, K. *J. Chem. Phys.* **2010,** *133,* 104901. doi:10.1063/1.3477981
59. Liu, Y.; Abetz, V.; Müller, A. H. E. *Macromolecules* **2003,** *36,* 7894–7898. doi:10.1021/ma0345551
60. Zhang, M.; Müller, A. H. E. *J. Polym. Sci., Part A: Polym. Chem.* **2005,** *43,* 3461–3481. doi:10.1002/pola.20900

61. Bates, F.; Fredrickson, G. *Annu. Rev. Phys. Chem.* **1990,** *41,* 525–557. doi:10.1146/annurev.pc.41.100190.002521
62. Bates, F. S.; Fredrickson, G. H. *Phys. Today* **1999,** *52,* 32–38. doi:10.1063/1.882522
63. Matsen, M. W. *J. Phys.: Condens. Matter* **2002,** *14,* R21. doi:10.1088/0953-8984/14/2/201
64. van Zoelen, W.; ten Brinke, G. *Soft Matter* **2009,** *5,* 1568–1582. doi:10.1039/b817093b
65. Park, C.; Yoon, J.; Thomas, E. L. *Polymer* **2003,** *44,* 6725–6760. doi:10.1016/j.polymer.2003.08.011
66. Bang, J.; Jeong, U.; Ryu, D. Y.; Russell, T. P.; Hawker, C. J. *Adv. Mater.* **2009,** *21,* 4769–4792. doi:10.1002/adma.200803302
67. Khandpur, A. K.; Foerster, S.; Bates, F. S.; Hamley, I. W.; Ryan, A. J.; Bras, W.; Almdal, K.; Mortensen, K. *Macromolecules* **1995,** *28,* 8796–8806. doi:10.1021/ma00130a012
68. Semenov, A. N. *Sov. Phys. JETP* **1985,** *61,* 733–742.
69. Dobrynin, A. V.; Erukhimovich, I. Ya. *Macromolecules* **1993,** *26,* 276–281. doi:10.1021/ma00054a005
70. Hadjichristidis, N.; Pispas, S. *Adv. Polym. Sci.* **2006,** *200,* 37–55. doi:10.1007/12_069
71. Ganesan, V.; Ellison, C. J.; Pryamitsyn, V. *Soft Matter* **2010,** *6,* 4010–4025. doi:10.1039/b926992d
72. Yerukhimovich, I. Ya. *Polym. Sci. USSR* **1982,** *24,* 2223–2232. doi:10.1016/0032-3950(82)90283-0
73. Benoit, H.; Hadziioannou, G. *Macromolecules* **1988,** *21,* 1449–1464. doi:10.1021/ma00183a040
74. Shinozaki, A.; Jasnow, D.; Balazs, A. C. *Macromolecules* **1994,** *27,* 2496–2502. doi:10.1021/ma00087a018
75. Palyulin, V. V.; Potemkin, I. I. *Polymer Science, Series A* **2007,** *49,* 473–481. doi:10.1134/S0965545X07040153
76. Palyulin, V. V.; Potemkin, I. I. *J. Chem. Phys.* **2007,** *127,* 124903. doi:10.1063/1.2768058
77. Nap, R. J.; Kok, C.; ten Brinke, G.; Kuchanov, S. I. *Eur. Phys. J. E* **2001,** *4,* 515–519. doi:10.1007/s101890170106
78. Nap, R. J.; ten Brinke, G. *Macromolecules* **2002,** *35,* 952–959. doi:10.1021/ma010519v
79. Pryamitsyn, V.; Ganesan, V. *J. Chem. Phys.* **2004,** *120,* 5824–5838. doi:10.1063/1.1649729
80. Chen, J. T.; Thomas, E. L.; Ober, C. K.; Mao, G.-p. *Science* **1996,** *273,* 343–346. doi:10.1126/science.273.5273.343
81. Olsen, B. D.; Segalman, R. A. *Mater. Sci. Eng., R* **2008,** *62,* 37–66. doi:10.1016/j.mser.2008.04.001
82. Zheng, W. Y.; Hammond, P. T. *Macromolecules* **1998,** *31,* 711–721. doi:10.1021/ma970940c
83. Sänger, J.; Gronski, W.; Maas, S.; Stühn, B.; Heck, B. *Macromolecules* **1997,** *30,* 6783–6787. doi:10.1021/ma970518w
84. Anthamatten, M.; Hammond, P. T. *Macromolecules* **1999,** *32,* 8066–8076. doi:10.1021/ma9910989
85. Vasilenko, S. V.; Shibaev, V. P.; Khokhlov, A. R. *Makromol. Chem.* **1985,** *186,* 1951–1960. doi:10.1002/macp.1985.021860922
86. Auriemma, F.; Corradini, P.; Vacatello, M. *J. Chem. Phys.* **1990,** *93,* 8314–8320. doi:10.1063/1.459314
87. Shibaev, V. P. *Polymer Science, Series A* **2009,** *51,* 1131–1193. doi:10.1134/S0965545X09110029
88. Wang, X. J.; Warner, M. *J. Phys. A: Math. Gen.* **1987,** *20,* 713–731. doi:10.1088/0305-4470/20/3/033
89. Hernández-Jiménez, M.; Westfahl, H., Jr.. *Eur. Phys. J. E* **2007,** *23,* 31–42. doi:10.1140/epje/i2006-10083-3
90. Hamley, I. W.; Castelletto, V.; Lu, Z. B.; Imrie, C. T.; Itoh, T.; Al-Hussein, M. *Macromolecules* **2004,** *37,* 4798–4807. doi:10.1021/ma0498619
91. Mao, G.; Wang, J.; Clingman, S. R.; Ober, C. K.; Chen, J. T.; Thomas, E. L. *Macromolecules* **1997,** *30,* 2556–2567. doi:10.1021/ma9617835
92. Verploegen, E.; McAfee, L. C.; Tian, L.; Verploegen, D.; Hammond, P. T. *Macromolecules* **2007,** *40,* 777–780. doi:10.1021/ma061684j
93. Albrecht, K.; Mourran, A.; Zhu, X.; Markkula, T.; Groll, J.; Beginn, U.; de Jeu, W. H.; Moeller, M. *Macromolecules* **2008,** *41,* 1728–1738. doi:10.1021/ma071317n
94. Anthamatten, M.; Hammond, P. T. *J. Polym. Sci., Part B: Polym. Phys.* **2001,** *39,* 2671–2691. doi:10.1002/polb.10027
95. Shah, M.; Pryamitsyn, V.; Ganesan, V. *Macromolecules* **2008,** *41,* 218–229. doi:10.1021/ma071566b
96. Potemkin, I. I.; Bodrova, A. S. *Macromolecules* **2009,** *42,* 2817–2825. doi:10.1021/ma802365y
97. Mkhonta, S. K.; Elder, K. R.; Grant, M. *Eur. Phys. J. E* **2010,** *32,* 349–355. doi:10.1140/epje/i2010-10636-9
98. Sheiko, S. S.; Möller, M. *Chem. Rev.* **2001,** *101,* 4099–4123. doi:10.1021/cr990129v
99. Potemkin, I. I.; Khokhlov, A. R.; Reineker, P. *Eur. Phys. J. E* **2001,** *4,* 93–101. doi:10.1007/s101890170147
100. Sheiko, S. S.; Sun, F. C.; Randall, A.; Shirvanyants, D.; Rubinstein, M.; Lee, H.-i.; Matyjaszewski, K. *Nature* **2006,** *440,* 191–194. doi:10.1038/nature04576
101. Potemkin, I. I. *Macromolecules* **2006,** *39,* 7178–7180. doi:10.1021/ma061235j
102. Panyukov, S.; Zhulina, E. B.; Sheiko, S. S.; Randall, G. C.; Brock, J.; Rubinstein, M. *J. Phys. Chem. B* **2009,** *113,* 3750–3768. doi:10.1021/jp807671b
103. Khalatur, P. G.; Khokhlov, A. R.; Prokhorova, S. A.; Sheiko, S. S.; Möller, M.; Reineker, P.; Shirvanyanz, D. G.; Starovoitova, N. *Eur. Phys. J. E* **2000,** *1,* 99–103. doi:10.1007/s101890050012
104. Potemkin, I. I. *Macromolecules* **2007,** *40,* 1238–1242. doi:10.1021/ma062099l
105. Sheiko, S. S.; Prokhorova, S. A.; Beers, K. L.; Matyjaszewski, K.; Potemkin, I. I.; Khokhlov, A. R.; Möller, M. *Macromolecules* **2001,** *34,* 8354–8360. doi:10.1021/ma010746x
106. Sheiko, S.; da Silva, M.; Shirvaniantz, D. G.; Rodrigues, C. A.; Beers, K.; Matyjaszewski, K.; Potemkin, I. I.; Moeller, M. *Polym. Prepr. (Am. Chem. Soc., Div. Polym. Chem.)* **2003,** *44,* 544–545.
107. Potemkin, I. *Eur. Phys. J. E* **2003,** *12,* 207–210. doi:10.1140/epje/i2003-10061-3
108. Potemkin, I. I.; Khokhlov, A. R.; Prokhorova, S.; Sheiko, S. S.; Möller, M.; Beers, K. L.; Matyjaszewski, K. *Macromolecules* **2004,** *37,* 3918–3923. doi:10.1021/ma021519d
109. Potemkin, I. I.; Popov, K. I. *J. Chem. Phys.* **2008,** *129,* 124901. doi:10.1063/1.2980050
110. de Jong, J.; Subbotin, A.; ten Brinke, G. *Macromolecules* **2005,** *38,* 6718–6725. doi:10.1021/ma050612+
111. Subbotin, A.; de Jong, J.; ten Brinke, G. *Eur. Phys. J. E* **2006,** *20,* 99–108. doi:10.1140/epje/i2005-10122-7
112. Birshtein, T. M.; Iakovlev, P. A.; Amoskov, V. M.; Leermakers, F. A. M.; Zhulina, E. B.; Borisov, O. V. *Macromolecules* **2008,** *41,* 478–488. doi:10.1021/ma071303h

113. Sun, F.; Sheiko, S. S.; Möller, M.; Beers, K.; Matyjaszewski, K. *J. Phys. Chem. A* **2004,** *108,* 9682–9686. doi:10.1021/jp047929g
114. Gallyamov, M.; Tartsch, B.; Khokhlov, A. R.; Sheiko, S. S.; Börner, H. G.; Matyjaszewski, K.; Möller, M. *Macromol. Rapid Commun.* **2004,** *25,* 1703–1707. doi:10.1002/marc.200400235
115. Gallyamov, M. O.; Tartsch, B.; Khokhlov, A. R.; Sheiko, S. S.; Börner, H. G.; Matyjaszewski, K.; Möller, M. *Chem.–Eur. J.* **2004,** *10,* 4599–4605. doi:10.1002/chem.200400174
116. Gallyamov, M. O.; Tartsch, B.; Mela, P.; Börner, H.; Matyjaszewski, K.; Sheiko, S.; Khokhlov, A.; Möller, M. *Phys. Chem. Chem. Phys.* **2007,** *9,* 346–352. doi:10.1039/b612654e
117. Gallyamov, M. O.; Tartsch, B.; Mela, P.; Potemkin, I. I.; Sheiko, S. S.; Börner, H.; Matyjaszewski, K.; Khokhlov, A. R.; Möller, M. *J. Polym. Sci., Part B: Polym. Phys.* **2007,** *45,* 2368–2379. doi:10.1002/polb.21253
118. Gallyamov, M. O.; Tartsch, B.; Potemkin, I. I.; Börner, H. G.; Matyjaszewski, K.; Khokhlov, A.; Möller, M. *Eur. Phys. J. E* **2009,** *29,* 73–85. doi:10.1140/epje/i2009-10451-5
119. Lord, S. J.; Sheiko, S. S.; LaRue, I.; Lee, H.-I.; Matjaszewski, K. *Macromolecules* **2004,** *37,* 4235–4240. doi:10.1021/ma035989z
120. Perelstein, O. E.; Ivanov, V. A.; Velichko, Y. S.; Khalatur, P. G.; Khokhlov, A. R.; Potemkin, I. I. *Macromol. Rapid Commun.* **2007,** *28,* 977–980. doi:10.1002/marc.200700009
121. Kellogg, G. J.; Walton, D. G.; Mayes, A. M.; Lambooy, P.; Russell, T. P.; Gallagher, P. D.; Satija, S. K. *Phys. Rev. Lett.* **1996,** *76,* 2503–2506. doi:10.1103/PhysRevLett.76.2503
122. Mansky, P.; Liu, Y.; Huang, E.; Russell, T. P.; Hawker, C. *Science* **1997,** *275,* 1458–1460. doi:10.1126/science.275.5305.1458
123. Busch, P.; Posselt, D.; Smilgies, D.-M.; Rheinländer, B.; Kremer, F.; Papadakis, C. M. *Macromolecules* **2003,** *36,* 8717–8727. doi:10.1021/ma034375r
124. Potemkin, I. I.; Busch, P.; Smilgies, D.-M.; Posselt, D.; Papadakis, C. M. *Macromol. Rapid Commun.* **2007,** *28,* 579–584. doi:10.1002/marc.200600764
125. Potemkin, I. I. *Macromolecules* **2004,** *37,* 3505–3509. doi:10.1021/ma035094m
126. Turner, M. S.; Rubinstein, M.; Marques, C. M. *Macromolecules* **1994,** *27,* 4986–4992. doi:10.1021/ma00096a021
127. Tsori, Y.; Andelman, D. *Europhys. Lett.* **2001,** *53,* 722–728. doi:10.1209/epl/i2001-00211-3
128. Kriksin, Y. A.; Neratova, I. V.; Khalatur, P. G.; Khokhlov, A. R. *Chem. Phys. Lett.* **2010,** *492,* 103–108. doi:10.1016/j.cplett.2010.04.028
129. Spatz, J. P.; Sheiko, S.; Möller, M. *Adv. Mater.* **1996,** *8,* 513–517. doi:10.1002/adma.19960080614
130. Spatz, J. P.; Möller, M.; Noeske, M.; Behm, R. J.; Pietralla, M. *Macromolecules* **1997,** *30,* 3874–3880. doi:10.1021/ma9607372
131. Spatz, J. P.; Eibeck, P.; Mößmer, S.; Möller, M.; Herzog, T.; Ziemann, P. *Adv. Mater.* **1998,** *10,* 849–852. doi:10.1002/(SICI)1521-4095(199808)10:11<849::AID-ADMA849>3.0.CO;2-5
132. Potemkin, I. I.; Kramarenko, E. Yu.; Khokhlov, A. R.; Winkler, R. G.; Reineker, P.; Eibeck, P.; Spatz, J. P.; Möller, M. *Langmuir* **1999,** *15,* 7290–7298. doi:10.1021/la9900730
133. Spatz, J. P.; Eibeck, P.; Mössmer, S.; Möller, M.; Kramarenko, E. Yu.; Khalatur, P. G.; Potemkin, I. I.; Khokhlov, A. R.; Winkler, R. G.; Reineker, P. *Macromolecules* **2000,** *33,* 150–157. doi:10.1021/ma990751p
134. Kramarenko, E. Yu.; Potemkin, I. I.; Khokhlov, A. R.; Winkler, R. G.; Reineker, P. *Macromolecules* **1999,** *32,* 3495–3501. doi:10.1021/ma981632x
135. Potemkin, I. I.; Möller, M. *Macromolecules* **2005,** *38,* 2999–3006. doi:10.1021/ma047576j
136. Patyukova, E. S.; Potemkin, I. I. *Langmuir* **2007,** *23,* 12356–12365. doi:10.1021/la701989s
137. Popov, K. I.; Potemkin, I. I. *Langmuir* **2007,** *23,* 8252–8256. doi:10.1021/la070035d
138. Grosberg, A. Y.; Khokhlov, A. R. *Statistical Physics of Macromolecules;* AIP Press: New York, 1994.

License and Terms

Beilstein Journal of Nanotechnology

Nanostructured, mesoporous Au/TiO_2 model catalysts – structure, stability and catalytic properties

Matthias Roos[1], Dominique Böcking[2], Kwabena Offeh Gyimah[1], Gabriela Kucerova[1], Joachim Bansmann[1], Johannes Biskupek[3], Ute Kaiser[3], Nicola Hüsing[4] and R. Jürgen Behm[*1]

Full Research Paper

Open Access

Address:
[1]Institute of Surface Chemistry and Catalysis, Ulm University, D-89069 Ulm, Germany, [2]Institute of Inorganic Chemistry, Ulm University, D-89069 Ulm, Germany, [3]Transmission Electron Microscopy Group, Ulm University, D-89069 Ulm, Germany and [4]Materials Chemistry, Paris-Lodron University Salzburg, Austria

Email:
R. Jürgen Behm[*] - juergen.behm@uni-ulm.de

* Corresponding author

Keywords:
Au catalysis; Au/TiO_2; CO oxidation; gold nanoparticles; model catalysts; thin-film catalyst

Beilstein J. Nanotechnol. **2011,** *2,* 593–606.
doi:10.3762/bjnano.2.63

Received: 08 May 2011
Accepted: 31 August 2011
Published: 15 September 2011

This article is part of the Thematic Series "Organic–inorganic nanosystems".

Guest Editor: P. Ziemann

Abstract

Aiming at model systems with close-to-realistic transport properties, we have prepared and studied planar Au/TiO_2 thin-film model catalysts consisting of a thin mesoporous TiO_2 film of 200–400 nm thickness with Au nanoparticles, with a mean particle size of ~2 nm diameter, homogeneously distributed therein. The systems were prepared by spin-coating of a mesoporous TiO_2 film from solutions of ethanolic titanium tetraisopropoxide and Pluronic P123 on planar Si(100) substrates, calcination at 350 °C and subsequent Au loading by a deposition–precipitation procedure, followed by a final calcination step for catalyst activation. The structural and chemical properties of these model systems were characterized by X-ray diffraction (XRD), transmission electron microscopy (TEM), N_2 adsorption, inductively coupled plasma ionization spectroscopy (ICP–OES) and X-ray photoelectron spectroscopy (XPS). The catalytic properties were evaluated through the oxidation of CO as a test reaction, and reactivities were measured directly above the film with a scanning mass spectrometer. We can demonstrate that the thin-film model catalysts closely resemble dispersed Au/TiO_2 supported catalysts in their characteristic structural and catalytic properties, and hence can be considered as suitable for catalytic model studies. The linear increase of the catalytic activity with film thickness indicates that transport limitations inside the Au/TiO_2 film catalyst are negligible, i.e., below the detection limit.

Introduction

There is a long history of studies in surface science of the elementary steps in catalytic reactions with idealized, planar model systems. In this way, a detailed mechanistic picture, on a molecular scale, has been derived from experimental and theoretical studies for a number of catalytic reactions on metal single crystal surfaces under ultrahigh vacuum (UHV) conditions [1]. It was soon realized, however, that because of the tremendous differences in the materials and reaction conditions between the idealized and realistic cases, the conclusions and results obtained from these model studies could not be easily transferred to the context of a realistic catalytic reaction [2-6]. Here it should be noted that many reactions are not accessible for investigations under surface science conditions, since the rates of specific reaction steps, or of the overall reaction, are too low under these conditions, a classical example of this situation being the synthesis of ammonia [7]. Accordingly, the last two decades saw increasing efforts to bridge the gaps between reaction conditions, often known as the "pressure gap", and between materials (the "materials gap") [2-6]. On the one hand, this includes the increasing use of techniques that can also be applied under or close to realistic reaction conditions, in the mbar to 1 bar range, such as high-pressure scanning tunneling microscopy (STM) [8-10], high-pressure X-ray photoelectron spectroscopy (HP-XPS) [11-14], polarization-modulation infrared reflection absorption spectroscopy (PM-IRAS) [15-17] or X-ray absorption spectroscopy (XAS) techniques [18,19], which allow us to gain detailed information on the structure, elemental/molecular chemical composition and electronic/vibrational properties of the catalyst surface and adlayers during reaction. On the other hand, more realistic, but nevertheless structurally well defined model systems were introduced, including in particular planar supported metal catalysts, where metal nanoparticles are supported on thin oxide or other compound films, or on massive oxide substrates [20-22]. These model catalysts were prepared in different ways, e.g., by deposition of the respective active metal phase by evaporation, deposition of preformed metal nanoparticles or chemical impregnation and subsequent activation procedures. While structurally and chemically still reasonably well defined, these systems are also more realistic than pure metal substrates in that they include, e.g., particle size effects or effects resulting from the interface between the support and the active material.

These model systems differ from realistic catalysts, however, in one important aspect with respect to their (internal) transport properties, as given, e.g., by the absence/presence of pore diffusion. Therefore, we recently started to develop a new type of model system, consisting of a nanoscale catalyst layer of a hundred to a few hundred nanometers thickness on a planar support. While both the preparation procedure and the internal surface chemistry and structure closely resemble those of realistic, dispersed catalysts, the transport properties in the nanostructured catalyst are much better controlled. Therefore, these model catalysts should be particularly suited for studies on the influence of the internal nanostructure and transport properties on the reaction characteristics. Furthermore, they may serve also as model systems for the development of catalytically active coatings.

In the following, we present initial results on the preparation, structural and spectroscopic characterization and catalytic properties of ultra-thin Au/TiO_2 catalyst films, which were prepared by spin-coating a thin film of mesoporous TiO_2 of 200–400 nm thickness on a flat Si(100) substrate and subsequent loading with Au nanoparticles. After describing the experimental procedures, we first present transmission electron microscopy images and XRD results characterizing the structure and morphology of these films and the distribution and particle size of the Au nanoparticles. The chemical state of the materials was characterized by XPS, and finally the catalytic activity of these model systems was characterized by a scanning mass spectrometer set-up that was modified for these measurements.

Experimental

Sample preparation and physical characterization

In a typical procedure, 0.32 g Pluronic® P123 (5 µmol) in 6 g ethanol (0.13 mol) were homogenized with a solution of 2.68 g titanium tetraisopropoxide (9.45 mmol) in 1.36 mL hydrochloric acid (conc.), resulting in a clear TiO_2 sol. After an aging period of 60 min at room temperature, the sol was spin-coated on the precleaned Si substrates with a spinning speed of 4000 rpm (for 280 nm thickness) for 30 s. To vary the film thickness of the titania films, spinning speeds of 2000 rpm (for 420 nm thickness) and 6000 rpm (for 190 nm thickness) were used instead for 30 s. The Si(100) wafer was cut into small pieces (9 mm × 9 mm) prior to the coating procedure. To remove possible organic contaminants, the wafer was cleaned with acetone, rinsed with distilled water and immersed into a piranha solution (2 H_2SO_4 : 1 H_2O_2 (30%)) for 5 min, followed by rinsing with water.

Subsequently, the films were aged in air for 8 h at room temperature, followed by drying in an oven (40 °C, 24 h, air). Finally, the structure-directing agent Pluronic® P123 was removed by calcination in air at 350 °C for 3 h, with a ramp rate of 1 K min^{-1}.

For the N_2 sorption and inductively coupled plasma ionization spectroscopy (ICP–OES) measurements, a larger quantity of the

titania material was needed: The remaining coating solution was cast in petri dishes and aged analogously to the thin coatings. After the aging step, the material was scraped off and calcined in air for 3 h at 350 °C with a heating ramp rate of 1 K min^{-1}.

The Au/TiO_2/Si catalysts were prepared following a deposition–precipitation (DP) procedure as described previously [23-25]. Up to 5 TiO_2/Si samples were immersed into 100 mL H_2O and heated to 60 °C. Then an aqueous solution of 0.01 M $HAuCl_4 \cdot 3H_2O$ was added at constant temperature, while the suspension was stirred and the pH of the solution was kept constant at about 5.5 by dropwise addition of 0.01 M K_2CO_3 solution. Subsequently, stirring was continued for additional 30 min, and the solution was then cooled to room temperature. Finally, the Au/TiO_2/Si precatalysts were washed several times with distilled H_2O to remove residual potassium and chloride ions as well as unreacted Au species, and then dried at room temperature in vacuum. Prior to the measurements, the Au/TiO_2 catalyst film was calcined for 1 h at 350 °C in 2 mbar O_2 (O350 treatment).

The Au/TiO_2 film thickness was either obtained from the transmission electron microscopy (TEM) measurements (see below) or by AFM profilometry by means of a Topometrix Explorer SPM (scan range: 100 µm) in contact mode. By mechanically removing part of the Au/TiO_2 film, we generated a free-standing edge of the film on the Si substrate around the sample center, whose height was measured by AFM. Evaluation of single line profiles across the step edge between the bare Si substrate and the region of the intact Au/TiO_2 film yielded statistically relevant data.

The surface area and the pore diameter of the titania (cast TiO_2 material, different batches) was determined by N_2 sorption measurements (Autosorb MP1 and Quadrasorb, Quantachrome). The specific surface area was calculated using the Brunauer–Emmett–Teller (BET) relation in the p/p_0 range of 0.05 to 0.3 [26]. The pore size distribution was evaluated from the desorption branch of the isotherms, by the procedure developed by Barrett, Joyner and Halenda (BJH) [27]. XRD measurements were performed on a PANalytical MPD PRO instrument, with Cu Kα radiation (λ = 0.154 nm).

X-ray photoelectron spectroscopy (XPS) measurements were performed using two different XPS systems: In the one system a hemispherical electron analyzer (SPECS, EA 200) was used together with a dual Al/Mg X-ray source (SPECS, RQ 20/38), using Al Kα radiation (1486 eV). Survey spectra were recorded with a pass energy of 197.76 eV, or for detail spectra with a pass energy of 43.95 eV. In the second, we used a PHI 5800 system (Physical Electronics) with a hemispherical electron analyzer in combination with an X-ray source for monochromatic Al Kα radiation. Here, survey spectra were recorded with a pass energy of 93.9 eV (detail spectra with 29.35 eV). ICP–OES measurements were performed on an Ultima 2 instrument (Horiba Jobin Yvon).

Electron microscopy measurements

The samples were cut into pieces (diamond wire saw) and glued together face-to-face for cross-sectional TEM measurements. These sandwich-like glued sample pieces were mechanical ground, dimpled and polished down to a thickness of <5 µm (Gatan dimple grinder). Low angle (10°) argon ion etching with energies of 5 to 1 keV (Fischione 1010 ion mill) was used to achieve electron transparency with lamella thicknesses of <100 nm. The TEM measurements were carried out on a FEI Titan 80–300 microscope operated at 300 kV in scanning mode (STEM). The microscope was equipped with a high-angle annular dark-field (HAADF) STEM detector (type Fischione). The mass sensitive HAADF contrast (intensity scales with ~Z^2) results in a very strong signal of the Au nanoparticles that could therefore be easily detected and measured by simple thresholding of the STEM images. X-ray spectroscopy to determine the composition was carried out using a Philips CM20 TEM operating at 200 kV equipped with an EDAX energy dispersive X-ray SiLi detector. Scanning electron microscopy was carried out on a Zeiss NVision 040 equipped with in-lens secondary electron detector and back-scatter detector and an EDAX energy dispersive silicon drift X-ray detector. For imaging, a voltage of 1 kV was used, and for EDX spectroscopy an energy of 5 kV was used.

CO oxidation activity measurements

The catalytic measurements were performed in a scanning mass spectrometer (SMS) system with a dedicated reaction chamber for reactions at pressures up to several mbar, and a separate second chamber containing a differentially pumped mass spectrometer (for details see [28,29]). The Au/TiO_2 samples were mounted on a heatable sample stage in the reaction chamber. For the reaction measurements, the reaction chamber was backfilled with the reaction gas mixture (in this case CO and O_2), with the gas flow being controlled by mass flow controllers (O_2: Hastings, HFC-302, 0–50 sccm, CO: MKS 1479A, 0–100 sccm).

The reaction chamber is connected to the analysis chamber by a quartz capillary with an inner diameter of 3 mm. At the lower end of the capillary, which reaches into the reaction chamber, a small cylindrical flow restrictor (channel length 3 mm, inner diameter 50 µm) is glued into the slightly widened orifice. The flow restrictor ends in a flat Ti cap (cylindrical volume with inner diameter of 2.5 mm and height of 0.1 mm) to collect the

gas species above a defined sample area. In this way, a much larger surface area of the underlying sample contributes to the measured signal than in the previous set-up [28], where the end of the capillary transformed into a tip with a constricted channel (inner diameter: 70 µm, outer diameter: 300 µm). The gas species are then guided towards the analysis chamber and, after leaving the quartz tube, directly into the ion source of a quadrupole mass spectrometer (QMS). A triple-axis, high precision, sample stage allows for free (relative) positioning of the sample underneath the Ti cap, at any lateral position on the sample surface (cf. Figure 1). For the measurements, the pressure in the reaction chamber was varied between 0.5 and 5 mbar, resulting in pressures within the analysis chamber of $1{\cdot}10^{-8}$–$3{\cdot}10^{-7}$ mbar. When the capillary head is fully approached towards the sample surface, we still find no measurable drop in the pressure underneath the Ti cap. Hence, the gas flow into the volume enclosed by the cap is high enough under these conditions that the outgoing flow through the capillary does not lead to a measurable pressure drop in the reaction volume under the Ti cap (cf. [29]). The slow flow of reactants into and out of the reaction volume also results in an accumulation of CO_2 product gas within the reaction volume, which in turn leads to an enhancement of the CO_2 signal such that this can be reproducibly detected.

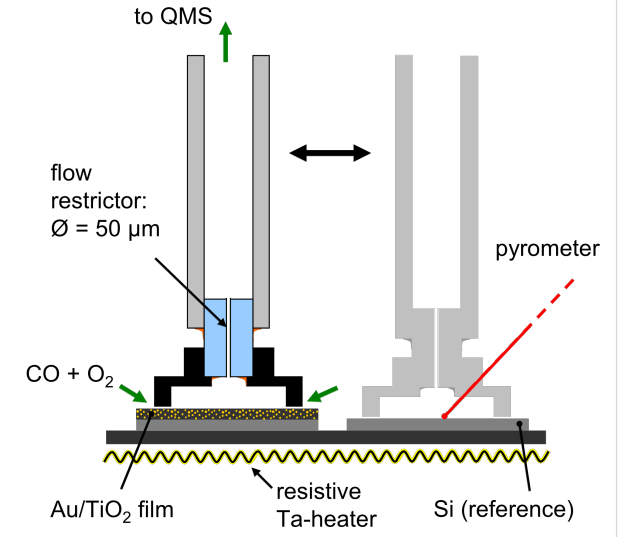

Figure 1: Schematic drawing of the end of the SMS capillary and the sample in the scanning mass spectrometer. Lower part: Sample holder with resistive heater and two separate samples (here: Au/TiO_2 film on Si and a catalytically inactive Si wafer), upper part: Capillary with flow constriction (can be moved from one sample to the next one).

To obtain background-corrected product gas concentrations in the reaction measurements, we performed additional measurements on a piece of Si wafer located next to the actual sample, and which served as reference sample. Since the Si surface is catalytically inactive, the CO_2 concentration above that sample can be considered as a measure of the background signal that is superposed on the CO_2 concentration arising from the catalytically active sample. This assumption is valid as long as the product gas concentration is low enough to not significantly affect the concentration and flow of the reactant gases (CO and O_2). Furthermore, the Si reference sample was used for measuring the temperature at the sample surface with a calibrated pyrometer (LumaSense - Impac IPE 140) during the time period when the capillary was located above the Au/TiO_2 sample (Figure 2). In this way, the temperature measurements are independent of any variations in the specific emissivity of the Au/TiO_2 films.

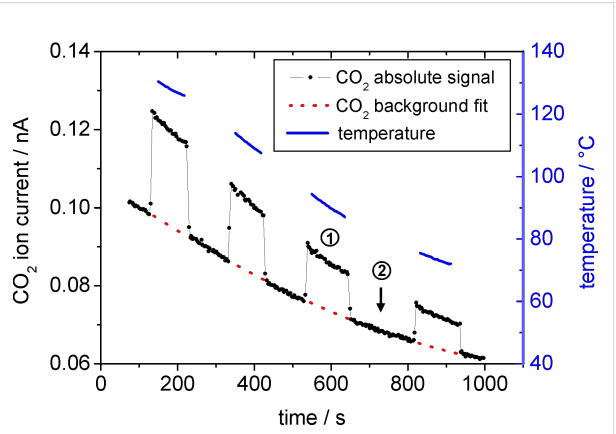

Figure 2: Principle of the SMS measurement on the mesoporous Au/TiO_2 film with CO oxidation as a test reaction. The CO_2 signal was measured for decreasing sample temperature (blue data) atop the catalytically active layer (1) and the bare Si reference (2).

CO conversions were calculated from the CO_2 content in the reaction gas as probed by the mass spectrometer, based on tabulated values for the ionization probability of the respective species CO, O_2 and CO_2 [30]. The gas flow into the mass spectrometer was calculated by assuming a maximum difference between the pressures in the reaction chamber and in the reactor (underneath the Ti cap) of 3%. This is justified by the fact that we did not detect any change in the gas flow to the mass spectrometer when approaching the Ti cap towards the sample surface. The incoming CO and O_2 stream entering the reactor from the outside (from the reaction chamber) was calculated by assuming that all molecules hitting the space between Ti cap and sample surface will enter the reaction volume, and the height of the Ti cap was adjusted relative to the sample surface such that the pressure difference of 3% (see above) was reached. This yields a minimum value for the incoming gas stream, but higher values are possible as well. Accordingly, the conversions given in the next section are maximum values; lower values are also possible.

Results and Discussion

Characterization of TiO_2 coatings and Au/TiO_2 catalysts

The thin-film Au/TiO_2 catalysts were prepared by an evaporation-induced self-assembly (EISA) approach, by spin-coating a Si(100) wafer with a TiO_2 sol containing a structure-directing agent [31], followed by precipitation–deposition of Au on these films. A stable and coatable sol was only obtained at very low pH (conc. HCl), due to the high reactivity of the titanium alkoxide precursor at higher pH values. The crystallinity and morphology of the coating depends critically on the posttreatment temperature. As synthesized, the coatings possess an amorphous network structure comprising mesopores. The mesoscopic ordering of the pore system after the heat treatment was confirmed by small angle X-ray scattering, displaying a broad maximum at $2\Theta = 1.35$, indicating repeating unit distances of 6.54 nm (data not shown). Upon calcination, the material crystallized and anatase nanocrystallites formed at temperatures above 350 °C; crystallization was completed with increasing temperature (600 °C). Further heat treatment resulted in the formation of the thermodynamically stable polymorph rutile, with complete transformation from anatase to rutile at about 1000 °C (cf. Figure 3). Concomitantly with crystallization, the organized mesopore system collapsed during the heat treatment as expected when structure-directing agents, such as Pluronic P123, are applied [32]. Nevertheless, a porous material was obtained, built up from anatase crystallites of 9 nm diameter (calculated from the Scherrer equation) with specific surface areas (after calcination at 350 °C) of 175 $m^2 \cdot g^{-1}$ and a monomodal, narrow, pore-size distribution with an average pore size of 3.1 nm (see Supporting Information File 1 for experimental data).

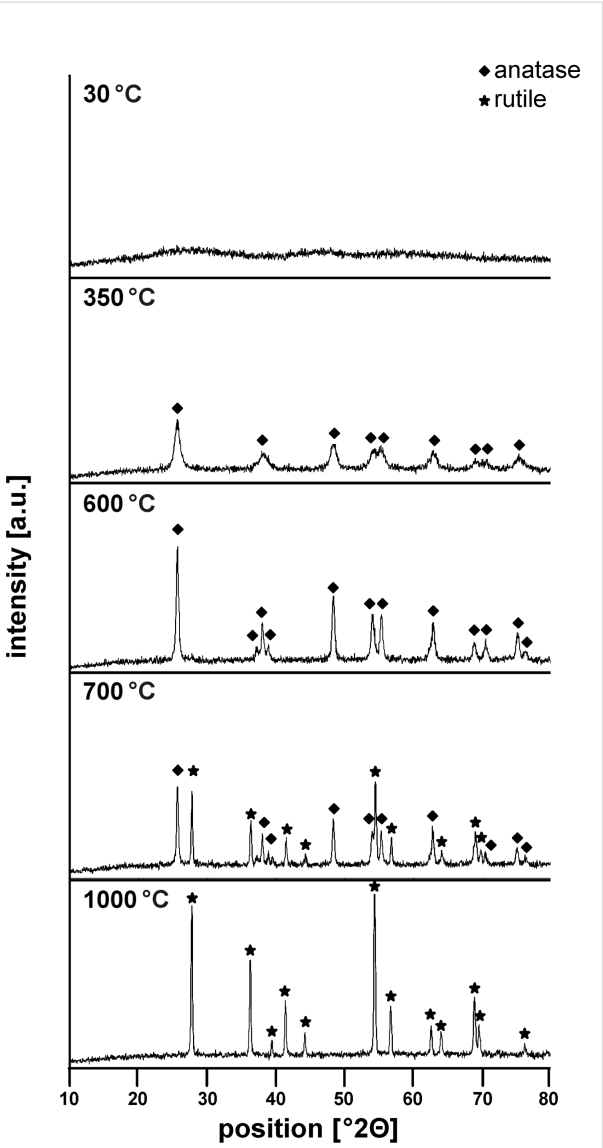

Figure 3: X-ray diffraction patterns obtained for TiO_2 coatings treated at different temperatures as indicated in the figure.

The DP method employed for Au loading of the oxide films was not expected to cause major changes in the structure of the oxide film because of the gentle conditions, which was also confirmed in previous studies of Au/TiO_2 catalysts based on highly dispersed mesoporous TiO_2 supports [33].

From the ICP–OES analysis of the Au/TiO_2 catalyst material (cast in the Petri dishes) we derived a Au content of 2.7 wt %. This is in the range of Au contents typical for realistic supported Au catalysts [25,34]. XPS measurements of the same cast material yielded a Au loading of 4.3 wt %, which is in reasonable agreement with the ICP–OES data. Contamination levels (e.g., Cl) were below the detection limit of XPS (XPS data on Au/TiO_2 films see in the following section).

Further information on the structural characteristics of the thin-film model catalysts was obtained from TEM analysis of the Au/TiO_2 layers. Using the procedures described in the experimental section, cross-sectional TEM measurements were performed directly on the nanoscaled Au/TiO_2 film, allowing for a detailed characterization of the structure of the TiO_2 layers and of the distribution of the Au nanoparticles (NPs) in the TiO_2 film and their size distribution. According to these measurements (see Figure 4), the mesoporous TiO_2 films on the Si(100) substrate form a compact, homogeneous layer of polycrystalline mesoporous TiO_2 with a uniform film thickness (~280 nm at 4000 rpm) and typical TiO_2 crystallites of 10–20 nm. The observation of very small Au NPs agrees well with earlier findings for DP prepared Au/TiO_2 catalysts, which generally yielded Au NPs with small sizes and a relatively uniform particle-size distribution [35].

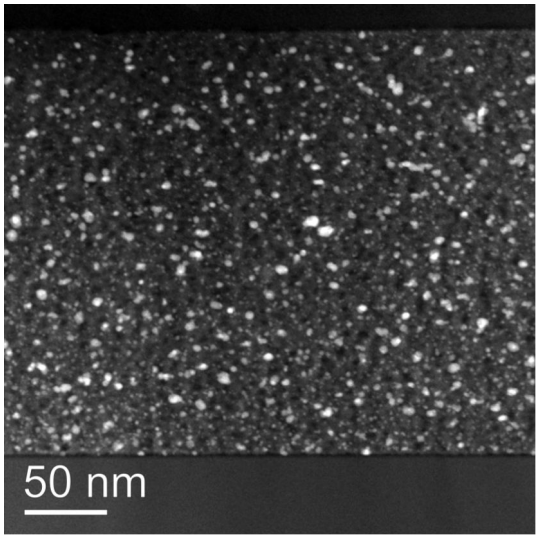

Figure 4: Cross-sectional scanning TEM image of a mesoporous Au/TiO_2 film spin-coated onto a Si(100) wafer and subsequently loaded with Au.

Based on the TEM analysis, the Au particles are homogenously distributed in the TiO_2 film, with a broad particle-size distribution ranging from 0.25 to 6–8 nm. On the O350 calcined catalyst film, before CO oxidation, the maximum of the particle-size distribution is located close to ~2.0 (mean particle size 2.0 ± 1.6 nm, Figure 5, left). As expected from the much higher temperature during the calcination pretreatment, we observed no substantial changes in the gold particle-size distribution after the CO oxidation reaction (see Figure 5 right, mean particle size 2.2 ± 1.3 nm). This result closely resembles previous findings on highly dispersed Au/TiO_2 catalysts, which also showed no significant growth of the Au NPs during reaction with similar pretreatment and reaction conditions/procedures [36-38].

Note that the size distribution of the Au nanoparticles differs significantly in the thin anatase films (280 nm thickness) compared to on the dispersed TiO_2 supports with approximately spherical TiO_2 particles of about 10–20 nm in diameter [33,39]. Despite the fact that we used the same preparation procedure for the Au deposition and formation of Au NPs on the TiO_2 film as on the dispersed TiO_2 support, the Au particles are measurably smaller than those obtained on a highly disperse mesoporous TiO_2 support (anatase, 175 $m^2 \cdot g^{-1}$, maximum of the particle-size distribution at about 3.0 nm) [33,39]. Furthermore, the particle-size distribution is broader for the mesoporous TiO_2 films. These differences may be related to

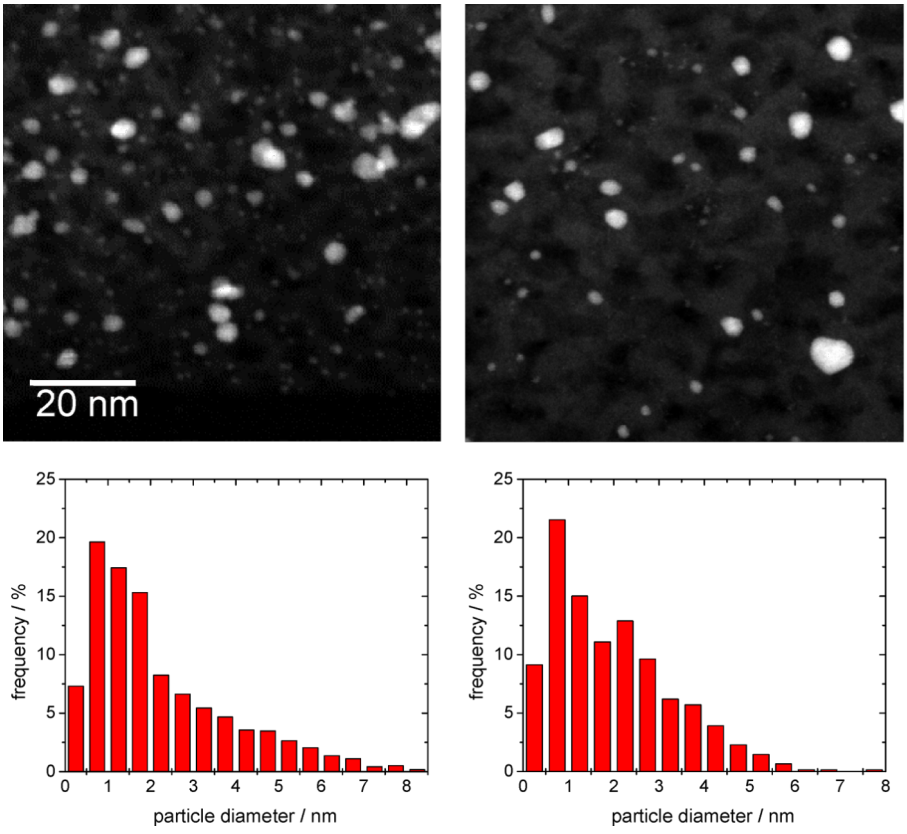

Figure 5: Upper part: High-magnification TEM images of the Au/TiO_2 thin-film catalyst after oxidative pretreatment (left) and after subsequent CO oxidation reaction (300 min on stream, right); lower part: Corresponding Au particle-size distribution.

differences in the Au particle growth process from a Au^{3+} solution, and specifically to the different diffusion pathways of Au^{3+} ions towards the TiO_2 surface in the two cases, the TiO_2 film and the TiO_2 powder. For deposition on the TiO_2 film samples, which were placed at the bottom of a beaker during stirring, the average diffusion path of the Au^{3+} complex to the TiO_2 surface was larger compared to deposition on the TiO_2 particles that were free to move in the whole volume of the solution. Consequently, the probability that an Au^{3+} ion meets the surface of a Au nanoparticle will be higher for deposition on dispersed TiO_2 than on the TiO_2 film. The broader Au particle-size distribution in the Au/TiO_2 film catalyst may be due to different reasons. First, earlier TEM analysis of powder Au catalysts was performed on a Philips CM 20 instrument (200 kV, thermionic electron emission) operated in conventional bright-field TEM mode with much lower sensitivity and spatial resolution than obtained on the present instrument (FEI Titan). On the former instrument, the smallest Au particles that could be detected within the background of the porous matrix were around 1.2 nm in diameter. In the current analysis, particles with sizes down to 0.3 nm could be detected since the scanning mode of a field emission STEM using a HAADF detector delivers a very good signal-to-background ratio, especially for particles consisting of heavy elements within a matrix of low-atomic-number elements (contrast scales with approximately Z^2). This may at least partly explain the higher probability of very small Au NPs in the present Au/TiO_2 film catalysts as compared to previous data on dispersed Au/TiO_2 catalysts. Second, although we have no direct evidence, we cannot rule out effects from residual Cl in the thin film catalysts. The presence of chloride anions is known to enhance the mobility and aggregation of Au NPs [40,41], and we cannot rule out that the residual Cl contents in the Au/TiO_2 film catalyst after the DP process are slightly higher than in a powder Au/TiO_2 catalyst. Even at levels far below the detection limit of XPS (~0.01 ML), Cl could have measurable effects.

XPS results

The composition of the Au/TiO_2 catalyst layer surface, in particular the oxidation state of the Au NPs and the amount of Au present in the film, was characterized by XPS, both before and after the oxidative pretreatment. Survey spectra showed the presence of Au, Ti, oxygen, and carbon species; significant carbon contributions are attributed to contaminations picked up during the sample transfer through air after drying or after calcination. Representative detail spectra of the Au(4f) region are displayed in Figure 6 (upper and lower panel). The Au(4f) spectrum of the dried catalyst, prior to calcination, includes two Au related contributions, a metallic Au^0 species with a $Au(4f_{7/2})$ signal at 84.5 eV as the main component (intensity ~66% of the total Au(4f) intensity), and a second pair of peaks related to ionic Au species [42-44]. The latter peaks appear at 1.9 eV higher binding energy compared to the metallic Au species, indicative of a Au^{3+} species [42,44]. The binding energy of the metallic $Au(4f_{7/2})$ peak was calibrated with respect to the $Ti(2p_{3/2})$ peak of the mesoporous TiO_2 (E_B = 459.0 eV) [33,44]. The total Au(4f) intensity corresponds to a Au content of 8.6 (as prepared) and 5.2 (after calcination) atom %, equivalent to 41 wt % (as prepared) and 26 wt % (after calcination). The loss in Au(4f) intensity upon O350 treatment results from Au^0 particle formation, which increases the absorption of Au(4f) electrons as compared to a dispersed distribution of Au^{3+} ions and very small Au^0 NPs. After calcination, the Au(4f) signal only shows the spin–orbit splitting of the Au(4f) state of Au^0 species, without any indication of ionic species.

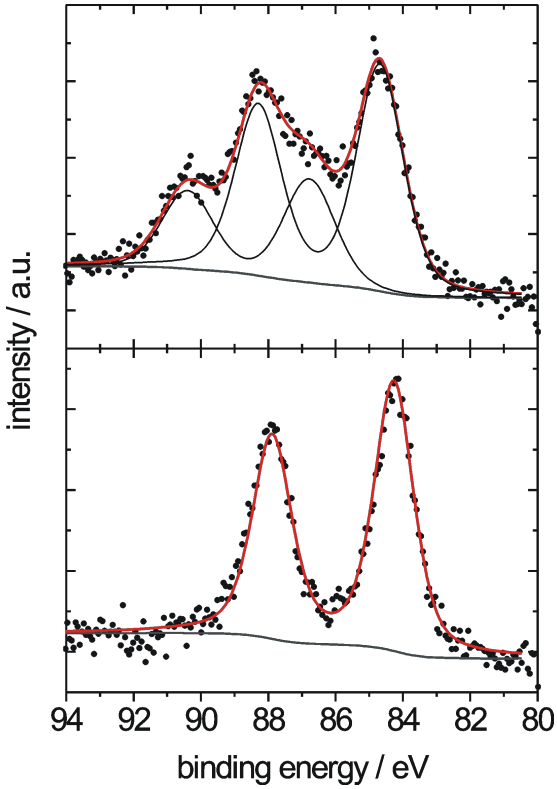

Figure 6: Au(4f) signals of the Au nanoparticles in mesoporous Au/TiO_2 catalyst films before (upper panel) and after (lower panel) oxidative pretreatment.

The significantly higher Au content in the Au/TiO_2 thin-film catalyst as compared to the dispersed Au/TiO_2 catalyst (cf. value of 4.3 wt % in the cast material given before) may arise from the fact that XPS measurements are sensitive only to the uppermost layers (a few nanometers) of the sample surface. An inhomogeneous distribution of the Au NPs in the film, with a pronounced enrichment at or close to the film surface, would result in much higher measured Au(4f) signals than obtained for

a homogeneous Au NP distribution, at identical total Au contents. The TEM results, however, clearly indicate a homogeneous distribution of the Au NPs in the film, and a similar result was also obtained from high resolution SEM measurements, which resolved a lateral distribution of Au NPs and surface sensitive conditions (at 1 keV beam energy), which is compatible with that observed in the TEM images. Finally, Au contents of 15 wt % and higher were obtained also in EDX spot measurements on Au/TiO_2 thin-film catalysts. These probe the entire film thickness, and even into the Si substrate, as evident from the presence of a visible Si peak. Hence, despite a similar Au loading process and process parameters, the DP process leads to significantly higher Au contents on the TiO_2 film samples than on highly disperse TiO_2 powder. Most easily, this can be explained by the much smaller mass and surface area of the TiO_2 films (~0.1 mg per batch with 4–5 film samples) as compared to that of the dispersed TiO_2 support (~10 mg per batch) during Au deposition in identical solution volumes.

In total, most of the structural properties of the mesoporous TiO_2 thin films on Si(100) substrates (crystallinity, pore size) are similar to those found in the mesoporous TiO_2 powder. Subsequent Au loading leads to a homogeneous distribution of the Au nanoparticles with a slightly smaller mean size, but a broader size distribution than obtained for disperse TiO_2 supports, for both mesoporous or nonporous (P25) supports. The Au content in the thin films, however, is significantly higher than in the disperse material, and must be reduced in future work. On the other hand, when comparing with typical planar Au/TiO_2 model systems, consisting, e.g., of Au nanoparticles deposited on single-crystalline TiO_2(110) supports by evaporation under UHV conditions, the size distributions are of comparable width. In contrast, depositing preformed Au nanoparticles, prepared by micellar techniques, yields model catalysts with much narrower size distributions and approximately spherical Au NPs of comparable size [36]. Hence, based on their structural characteristics, mesoporous Au/TiO_2 thin film catalysts can be regarded as structurally well-defined planar model systems, which are closer to realistic catalysts than conventional planar model catalysts, but are nevertheless structurally well defined and thus are a suitable candidate to bridge the materials gap.

Catalytic properties of the mesoporous Au/TiO_2 films

CO_2 formation as function of time

The catalytic activity of the Au/TiO_2 films for CO oxidation was investigated in different ways. First, we tested the initial activity and the tendency for deactivation as a function of time in stream.

Figure 7 shows the catalytic activity of the mesoporous Au/TiO_2 films as a function of time (CO:O_2 = 1:1, total pressure: 2 mbar) in two different temperature regimes, at 140 °C

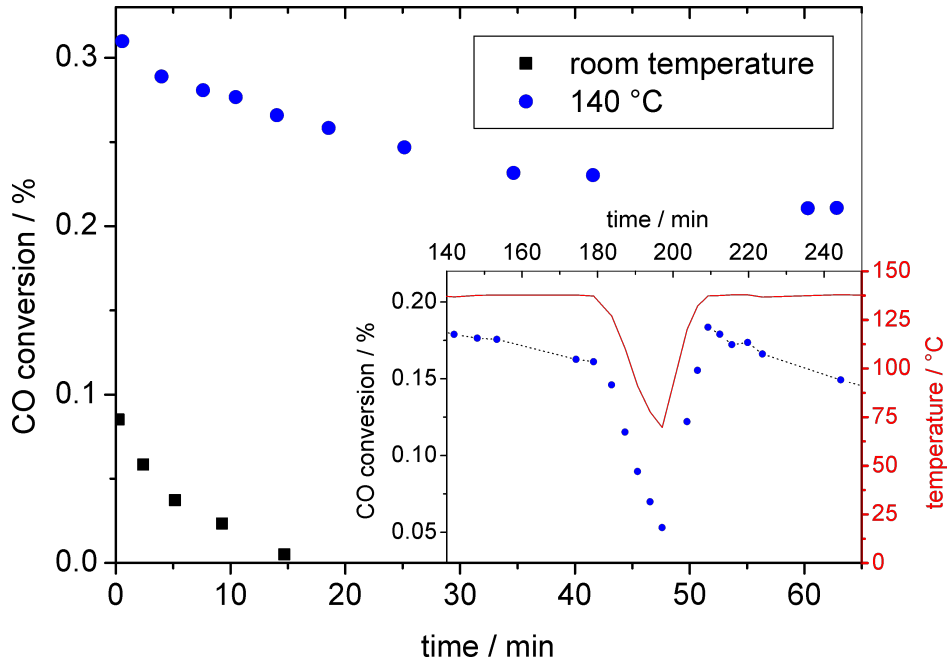

Figure 7: CO conversion during CO oxidation over a mesoporous Au/TiO_2 film as a function of time and sample temperature, at room temperature and at 140 °C. The inset shows the further development of the CO conversion at 140 °C (blue dots) up to 3 h (180 min) under identical conditions and the effect of subsequently modifying the temperature (red curve). Dotted lines serve as guides for eye.

(blue dots) and at room temperature (black squares). The data reveal a rapid deactivation of the film catalyst at room temperature (50% of initial activity value is lost within a few minutes), whereas at 140 °C the decrease in activity is much slower (50% after 3 h, see inset before temperature modulation).

Possible reasons for the deactivation of TiO_2 supported Au catalysts are the agglomeration/sintering of Au particles ("irreversible deactivation") and the accumulation of stable adsorbed species, such as surface carbonates or water, on the catalyst surface [23,24,38,45,46]. The latter deactivation process is reversible, if the adsorbed species can be removed without affecting the catalyst itself, e.g., by thermal desorption. Since, based on the TEM measurements, there was no significant change in the mean particle size during the reaction, Au NP sintering can be ruled out as the main reason for the rapid deactivation. Moreover, since particle agglomeration/sintering is a thermally activated process, this process should be faster at higher temperatures, which is in contrast to our observation. The much faster deactivation of the catalyst at room temperature instead points to an enhanced accumulation of stable adsorbed species, which may cause blocking of active sites [23,24,38,45,46]. At higher temperatures, the enhanced desorption/decomposition of these surface species results in slower accumulation rates and hence slower deactivation, in agreement with our findings [38]. The nature of the site-blocking adsorbate, however, is not clear from these experiments. It is likely that, similar to previous findings based on combined in situ IR and reaction measurements on dispersed Au/TiO_2 catalysts [23], surface carbonates are mainly responsible for the deactivation [24,38,45,46]. However, additional effects from other species, e.g., residues of the synthesis process that are still present in the support material after the calcination procedures prior to the reaction measurement, cannot be ruled out. Evidence for an important role of surface carbonates in the deactivation process comes from a measurement in which the CO_2 evolution was followed while lowering the reaction temperature from 140 °C to 70 °C and then returning to 140 °C again, where it was held for 1 h (inset of Figure 7). In that measurement, we found that the CO_2 production after the initial decay increased to even higher values after the reheating to 140 °C than were measured before the temperature variation, that is from 50% to 60% of the initial signal intensity. Afterwards, the CO_2 signal slowly returned to values as they would have been expected without the intermittent temperature variation. Most simply, the higher CO_2 formation rate after the heat-up procedure can be understood by additional CO_2 formation due to the decomposition of carbonate species that were accumulated on the surface at the previously lower temperature [46]. Once the excess surface carbonates are removed, the CO_2 formation rate returns to its 'normal' value. While this argument appears plausible, definite proof for this hypothesis must wait for in situ IR measurements on the Au/TiO_2 thin-film catalyst, which are planned for the future.

The fact that the deactivation at 140 °C is still faster than observed on a dispersed Au/TiO_2 catalyst supported on nonporous P25 (Degussa) at the same temperature [38] may be explained by the smaller TiO_2 surface area available per Au NP in the thin film catalysts, which results from a combination of a much higher Au loading (~25 wt % versus 3.3 wt % in [38]), a smaller Au NP size (2.0 nm versus 3.2 nm in [38]), and a higher surface area (175 $m^2 \cdot g^{-1}$ versus 56 $m^2 \cdot g^{-1}$ in [38]). In total, the surface area per Au NP decreases to below one third of the value in the Au/P25 catalysts, and therefore surface blocking by stable adsorbed reaction by-products could be correspondingly faster. Similar effects were proposed recently by van den Berg et al. for a Au/TiO_2-MCM-48 catalyst [47]. On the other hand, the fact that there was little difference in deactivation between dispersed mesoporous and nonporous TiO_2 supported Au/TiO_2 catalysts, despite the much higher surface area of the mesoporous catalysts [38,48], contradicts this proposal. Furthermore, the very rapid deactivation at room temperature, which is considerably faster than observed for dispersed Au/TiO_2 catalysts at similar reaction temperatures (not shown), indicates that in that case contributions from other site-blocking adsorbates that are not present on P25 based Au/TiO_2 catalysts, play a role as well. In summary, the physical origin for the rapid deactivation is not yet clear, but most likely it is related to more than a single effect. Finally it should be noted that absolute rates cannot be derived from these measurements at present, and further work focusing on that aspect is in progress.

CO oxidation activity as a function of film thickness

A second important aspect in the catalytic properties of these film catalysts is related to transport effects, specifically to the accessibility of deeper lying regions within the mesoporous Au/TiO_2 films by the reaction gases. This was investigated by measuring the activity of three samples with different film thicknesses (190 nm, 280 nm and 420 nm), which were fabricated with different rotation speeds (2000 rpm, 4000 rpm and 6000 rpm) during the spin-coating process. For direct comparison, the different TiO_2 film samples were loaded with Au simultaneously, using the same aqueous solution of $HAuCl_4 \cdot 3H_2O$. The catalytic activity of the Au/TiO_2 film samples towards CO oxidation was measured at 140 °C in a 1:1 mixture of CO and O_2 (total pressure 2 mbar). To reduce the effect of deactivation before or during the measurements, the samples were heated to 140 °C before adding the reactant gases, and the catalytic activity was evaluated within the first minutes after adjusting the CO and O_2 gas flows. The resulting CO conversions, corrected for contributions from the background intensity (see Experimental section), were plotted versus the

respective film thickness (Figure 8). Considering also that the background corrected CO_2 signal (CO conversion) on the bare Si wafer (film thickness: 0 nm) must be zero by definition, we obtain a linear fit to the data with a slope corresponding to an increase of the CO conversion of 0.037% per 100 nm Au/TiO_2 film layer.

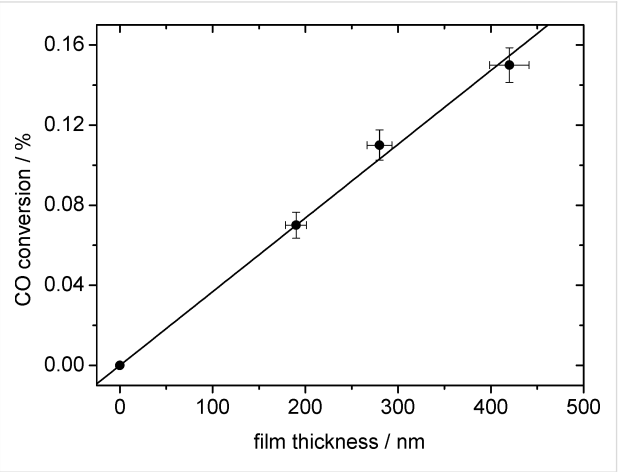

Figure 8: CO conversion measured above mesoporous Au/TiO_2 films of different thicknesses.

The linear increase of the CO_2 evolution/CO conversion with increasing film thickness is clear proof that under the given reaction conditions transport effects within the mesoporous Au/TiO_2 film are negligible. This together with a low conversion leads to identical reaction conditions at all locations on and in the film sample. This result implies that in further catalytic reaction measurements on these film catalysts, the product gas evolution detected atop a certain position on the film surface is representative for the entire underlying layer volume, and can be normalized accordingly. Lateral transport of product molecules within the film can be neglected considering that the diameter of the sampled surface area (2.5 mm) is large in comparison to the film thickness of 200–400 nm.

CO oxidation: Apparent activation energy and reaction orders

A third aspect deals with inherent reaction properties such as the apparent activation energy (temperature dependence of the reaction rate) and the reaction orders (partial pressure dependence of the reaction rate). Here it is of interest whether the model systems exhibit characteristics that are comparable to those of realistic dispersed catalysts, in this case to those of dispersed Au/TiO_2 catalysts.

The apparent activation energy E_A was determined on a 280 nm thick Au/TiO_2 film by varying the temperature during the measurement between 70 and 130 °C while recording the CO_2 production ($CO:O_2$ = 1:1, total pressure 2 mbar). In order to reduce the impact of contributions from catalyst deactivation (see above), we started with the high temperatures. The resulting logarithmic CO conversions are plotted versus the inverse temperature in Figure 9. The gaps in between the four groups of data points result from measurements on the reference sample (cf. Figure 2). The apparent activation energy of $E_A = 23.9 \pm 0.2$ kJ·mol^{-1}, obtained from the Arrhenius plot, is comparable in size to results obtained under similar reaction conditions on other model systems (Diemant et al. [49]: 27 kJ·mol^{-1}, Valden et al. [50]: 15–23 kJ·mol^{-1}) or on dispersed catalysts (Bollinger et al. [51]: 29 kJ·mol^{-1}, Liu et al. [52]: 24 kJ·mol^{-1}, Haruta et al. [35]: 34 kJ·mol^{-1}, and Schumacher et al. [53]: 27 kJ·mol^{-1}). Considering the still-existing differences in reaction conditions (reaction gas pressure and composition, catalyst pretreatment), the numbers indicate a good agreement in the reaction characteristics of the Au/TiO_2 film catalysts and the realistic Au/TiO_2 catalysts.

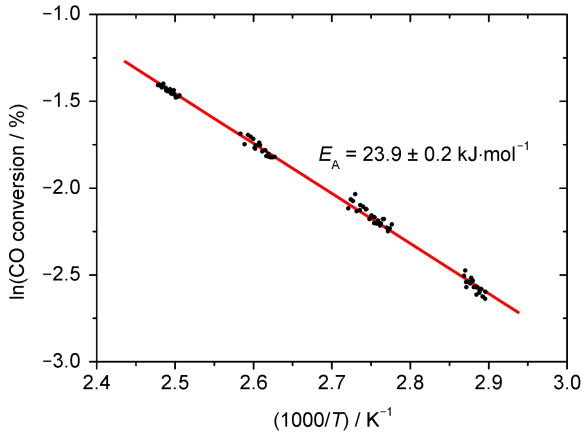

Figure 9: Arrhenius plot of the CO conversion, which is proportional to the CO oxidation rate, to determine the apparent activation energy E_A for Au nanoparticles in a mesoporous TiO_2 film.

Further information on the reaction characteristics comes from the reaction orders, i.e., the pressure dependence of the reaction rate r_{CO2} in a power law rate description:

$$r_{CO2} = k \cdot p_{O2}^{\alpha_{O2}} \cdot p_{CO}^{\alpha_{CO}} \quad (1)$$

with the total reaction order n being the sum of the partial reaction orders α_{CO} and α_{O2}. In order to determine the total reaction order n, we performed a series of measurements in which we varied the total pressure in the reaction chamber between 0.5 and 5 mbar, while keeping the composition of the gas mixture constant at $CO:O_2$ = 1:1. Similar measurements were performed for three different temperatures, 100 °C, 115 °C and 135 °C.

For reaction at 135 °C, the partial reaction orders α_{O2} and α_{CO} were additionally determined by varying either the CO (p_{CO}) or the O_2 partial pressure (p_{O2}), while keeping the other component constant (1 mbar). The resulting data were evaluated according to Equation 1, by plotting the logarithmic CO conversion versus the logarithmic total pressure (total reaction order n, Figure 10a) or versus the logarithmic CO or O_2 partial pressure (partial reaction orders α_{O2} and α_{CO}, Figure 10b).

The calculated total reaction orders n vary between 0.9 for 100 °C and 1.7–1.8 for 115 °C and 135 °C. The reaction order at T = 100 °C obtained in these experiments ($n = 0.9 \pm 0.1$) is in good agreement with results from our group on model systems (Diemant et al.: n = 0.88 [49]). Comparison with corresponding reaction data for dispersed, realistic, Au/TiO_2 catalysts is limited by large differences in the reaction conditions, in particular in the composition of the reaction gas, but including also the total pressure, and the reaction temperature. Accordingly, typical total reaction orders measured on Au/TiO_2 powder catalysts were found to vary between n = 0.3 and 2.1 (e.g., Haruta et al. [35]: n = 0.3; Bollinger et al. [51], Liu et al. [52], Cant et al. [54]: n = 0.65; Lin et al. [55]: n = 0.9; Bondzie et al. [56]: n = 2.1), an overview is given in [34]. In addition to the reaction gas composition, also the preparation method and the pretreatment of the catalyst may affect these values. Concentrating on reaction conditions comparable to the present measurements, Schumacher et al. reported a total reaction order of n = 1.11 for reaction at 80 °C [53]. Considering the trend in our experimental data, which reveals a pronounced decrease of the reaction order with decreasing temperature, we expect a value of below n = 0.8 for the total reaction order at 80 °C, which fits well with the above numbers.

Comparison of the partial reaction orders in these measurements and those reported in previous studies equally suffers from the variation in reaction conditions. Nevertheless, we can summarize a few of the characteristics which seem to be valid over a large range of reaction conditions. For instance, in most studies (except for that by Liu et al. [52]), the reaction order of CO was larger than that for O_2, and it was always positive. The latter finding, which is in contrast to observations on platinum metal catalysts in the low-rate branch, indicates that the reaction is not limited by CO_{ad}-induced blocking of active sites, but by a lack of CO_{ad}. The partial reaction orders determined in these experiments at 135 °C (cf. Figure 10a) follow these trends, the CO reaction order (α_{CO} = 1.0) is higher than the corresponding O_2 value (α_{O2} = 0.8). This is also compatible with the previous observation that at 1 mbar and 140 °C the steady-state CO_{ad} coverage is very low already in the absence of O_2, due to rapid CO_{ad} desorption, and is even less in the presence of O_2 [38]. For CO oxidation on dispersed Au/TiO_2 catalysts, CO and O_2 reaction orders of n = 0.34 (at 1 mbar O_2, CO variable) and n = 0.32 [24] or 0.38 [57], respectively (at 1 mbar CO, O_2 variable), were reported for reaction at 80 °C and comparable gas-phase compositions. The much lower reaction orders in the above two studies can be explained by the lower reaction temperatures in those cases. Considering the steep increase of the total reaction order with temperature, by almost 100% upon increasing from 90 °C to 135 °C, we would expect a similar effect also for the partial reaction orders. The resulting values of around n = 0.4 for the partial reaction orders would agree perfectly with the findings in the earlier studies.

In summary, we demonstrated that the local catalytic properties of these nanoscaled mesoporous Au/TiO_2 films largely

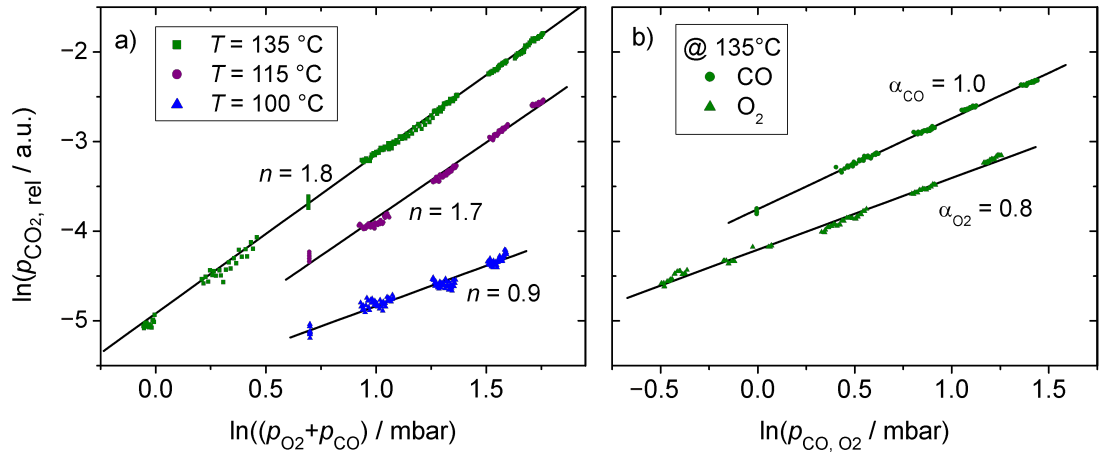

Figure 10: a) Determination of the total reaction order n in the CO oxidation reaction at temperatures of 100 °C, 115 °C and 135 °C by varying the total pressure from 0.5 to 5 mbar at constant reaction gas composition ($CO:O_2$ = 1:1). b) Partial reaction orders of O_2 and CO at a reaction temperature of 135 °C and constant partial pressure of the other reactant (1 mbar).

resemble those of commonly investigated Au/TiO_2 catalysts supported by highly disperse, nonporous or mesoporous TiO_2. This is a precondition for their use as a model catalyst. Future research will concentrate on i) clarifying the physical origin of the faster deactivation at room temperature, and in particular on ii) exploring the role of transport effects in these films on the reaction characteristics, both by locally resolved measurements on microstructured samples by means of higher resolution scanning mass spectrometry and by time-resolved measurements, e.g., in a temporal analysis of products reactor.

Conclusion

Aiming at model catalyst systems with close-to-realistic internal transport properties**,** we have prepared nanoscaled mesoporous Au/TiO_2 films of 200–400 nm thickness, with Au nanoparticles embedded in a mesoporous TiO_2 film, and investigated their structural, chemical and catalytic properties. The systems were prepared by spin-coating of a mesoporous TiO_2 film from solutions of ethanolic titanium tetraisopropoxide and Pluronic P123 on planar Si(100) substrates, calcination at 350 °C and subsequent Au loading by a deposition-precipitation procedure, followed by a final calcination step for catalyst activation. N_2 adsorption and XRD measurements revealed a surface area of 175 $m^2 \cdot g^{-1}$ and a repeat unit of ~6.5 of the mesostructured anatase TiO_2 films after calcination. After Au loading, XPS and EDX measurements determined Au contents of between 15 and 30 wt %, which is much higher than obtained by the same DP procedure on otherwise similar highly disperse TiO_2 material (cast material, 3–4 wt %). After calcination, only metallic Au^0 was detected in the film, which was present as Au NPs, in agreement with previous findings for dispersed Au/TiO_2 catalysts. Cross-sectional TEM measurements revealed a homogeneous distribution of very small Au nanoparticles in the TiO_2 film, with a maximum in the size distribution at 2.0 nm; these findings were supported also by highly surface sensitive SEM images (no enrichment of Au NPs at the film surface). Reaction measurements of the CO oxidation reaction, performed with a scanning mass spectrometer directly above the film, yielded reaction characteristics that are very close to those of highly dispersed Au/TiO_2 catalysts at comparable reaction conditions, with an activation energy of 23.9 $kJ \cdot mol^{-1}$ and temperature-dependent positive reaction orders (at 135 °C $\alpha_{CO} \approx 1.0$ and $\alpha_{O2} \approx 0.8$). Furthermore, the observation of a linear increase of the activity with increasing film thickness indicates that mass transport limitations inside the film are essentially absent (below the detection limit), and the reaction conditions (partial pressures) inside the film are independent of the location.

The good agreement between the results presented here and those for dispersed Au/TiO_2 powder catalysts illustrates that this model system is well suited to further bridge the materials gap between model studies and real catalysts. The absence of transport limitations in the Au/TiO_2 films, as evidenced by the linear increase of activity with thickness, together with the ability of locally resolved mass spectrometric measurements will allow us to investigate possible transport effects. Accordingly, future work will include studies of microstructured Au/TiO_2 film patterns for investigating transport effects, and more detailed studies of structural effects imposed, e.g., by changes in the film morphology or in the Au particle size, and finally such work will focus on establishing in situ spectroscopy techniques.

Supporting Information

Supporting Information features details on the nitrogen sorption measurement of porous titania.

Supporting Information File 1

Details of sorption measurements.
[http://www.beilstein-journals.org/bjnano/content/supplementary/2190-4286-2-63-S1.pdf]

Acknowledgements

This work was supported by the Deutsche Forschungsgemeinschaft, through the Collaborative Research Center (SFB) 569. We thank M. Lang, S. Blessing, T. Diemant, and M. Eyrich for the ICP–OES, XRD and XPS measurements and S. Grözinger for TEM sample preparation (all Ulm University).

References

1. Sinfelt, J. H. *Surf. Sci.* **2002,** *500,* 923. doi:10.1016/S0039-6028(01)01532-1
2. Stoltze, P.; Nørskov, J. K. *Phys. Rev. Lett.* **1985,** *55,* 2502. doi:10.1103/PhysRevLett.55.2502
3. Aßmann, J.; Löffler, E.; Birkner, A.; Muhler, M. *Catal. Today* **2003,** *85,* 235. doi:10.1016/S0920-5861(03)00391-2
4. Over, H.; Muhler, M. *Prog. Surf. Sci.* **2003,** *72,* 3. doi:10.1016/S0079-6816(03)00011-X
5. Imbihl, R.; Behm, R. J.; Schloegl, R. *Phys. Chem. Chem. Phys.* **2007,** *9,* 3459. doi:10.1039/B706675A
6. Vang, R. T.; Lægsgaard, E.; Besenbacher, F. *Phys. Chem. Chem. Phys.* **2007,** *9,* 3460. doi:10.1039/b703328c
7. Ertl, G. *Angew. Chem., Int. Ed.* **2008,** *47,* 3524. doi:10.1002/anie.200800480
8. Rasmussen, P. B.; Hendriksen, B. L. M.; Zeijlemaker, H.; Ficke, H. G.; Frenken, J. W. M. *Rev. Sci. Instrum.* **1998,** *69,* 3879. doi:10.1063/1.1149193
9. Kolmakov, A.; Goodman, D. W. *Rev. Sci. Instrum.* **2003,** *74,* 2444. doi:10.1063/1.1544086
10. Tao, F.; Tang, D.; Salmeron, M.; Somorjai, G. A. *Rev. Sci. Instrum.* **2008,** *79,* 084101. doi:10.1063/1.2960569

11. Pantförder, J.; Pöllmann, S.; Zhu, J. F.; Borgmann, D.; Denecke, R.; Steinrück, H.-P. *Rev. Sci. Instrum.* **2005,** *76,* 014102. doi:10.1063/1.1824351
12. Salmeron, M.; Schlögl, R. *Surf. Sci. Rep.* **2008,** *63,* 169. doi:10.1016/j.surfrep.2008.01.001
13. Ogletree, F. D.; Bluhm, H.; Hebenstreit, E. D.; Salmeron, M. *Nucl. Instrum. Methods Phys. Res., Sect. A* **2009,** *601,* 151–160. doi:10.1016/j.nima.2008.12.155
14. Knop-Gericke, A.; Kleimenov, E.; Hävecker, M.; Blume, R.; Teschner, D.; Zafeiratos, S.; Schlögl, R.; Bukhtiyarov, V. I.; Kaichev, V. V.; Prosvirin, I. P.; Nizovskii, A. I.; Bluhm, H.; Barinov, A.; Dudin, P.; Kiskinova, M. *Adv. Catal.* **2009,** *52,* 213. doi:10.1016/S0360-0564(08)00004-7
15. Beitel, G. A.; Laskov, A.; Oosterbeek, H.; Kuipers, E. W. *J. Phys. Chem.* **1996,** *100,* 12494. doi:10.1021/jp960045f
16. Zhao, Z.; Diemant, T.; Häring, T.; Rauscher, H.; Behm, R. J. *Rev. Sci. Instrum.* **2005,** *76,* 123903. doi:10.1063/1.2140449
17. Dupont, C.; Loffreda, D.; Delbecq, F.; Santos Aires, F. J. C.; Ehret, E.; Jugnet, Y. *J. Phys. Chem. C* **2008,** *112,* 10862. doi:10.1021/jp802416f
18. Weckhuysen, B. M., Ed. *In-situ Spectroscopy of Catalysts;* Utrecht University: Utrecht, The Netherlands, 2004.
19. Singh, J.; Lamberti, C.; van Bokhoven, J. A. *Chem. Soc. Rev.* **2010,** *39,* 4754. doi:10.1039/c0cs00054j
20. Rainer, D. R.; Goodman, D. W. *J. Mol. Catal. A* **1997,** *131,* 259. doi:10.1016/S1381-1169(97)00270-7
21. Kielbassa, S.; Kinne, M.; Behm, R. J. *J. Phys. Chem. B* **2004,** *108,* 19184. doi:10.1021/jp048547d
22. Freund, H.-J.; Pacchioni, G. *Chem. Soc. Rev.* **2008,** *37,* 2224. doi:10.1039/b718768h
23. Schumacher, B.; Plzak, V.; Kinne, M.; Behm, R. J. *Catal. Lett.* **2003,** *89,* 109. doi:10.1023/A:1024731812974
24. Schumacher, B.; Denkwitz, Y.; Plzak, V.; Kinne, M.; Behm, R. J. *J. Catal.* **2004,** *224,* 449. doi:10.1016/j.jcat.2004.02.036
25. Schumacher, B.; Plzak, V.; Cai, J.; Behm, R. J. *Catal. Lett.* **2005,** *101,* 215. doi:10.1007/s10562-004-4895-6
26. Brunauer, S.; Emmett, P. H.; Teller, E. *J. Am. Chem. Soc.* **1938,** *60,* 309. doi:10.1021/ja01269a023
27. Barrett, E. P.; Joyner, L. G.; Halenda, P. P. *J. Am. Chem. Soc.* **1951,** *73,* 373. doi:10.1021/ja01145a126
28. Roos, M.; Kielbassa, S.; Schirling, C.; Häring, T.; Bansmann, J.; Behm, R. J. *Rev. Sci. Instrum.* **2007,** *78,* 084104. doi:10.1063/1.2777167
29. Roos, M.; Bansmann, J.; Zhang, D.; Deutschmann, O.; Behm, R. J. *J. Chem. Phys.* **2010,** *133,* 094504. doi:10.1063/1.3475518
30. *Partial Pressure Measurements in Vacuum Technology;* Inficon AG: Balzers, Liechtenstein, 2001.
31. Frindell, K. L.; Bartl, M. H.; Popitsch, A.; Stucky, G. D. *Angew. Chem., Int. Ed.* **2002,** *41,* 959. doi:10.1002/1521-3773(20020315)41:6<959::AID-ANIE959>3.0.CO;2-M
32. Thomas, A.; Schlaad, H.; Smarsly, B.; Antonietti, M. *Langmuir* **2003,** *19,* 4455. doi:10.1021/la0340807
33. Geserick, J.; Fröschl, T.; Hüsing, N.; Kucerova, G.; Makosch, M.; Diemant, T.; Eckle, S.; Behm, R. J. *Dalton Trans.* **2011,** *40,* 3269. doi:10.1039/c0dt00911c
34. Aguilar-Guerrero, V.; Gates, B. C. *Catal. Lett.* **2009,** *130,* 108. doi:10.1007/s10562-009-9906-1
35. Haruta, M.; Tsubota, S.; Kobayashi, T.; Kageyama, H.; Genet, M. J.; Delmon, B. *J. Catal.* **1993,** *144,* 175. doi:10.1006/jcat.1993.1322
36. Kielbassa, S.; Häbich, A.; Schnaidt, J.; Bansmann, J.; Weigl, F.; Boyen, H.-G.; Ziemann, P.; Behm, R. J. *Langmuir* **2006,** *22,* 7873. doi:10.1021/la0610102
37. Comotti, M.; Li, W.-C.; Spliethoff, B.; Schüth, F. *J. Am. Chem. Soc.* **2006,** *128,* 917. doi:10.1021/ja0561441
38. Denkwitz, Y.; Schumacher, B.; Kučerová, G.; Behm, R. J. *J. Catal.* **2009,** *267,* 78. doi:10.1016/j.jcat.2009.07.018
39. Denkwitz, Y.; Makosch, M.; Geserick, J.; Hörmann, U.; Selve, S.; Kaiser, U.; Hüsing, N.; Behm, R. J. *Appl. Catal., B* **2009,** *91,* 470. doi:10.1016/j.apcatb.2009.06.016
40. Bowker, M.; Nuhu, A.; Soares, J. *Catal. Today* **2007,** *122,* 245. doi:10.1016/j.cattod.2007.01.021
41. Carabineiro, S. A. C.; Silva, A. M. T.; Dražić, G.; Tavares, P. B.; Figueiredo, J. L. *Catal. Today* **2010,** *154,* 293. doi:10.1016/j.cattod.2009.12.017
42. Dickinson, T.; Povey, A. F.; Sherwood, P. M. A. *J. Chem. Soc., Faraday Trans. 1* **1975,** *71,* 298. doi:10.1039/f19757100298
43. Denkwitz, Y.; Zhao, Z.; Hörmann, U.; Kaiser, U.; Plzak, V.; Behm, R. J. *J. Catal.* **2007,** *251,* 363. doi:10.1016/j.jcat.2007.07.029
44. Holm, R.; Storp, S. *Appl. Phys.* **1976,** *9,* 217. doi:10.1007/BF00900608
45. Konova, P.; Naydenov, A.; Venkov, C.; Mehandjiev, D.; Andreeva, D.; Tabakova, T. *J. Mol. Catal. A* **2004,** *213,* 235. doi:10.1016/j.molcata.2003.12.021
46. Clark, J. C.; Dai, S.; Overbury, S. H. *Catal. Today* **2007,** *126,* 135. doi:10.1016/j.cattod.2006.10.008
47. van den Berg, M. W. E.; De Toni, A.; Bandyopadhyay, M.; Gies, H.; Grünert, W. *Appl. Catal., A* **2011,** *391,* 268. doi:10.1016/j.apcata.2010.06.022
48. Denkwitz, Y.; Geserick, J.; Hörmann, U.; Plzak, V.; Kaiser, U.; Hüsing, N.; Behm, R. J. *Catal. Lett.* **2007,** *119,* 199. doi:10.1007/s10562-007-9229-z
49. Diemant, T. Adsorptions- und Reaktionseigenschaften planarer PtRu/Ru(0001)- und Au/TiO2/Ru(0001)-Modellkatalysatoren: Von der Oberflächenchemie zur Katalyse. Ph.D. Thesis, Ulm University, Ulm, Germany, 2008.
50. Valden, M.; Pak, S.; Lai, X.; Goodman, D. W. *Catal. Lett.* **1998,** *56,* 7. doi:10.1023/A:1019028205985
51. Bollinger, M. A.; Vannice, M. A. *Appl. Catal., B* **1996,** *8,* 417. doi:10.1016/0926-3373(96)90129-0
52. Liu, H.; Kozlov, A. I.; Kozlova, A. P.; Shido, T.; Asakura, K.; Iwasawa, Y. *J. Catal.* **1999,** *185,* 252. doi:10.1006/jcat.1999.2517
53. Schumacher, B. Investigation of the CO Oxidation on highly disperse Au/TiO_2 Catalysts in H_2-rich and H_2-free Atmosphere – A kinetic and mechanistic Study. Ph.D. Thesis, Ulm University, Ulm, Germany, 2005.
54. Cant, N. W.; Ossipoff, N. J. *Catal. Today* **1997,** *36,* 125. doi:10.1016/S0920-5861(96)00205-2
55. Lin, S. D.; Bollinger, M.; Vannice, M. A. *Catal. Lett.* **1993,** *17,* 245. doi:10.1007/BF00766147
56. Bondzie, V. A.; Parker, S. C.; Campbell, C. T. *Catal. Lett.* **1999,** *63,* 143. doi:10.1023/A:1019012903936
57. Widmann, D.; Behm, R. J. *Angew. Chem., Int. Ed.* **2011,** in press. doi:10.1002/anie.201102062

Beilstein Journal of Nanotechnology

Deconvolution of the density of states of tip and sample through constant-current tunneling spectroscopy

Holger Pfeifer, Berndt Koslowski* and Paul Ziemann

Full Research Paper

Open Access

Address:
Institut für Festkörperphysik, Universität Ulm, D-89069 Ulm, Germany

Email:
Holger Pfeifer - h.pfeifer@uni-ulm.de; Berndt Koslowski* - berndt.koslowski@uni-ulm.de; Paul Ziemann - paul.ziemann@uni-ulm.de

* Corresponding author

Keywords:
deconvolution; Nb DOS; STM; STS

Beilstein J. Nanotechnol. **2011,** *2,* 607–617.
doi:10.3762/bjnano.2.64

Received: 06 June 2011
Accepted: 06 September 2011
Published: 19 September 2011

This article is part of the Thematic Series "Organic–inorganic nanosystems".

Associate Editor: A. Gölzhäuser

Abstract

We introduce a scheme to obtain the deconvolved density of states (DOS) of the tip and sample, from scanning tunneling spectra determined in the constant-current mode (z–V spectroscopy). The scheme is based on the validity of the Wentzel–Kramers–Brillouin (WKB) approximation and the trapezoidal approximation of the electron potential within the tunneling barrier. In a numerical treatment of z–V spectroscopy, we first analyze how the position and amplitude of characteristic DOS features change depending on parameters such as the energy position, width, barrier height, and the tip–sample separation. Then it is shown that the deconvolution scheme is capable of recovering the original DOS of tip and sample with an accuracy of better than 97% within the one-dimensional WKB approximation. Application of the deconvolution scheme to experimental data obtained on Nb(110) reveals a convergent behavior, providing separately the DOS of both sample and tip. In detail, however, there are systematic quantitative deviations between the DOS results based on z–V data and those based on I–V data. This points to an inconsistency between the assumed and the actual transmission probability function. Indeed, the experimentally determined differential barrier height still clearly deviates from that derived from the deconvolved DOS. Thus, the present progress in developing a reliable deconvolution scheme shifts the focus towards how to access the actual transmission probability function.

Introduction

Undoubtedly, the power of scanning tunneling microscopy (STM) is based on its capability to map the surface topology of a conductive sample with resolution down to the atomic scale in real space [1]. Moreover, previous experience on metal–insulator–metal tunnel junctions [2] immediately suggested extending STM to become a local analytical tool, opening up

the field of scanning tunneling spectroscopy (STS). The most prominent property that can be accessed by STS is the local electronic density of states (LDOS). For that purpose, the applied tunneling bias, V, is ramped while the probe–sample separation is kept constant (commonly denoted as I–V spectroscopy) [1,3]. However, determination of the sample LDOS from such a measurement is always obscured by unavoidable interfering influences from other STS constituents such as the tunneling barrier, with its bias-dependent transmission probability, as well as from the LDOS of the probing tip. The problem becomes most clearly visible when referring to the semiclassical Wentzel–Kramers–Brillouin (WKB) description of tunneling processes. There, the experimentally determined tunneling current, I, is expressed as a convolution integral involving the sample and tip LDOS as well as the barrier behavior on equal footing. Thus, if there is just one I–V characteristic available for a given tunneling barrier, extraction of the sample LDOS is in principle impossible. That used to be the standard situation for previous tunnel junctions with their fixed oxide barriers. In STS, however, at any given sample location, barriers can be experimentally adjusted. In this way, additional information is provided by taking I–V curves at different fixed z values.

Based on this additional degree of freedom when applying STS, much work has been devoted in the past to unraveling the different contributions to the tunneling current. Most of the work was concerned with removing at least a proposed tunneling probability from the measured quantity, assuming validity of the WKB approximation. This, however, still leaves a kind of a convolved LDOS of tip and sample [4-12]. Recently, it was shown that the tunneling current as described by the WKB approximation can be transformed into a Volterra integral equation of the second kind and, therefore, well-known schemes can be applied to solve such an equation numerically [7,8]. Taking this one step further, it was demonstrated that, taking I–V curves at different tip–sample distances, these Volterra equations form a set of coupled integro-differential equations, which allow for a deconvolution of the transmission probability as well as of the LDOS of tip and sample [13].

I–V spectroscopy is not the only STS measurement mode to determine the LDOS of a sample. Though less commonly used, z–V spectroscopy, alias constant-current spectroscopy, offers an interesting alternative to the I–V mode. In constant-current mode, the topographic feedback loop is left on and, thus, the tunneling current is held constant while the bias, V, is scanned and the derivative of I with respect to V, $\partial_V I(V)$, as well as the varying tip–sample separation, $z(V)$, is acquired. In a number of cases, z–V may be superior to I–V spectroscopy. Examples are the common case of a limited dynamic range in the current measurement, the need to keep the tunneling current below a certain upper limit in order to avoid local damage of a delicate sample, or the necessity of a measurement over a wide range of biases, such as in case of samples with adsorbed organic molecules in order to resolve the lowest unoccupied molecular orbital (LUMO) [14-16]. Ziegler et al. showed that an approximation, originally derived for I–V spectroscopy in reference [7], can be used to obtain a joint LDOS of tip and sample from such a measurement [17]. However, so far such a deconvolution scheme as that for I–V spectroscopy is not yet available for z–V spectroscopy.

Consequently, it is the aim of the present contribution to provide such a scheme by extending the previous deconvolution derived for I–V spectroscopy and tailoring it for the z–V mode. After a short introduction to the theory, the deconvolution scheme is applied to different LDOS model functions for tip and sample. By numerically calculating the related I–V curves for various barrier and LDOS parameters, insight is gained into how these parameters may influence "experimental" data. The newly developed deconvolution is adopted to analyze experimental STS data obtained on Nb(110). By comparison with earlier results we find that the commonly used transmission probability function (TPF) according to the one-dimensional WKB approximation is deficient, at least in the case of Nb(110). We propose that the differential barrier height is a sensitive indicator of how to adjust the TPF to obtain a more realistic description of the tunneling probability.

Results and Discussion

Theory

The underlying theory for z–V spectroscopy is closely related to that applied to I–V spectroscopy [7] except for an explicit dependence on the tip–sample separation, z. The starting point of the calculation is the tunneling current, I, as given by the one-dimensional WKB approximation for a barrier characterized by an energy-dependent transmission probability function (TPF), $T(E,V,z)$. Assuming zero temperature, application of a bias, V, results in a tunneling current which, according to WKB, can be written as

$$I(V,z) \propto \int_0^V \rho_S(E) \cdot \rho_T(E-V) \cdot T(E,V,z)\,\mathrm{d}E, \qquad (1)$$

where ρ_S and ρ_T are the sample and tip density of states (DOS), respectively, and E is the energy of electrons participating in the tunneling process; z is considered as being an independent variable with $\partial_V z = 0$. If, in a z–V measurement, z is the response of the tip–sample separation on ramping the bias voltage for a preset constant current, I_0, we denote z as $z(V)\big|_{I_0}$ or for

simplicity $z(V)$. According to Simmons [18,19] the TPF, $T(E,V,z)$, can be approximated by assuming a trapezoidal shape of the barrier, leading to

$$T\left(E,V,z\right)=\exp\left[-\sqrt{\alpha\cdot\left(\varphi+\frac{V}{\beta}-\gamma E\right)}\cdot z\right], \qquad (2)$$

where φ is the height of the tunneling barrier at zero bias and $\alpha=8m/\hbar^2$. We introduced here the dimensionless parameters β and γ. For the trapezoidal approximation in 1-D, β = 2 and γ = 1. The parameter β may be increased slightly, e.g., to account for the image potential, while γ may be used to consider the energy dependence of the TPF on the dispersion relation of the electrons [7,20]; for a surface state with no energy component perpendicular to the surface and perfect parabolic dispersion, γ = 0. Note, that γ × E may be replaced by any continuous energy-dependent function with no impact on the proposed formalism. This way, a wide range of energy-dependent decay lengths of the electron states into the vacuum may be implemented in the deconvolution scheme.

Taking the derivative of Equation 1 with respect to bias delivers

$$\partial_V I(V,z)\propto\rho_S(V)\rho_T(0)\cdot T\left(E=V,z\right)$$
$$-\int_0^V\rho_S(E)T(E,V,z)\cdot\left(\begin{array}{l}\partial_E\rho_T(E-V)\\+\rho_T(E-V)\cdot\dfrac{\sqrt{\alpha}\cdot z}{2\beta\cdot\sqrt{\varphi+\dfrac{V}{\beta}-\gamma E}}\end{array}\right)\mathrm{d}E, \qquad (3)$$

where we used $-\partial_V\rho(E-V)=\partial_E\rho(E-V)$. Comparing Equation 3 with Equation 5 in [17] we set $\partial_V z=0$ since z is an independent variable. If we set $z=z(V)\big|_{I_0}$, $\partial_V I(V,z(V))$ would necessarily be zero. Equation 3 can now be solved formally for $\rho_S(V)$, giving

$$\rho_S(V)\propto\frac{1}{\rho_T(0)\cdot T\left(E=V,z\right)}\cdot$$
$$\left[\partial_V I(V,z)+\int_0^V\rho_S(E)T(E,V,z)\cdot\left(\begin{array}{l}\partial_E\rho_T(E-V)+\\\sqrt{\alpha}\,\rho_T(E-V)\dfrac{z}{2\beta\cdot\sqrt{\varphi+\dfrac{V}{\beta}-\gamma E}}\end{array}\right)\mathrm{d}E\right]. \qquad (4)$$

This is a Volterra integral equation of the second kind. For a known $\rho_T(V)$ it can be solved numerically by means of the Neumann approximation scheme, by replacing $\rho_S(V)$ on the left side by $\rho_S(V)_{n+1}$ and on the right side by $\rho_S(V)_n$. Assuming a constant tip DOS, φ > V, and applying the mean value theorem of integrals, we arrive at an equation that has been introduced already in [7] for I–V spectroscopy and extended to z–V spectroscopy in [17]:

$$\rho_S\left(V\right)\propto\frac{1}{T\left(E=V,z\right)}\left[\partial_V I(V,z)+\frac{\sqrt{\alpha}\cdot z}{2\beta\cdot\sqrt{\varphi}}\cdot I_0\right]. \qquad (5)$$

As the tunneling junction is symmetric, we may change the reference frame from the sample to the tip. We then obtain similarly a Volterra integral equation for the tip DOS:

$$\rho_T\left(V_T\right)\propto\frac{1}{\rho_S\left(V_T=0\right)\cdot T\left(E=V_T,z\right)}\cdot$$
$$\left[\partial_{V_T}I(-V_T,z)+\int_0^V\rho_T(E)T(E,V_T,z)\left(\begin{array}{l}\partial_E\rho_S(E-V_T)+\\\sqrt{\alpha}\rho_S(E-V_T)\dfrac{z}{2\beta\cdot\sqrt{\varphi+\dfrac{V_T}{\beta}-\gamma E}}\end{array}\right)\mathrm{d}E\right]. \qquad (6)$$

where $V_T=-V$ is the bias with respect to the Fermi level of the tip. Note that this equation is identical to Equation 4 in the respective reference frame, but $\partial_V I$ has to be mirrored at $V=0$ because $\partial_V I$ has been measured in the reference frame of the sample.

With Equation 4 and Equation 6 we have a set of two coupled integro-differential equations for the sought properties $\rho_S(V)$ and $\rho_T(V)$ based on the measurable data $\partial_V I$ and $z(V)$. The additionally required parameter φ can be determined from, e.g., I–z spectroscopy and the absolute tip–sample separation, $z(V)\big|_{I_0}=z_0+\Delta z(V)\big|_{I_0}$, can be reasonably guessed or estimated through recently proposed methods [12].

This set of Volterra integral equations is applied in order to deconvolve the DOS of both sample and tip, by referring to a previously described scheme [13]. There, the basic idea was to take advantage of the additional information provided by different $\partial_V I$–V curves, taken at different tip–sample separations. Presently, the additional information is provided by different $\partial_V I$–V and $z(V)$ curves taken at different set currents, I_0. Note that it is the TPF that makes the difference. As it is not symmetric in E, V, or z, it allows deconvolution of the tip and sample DOS .

In the following section we will demonstrate this deconvolution scheme for z–V spectroscopy. Starting with model functions for $\rho_S(V)$ and $\rho_T(V)$, the "experimental" data $I(V,z)$ for a given V and z are calculated according to Equation 1. Additionally, $z(V)\big|_{I_0}$ for a given set current, I_0, is determined by calculating $I(V,z)$ and varying z until $|I(V,z)-I_0|/I_0<0.001$. Next,

$\partial_V I$ is calculated from Equation 3 with the afore-determined $z(V)\big|_{I_0}$ for a given I_0. In this way, two sets of $\partial_V I$ and $z(V)$ curves for set currents $I_{0,1}$ and $I_{0,2}$ are obtained and mimic experimental data, which form the starting point of the deconvolution procedure. Assuming that on entry to the deconvolution scheme no specific information is available for $\rho_S(V)$ and $\rho_T(V)$, both entries are initialized as unity for the iteration.

It should be noted that, due to the coupled equations, one may commence the iteration with data for either the larger or the smaller set current. There is no criterion available to determine a better choice. In the following examples we achieved better results, i.e., faster convergence and better accuracy, when starting with data for the smaller set current. Note also, as previously reported [7,13], that numerical errors may accumulate during the iterations leading to a divergence of the DOS at the boundaries. For a sufficient optimization we found that it is necessary to repeat the iteration at least four times but not more than six times, which, according to the numerical examples presented below, will lead to acceptably accurate results.

Equation 6 and Equation 4 exhibit an apparent singularity with $z \to -\infty$ for $V \to 0$. However, this singularity is not substantial in theory and is of no practical relevance, since experimental data can be safely measured only above a minimal bias, V_{min}. Below V_{min} the tip or sample could be damaged. Assuming that the measurement is started at that sufficiently small bias, V_{min}, such that ρ_S, $\rho_T \approx$ constant for $|E| < |V_{min}|$ and $V_{min} << \varphi$, we replace in Equation 4 the integral

$$\int_0^V \ldots \mathrm{d}E = \int_0^{V_{min}} \ldots \mathrm{d}E + \int_{V_{min}}^{V-V_{min}} \ldots \mathrm{d}E + \int_{V-V_{min}}^{V} \ldots \mathrm{d}E.$$

The first term on the right then gives

$$\int_0^{V_{min}} \ldots \mathrm{d}E \approx \rho_S(0) \int_0^{V_{min}} T\left(E,V,z(V)\right) \left[\frac{\partial_E \rho_T(-V) + \dfrac{\rho_T(-V)\cdot\sqrt{\alpha}\cdot z(V)}{2\beta\sqrt{\varphi + V/\beta - \gamma E}}} \right] \mathrm{d}E$$

$$\approx \rho_S(0)\cdot T\left(E=0,V,z(V)\right)\cdot V_{min} \left[\frac{\partial_E \rho_T(-V) + \dfrac{\rho_T(-V)\cdot\sqrt{\alpha}\cdot z(V)}{2\beta\sqrt{\varphi + V/\beta}}} \right],$$

and similarly the last term gives

$$\int_{V-V_{min}}^{V} \ldots \mathrm{d}E \approx \rho_S(V)\cdot T\left(E=V,z(V)\right)\cdot V_{min} \left[\frac{\partial_E \rho_T(0) + \dfrac{\rho_T(0)\cdot\sqrt{\alpha}\cdot z(V)}{2\beta\sqrt{\varphi - V/\beta}}} \right].$$

These approximations simplify the numerical integration of experimental data. However, to account for the missing data in the range $0 \le V \le V_{min}$, extrapolation of the experimental data towards zero bias is carried out. For this purpose, in the case of $\partial_V I$ being linear and for $z(V)$ being logarithmic the extrapolations delivered satisfying results.

Numerical Examples

Analysis of peak positions

Before we start applying the deconvolution procedure, we analyze how different characteristic features of the sample and tip DOS appear in the "experimental" $\partial_V I$–V curves or the derived quantity $\partial_V I \times V$ within the one-dimenional WKB approximation. For that purpose, we start with a Gaussian peak of a given width and height, at various peak positions within the range −1.8 eV to +1.8 eV, in an otherwise constant DOS of the sample while the tip DOS is kept constant. In Figure 1a the corresponding conductivity, $\partial_V I$, is presented showing the following characteristics: (i) There is a hyperbolic background in the conductivity, since the TPF can be approximately described by $T \sim V^{-1}$ at low bias for a constant DOS and constant tunneling current (the already discussed singularity at zero bias is excluded). (ii) For DOS peaks in the negative energy range (occupied states) only weak shoulders are visible, while DOS peaks in the positive energy range (empty states) result in pronounced peaks with increasing amplitude for increasing peak bias positions. This is an immediate consequence of the growing TPF for increasing energies, E. In the present case, the resulting conductivity peaks in the negative bias range are so weak that a reasonable analysis of their position is not possible. (iii) The pronounced peaks in $\partial_V I$ at positive bias shift in energy with respect to the original position in the DOS. The shift is always negative and amounts to −0.15 eV in Figure 1a. Furthermore, this peak shift depends on the position, $E_{max,0}$ of the Gaussian in the model DOS as well as on its width, w, the set current, I_0, and the barrier height, φ. The corresponding numerically determined peak positions, as depending on these parameters, are presented in Figure 1c–f. Due to the hyperbolic background, the peak shift in $\partial_V I$ is larger the closer the original DOS peak is to zero bias. The dependence on its width, w, and the set current, I_0, is as expected: The broader the original DOS peak and the smaller the set current, the larger the shift of the corresponding peak in $\partial_V I$. Thus, it is worth noting that for lifetime-broadened states in transition metals or molecular states on top of a metal surface, which may approach ~1 eV, the expected peak shifts in $\partial_V I$ will be of similar order. The peak shift in dependence on the barrier height (Figure 1d) is larger the lower the barrier. However, for a reasonable barrier height ranging from 2 eV to 4.5 eV the shift is relatively small.

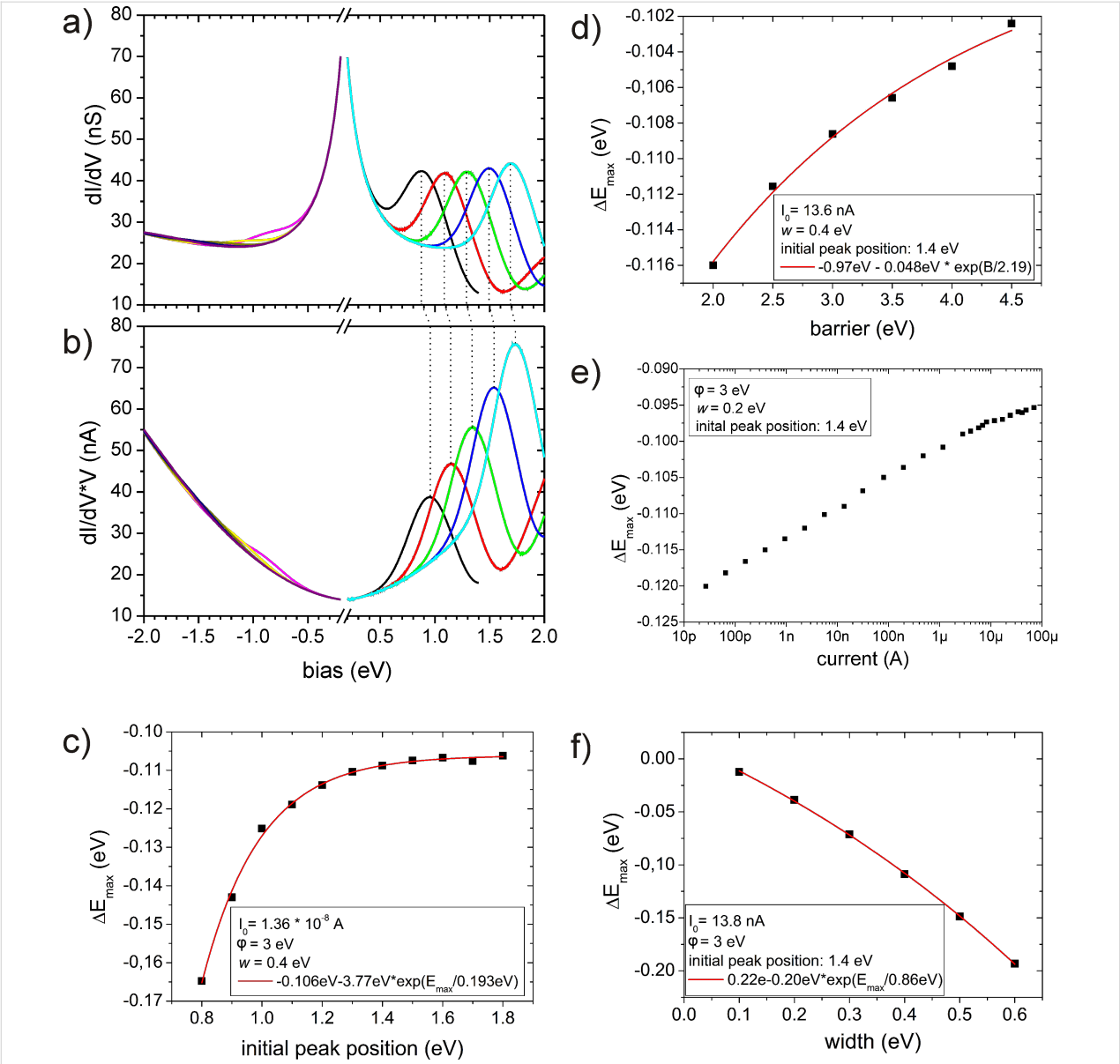

Figure 1: Calculated $\partial_V I$–V curves (a) and ($\partial_V I \times V$)–V curves (b) for different peak positions in the sample DOS ranging from −1.8 eV to +1.8 eV. The model DOS of tip and sample are constant with an additional Gaussian peak in the sample DOS at the given position. Parameters are: Barrier height φ = 3 eV, I_0 = 13.7 nA. The initial peak positions were ±[1.0 (black, magenta), 1.2 (red, yellow), 1.4 (green, dark yellow), 1.6 (blue, navy), 1.8 (cyan, purple)] eV. Panels (c) through (f) show the dependence of the peak positions in $\partial_V I$ on the barrier height, φ, the set current, I_0, the initial peak position, $E_{max,0}$, and the width of the peak, w, respectively. The values of the set currents result from the particular choice of the tip–sample separation at zero bias.

The hyperbolic background around zero bias can be removed by plotting $\partial_V I \times V$ versus V (Figure 1b), which corresponds to setting $I_0 = 0$ and $T \sim V^{-1}$ in Equation 5. Accordingly, the peaks at positive bias shift back towards the original positions as given by the sample DOS. Peaks in the negative bias range, however, remain hardly detectable while those in the positive range are largely enhanced at increasing bias positions, even though the peak heights are all equal in the original DOS. Thus, the results presented in Figure 1 may serve as a warning that experimentally observed peak-like features in $\partial_V I$ cannot immediately be assigned to corresponding DOS characteristics. For that purpose, a complete deconvolution procedure must be applied as presented in the following.

Recovery and deconvolution of the DOS

In the first example we focus on the positive bias range (in the reference frame of the sample). Again, a model DOS of the sample is defined by setting it to unity with an additional Gaussian peak centered at 0.6 eV (height h = 1, width w = 0.2 eV). Similarly, the model DOS of the tip is taken as

unity with a Gaussian peak at −1.2 eV (h = 1, w = 0.2 eV). For two set currents $I_{0,1}$ = 80.7 nA and $I_{0,2}$ = 0.386 nA, and an effective barrier height of φ = 3 eV the resulting z–V curves and the corresponding $\partial_V I$–V curves were calculated. The results are displayed in Figure 2a and represent "experimental" data as before. The curves show the expected behavior: Decreasing the set current from $I_{0,1}$ to $I_{0,2}$ leads to a shift of $z(V)$ to larger values. The $\partial_V I$–V curves (inset in Figure 2a) roughly scale with the ratio of the set currents. In detail, however, there are small deviations from a constant shift of $z(V)$ or from a linear scaling of $\partial_V I$ with the set currents. It is exactly these deviations that allow for the deconvolution of the DOS. Both z–V curves exhibit a logarithmic behavior with two shoulders, one at about 0.7 eV and a very small one at 1.6 eV. The conductivity $\partial_V I$ shows a shoulder at around 0.5 eV and a broad peak at around 1.5 eV, both on top of a hyperbolic background ($\sim V^{-1}$) as discussed above.

When applying the deconvolution scheme to these data it turned out that the best results were achieved by starting the iteration from Equation 4 with data related to the smaller set current, $I_{0,2}$. After six iterations the Gaussian peaks in the sample and tip DOS clearly emerged (Figure 2b) with an accuracy of better than ±0.03 when compared to the given model DOS.

As a second example, the deconvolution scheme was applied to the negative bias range (in the reference frame of the sample). Again, the model DOS used as input consists of a Gaussian peak on top of a constant background at unity. The peak in the sample DOS is centered at −1.2 eV (h = 1, w = 0.2 eV) and in the tip DOS at +1.2 eV (h = 1, w = 0.2 eV). It should be noted, that both peaks should lead to a superposed feature appearing at a bias of −1.2 eV in the "experimental" $\partial_V I$ curves. With the two set currents, $I_{0,1}$ = −80.7 nA and $I_{0,2}$ = −0.386 nA, we obtained the two z–V curves displayed in Figure 2c. Both z–V

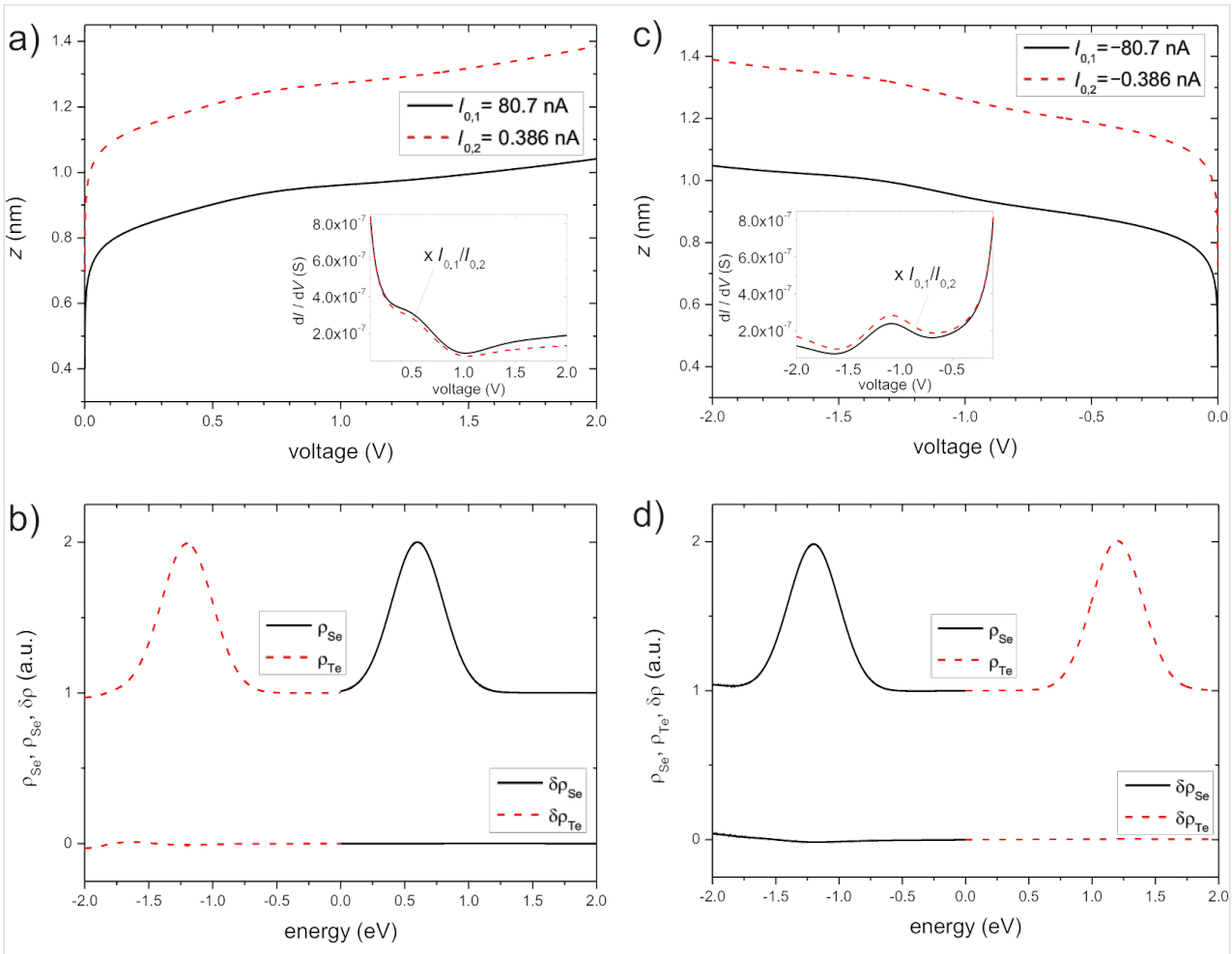

Figure 2: Numerically calculated $z(V)$–V curves in the a) positive and c) negative bias range with respect to the sample. The two set currents are a) $I_{0,1}$ = 80.7 nA and $I_{0,2}$ = 0.386 nA and c) $I_{0,1}$ = −80.7 nA and $I_{0,2}$ = −0.386 nA. The inset displays the corresponding $\partial_V I$–V curves. For better comparison, the $\partial_V I$–V curve for $I_{0,2}$ has been scaled by $I_{0,1}/I_{0,2}$. b) and d) are the corresponding recovered and deconvolved DOS for the positive and negative bias range, respectively, together with the errors (δ) relative to the model DOS (upper curves, ρ_{Se}: black solid, ρ_{Te}: red dashed; lower curves, $\delta\rho_{Se}$: black solid, $\delta\rho_{Te}$: red dashed). The values of the set currents result from the particular choice of the tip–sample separation at zero bias.

curves show a logarithmic behavior with a shoulder at about −1.2 eV. The related $\partial_V I$–V curves are displayed in the inset of Figure 2c. Both have a peak at −1.1 eV. The shift of about 0.1 eV relative to the model value has already been discussed in section "Analysis of peak positions". When applying our deconvolution scheme at negative bias the best results were achieved when starting from Equation 6 with data for the lower set current. After six iterations the deconvolved DOS of tip and sample emerged as shown in Figure 2d. In comparison to the model DOS the accuracy is better than 0.0042 over the complete bias range under study.

Both examples clearly demonstrate successful recovery and deconvolution of the density of states of tip and sample within the framework of the one-dimensional WKB approximation with data obtained from z–V spectroscopy. As in the case of I–V spectroscopy, we found (besides numerical/technical issues) only one restriction to the successful implementation of the formalism: The DOS of tip and sample must be continuously differentiable, and slopes that are too steep will reduce the accuracy of the result. It turned out, as might have been expected, that the larger the difference between the two set currents the better the recovery and the deconvolution of the DOS of the tip and sample.

Application to experimental data

In the following we apply the above-described scheme to experimental data obtained on Nb(110) [21]. The measurements were performed on a home-built low-temperature STM operated at a base pressure of ~10^{-10} mbar and a base temperature of 5.2 K [22]. The $\partial_V I$–V curves were recorded at different set currents by employing a lock-in technique with a modulation frequency of ~500 Hz, which is well above the bandwidth of the topographic feedback loop. As tunneling tip, we used an electrochemically etched tungsten wire, which was subsequently heated in UHV to ~2000 °C and conditioned by field emission and desorption.

In analogy to [13] we measured a set of five $\partial_V I$–V curves together with the corresponding z–V curves for both positive and negative bias. For each sign of the bias, two of these $\partial_V I$–V curves are displayed in Figure 3. The $\partial_V I$–V curves for the smaller set current, $I_{0,2}$, have been scaled by the ratio of the set currents, $I_{0,2}/I_{0,1}$, in order to make the small separation-dependent differences apparent. The insets depict the corresponding z–V curves, which were recorded simultaneously. We applied the deconvolution scheme pairwise to the data sets, on each occasion cycling three times through the iteration in order to avoid divergence of the DOS at the interval boundaries. The resulting tip DOS's were averaged and the result, ρ_{Te} (cf. Figure 4b), was used to calculate the sample DOS. The averaged result for the sample is presented in Figure 4a as "experimental sample DOS", ρ_{Se}. The tunneling barrier height was determined from a separate I–z measurement at low bias at the same spot as the $\partial_V I$–V curves, and a value of $\varphi = 4.1$ eV was extracted. The coefficients β and γ in the TPF (Equation 2) were set to $\beta = 2$ and $\gamma = 1$ for negative energy and $\gamma = 1.11$ for positive energy. This choice of γ for positive energy results from an adjustment of the tunneling probability to the measured differential barrier height, as proposed in [20] (see below).

Inspecting first ρ_{Se}, one finds two broad maxima centered at around ±1.2 eV with a plateau in between from −0.5 eV to +0.4 eV. There are several minor peaks and shoulders in the negative energy range at [−1.8, −1.6, −1.25, −1.0, −0.8, −0.6, −0.3, −0.15] eV, and at [0.5, 0.8, 1.1, 1.4, 1.8] eV in the positive energy range. Most probably due to the limited accuracy of data and/or the calculation, the specific development of those features depends on the course of the iteration and the details of the data processing. The tip DOS, ρ_{Te} (Figure 4b), is smooth in

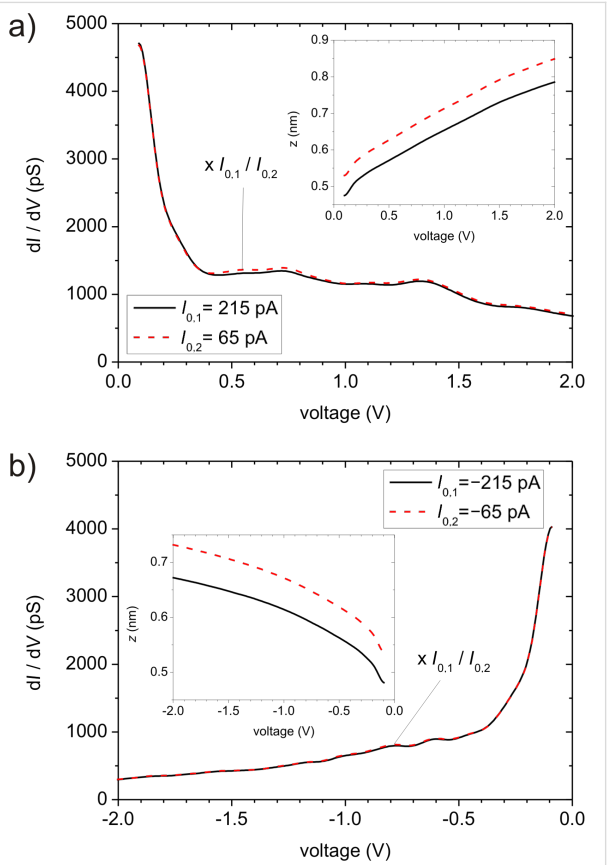

Figure 3: $\partial_V I$-V curves measured on Nb(110) a) in the positive bias range at two different set currents ($I_{0,1}$ = 215 pA and $I_{0,2}$ = 65 pA), and b) in the negative voltage range at $I_{0,1}$ = −215 pA and $I_{0,2}$ = −65 pA. The insets depict the corresponding $z(V)$–V curves, which were measured simultaneously. (φ = 4.1 eV). The given values of the set currents are the averages of the tunneling current during the measurement at an accuracy of ±5%.

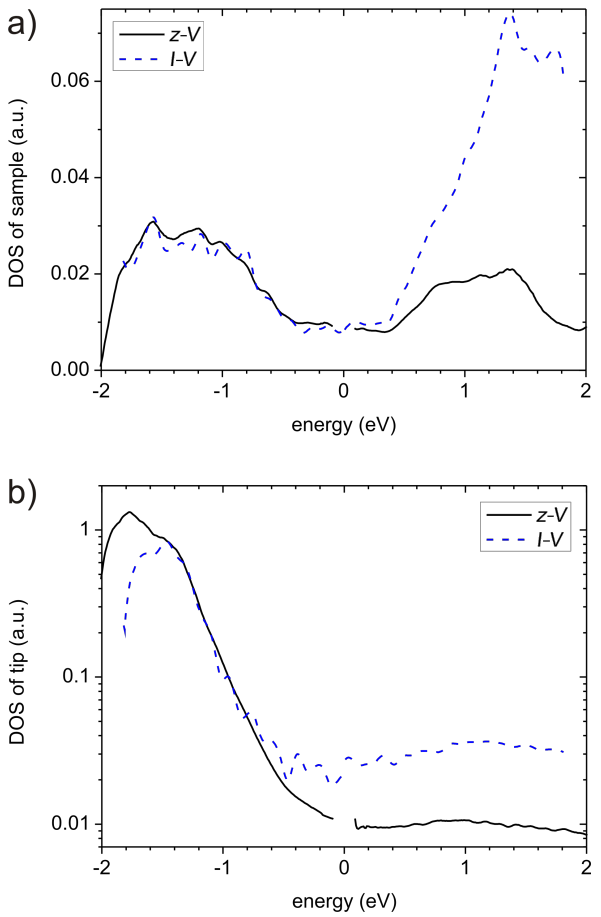

Figure 4: Recovered and deconvolved DOS's of the sample derived from *z*–*V* measurements (black solid) and *I*–*V* measurements (dashed). Parameters used in the calculations are: z_0 = 0.4 nm for *z*–*V* and z_0 = 0.6 nm for *I*–*V* spectroscopy, β = 2, γ = 1.11 for positive and γ = 1.0 for negative energy.

the positive energy range, with a weak and broad maximum at about 1 eV. In the negative energy range, however, there is an exponential increase with a pronounced maximum at −1.8 eV.

For comparison we performed additionally constant-separation spectroscopy at the same location and applied the related deconvolution scheme [13] to those data using the same parameters β and γ. The result is included in Figure 4 (dashed blue lines). It agrees very well with the DOS obtained from *z*–*V* spectroscopy except for a much stronger increase (a factor of ~7 instead of a factor of 2) in the sample DOS at positive energy. We interpret this as an indication that the assumed TPF needs to be modified. The stronger increase in the sample DOS is related to the less pronounced peak of the tip DOS at negative energy. It is important to note that the energetic position of the characteristic DOS features is almost identical in *I*–*V* and *z*–*V* spectroscopy. The features, however, are palpably more pronounced in *I*–*V* spectroscopy. Comparing results obtained here with those published previously [13,21] or with theory [23-26], the energetic positions are similar, but the overall behavior of the DOS is considerably different. Consequently, in the following we focus on the overall behavior of the DOS.

There are several reasons why the experimental DOS obtained here may or even should be different from the theoretical/expected DOS. Firstly, with STM local measurements are performed revealing correspondingly local DOS variations due to the imperfections of a real Nb(110) surface. Secondly, one should be aware that at negative energies, i.e., for occupied states, recovery and deconvolution of the DOS is much more challenging, because these states contribute little to the total tunneling current. This is most clearly demonstrated in Figure 1a and b, where identical peaks in the sample DOS change from being pronounced in STS spectra when centered at positive energies, to being hardly detectable when shifted to negative energies. As a consequence, even small deviations from our assumptions (1-D WKB and trapezoidal approximation; dispersion) or measurement errors have a strong impact on the result, especially in the negative energy range (on the sample and the tip side). A rough estimate of the required accuracy in the measurement is given by considering the fractional contribution of the TPF to the total $\partial_V I$, δ_c that arises from electron states at the Fermi level of the tip compared to that which arises from the states at the Fermi level of the sample. This contribution is approximately given by

$$\delta_c \approx \frac{\rho_S(V)\cdot\rho_T(0)}{\rho_S(0)\cdot\rho_T(-V)}\frac{T(V,V,z)}{T(V,0,z)} = \frac{\rho_S(V)}{\rho_S(0)}\frac{T(V,V,z)}{T(V,0,z)}$$

assuming $\rho_T(E) = 1$ and $V \ll 0$ V. If now $\rho_S(E) = 1 + \delta_S\Theta(E - V)$ with the Heaviside function, Θ, i.e., ρ_S changes at $E = V$ by a step of size $-\delta_S$ to unity, the contribution of states at energy $E = V$ changes at bias, V, by

$$\delta = \delta_c(V-\varepsilon) - \delta_c(V+\varepsilon) = \delta_S\frac{T(V,V,z)}{T(V,0,z)} \approx \delta_S\cdot\exp\left(\frac{Vz}{2}\sqrt{\frac{\alpha}{\varphi}}\right)$$

Solving for V and setting the inequality correctly, leads to

$$V > \frac{2\sqrt{\varphi}}{z\sqrt{\alpha}}\ln\left(\frac{\delta}{\delta_S}\right) \qquad (7)$$

δ corresponds to the required accuracy to detect a relative change of δ_S in the sample DOS at bias V. In our experiments, an accuracy of 1% corresponds to a detectable change of ~9% in the sample DOS at −2 eV. The accuracy of the deconvolved DOS is probably even lower.

A third and probably the most important reason why the experimental sample DOS would be different from expectations is the fact that we used effectively a one-dimensional WKB approximation. To correct for this to first order, we introduced the parameter γ in Equation 2 where, for the sake of simplicity, we assumed γ to be constant, i.e., the parallel energy component $E_p = (1 - \gamma)E$. Such a correction has a tremendous impact on the resulting DOS especially at negative energy. In order to elucidate that problem, we show in Figure 5 a comparison of the experimental sample DOS displayed in Figure 4 (black curve) with results of the calculation obtained by changing γ just by ±0.01. Such a tiny change of γ leads to a variation of the DOS by ±40% at +2 eV, and at −2 eV the DOS even goes negative. Thus, the difficulty shifts from the original problem of developing a deconvolution scheme to the problem of finding the correct TPF.

Elaborating on that point, we employ the differential barrier height (DBH) as introduced previously in [7]. A subsumption of the DBH approach is as follows: All electron states in the energy range $E = 0...V$ contribute to the apparent barrier height, $\varphi_{app} = 1/\alpha \times (\partial_z I/I)^2$, weighted by their individual tunneling probability and the product of the DOS $\rho_S(E) \times \rho_T(E-V)$ [7]. Consequently, the apparent barrier height is relatively insensitive to changes of the DOS. The DBH, $\varphi_{diff} = 1/\alpha \times (\partial_z \partial_V I/\partial_V I)^2$, however, selects predominantly contributions from the limiting energies $E = 0$ and $E = V$ and, thus, is extremely sensitive to changes of the DOS at the Fermi levels. Figure 6 shows the DBH as calculated from measured $\partial_V I$–z curves taken at the given biases (blue dashed curve) and the DBH as calculated from the deconvolved DOS shown in Figure 4 with the given values for β, γ, and $z_0 = 0.6$ nm. Additionally, we calculated and plotted the DBH for constant DOS and the given separation (black dash-dotted curve) according to:

$$\varphi_{\mathrm{diff,cc}}(V,z) = \left(-\frac{\sqrt{\varphi + \frac{V}{\beta}}T^{-1}(E=V,z) + \sqrt{\varphi - \frac{V}{\beta}}T^{-1}(E=0,V,z)}{T^{-1}(E=V,z) + T^{-1}(E=0,V,z)} \right)^2 . \quad (8)$$

This entity can be interpreted as the square of a weighted average of the inverse tunneling decay lengths. In the case of varying DOS an additional weight factor would appear in front of the inverse decay lengths containing the DOS.

The agreement between the experimental and the calculated DBH from the deconvolved DOS is, however, unsatisfactory. This is a clear indication that the TPF used in the calculation does not yet reflect the true TPF accurately. The most prominent difference occurs in the energy range $E > 0.5$ eV where the experimental DBH falls off linearly as $\varphi_{diff} \approx 4.4\ \mathrm{eV} - 0.7E$, whereas the calculated DBH increases linearly. Note that the DBH depends on the tip DOS, which decreases exponentially in the corresponding negative energy range (see Figure 4b). The

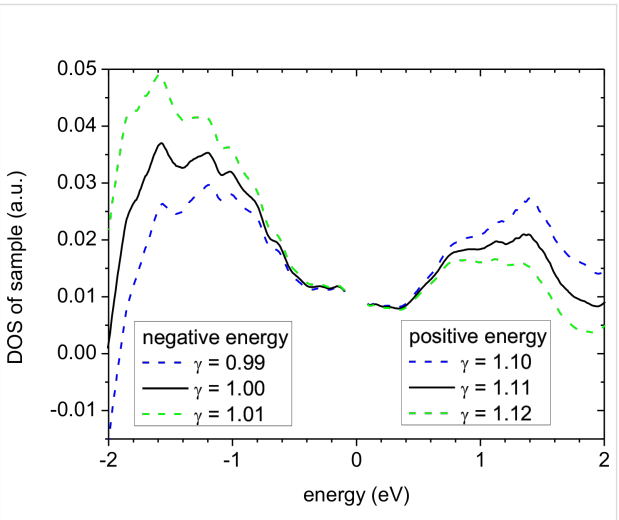

Figure 5: Influence of the parameter γ on the resulting experimental sample DOS. Three DOS are shown in the positive energy range for γ = 1.11 as in Figure 3a (black solid curve), γ = 1.10 (blue dashed), γ = 1.12 (green dashed) and in the negative energy range for γ = 1.00 as in Figure 3a (black solid curve), γ = 0.99 (blue dashed), γ = 1.01 (green dashed). Note that changing γ has an asymmetric influence on the DOS.

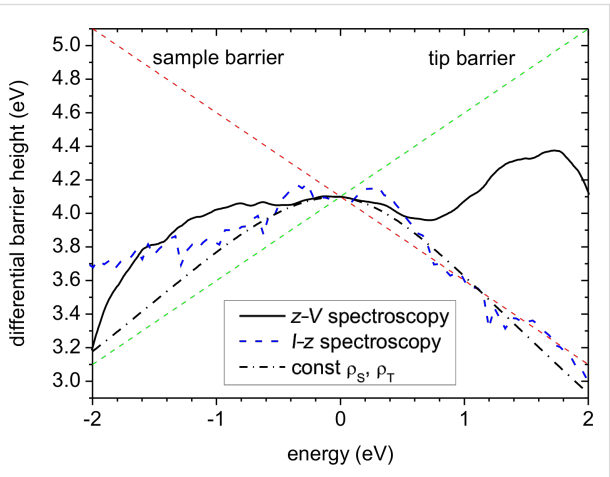

Figure 6: Differential barrier height ($z = 0.6$ nm, $\varphi = 4.1$ eV) as derived from the deconvolved DOS (Figure 4, solid curves) according to the WKB approximation, and as obtained from an independent $\partial_V I$–z measurement with the same tip on the same sample at the same position (dashed blue). The black dash-dotted curve is the calculated DBH for constant DOS using the same TPF as for the other data, i.e., β = 2, γ = 1.11 for positive bias and γ = 1.0 for negative bias. The sample and tip barriers indicate the barriers experienced by electrons at the Fermi level of the tip and of the sample, respectively, according to the one-dimensional WKB approximation.

exponential decrease of the tip DOS at negative bias favors increasingly deeper-lying states at the Fermi level of the sample and thus pushes the DBH towards the higher tip barrier. If this exponential decrease does not describe reality correctly, one has to compensate for the changing DOS by an appropriately changing tunneling probability. A first guess could be adjusting φ and γ such that they fit to $\varphi_{\mathrm{diff}} = \varphi + V/2 - \gamma V$ [20]. In our case we would obtain $\gamma \approx 1.2$, which is too great since the weighting is neglected. Consequently, we took half of the change, giving $\gamma \approx 1.1$ for our calculations at positive bias. However, it must be left to future work to find a better adjustment of the TPF, e.g., by using an energy dependent $\gamma = \gamma(E)$, or to consider a possible dependence of the TPF on the symmetry of the involved electronic states [27].

Conclusion

A formalism that was introduced in [13] to recover and deconvolve the DOS of tip and sample from *I–V* spectra was extended to allow application also to *z–V* spectroscopy data within the framework of the WKB approximation including the trapezoidal approximation. Successful recovery/deconvolution was demonstrated with simulated data. The corresponding results provide information on how the energy position of characteristic DOS features depends on relevant parameters such as the barrier height and width, the tip–sample separation, and true energetic position of such a feature. It is instructive to see here how the sensitivity of STS to variations of the DOS changes with energy and how little the occupied states contribute to the tunneling current and its derivative. The newly developed scheme was applied to experimental data obtained on Nb(110) by *z–V* spectroscopy and compared to corresponding results based on the previous formalism introduced for *I–V* spectroscopy. We find comparable accuracy for both approaches. Thus, the advantages of *z–V* spectroscopy as mentioned in the introduction can, if necessary, be exploited without losing accuracy in the course of the deconvolution procedure.

Comparison with earlier experimental [13] and theoretical results suggest, however, that the major deficiency of the STS analysis lies in the assumed transmission probability function (TPF). Thus, the problem has shifted from developing a deconvolution procedure to finding an adequate TPF that describes tunneling between tip and sample in a more realistic way. To tackle this problem it is presently suggested to elaborate on the properties of the differential barrier height (DBH) as obtained from measurements and the deconvolved DOS. For a proper deconvolution procedure, both DBHs should agree. In the case of discrepancies, however, one should re-iterate the procedure with an adjusted TPF until satisfactory agreement is obtained. Failure of such an adjustment could imply a principal limitation of the WKB approximation.

Acknowledgments

The authors would like to thank the Deutsche Forschungsgemeinschaft (DFG) for financial support within SFB569 TP B6.

References

1. Binnig, G.; Rohrer, H.; Gerber, C.; Weibel, E. *Phys. Rev. Lett.* **1982,** *49,* 57. doi:10.1103/PhysRevLett.49.57
2. Geerk, J.; von Löhneysen, H. *Phys. Rev. Lett.* **2007,** *99,* 257005. doi:10.1103/PhysRevLett.99.257005
3. Tersoff, J.; Hamann, D. R. *Phys. Rev. B* **1985,** *31,* 805. doi:10.1103/PhysRevB.31.805
4. Martensson, P.; Feenstra, R. M. In *Methods of Experimental Physics;* Stroscio, J. A.; Kaiser, W. J., Eds.; Academic Press: New York, 1993; Vol. 27.
5. Feenstra, R. M. *Phys. Rev. B* **1994,** *50,* 4561. doi:10.1103/PhysRevB.50.4561
6. Ukraintsev, V. A. *Phys. Rev. B* **1996,** *53,* 11176. doi:10.1103/PhysRevB.53.11176
7. Koslowski, B.; Dietrich, C.; Tschetschetkin, A.; Ziemann, P. *Phys. Rev. B* **2007,** *75,* 035421. doi:10.1103/PhysRevB.75.035421
8. Wagner, C.; Franke, R.; Fritz, T. *Phys. Rev. B* **2007,** *75,* 235432. doi:10.1103/PhysRevB.75.235432
9. Passoni, M.; Bottani, C. E. *Phys. Rev. B* **2007,** *76,* 115404. doi:10.1103/PhysRevB.76.115404
10. Passoni, M.; Donati, F.; Li Bassi, A.; Casari, C. S.; Bottani, C. E. *Phys. Rev. B* **2009,** *79,* 045404. doi:10.1103/PhysRevB.79.045404
11. Wahl, P.; Diekhöner, L.; Schneider, M. A.; Kern, K. *Rev. Sci. Instrum.* **2008,** *79,* 043104. doi:10.1063/1.2907533
12. Naydenov, B.; Boland, J. J. *Phys. Rev. B* **2010,** *82,* 245411. doi:10.1103/PhysRevB.82.245411
13. Koslowski, B.; Pfeifer, H.; Ziemann, P. *Phys. Rev. B* **2009,** *80,* 165419. doi:10.1103/PhysRevB.80.165419
14. Doughert, D. B.; Maksymovych, P.; Lee, J.; Yates, J. T., Jr. *Phys. Rev. Lett.* **2006,** *97,* 236806. doi:10.1103/PhysRevLett.97.236806
15. Ploigt, H.-C.; Brun, C.; Pivetta, M.; Patthey, F.; Schneider, W.-D. *Phys. Rev. B* **2007,** *76,* 195404. doi:10.1103/PhysRevB.76.195404
16. Feng, M.; Zhao, J.; Petek, H. *Science* **2008,** *320,* 359. doi:10.1126/science.1155866
17. Ziegler, M.; Néel, N.; Sperl, A.; Kröger, J.; Berndt, R. *Phys. Rev. B* **2009,** *80,* 125402. doi:10.1103/PhysRevB.80.125402
18. Simmons, J. G. *J. Appl. Phys.* **1963,** *34,* 1793. doi:10.1063/1.1702682
19. Simmons, J. G. *J. Appl. Phys.* **1964,** *35,* 2655. doi:10.1063/1.1713820
20. Koslowski, B.; Tschetschetkin, A.; Maurer, N.; Ziemann, P. *Phys. Chem. Chem. Phys.* **2011,** *13,* 4045. doi:10.1039/C0CP02162H
21. Koslowski, B.; Dietrich, C.; Ziemann, P. *Surf. Sci.* **2004,** *557,* 255. doi:10.1016/j.susc.2004.03.053
22. Koslowski, B.; Dietrich, C.; Tschetschetkin, A.; Ziemann, P. *Rev. Sci. Instrum.* **2006,** *77,* 063707. doi:10.1063/1.2213171
23. Kilimis, D. A.; Lekka, C. E. *Mater. Sci. Eng., B* **2007,** *144,* 27. doi:10.1016/j.mseb.2007.07.079
24. Heinze, S. (unpublished), compare Reference [13].
25. Lekka, C. E.; Mehl, M. J.; Bernstein, N.; Papaconstantopoulos, D. A. *Phys. Rev. B* **2003,** *68,* 035422. doi:10.1103/PhysRevB.68.035422
26. Pan, X.; Johnson, P. D.; Weinert, M.; Watson, R. E.; Davenport, J. W.; Fernando, G. W.; Hulbert, S. L. *Phys. Rev. B* **1988,** *38,* 7850. doi:10.1103/PhysRevB.38.7850
27. Donati, F.; Piccoli, S.; Bottani, C. E.; Passoni, M. *New J. Phys.* **2011,** *13,* 053058. doi:10.1088/1367-2630/13/5/053058

Beilstein Journal of Nanotechnology

Femtosecond time-resolved photodissociation dynamics of methyl halide molecules on ultrathin gold films

Mihai E. Vaida, Robert Tchitnga and Thorsten M. Bernhardt*

Full Research Paper

Open Access

Address:
Institute of Surface Chemistry and Catalysis, University of Ulm, Albert-Einstein-Allee 47, 89069 Ulm, Germany

Email:
Thorsten M. Bernhardt* - thorsten.bernhardt@uni-ulm.de

* Corresponding author

Keywords:
femtosecond laser spectroscopy; gold; methyl halide photodissociation; surface chemistry; time-of-flight mass spectrometry

Beilstein J. Nanotechnol. **2011,** *2,* 618–627.
doi:10.3762/bjnano.2.65

Received: 08 June 2011
Accepted: 16 September 2011
Published: 20 September 2011

This article is part of the Thematic Series "Organic–inorganic nanosystems".

Guest Editor: P. Ziemann

Abstract

The photodissociation of small organic molecules, namely methyl iodide, methyl bromide, and methyl chloride, adsorbed on a metal surface was investigated in real time by means of femtosecond-laser pump–probe mass spectrometry. A weakly interacting gold surface was employed as substrate because the intact adsorption of the methyl halide molecules was desired prior to photo-excitation. The gold surface was prepared as an ultrathin film on Mo(100). The molecular adsorption behavior was characterized by coverage dependent temperature programmed desorption spectroscopy. Submonolayer preparations were irradiated with UV light of 266 nm wavelength and the subsequently emerging methyl fragments were probed by photoionization and mass spectrometric detection. A strong dependence of the excitation mechanism and the light-induced dynamics on the type of molecule was observed. Possible photoexcitation mechanisms included direct photoexcitation to the dissociative A-band of the methyl halide molecules as well as the attachment of surface-emitted electrons with transient negative ion formation and subsequent molecular fragmentation. Both reaction pathways were energetically possible in the case of methyl iodide, yet, no methyl fragments were observed. As a likely explanation, the rapid quenching of the excited states prior to fragmentation is proposed. This quenching mechanism could be prevented by modification of the gold surface through pre-adsorption of iodine atoms. In contrast, the A-band of methyl bromide was not energetically directly accessible through 266 nm excitation. Nevertheless, the one-photon-induced dissociation was observed in the case of methyl bromide. This was interpreted as being due to a considerable energetic down-shift of the electronic A-band states of methyl bromide by about 1.5 eV through interaction with the gold substrate. Finally, for methyl chloride no photofragmentation could be detected at all.

Introduction

The understanding of the mechanisms involved in the light-induced excitation and fragmentation of organic molecules on metal substrates is of great importance in several research areas and applications connected to surface chemistry and catalysis. Photostability, photooxidation, and photocatalysis are important concepts in this respect that attract considerable interest in the fields of nanotechnology and surface engineering [1,2]. The present investigation focuses on fundamental mechanistic aspects associated with the interaction of small organic molecules with metal surfaces. For this purpose, ultrafast, time-resolved laser spectroscopy was applied to provide insight into light-induced molecular fragmentation on surfaces on the time-scale of nuclear motion. The system under investigation was a nanoscale organic–inorganic layer structure composed of an organic overlayer adsorbed on a weakly interacting ultrathin gold film on a Mo(100) single crystal substrate. Methyl halide molecules are simple pseudo-diatomic photochemical model systems, which have been studied in great detail in the gas phase (see, e.g., [3-7]) as well on several metallic and nonmetallic solid substrates (see, e.g., [8-14]). The adsorption of methyl iodide on a gold surface has been previously investigated [9,11]. However, nothing has been reported so far about the adsorption of methyl bromide or methyl chloride on gold. Also, no ultrafast time-resolved laser investigations of methyl halide molecules on metal substrates have been performed so far. Only recently, the femtosecond (fs)-laser time-resolved photodissociation of methyl iodide and methyl bromide on oxide-supported gold nanoparticles was investigated [15-17]. The gold films employed in the presented experiment for the investigation of photoinduced reaction dynamics of methyl halide molecules on metallic supports were grown on Mo(100).

The central questions of the present investigation are concerned with the dependence of the photoexcitation and the subsequent photodissociation dynamics on the electronic structure of the organic adsorbates and, even more importantly, on the interaction with the substrate surface. Furthermore, the obtained results provide insight into fundamental issues of the ultrafast reaction dynamics of molecules on metallic surfaces and the influence of organic-molecule–inorganic-substrate interactions on the molecular photoreaction dynamics.

Results and Discussion

In the following, the results of the molecular adsorption studies and the investigations of the photodissociation dynamics are presented for the three molecular-adsorbate systems investigated. The characterization of the ultrathin gold films on Mo(100) that have been employed as a substrate in the present study is detailed in Supporting Information File 1.

Adsorption of methyl halide molecules on Au/Mo(100)

Methyl iodide

Figure 1a shows temperature-programmed desorption (TPD) spectra recorded after dosing different amounts of CD_3I molecules at 90 K onto a 10 ML gold film grown on Mo(100). Similar to the TPD investigations of methyl iodide on Au(100) [11] and on Au(111) [9] surfaces that have been reported in the literature, we found that most of the first layer desorbs without fragmentation. At submonolayer coverage just one desorption peak, which shifts to lower temperature with increasing coverage, appears in the TPD spectra. A similar desorption feature has been observed for CH_3I [10,18] and CH_3Br [12] on MgO, CH_3Br on LiF [19], and CH_3Cl on Pd(100) [20], as well as for CH_3Cl, CH_3Br and CH_3I on GaAs(110) [21,22], and the coverage dependence is attributed to the adsorbate–adsorbate repulsion that results from the interaction between the static dipole moments of adsorbed molecules. Due to this lateral repulsion between the adsorbate molecules, the activation energy for desorption decreases with increasing coverage and, hence, the desorption temperature decreases. The completion of the first monolayer of CD_3I molecules appears for doses just below 4.75 L, in agreement with the previous investigations on Au(100) [11]. The peak below 140 K in Figure 1a is due to the multilayer desorption. Higher coverages were not investigated in this experiment.

About 4% of the CD_3I molecules of the first layer dissociate and produce ethane. The inset in Figure 1a shows the evolution of the ethane signal in the temperature-programmed reaction of CD_3I molecules on the 10 ML Au film on Mo(100). The ethane signal starts just below 300 K, extends up to 400 K and presents a maximum at 350 K. Based on similar results for Au(100) [11] and Au(111) [9], the ethane formation is thought to be a consequence of methyl iodide dissociation followed by coupling between the methyl radicals. Since the temperature at which ethane appears is higher than that for the ethane molecular desorption (below 100 K), it was concluded that the ethane formation is the rate-determining step as opposed to the desorption [11]. Furthermore, it can be assumed that the methyl iodide molecules involved in the thermal reaction are adsorbed on defect sites and dissociate close to the ethane-appearance temperature (300 K) [11]. The remaining iodine atoms resulting from dissociation should desorb from the surface as atoms at temperatures higher than 650 K [23] (not investigated here). The intensity of the ethane signal saturates at a CD_3I coverage corresponding to an exposure of about 0.75 L in agreement with the previous investigation of Yang et al. [11]. No other thermal reaction products were detected.

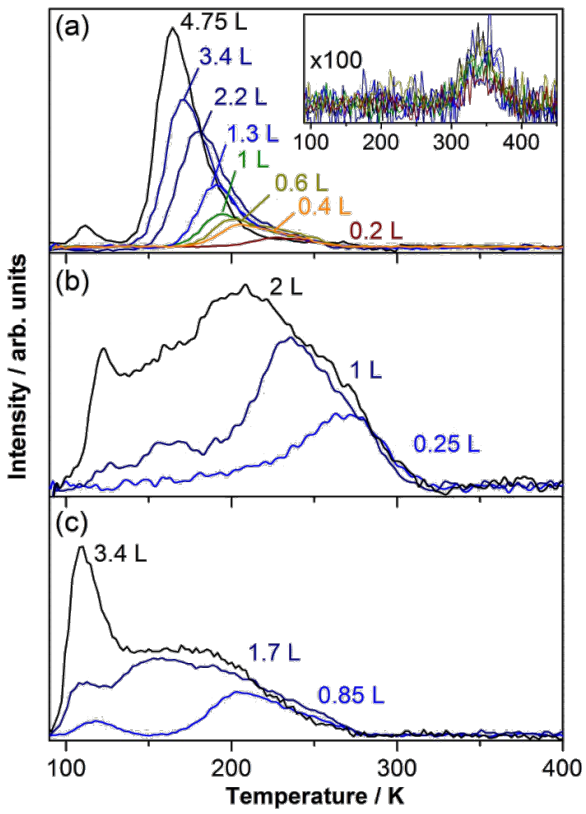

Figure 1: Temperature-programmed desorption/reaction spectra showing the molecular desorption of: (a) CD_3I, (b) CH_3Br and (c) CH_3Cl from a 10 ML Au film on Mo(100). The numbers indicated next to the spectra represent the methyl halide exposure in units of Langmuir. The inset displays the C_2D_6 signal evolution. The C_2D_6 signal intensity has been multiplied by a factor of 100. All spectra were obtained with a heating rate of 2 K/s.

Methyl bromide

The adsorption behavior of methyl bromide on a gold surface was also investigated by means of TPD spectroscopy, and the results are displayed in Figure 1b. Methyl bromide generally desorbed at higher temperatures from the gold substrate as compared to methyl iodide. For an exposure of 0.25 L the CH_3Br desorption began at around 150 K and extended to 310 K, with an intensity maximum at about 275 K. For an exposure of 1 L CH_3Br, a decrease of the maximum desorption temperature to about 235 K was observed. Additionally, a new desorption feature appeared below 200 K. When 2 L of CH_3Br were dosed onto the Au film, a distinct desorption peak at 120 K was observed separate from the main desorption peak as observed at lower coverages, with the maximum now shifted to 205 K. No investigations of the adsorption of methyl bromide molecules on a gold surface have been reported so far in the literature. The interpretation of the features displayed in Figure 1b is therefore based on TPD experiments with methyl halide molecules adsorbed on different substrates, which have been reported in the literature (see above). The desorption peak above 170 K is assigned to the molecular desorption of CH_3Br molecules from the gold surface. Its shift to lower temperature with increasing adsorbate coverage is attributed also to a repulsive desorption that is caused by the interaction between the static dipole moments of the adsorbed molecules. A similar desorption characteristic was observed for submonolayer coverages of CH_3Br on Ru(001) [13]. The distinct peak at 120 K is assigned to the onset of the CH_3Br multilayer desorption, which was observed to start at an exposure of 3.4 L on Ru(001) [13]. In contrast to methyl iodide adsorbed on a gold surface, no thermally induced reaction products of CH_3Br, such as methane or ethane, were detected. As well, no evidence for methyl bromide dissociation subsequent to adsorption on the Au substrate was found.

Methyl chloride

Similar to the case of methyl bromide, no desorption studies of methyl chloride on a gold surface have been reported so far. Our results are depicted in Figure 1c. Already at 0.85 L exposure two desorption features were observed. The high-temperature peak shifts to lower temperatures with increasing coverage, indicating again repulsive adsorbate–adsorbate interactions. Interestingly, already at 0.85 L exposure a low-temperature desorption peak also emerges at around 110 K. This peak might indicate early multilayer desorption, which would be in accordance with similar results of CH_3Cl adsorbed on Ru(001) [13]. In this case the authors reported the onset of multilayer desorption for a methyl chloride exposure of 1.6 L. Also for methyl chloride no thermally induced reaction products were detected.

Molecular photodissociation dynamics

Molecular photoexcitation on solid surfaces is generally believed to proceed through one of the two following mechanisms:

1. Electron attachment leading to transient negative molecular ions, which in the case of the methyl halide molecules are unstable and subsequently decompose, or
2. direct photoexcitation of the adsorbed molecules to electronically excited states, which will determine the following photoreaction dynamics. For the methyl halide molecules the first optically accessible states belong to the dissociative A-band.

These two principally possible photoexcitation scenarios are schematically illustrated in Figure 2 for the methyl halide molecules adsorbed on a metal surface. For methyl iodide both reaction pathways are energetically possible with the absorption of one pump-laser photon of 266 nm wavelength. For methyl bromide and methyl chloride the A-band absorption maximum is

6.2 and 7.3 eV, respectively, above the electronic ground state of the free molecules [3] and thus not accessible through one-photon excitation at 266 nm (4.7 eV).

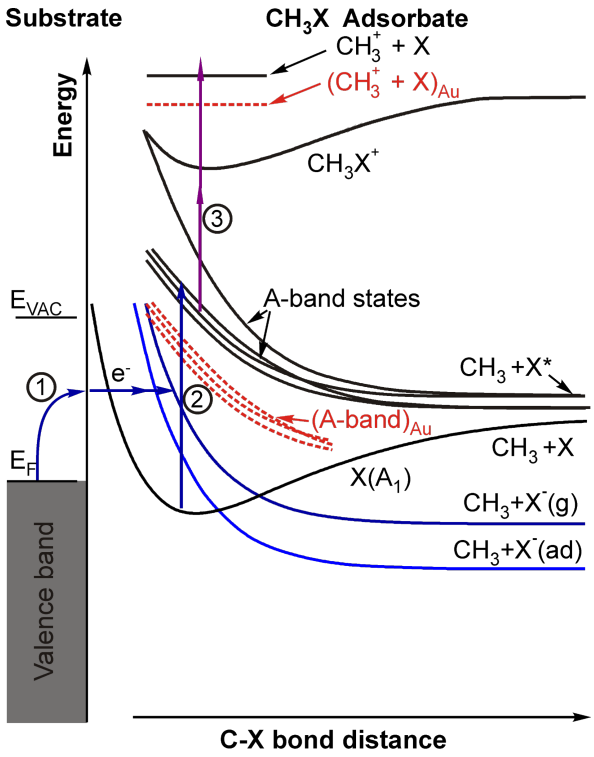

Figure 2: Schematic potential energy diagram for CH_3X (X = I, Br, Cl) molecules adsorbed on a metal surface. The shape of the potentials and the general idea have been adapted from data on CH_3Br in [7,24-27]. The numbers of the excitation and detection mechanisms refer to the discussion in the text. The electronic levels that are proposed to be involved in the excitation and detection mechanism on the gold surface are indicated by the dashed red lines.

Methyl iodide

Methyl iodide photodissociation on gold: CD_3I was adsorbed at submonolayer coverage on a 10 ML Au film on Mo(100) and irradiated with fs-laser pulses of 266 nm wavelength (pump beam, 80 fs, p-polarized, 1–2 mW/cm^2). For the subsequent fragment ionization a probe laser beam with a wavelength of 333 nm (80 fs, p-polarized, 600 mW/cm^2) was employed. However, neither photodissociation products nor the parent molecule were detected, independent on the pump–probe delay time. Similar results were reported by White and coworkers for methyl iodide adsorbed on Pt(111) [28-31]. In their work, methyl iodide molecules that were adsorbed on the metal surface were exposed to the full spectrum of an Hg arc lamp. The photodissociation and the desorption of the molecules from the surface was subsequently monitored by means of X-ray photoemission spectroscopy. White and coworkers reported that only 10% of the first CH_3I layer adsorbed on the Pt(111) substrate dissociated when the sample was irradiated for 120 min with a 100 W Hg arc lamp [29]. In contrast, a facile cleavage of the second layer was observed. According to vibrational spectroscopy investigations, the methyl iodide molecules adsorb on a Pt(111) surface with the halogen atom bound to the surface and with the C–I axis considerably tilted away from the surface normal [32]. On Au(100) an adsorption geometry with the C–I axis almost parallel to the surface plane is even expected for CH_3I at submonolayer coverages [11]. Under these circumstances, the ground state of the CH_3I molecule is only slightly perturbed from the gas phase. In contrast, the excited state is strongly bound to the metal surface, which facilitates the recapturing of the ground state before the C–I bond stretches considerably. As a consequence, the molecule will almost instantaneously relax back to the ground state after excitation, and the molecular dissociation will be quenched [29]. Also on an Ag(111) surface the methyl iodide molecules adsorbed at monolayer coverage are photodissociated at a slower rate compared to those adsorbed at multilayer coverages, which also indicates a substantial quenching of the photodissociation when the molecules are in contact with the metal substrate [33,34]. In contrast to CH_3I, however, the photodissociation of the first monolayer of CH_3Br and CH_3Cl is easily promoted on the Pt(111) surface through UV irradiation [24,31,35,36].

Trapping of iodine atoms at the surface subsequent to CD_3I photodissociation on gold: Figure 3 displays the time evolution of the CD_3^+ signal during continuous admission of CD_3I to a 10 ML Au film on Mo(100). The surface temperature was held at 120 K to ensure a maximum CD_3I coverage of just about one monolayer (Figure 1a and [11]). In the beginning (period A in Figure 3), the surface was continuously irradiated by the pump- and probe-laser beams. An increase of the CD_3^+ signal intensity was observed, starting after a few tens of seconds. The saturation of the CD_3^+ signal appeared close to 2000 s. The CD_3^+ signal up to 2000 s approximates to an exponential rise function. The obtained time constant is τ_A = 410 ± 20 s. After 2000 s (period B in Figure 3), the CD_3I admission was stopped, but the surface was further irradiated by the laser beams. The CD_3^+ signal immediately started to decrease. This decay is best fitted by a second-order exponential decay function. The time constants of the fast and slow decaying parts are τ_{B1} = 55 ± 5 s and τ_{B2} = 300 ± 100 s, respectively. After 3000 s the CD_3I gas admission was restarted (period C in Figure 3) and the CD_3^+ signal exhibited an abrupt increase. The best fit to this signal with an exponential rise function gives a time constant of τ_C = 75 ± 22 s.

The initial rise of the CD_3^+ signal in Figure 3 (period A) cannot be attributed to the continuous accumulation of CD_3I molecules onto the surface, since the saturation of the monolayer is

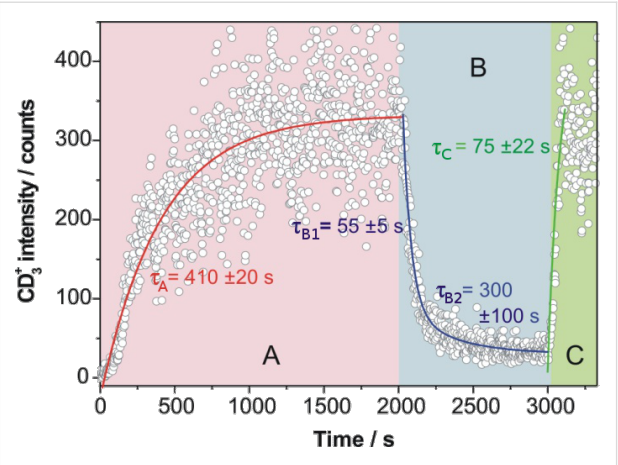

Figure 3: Time evolution of the integral CD_3^+ intensity (open circles) during the continuous admission of CD_3I to a 10 ML Au film on Mo(100). The surface temperature was 120 K. At 2000 s the gas admission was stopped for 1000 s. The solid lines represent the best fits to the different parts of the measured data (A, B and C) with exponential growth and decay functions, as appropriate (see text for more details). Pump pulse: 266 nm, 2 mW/cm²; probe pulse: 333 nm, 600 mW/cm²; pump–probe delay time: 130 fs.

expected within less than 10 s. Moreover, a subsequent irradiation of a new (but already covered with CD_3I) surface area, of the same sample, gave a similar exponential rise of the CD_3^+ signal. Therefore, it must be assumed that the result shown in Figure 3 indicates a change in the nature of the surface during laser irradiation. As discussed in the previous section, just a small amount of C–I bond cleavage of CH_3I at monolayer coverage on Pt(111) was observed after a long period (120 min) of irradiation with a 100 W Hg arc lamp [29]. In the present experiment a much more intense light source, i.e., a fs-laser, was employed. Therefore, in our experiment the dissociation of the CD_3I adsorbed at monolayer coverage on Au can be assumed to occur at a somewhat faster rate (on the time scale of tens of seconds in contrast to tens of minutes). According to the adsorption geometry and binding energy of methyl iodide molecules on the Au surface [11], we expect the trapping of the iodine atoms at the surface subsequent to CD_3I photodissociation. Consequently, during the laser irradiation of the sample an iodine film (or a gold–iodine layer) might be formed between the Au surface and the subsequently adsorbed CD_3I molecules. On this iodine film, the photodissociation of the CD_3I molecules should not be quenched anymore. The suggestion of the formation of an iodine layer, or at least an iodine containing gold layer, in the present experiment is supported by the investigations of White and coworkers, who observed that the CH_3I photodissociation on a Pt(111) surface precovered with a monolayer of iodine atoms was not quenched either [37].

The rise time of the CD_3^+ signal in Figure 3 (period A) should be related to the formation of the iodine layer. Once the sample is modified, i.e., the light-induced transformation CD_3I/10 ML Au/Mo(100) → CD_3I/I/10 ML Au/Mo(100) is completed, the laser can induce the dissociation and fragment desorption of an significant fraction of the CH_3I molecules that are adsorbed on the iodine layer. The dissociated and desorbed amount of CD_3I is immediately restored owing to the continuous admission, and a stable methyl desorption signal is established at the end of period A in Figure 3. In period B of Figure 3, the fast decaying part is attributed to the dissociation of the uppermost CD_3I molecules that were weakly adsorbed on the iodine layer. The slowly decaying part in period B could be attributed to the dissociation of strongly bound CD_3I molecules, which were possibly surrounded by iodine atoms. Towards the end of period B in Figure 3 it can be expected that the sample surface consisted mostly of iodine atoms adsorbed on the gold film on Mo(100). The considerably faster rise of the methyl signal in period C of Figure 3, when the gas admission was restarted, compared to the one obtained in the beginning of the experiment (see period A in Figure 3), supports the assumption that a change of the surface composition after laser irradiation during continuous methyl iodide admission had occurred. The CD_3^+ signal in period C is attributed to the dissociation of CD_3I molecules adsorbed on the new iodide film that was formed during the previous laser irradiation. The fast rise of the CD_3^+ signal then reflects the time needed to saturate this iodine film surface with CD_3I molecules. The maximum CD_3^+ signal intensities reached in both periods B and C coincide. The exact values of the time constants presented in Figure 3 depend of course strongly on the laser intensity. In particular, the rise time in period A can be considerably extended at reduced laser intensity.

In Figure 4 laser desorption mass spectra recorded from the sample surface employed in the previous experiment (Figure 3) after 3500 s are shown. At a surface temperature of 150 K (Figure 4a), signals corresponding to atomic and molecular iodine are detected separate from the methyl mass peak. At 150 K the CD_3I coverage is below one monolayer (Figure 1a) and therefore, iodine atoms and molecules can also be desorbed by laser irradiation from the iodine layer on the gold surface, which also supports the assumption that iodine atom fragments have been previously trapped on the gold surface.

In contrast, at 100 K surface temperature multilayer coverages of CD_3I are possible. The mass spectrum in Figure 4b was obtained at this surface temperature and confirms that, under these multilayer conditions, the atomic and molecular iodine desorption from the iodine layer on the gold surface is suppressed because the iodine layer is completely covered by CD_3I. In addition, when the sample was held at 100 K the methyl peak intensity was about 35 times higher than that at

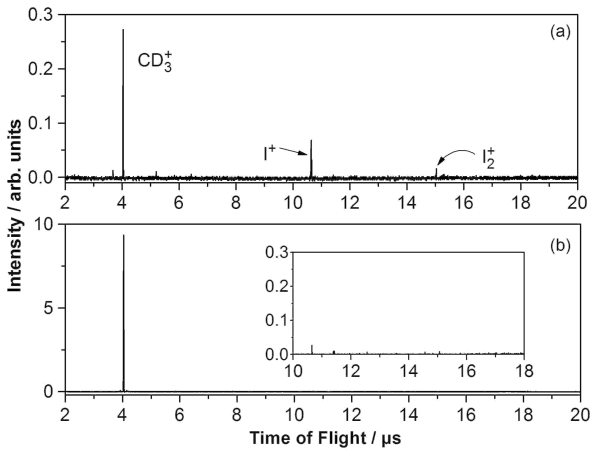

Figure 4: Mass spectra recorded at (a) 150 K and (b) 100 K from the same sample surface as in Figure 3 period C, after 3500 s. The inset presents a zoom-in to the mass spectrum (b). During the recording of the mass spectra, CD_3I was continuously dosed onto the surface. Pump pulse: 266 nm, 2 mW/cm²; probe pulse: 333 nm, 600 mW/cm²; pump–probe delay time: 130 fs.

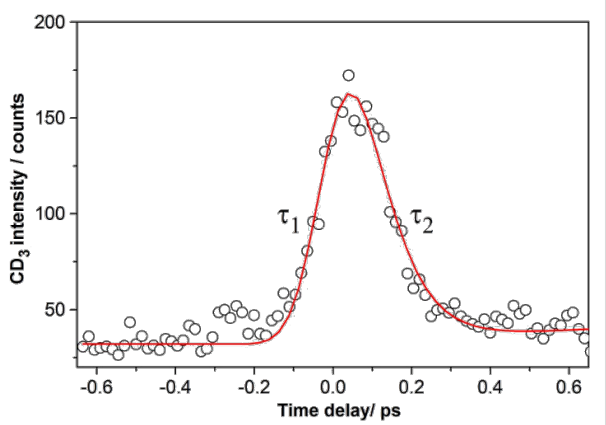

Figure 5: Femtosecond photodissociation reaction of multilayer methyl iodide adsorbed on 10 ML Au/Mo(100) recorded by monitoring the transient methyl cation signal intensity as a function of the pump–probe delay time (pump: 266 nm, 2 mW/cm² and probe: 333 nm 60 mW/cm²). The solid line is the best fit of an exponential "rise and decay" model to the experimental data, yielding the indicated time constants τ_1 and τ_2.

150 K owing to the CD_3I multilayer formation (note that at the chosen delay time of 130 fs no iodine atoms or I_2 molecules resulting from molecular CH_3I photodissociation were detected with the employed probe laser beam [38]; the detected I-atoms and I_2 molecules in the mass spectrum must therefore originate from the iodine layer on the gold surface). On the modified gold surface (I/Au/Mo(100)) it was then possible to record the fs photodissociation dynamics of CD_3I by monitoring the transient methyl cation signal intensity as a function of the pump–probe delay. The result is shown in Figure 5. The CD_3^+ transient signal consists of a peak structure with a maximum at 50 fs. The interpretation of this transient is based on earlier experiments with methyl iodide on an insulating magnesia surface and on the power dependences of the pump and the probe laser, which support a single-photon excitation followed by a two-photon ionization [18,38,39].

Dissociative electron attachment according to excitation mechanism (1) in Figure 2 might be possible. In this way transient CH_3I^- ions would be generated, which would subsequently decompose. However, the formation of methyl cations would in this case involve a transition from the anion, via the neutral, to the cation. Of course, the exact locations of the respective potential energy surfaces are not known, but owing to the steep slope of the potentials at short distances (Figure 2) it is likely that this would require a three-photon transition, which is not in accordance with our observed two-photon ionization probe process. Therefore, it is assumed instead that one single photon of 266 nm excited the adsorbed methyl iodide molecule to the A-band (excitation mechanism (2) in Figure 2). The peak structure is then attributed to the dynamics of the dissociating excited transition state of methyl iodide in the A-band, which can be directly ionized with the highest cross section after 50 fs by two photons of the probe pulse at 333 nm wavelength (excitation mechanism (3) in Figure 2). Subsequent rapid decomposition of the excited methyl iodide cation is proposed to lead to the observed methyl fragment signal. Fitting the experimental data with an exponential "rise and decay" model (convoluted with the laser cross correlation function) yielded the time constants of $\tau_1 = 60 \pm 10$ fs and $\tau_2 = 70 \pm 10$ fs for the rise and decay of the peak structure, respectively.

Methyl bromide

In contrast to methyl iodide molecules adsorbed at submonolayer coverage on the gold surface, which did not photodissociate, methyl bromide adsorbed on the same substrate at submonolayer coverage was easily photodissociated. Figure 6a displays a mass spectrum recorded from submonolayer (0.25 ML) CH_3Br adsorbed on 10 ML Au/Mo(100). The spectrum was recorded at 90 K. The pump and probe wavelengths were 266 nm and 333 nm, respectively. The pump–probe delay time was fixed to 140 fs. As can be seen, the only observed photoreaction product was CH_3^+. Mass spectra recorded under different experimental conditions, i.e., different pump–probe delay times, laser intensities, coverages, and temperatures, did not lead to the detection of other reaction products.

The time evolution of this methyl cation signal is shown in Figure 6b. Similar to the real-time photodissociation of CD_3I molecules on I/Au/Mo(100), which was discussed above, the CH_3^+ transient signal in Figure 6b exhibits a peak structure. The signal starts at 0 fs and no CH_3^+ transient signal was detected

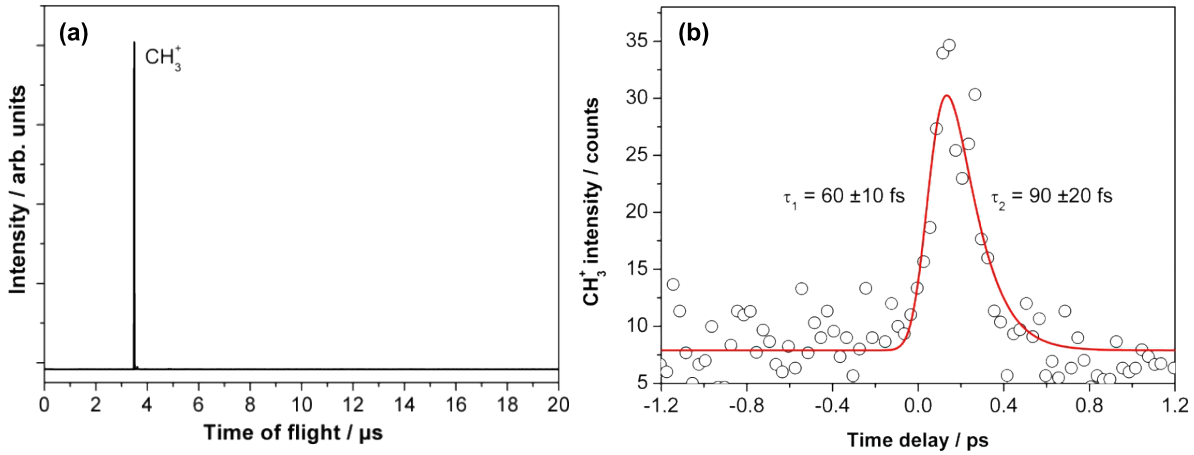

Figure 6: (a) Time-of-flight mass spectrum obtained from 0.25 ML methyl bromide adsorbed on a 10 ML Au film on Mo(100) at 140 fs pump–probe delay time. (b) Transient fs-photodissociation dynamics of CH_3Br molecules adsorbed on Au(100)/Mo(100) recorded by monitoring the CH_3^+ signal as a function of the pump–probe time delay. The surface temperature was 150 K. The solid line is the best fit of an exponential "rise and decay"-model to the experimental data, yielding the indicated time constants τ_1 and τ_2. For the shown transient, four single transients were averaged to improve the signal-to-noise ratio. The transient was obtained with 2 mW/cm² pump (266 nm) and 200 mW/cm² probe (333 nm) laser power.

for reaction times longer than 600 fs. The measured data were also fitted with an exponential "rise and decay" model. The determined rise and decay time constants were $\tau_1 = 60 \pm 10$ fs and $\tau_2 = 90 \pm 20$ fs, respectively. The maximum of the peak structure was located at 140 ± 20 fs. The error of ±20 fs, in determining the maximum intensity, was derived from several transients recorded under similar conditions, i.e., similar substrate preparation, molecular coverage, and laser parameters. The other errors in determining the time constants were acquired directly from the fitting procedure.

Laser power dependence measurements indicated that the fundamental mechanism of the CH_3Br photodissociation on the gold film is similar to that of methyl iodide on I/Au/Mo(100). The pump and probe power dependences of the CH_3^+ signal intensity at 140 fs pump–probe delay time are depicted in Figure 7 in a double-logarithmic representation. The slope of the graphs is an indication of the number of photons involved in the respective processes. From Figure 7 it can be seen that one pump photon was needed to excite the adsorbed CH_3Br molecules. Therefore, the electron attachment mechanism might be possible, however, the two-photon probe power dependence renders this option again unlikely because rather three photons of 333 nm would be expected to be required to excite CH_3Br^- to CH_3Br^+. The A-band of the free methyl bromide molecule has its maximum absorption cross section at around 6.2 eV [3]. The observation that CH_3Br adsorbed on Au can be excited by means of a single photon with a central wavelength of 266 nm (4.7 eV) to a dissociative state, which is most likely the A-band, thus strongly indicates that the gold substrate induces a red-shift of the CH_3Br A-band of about 1.5 eV. This energetic down-shift of the A-band states due to the interaction of the molecules with the gold surface is schematically indicated by the red dashed lines in Figure 2. Similar results were reported in the literature for CH_3Br adsorbed on Ag(111) [34]. Figure 7b displays the quadratic power dependence measured for the probe laser beam, which confirms that two probe photons are most likely required to generate the ionized methyl fragments.

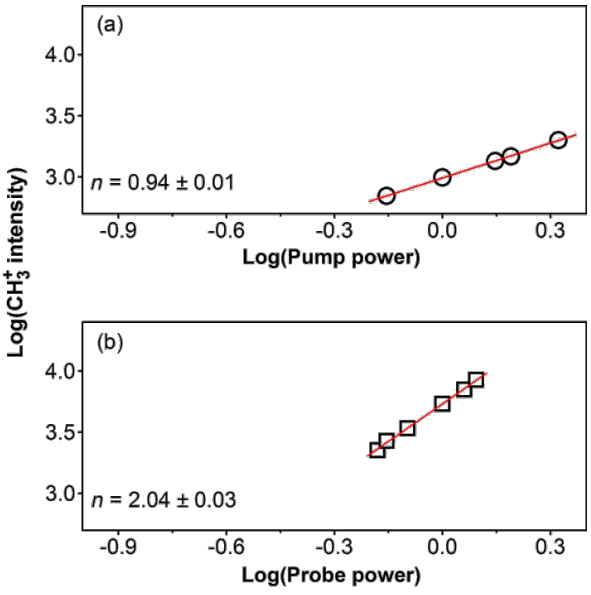

Figure 7: Intensity of the CH_3^+ signal as a function of (a) pump power and (b) probe power. Both measurements (a) and (b) were performed for a pump–probe delay time of 140 fs. The straight lines represent linear fits to the experimental data yielding the indicated slopes *n*.

Therefore, it is assumed that the excited adsorbate molecules were ionized by two nonresonant photons of 333 nm wavelength, and the ionized excited transition state decomposed yielding the CH_3^+ fragment.

The maximum intensity of the CH_3^+ transient peak obtained from the CH_3Br photodissociation on gold is located at 140 fs (Figure 6b), whereas the transient peak of the CD_3^+ signal resulting from CD_3I photodissociation on I/Au/Mo(100) was located at 50 fs with slightly different time constants for the rise and the decay of the signal. This is a clear indication of the different interaction of CH_3Br with Au/Mo(100) compared to that of CD_3I with I/Au/Mo(100). Thus, if the molecules dissociate by direct photoexcitation through the A state (which is proposed for methyl iodide and bromide), then these data represent intramolecular dynamics of the weakly perturbed molecule sitting on the Au surface, i.e., the dynamics in the transition-state region of photodissociation, which is intimately influenced by the detailed interaction with the surface. Clearly, further insight from first principles simulations on these systems would be highly desirable to complement the experimental data.

Methyl chloride

No light-induced formation of fragments was observed in the case of methyl chloride. This is most likely due to the fact that the A-band of CH_3Cl with an absorption maximum at 7.3 eV above the electronic ground state of the free molecule [3] cannot be energetically lowered enough to become accessible to the 4.7 eV photons of the 266 nm pump laser beam.

Conclusion

The present investigation demonstrates that time resolved pump–probe fs-laser time-of-flight mass spectrometry is able to probe the photodissociation dynamics of organic molecules on metallic substrates. The observed molecular dynamics varies strongly for the three investigated methyl halide molecules and reflects the different electronic structure of the molecules as well as the interaction with the gold substrate surface. The dissociation of methyl iodide on gold after UV irradiation was found to be quenched. In contrast, a modification of the gold substrate by slowly emerging iodine fragments was observed, which inhibited the quenching mechanism and enabled the measurement of transient methyl fragment signals. In the case of methyl bromide one-photon excitation was found to lead to the decomposition of the molecules on the gold surface. This was interpreted as an indication for a considerable red-shift of the A-band excitation of methyl bromide due to the interaction with the substrate. The alternative mechanism of dissociative electron attachment was found to be unlikely to be responsible for the observed dynamics of both molecules. Methyl chloride did not yield any detectable photofragments.

Experimental

The experiments were performed in an ultrahigh vacuum (UHV) chamber equipped with standard tools for surface preparation and characterization [15,18,40]. Prior to deposition of the gold film, the surface was cleaned by heating the Mo(100) crystal to 2000 K by means of electron bombardment. Subsequently, the surface temperature was ramped down to 1000 K. In order to avoid the surface contamination, the Mo crystal was held at 1000 K by resistive heating until the background pressure restored ($<5 \times 10^{-10}$ mbar). Subsequently the surface was cooled down to the deposition temperature of 400 K. The gold evaporator was initially degassed and subsequently gave stable deposition rates over extended periods of time. In order to ensure the constant evaporation rate, prior to each deposition, the Au oven was preheated for 15 min. Subsequently, the substrate was positioned 10 mm away from the gold source and the support was held at 400 K. The gold evaporation was performed at normal incidence. The maximum background pressure in the UHV chamber reached throughout the gold evaporation process was less than 2×10^{-9} mbar. Deuterated methyl iodide was employed in the present study, but test measurements with CH_3I yielded identical results. CD_3I, CH_3Br, and CH_3Cl (all from Sigma-Aldrich, >99.5%, additionally purified by several freeze–pump–thaw cycles) were dosed onto the gold substrate at 90 K by means of an UHV compatible pulsed valve that was connected to a stainless steel tube ending close to the surface.

The fs pump (266 nm, third harmonic of fundamental, 80 fs, 1 mW/cm² average power, p-polarized) and probe (333 nm central wavelength, tuned by an OPA, 80 fs, 600 mW/cm² average power, p-polarized) were generated by a commercial amplified 1 kHz Ti:sapphire laser system (Spectra Physics Spitfire). The time zero in the experiments was determined in situ by monitoring the integral pump–probe time-dependent two-photon electron emission signal from the molybdenum surface.

Mass measurements were carried out on a homebuilt time-of-flight mass spectrometer [18,39]. The grounded Au/Mo(100) substrate served as the repeller electrode of a Wiley–McLaren-type acceleration lens arrangement [41]. The pump and probe laser beams collinearly irradiated the surface at an angle of 45°. Reaction products and intermediates that were ionized by the probe laser pulse were immediately removed from the surface and directed into the time-of-flight mass spectrometer by the static electric field between the substrate surface and the first acceleration electrode of the mass spectrometer. The ions pass a field free drift tube with different velocities according to their mass-to-charge ratio and are finally detected by a multichannel plate amplifier arrangement as a function of their flight time. To obtain the transient evolution of the product ion mass signals,

the mass peaks were averaged over 2500 laser pulses for a fixed pump–probe delay time. The initial coverage was subsequently restored by admitting an identical amount of compound to the surface with the pulsed valve. Subsequently, the procedure was repeated for a new pump–probe delay time. Several of the thus obtained transients were averaged to yield the shown data.

Supporting Information

Supporting information features the description of the characterization of the gold ultrathin films on Mo(100).

Supporting Information File 1

Characterization of ultrathin gold films on Mo(100).
[http://www.beilstein-journals.org/bjnano/content/supplementary/2190-4286-2-65-S1.pdf]

Acknowledgements

The work presented was supported by the Deutsche Forschungsgemeinschaft (SFB 569) and by the Fonds der Chemischen Industrie. MEV acknowledges a fellowship from the DAAD.

References

1. Pickett, J. E.; Moore, J. E. In *Polymer Durability;* Clough, R. L.; Billingham, N. C.; Gillen, K. T., Eds.; ACS Publications: Washington, DC, 1996; Vol. 249, p 287. doi:10.1021/ba-1996-0249.ch019
2. Esswein, A. J.; Nocera, D. G. *Chem. Rev.* **2007,** *107,* 4022. doi:10.1021/cr050193e
3. Felps, W. S.; Rupnik, K.; McGlynn, S. P. *J. Phys. Chem.* **1991,** *95,* 639. doi:10.1021/j100155a028
4. Alekseyev, A. B.; Liebermann, H.-P.; Buenker, R. J. *J. Chem. Phys.* **2007,** *126,* 234103. doi:10.1063/1.2736696
5. Alekseyev, A. B.; Liebermann, H.-P.; Buenker, R. J.; Yurchenko, S. N. *J. Chem. Phys.* **2007,** *126,* 234102. doi:10.1063/1.2736695
6. de Nalda, R.; Durá, J.; Garcia-Vela, A.; Izquierdo, J. G.; González-Vázquez, J.; Bañares, L. *J. Chem. Phys.* **2008,** *128,* 244309. doi:10.1063/1.2943198
7. Blanchet, V.; Samartzis, P. C.; Wodtke, A. M. *J. Chem. Phys.* **2009,** *130,* 034304. doi:10.1063/1.3058730
8. Kutzner, J.; Lindeke, G.; Welge, K. H.; Feldmann, D. *J. Chem. Phys.* **1989,** *90,* 548. doi:10.1063/1.456506
9. Paul, A. M.; Bent, B. E. *J. Catal.* **1994,** *147,* 264. doi:10.1006/jcat.1994.1137
10. Holbert, V. P.; Garrett, S. J.; Bruns, J. C.; Stair, P. C.; Weitz, E. *Surf. Sci.* **1994,** *314,* 107. doi:10.1016/0039-6028(94)90217-8
11. Yang, M. X.; Jo, S. K.; Paul, A.; Avila, L.; Bent, B. E.; Nishikida, K. *Surf. Sci.* **1995,** *325,* 102. doi:10.1016/0039-6028(94)00722-5
12. Garrett, S. J.; Heyd, D. V.; Polanyi, J. C. *J. Chem. Phys.* **1997,** *106,* 7847. doi:10.1063/1.473743
13. Livneh, T.; Asscher, M. *Langmuir* **1998,** *14,* 1348. doi:10.1021/la970712b
14. Osgood, R. *Chem. Rev.* **2006,** *106,* 4379. doi:10.1021/cr050175x
15. Vaida, M. E.; Bernhardt, T. M. *Eur. Phys. J. D* **2009,** *52,* 119. doi:10.1140/epjd/e2009-00064-2
16. Vaida, M. E.; Gleitsmann, T.; Tchitnga, R.; Bernhardt, T. M. *Phys. Status Solidi B* **2010,** *247,* 1139. doi:10.1002/pssb.200945518
17. Vaida, M. E.; Bernhardt, T. M. In *AIP Conference Proceedings, Vol. 1387,* PHYSICS CONFERENCE TIM-10, Timisoara, Romania, Nov 25–27, 2010; Bunoiu, M.; Malaescu, I., Eds.; American Institute of Physics: Melville, NY, 2011.
18. Vaida, M. E.; Hindelang, P. E.; Bernhardt, T. M. *J. Chem. Phys.* **2008,** *129,* 011105. doi:10.1063/1.2953578
19. Garrett, S. J.; Heyd, D. V.; Polanyi, J. C. *J. Chem. Phys.* **1997,** *106,* 7834. doi:10.1063/1.473742
20. Berko, A.; Erley, W.; Sander, D. *J. Chem. Phys.* **1990,** *93,* 8300. doi:10.1063/1.459312
21. Lasky, P. J.; Lu, P. H.; Yang, M. X.; Osgood, R. M., Jr.; Bent, B. E.; Stevens, P. A. *Surf. Sci.* **1995,** *336,* 140. doi:10.1016/0039-6028(95)00493-9
22. Lu, P. H.; Lasky, P. J.; Yang, Q. Y.; Osgood, R. M., Jr. *Chem. Phys.* **1996,** *205,* 143. doi:10.1016/0301-0104(95)00377-0
23. Neumann, A.; Christmann, K.; Solomun, T. *Surf. Sci.* **1993,** *287–288,* 593. doi:10.1016/0039-6028(93)91034-M
24. Ukraintsev, V. A.; Long, T. J.; Gowl, T.; Harrison, I. *J. Chem. Phys.* **1992,** *96,* 9114. doi:10.1021/j100202a009
25. Camillone, N., III; Khan, K. A.; Yarmoff, J. A.; Osgood, R. M., Jr. *Phys. Rev. Lett.* **2001,** *87,* 056101. doi:10.1103/PhysRevLett.87.056101
26. Escure, C.; Leininger, T.; Lepetit, B. *J. Chem. Phys.* **2009,** *130,* 244306. doi:10.1063/1.3152865
27. Escure, C.; Leininger, T.; Lepetit, B. *J. Chem. Phys.* **2009,** *130,* 244305. doi:10.1063/1.3154140
28. Costello, S. A.; Roop, B.; Liu, Z. M.; White, J. M. *J. Phys. Chem.* **1988,** *92,* 1019. doi:10.1021/j100316a006
29. Liu, Z. M.; Akhter, S.; Roop, B.; White, J. M. *J. Am. Chem. Soc.* **1988,** *110,* 8708. doi:10.1021/ja00234a029
30. Liu, Z. M.; Costello, S. A.; Roop, B.; Coon, S. R.; Akhter, S.; White, J. M. *J. Phys. Chem.* **1989,** *93,* 7681. doi:10.1021/j100359a030
31. Roop, B.; Lloyd, K. G.; Costello, S. A.; Campion, A.; White, J. M. *J. Chem. Phys.* **1989,** *91,* 5103. doi:10.1063/1.457602
32. Henderson, M. A.; Mitchell, G. E.; White, J. M. *Surf. Sci.* **1987,** *184,* L325. doi:10.1016/S0039-6028(87)80258-3
33. Domen, K.; Chuang, T. J. *J. Chem. Phys.* **1989,** *90,* 3332. doi:10.1063/1.455887
34. Zhou, X.-L.; White, J. M. *Surf. Sci.* **1991,** *241,* 270. doi:10.1016/0039-6028(91)90087-9
35. Jo, S. K.; Zhu, X.-Y.; Lennon, D.; White, J. M. *Surf. Sci.* **1991,** *241,* 231. doi:10.1016/0039-6028(91)90084-6
36. Ukraintsev, V. A.; Long, T. J.; Harrison, I. *J. Chem. Phys.* **1992,** *96,* 3957. doi:10.1063/1.461898
37. Zhou, X.-L.; White, J. M. In *Laser spectroscopy and photochemistry on metal surfaces;* Dai, H.-L.; Ho, W., Eds.; Advanced Series in Physical Chemistry, Vol. 5; World Scientific: Singapore, 1995.
38. Vaida, M. E.; Bernhardt, T. M. *ChemPhysChem* **2010,** *11,* 804. doi:10.1002/cphc.200900920
39. Vaida, M. E.; Bernhardt, T. M. *Rev. Sci. Instrum.* **2010,** *81,* 104103. doi:10.1063/1.3488098
40. Gleitsmann, T.; Vaida, M. E.; Bernhardt, T. M.; Bonačić-Koutecký, V.; Bürgel, C.; Kuznetsov, A. E.; Mitrić, R. *Eur. Phys. J. D* **2007,** *45,* 477. doi:10.1140/epjd/e2007-00257-7
41. Wiley, W. C.; McLaren, I. H. *Rev. Sci. Instrum.* **1955,** *26,* 1150. doi:10.1063/1.1715212

Beilstein Journal of Nanotechnology

Optical properties of fully conjugated cyclo[*n*]thiophenes – An experimental and theoretical approach

Elena Mena-Osteritz[1], Fan Zhang[1], Günther Götz[1], Peter Reineker[2] and Peter Bäuerle[*1]

Full Research Paper

Open Access

Address:
[1]Institute of Organic Chemistry II and Advanced Materials, University of Ulm, Albert-Einstein-Allee 11, 89081 Ulm, Germany and [2]Institute of Theoretical Physics, University of Ulm, Albert-Einstein-Allee 11, 89081 Ulm, Germany

Email:
Elena Mena-Osteritz - elena.mena-osteritz@uni-ulm.de;
Fan Zhang - hamburgzhang@yahoo.de;
Günther Götz - guenther.goetz@uni-ulm.de;
Peter Reineker - peter.reineker@uni-ulm.de;
Peter Bäuerle* - peter.baeuerle@uni-ulm.de

* Corresponding author

Keywords:
conjugated macrocycles; Frenkel exciton model; oligothiophene; photophysical properties

Beilstein J. Nanotechnol. **2011,** *2,* 720–726.
doi:10.3762/bjnano.2.78

Received: 06 July 2011
Accepted: 30 September 2011
Published: 25 October 2011

This article is part of the Thematic Series "Organic–inorganic nanosystems".

Guest Editor: P. Ziemann

Abstract

Optical properties of two series of fully conjugated cyclo[*n*]thiophenes were analyzed experimentally and theoretically. The absorption spectra reveal a shift to higher wavelengths with increasing size of the cycles, which can be successfully described by an excitonic approach based on a Frenkel exciton Hamiltonian. Furthermore, intriguing new bands in the absorption and fluorescence spectra of the smaller macrocycles disclose the dominance of their ring strain.

Introduction

In the last few decades organic conjugated polymers and oligomers, in particular poly- and oligothiophenes, have attracted a broad interest due to their excellent electronic and transport properties in the solid state, which allow their application in a variety of organic-electronic devices, such as organic field-effect transistors, organic solar cells, and sensors [1-4]. Typically, such π-conjugated systems comprise extended linear one-dimensional (1D) structures showing interesting optoelectronic properties. In the solid state they represent organic semiconductors, whereas by doping with oxidants metallic states with higher conductivities can be achieved. For various series of 1D linear oligothiophenes, which, in contrast to their polydisperse polymeric counterparts, exhibit defined molecular structures, it was proven that the physical properties correlate well

with the length of the conjugated chain [5-8]. However, in particular for the shorter oligomers, end-effects imposed by the end groups perturb structure–property correlations, whereas for longer derivatives saturation of, e.g., optical transitions occurs leading to a limiting value. In this respect, 2D macrocyclic systems, cyclo[*n*]thiophenes (C*n*T) [9-11], which are shape-persistent and cyclically conjugated, were recently introduced by our group. They are not only theoretically most-interesting systems [12-16] providing an infinite π-conjugated chain like an idealized polymer, but they also represent a novel class of organic semiconductors without end-effects exhibiting fascinating optical [17-20] and self-assembling properties [21-23].

In a statistical macrocyclization approach under high-dilution conditions, the first cyclic representatives **C12T**, **C16T**, and **C18T** were prepared starting from terminally ethynylated terthiophenes, in only low yields and quantities, which is a general observation for the statistical synthesis of macrocycles [24-26]. Somewhat later, we developed a novel method using the same ethynylated oligothiophenes and Pt(II)-precursors as templates leading to stable coordinatively bound metallomacrocycles, which were transformed to the corresponding diacetylene-bridged macrocycles by elimination of the metal centers and simultaneous C–C bond formation. In a final step, the diacetylene units were subsequently transformed to thiophene units forming the final cyclothiophene. By this "metal–template approach", among other derivatives the series was extended to **C8T** as the smallest member and the overall yield was improved to around 10% [6,7]. More recently, by applying Pt(II)-oligothienyl complexes [27], a more direct general and highly effective "one-pot" synthesis of cyclo[*n*]thiophenes was developed. By using linear pentameric quinquethiophene **L5T** as a building block, a series of individual macrocycles C*n*T, from **C10T** to an unprecedented size up to **C35T**, was obtained in an excellent overall yield of around 60%. For the first time, C*n*Ts including members with an odd number of repeating units became available on a preparative scale. Thus, the following macrocycles were isolated and characterized: **C10T**, **C15T**, **C20T**, **C25T**, **C30T**, and **C35T** [28]. X-ray structural analysis of **C10T** and characterization of its charged states revealed an unusual polaron pair structure of doubly oxidized $\mathbf{C10T^{2+}}$ serving as a model for charged and conducting states in linear oligo- and polythiophenes [29].

In this article, we present and analyze optical data on two larger series of cyclo[*n*]thiophenes C*n*T, series I and series II, which differ in ring size and substitution pattern of the solubilizing butyl side chains. The obtained structure–property relationships were further analyzed by our theoretical model based on Frenkel exciton theory. The comparison of the experimental with the theoretical spectral parameters gave valuable insights into the electronic structure, because they correlate the monomer transition energy (ω_0), the magnitude of the electronic coupling between the thiophene monomers in the macromolecules (J), and the extent of the delocalized π-conjugated system [17].

Experimental

The solutions were freshly prepared with chloroform (Merck, UVASOL). UV–vis absorbance spectra were recorded on a Perkin-Elmer Lambda 19 spectrometer, and corrected fluorescence spectra were recorded on a Perkin-Elmer LS 55 under ambient conditions.

Results and Discussion

The macrocycles examined in this study are depicted in Scheme 1.

The first family of compounds (series I) is represented by alternately substituted thiophene units, every second unit having two butyl side chains in the ß-positions leading to highly symmetrical derivatives: **C8T**, **C12T**, **C16T**, and **C18T**. Due to the

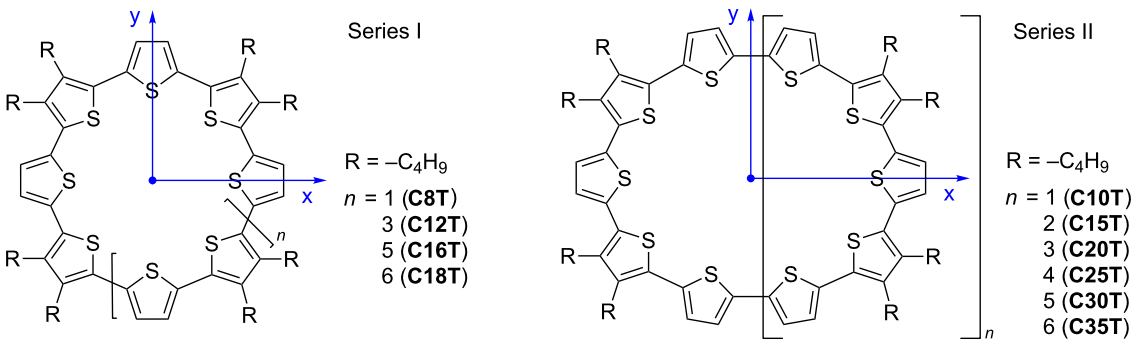

Scheme 1: Chemical structure of the oligothiophene macrocycles (series I and II). The coordinate system used in the theoretical description is included.

pentameric starting material **L5T** with dibutyl substitution at thiophenes 2 and 4, in series II a different alkyl chain substitution pattern resulted and allowed synthesis of macrocycles composed of an even or odd number of thiophene rings. Therefore, a much more extended series from **C10T** (cyclodimer) as the smallest member to **C35T** (cycloheptamer) as the largest was obtained.

The photophysical properties of the two series of macrocycles were analyzed by absorption and fluorescence spectroscopy. The data are summarized in Table 1. Two linear oligothiophenes, **L5T** and **L10T**, are included in the table as references having an identical substitution pattern to the macrocycles in series II. **L5T** is the building block used for the cyclization reactions and **L10T** the linear dimer.

Absorption spectra of the macrocycles in dichloromethane (DCM) at room temperature were characterized by several broad unstructured bands in the UV–vis region (Figure 1 and Figure 2).

In each series, the position of the low energy band, related to the π–π* transition of the macrocyclic systems, shifts on going from the smaller cycles to the larger ones. The absorption band (λ_{max} in Table 1) shifts to higher wavelengths with increasing number of thiophene units in the macrocycle ($\Delta\lambda$ = 25 nm and $\Delta\lambda$ = 28 nm in series I and II, respectively). The corresponding transition dipole lies in the molecular plane and is oriented almost parallel to the π-conjugated backbone, strongly dependent on the number of thiophene units composing the delocalized π-system, as in the case of the linear analogues [12].

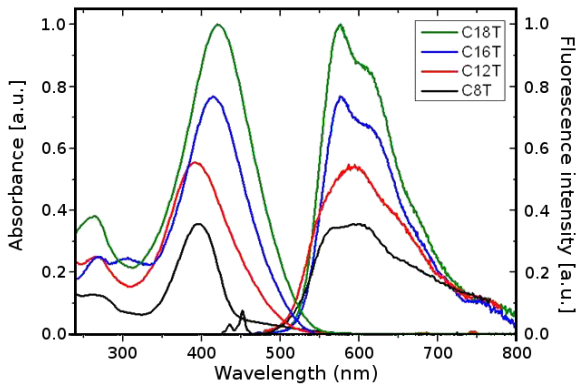

Figure 1: Absorption and fluorescence spectra of the macrocycles of Series I in dichloromethane (the excitation wavelength was chosen at the maximum of the absorption band).

Table 1: Photophysical data of the cyclothiophenes belonging to series I and II in comparison to the linear reference compounds. Maxima at the absorption and emission wavelengths, λ_{max}^{abs} and λ_{max}^{em} (absolute maximum underlined), the extinction coefficient ε and the normalized extinction coefficient (ε/N_r). **L5T** and **L10T** denote the linear homologues. Data of series II were taken from [28].

C*n*T series I	C*n*T series II	λ_{max}^{abs} [nm]([eV])[a]	ε [L·mol^{-1}·cm^{-1}][a]	ε/N_r [L·mol^{-1}·cm^{-1}][a] I	ε/N_r [L·mol^{-1}·cm^{-1}][a] II	λ_{max}^{em} [nm]([eV])[a]
8		396, ~500 (3.13, ~2.48)	51300	6413		435, 452 (2.85, 2.74) // 567, 602 (2.19, 2.06)
	10	417, ~500 (2.97, ~2.48)	86000		8600	~568, ~629, 685 (~2.18, ~1.97, 1.81)
12		392 (3.16)	55000	4583		~556, 593, ~660 (~2.23, 2.09, ~1.88)
	15	423 (2.93)	119000		7933	582, ~603 (2.13, ~2.06)
16		414 (3.00)	97000	6106		577, ~615 (2.15, ~2.02)
18		421 (2.95)	123000	6833		575, ~610 (2.16, ~2.03)
	20	434 (2.86)	130000		6500	572, ~603 (2.17, ~2.06)
	25	440 (2.82)	163000		6520	570, ~607 (2.18, ~2.04)
	30	444 (2.79)	183000		6100	568, 607 (2.18, 2.04)
	35	445 (2.79)	196000		5600	567, 604 (2.19, 2.06)
L5T		392 (3.16)	28000	5600		
L10T		435 (2.85)	51000	5100		553, ~587 (2.24, ~2.11)

[a]Solvent: Dichloromethane.

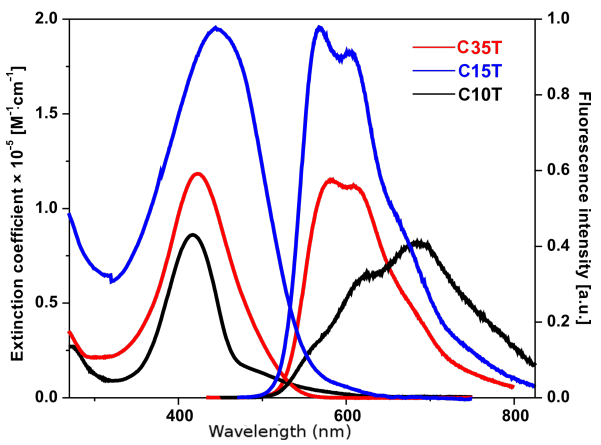

Figure 2: Representative absorption and fluorescence spectra of the smallest and largest macrocycles of series II in dichloromethane (taken from [28]). The excitation wavelength was chosen at the maximum of the absorption band.

Although a direct cross-correlation between the absorption of the two series seems inappropriate, the general trend shows that the macrocycles in series I absorb at higher energies than those of series II: **C15T** (λ_{max} = 423 nm) absorbs at a higher wavelength compared to the next higher macrocycle **C16T** (λ_{max} = 414 nm): The blue-shift of the absorption band in series I indicates slightly lower π-conjugation due to bigger distorsions of the thiophenes induced by steric interactions of the increased number of alkyl chains (8 versus 6 for **C16T** and **C15T**, respectively).

A closer look at the smallest macrocycles (**C8T** and **C10T**) reveals a weak, but clear absorption band at lower energies (~500 nm), which in the case of the bigger macrocycles is overlapped and covered by the stronger main absorption band (Figure 1 and Figure 2). Because the selection rules for the electronic transitions of cyclic molecules substantially differ from those of the linear homologues, the transition to the lowest excited state in the macrocycles, which appears at ~2.48 eV independently of the ring size, is not allowed, whereas the degenerate second transition (corresponding to the intense absorption band) is permitted and ring-size dependent (see above) [12]. Figure 3 shows a sketch of the possible electronic transitions depending on the macrocycle size and taking into account the relative energies of the involved ground and excited states. The lack of vibronic structure in the absorption bands of all macrocycles indicates a nonplanar delocalized π-system with more or less well-pronounced torsion angles between the thiophene rings. This is in accordance with the behavior of the linear oligomers, which as well show a more pronounced aromatic structure in their ground state.

In both series the extinction coefficient increases with increasing macrocyclic ring size, although the values for series I are smaller than for series II (Table 1 and Figure 4, also see below Equation 6 and Equation 7). This effect can be attributed to the already mentioned distinct substitution pattern for both series. The extinction coefficient versus number of thiophenes in the cycle for series II fits well to a linear trend (red curve in Figure 4) with a slope of 4428 L·mol^{-1}·cm^{-1} per thiophene. This value is much lower than the normalized extinction coefficients (ε value/N_T the number of thiophenes in the macrocycle) in this series, which decay linearly with the macrocycle size (Table 1) reaching the normalized value for the linear oligomers **L5T** and **L10T** (~5100 L·mol^{-1}·cm^{-1}). Due to this discrepancy, a better fit can be calculated taking the last value as a supplementary point into account: A second linear fit can be calculated for the smaller macrocycles (up to **C15T**) with a slope of 8058 L·mol^{-1}·cm^{-1}. Interestingly, the normalized extinction

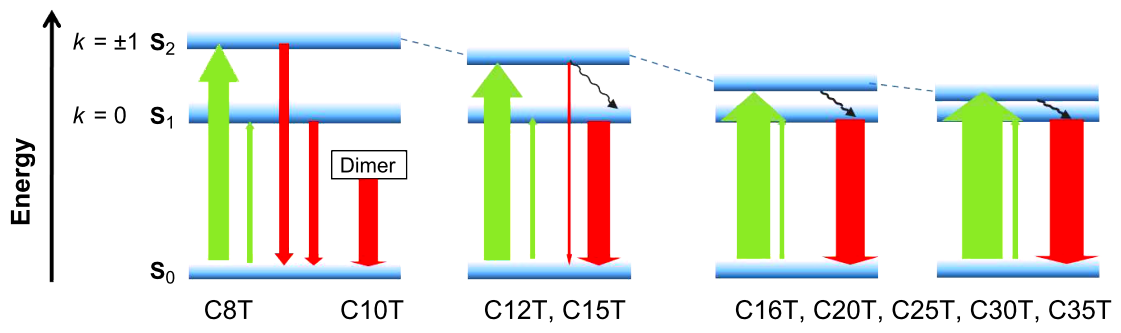

Figure 3: Sketch of the electronic transitions in the macrocycles: Ground state (S_0), first (S_1) and second (S_2) excited state. Plain arrows are weighted by the transition probability. The black wavy arrows represent nonradiative deactivation.

coefficient remains almost constant in series I (exception **C12T**) with a value of about 6500 L·mol^{-1}·cm^{-1}.

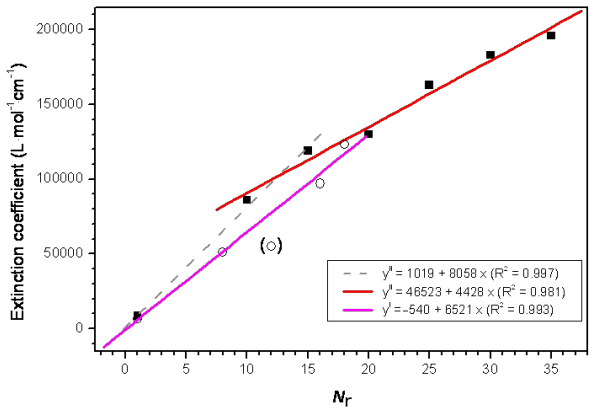

Figure 4: Extinction coefficient for the macrocycles of series I (circles) and II (squares) versus the number of thiophenes including the corresponding least-squares fit (y^I and y^{II}) for the fit function $\varepsilon = a + bN_r$. Compound **C12T** (circle in parentheses) was not included in the linear fit of series I.

The fluorescence spectra revealed a structured emission band, in which up to four vibronic contributions can be observed. In contrast to the discussed torsion of thiophene units in the ground state of the macrocycles, we assume that in the excited state the macrocyclic conjugated backbone tends to planarize reducing the torsional angles of the thiophene units and in accordance to the linear analogues tends to a more quinoidal structure.

The fluorescence spectra of the larger macrocycles are alike with respect to their shape and energy position with maxima at around 2.15 eV (series I) and 2.18 eV (series II). For the small macrocycles, however, striking differences concerning the emission-band shape emerge and new bands appear, pointing to a special behavior most probably related to the inherent ring strain in these smaller homologues. The most relevant features concern the appearance of a very weak fluorescence band in the case of **C8T** at ~450 nm and a more red-shifted emission in the case of **C10T**. The latter can be explained by the tendency of **C10T** to form dimers (excimers) in the excited state [29], which emit at lower energies with respect to the monomers (1.81 eV versus 2.18 eV). For the smallest cycle, **C8T**, we observe a weak structured emission band at much higher energy than the $S_0 \leftarrow S_1$ transition, whose origin can be attributed to the emission from the second excited state, S_2 (Figure 1, Table 1 and Figure 3). This double fluorescence behavior becomes possible because an incomplete energy transfer to the S_1 state occurs allowing partially the emission from the populated higher excited state S_2.

In a previous theoretical work we showed that the optical excitations of thiophene-based linear and cyclic oligomers can be described by Frenkel excitons, which are delocalized over the oligomeric π-system [12,30]. Concerning the macrocycles of series I and II, we assume, as a first approach, that the electronic excitations of a thiophene subunit can be described by two relevant energy levels corresponding to the HOMO and the LUMO level. We assume that the energies of these states and the transition-matrix elements are essentially unmodified by the side chains. The Hamiltonian of the model then reads

$$\begin{aligned} H_{\mathrm{ex}} &= \omega_0 \sum_{n=1}^{N_\mathrm{r}} |n\rangle\langle n| \\ &= -J \sum_{n=1}^{N_\mathrm{r}} \left(|n\rangle\langle n+1| + |n+1\rangle\langle n| \right), \end{aligned} \tag{1}$$

ω_0 is the excitation energy, N_r the number of thiophene units in the macrocycle, J describes the transfer of the excitation energy between neighboring thiophenes and $|n\rangle$ is the excited state at thiophene n. Throughout, we assume periodic boundary conditions, i.e., thiophenes 1 and N_r are nearest neighbors and complete the macrocyclic shape. The Schrödinger equation for this Hamiltonian can be represented as a difference equation. The energy eigenvalues and the eigenfunctions are given by the following expressions:

$$\begin{aligned} &E_k = \omega_0 - 2J \cos\left(\frac{2\pi}{N_\mathrm{r}} k\right), \\ &k = 0, \pm 1, \pm 2, \ldots, \begin{cases} \pm(N_\mathrm{r}-1)/2, & N_\mathrm{r} \text{ odd} \\ +N_\mathrm{r}/2, & N_\mathrm{r} \text{ even} \end{cases} \end{aligned} \tag{2}$$

$$|\psi_k\rangle = \sum_{m=1}^{N_\mathrm{r}} D_k(m) |m\rangle, \tag{3}$$

$$D_k(m) = \frac{1}{\sqrt{N_\mathrm{r}}} \exp\left(\mathrm{i} \frac{2\pi}{N_\mathrm{r}} km \right). \tag{4}$$

The allowed optical transitions between the ground state $|0\rangle$ and the excited states (3) with energies given by (2) are determined by the matrix elements of the ring dipole operator:

$$\vec{\mu} = \sum_{n=1}^{N_\mathrm{r}} \vec{\mu}_n \left(|0\rangle\langle n| + |n\rangle\langle 0| \right). \tag{5}$$

Here $\vec{\mu}_n$ is the local optical dipole moment between the molecular ground and excited states. We assume that these dipole moments can have a component $\mu_{\parallel}$ parallel to the z-axis and a component $\mu_{\perp}$ perpendicular to the z-axis, i.e., lying in the ring plane (x–y plane) and oriented in a tangential manner around the ring (Scheme 1) [31].

The evaluation of the z-component of the ring dipole moment μ_z for the case that all molecular dipole moments $\mu_{||}$ are equal results in the following selection rule:

$$\left|\langle 0|\mu_z|k\rangle\right|^2 = \mu_{||}^2 N_r \delta_{k,0} \quad (6)$$

For the evaluation of the x-component of the ring dipole moment μ_x we again assume that the molecular dipole moments have the same $\mu_\perp$. However, the in-plane component for each molecule is oriented parallel to the ring tangent and thus its orientation is shifted by $2\pi/N_r$ as compared to those of the neighboring molecules. The evaluation of the dipole moment operator gives in this case

$$\left|\langle 0|\mu_x|k\rangle\right|^2 = \mu_\perp^2 \frac{N_r}{4}\left(\delta_{k,-1} + \delta_{k,1}\right) \quad (7)$$

According to Equation 2 the two selection rules (Equation 6 and Equation 7) result in two different absorption lines, which agrees with our experimental finding of two absorption bands, more clearly observed for the small macrocycles. The first transition given for the component of the dipole moment perpendicular to the x–y plane has the selection rule $k = 0$ and their energy reads $E_k = \omega_0 - 2J$, independent of the macrocycle size. The line position given for the component of the dipole moment in the x–y plane has the selection rule $k = \pm 1$ and the line position reads $E_k = \omega_0 - 2J\cos(2\pi/N_r)$. In the fit, using a least-squares procedure in the Maple software, we determine the parameters ω_0 and J, related to the monomer transition energy (ω_0) and the coupling energy between thiophene units (J). The results of the fit (in eV) are shown in Figure 5. The values corresponding to the smallest macrocycles in both series (**C8T** and **C10T**) were not included in the fitting, because of their evident deviation from the general trend. The reason for this behavior might be the ring strain of the macrocycle and the torsion that the individual thiophene rings experience due to their small ring size. This guess is supported by geometry calculations for **C8T** and X-ray structure analysis for **C10T** [10,29].

The macrocycles show an energetic decrease of their line positions, i.e., an increase of their wavelengths, with increasing ring size, which can be successfully described by Equation 2 and was observed experimentally. The circles show the experimental line positions of the macrocycle series I, and the squares show those of series II. The parameters of the fit are $\omega_0^{I} = 5.713$ eV, and $J^{I} = 1.472$ eV (series I, excluding **C8T**), and $\omega_0^{II} = 4.853$ eV, and $J^{II} = 1.051$ eV (series II, excluding **C10T**). We must stress here that the parameters obtained for the fit to series I should be treated with care because of the low number of macrocycles in the series (3 elements). The difference between the ω_0 values can be attributed to the limitation of the theory, which does not take into account the thiophene substitution pattern. For comparison, the parameters obtained for the homologous linear oligomers are $\omega_0 = 5.5$ eV and $J = 1.3$ eV [30]. Because of the strong sensitivity of the fit to the ω_0 parameter, a better comparison can be performed by applying the well-established linear ω_0 parameter to the two cyclic series, using it as a fixed value in the fitting and comparing the obtained coupling constants. These amount to $J^{I} = 1.355$ eV and $J^{II} = 1.388$ eV and reveal a slightly better electronic coupling for macrocycles of series II and therefore a reduced transition energy, which agrees with the experimentally red-shifted absorption of this series as compared to series I.

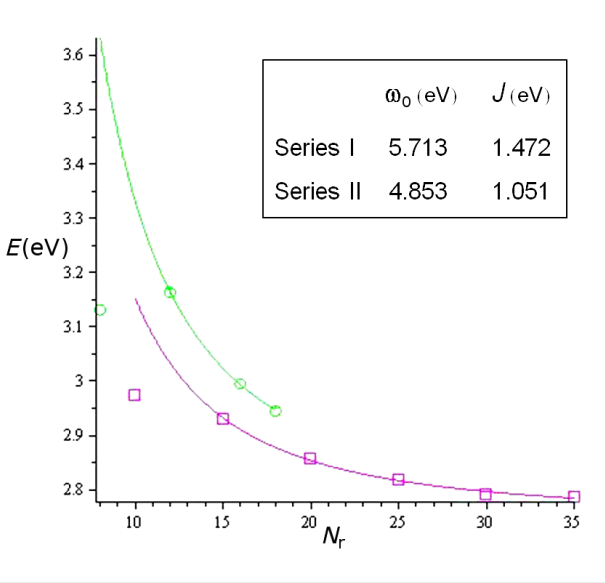

Figure 5: Diagram of the energy of the absorption band (eV) versus the number of thiophenes in the macrocycles of series I (circles) and II (squares), including the least-squares fit to Equation 2.

The experimentally observed linear increase of the extinction coefficients with increasing ring size (Figure 4) was also predicted by Equation 6 and Equation 7, confirming that the electronic excitation is distributed along the ring. These findings strongly corroborate the description of the electronic excitations by the model based on Frenkel excitons, despite the limitations assumed in this approach. A series of improvements of the model can be adopted in the future.

Conclusion

Oligothiophene macrocycles exhibit interesting photophysical properties. Due to the ring geometry, the electronic transitions follow distinct selection rules and the transition dipoles are mainly arranged in the macrocycle plane. Similar to the behaviour of linear oligomers, the absorption maxima positions

tended towards a fixed value with increasing size of the macrocycle. The size-dependent effects on the absorption spectra (energy and extinction coefficient) can be described in the framework of a Frenkel exciton theory. The small macrocycles show most interesting photophysical behaviour (dual fluorescence), mostly due to their strong ring strain.

Acknowledgements

The authors gratefully acknowledge the financial support of the Deutsche Forschungsgemeinschaft within the collaborative research center SFB 569.

References

1. Fichou, D., Ed. *Handbook of Oligo- and Polythiophenes;* Wiley-VCH: Weinheim, Germany, 1999.
2. Bäuerle, P. *Electronic Materials: The Oligomer Approach*. Müllen, K.; Wegner, G., Eds.; Wiley-VCH: Weinheim, Germany, 1998; pp 105–197.
3. Roncali, J. *Chem. Rev.* **1997,** *97,* 173. doi:10.1021/cr950257t
4. Mishra, A.; Ma, C.-Q.; Bäuerle, P. *Chem. Rev.* **2009,** *109,* 1141. doi:10.1021/cr8004229
5. Kirschbaum, T.; Bäuerle, P. *Synth. Met.* **2001,** *119,* 127. doi:10.1016/S0379-6779(00)01206-6
6. Kirschbaum, T.; Azumi, R.; Mena-Osteritz, E.; Bäuerle, P. *New J. Chem.* **1999,** *23,* 241. doi:10.1039/A808026G
7. Mitschke, U.; Mena-Osteritz, E.; Debaerdemaeker, T.; Sokolowski, M.; Bäuerle, P. *Chem.–Eur. J.* **1998,** *4,* 2211. doi:10.1002/(SICI)1521-3765(19981102)4:11<2211::AID-CHEM2211>3.3.CO;2-Z
8. Bäuerle, P.; Fischer, T.; Bidlingmeier, B.; Rabe, J. P.; Stabel, A. *Angew. Chem., Int. Ed.* **1995,** *34,* 303. doi:10.1002/anie.199503031
9. Krömer, J.; Rios-Carreras, I.; Fuhrmann, G.; Musch, C.; Wunderlin, M.; Debaerdemaeker, T.; Mena-Osteritz, E.; Bäuerle, P. *Angew. Chem., Int. Ed.* **2000,** *39,* 3481. doi:10.1002/1521-3773(20001002)39:19<3481::AID-ANIE3481>3.0.CO;2-O
10. Fuhrmann, G.; Debaerdemaeker, T.; Bäuerle, P. *Chem. Commun.* **2003,** 948. doi:10.1039/b300542a
11. Fuhrmann, G. Synthesis and Characterization of Oligothiophene – based Fully π-Conjugated Macrocycles. Ph.D. Thesis, University of Ulm, Ulm, Germany, 2006.
12. Zade, S. S.; Bendikov, M. *J. Org. Chem.* **2006,** *71,* 2972. doi:10.1021/jo0525229
13. Fomine, S.; Guadarrama, P. *J. Phys. Chem. A* **2006,** *110,* 10098. doi:10.1021/jp063065i
14. Fabian, J.; Hartmann, H. *J. Phys. Org. Chem.* **2007,** *20,* 554. doi:10.1002/poc.1203
15. Fomine, S.; Guadarrama, P.; Flores, P. *J. Phys. Chem. A* **2007,** *111,* 3124. doi:10.1021/jp0677750
16. Flores, P.; Guadarrama, P.; Ramos, E.; Fomine, S. *J. Phys. Chem. A* **2008,** *112,* 3996. doi:10.1021/jp710654k
17. Bednarz, M.; Reineker, P.; Mena-Osteritz, E.; Bäuerle, P. *J. Lumin.* **2004,** *110,* 225. doi:10.1016/j.jlumin.2004.08.013
18. Casado, J.; Hernández, V.; Ponce Ortiz, R.; Ruiz Delgado, M. C.; López Navarrete, J. T.; Fuhrmann, G.; Bäuerle, P. *J. Raman Spectrosc.* **2004,** *35,* 592. doi:10.1002/jrs.1202
19. Bhaskar, A.; Ramakrishna, G.; Hagedorn, K.; Varnavski, O.; Mena-Osteritz, E.; Bäuerle, P.; Goodson, T., III. *J. Phys. Chem. B* **2007,** *111,* 946. doi:10.1021/jp066766o
20. Varnavski, O.; Bäuerle, P.; Goodson, T., III. *Opt. Lett.* **2007,** *32,* 3083. doi:10.1364/OL.32.003083
21. Mena-Osteritz, E.; Bäuerle, P. *Adv. Mater.* **2001,** *13,* 243. doi:10.1002/1521-4095(200102)13:4<243::AID-ADMA243>3.0.CO;2-X
22. Mena-Osteritz, E. *Adv. Mater.* **2002,** *14,* 609. doi:10.1002/1521-4095(20020418)14:8<609::AID-ADMA609>3.0.CO;2-7
23. Mena-Osteritz, E.; Bäuerle, P. *Adv. Mater.* **2006,** *18,* 447. doi:10.1002/adma.200501575
24. Mayor, M.; Didschies, C. *Angew. Chem., Int. Ed.* **2003,** *42,* 3176. doi:10.1002/anie.200250763
25. Jung, S.-H.; Pisula, W.; Rouhanipour, A.; Räder, H. J.; Jacob, J.; Müllen, K. *Angew. Chem., Int. Ed.* **2006,** *45,* 4685. doi:10.1002/anie.200601131
26. Nakao, K.; Nishimura, M.; Tamachi, T.; Kuwatani, Y.; Miyasaka, H.; Nishinaga, T.; Iyoda, M. *J. Am. Chem. Soc.* **2006,** *128,* 16740. doi:10.1021/ja067077t
27. Zhang, F.; Bäuerle, P. *J. Am. Chem. Soc.* **2007,** *129,* 3090. doi:10.1021/ja070083k
28. Zhang, F.; Götz, G.; Winkler, H. D. F.; Schalley, C. A.; Bäuerle, P. *Angew. Chem., Int. Ed.* **2009,** *48,* 6632. doi:10.1002/anie.200900101
29. Zhang, F.; Götz, G.; Mena-Osteritz, E.; Weil, M.; Sarkar, B.; Kaim, W.; Bäuerle, P. *Chem. Sci.* **2011,** *2,* 781. doi:10.1039/c0sc00560f
30. Bednarz, M.; Reineker, P.; Mena-Osteritz, E.; Bäuerle, P. *Chem. Phys.* **2007,** *342,* 191. doi:10.1016/j.chemphys.2007.09.052
31. Bednarz, M.; Knoester, J. *J. Phys. Chem. B* **2001,** *105,* 12913. doi:10.1021/jp012371n

License and Terms

Beilstein Journal of Nanotechnology

STM study on the self-assembly of oligothiophene-based organic semiconductors

Elena Mena-Osteritz*[1], Marta Urdanpilleta[1,2], Erwaa El-Hosseiny[1], Berndt Koslowski[3], Paul Ziemann[3] and Peter Bäuerle[1]

Full Research Paper

Open Access

Address:
[1]Institute of Organic Chemistry II and Advanced Materials, Ulm University, Albert-Einstein-Allee 11, D 89081 Ulm, Germany, [2]Department of Applied Physics, University of the Basque Country (UPV/EHU), Plaza de Europa, 1, 20018 Donostia - San Sebastián, Spain and [3]Department of Solid State Physics, Ulm University, Albert-Einstein-Allee 11, D 89081 Ulm, Germany

Email:
Elena Mena-Osteritz* - elena.mena-osteritz@uni-ulm.de; Marta Urdanpilleta - marta.urdanpilleta@ehu.es; Berndt Koslowski - berndt.koslowski@uni-ulm.de; Paul Ziemann - paul.ziemann@uni-ulm.de; Peter Bäuerle - peter.baeuerle@uni-ulm.de

* Corresponding author

Keywords:
2-D crystals; functionalized oligothiophenes; H-bonding; intermolecular interaction; scanning tunneling microscopy

Beilstein J. Nanotechnol. **2011,** *2,* 802–808.
doi:10.3762/bjnano.2.88

Received: 28 June 2011
Accepted: 20 November 2011
Published: 07 December 2011

This article is part of the Thematic Series "Organic–inorganic nanosystems".

Associate Editor: U. D. Schwarz

Abstract

The self-assembly properties of a series of functionalized regioregular oligo(3-alkylthiophenes) were investigated by using scanning tunneling microscopy (STM) at the liquid–solid interface under ambient conditions. The characteristics of the 2-D crystals formed on the (0001) plane of highly ordered pyrolitic graphite (HOPG) strongly depend on the length of the π-conjugated oligomer backbone, on the functional groups attached to it, and on the alkyl substitution pattern on the individual thiophene units. Theoretical calculations were performed to analyze the geometry and electronic density of the molecular orbitals as well as to analyze the intermolecular interactions, in order to obtain models of the 2-D molecular ordering on the substrate.

Introduction

In the last few decades conjugated organic polymers and oligomers have attracted a broad interest due to their excellent electronic and transport properties in the solid state, which allow their application in a variety of organic-electronic devices [1]. Among others, organic semiconductors based on thiophenes are very promising materials in the field, because of their superior stability and the possibility to chemically functionalize them without affecting their electronic properties. The most prominent example is given by the regioregular (head-to-tail-coupled) poly(3-hexylthiophene), which is among the best-performing photoactive materials in polymer solar cells [2-4]. The self-organization of the polymer chains in the bulk seems to

be a key factor, which determines the efficiency of the charge transport through the material and ultimately the performance in organic-electronic devices. In recent years, various approaches have been followed to elucidate the ordering principles of conjugated polymers, by X-ray diffraction and scanning tunneling microscopy. Valuable information about intermolecular interactions taking place on substrates has been obtained [5-7].

Although the substitution pattern is regioregular and chemically controlled, the inherent chain length dispersity of poly(3-alkylthiophenes) leads to a mesoscopic structure of the resulting films, which are composed of polycrystalline domains embedded in a disordered matrix [7]. Furthermore, the knowledge of clear structure–property relationships, connecting the physical properties with the length of the conjugated system, and the recent success in the field of small-molecule organic devices have restored huge interest in structurally well-defined and therefore monodisperse, crystalline oligomers [8].

The method of choice to investigate the ordering of organic semiconductors adsorbed on flat metallic surfaces, at the desired molecular level in the subnanometer range, is scanning tunneling microscopy (STM). With this method, the self-assembly of oligo- and polythiophenes on surfaces has been successfully investigated in the last few years [5,6,9-14]. The 2-D crystalline arrangement on surfaces is a result of a delicate balance between several weak intermolecular van der Waals forces and molecule–substrate interactions, as well as intermolecular hydrogen bonding in the case of functionalized oligothiophenes [15-17]. The typical flat metallic substrates (HOPG, Au(111), Ag(111), etc.) employed in STM differ from the ITO electrodes used in the devices, which are usually rendered flat by an organic hole-transporting layer. Despite the differences, a good approach to elucidate the bulk properties of the active molecules is to probe their intermolecular interactions on nonreactive substrates, such as HOPG, by means of STM.

In this paper, we report the investigation of the self-assembly properties of a series of carbonic acid functionalized regioregular (head-to-tail-coupled) oligo(3-hexylthiophenes) on HOPG at the liquid–solid interface as examined by STM at room temperature. The ambient and environmental conditions employed in this study are essential in order to mimic the deposition conditions for real devices. Supported by quantum-chemical calculations, the interpretation of the STM images and the analysis of the intermolecular forces will be highlighted.

Results and Discussion

The molecules analyzed in this study, carboxylic acid-functionalized regioregular oligo(3-hexylthiophenes), **H*n*TCOOH**, are sketched in Figure 1. The π-conjugated system, comprising the aromatic thiophene rings and being responsible for the electronic properties of the molecule, extends from 4 to 12 thiophene repeating units, and the molecular size stretches accordingly from 1.7 nm to 5.4 nm. The carboxylic acid group (**COOH**) at the terminal α-position of the oligothiophene backbone allows the formation of effective intermolecular hydrogen bonding through dimer formation. The regioregular hexyl-side-chain substitution pattern enhances the solubility of the compounds in organic solvents and their crystallinity on the substrate.

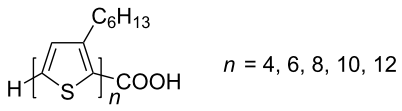

Figure 1: General formula of carboxylic acid functionalized oligothiophenes **H*n*TCOOH**.

Figure 2 shows a large-scale STM image of a monolayer of tetramer **H4TCOOH** adsorbed at the solution–HOPG interface. Several terraces of the graphite substrate are visible in the image. On the terraces, a very well ordered monolayer of **H4TCOOH** can be seen extending over the micrometer range.

In the first images after deposition, several domains with sizes ranging from tens to hundreds of nanometers can be recognized. In Figure 2 (left) four out of six possible domains (labeled “A” to “D”) can be seen. The six domains correspond to the two enantiomorphic molecular arrangements (with a relative angle of 10°) combined with the three crystallographic axes of the underlying HOPG substrate. In Figure 2 (left) “A” and “C” correspond to two orientations (at an angle of 120°) of the same enantiomorph, as do “B” and “D”.

The molecules are lying flat on the nonreactive HOPG surface. The oligothiophene backbone carrying the delocalized π-electron system is recognized in STM images as bright spots under the given scanning conditions, which correspond to a higher tunneling probability. On the contrary, the alkyl side chains, corresponding to the insulating part of the molecules, are extended perpendicular to the oligothiophene backbone and can be recognized as dark regions, reflecting the expected lower tunneling probability.

Figure 2 (center) shows a short range image of **H4TCOOH** adsorbed on HOPG, exhibiting submolecular resolution. The unit cell contains two molecules and the cell parameters are $a = 3.6 \pm 0.1$ nm, $b = 2.1 \pm 0.1$ nm and $\alpha = 42 \pm 2°$ (Table 1).

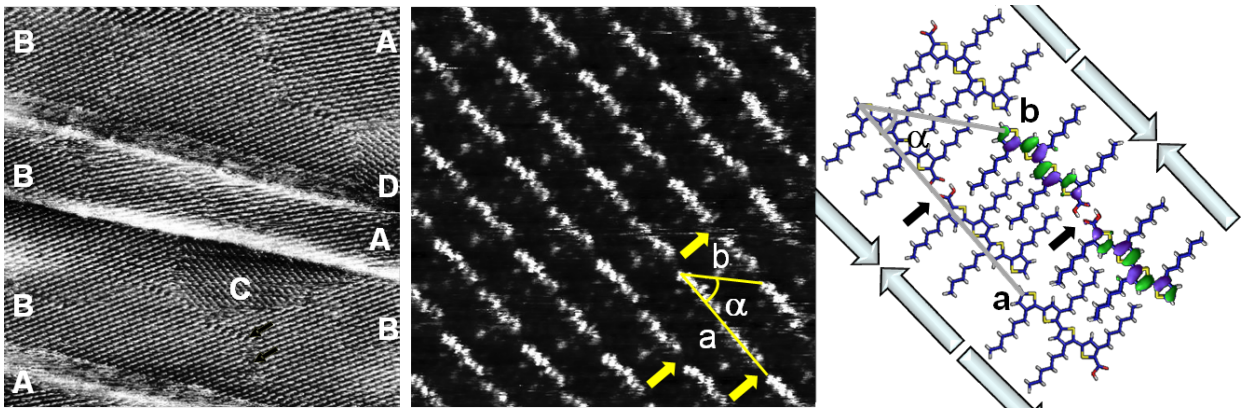

Figure 2: Left: STM image of **H4TCOOH** on HOPG (100 × 100 nm^2, U = −120 mV, I = 50 pA). The letters label the different domains as explained in the text. Center: STM current image of **H4TCOOH** on HOPG (10 × 10 nm^2, U = −100 mV, I = 50 pA). The arrows label the positions of the carboxylic groups. Right: Quantum chemical model of the adsorbate, including the electron-density distribution of the HOMO and HOMO−1 for the dimer.

The molecules are ordered in lamellae with an interlamellar distance of 1.4 nm. This value correlates very well with data published for ordered monolayers of hexyl-substituted oligo- and polythiophenes and can be explained by van der Waals interaction driven full interdigitation of the alkyl chains of two opposite molecules in their all-*trans* conformation in different rows [9-12,18].

Theoretical calculations on a group of four molecules, excluding the substrate, support the dimer formation and are in very good agreement with the observed unit-cell parameters, with a = 3.6 ± 0.1 nm, b = 2.1 ± 0.1 nm and α = 39 ± 1° (Figure 2, right, and Table 1). In the lamellae the molecules form an angle of 8° between the molecular axis and the row direction. The two molecules building the pair are separated by small regions of low tunneling current (labeled with an arrow in Figure 2, center), which we assign to the carboxylic acid ends of two **H4TCOOH** molecules in a head-to-head arrangment. It is widely observed in STM images that carboxylic acid groups appear as dark spots under negative bias [19,20]. Our theoreti-

Table 1: STM and theoretical parameters of 2-D crystals of the investigated carboxylic acid functionalized oligothiophenes H*n*TCOOH.

Compound	Molecular and Lattice Parameters	STM	Calculations
H4TCOOH	Molecule length [nm]	1.7	1.8
	a [nm]	3.6	3.6
	b [nm]	2.1	2.1
	α [°]	42	39
H6TCOOH	Molecule length [nm]	2.6	2.6
	a [nm]	5.3	5.4
	b [nm]	3.0	2.9
	α [°]	29	27
H8TCOOH	Molecule length [nm]	3.5	3.4
	a [nm]	7.0	6.8
	b [nm]	3.8	3.7
	α [°]	21	22
H10TCOOH	Molecule length [nm]	4.3	4.2
	a [nm]	9.0	8.5
	b [nm]	4.2	4.5
	α [°]	19	18
H12TCOOH	Molecule length [nm]	4.6	4.7
	a [nm]	9.6	9.5
	b [nm]	4.9	4.9
	α [°]	17	16

cal calculations support the experimental findings (Figure 2, right), showing no contribution of the end-function to the occupied frontier orbitals (HOMO and HOMO−1) close to the Fermi level. This arrangement stabilizes the monolayer by neutralizing the dipole moments of the molecules, which are oriented along the molecular axis (Figure 2, right; plain arrows). The carboxylic acid groups of two head-to-head arranged molecules are able to undergo hydrogen-bond formation, additionally stabilizing the monolayer (Figure 2, right).

In the current image (Figure 2, center) submolecular resolution was obtained for the oligothiophene backbones. Due to the low negative bias applied and at the limit given by the tunneling barrier of this compound, we can assume that the observed eight lobes per molecule correspond to the local density of states (LDOS) of the molecule, which are very close to the Fermi level and are coupled, at this bias, to an almost anisotropic contribution from the LDOS of the substrate.

In Figure 3, STM images of a 2-D crystal of the next higher homologue, hexamer **H6TCOOH**, are depicted. Figure 3, left, shows a large-scale STM image of a densely packed monolayer. The molecules are perfectly arranged in lamellae and two domains (out of six possibilities, see above) can be observed. The lamellae are separated by about 1.3 nm, like in the case of **H4TCOOH.** In these regions the insulating hexyl chains interdigitate (Figure 3, right). Despite a high degree of crystallinity, the monolayer reveals a few defects (Figure 3, left), which are noticeable as faint depressions, probably related to molecules adsorbed at unstable sites. Adsorption and desorption processes equilibrating at the liquid–solid interface induce, in turn after 10–20 minutes, a self-healing process to form a perfectly ordered monolayer over several micrometers.

Figure 3 (center) shows a small-scale image of a single domain. The molecular resolution allows the determination of the unit-cell parameters: a = 5.3 ± 0.1 nm, b = 3.0 ± 0.1 nm and α = 29 ± 2°. In the unit cell two molecules arrange as a dimer, with their carboxylic acid functional groups facing each other due to H-bonding, like in the case of **H4TCOOH**. With the help of theoretical calculations a model of the molecular packing can be obtained (Figure 3, right). The unit-cell parameters are calculated to be a = 5.4 nm, b = 2.9 nm, and α = 27° in very good agreement with the experimental data. The plain arrows depicted in the model show that this molecular arrangement allows the full neutralization of the molecular dipoles within the plane.

In Figure 4 and Figure 5, STM images of compounds **H8TCOOH** and **H10TCOOH** adsorbed at the HOPG surface are shown. The large-scale images (Figure 4 and Figure 5, left) reveal monolayers with different orientations (see above). The STM image of octamer **H8TCOOH** was taken immediately after adsorption and therefore reveals an increased number of vacancies relative to monolayers of the shorter oligomers. This phenomenon can be explained by a decrease in diffusivity as the size of the oligomers increase. However, the adsorption–desorption dynamics at the surface and the observed Ostwald ripening [21,22] lead to an almost perfect monolayer with time. The arrangement of the molecules reveals a more columnar than lamellar ordering, although after careful analysis, the dimer formation can also be determined for these long oligomers (Figure 4 and Figure 5, center). The unit cell calculated for the crystalline regions of **H8TCOOH** and **H10TCOOH** monolayers contains two molecules and the parameters correlate very well with the quantum-chemical model displayed in Figure 4 and Figure 5, right, and in Table 1. The more extended π-system of **H8TCOOH** and **H10TCOOH** induces a face-to-face molecular arrangement with a negligible offset and therefore a more columnar structure. The distance between the columns amounts to 1.3 nm and the space is filled by interdigitating alkyl chains (Figure 4 and Figure 5, right).

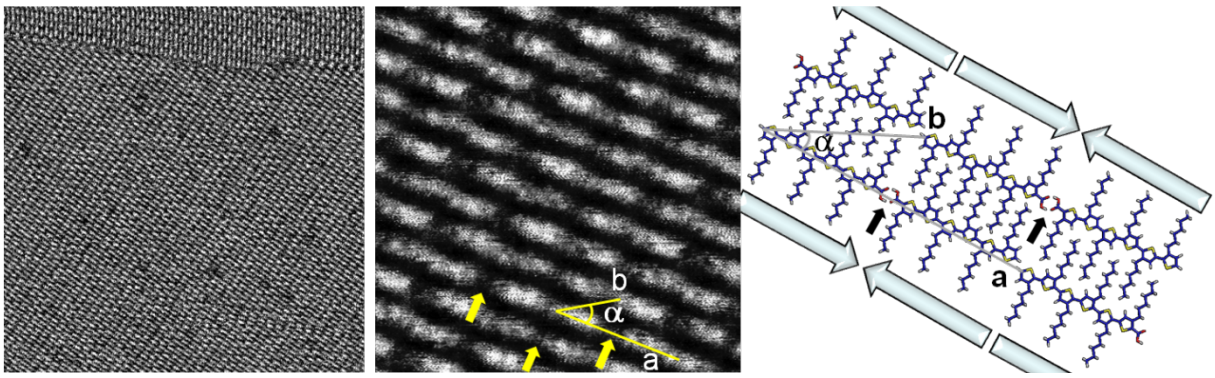

Figure 3: STM image of **H6TCOOH**. Left: 70 × 70 nm^2, U = −360 mV, I = 50 pA. Center: 20 × 20 nm^2, U = −361 mV, I = 50 pA. Right: Theoretical model. The small black arrows emphasize the H-bonding position. The big arrows indicate the orientation of the molecular dipole moments.

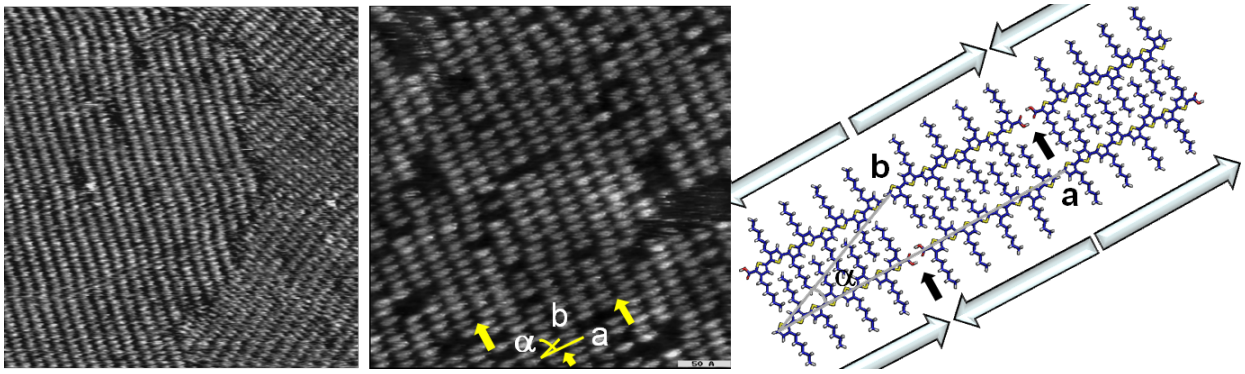

Figure 4: STM images of **H8TCOOH**. Left: 60 × 60 nm^2, *U* = −640 mV, *I* = 44 pA. Center: 30 × 30 nm^2, *U* = −725 mV, *I* = 35 pA. Right: Theoretical model. The small black arrows indicate the H-bonds. The big arrows show the orientation of the molecular dipole moments.

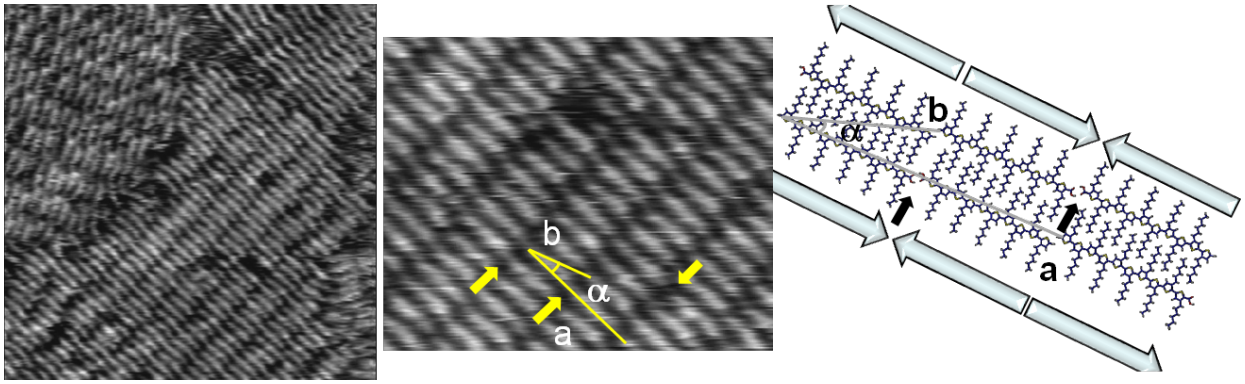

Figure 5: STM images of **H10TCOOH**. Left: 50 × 50 nm^2, *U* = −200 mV, *I* = 73 pA. Center: 24 × 19 nm^2, *U* = −100 mV, *I* = 22 pA. Right: Theoretical model. The small black arrows point out the H-bonding position. The big arrows show the orientation of the molecular dipole moments.

The 2-D crystal of the longest oligomer, **H12TCOOH**, is shown in Figure 6, left. A densely packed monolayer can be seen. One can easily recognize the molecules, which are arranged in columns and domains related to the crystallographic axes of the HOPG substrate. The columns are not perfectly straight, in contrast to the stacks of derivatives

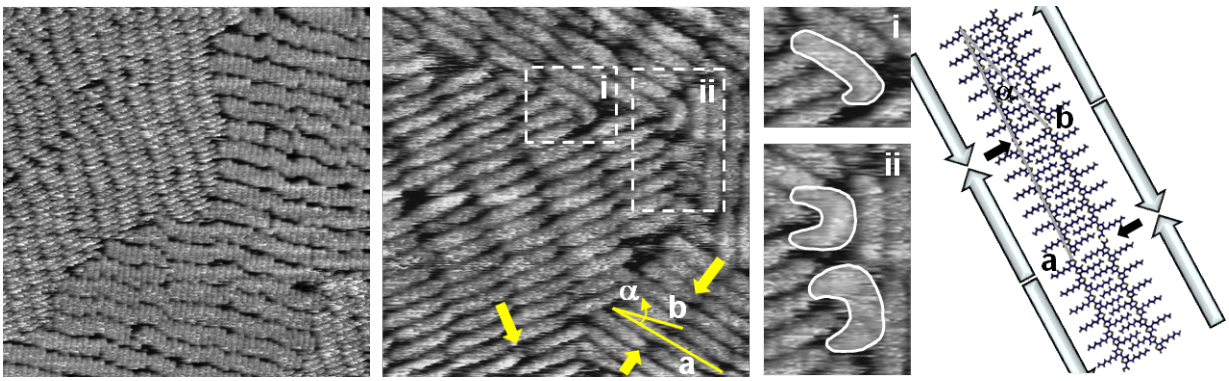

Figure 6: STM images of **H12TCOOH**. Left: 80 × 80 nm^2, *U* = −200 mV, *I* = 73 pA. Center: 20 × 20 nm^2, *U* = −750 mV, *I* = 68 pA. Details of the regions in the dashed rectangles are given in (i) and (ii). Right: Theoretical model. The small black arrows point out the H-bonding position. The big arrows show the orientation of the molecular dipole moments.

H8TCOOH and **H10TCOOH**, due to several possibilities for an offset in the pseudo face-to-face arrangement of the long **H12TCOOH** molecules.

In the small-scale STM images of **H12TCOOH** some very interesting effects can be seen (Figure 6, center). At the domain boundaries, molecules in a nonlinear, bent shape can be distinguished (Figure 6, center right (i) and (ii)). In order to fill the space between the domains, the adsorbed molecules partially change their conformation from the usual linear shape to a crescent shape. In Figure 6, center right (i), the five terminal thiophenes are arranged in a *syn*-conformation causing the observed hairpin bend. In Figure 6, center right (ii), an oligomer conformation, in which several thiophene units are in *syn*-arrangement, seems to be responsible for the observed crescent shape of the adsorbed **H12TCOOH** molecules. The hairpin conformation was already observed for corresponding regioregular poly(3-alkylthiophenes) adsorbed on a HOPG surface [5], but for an oligothiophene this behavior is shown here for the first time. More detailed analysis on the adsorption conformation at different solution concentrations of all the oligomers presented in this communication reveals that only the longest oligothiophene, **H12TCOOH**, changes the typical all-*anti* conformation to *syn*-containing ones at the domain boundaries. X-ray structure analyses on different series of alkylated oligothiophenes [12,18] have shown that, with a unique exception, smaller oligomers throughout prefer an all-*anti* conformation [23], whereas for longer oligomers *syn*-conformations at the terminal thiophene units typically seem to be more favored.

Conclusion

The self-assembling properties of a series of regioregularly alkylated oligothiophenes on HOPG were studied by STM at the solid–liquid interface. The experimental unit-cell parameters were compared with the results of quantum chemical calculations and a very good agreement was found. This result demonstrates a major contribution of intermolecular van der Waals and H-bonding interactions to the stabilization of the monolayer on the HOPG surface. Conformational changes of the **H12TCOOH** molecules at the domain boundaries of the adsorbate were shown for the first time for self-assembling oligothiophenes. This effect appears to be closely related to the already known hairpin conformation of the related regioregular poly(3-alkylthiophenes).

Experimental

The solutions were freshly prepared with 1,2,4-trichlorobenzene (Aldrich). STM measurements were carried out under ambient conditions with a low-current STM (RHK Rochester Hills, Michigan, USA) equipped with an STM 1000 control system. Details concerning the set-point current and bias applied are given in the figure captions. Mechanically cut Pt/Ir (80/20) tips were used. For the measurements at the solution–substrate interface, a solution of the compound in 1,2,4-trichlorobenzene was applied onto a freshly cleaved (0001) face of highly oriented pyrolytic graphite (HOPG). Measurements were repeated with different tips and different samples to confirm reproducibility and to ensure that the images were not affected by tip and sample artifacts. Theoretical calculations were performed on a semi-empirical basis with the Austin Model 1 (AM1) and the Parameterized Model 3 (PM3) by using the Hyperchem (Hypercube, Inc., FL) software package. No constraints or annealing simulations were applied.

Acknowledgements

The authors gratefully acknowledge the financial support of the Deutsche Forschungsgemeinschaft within the collaborative research unit SFB 569.

References

1. Fichou, D. *Handbook of Oligo- and Polythiophenes;* Wiley-VCH: Weinheim, Germany, 1999.
2. Sirringhaus, H.; Brown, P. J.; Friend, R. H.; Nielsen, M. M.; Bechgaard, K.; Langeveld-Voss, B. M. W.; Spiering, A. J. H.; Janssen, R. A. J.; Meijer, E. W.; Herwig, P.; de Leeuw, D. M. *Nature* **1999,** *401,* 685–688. doi:10.1038/44359
3. Sirringhaus, H.; Tessler, N.; Friend, R. H. *Science* **1998,** *280,* 1741–1744. doi:10.1126/science.280.5370.1741
4. Ong, B. S.; Wu, Y.; Liu, P.; Gardner, S. *Adv. Mater.* **2005,** *17,* 1141–1144. doi:10.1002/adma.200401660
5. Mena-Osteritz, E.; Meyer, A.; Langeveld-Voss, B. M. W.; Janssen, R. A. J.; Meijer, E. W.; Bäuerle, P. *Angew. Chem., Int. Ed.* **2000,** *39,* 2679–2684. doi:10.1002/1521-3773(20000804)39:15<2679::AID-ANIE2679>3.0.CO;2-2
6. Grévin, B.; Rannou, P.; Payerne, R.; Pron, A.; Travers, J. P. *J. Chem. Phys.* **2003,** *118,* 7097–7102. doi:10.1063/1.1561435
7. Sirringhaus, H.; Brown, P. J.; Friend, R. H.; Nielsen, M. M.; Bechgaard, K.; Langeveld-Voss, B. M. W.; Spiering, A. J. H.; Janssen, R. A. J.; Meijer, E. W. *Synth. Met.* **2000,** *111-112,* 129–132. doi:10.1016/S0379-6779(99)00326-4
8. Fitzner, R.; Reinold, E.; Mishra, A.; Mena-Osteritz, E.; Ziehlke, H.; Körner, C.; Leo, K.; Riede, M.; Weil, M.; Tsaryova, O.; Weiß, A.; Uhrich, C.; Pfeiffer, M.; Bäuerle, P. *Adv. Funct. Mater.* **2011,** *21,* 897–910. doi:10.1002/adfm.201001639
9. Kirschbaum, T.; Azumi, R.; Mena-Osteritz, E.; Bäuerle, P. *New J. Chem.* **1999,** *23,* 241–250. doi:10.1039/a808026g
10. Mena-Osteritz, E. *Adv. Mater.* **2002,** *14,* 609–616. doi:10.1002/1521-4095(20020418)14:8<609::AID-ADMA609>3.0.CO;2-7
11. Mena-Osteritz, E.; Bäuerle, P. *Adv. Mater.* **2006,** *18,* 447–451. doi:10.1002/adma.200501575
12. Azumi, R.; Mena-Osteritz, E.; Boese, R.; Benet-Buchholz, J.; Bäuerle, P. *J. Mater. Chem.* **2006,** *16,* 728–735. doi:10.1039/b513427g
13. Grévin, B.; Maggio-Aprile, I.; Bentzen, A.; Ranno, L.; Llobet, A.; Fischer, Ø. *Phys. Rev. B* **2000,** *62,* 8596–8599. doi:10.1103/PhysRevB.62.8596

14. Grévin, B.; Maggio-Aprile, I.; Bentzen, A.; Kuffer, O.; Joumard, I.; Fischer, Ø. *Appl. Phys. Lett.* **2002,** *80,* 3979–3981. doi:10.1063/1.1481787
15. Xu, L.-P.; Gong, J.-R.; Wan, L.-J.; Jin, T.-G.; Li, Y.-L.; Zhu, D.-B.; Deng, K. *J. Phys. Chem. B* **2006,** *110,* 17043–17049. doi:10.1021/jp063240v
16. Wang, L.; Yan, H.-J.; Wan, L.-J. *J. Nanosci. Nanotechnol.* **2007,** *7,* 3111–3116. doi:10.1166/jnn.2007.690
17. MacLeod, J. M.; Ivasenko, O.; Fu, C.; Taerum, T.; Rosei, F.; Perepichka, D. F. *J. Am. Chem. Soc.* **2009,** *131,* 16844–16850. doi:10.1021/ja906206g
18. Azumi, R.; Götz, G.; Debaerdemaeker, T.; Bäuerle, P. *Chem.–Eur. J.* **2000,** *6,* 735–744. doi:10.1002/(SICI)1521-3765(20000218)6:4<735::AID-CHEM735>3.0.CO;2-A
19. Hibino, M.; Sumi, A.; Hatta, I. *Jpn. J. Appl. Phys.* **1995,** *34,* 610–614. doi:10.1143/JJAP.34.610
20. Hibino, M.; Sumi, A.; Hatta, I. *Jpn. J. Appl. Phys.* **1995,** *34,* 3354–3359. doi:10.1143/JJAP.34.3354
21. Ostwald, W. *Z. Phys. Chem.* **1900,** *34,* 495–503.
22. Heinz, R.; Stabel, A.; De Schryver, F. C.; Rabe, J. P. *J. Phys. Chem.* **1995,** *99,* 505–507. doi:10.1021/j100002a009
23. Unpublished X-Ray structure analysis of a regioregular head-to-tail 3-hexylquaterthiophene showing two polymorph crystals; one with the molecules in an all-*anti* conformation and a second one with a terminal thiophene in a *syn*-conformation.

License and Terms